

AD A 137265

12

DNA-TR-81-223

PLACES AIRCRAFT EXPERIMENT TEST RESULTS

ESL, Incorporated
495 Java Drive
Sunnyvale, California 94086

1 May 1982

Technical Report

CONTRACT No. DNA 001-81-C-0149

APPROVED FOR PUBLIC RELEASE;
DISTRIBUTION UNLIMITED.

DTIC FILE COPY

THIS WORK WAS SPONSORED BY THE DEFENSE NUCLEAR AGENCY
UNDER RDT&E RMSS CODE B322981466 S99QAXHB00007 H2590D.

Prepared for
Director
DEFENSE NUCLEAR AGENCY
Washington, DC 20305

DTIC
ELECTE
JAN 25 1984
S B

83 11 23 006

Destroy this report when it is no longer
needed. Do not return to sender.

PLEASE NOTIFY THE DEFENSE NUCLEAR AGENCY,
ATTN: STTI, WASHINGTON, D.C. 20305, IF
YOUR ADDRESS IS INCORRECT, IF YOU WISH TO
BE DELETED FROM THE DISTRIBUTION LIST, OR
IF THE ADDRESSEE IS NO LONGER EMPLOYED BY
YOUR ORGANIZATION.



UNCLASSIFIED

SECURITY CLASSIFICATION OF THIS PAGE (When Data Entered)

REPORT DOCUMENTATION PAGE		READ INSTRUCTIONS BEFORE COMPLETING FORM
1. REPORT NUMBER DNA-TR-81-223	2. GOVT ACCESSION NO. AD-A137 265	3. RECIPIENT'S CATALOG NUMBER
4. TITLE (and Subtitle) PLACES AIRCRAFT EXPERIMENT TEST RESULTS		5. TYPE OF REPORT & PERIOD COVERED Technical Report
		6. PERFORMING ORG. REPORT NUMBER ESL-TM1466
7. AUTHOR(s) Dr J. M. Marshall W. E. Solbrig J. W. Lehman		8. CONTRACT OR GRANT NUMBER(s) DNA 001-81-C-0149
9. PERFORMING ORGANIZATION NAME AND ADDRESS ESL Incorporated 495 Java Drive Sunnyvale, California 94086		10. PROGRAM ELEMENT, PROJECT, TASK AREA & WORK UNIT NUMBERS Task S99QAXHB-00007
11. CONTROLLING OFFICE NAME AND ADDRESS Director Defense Nuclear Agency Washington, DC 20305		12. REPORT DATE 1 May 1982
		13. NUMBER OF PAGES 354
14. MONITORING AGENCY NAME & ADDRESS (if different from Controlling Office)		15. SECURITY CLASS (of this report) UNCLASSIFIED
		15a. DECLASSIFICATION/DOWNGRADING SCHEDULE N/A since UNCLASSIFIED
16. DISTRIBUTION STATEMENT (of this Report) Approved for public release; distribution unlimited.		
17. DISTRIBUTION STATEMENT (of the abstract entered in Block 20, if different from Report)		
18. SUPPLEMENTARY NOTES This work was sponsored by the Defense Nuclear Agency under RDT&E RMSS Code B322081466 S99QAXHB00007 H2590D.		
19. KEY WORDS (Continue on reverse side if necessary and identify by block number) PLACES Experiment Satellite Communications Barium Release Navigation Amplitude and Phase Scintillation Striations Fading Propagation LES-879		
20. ABSTRACT (Continue on reverse side if necessary and identify by block number) During December 1980 the Position Location and Communication Effects Simu- lations (PLACES) Experiment was conducted to investigate the effects of structured ionospheric plasmas on satellite communications and navigation systems. A series of four separate artificial ionospheric plasma environ- ments were created on separate evenings by 48 kg barium releases from rockets launched from Eglin AFB, Florida. This report describes the measurements of propagation effects on CW tone signals from the LES-8 satellite over the		

DD FORM 1473
1 JAN 73

EDITION OF 1 NOV 65 IS OBSOLETE

UNCLASSIFIED

SECURITY CLASSIFICATION OF THIS PAGE (When Data Entered)

UNCLASSIFIED

SECURITY CLASSIFICATION OF THIS PAGE(When Data Entered)

20. ABSTRACT (Continued)

Pacific Ocean to a KC135/662 aircraft operating in the Florida area. Measurements were conducted simultaneously with both a 250 MHz downlink signal and a 349 MHz uplink signal. The measurement of the amplitude and phase scintillation on these tone signals makes possible the back-propagation calculations of the plasma integrated electron content. The plasma integrated electron content reflects the plasma evolution from a smooth early-time cloud through striation formation to a dispersed late-time cloud.

UNCLASSIFIED

SECURITY CLASSIFICATION OF THIS PAGE(When Data Entered)

PREFACE

The PLACES Aircraft Experiment has produced a significant amount of data, only a portion of which have been examined in detail. The goal of this report is to present a summary of those data that are believed to be of most interest to the DNA community and to provide an overview of the data availability.

The authors would like to acknowledge the valuable cooperation and assistance of the Air Force Avionics Laboratory (AFWAL/AAAD) throughout the planning and execution of the experiment, without which this experiment would not have been possible. The authors would also like to single out the assistance of Dr. Clifford Prettie of Berkeley Research Associates for his continued participation and assistance throughout this data reduction effort.

Accession For	
NTIS GRA&I	<input checked="checked" type="checkbox"/>
DTIC TAB	<input type="checkbox"/>
Unannounced	<input type="checkbox"/>
Justification	
By _____	
Distribution/	
Availability Codes	
Dist	Avail and/or Special
A-1	

DATA
COPY
INSPECTED

TABLE OF CONTENTS

<u>Section</u>		<u>Page</u>
	PREFACE - - - - -	1
	LIST OF ILLUSTRATIONS ● - - - - -	5
	LIST OF TABLES - - - - -	16
1	INTRODUCTION - - - - -	17
	1-1 GENERAL - - - - -	17
	1-2 TEST EVENTS - - - - -	18
	1-3 AIRCRAFT EXPERIMENT TEST CONCEPT - - - - -	18
	1-4 AIRCRAFT EXPERIMENT RESULTS - - - - -	19
2	GAIL OVERVIEW - - - - -	24
	2-1 GENERAL - - - - -	24
	2-2 RELEASE GEOMETRY - - - - -	24
	2-3 FADING DATA SUMMARY - - - - -	26
3	GAIL DOWNLINK TONE DATA - - - - -	34
	3-1 INTRODUCTION - - - - -	34
	3-2 DOWNLINK PROPAGATION MEASUREMENTS DURING GAIL - - - - -	34
	3-3 GAIL SUMMARY - - - - -	45
4	HOPE OVERVIEW - - - - -	48
	4-1 GENERAL - - - - -	48
	4-2 RELEASE GEOMETRY - - - - -	48
	4-3 FADING DATA SUMMARY - - - - -	54
5	HOPE DOWNLINK TONE DATA - - - - -	57
	5-1 INTRODUCTION - - - - -	57
	5-2 DOWNLINK PROPAGATION MEASUREMENTS DURING HOPE - - - - -	57
	5-3 HOPE DOWNLINK SUMMARY - - - - -	76
6	HOPE UPLINK TONE DATA - - - - -	78
	6-1 INTRODUCTION - - - - -	78
	6-2 UPLINK PROPAGATION MEASUREMENTS DURING HOPE - - - - -	78
	6-3 HOPE UPLINK SUMMARY - - - - -	89

TABLE OF CONTENTS (Continued)

Section	Page
7 BACK-PROPAGATION PROCESSING FOR HOPE - - - - -	90
7-1 INTRODUCTION - - - - -	90
7-2 HOPE BACK-PROPAGATION SUMMARY - - - - -	91
7-3 BACK-PROPAGATED HOPE DOWNLINK DATA - - - - -	96
7-4 PHASE PSD PARAMETER ESTIMATION - - - - -	102
8 IRIS OVERVIEW - - - - -	167
8-1 GENERAL - - - - -	167
8-2 RELEASE GEOMETRY - - - - -	167
8-3 FADING DATA SUMMARY - - - - -	173
9 IRIS DOWNLINK TONE DATA - - - - -	177
9-1 INTRODUCTION - - - - -	177
9-2 DOWNLINK PROPAGATION MEASUREMENTS DURING IRIS - - - - -	177
9-3 IRIS SUMMARY - - - - -	193
10 JAN OVERVIEW - - - - -	195
10-1 GENERAL - - - - -	195
10-2 RELEASE GEOMETRY - - - - -	195
10-3 FADING DATA SUMMARY - - - - -	196
11 JAN DOWNLINK TONE DATA - - - - -	204
11-1 INTRODUCTION - - - - -	204
11-2 DOWNLINK PROPAGATION MEASUREMENTS DURING JAN - - - - -	204
11-3 JAN SUMMARY - - - - -	231
12 JAN UPLINK TONE DATA - - - - -	232
12-1 INTRODUCTION - - - - -	232
12-2 UPLINK PROPAGATION MEASUREMENTS DURING JAN - - - - -	232
12-3 JAN UPLINK SUMMARY - - - - -	257
13 BACK-PROPAGATION PROCESSING FOR JAN DOWNLINK - - - - -	258
13-1 INTRODUCTION - - - - -	258
13-2 JAN BACK-PROPAGATION SUMMARY - - - - -	258
13-3 BACK-PROPAGATED JAN DOWNLINK DATA - - - - -	260
13-4 BACK-PROPAGATED JAN UPLINK DATA - - - - -	298

TABLE OF CONTENTS (Continued)

<u>Section</u>		<u>Page</u>
14	REFERENCES - - - - -	305
<u>Appendix</u>		
A	AIRCRAFT EQUIPMENT CONFIGURATION - - - - -	307
B	DATA PROCESSING AND DISPLAY OVERVIEW - - - - -	311
C	DOWNLINK TONE DATA PROCESSING SUMMARY - - - - -	319
D	UPLINK TONE DATA PROCESSING SUMMARY - - - - -	325
E	BACK-PROPAGATION PROCESSING - - - - -	339
F	AIRCRAFT EXPERIMENT LINK CALCULATIONS - - - - -	345

LIST OF ILLUSTRATIONS

Figure		Page
1-1	Azimuth and Elevation Angle to LES-8 Versus Time During PLACES - - - - -	21
2-1	Ion Cloud Track Projection for GAIL - - - - -	25
2-2	Aircraft Ground Track for GAIL - - - - -	27
2-3	Aircraft Ground Track for GAIL from 23:25 to 00:00Z. No Strong Fading Observed - - - - -	28
2-4	Aircraft Ground Track for GAIL from 00:00 to 01:00Z. Periods of Deep Fading are Shaded - - - - -	29
2-5	Aircraft Ground Track for GAIL from 01:00 to 01:37Z. Periods of Deep Fading are Shaded - - - - -	30
3-1	GAIL Pass-3 Downlink Amplitude and Phase - - - - -	35
3-2	GAIL Pass-2 Downlink Amplitude and Phase - - - - -	36
3-3	GAIL Pass-1 Downlink Amplitude and Phase - - - - -	37
3-4	GAIL Pass 8 Downlink Amplitude and Phase - - - - -	38
3-5	GAIL Pass 10 Downlink Amplitude and Phase - - - - -	39
3-6	GAIL Pass 11 Downlink Amplitude and Phase - - - - -	40
3-7	GAIL Pass 12 Downlink Amplitude and Phase - - - - -	41
3-8	GAIL Pass 18 Downlink Amplitude - - - - -	42
3-9	GAIL Pass 19 Downlink Amplitude - - - - -	43
3-10	GAIL Pass 24 Downlink Amplitude - - - - -	44
3-11	Ground Optics Site Locations - - - - -	46
4-1	Ion Cloud Track Projection for HOPE - - - - -	49
4-2	Aircraft Ground Track for HOPE - - - - -	50
4-3	Aircraft Ground Track for HOPE from 23:06 to 00:00Z. Periods of Deep Fading are Shaded - - - - -	51

LIST OF ILLUSTRATIONS (Continued)

Figure		Page
4-4	Aircraft Ground Track for HOPE from 00:00 to 01:00. Periods of Deep Fading are Shaded - - - - -	52
4-5	Aircraft Ground Track for HOPE from 01:00 to 02:07. Periods of Deep Fading are Shaded - - - - -	53
5-1	HOPE Pass 1 Downlink Amplitude - - - - -	58
5-2	HOPE Pass 3 Downlink Amplitude & Phase - - - - -	59
5-3	HOPE Pass 6 Downlink Amplitude & Phase - - - - -	60
5-4	HOPE Pass 7 Downlink Amplitude & Phase - - - - -	61
5-5	HOPE Pass 8 Downlink Amplitude & Phase - - - - -	62
5-6	HOPE Pass 9 Amplitude & Phase - - - - -	63
5-7	HOPE Pass 10 Amplitude & Phase - - - - -	64
5-8	HOPE Pass 14 Downlink Amplitude & Phase - - - - -	65
5-9	HOPE Pass 15 Downlink Amplitude & Phase - - - - -	66
5-10	HOPE Pass 17 Downlink Amplitude & Phase - - - - -	67
5-11	HOPE Pass 19 Downlink Amplitude & Phase - - - - -	68
5-12	HOPE Pass 20 Downlink Amplitude & Phase - - - - -	69
5-13	HOPE Pass 21 Downlink Amplitude & Phase - - - - -	70
5-14	HOPE Pass 22 Downlink Amplitude & Phase - - - - -	71
5-15	HOPE Pass 23 Downlink Amplitude & Phase - - - - -	72
5-16	HOPE Pass 29 Amplitude & Phase - - - - -	73
5-17	Integrated Electron Content Versus Time for HOPE - - - - -	77
6-1	HOPE Pass 3 Uplink Amplitude & Phase - - - - -	79
6-2	HOPE Pass 6 Uplink Amplitude & Phase - - - - -	80

LIST OF ILLUSTRATIONS (Continued)

<u>Figure</u>		<u>Page</u>
6-3	HOPE Pass 9 Uplink Amplitude & Phase - - - - -	81
6-4	HOPE Pass 14 Uplink Amplitude & Phase - - - - -	82
6-5	HOPE Pass 17 Uplink Amplitude & Phase - - - - -	83
6-6	HOPE Pass 19 Uplink Amplitude & Phase - - - - -	84
6-7	HOPE Pass 20 Uplink Amplitude & Phase - - - - -	85
6-8	HOPE Pass 21 Uplink Amplitude & Phase - - - - -	86
6-9	HOPE Pass 22 Uplink Amplitude & Phase - - - - -	87
7-1	Transverse Velocity Calculation - - - - -	103
7-2	HOPE Pass 7 Downlink Back-Propagated Amplitude & Phase - - - -	104
7-3	HOPE Pass 7 Downlink Back-Propagated Phase PSD - - - - -	105
7-4	HOPE Pass 7 Downlink Angular Spectrum - - - - -	106
7-5	HOPE Pass 9 Downlink Back-Propagated Amplitude & Phase - - - -	107
7-6	HOPE Pass 9 Back-Propagated Phase PSD - - - - -	108
7-7	HOPE Pass 9 Downlink Angular Spectrum - - - - -	109
7-8	HOPE Pass 10 Downlink Back-Propagated Amplitude & Phase - - -	110
7-9	HOPE Pass 10 Downlink Back-Propagated Phase PSD - - - - -	111
7-10	HOPE Pass 10 Downlink Angular Spectrum - - - - -	112
7-11	HOPE Pass 14 Downlink Back-Propagated Amplitude & Phase - - -	113
7-12	HOPE Pass 14 Back-Propagated Phase PSD - - - - -	114
7-13	HOPE Pass 14 Downlink Angular Spectrum - - - - -	115
7-14	HOPE Pass 15 Downlink Back-Propagated Amplitude & Phase - - -	116
7-15	HOPE Pass 15 Received Phase PSD at Aircraft - - - - -	117

LIST OF ILLUSTRATIONS (Continued)

<u>Figure.</u>		<u>Page</u>
7-16	HOPE Pass 15 Back-Propagated Phase PSD	118
7-17	HOPE Pass 15 Downlink Angular Spectrum	119
7-18	HOPE Pass 17 Downlink Back-Propagated Amplitude & Phase . . .	120
7-19	HOPE Pass 17 Back-Propagated Phase PSD	121
7-20	HOPE Pass 17 Downlink Angular Spectrum	122
7-21	HOPE Pass 19 Downlink Back-Propagated Amplitude & Phase . . .	123
7-22	HOPE Pass 19 Back-Propagated Phase PSD	124
7-23	HOPE Pass 19 Downlink Angular Spectrum	125
7-24	HOPE Pass 21 Downlink Back-Propagated Amplitude & Phase . . .	126
7-25	HOPE Pass 21 Back-Propagated Phase PSD	127
7-26	HOPE Pass 21 Downlink Angular Spectrum	128
7-27	HOPE Pass 22 Downlink Back-Propagated Amplitude & Phase . . .	129
7-28	HOPE Pass 22 Back-Propagated Phase PSD	130
7-29	HOPE Pass 22 Downlink Angular Spectrum	131
7-30	HOPE Pass 23 Downlink Back-Propagated Amplitude & Phase . . .	132
7-31	HOPE Pass 23 Back-Propagated Phase PSD	133
7-32	HOPE Pass 23 Downlink Angular Spectrum	134
7-33	HOPE Pass 29 Back-Propagated Amplitude & Phase	135
7-34	HOPE Pass 29 Back-Propagated Phase PSD	136
7-35	HOPE Pass 29 Angular Spectrum	137
7-36	Phase PSD Template for Slopes from 30 to 40 dB/Decade	143
7-37	Phase PSD Template for Slopes from 40 to 50 dB/Decade	144

LIST OF ILLUSTRATIONS (Continued)

<u>Figure</u>		<u>Page</u>
7-38	Best Fit to HOPE Pass 9 Back-Propagated Phase PSD - - - - -	145
7-39	Alternate Fit to HOPE Pass 9 Back-Propagated Phase PSD - - - - -	146
7-40	Best Fit to HOPE Pass 14 Back-Propagated Phase PSD - - - - -	147
7-41	Alternate Fit to HOPE Pass 14 Back-Propagated Phase PSD - - - - -	148
7-42	Best and Alternate Fits to HOPE Pass 15 Back-Propagated Phase PSD - - - - -	149
7-43	Extreme Fit to HOPE Pass 15 Back-Propagated Phase PSD - - - - -	150
7-44	Best Fit to HOPE Pass 17 Back-Propagated Phase PSD - - - - -	151
7-45	Alternate Fit to HOPE Pass 17 Back-Propagated Phase PSD - - - - -	152
7-46	Best and Alternate Fit to HOPE Pass 19 Back-Propagated Phase PSD - - - - -	153
7-47	Alternate Fit to HOPE Pass 19 Back-Propagated Phase PSD - - - - -	154
7-48	Best Fit to HOPE Pass 21 Back-Propagated Phase PSD - - - - -	155
7-49	Alternate Fit to HOPE Pass 21 Back-Propagated Phase PSD - - - - -	156
7-50	Best Fit to HOPE Pass 22 Back-Propagated Phase PSD - - - - -	157
7-51	Alternate Fit to HOPE Pass 22 Back-Propagated Phase PSD - - - - -	158
7-52	Best Fit to HOPE Pass 23 Back-Propagated Phase PSD - - - - -	159
7-53	Alternate Fit to HOPE Pass 23 Back-Propagated Phase PSD - - - - -	160
7-54	Second Alternate Fit to HOPE Pass 23 Back-Propagated Phase PSD - - - - -	161
7-55	Best and Alternate Fit to HOPE Pass 29 Back-Propagated Phase PSD - - - - -	162
7-56	Outer Scale Versus Time for HOPE - - - - -	163
7-57	Back-Propagated Phase PSD Slope Versus Time for HOPE - - - - -	164
7-58	RMS Phase Versus Time for HOPE - - - - -	165

LIST OF ILLUSTRATIONS (Continued)

<u>Figure</u>		<u>Page</u>
8-1	Ion Cloud Track Projection for IRIS - - - - -	168
8-2	Aircraft Ground Track for IRIS - - - - -	169
8-3	Aircraft Ground Track for IRIS from 23:12 to 00:00Z. Periods of Deep Fading are Shaded. - - - - -	170
8-4	Aircraft Ground Track for IRIS from 00:00 to 01:00Z. Periods of Deep Fading are Shaded. - - - - -	171
8-5	Aircraft Ground Track for IRIS from 01:00 to 02:04Z. Periods of Deep Fading are Shaded - - - - -	172
9-1	IRIS Pass 4 Downlink Amplitude & Phase - - - - -	178
9-2	IRIS Pass 5 Downlink Amplitude & Phase - - - - -	179
9-3	IRIS Pass 6 Downlink Amplitude & Phase - - - - -	180
9-4	IRIS Pass 7 Downlink Amplitude - - - - -	181
9-5	IRIS Pass 8 Downlink Amplitude - - - - -	182
9-6	IRIS Pass 9 Downlink Amplitude - - - - -	183
9-7	IRIS Pass 10 Downlink Amplitude - - - - -	184
9-8	IRIS Pass 11 Downlink Amplitude - - - - -	185
9-9	IRIS Pass 12 Downlink Amplitude - - - - -	186
9-10	IRIS Pass 20 Downlink Amplitude - - - - -	187
9-11	IRIS Pass 25 Downlink Amplitude - - - - -	188
9-12	IRIS Pass 5 Aircraft Occultation Geometry - - - - -	190
9-13	IRIS Pass 6 Aircraft Occultation Geometry - - - - -	191
10-1	Ion Cloud Track Projection for JAN - - - - -	199
10-2	Aircraft Ground Track for JAN - - - - -	200
10-3	Aircraft Ground Track for JAN from 23:13 to 00:00Z. Periods of Deep Fading are Shaded - - - - -	201

LIST OF ILLUSTRATIONS (Continued)

<u>Figure</u>		<u>Page</u>
10-4	Aircraft Ground Track for JAN from 00:00 to 01:00Z. Periods of Deep Fading are Shaded - - - - -	202
10-5	Aircraft Ground Track for JAN from 01:00 to 02:15Z. Periods of Deep Fading are Shaded - - - - -	203
11-1	JAN Pass 1 Downlink Amplitude & Phase - - - - -	205
11-2	JAN Pass 2 Downlink Amplitude & Phase - - - - -	206
11-3	JAN Pass 3 Downlink Amplitude & Phase - - - - -	207
11-4	JAN Pass 4 Downlink Amplitude & Phase - - - - -	208
11-5	JAN Pass 5 Amplitude & Phase - - - - -	209
11-6	JAN Pass 6 Amplitude & Phase - - - - -	210
11-7	JAN Pass 7 Downlink Amplitude & Phase - - - - -	211
11-8	JAN Pass 10 Downlink Amplitude & Phase - - - - -	212
11-9	JAN Pass 11 Downlink Amplitude & Phase - - - - -	213
11-10	JAN Pass 12 Downlink Amplitude - - - - -	214
11-11	JAN Pass 13 Downlink Amplitude & Phase - - - - -	215
11-12	JAN Pass 14 Downlink Amplitude & Phase - - - - -	216
11-13	JAN Pass 15 Downlink Amplitude & Phase - - - - -	217
11-14	JAN Pass 18 Downlink Amplitude & Phase - - - - -	218
11-15	JAN Pass 20 Downlink Amplitude & Phase - - - - -	219
11-16	JAN Pass 21 Downlink Amplitude & Phase - - - - -	220
11-17	JAN Pass 23 Downlink Amplitude & Phase - - - - -	221
11-18	JAN Pass 24 Downlink Amplitude & Phase - - - - -	222
11-19	JAN Pass 25 Downlink Amplitude & Phase - - - - -	223
11-20	JAN Pass 26 Downlink Amplitude & Phase - - - - -	224

LIST OF ILLUSTRATIONS (Continued)

<u>Figure</u>		<u>Page</u>
11-21	JAN Pass 27 Amplitude & Phase - - - - -	225
11-22	JAN Pass 29 Downlink Amplitude & Phase - - - - -	226
11-23	Integrated Electron Content Versus Time for JAN - - - - -	230
12-1	JAN Pass 2 Uplink Amplitude & Phase - - - - -	233
12-2	JAN Pass 3 Uplink Amplitude & Phase - - - - -	234
12-3	JAN Pass 4 Uplink Amplitude & Phase - - - - -	235
12-4	JAN Pass 5 Uplink Amplitude & Phase - - - - -	236
12-5	JAN Pass 6 Uplink Amplitude & Phase - - - - -	237
12-6	JAN Pass 7 Uplink Amplitude & Phase - - - - -	238
12-7	JAN Pass 10 Uplink Amplitude and Phase - - - - -	239
12-8	JAN Pass 11 Uplink Amplitude & Phase - - - - -	240
12-9	JAN Pass 12 Uplink Amplitude & Phase - - - - -	241
12-10	JAN Pass 13 Uplink Amplitude & Phase - - - - -	242
12-11	JAN Pass 14 Uplink Amplitude & Phase - - - - -	243
12-12	JAN Pass 15 Uplink Amplitude & Phase - - - - -	244
12-13	JAN Pass 16 Uplink Amplitude & Phase - - - - -	245
12-14	JAN Pass 18 Uplink Amplitude & Phase - - - - -	246
12-15	JAN Pass 19 Uplink Amplitude & Phase - - - - -	247
12-16	JAN Pass 20 Uplink Amplitude & Phase - - - - -	248
12-17	JAN Pass 23 Uplink Amplitude & Phase - - - - -	249
12-18	JAN Pass 24 Uplink Amplitude & Phase - - - - -	250
12-19	JAN Pass 25 Uplink Amplitude & Phase - - - - -	251

LIST OF ILLUSTRATIONS (Continued)

<u>Figure</u>		<u>Page</u>
12-20	JAN Pass 26 Uplink Amplitude & Phase - - - - -	252
12-21	JAN Pass 27 Uplink Amplitude & Phase - - - - -	253
12-22	JAN Pass 29 Uplink Amplitude & Phase - - - - -	254
13-1	JAN Pass 2 Downlink Back-Propagated Amplitude & Phase - - - -	261
13-2	JAN Pass 2 Downlink Back-Propagated Phase PSD - - - - -	262
13-3	JAN Pass 2 Downlink Angular Spectrum - - - - -	263
13-4	JAN Pass 3 Downlink Back-Propagated Amplitude & Phase - - - -	264
13-5	JAN Pass 3 Downlink Back-Propagated Phase PSD - - - - -	265
13-6	JAN Pass 3 Downlink Angular Spectrum - - - - -	266
13-7	JAN Pass 4 Downlink Back-Propagated Amplitude & Phase - - - -	267
13-8	JAN Pass 4 Downlink Back-Propagated Phase PSD - - - - -	268
13-9	JAN Pass 4 Downlink Angular Spectrum - - - - -	269
13-10	JAN Pass 10 Downlink Back-Propagated Amplitude & Phase - - - -	270
13-11	JAN Pass 10 Downlink Back-Propagated Phase PSD - - - - -	271
13-12	JAN Pass 10 Downlink Angular Spectrum - - - - -	272
13-13	JAN Pass 11 Downlink Back-Propagated Amplitude & Phase - - - -	273
13-14	JAN Pass 11 Downlink Back-Propagated Phase PSD - - - - -	274
13-15	JAN Pass 11 Downlink Angular Spectrum - - - - -	275
13-16	JAN Pass 12 Downlink Back-Propagated Amplitude & Phase - - - -	276
13-17	JAN Pass 12 Downlink Back-Propagated Phase PSD - - - - -	277
13-18	JAN Pass 12 Downlink Angular Spectrum - - - - -	278
13-19	JAN Pass 21 Downlink Back-Propagated Amplitude & Phase - - - -	279

LIST OF ILLUSTRATIONS (Continued)

<u>Figure</u>		<u>Page</u>
13-20	JAN Pass 21 Downlink Back-Propagated Phase PSD - - - - -	280
13-21	JAN Pass 21 Downlink Angular Spectrum - - - - -	281
13-22	JAN Pass 23 Downlink Back-Propagated Amplitude & Phase - - - -	282
13-23	JAN Pass 23 Downlink Back-Propagated Phase PSD - - - - -	283
13-24	JAN Pass 23 Downlink Angular Spectrum - - - - -	284
13-25	JAN Pass 25 Downlink Back-Propagated Amplitude & Phase - - - -	285
13-26	JAN Pass 25 Downlink Back-Propagated Phase PSD - - - - -	286
13-27	JAN Pass 25 Downlink Angular Spectrum - - - - -	287
13-28	JAN Pass 26 Downlink Back-Propagated Amplitude & Phase - - - -	288
13-29	JAN Pass 26 Downlink Back-Propagated Phase PSD - - - - -	289
13-30	JAN Pass 26 Downlink Angular Spectrum - - - - -	290
13-31	JAN Pass 27 Downlink Back-Propagated Amplitude & Phase - - - -	291
13-32	JAN Pass 27 Downlink Back-Propagated Phase PSD - - - - -	292
13-33	JAN Pass 27 Downlink Angular spectrum - - - - -	293
13-34	JAN Pass 29 Downlink Back-Propagated Amplitude & Phase - - - -	294
13-35	JAN Pass 29 Downlink Back-Propagated Phase PSD - - - - -	295
13-36	JAN Pass 29 Downlink Angular Spectrum - - - - -	296
13-37	JAN Pass 10 Uplink Back-Propagated Amplitude and Phase - - - -	299
13-38	JAN Pass 10 Uplink Back-Propagated Phase PSD - - - - -	300
13-39	JAN Pass 10 Uplink Angular Spectrum - - - - -	301
13-40	JAN Pass 23 Uplink Back-Propagated Amplitude & Phase at 120 Kilometers - - - - -	302

LIST OF ILLUSTRATIONS (Continued)

<u>Figure</u>		<u>Page</u>
13-41	JAN Pass 23 Uplink Back-Propagated Amplitude & Phase at 140 Kilometers - - - - -	303
A-1	Aircraft Equipment Configuration - - - - -	308
B-1	HOPE Pass 20 Uplink Amplitude & Phase Before Filtering - - - -	313
B-2	HOPE Pass 20 Uplink Angular Spectrum Before Filtering - - - -	314
B-3	HOPE Pass 20 Uplink Phase Spectrum Before Filtering - - - - -	315
B-4	HOPE Pass 20 Uplink Amplitude and Phase After Filtering - - - -	316
B-5	HOPE Pass 20 Uplink Angular Spectrum After Filtering - - - - -	317
B-6	HOPE Pass 20 Uplink Phase Spectrum After Filtering - - - - -	318
C-1	Conceptual Downlink Data Doppler Correction - - - - -	320
C-2	Conceptual Measurement of Downlink Tone Fading from LES-9. Note that in Use with LES-8 the Output of the ATR is Conceptually $f_u = 500 + f_{k\text{dop}}/N$ and the Intermediate Doppler Inversion Process is Bypassed - - - - -	321
C-3	Software Processing of the Downlink Tone Fading Data - - - - -	322
D-1	Simplified Uplink Doppler Correction - - - - -	326
D-2	Uplink Data Tone LES Satellite Signal Path - - - - -	327
D-3	Satellite Down Converter and Sampler - - - - -	328
D-4	Aircraft Equipment for Uplink Tone Data Processing - - - - -	330
D-5	Flowchart for Determination of Histograms to Set Uplink Data Processing Parameters - - - - -	334
D-6	Flowchart for Uplink Data Signal Recovery Software - - - - -	335
D-7	Plot of a Typical Look-up Table Value Versus Sample Value - - -	337
E-1	Flowchart of PATS Code for Free-Space Propagation - - - - -	341

LIST OF TABLES

<u>Table</u>		<u>Page</u>
1-1	Aircraft Data Summary - - - - -	20
2-1	Aircraft Data Summary for GAIL - - - - -	31
4-1	Aircraft Data Summary for HOPE - - - - -	55
7-1	HOPE Downlink Back-Propagation Summary - - - - -	94
7-2	Transverse Pattern Velocity, V_{\perp} - - - - -	95
8-1	Aircraft Data Summary for IRIS - - - - -	174
10-1	Aircraft Data Summary for JAN - - - - -	197
13-1	JAN Downlink Back-Propagation Summary - - - - -	259
F-1	Link Calculation Downlink Tone to Aircraft - - - - -	346
F-2	Link Calculation Uplink Tone Aircraft-to-Satellite - - - - -	348
F-3	Approximate K-band Downlink Calculation - - - - -	349

SECTION 1

INTRODUCTION

1-1 GENERAL.

During December 1980 the Position Location and Communications Effects Simulations (PLACES) Experiment was conducted to investigate the effects of structured ionospheric plasmas on satellite communications and navigation systems. A structured plasma environment was created by a 48 kgm barium release from a rocket launched from Eglin AFB, FL. During what is referred to here as the Aircraft Experiment^[1,2], measurements of propagation effects on signals from the LES-8 satellite over the Pacific Ocean to a KC 135 aircraft operating in the Florida area was conducted. Additionally, measurements of the time-of-arrival spread of energy were accomplished during the Beacon Experiment on signals emanating from a rocket transiting behind the barium cloud as viewed from ground receiving sites in northern Florida^[1,3]. This report is intended to provide a summary of the Aircraft Experiment test results.

An aircraft experiment was flown to measure flat fading scintillation effects at UHF. The primary purpose of the aircraft experiment was to measure the barium cloud fading channel in order to provide data for back-propagation diagnostics of the plasma structure evolution. The secondary purpose was to generate real-time diagnostic information about the barium cloud plasma structure that could be used to guide the beacon rocket transmission experiment launch timing. Additionally, the aircraft experiment data is an aid to the interpretation of the beacon experiment data. An enduring feature of the aircraft experiment data is the ability to obtain diagnostic data on plasma structure evolution and dissipation. Similar data was successfully collected during a preceding program called the STRESS Experiment during February and March of 1977. Both the PLACES and STRESS^[4] Experiments were sponsored by the Defense Nuclear Agency and supported by the Avionics Laboratory (AFWAL/AAAD) of the Air Force

Wright Aeronautical Laboratories, the 4950th test aircraft, and the Eglin Test Range/ADTC. The aircraft and beacon experiments were conceived and implemented by ESL Incorporated.

1-2 TEST EVENTS.

A total of four 48 kgm barium releases were conducted. These releases were named GAIL (12/4/80), HOPE (12/6/80), IRIS (12/8/80), and JAN (12/12/80). The release altitudes were between 180 and 185 kilometers. The ionizing action of the sun's ultraviolet rays on the barium generates the ionized plasma which becomes elongated along the earth's magnetic field. Subsequent neutral wind cross-field drag causes the field aligned irregularities (striations) to be created.

1-3 AIRCRAFT EXPERIMENT TEST CONCEPT.

The aircraft experiment used two UHF tone signals, one transmitted from the aircraft (Doppler precorrected) at 349 MHz to LES-8 and one received (Doppler corrected) from LES-8 at the aircraft at 250 MHz. Doppler correction is provided by a K-band (39.6 GHz) reference signal generated at the satellite coherently with the UHF signal. The inphase and quadrature components of the signal received at the satellite were sampled and sent back down on the K-band data link to the aircraft. Appendix A summarizes the aircraft equipment configuration used during the test. The aircraft is positioned to fly in the shadow of the barium ion cloud. The proper location is calculated in real time from the measured ion cloud position and the precomputed satellite position. The ion cloud location was tracked using a UHF radar. A link from the aircraft through FLTSATCOM was also provided to the experiment director at Eglin AFB giving amplitude and phase fading data as received at the aircraft in real time.

The flight path of the aircraft in the shadow of the barium ion cloud was designed to cut across the striations and to measure the signal fading caused by the diffraction pattern of the striations. Using sophisticated data processing techniques (back-propagation), the propagation effects of the plasma

can be removed from a cross-field diffraction pattern to give the integrated electron content fluctuations of the plasma, a quantity useful in assessing barium phenomenology.

1-4 AIRCRAFT EXPERIMENT RESULTS.

The aircraft experiment employed LES-8 throughout the experiment. The uplink and downlink tone processing equipment built by ESL under the STRESS program performed reliably. There was no apparent degradation over the past 3 years in the overall signal quality. In fact, 2 or 3 dB of SNR improvement appears to have been realized, possibly through a combination of more favorable geometry and hardware/antenna changes on the aircraft. A quick look at the downlink C/kT indicated approximately 51 dB-Hz compared to 46 to 47 dB-Hz measured during STRESS.

Table 1-1 summarizes each event. The release point location is the center as derived from photographic triangulation^[5]. Following each release approximately 30 passes of the aircraft through the ion cloud shadow were achieved. Both uplink and downlink data are available except during periods when K-band phase lock was lost. Without K-lock the uplink tone data is lost, since the uplink signal is split into inphase and quadrature components at the satellite, each component one bit sampled at a 50 kHz rate, and these samples are sent down to the aircraft on the K-band signal using a 100 Kbps DPSK mode. A detailed summary for each release and each pass is provided in the subsequent sections.

A plot of azimuth angle variation from the 662 aircraft to the LES-8 satellite for all four PLACES releases is given in Figure 1-1. By far the largest component of the change with time is due to the satellite motion. The azimuth and elevation both increase by approximately 18 degrees over a typical 3 hour period. The azimuth angle typically started near 207 degrees at 2300 (GMT) and ended near 227 degrees at 0200 (GMT). Likewise, the elevation angle started near 34 degrees at 2300 (GMT) and ended near 51 degrees at 0200 (GMT). Generally, it was desired to have an elevation angle in excess of 30 degrees throughout the test.

Table 1-1. Aircraft Data Summary

Release	Release Time	Release Altitude	Release Location	No. of Passes	Data Period
GAIL 12/4/80	2305:35	181.3 km	29.317 87.420	32	2307:10 --- 0148 0136 Last Strong Fading (R+2:29)
HOPE 12/6/80	2307:37	182.6 km	29.263 87.041	33	2307:40 --- 0206 0113 Last Strong Fading (R+2:06)
IRIS 12/8/80	2313:08	182.2 km	28.763 87.185	31	2329 --- 0205 0150 Last Fading Data (R+2:37)
JAN 12/12/80	2313:42Z	183.7 km	29.176 86.978	35	2314:06 --- 0200 0157 Last Strong Fading (R+2:43)

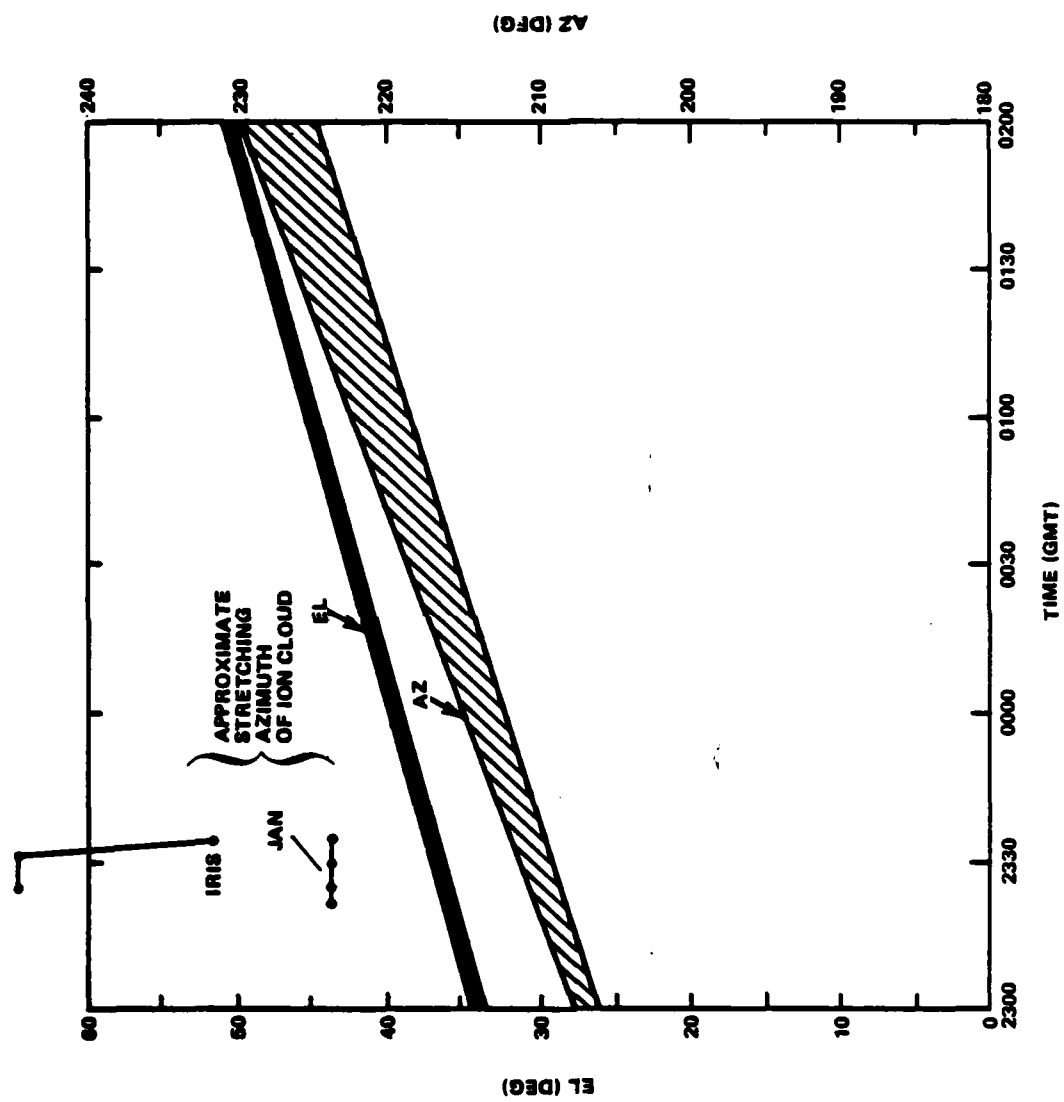


Figure 1-1. Azimuth and Elevation Angle to LES-8 Versus Time During PLACES

Of particular interest is the orientation of the propagation path with respect to the stretching direction of the ion cloud. The stretching direction of the ion cloud can be estimated from photographs locating the center of the neutral cloud and the center of the striation mass. This was done for IRIS and JAN as shown on Figure 1-1. For JAN the propagation path is very nearly along the stretching direction of the cloud. In particular, approximately 2 hours after release, if that initial alignment were preserved, the propagation path would be aligned along the ion sheet defined by the magnetic field and stretching direction. This may in some way account for the difficulties in back-propagating the JAN data between Passes 10 and 20 (0000Z to 0110Z). The initial behavior of HOPE and GAIL were similar to JAN, but stretching directions have not been estimated.

The propagation results from the tone data were much as expected and similar in most respects to that obtained during the STRESS Experiment. During the early lifetime of the cloud, fading and phase effects had the characteristics of the classical diffraction pattern of a single striation; i.e., a ringing pattern on the edges of a long defocus associated with a bell shaped phase structure with many cycles of phase excursion. As the striations develop the fading becomes Rayleigh-like. Very old clouds and when transiting the cloud at very high or very low altitudes produce less intense Rician-like fading until eventually the cloud track is lost.

Back-propagation processing of the uplink and downlink tone data taken simultaneously has shown good agreement between the integrated electron contents obtained from the separate links.

Scintillation effects or striation lifetimes of the order of 3 hours were observed. Evident in the data is a decay in the total integrated electron content. Apparently the fading effects of the striations observed during PLACES dissipated because of the decrease in total integrated electron content associated with the extensive stretching of the barium structure. The decay in integrated electron content has been noted to follow a linear decay when plotted linearly versus the logarithm of time.

The aircraft data measurements have provided the first strong indication of an outer scale associated with barium plasma striations. The back-propagated phase data is expected to aid theoretical developments on striation evolution. Unfortunately, estimates of the outer scale are not available throughout each release. Only those data that were relatively easy to process were examined. It may be possible through additional processing to provide greater continuity. On the surface, the data would appear to support the notion of striation freezing. Freezing is a postulated late-time phenomenon wherein striation bifurcation stops and the striations move as a unit. This is evidenced by the fact that the outer scale sizes measured appear to remain of the order of about one half the typical initial barium ion density e^{-1} halfwidth.

The scintillation effects observed are similar to those observed during the STRESS program with the exception of the long defocusing seen at early times. During HOPE a -20 dB defocus lasted for approximately 75 seconds. These data are presented in the subsequent sections.

This report has been organized such that the data from each release is grouped together. First the measured amplitude and phase data are presented for the downlink, then as a separate section for the uplink, if available, and then followed by another section on the back-propagation processing, if performed.

SECTION 2

GAIL OVERVIEW

2-1 GENERAL.

A number of operational difficulties following release precluded the consistent collection of data during the first release (GAIL). For this reason only a limited effort has been expended processing this data. Backpropagation processing was not performed for GAIL nor were the uplink scintillation data processed. The downlink propagation data are presented in Section 3 showing the expected progression of propagation effects over the ion cloud lifetime.

2-2 RELEASE GEOMETRY.

The barium cloud for the first experiment, GAIL, was released on 4 December 1980 at 23:07:35Z. The center of the initial release was at an altitude of 181.3 kilometers located approximately 87.4197°W, 29.3172°N. The projection of the release point from the LES-8 satellite down to the 10.668 kilometer aircraft altitude is 86.2082°W, 31.5310°N. This is slightly southwest of the planned projection of 86.1919°W, 31.5169°N. The cloud quickly moved northeast from this point, stopped for a few minutes, then moved southwest at a slower pace for the rest of the experiment. The apparent projection from the satellite to the aircraft operating altitude appears to follow a somewhat different pattern due to the satellite motion as shown in Figure 2-1. The cloud projection was about 1 degree south and 1 degree west of the release point at R+2 hours 28 minutes.

The early time cloud drift was more northerly than previously observed. This northerly drift in conjunction with an optical tracking error resulted in the apparent cloud drifting outside the range safety firing limits for the beacon and the probe rocket experiments before striations were clearly evident.

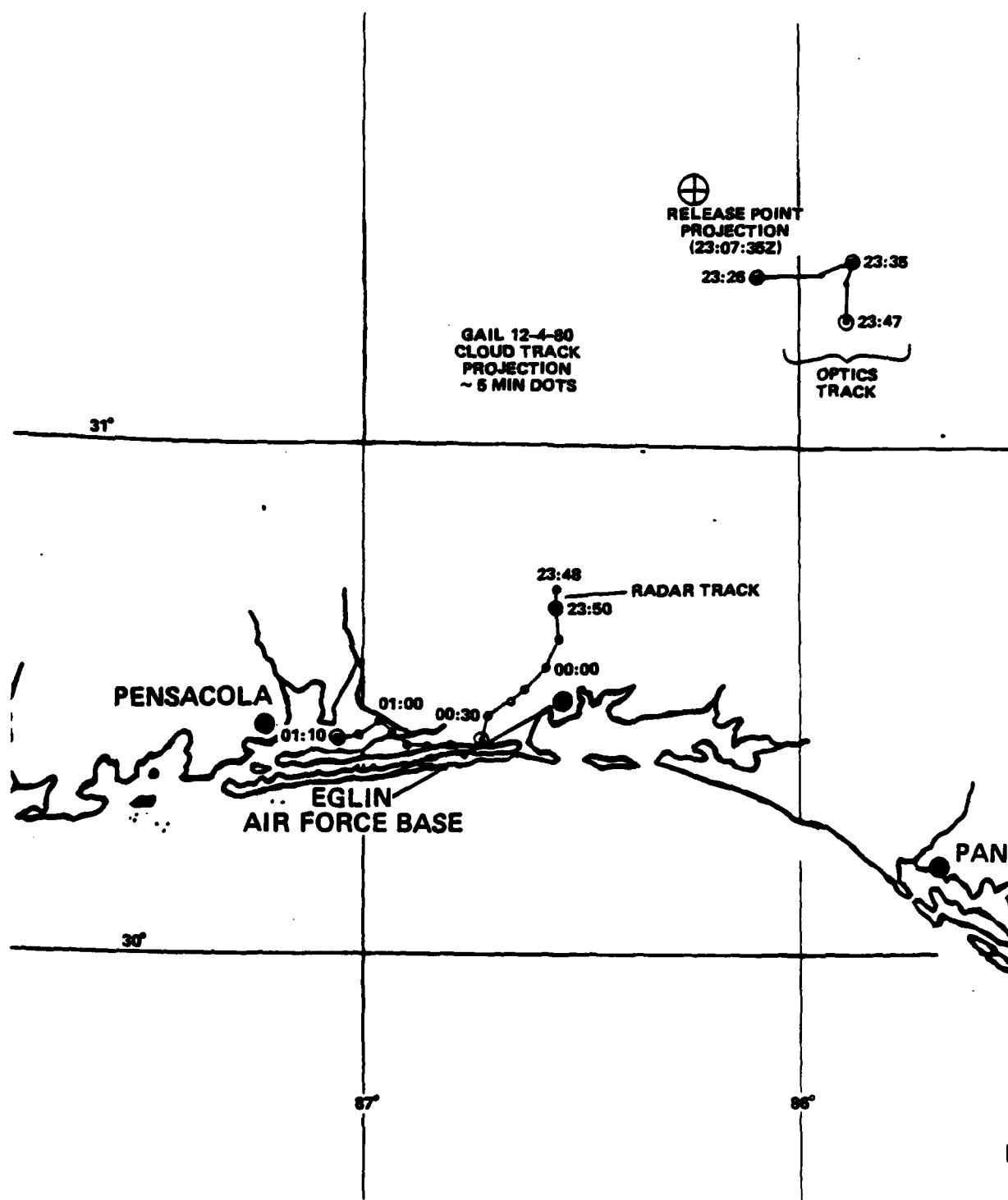


Figure 2-1. Ion Cloud Track Projection for GAIL

The optical tracking system used two ground sites to follow the cloud, and from these determines the cloud position. During this release, the D3A ground site tracked the neutral cloud, not the striated ion cloud, causing the projection of the ion cloud position to be significantly northeast of its actual position. The FPS-85 radar was not working from release (R) to R+20 minutes due to a cable failure. The tracking error is clearly evident in the large jump in the cloud projection point around 2347Z when the track was switched from optics to radar. The aircraft tracking radar was held for missile tracking for the first 21 minutes; thus, the aircraft position during this time must be derived from the less accurate onboard INS data. As a further complication, the radar provided the projection data using the LES-9 ephemeris rather than LES-8 (LES-9 was near LES-8). These difficulties resulted in no useful data until approximately 1 hour after release. Figure 2-2 shows the aircraft ground track which reflects this difficulty in obtaining good projection data.

Figures 2-3, 2-4, and 2-5 show the aircraft ground track during each hour and also show the periods of strong (deep) fading. Since the radar projection was south of the true projection, the first pass of the aircraft through the radar track around 0000Z resulted in no fading and the aircraft was vectored north back toward the last optics track data. It was along this flight path that strong fading was observed (see Figure 2-4). From that point on the real time aircraft track display and real time fading display were used to position the aircraft.

2-3 FADING DATA SUMMARY.

A total of 32 passes were made with fading seen as late as R+2 hours 45 minutes. A summary of these passes is given in Table 2-1. Uplink tone data is available when the K-band signal is in phase lock. Moderate to strong fading was seen during 18 of the 19 passes between R+50 minutes and R+1 hour 32 minutes. Weak fading and diffraction ringing were observed between R+1 minute and R+50 minutes. During most of this first 50 minutes, the aircraft was following the incorrect optics track point projection data causing it to traverse the high altitude, low-ion density part of the cloud, northeast of the cloud center. These high altitude data may be of some interest to studies of F-region image

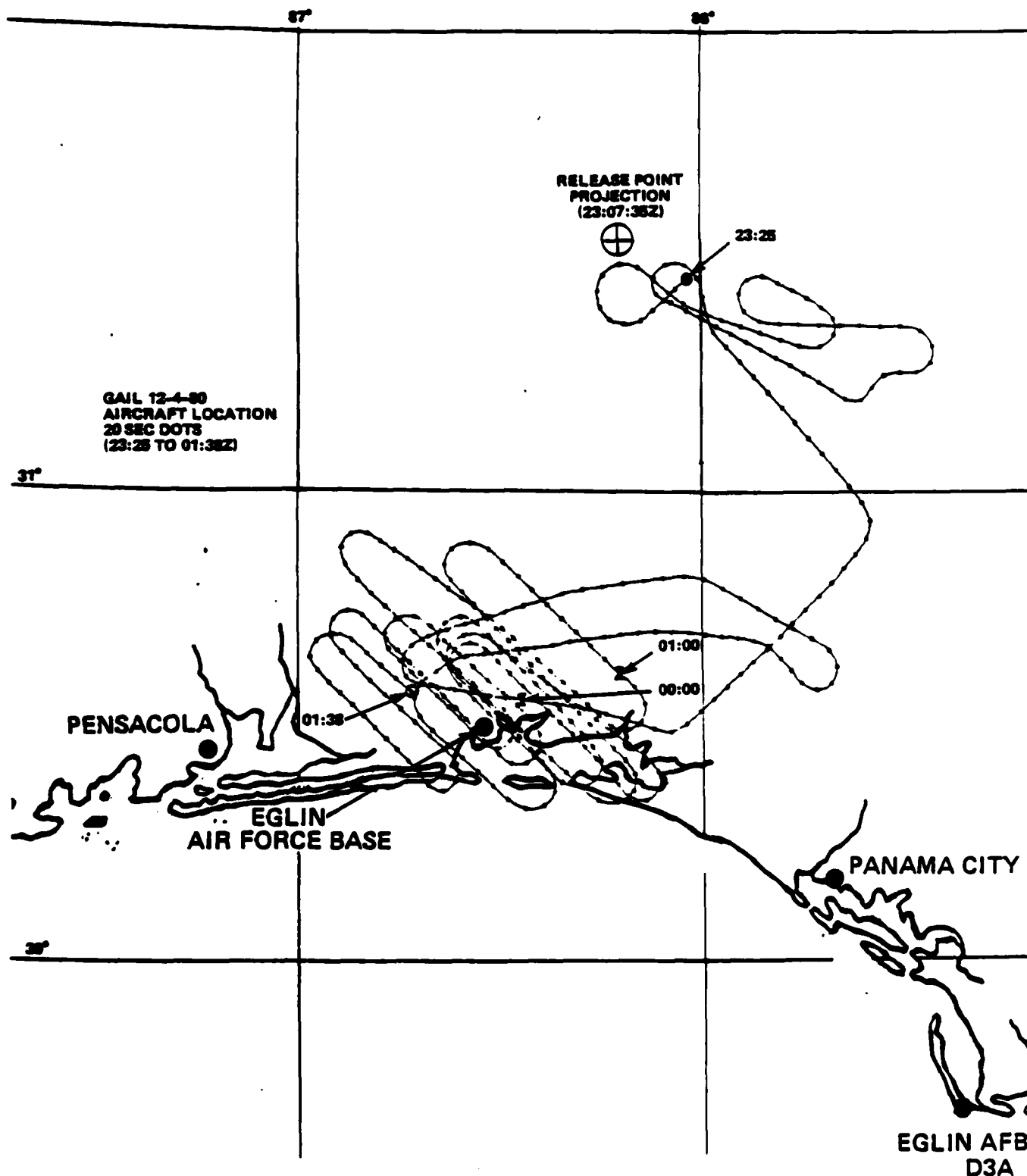


Figure 2-2. Aircraft Ground Track for GAIL

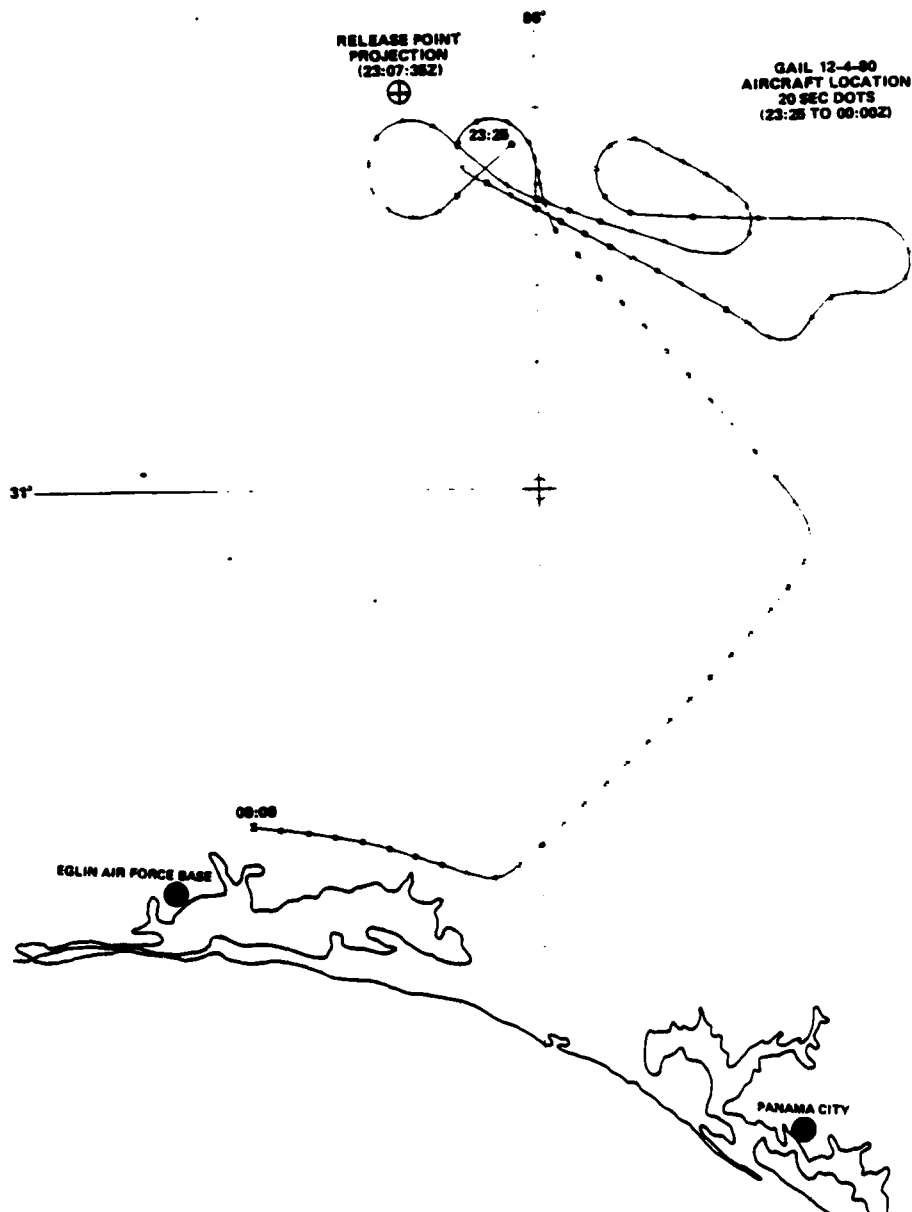


Figure 2-3. Aircraft Ground Track for GAIL from 23:25 to 00:00Z.
No Strong Fading Observed

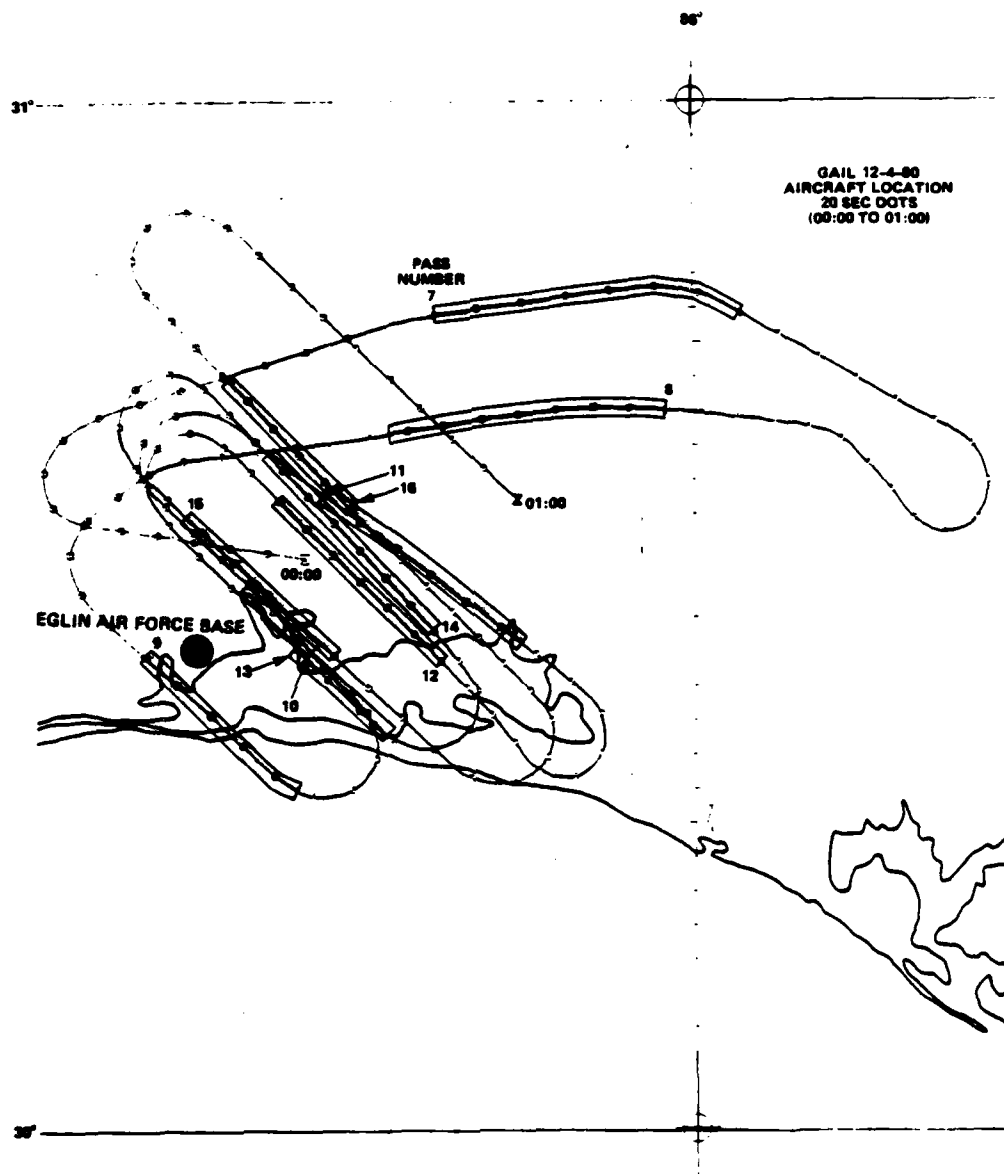


Figure 2-4. Aircraft Ground Track for GAIL from 00:00 to 01:00Z.
Periods of Deep Fading are Shaded

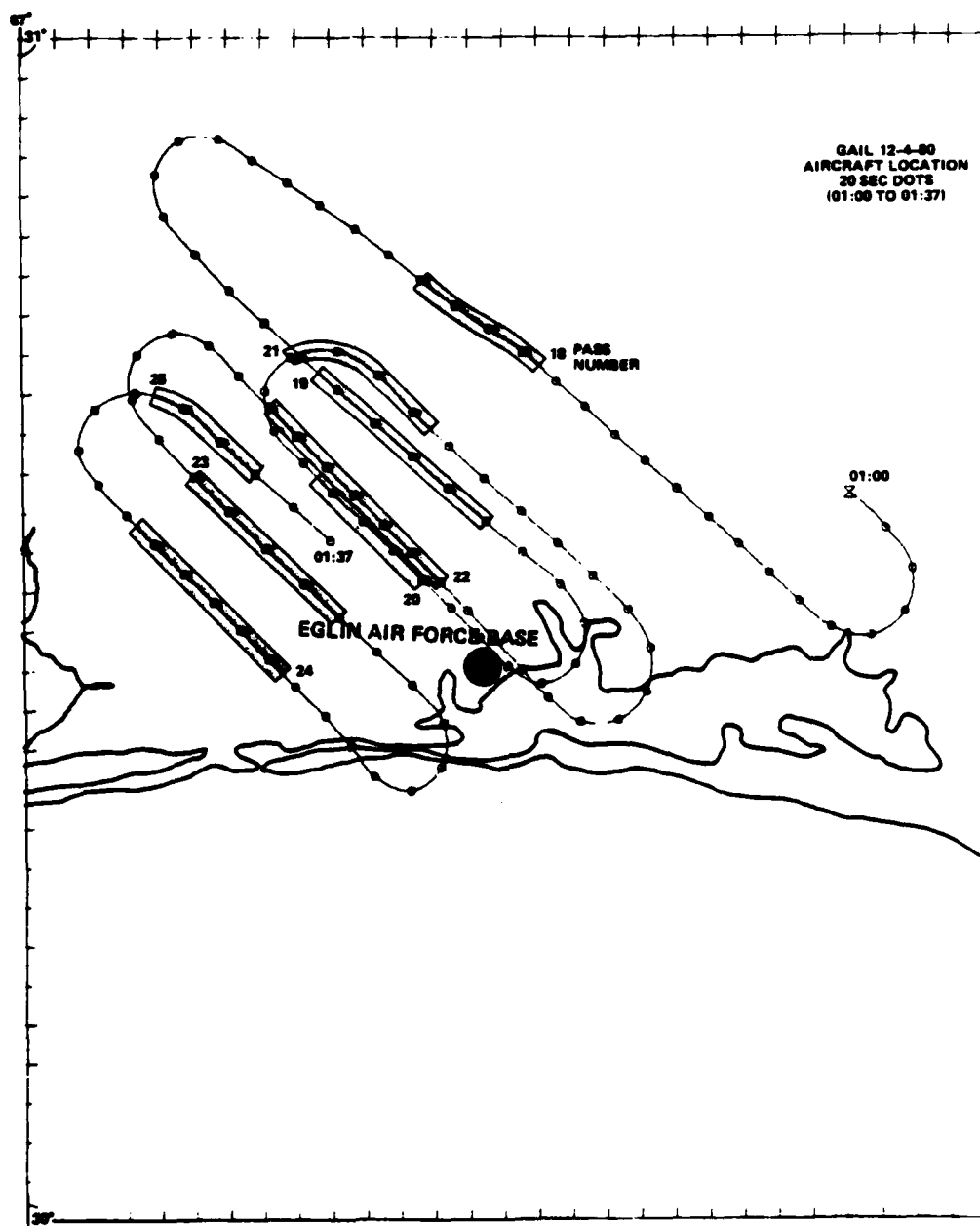


Figure 2-5. Aircraft Ground Track for GAIL from 01:00 to 01:37Z.
Periods of Deep Fading are Shaded

Table 2-1. Aircraft Data Summary for GAIL

Pass No.	Time	K-Lock ⁽¹⁾	Comments
-3	23:07:40-23:09:30	Yes	Diffraction ringing
-2	23:11:50-23:13:30	↓	Diffraction ringing
-1	23:17:40-23:19:30		Weak fading
0	23:24:00-23:26:20		Weak fading
1	23:29:50-23:31:40		Weak fading
2	23:32:40-23:34:20	↓	Weak fading
3	23:35:30-23:37:30	No	Weak fading
4	23:41:40-23:43:20	↓	Weak fading
5	23:48:20-23:50:10		Weak fading
6	23:59:00-00:02:00	No, manual ⁽²⁾ doppler correction	Weak fading
7	00:06:00-00:08:40	No, manual ⁽²⁾ doppler correction	Strong fading
8	00:14:20-00:17:10	Yes	Strong fading
9	00:20:20-00:22:30	↓	Moderate fading
10	00:23:40-00:25:40		Moderate fading
11	00:28:40-00:30:40		Strong fading
12	00:33:00-00:35:50		Strong fading
13	00:37:50-00:39:10		Moderate fading
14	00:41:30-00:44:00	No	Strong fading
15	00:46:30-00:48:30	↓	Strong fading
16	00:49:40-00:55:30		Strong fading, three pieces to cloud
17	00:57:20-01:00:00	No, manual ⁽²⁾ doppler correction	Weak fading
18	01:04:40-01:06:30	No, manual ⁽²⁾ doppler correction	Strong fading

Table 2-1. --Continued

Pass No.	Time	K-Lock ⁽¹⁾	Comments
19	01:10:40-01:12:10	No, manual ⁽²⁾ doppler correction	Strong fading
20	01:14:40-01:16:20	No, manual ⁽²⁾ doppler correction	Strong fading
21	01:17:30-01:18:50	No, manual ⁽²⁾ doppler correction	Strong fading
22	01:23:20-01:25:40	No, manual ⁽²⁾ doppler correction	Strong fading
23	01:27:20-01:29:20	No, manual ⁽²⁾ doppler correction	Strong fading
24	01:32:00-01:34:00	No, manual ⁽²⁾ doppler correction	Strong fading
25	01:35:20-01:36:40	No, manual ⁽²⁾ doppler correction	Strong fading, short interval
26	01:39:30-01:42:00	No, manual ⁽²⁾ doppler correction	No fading
27	01:42:00-01:46:00	No, manual ⁽²⁾ doppler correction	No fading/possibly weak fading
28	01:48:00-01:52:00	No, manual ⁽²⁾ doppler correction	No fading/possibly weak fading

(1) Loss of k-lock implies loss of uplink tone data.

(2) Manual doppler correction on downlink tone.

coupling. Only weak fading was seen during the last two passes. Uplink data is available for 12 of the 32 passes while downlink data is available for all 32 passes. Most of the passes where uplink data is available show no fading and were not processed.

The data received from each of these releases shows the expected progression of effects from diffraction ringing, large defocusing from the background ion cloud, large defocus with superimposed fading from developing striations, and eventually random fading at late times. Representative downlink data are discussed in detail in Section 3.

SECTION 3

GAIL DOWNLINK TONE DATA

3-1 INTRODUCTION.

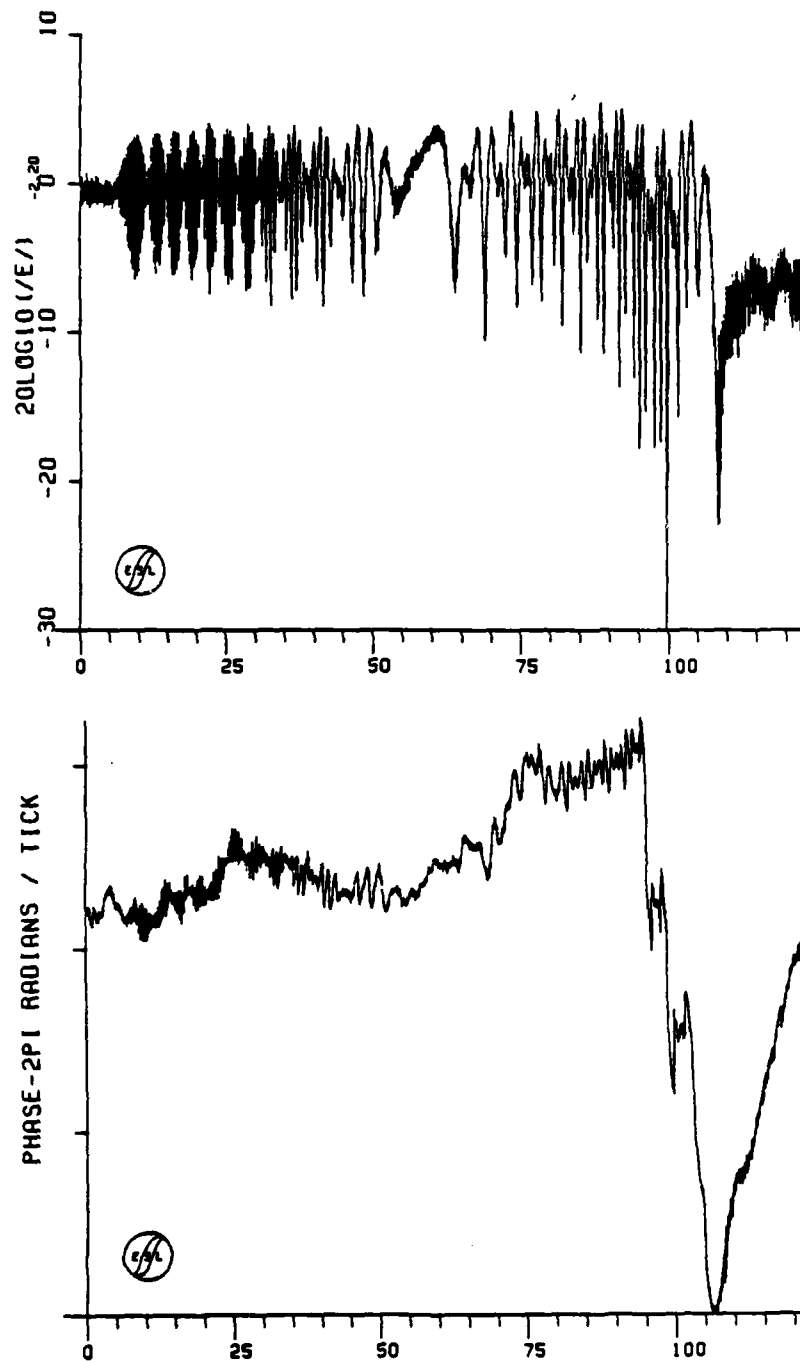
Measurements of the downlink amplitude and phase were made following each PLACES release; GAIL, HOPE, IRIS, and JAN. These measurements were made using a 250 MHz signal transmitted from LES-8 through the barium cloud to the aircraft. This section describes the GAIL downlink propagation data. The signal processing employed is described in Appendix B.

3-2 DOWNLINK PROPAGATION MEASUREMENTS DURING GAIL.

A total of 32 passes were made during GAIL with fading seen as late as R+2 hours 45 minutes. A brief description of these passes were given in Table 2-1. Plots of the received amplitude and phase are given in Figures 3-1 through 3-10. The data show what is perhaps best described as diffraction ringing during the first two passes, weak fading for the next eight passes, strong fading for the next few passes, followed by moderate late-time fading for the last 10 passes. These data generally reflect the operation difficulties in positioning the aircraft described in Section 2.

Figures 3-1 and 3-2 show the first two passes of GAIL. These passes start at release (R+0) and R+4 minutes, respectively, and lasted about 2 minutes each. There is no indication of plasma structuring during the first pass (Pass-3). Rather, the ringing is reminiscent of one or two ray multipath interference from gross plasma refracted energy. The second pass (Pass-2) at R+4 minutes may indicate some initial bifraction taking place on the eastern side. Generally the aircraft was transiting high along the magnetic field lines containing the barium plasma.

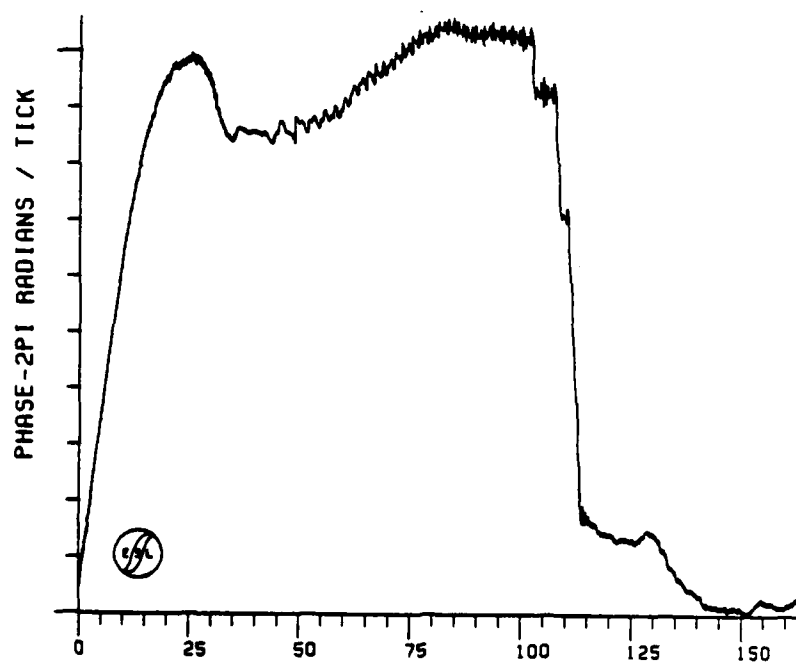
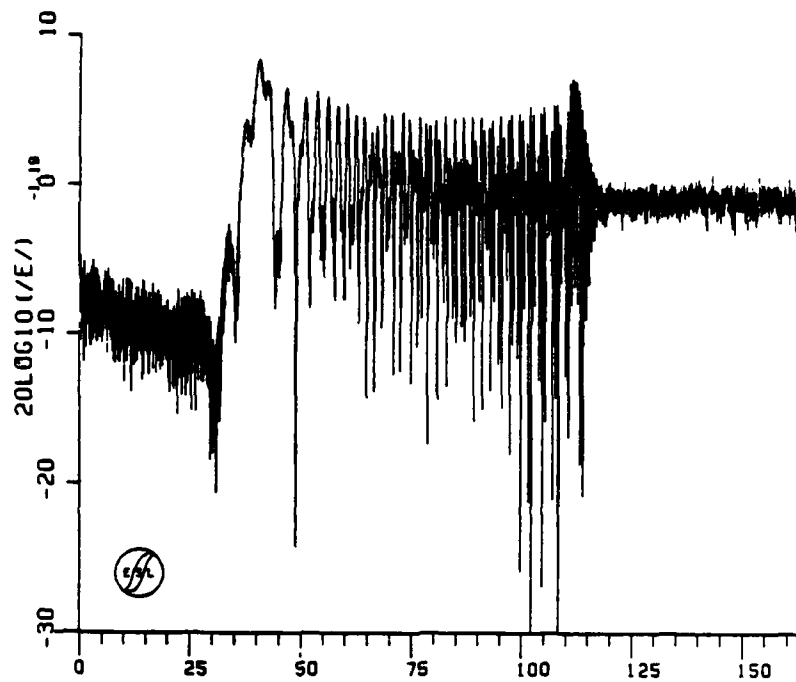
The third pass (Pass-1) recorded during GAIL started at R+11 minutes and lasted 2-1/2 minutes as shown in Figure 3-3. The cloud is structuring at



TIME-- SECONDS

PHASE OF FIELD
GN3052081100HZ
START TIME- 23:07:38.480

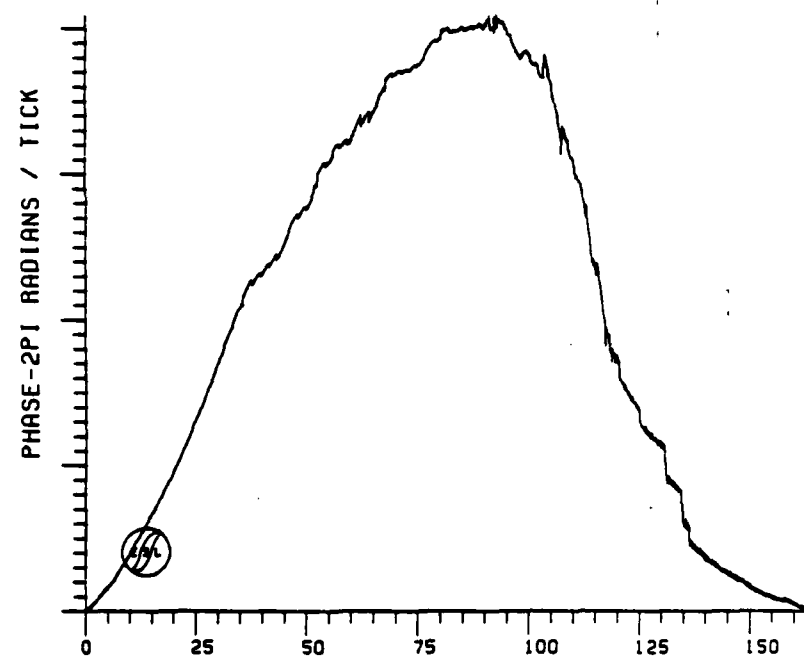
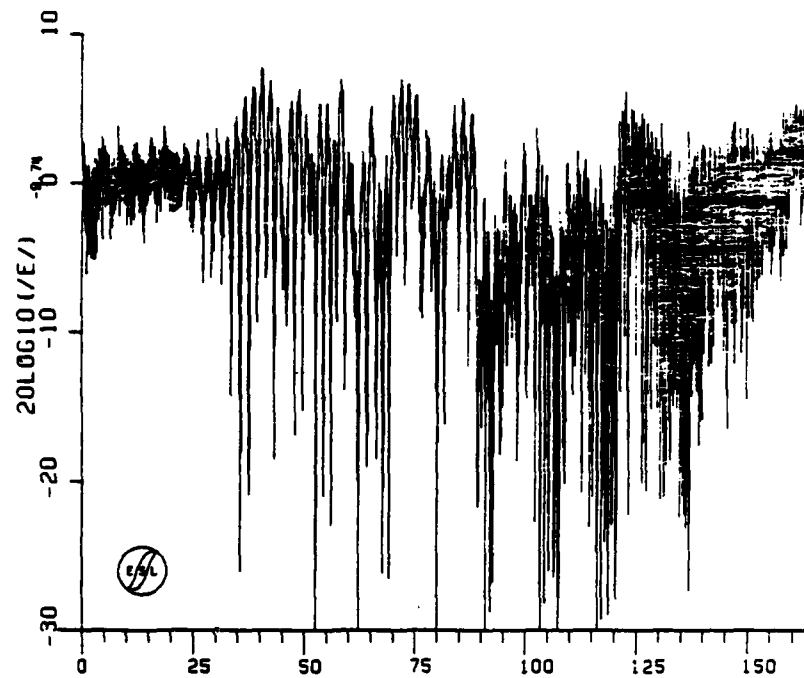
Figure 3-1. GAIL Pass-3 Downlink Amplitude and Phase



TIME-- SECONDS

PHASE OF FIELD
 GN2052081100HZ
 START TIME- 23:11:28.000

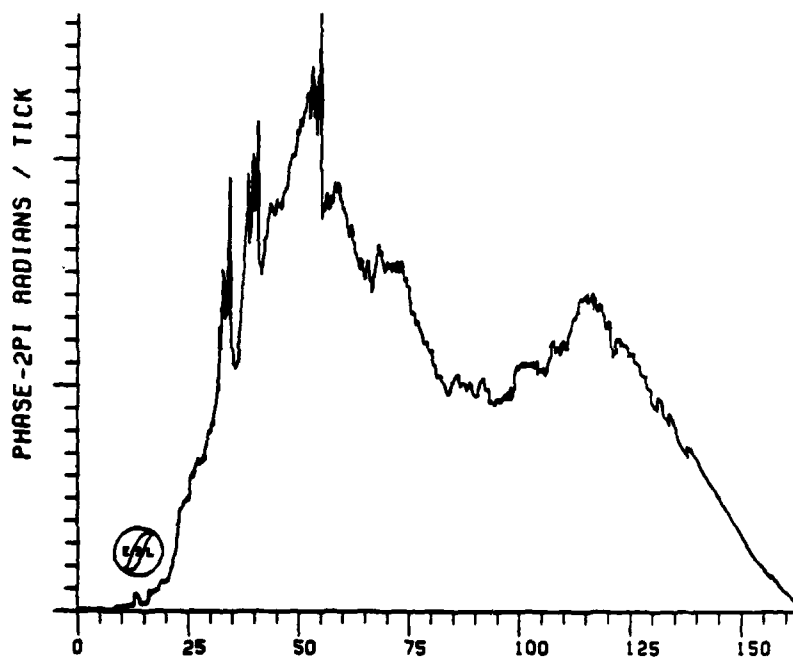
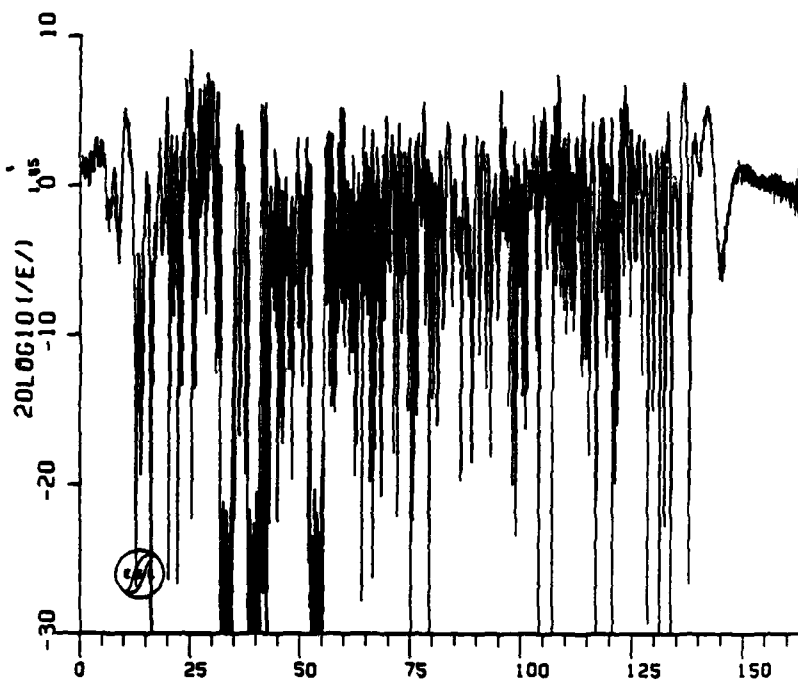
Figure 3-2. GAIL Pass-2 Downlink Amplitude and Phase



TIME-- SECONDS

PHASE OF FIELD
GM1052081100HZ
START TIME- 23:17:26.000

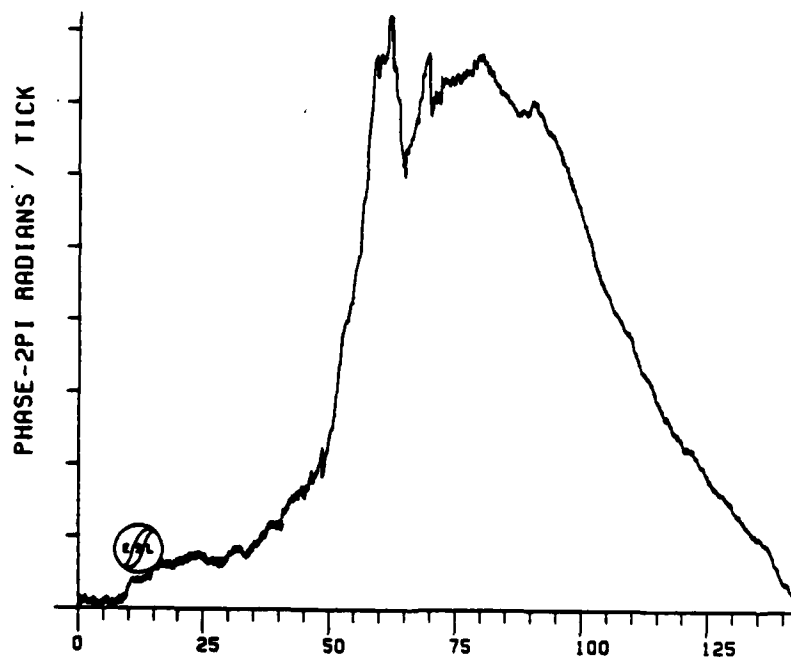
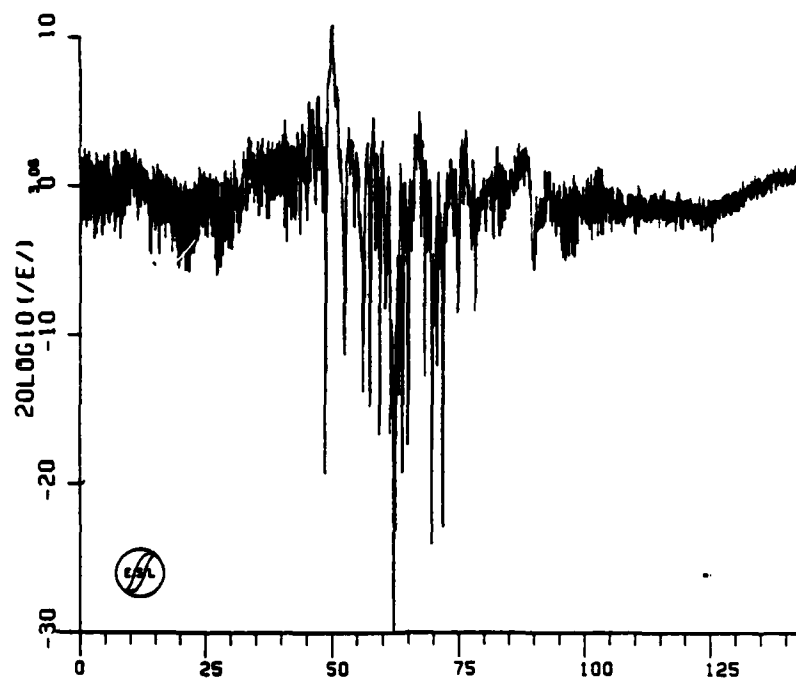
Figure 3-3. GAIL Pass-1 Downlink Amplitude and Phase



TIME-- SECONDS

PHASE OF FIELD
G08052081100HZ
START TIME- 00:14:28.495

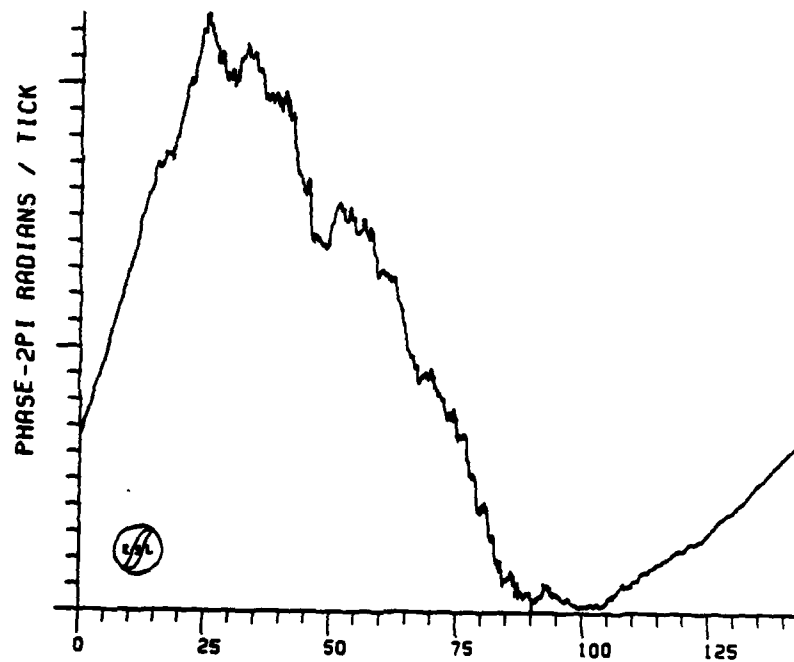
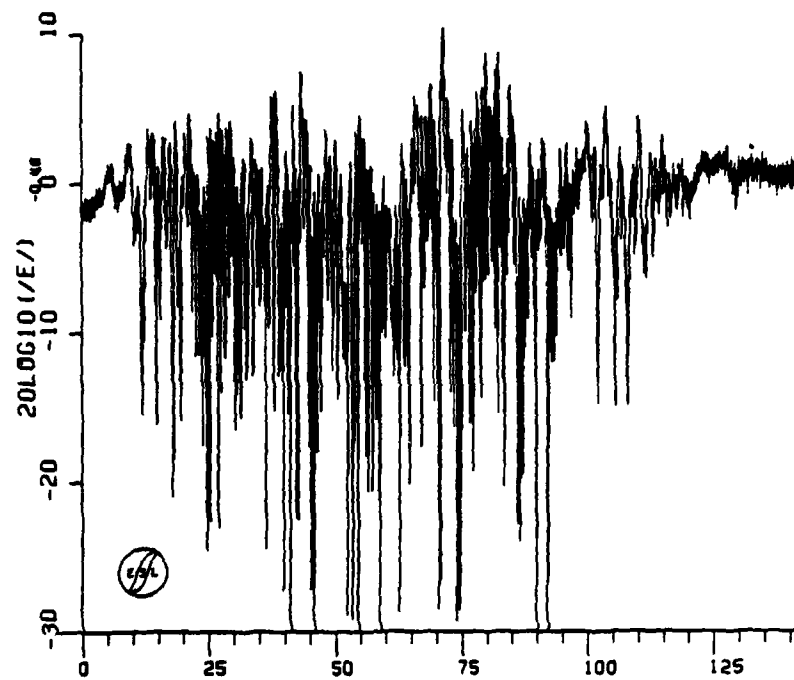
Figure 3-4. GAIL Pass 8 Downlink Amplitude and Phase



TIME-- SECONDS

PHASE OF FIELD
G10052081100HZ
START TIME- 00:23:56.495

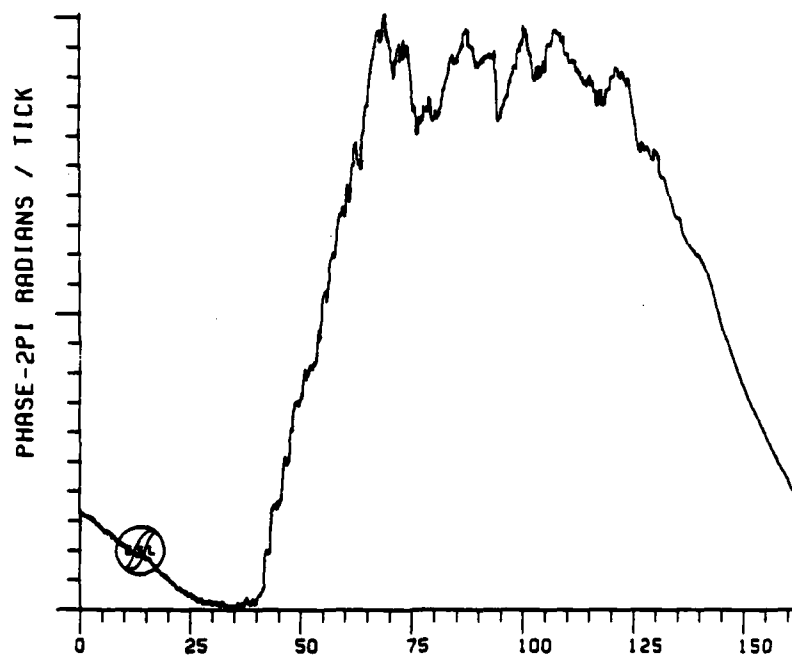
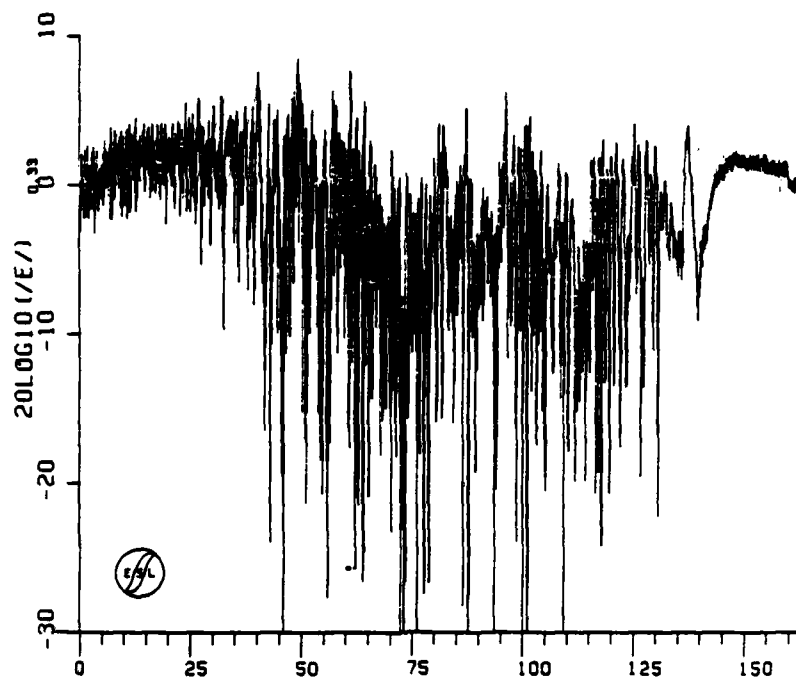
Figure 3-5. GAIL Pass 10 Downlink Amplitude and Phase



TIME-- SECONDS

PHASE OF FIELD
 G110S2081100HZ
 START TIME- 00:28:28.015

Figure 3-6. GAIL Pass 11 Downlink Amplitude and Phase



TIME-- SECONDS

PHASE OF FIELD
G12052081100HZ
START TIME- 00:33:19.935

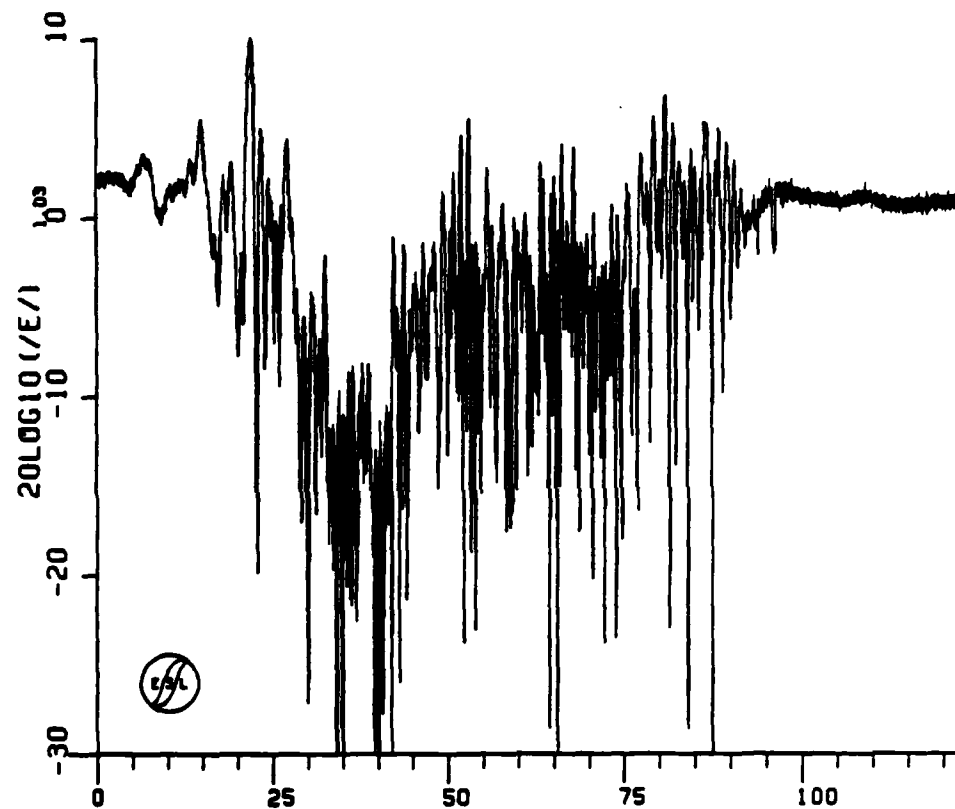
Figure 3-7. GAIL Pass 12 Downlink Amplitude and Phase

OSN=ESL3913.GAIL.PAS18.TOPAS24.ON
REC. NO. 1 2 3 4 5 6

PSD318
OTRM

11/23/81

15:43:04



TIME-- SECONDS

MAGNITUDE OF FIELD

G18052081100HZ

START TIME- 01:04:38.015

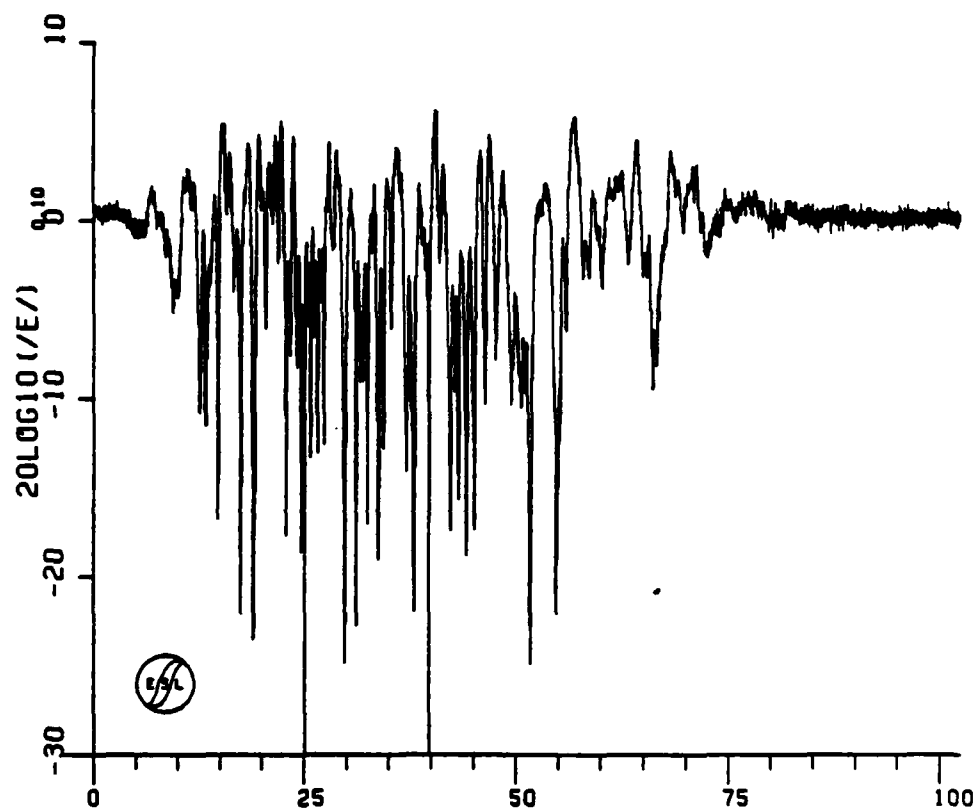
Figure 3-8. GAIL Pass 18 Downlink Amplitude

DSN-ESL3913.GAIL.PAS18.TOPAS24.ON
REC. NO. 10 11 12 13 14

PS0318
OTAN

11/23/81

15:43:31



TIME-- SECONDS

MAGNITUDE OF FIELD

G19052081100HZ

START TIME- 01:10:48.495

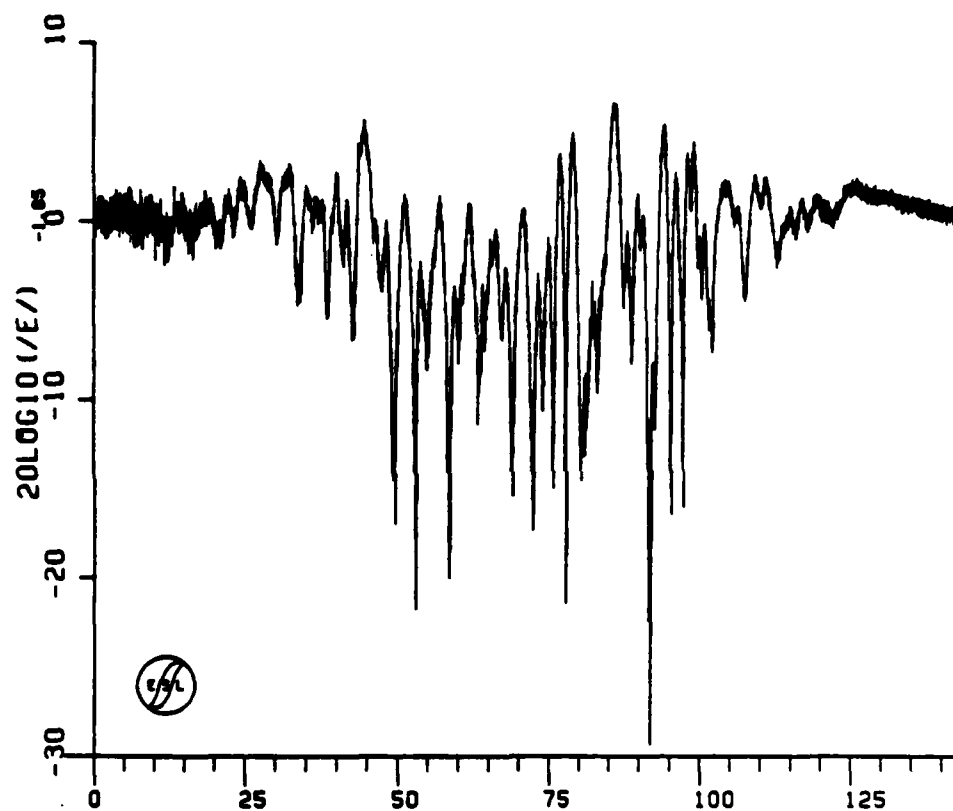
Figure 3-9. GAIL Pass 19 Downlink Amplitude

DSN-ESL3913.GAIL.PAS18.TOPAS24.ON
REC. NO. 48 50 51 52 53 54 55

PS0318
DTAM

11/23/81

15:43:52



TIME-- SECONDS

MAGNITUDE OF FIELD

G24052081100HZ

START TIME- 01:31:48.015

Figure 3-10. GAIL Pass 24 Downlink Amplitude

this time as can be seen by the strong fading and the roughness of the phase on the eastern side of the cloud.

It is interesting to note that the striation on-set times as observed from A-105 near the launch complex, from C-6 and from Tyndall were $R+10^m14^s$, $R+10^m14^s$ and $R+9^m30^s$, respectively. These are the times at which the first observable separated structure could be discerned. Figure 3-11 shows the locations of these sites. The center of Pass-2 was at $R+5$ minutes which exhibited a sharp steepening of the phase slope on the eastern side along with some possible initial structuring. Pass-1 centered at $R+11^m30^s$ shows the on-set of strong scintillation effects.

The aircraft continued to transit progressively higher along the field during the next seven passes, as discussed in Section 2, as the cloud projection moved southward. No plots are included here as little or no fading was observed. These data may be of interest to field line coupling studies as good optical coverage to locate the cloud during these passes are available.

Fading records for the rest of the event followed the expected progression from strong fading to moderate and weak late time fading. Figures 3-4 through 3-7 show the strong fading from Passes 8, 10, 11, and 12. They span $R+1^h7^m$ to $R+1^h30^m$. Passes 8, 11, and 12 show strong fading which is caused by the main cloud while Pass 10 shows moderate fading from a region of the cloud lower down the field lines. Figure 3-8 shows the moderate late-time fading from Pass 18 at $R+1^h55^m$. Passes 19 and 24, given in Figures 3-9 and 3-10 are examples of the weak late-time fading seen during GAIL. They occurred at $R+2^h5^m$ and $R+2^h25^m$. No phase data are presented for Passes 18, 19, and 24 because the K-band antenna needed for Doppler correction was misaligned during these passes.

3-3 GAIL SUMMARY.

Summarizing, the downlink propagation data for Event GAIL shows diffraction ringing during the first two passes, followed by a strong fading pass, followed by seven passes with little or no fading, while, the last 22 passes yielded typical fading with the expected progression from strong Rayleigh fading

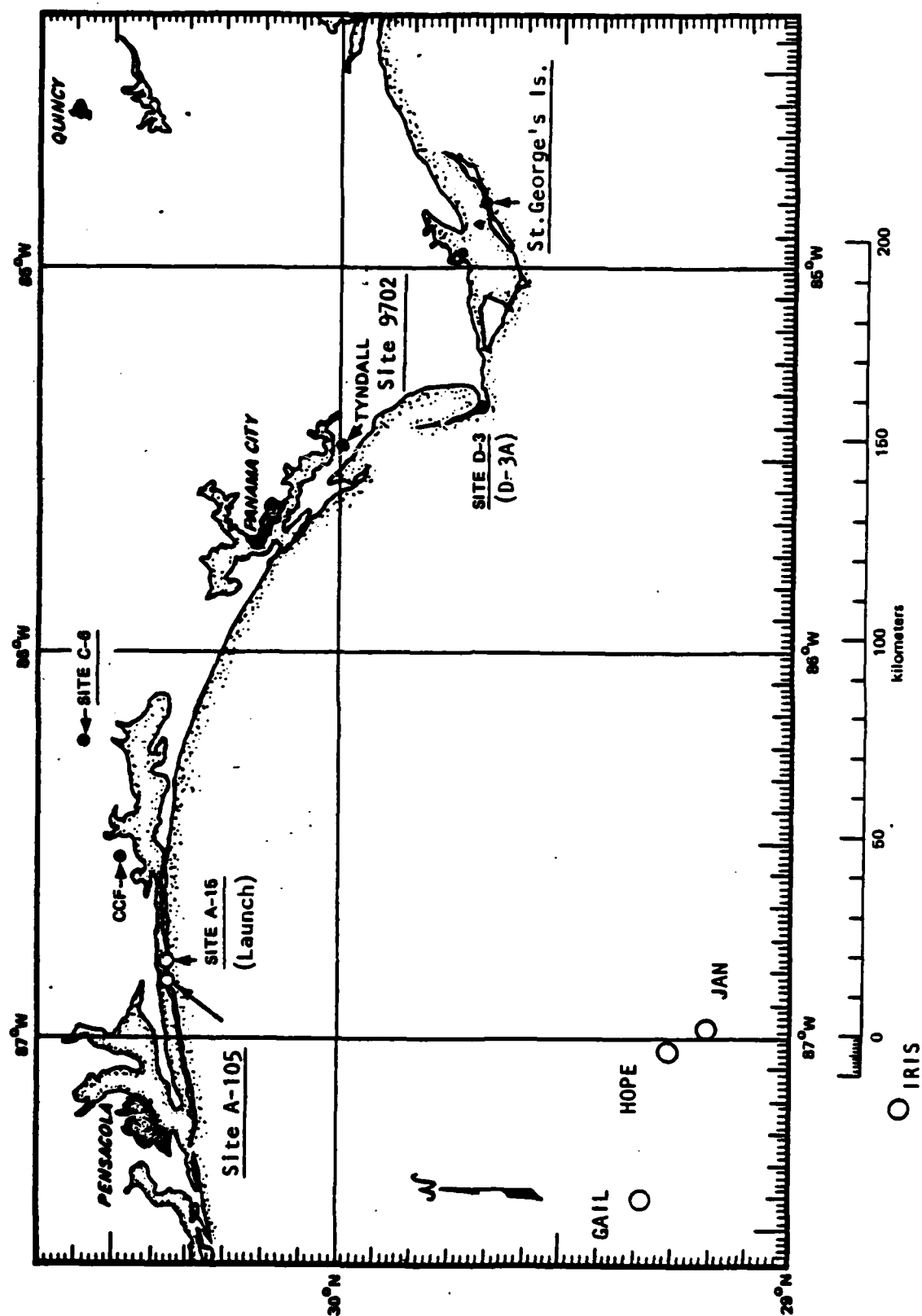


Figure 3-11. Ground Optics Site Locations

to weak late time fading. Because of the lesser interest in this event, no further data for GAIL are presented.

SECTION 4

HOPE OVERVIEW

4-1 GENERAL.

HOPE, the second release, provided the best overall propagation data of the four releases. It is somewhat better than JAN in that consistent radar tracking for positioning the aircraft following the loss of optics at sunset was obtained following HOPE but not following JAN. Downlink propagation data are presented in Section 5 and the uplink propagation data are shown in Section 6. Back-propagation of the downlink data are presented in Section 7. A few uplink data passes were examined but did not back-propagate well and are not presented.

4-2 RELEASE GEOMETRY.

The second barium release, HOPE, occurred on 6 December 1980 at 23:07:37. It was released at an altitude of 182.6 kilometers at a latitude and longitude of 29.2633°N and 87.0414°W. This release point was about 5 minutes southwest of the planned release point. This cloud appears to have moved north for a few minutes, stopped, then moved south-southwest at a moderate velocity for the rest of the night. The cloud projection was located about 2 degrees south and 1.5 degrees west of release at R+2 hours 38 minutes. A plot of the available cloud projection data is shown on Figure 4-1. The aircraft ground track is shown in Figure 4-2.

Optical track data was used until about R+55 minutes with radar track being used for the remainder of the experiment. The optics track located the cloud somewhat north of the radar track. The radar track appears to have been more consistent with the observed fading. As shown on Figure 4-2 the aircraft was vectored nearly 0.5 degree south of the optics track around 0000Z by the radar. The intervals of strong fading are indicated by the shading on Figures 4-3, 4-4, and 4-5 which show the aircraft ground track for each hour period.

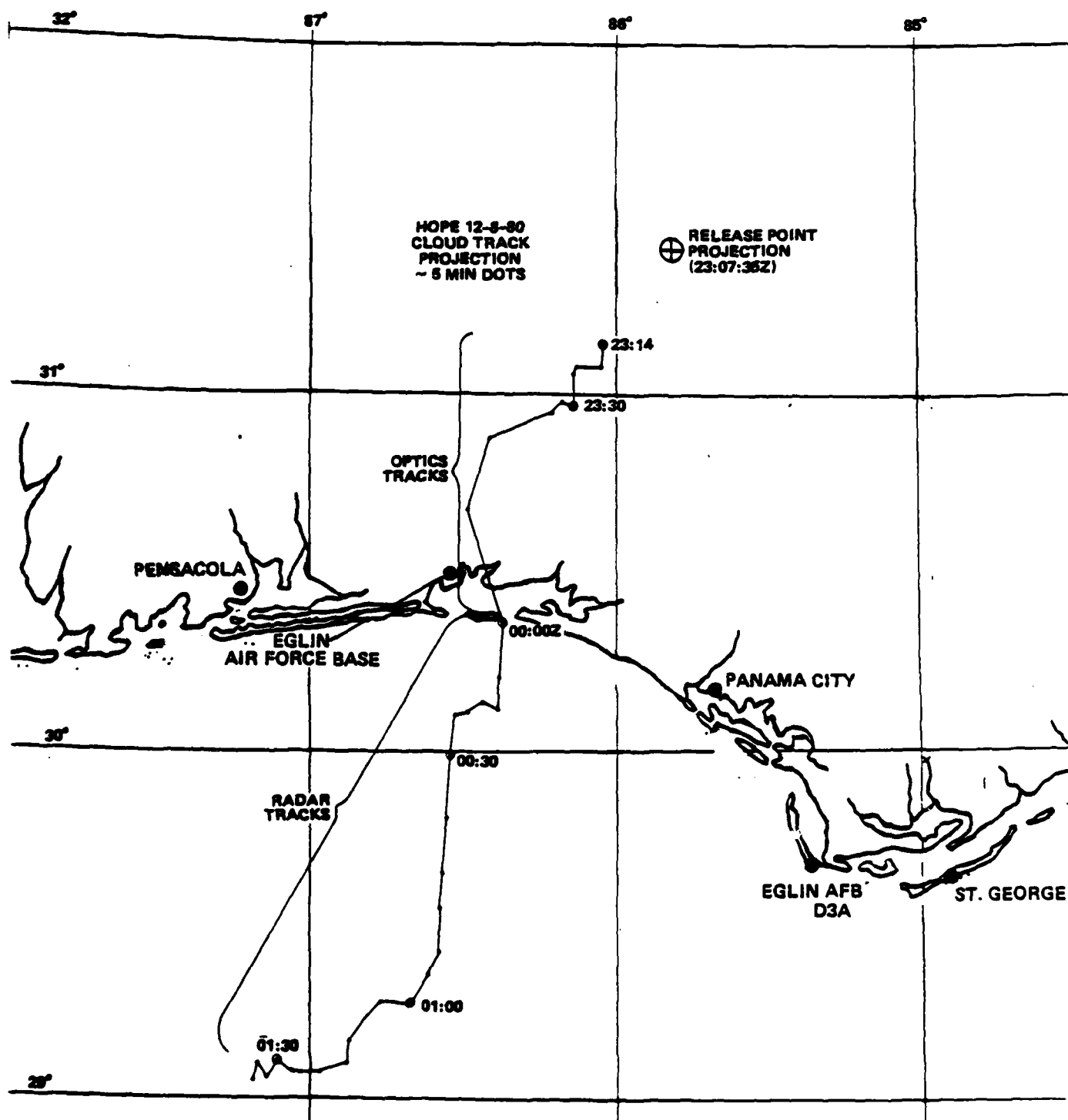


Figure 4-1. Ion Cloud Track Projection for HOPE

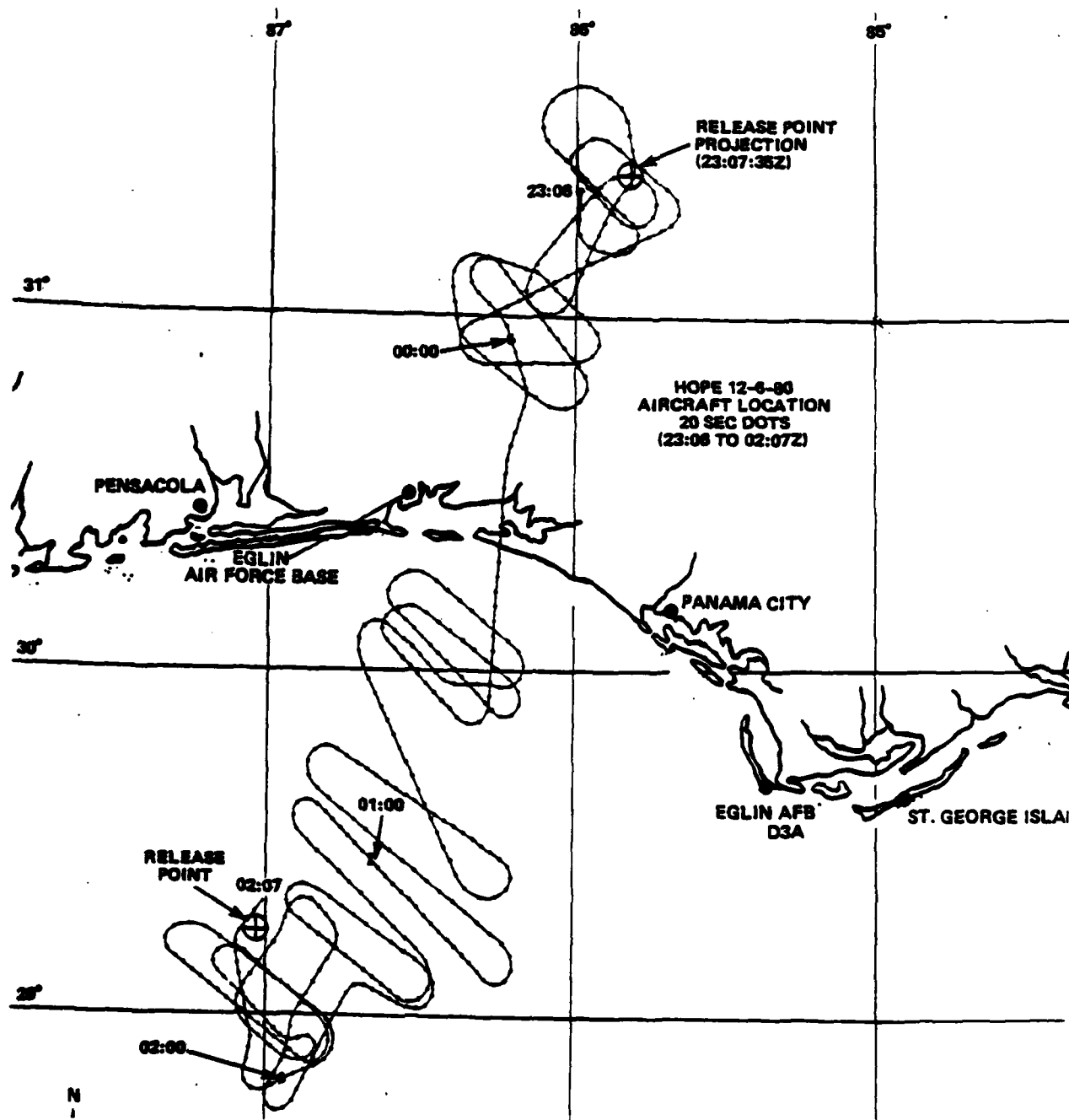


Figure 4-2. Aircraft Ground Track for HOPE

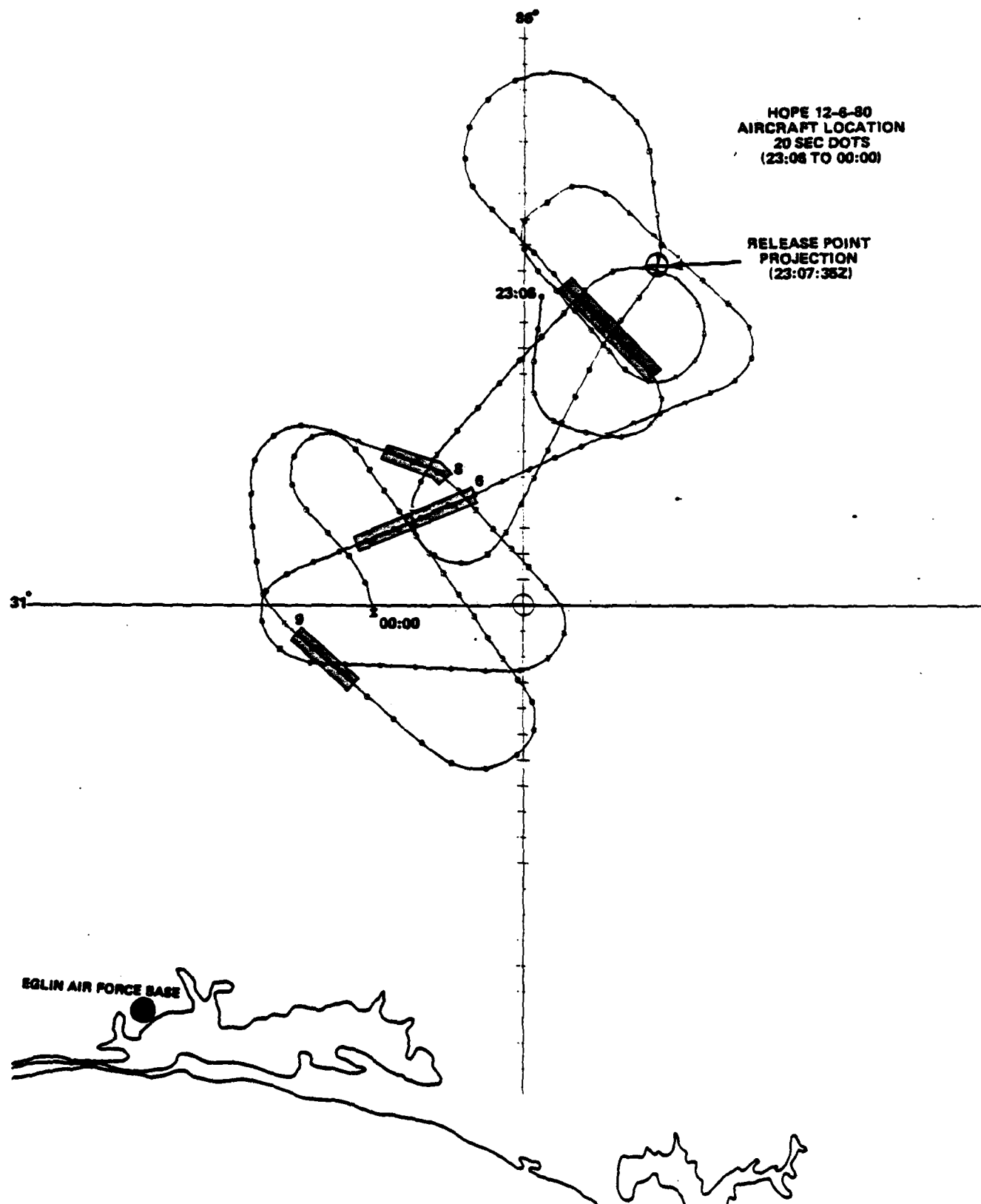


Figure 4-3. Aircraft Ground Track for HOPE from 23:06 to 00:00Z.
Periods of Deep Fading are Shaded

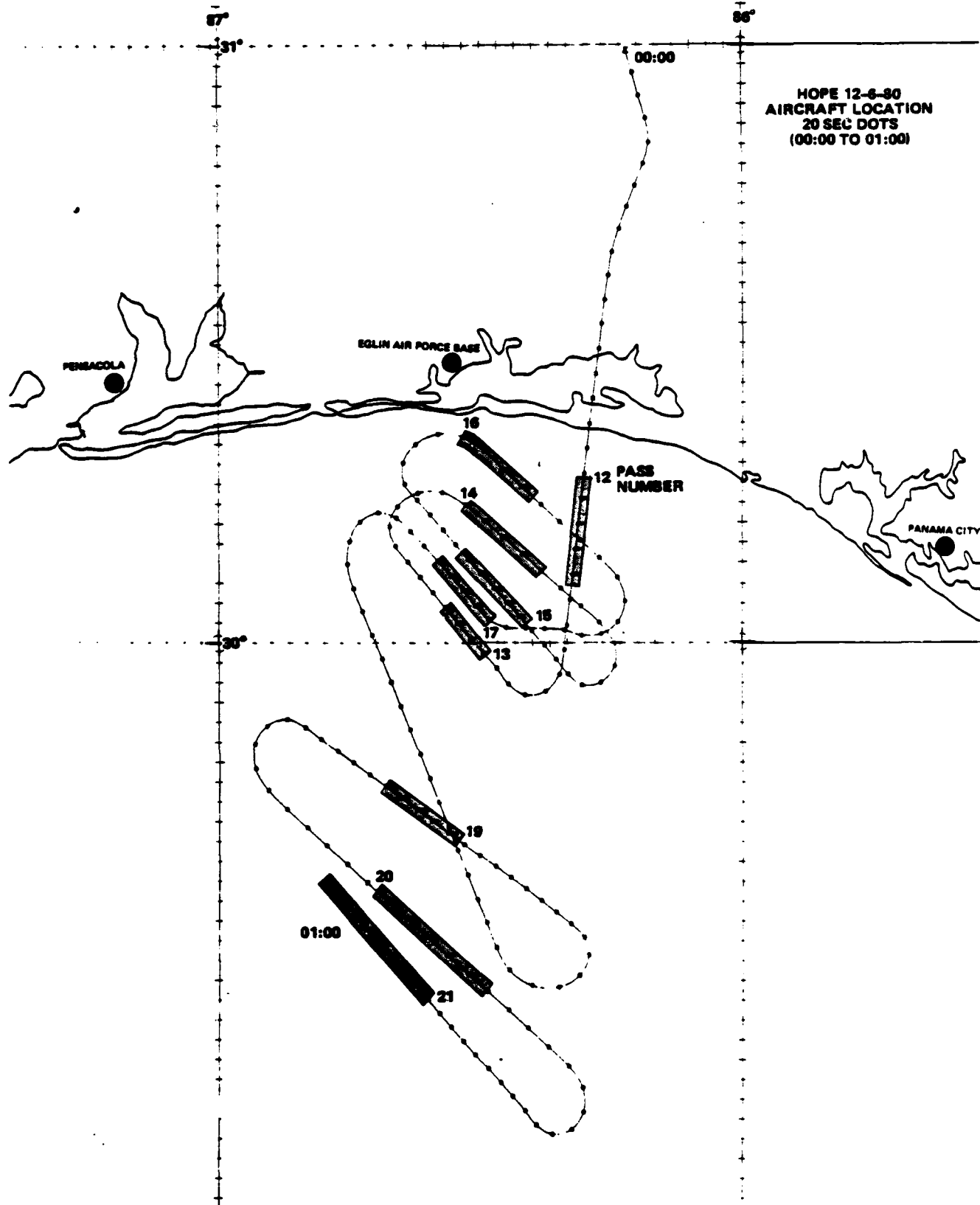


Figure 4-4. Aircraft Ground Track for HOPE from 00:00 to 01:00.
Periods of Deep Fading are Shaded

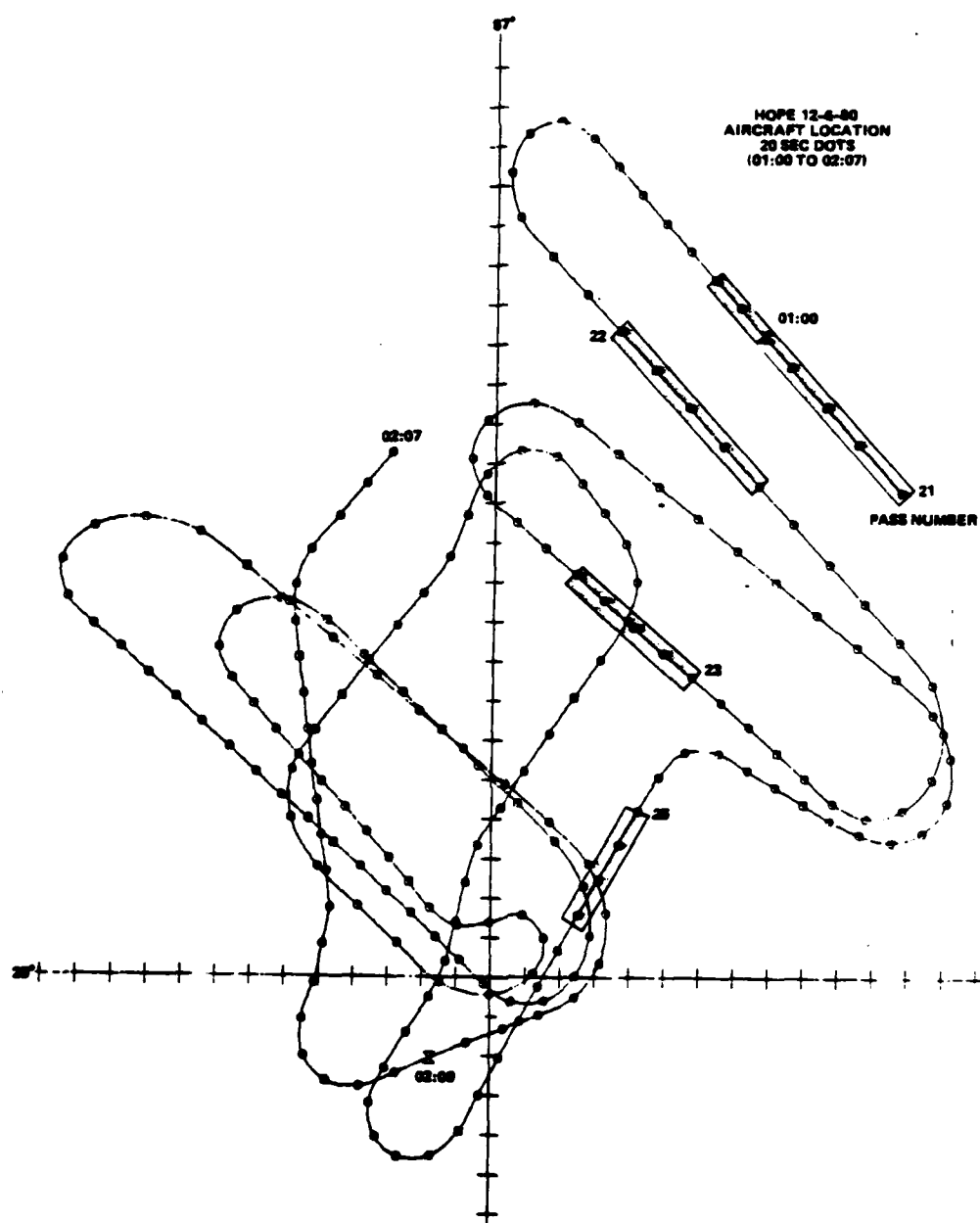


Figure 4-5. Aircraft Ground Track for HOPE from 01:00 to 02:07.
Periods of Deep Fading are Shaded

4-3. FADING DATA SUMMARY.

A total of 33 passes were made during this release with 14 showing moderate to strong fading. A summary of all of the passes is given in Table 4-1. The last pass ended at R+2^h57^m while the last pass with moderate fading observed ended at R+2^h22^m. The first 11 passes, which were between release and R+55 minutes, showed strong fading in only two passes and diffraction ringing in one. These passes were made while the aircraft followed the optics cloud track. The time between R+55 minutes and R+1^h3^m was spent catching up with the cloud which was south of the aircraft. Twelve of the next 15 passes showed moderate to strong fading yielding the total of 14 good passes. The last seven passes showed weak fading or no fading. It is believed that the striations may have continued moving southwest while the radar track point moved northwest.

Uplink data is available for 32 of the 33 passes and downlink data is available for all 33 passes. K-band lock was lost during part of one pass making the uplink data questionable during that pass. Occasionally, as noted in Table 4-1, a loss of lock indication was obtained, but, the uplink data appeared unperturbed. The data received during this event are shown in the next two sections.

Table 4-1. Aircraft Data Summary for HOPE

Pass No.	Time	K-Lock	Comments
1	23:07:30-23:11:40	No	Diffraction ringing, large defocus of ~15 dB
2	23:17:40-23:20:00	Yes	No fading
3	23:22:00-23:24:00	↓	Weak diffraction ringing
4	23:27:30-23:29:10	↓	Very little fading
5	23:30:50-23:32:20	↓	Very little fading
6	23:36:20-23:38:40	?, uplink OK	Strong fading, large defocus of ~15 dB
7	23:40:30-23:42:00	Yes	Little fading
8	23:45:00-23:47:00	↓	Strong fading, partially in turn
9	23:49:50-23:51:30	↓	Moderate fading
10	23:54:00-23:57:00	↓	No fading
11	00:00:00-00:01:00	↓	No fading
12	00:05:40-00:07:50	↓	Moderate diffraction ringing
13	00:10:00-00:12:00	↓	No fading
14	00:14:00-00:16:20	↓	Strong fading
15	00:18:20-00:21:40	↓	Strong fading
16	00:23:30-00:15:00	↓	Strong fading
17	00:29:00-00:31:20	↓	Strong fading
18	00:36:30-00:38:00	↓	Little fading
19	00:42:30-00:45:20	↓	Strong fading
20	00:50:00-00:52:10	↓	Strong fading first minute
21	00:56:00-01:02:00	↓	Strong fading in 00:59:20 to 01:01:20
22	01:04:30-01:06:20	↓	Strong fading
23	01:10:50-01:12:40	↓	Moderate fading
24	01:15:30-01:17:00	?, uplink OK	Moderate fading
25	01:21:00-01:23:20	Yes	Weak fading
26	01:28:20-01:29:30	↓	One deep fade

Table 4-1. --Continued

Pass No.	Time	K-Lock	Comments
27	01:34:00-01:36:00	Yes ↓	Weak fading
28	01:36:00-01:37:00		Weak fading
29	01:39:20-01:41:10		Weak fading
30	01:44:00-01:45:00		No fading
31	01:49:00-01:53:00		No fading
32	01:53:00-01:55:00		No fading
33	02:02:00-02:04:00		Weak fading

SECTION 5

HOPE DOWNLINK TONE DATA

5-1 INTRODUCTION.

Measurements of the downlink amplitude and phase were made following the HOPE release. These measurements were made using a 250 MHz signal transmitted from LES-8 through the barium cloud to the KC135/662 aircraft. The signal processing employed is described in Appendix B.

5-2 DOWNLINK PROPAGATION MEASUREMENTS DURING HOPE.

A total of 33 passes were made following this release with fading seen as late as R+2 hours 22 minutes. A summary of these passes were given in Table 4-1. Plots of the received downlink amplitude and phase are given in Figures 5-1 through 5-16. The data show the usual progression of effects from diffraction ringing at early times to strong scintillation as the striations develop, eventually weakening as the ionization diminishes. An exception to this usual pattern was observed during the first pass, however.

Pass 1, beginning at R+1 minute 40 seconds, shown in Figure 5-1 shows an unusually large defocus of nearly -20 dB with extensive diffraction ringing at the edges. (Note that the 0 dB point on this figure corresponds to -5.01 dB) the depth and duration of this defocus, lasting approximately 75 seconds is remarkable. This defocus is followed by about 1 minute of diffraction ringing. The aircraft was following a northwest path which may have coincided with the initial movement of the ion cloud. This large defocus was undoubtedly caused by the aircraft flying directly underneath the shadow of the ion cloud. Why the fade depth should be so uniform and end so abruptly is not so obvious. The ringing seen prior to and just past the defocus is very similar to the ringing seen in GAIL Pass 2. No phase plot is available for this pass because of loss of K-band lock.

DSN-ESL3913.HOPE.PAS01.TOPAS07.ON
REC. NO. 5 6 7 8 9

PS0318
DTAN

01/29/82 14:24:45

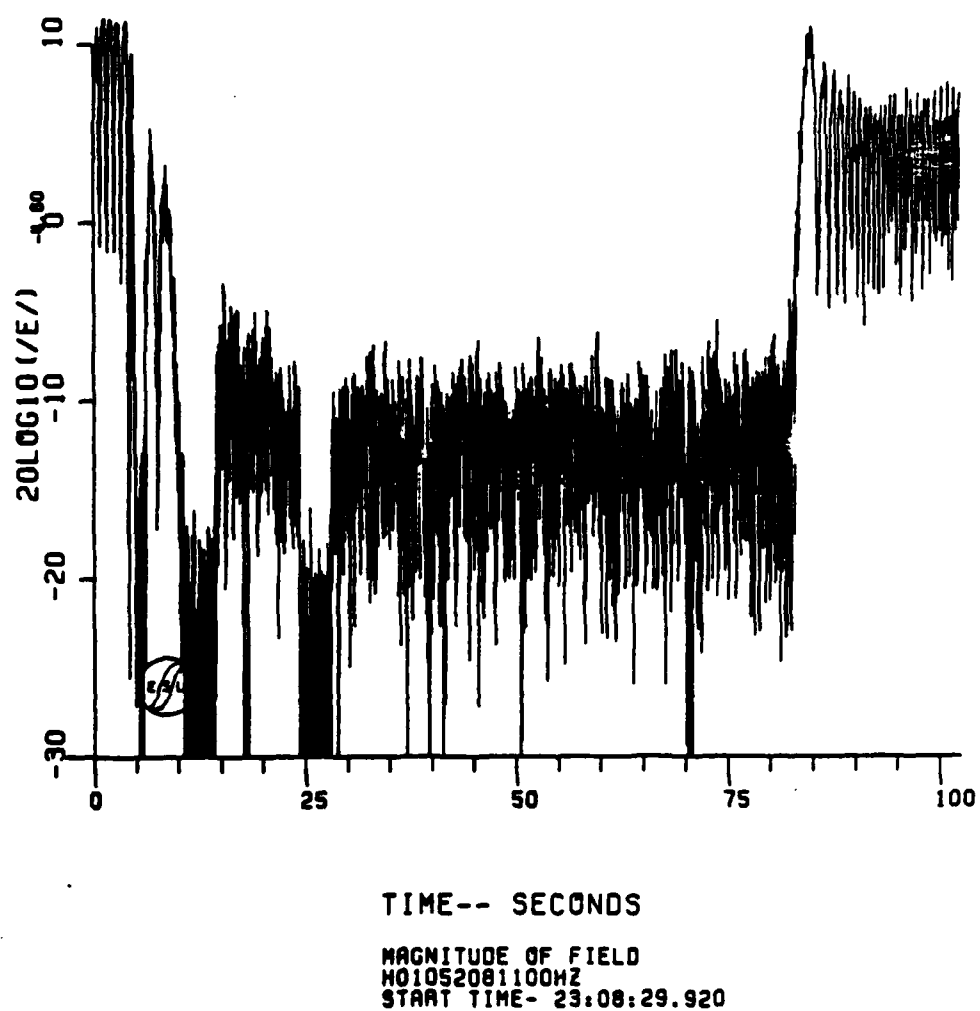


Figure 5-1. HOPE Pass 1 Downlink Amplitude

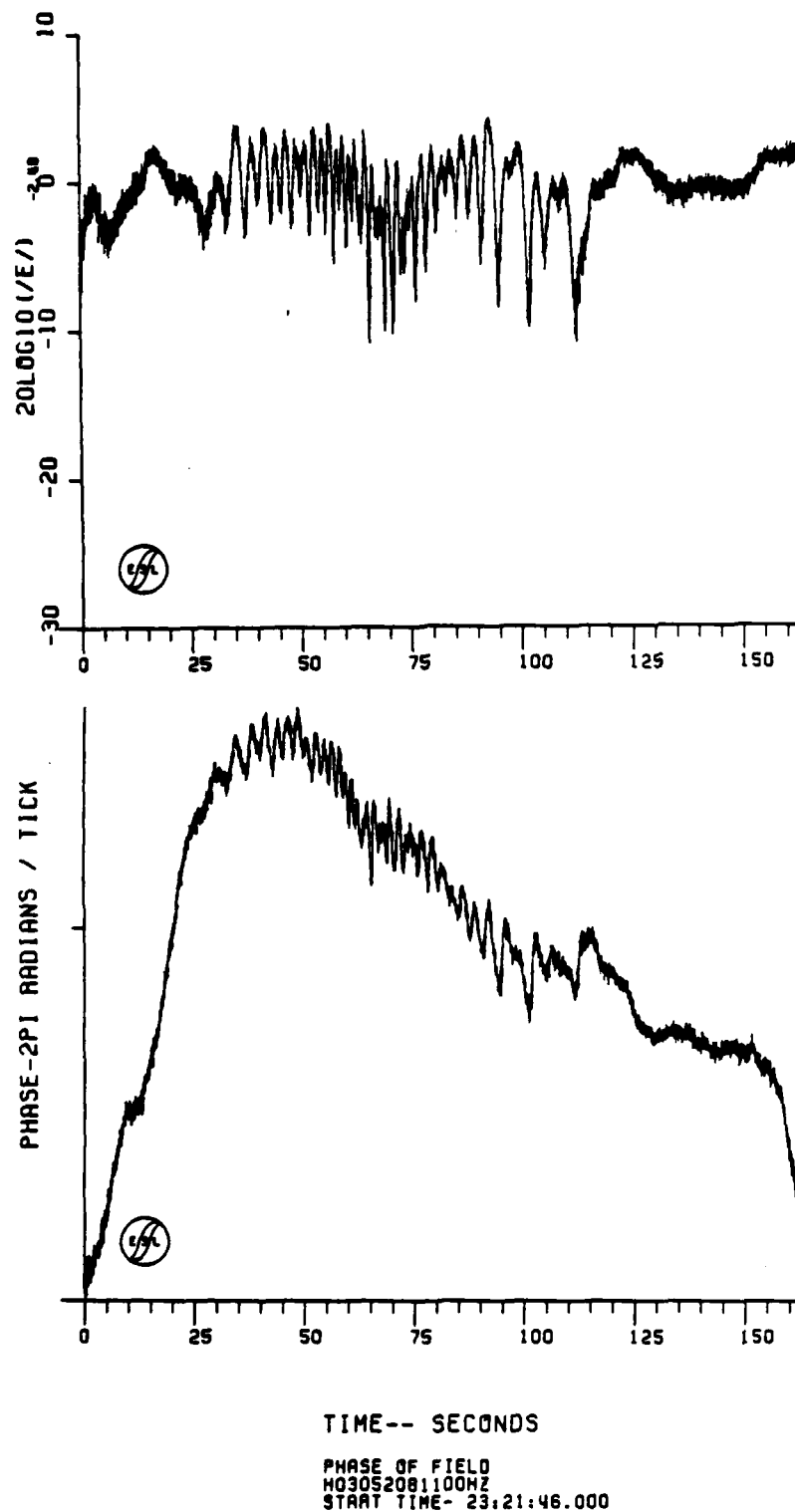
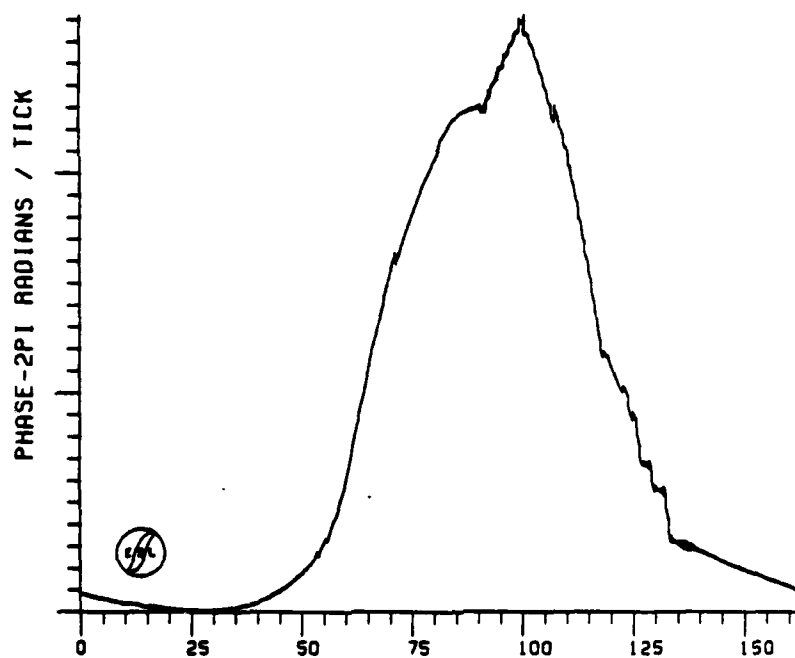
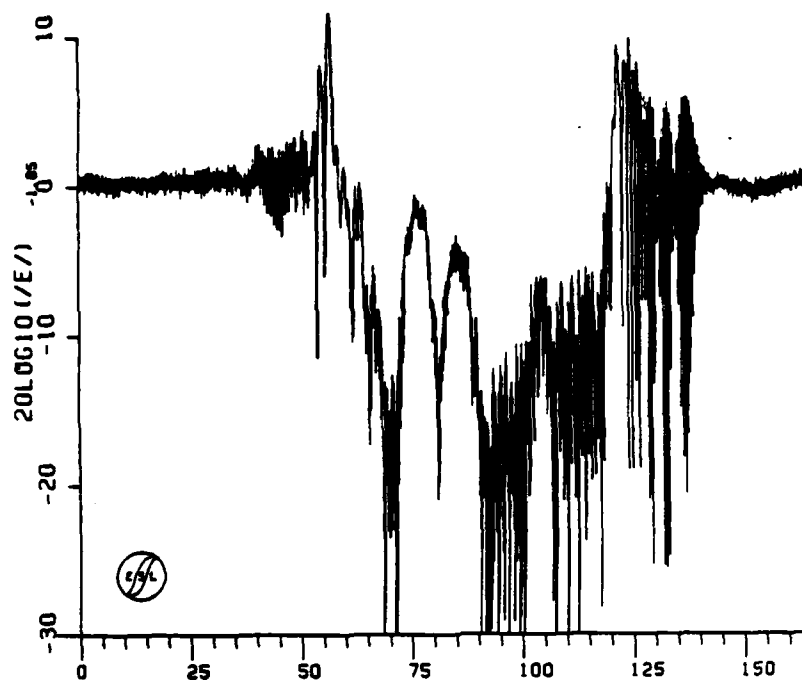


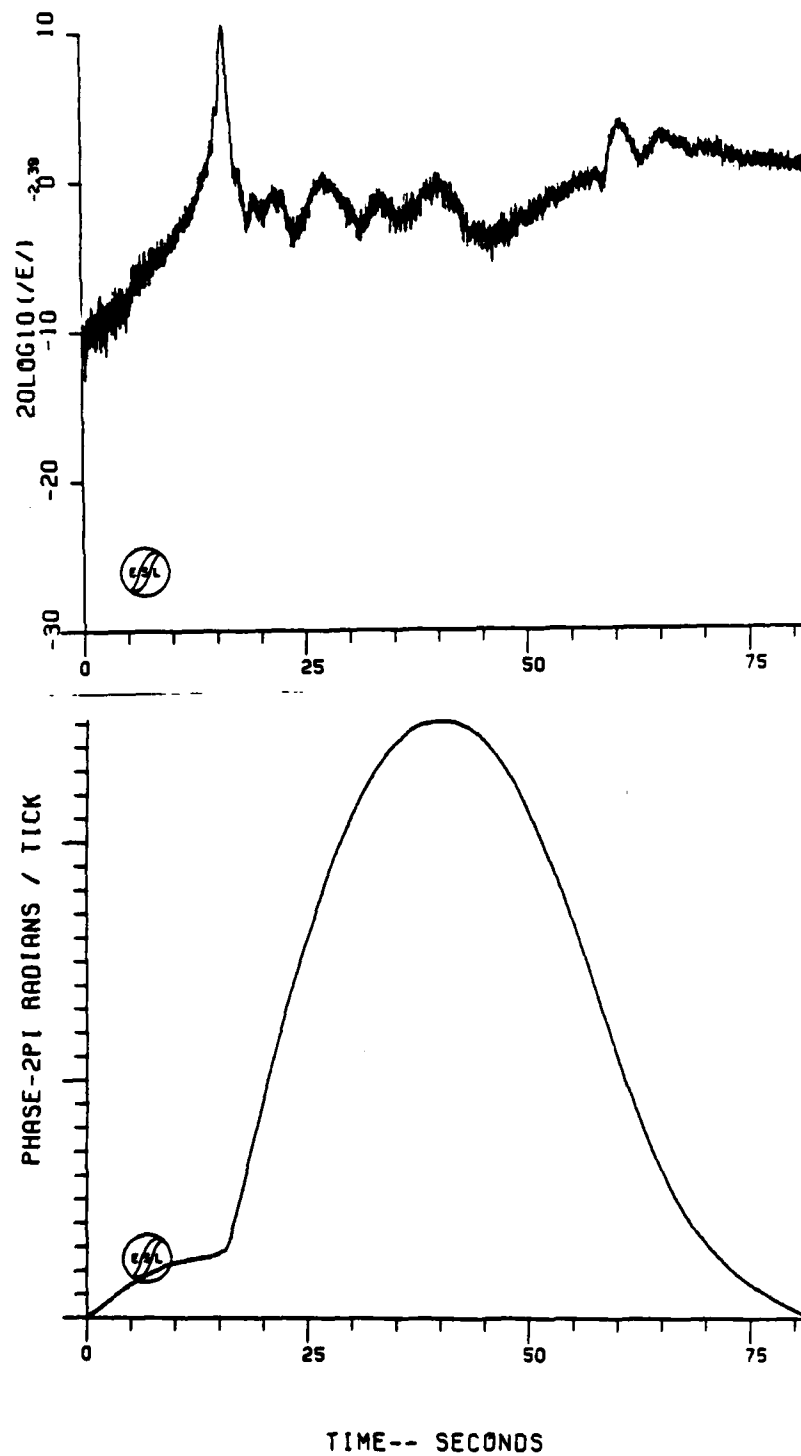
Figure 5-2. HOPE Pass 3 Downlink Amplitude & Phase



TIME-- SECONDS

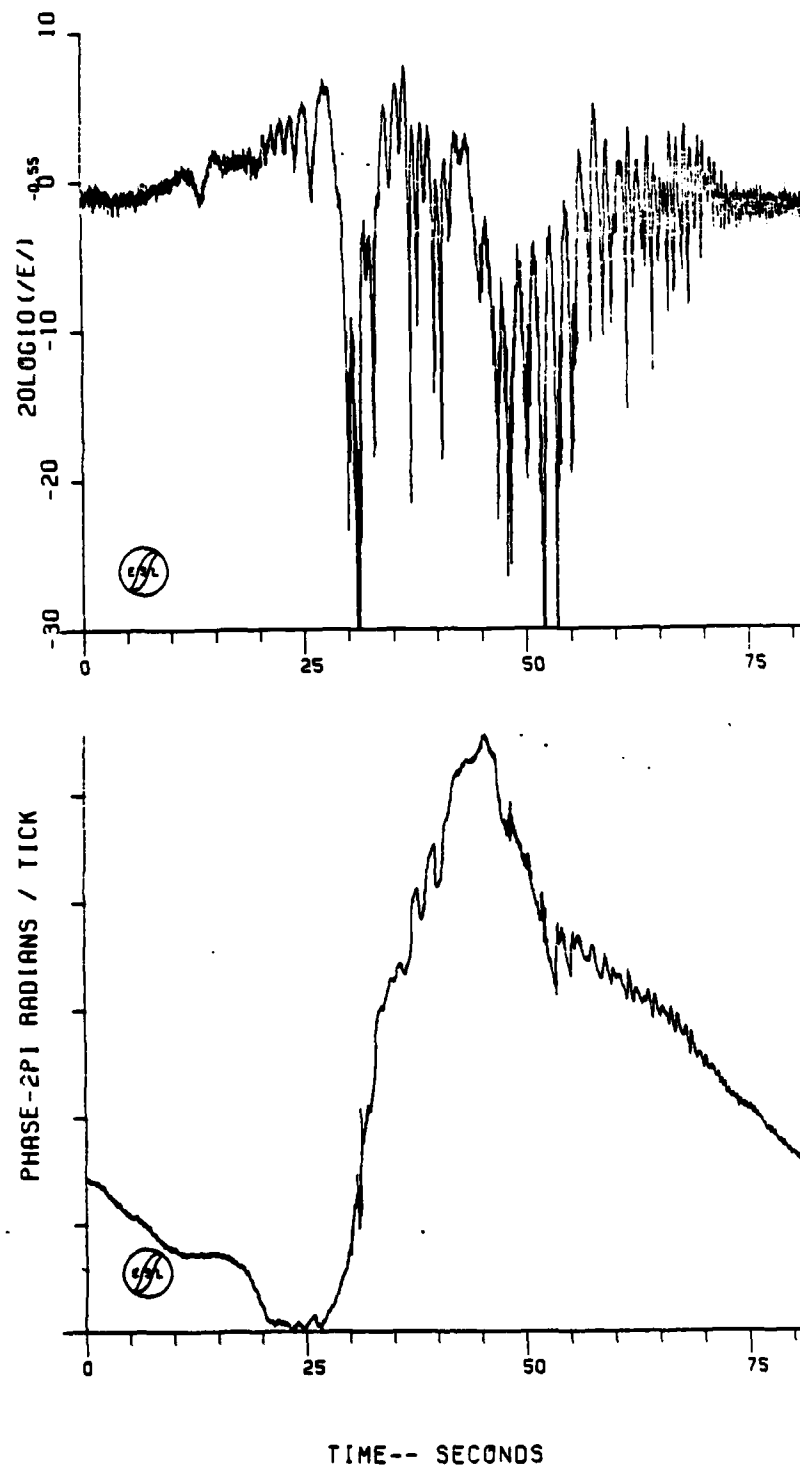
PHASE OF FIELD
 H06052081100HZ
 START TIME- 23:36:04.000

Figure 5-3. HOPE Pass 6 Downlink Amplitude & Phase



PHASE OF FIELD
H06052001100HZ
START TIME- 23:40:12.000

Figure 5-4. HOPE Pass 7 Downlink Amplitude & Phase



TIME-- SECONDS

PHASE OF FIELD
H08052081:03HZ
START TIME- 23:45:08.480

Figure 5-5. HOPE Pass 8 Downlink Amplitude & Phase

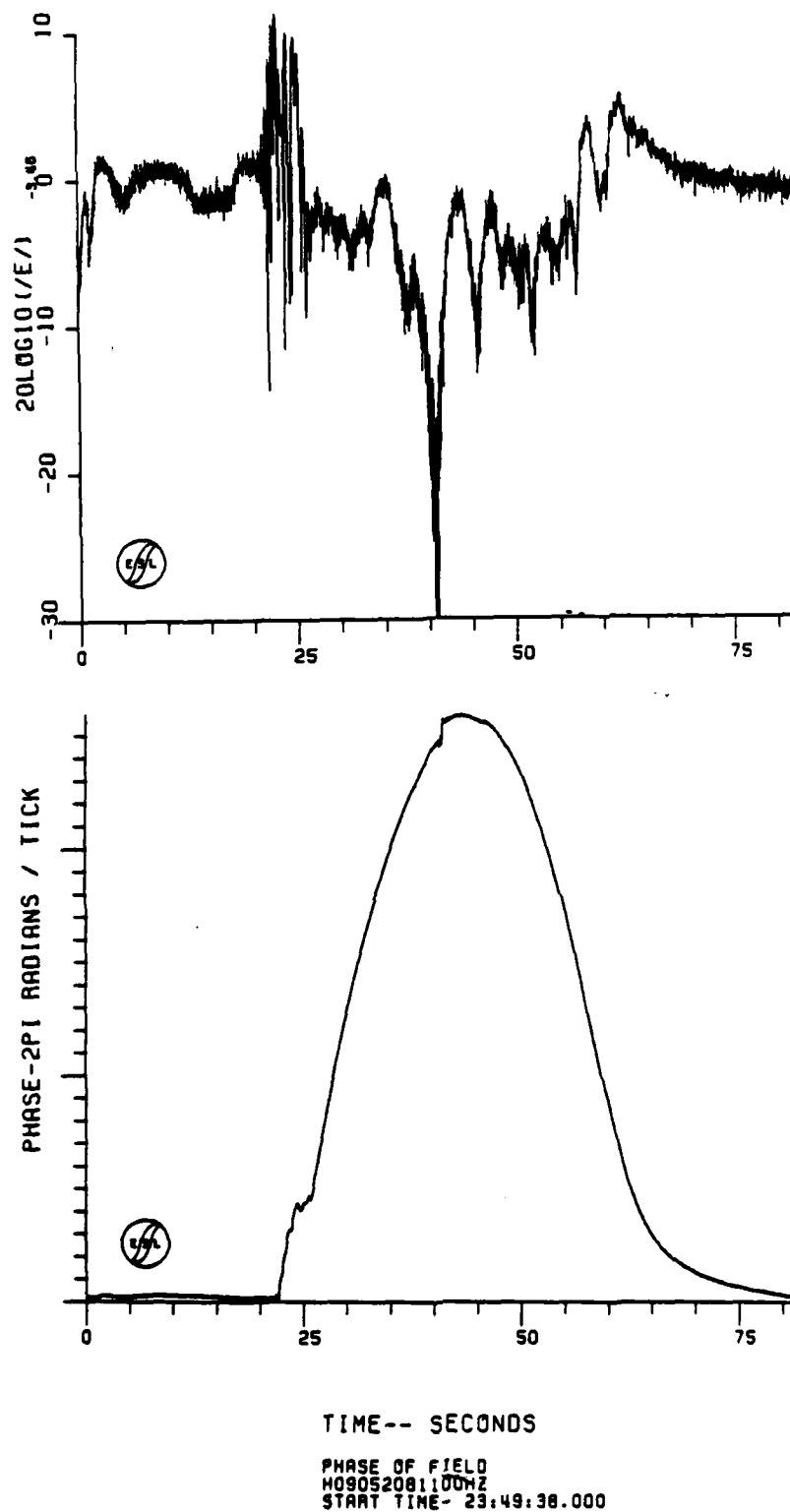
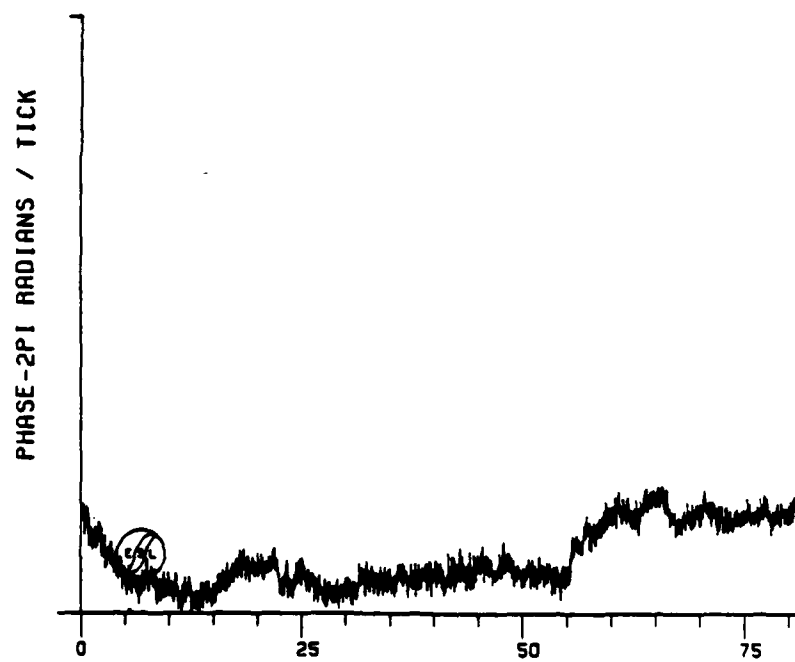
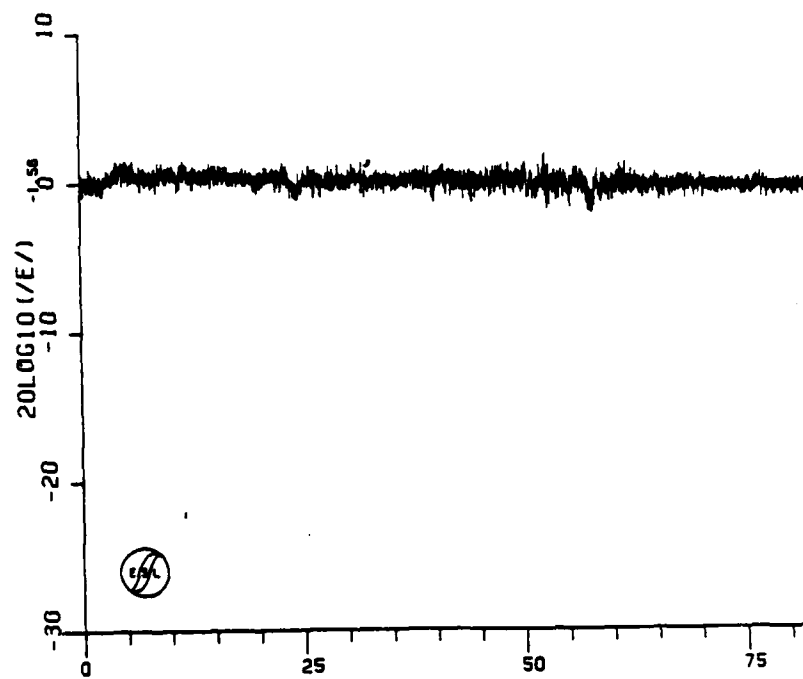


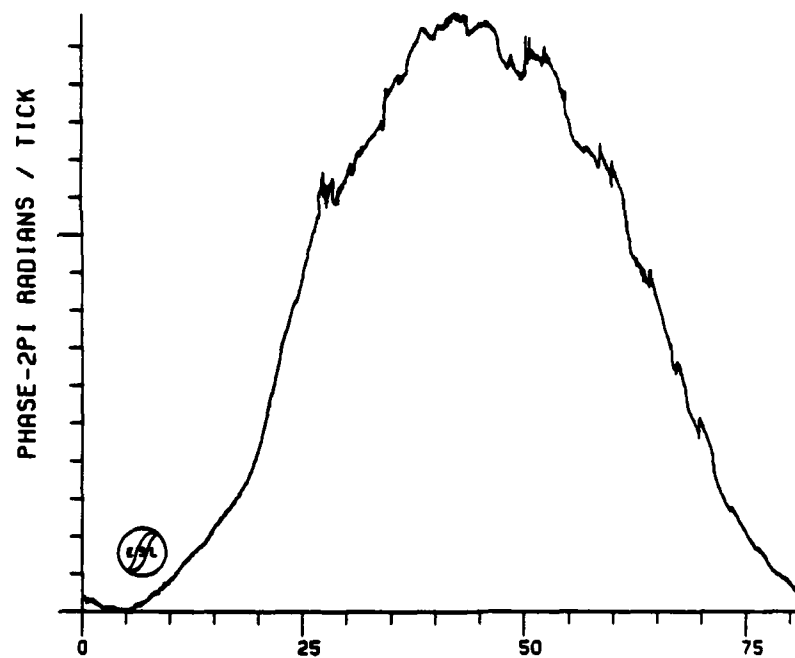
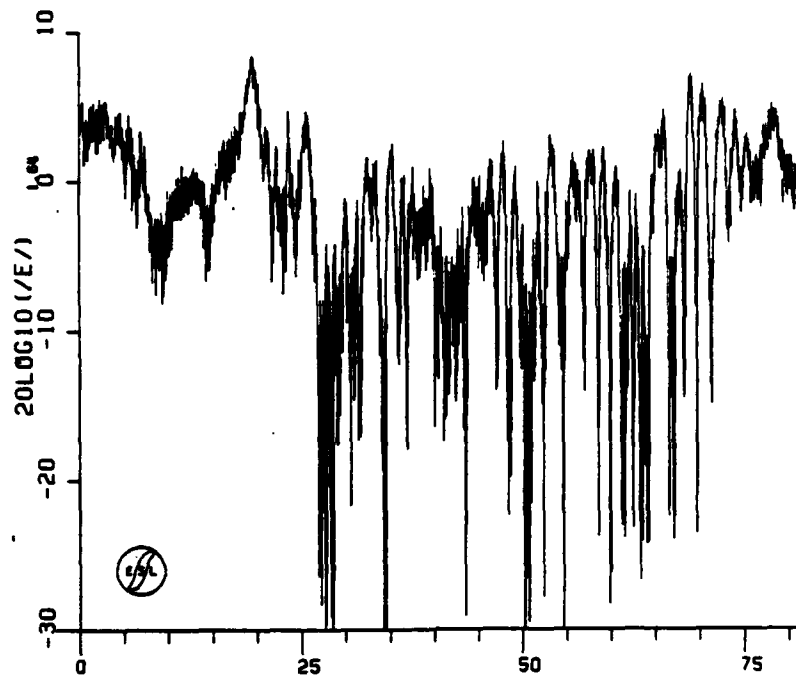
Figure 5-6. HOPE Pass 9 Amplitude & Phase



TIME-- SECONDS

PHASE OF FIELD
H10052081100HZ
START TIME- 23:54:06.480

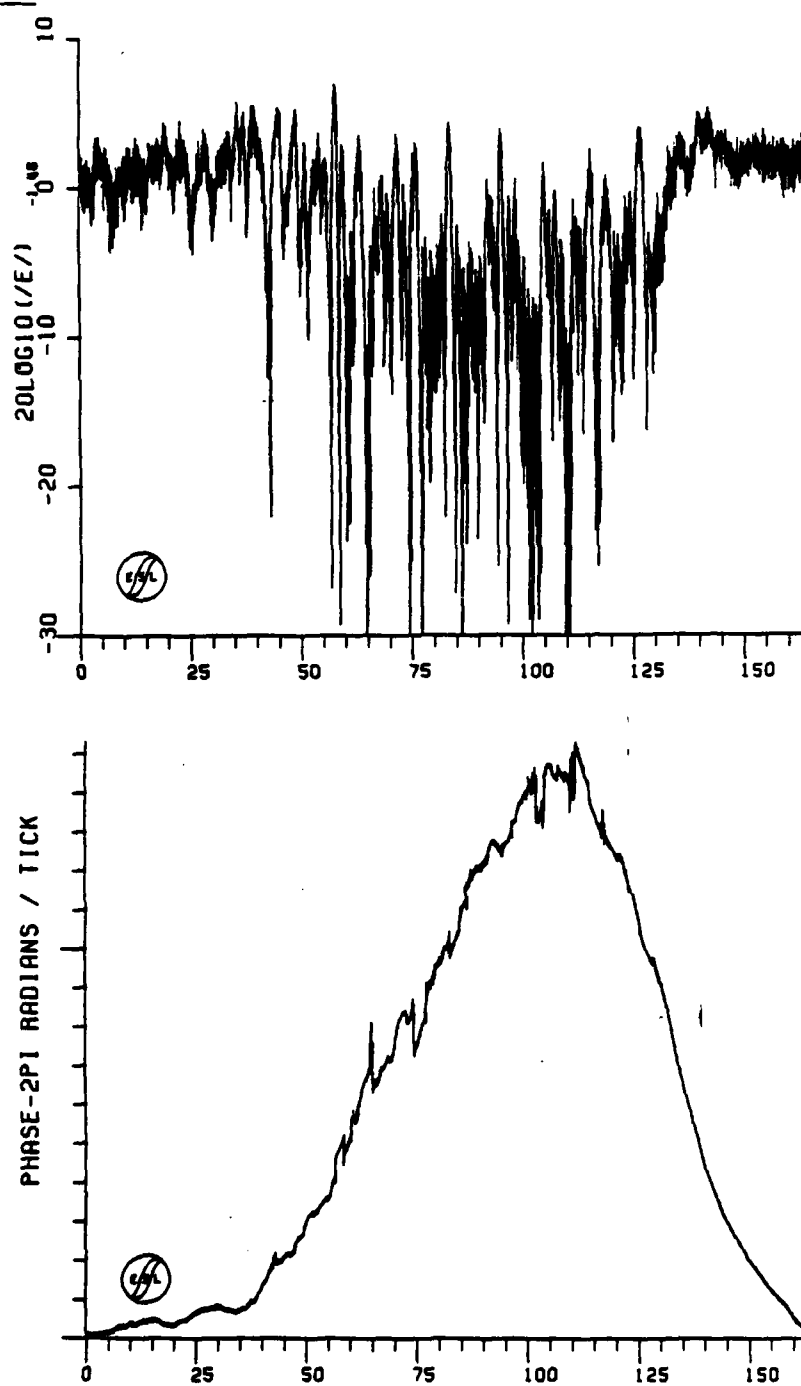
Figure 5-7. HOPE Pass 10 Amplitude & Phase



TIME-- SECONDS

PHASE OF FIELD
H14052081100HZ
START TIME- 00:14:14.480

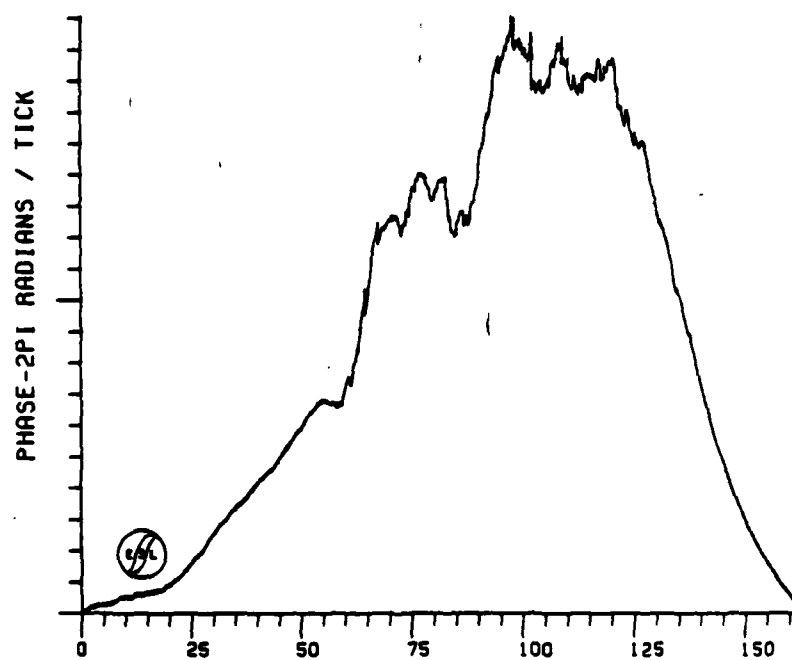
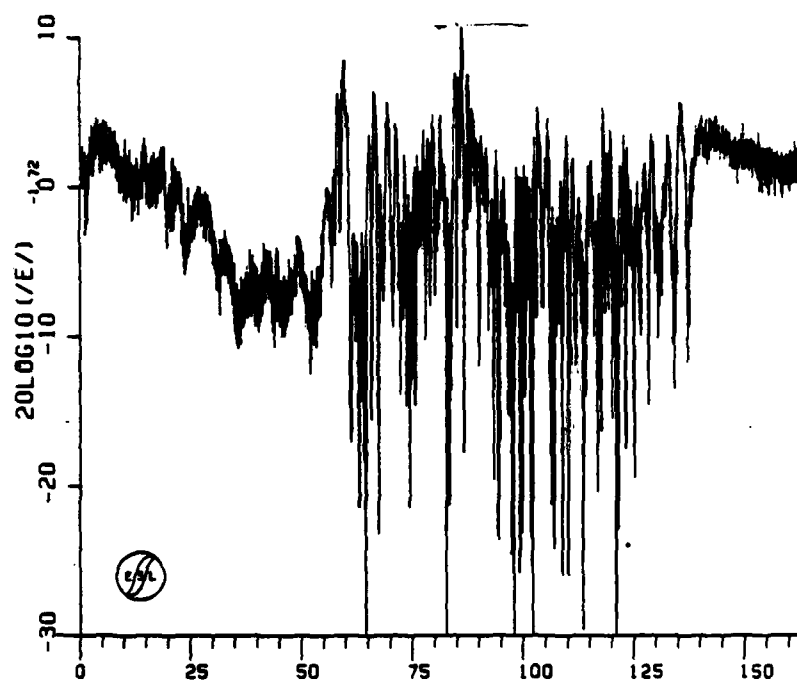
Figure 5-8. HOPE Pass 14 Downlink Amplitude & Phase



TIME-- SECONDS

PHASE OF FIELD
W15061801100HZ
START TIME- 00:18:53.920

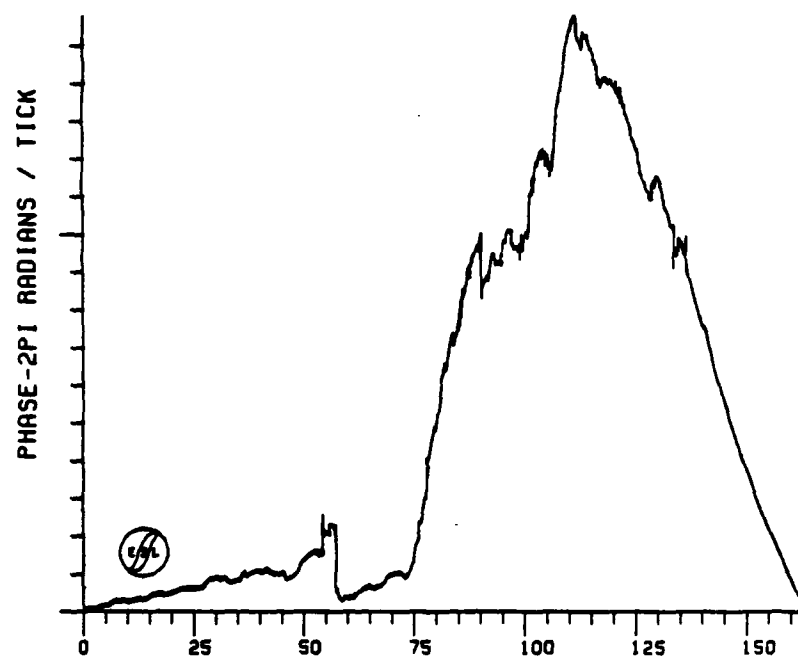
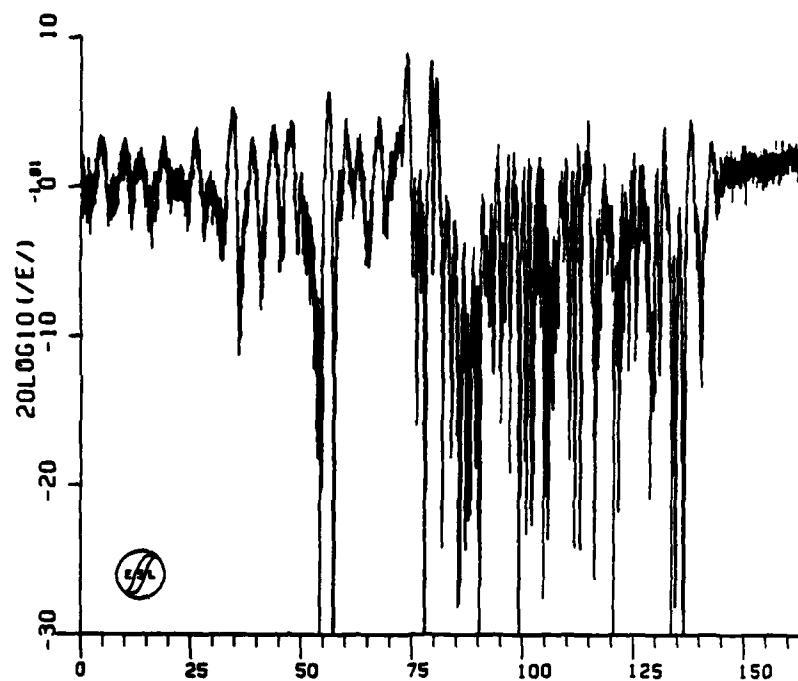
Figure 5-9. HOPE Pass 15 Downlink Amplitude & Phase



TIME-- SECONDS

PHASE OF FIELD
 H17052281100HZ
 START TIME- 00:28:47.999

Figure 5-10. HOPE Pass 17 Downlink Amplitude & Phase



TIME-- SECONDS

PHASE OF FIELD
H19052201100HZ
START TIME- 00:42:36.479

Figure 5-11. HOPE Pass 19 Downlink Amplitude & Phase

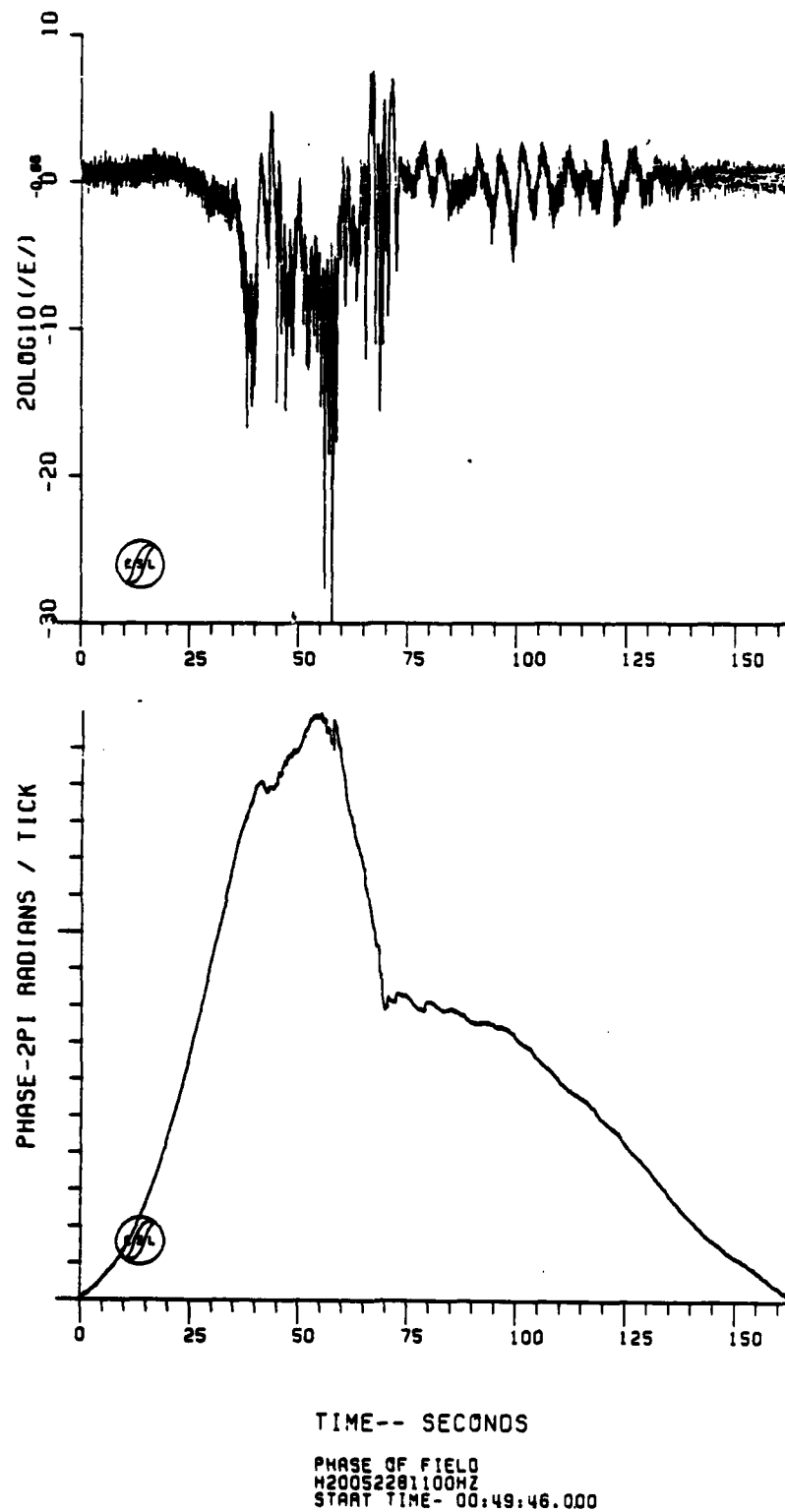
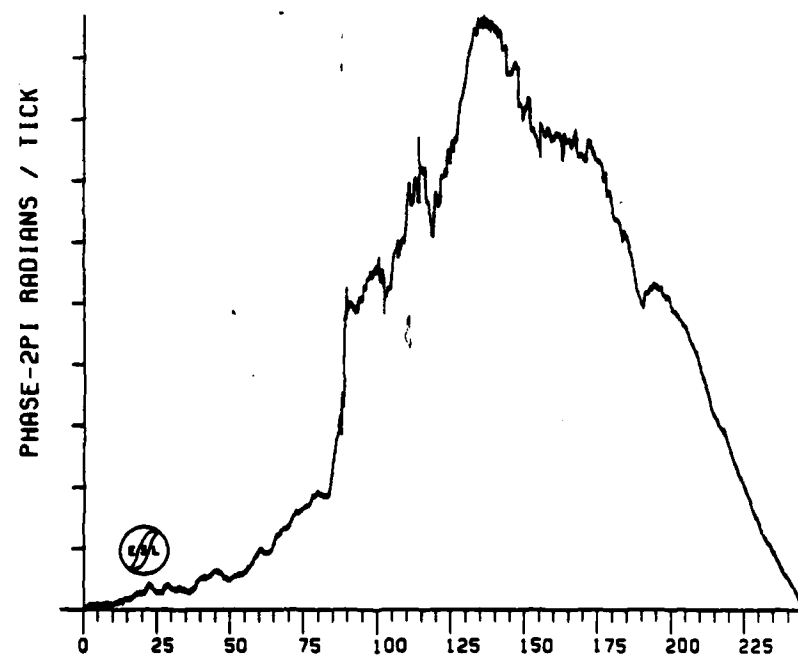
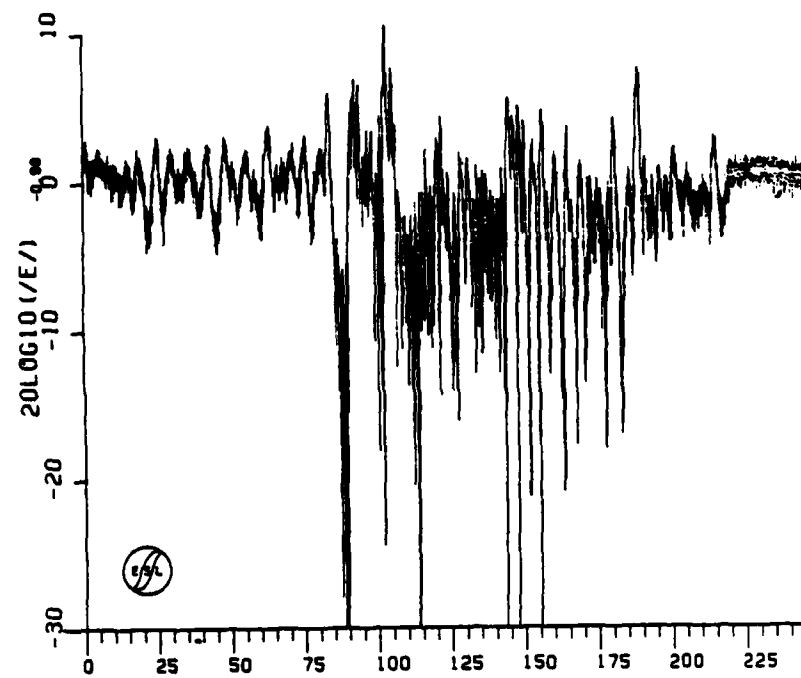


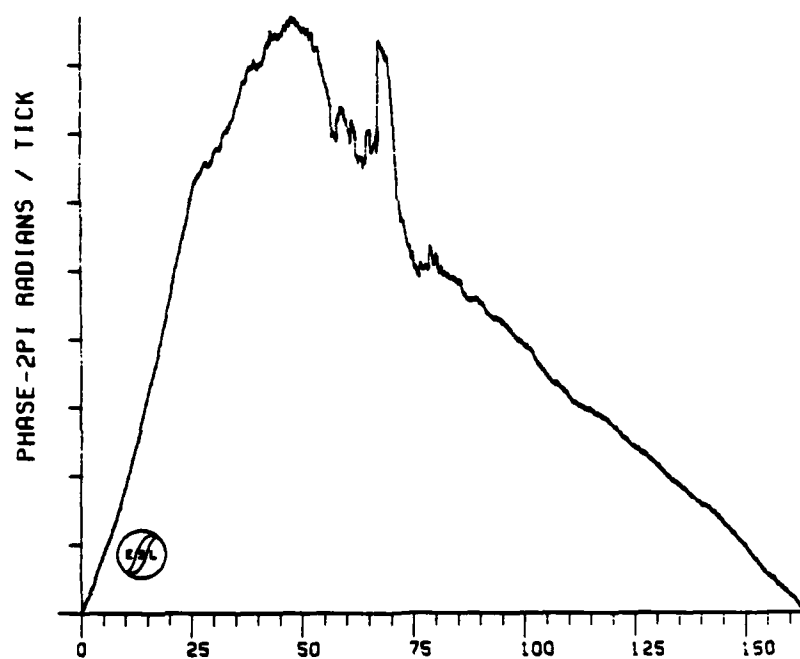
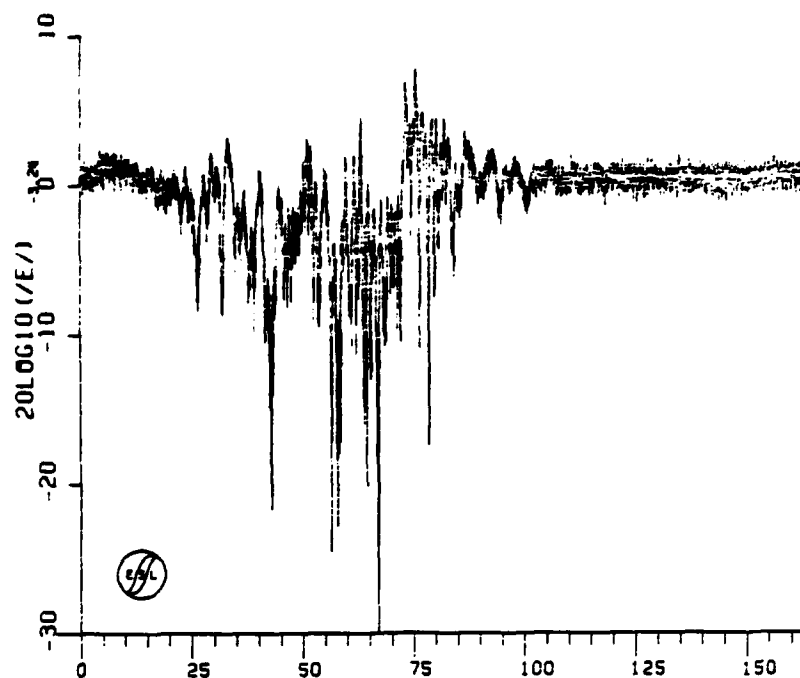
Figure 5-12. HOPE Pass 20 Downlink Amplitude & Phase



TIME-- SECONDS

PHASE OF FIELD
H21052281100HZ
START TIME- 00:58:00.000

Figure 5-13. HOPE Pass 21 Downlink Amplitude & Phase



TIME-- SECONDS

PHASE OF FIELD
M22052281100HZ
START TIME- 01:04:20.000

Figure 5-14. HOPE Pass 22 Downlink Amplitude & Phase

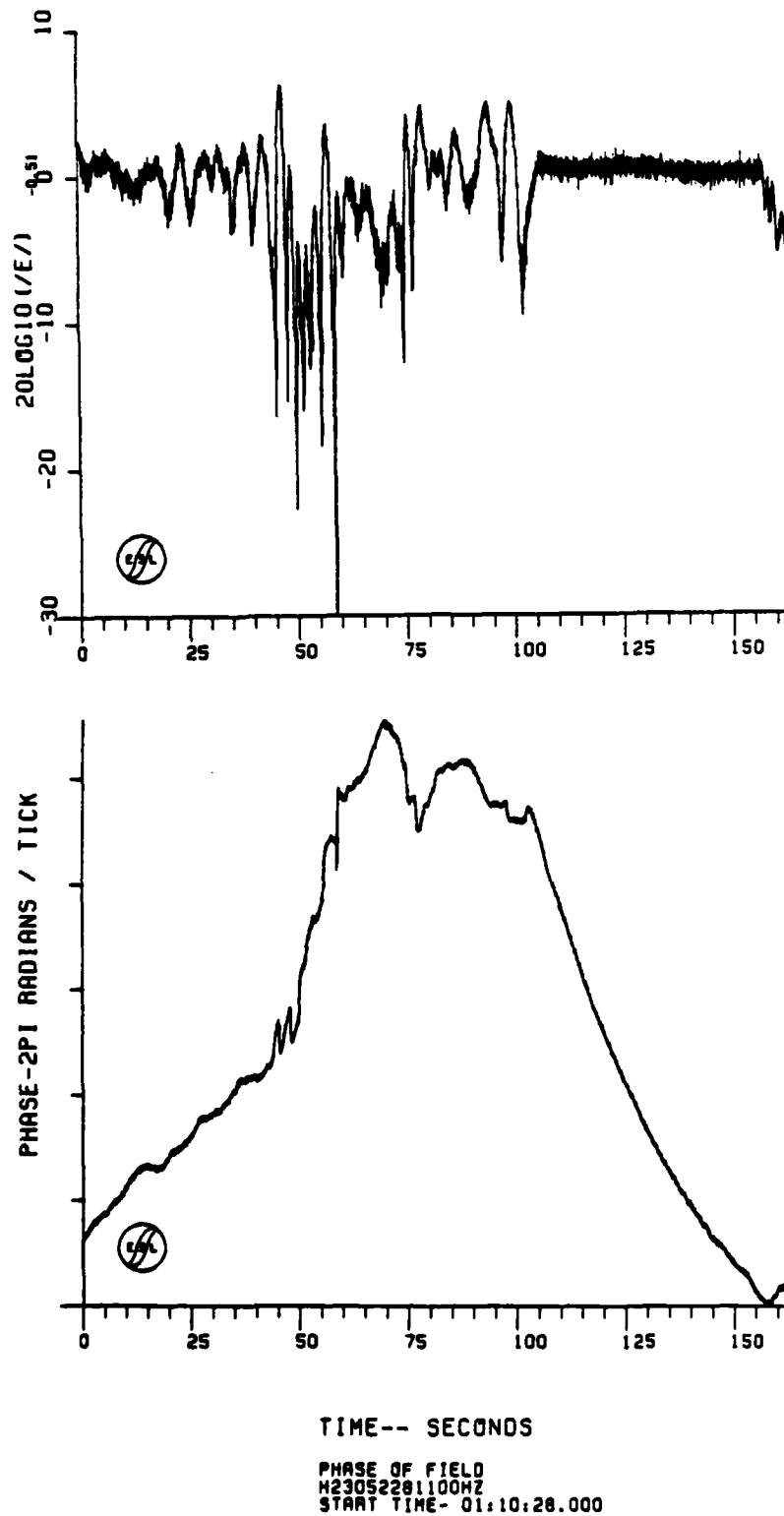
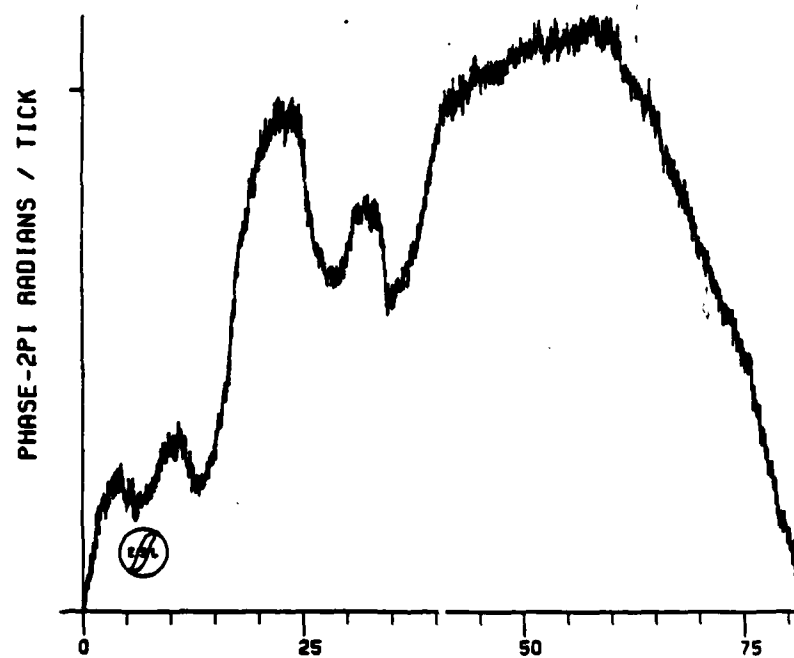
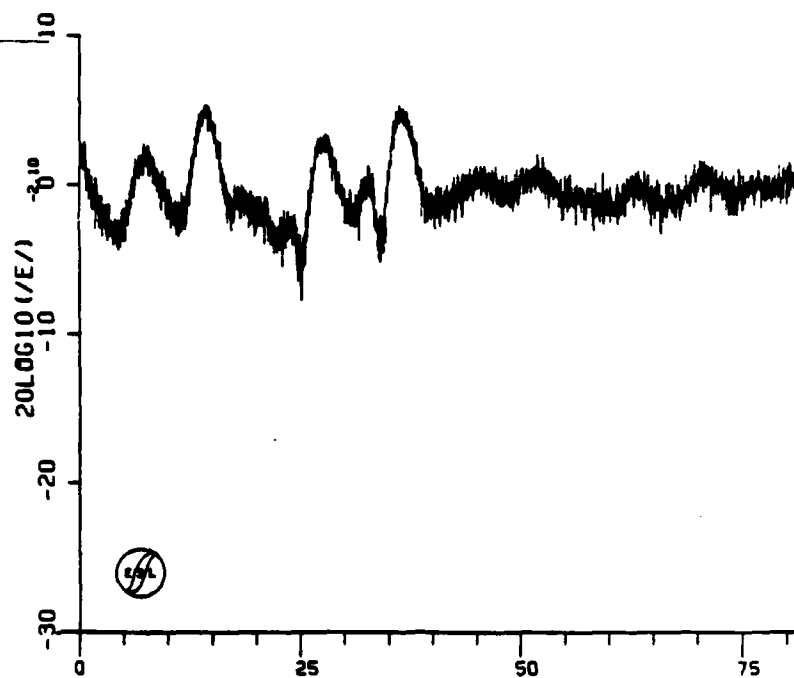


Figure 5-15. HOPE Pass 23 Downlink Amplitude & Phase



TIME-- SECONDS

PHASE OF FIELD
H29052281100HZ
START TIME- 01:39:48.960

Figure 5-16. HOPE Pass 29 Amplitude & Phase

The second pass missed the cloud shadow. Pass 3 exhibits some ringing as shown in Figure 5-2. This pass was apparently to the northeast of the cloud transiting high along the field lines without the propagation path cutting the bulk of the background ion cloud. Although the transit direction is different, it is similar to Pass 8. This pass was near the striation on-set time observed optically. The striation on-set times as observed from A-105, C-6 and Tyndall were $R+15^m20^s$ (2322:57Z), $R+17^m10^s$ (2324:47Z) and $R+17^m13^s$ (2324:50Z), respectively.

The next two passes missed the cloud shadow, reflecting the difficulty of obtaining good optical track data during this period. Pass 6 at $R+30$ minutes was the first pass to show deep fading superimposed on a large defocus as shown in Figure 5-3. This pass is very similar to JAN Pass 11 and several passes seen during the STRESS Experiment.

Passes 6, 7, 8, and 9 shown in Figures 5-3 through 5-6 provide an interesting set of data. By comparing the aircraft ground track in Figure 4-3 with the fading data observed, the occultation geometry relative to the striated portion of the ion cloud can be inferred. It would appear from the ground track that Pass 6 was likely to have been through the most intense scintillation region. Pass 7 interestingly appears to have gone through the unstructured portion of the ion cloud tail to the south of the structured portion as the total phase windup shown in Figure 5-4 is nearly the same as that observed in Figure 5-3 for Pass 6. However, there are only minor amplitude fluctuations associated with Pass 7. It is interesting to note the similarity between Passes 6 and 8. Pass 8, occurring approximately 9 minutes 26 seconds after Pass 6, transited higher up the field lines. Moreover, Pass 8 unlike Pass 6 did not appear to penetrate the ion cloud tail. The total phase windup was approximately five cycles as opposed to approximately 27 cycles during Pass 6. The net effect appears to be less defocusing. The diffraction effects are remarkably similar indicating good coupling up the field lines, but more importantly suggest that freezing may already have occurred by $R+30$ minutes and the striations are now moving as a unit. Alternatively, this may also be a result of the slower drift velocity at this time.

The radar data given in Reference 8 shows that beginning at R+30 minutes the cloud began to change its drift direction from northwest to slightly west of south. During these four passes the cloud was only slowly moving southward. Thus, we view the structured cloud to the north and the gross ion cloud tail to the south. Pass 9 again transits the ion cloud tail and appears to catch a few major striations low along the field line altitude. Again the one prominent fade feature is evident and closely resembles that observed in Passes 6 and 8.

The radar data indicates that there was a substantial southward drift velocity around this time. Passes 10, 11, and 13 show very little fading or phase activity. Pass 12 showed moderate fading as the aircraft caught up to the ion cloud, but has not been included here. Figure 5-7 showing Pass 10 which was just south of Pass 8 shows virtually no ionization present. This is consistent with Pass 8 just catching the high altitude portion of the striations. Pass 10 is included as a good example of the normal non-fading signal quality. The minor bump in amplitude and phase around 60 seconds into this plot coincides with the region that an occultation would have occurred had the cloud remained stationary. Thus, the small bump may be due to small residue ionization.

HOPE Passes 14, 15, 16, 17, and 19 all show strong fading. These, with the exception of Pass 16 which was partially lost when the analog tapes were being changed on the aircraft, are plotted in Figures 5-8 through 5-11. They all show strong fading with the peak phase decreasing from pass to pass. These passes occurred between R+1^h7^m and R+2^h5^m. HOPE Pass 18 showed no fading and is not included.

Passes 20 through 23 are included in Figures 5-12 through 5-15. They show moderate late-time fading with little phase windup. Pass 29 ended at R+2^h34^m and is shown in Figure 5-16 as an example of the very late time fading observed.

HOPE Passes 20 and 21 (Figures 5-12 and 5-13) show a weak structuring outside the main ion cloud to the west. This may be the result of transiting some striations high up the field. This does not seem plausible as the phase shown in

Figure 5-12 for Pass 20 would indicate a lower altitude transit than for Pass 21 with the same level of amplitude perturbation. This may be an indication of weak structuring in the ion tail, or it may indicate that the leading striations have drifted apart where they have become isolated and are diffusing away.

It was observed during the STRESS Experiment that the total integrated electron content or peak phase windup along the aircraft line-of-sight followed a linear slope when plotted versus the logarithm of time. The peak phase windup given on these plots is corrupted by diffraction effects, but is close to the peak dispersive phase obtained on back-propagation. Figure 5-17 is a plot of the integrated electron content versus time using the peak phase windup from the downlink tone data. The resulting curve obtained for JAN is shown for comparison. Generally, the data indicates that the early time passes did not transit the maximum electron density region of the barium ion cloud. It also suggests that as the cloud ion density decayed the radar had difficulty tracking and, thus, the striations may have continued southward rather than to the west as the radar indicated.

5-3 HOPE DOWNLINK SUMMARY.

Summarizing, the downlink propagation data for event HOPE is of high quality. Several interesting passes are available that provide data on high and low altitude plasma coupling. In particular, Pass 8 provides a high altitude transit that appears to have cut the bulk of the striations without cutting a significant portion of the background ion cloud. With the exception of the large defocus seen during Pass 1, the data are as one would expect based on the STRESS Experiment.

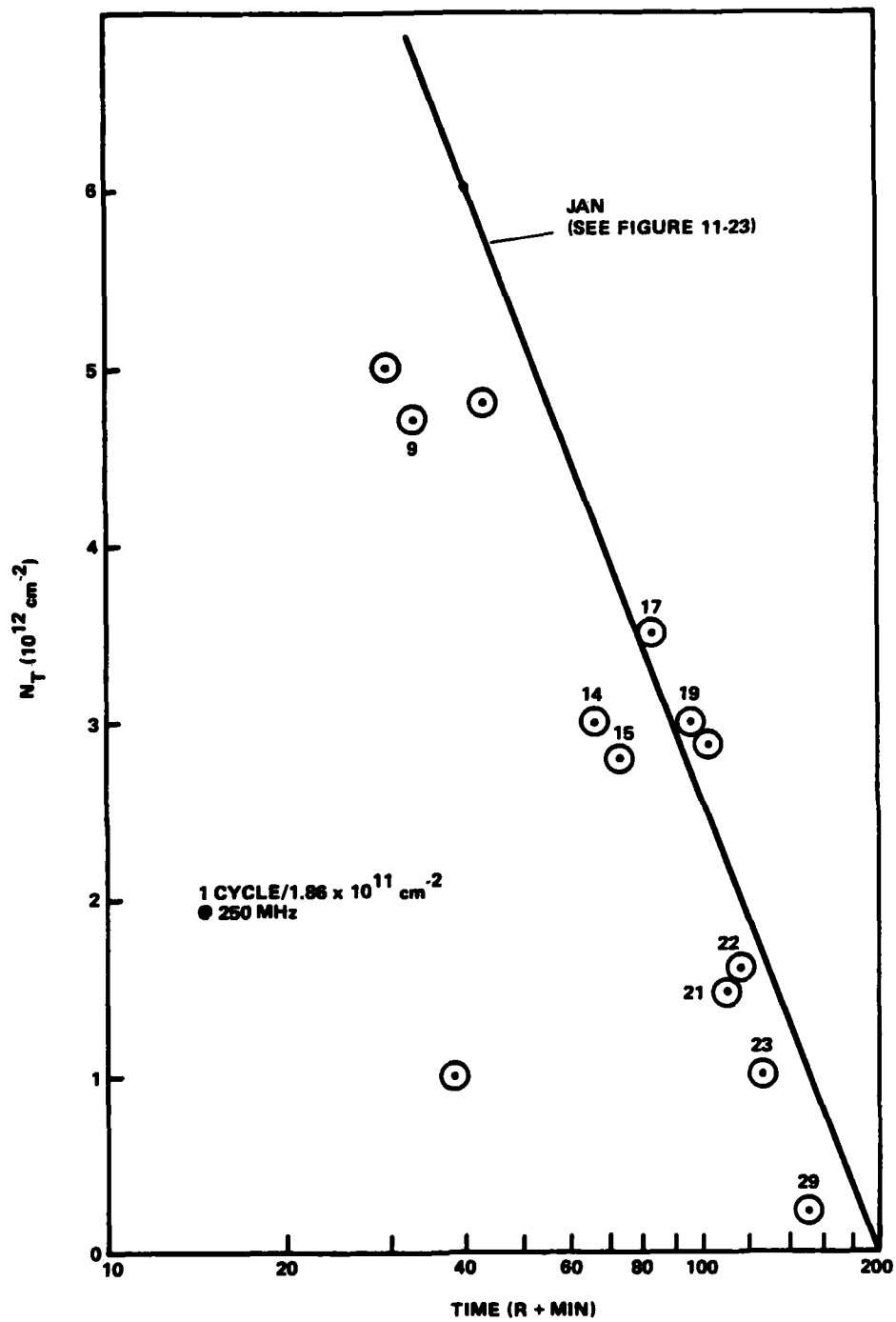


Figure 5-17. Integrated Electron Content Versus Time for HOPE

SECTION 6

HOPE UPLINK TONE DATA

6-1 INTRODUCTION.

The uplink tone signal is transmitted from the aircraft (Doppler precorrected) at 341 MHz to the LES-8 satellite. Doppler correction is provided by a K-band (39.6 GHz) reference signal generated at the satellite coherently with the downlink tone. At the satellite, the inphase and quadrature components of the signal are sampled and sent back down on the K-band data link (reference signal) to the aircraft.

Reception of the uplink tone data requires K-band phase lock for Doppler pre-correction. Loss of lock also results in the loss of data demodulation on the K-band data link. Loss of K-band phase lock was a problem during GAIL due to an antenna misalignment on the aircraft. Just prior to release on IRIS an oscillator failed in the airborne K-band receiver resulting in no usable uplink data for IRIS. Good uplink data was obtained following HOPE and JAN.

6-2 UPLINK PROPAGATION MEASUREMENTS DURING HOPE.

Uplink data was received for 32 of the 33 passes during HOPE. No data was received for Pass 1 due to loss of the K-band Doppler correction signal. Moderate to strong fading was observed during several of the 32 passes. A summary of these passes were given in Table 4-1. Plots of the received uplink amplitude and phase are given in Figures 6-1 through 6-9. These plots can be compared with plots of the HOPE downlink data given in Figures 5-2 through 5-14. Except for the satellite processing non-idealities described in Appendix B, the uplink data should provide a better estimate for the cloud integrated electron content on back-propagation processing, since the link frequency is 341 MHz as opposed to 250 MHz where the diffraction effects are worse. That is, the received signal phase should more closely resemble the actual integrated electron content profile.

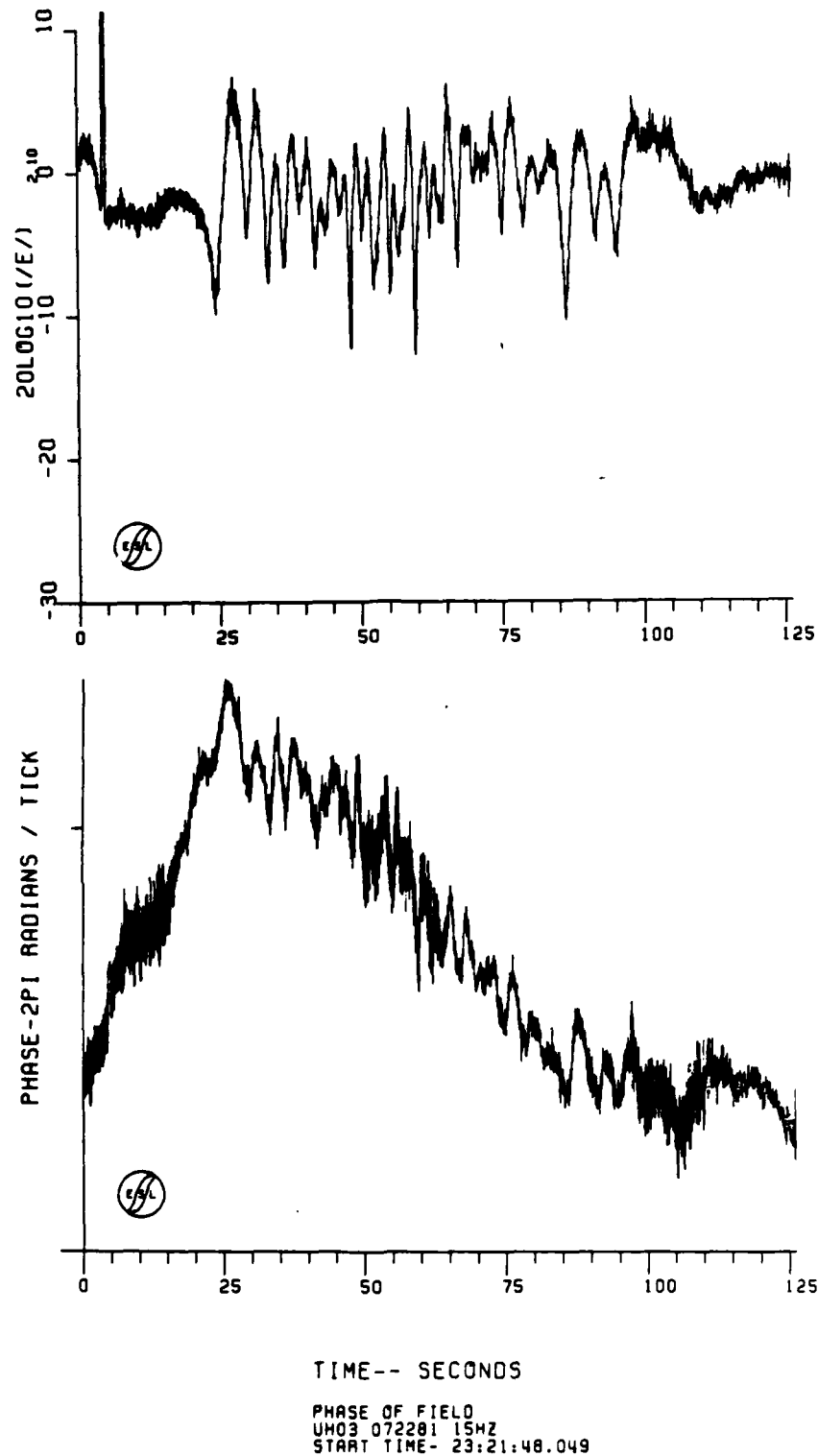
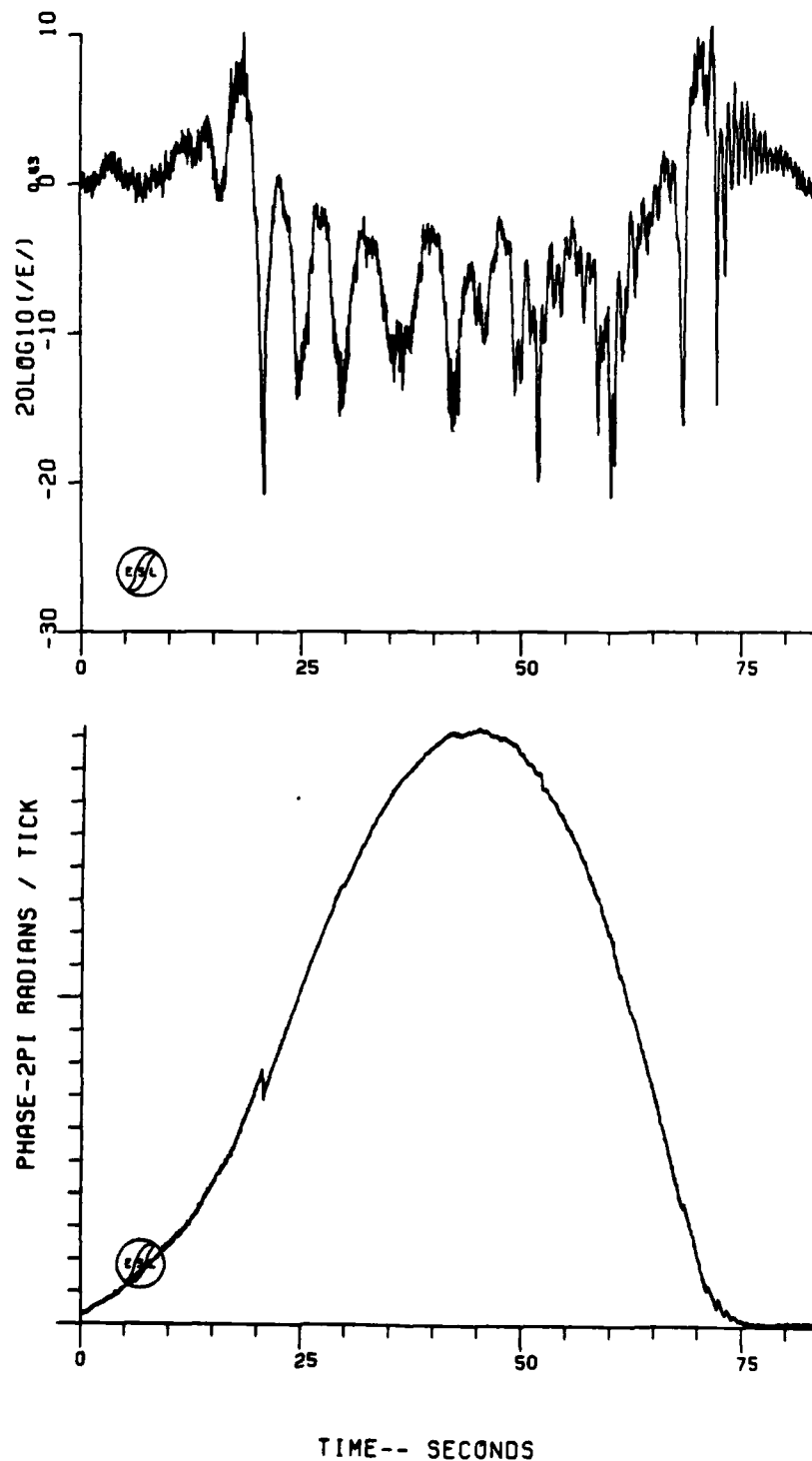


Figure 6-1. HOPE Pass 3 Uplink Amplitude and Phase



TIME-- SECONDS

PHASE OF FIELD
UH06 072281 15HZ
START TIME- 23:36:50.552

Figure 6-2. HOPE Pass 6 Uplink Amplitude and Phase

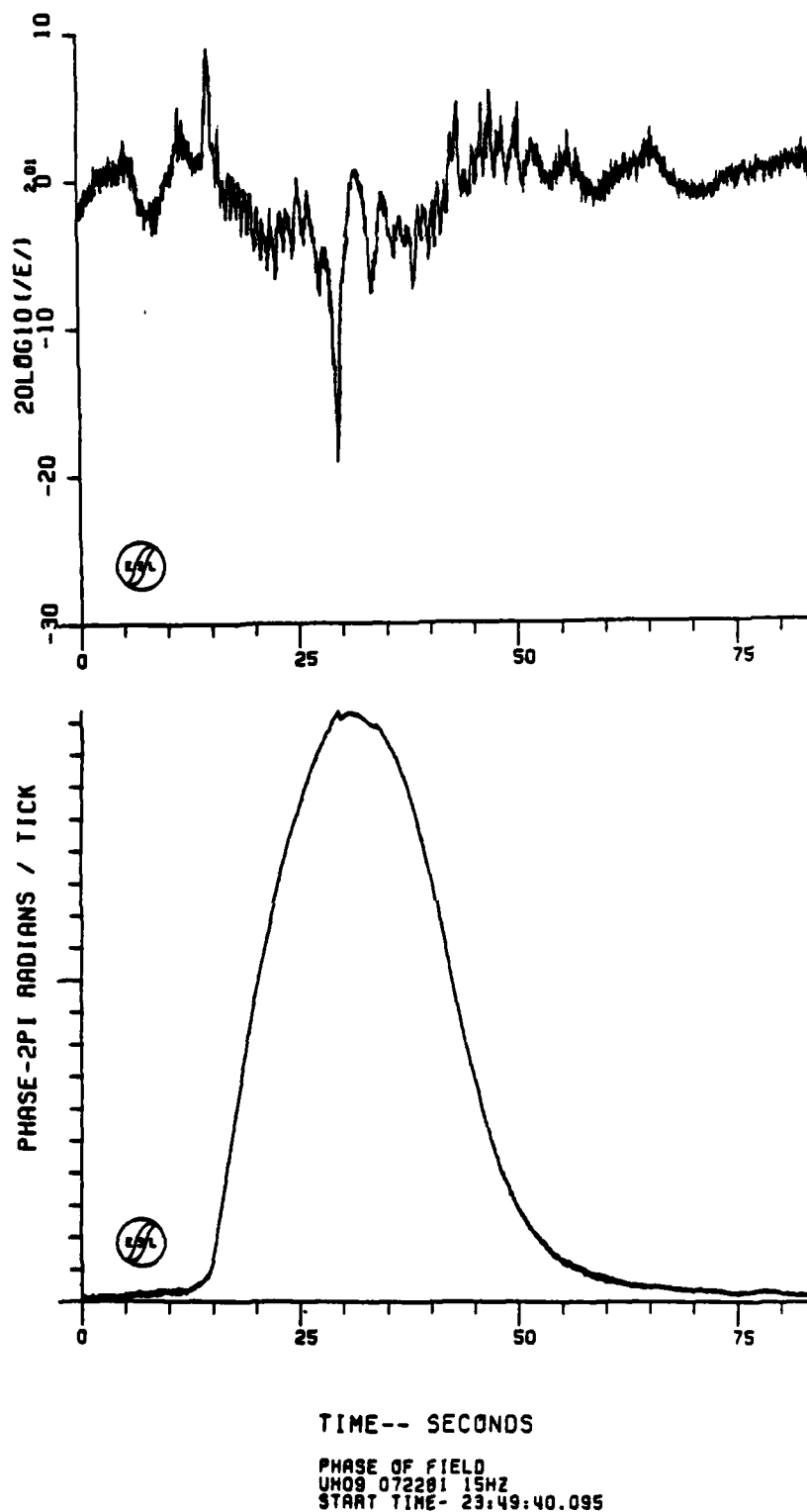
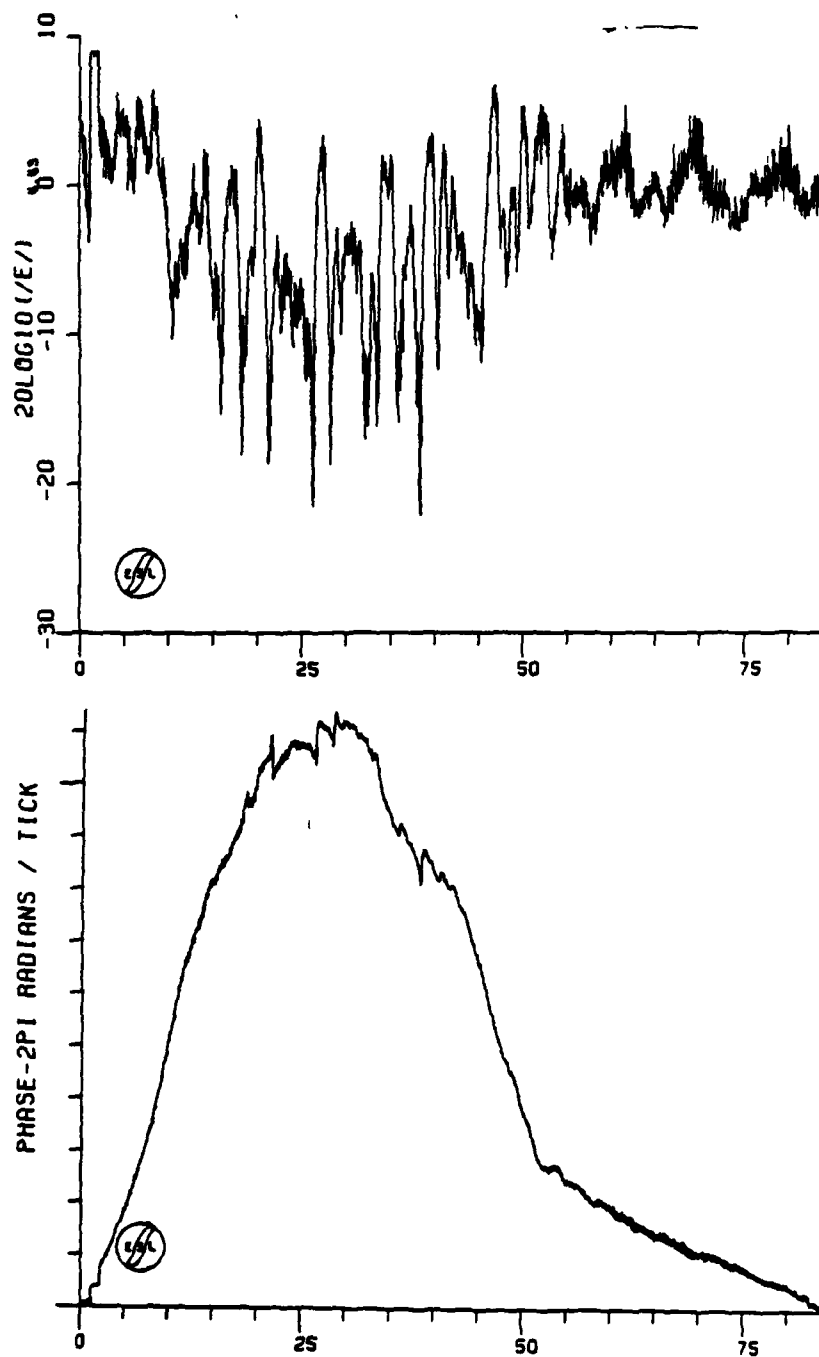


Figure 6-3. HOPE Pass 9 Uplink Amplitude and Phase



TIME-- SECONDS

PHASE OF FIELD
UH14 072201 15HZ
START TIME- 00:14:20.971

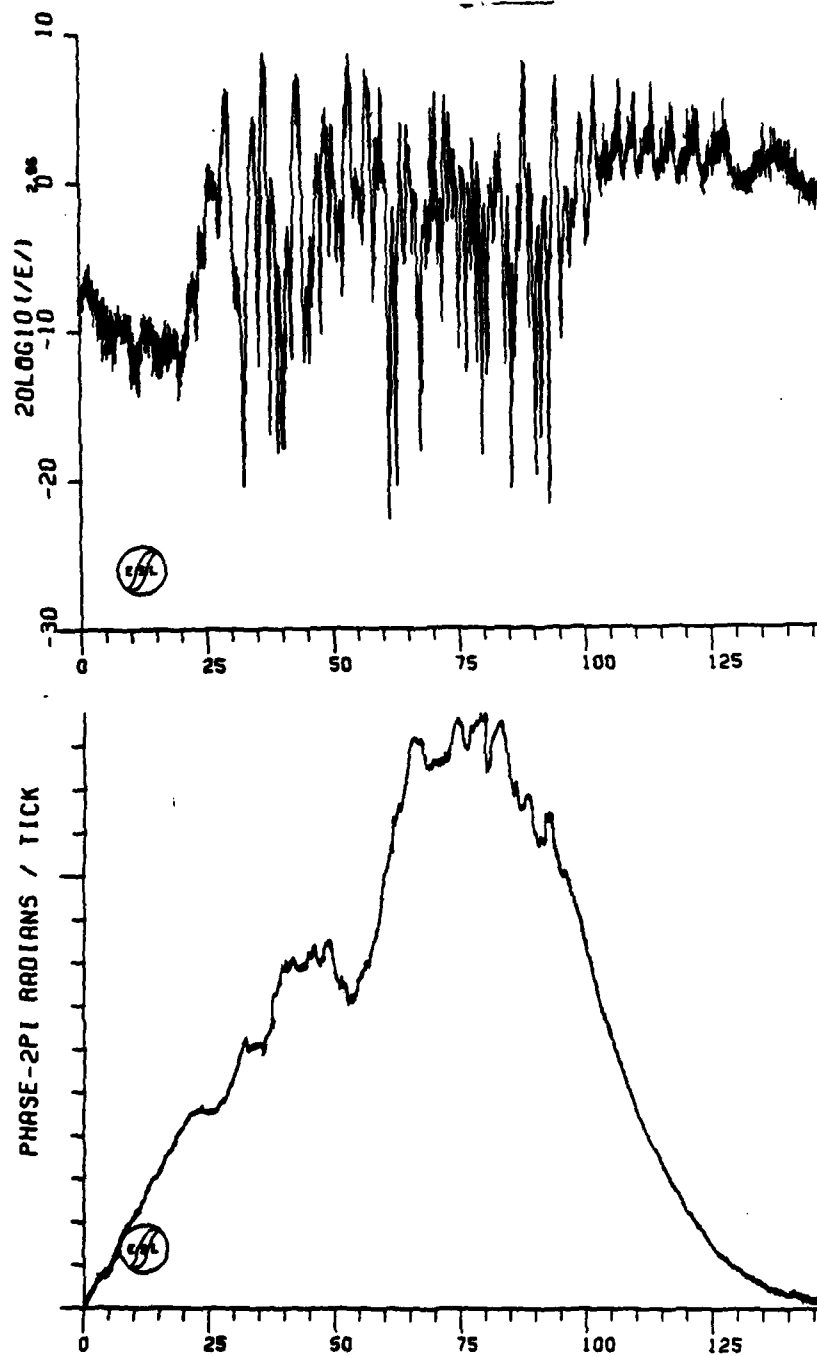
Figure 6-4. HOPE Pass 14 Uplink Amplitude and Phase

QSN=ESL3913.HOPE.PAS17.TOPAS22.UP
REC. NO. 2 3 4 5 6 7 8

PS0318
DTM

12/14/81

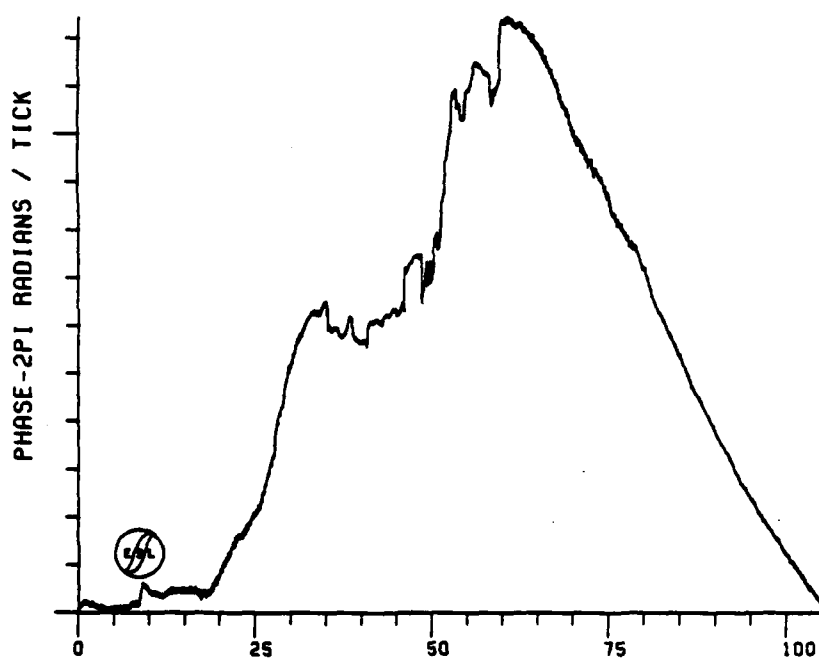
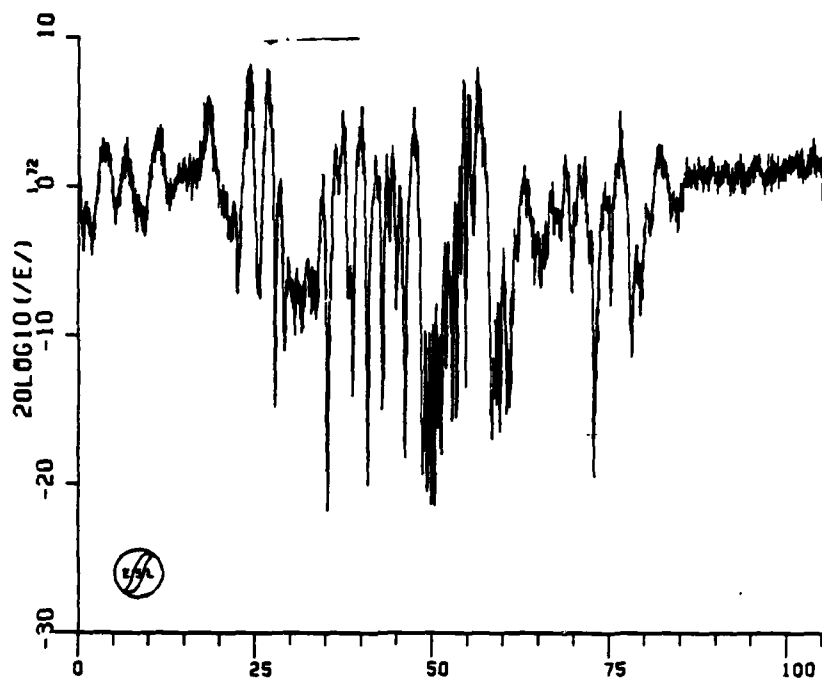
17:45:13



TIME-- SECONDS

PHASE OF FIELD
UH17 092181 15HZ
START TIME- 00:29:20.826

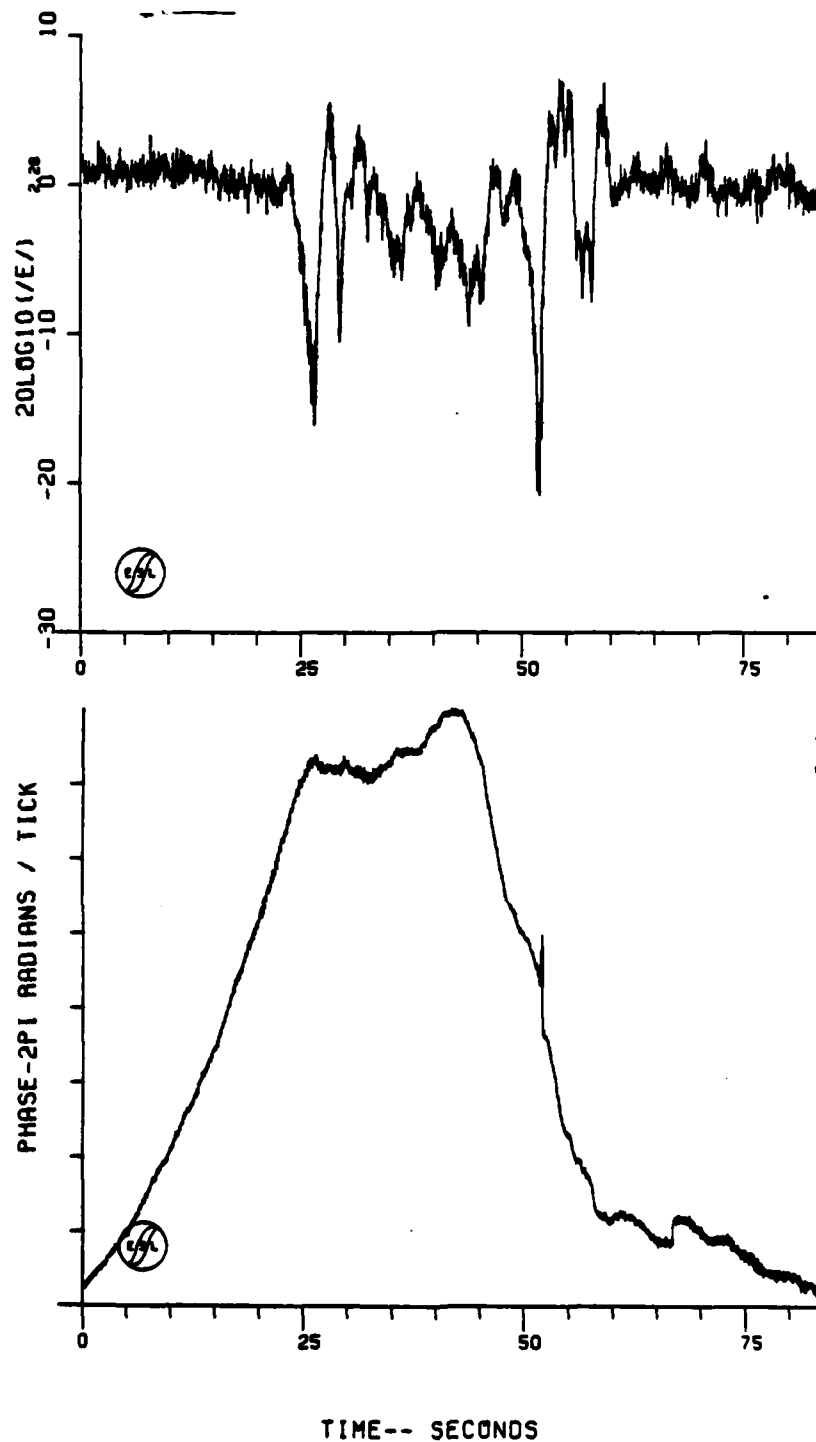
Figure 6-5. HOPE Pass 17 Uplink Amplitude and Phase



TIME-- SECONDS

PHASE OF FIELD
UN19 092181 15HZ
START TIME- 00:43:32.648

Figure 6-6. HOPE Pass 19 Uplink Amplitude and Phase



TIME-- SECONDS

PHASE OF FIELD
UM20 092181 15HZ
START TIME- 00:49:47.953

Figure 6-7. HOPE Pass 20 Uplink Amplitude and Phase

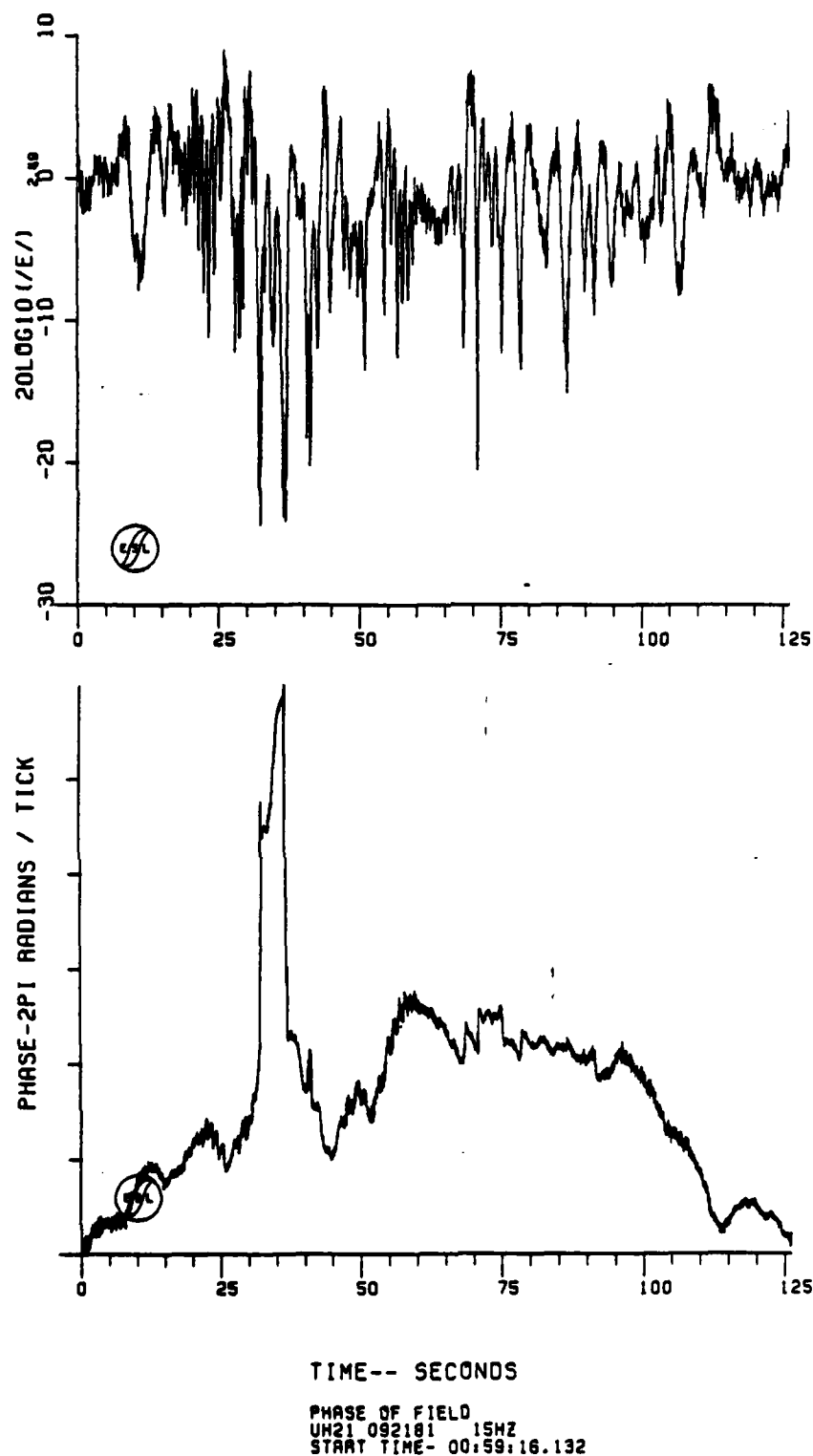
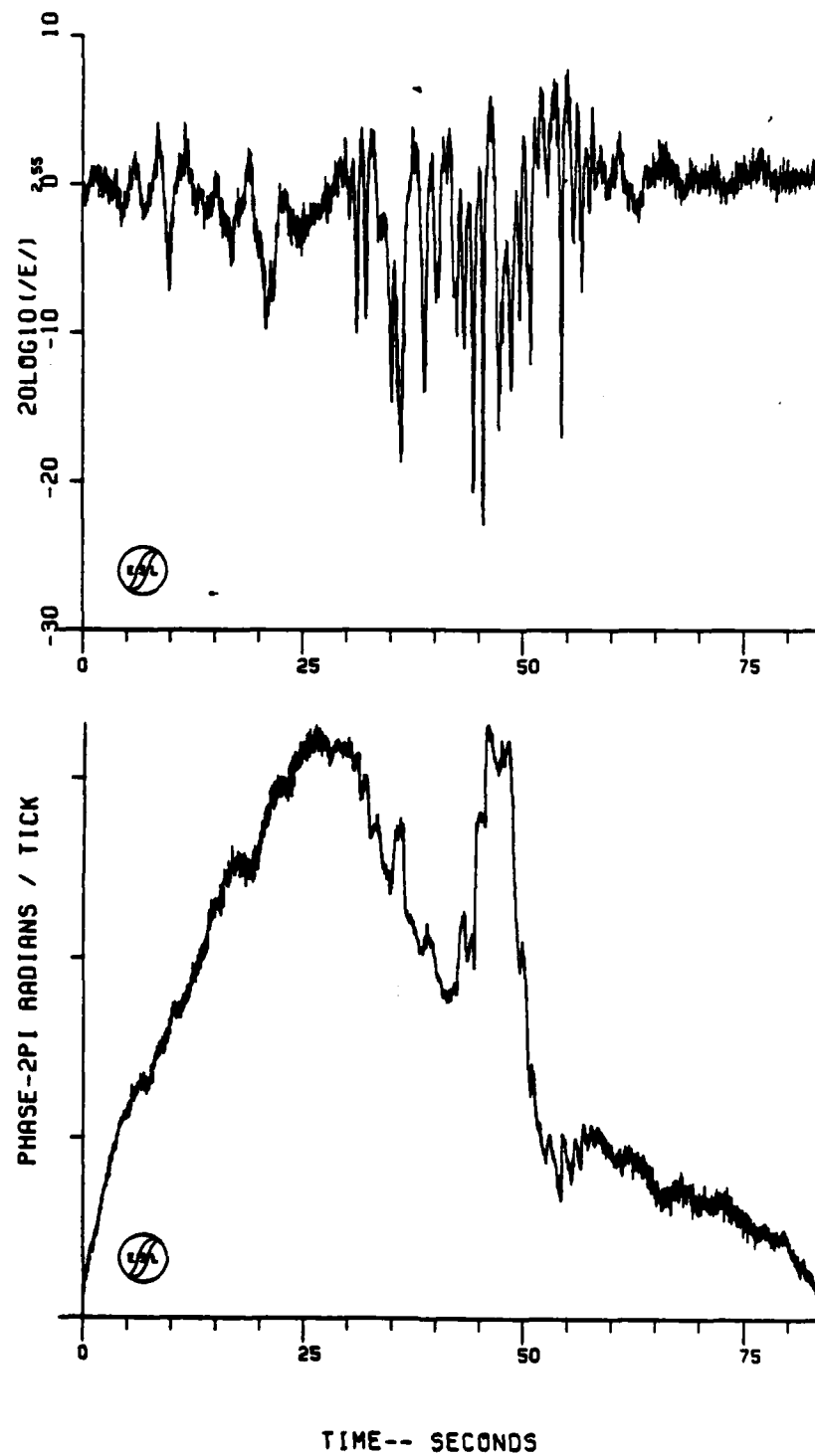


Figure 6-8. HOPE Pass 21 Uplink Amplitude and Phase



TIME-- SECONDS

PHASE OF FIELD
UM22 072281 15HZ
START TIME- 01:04:42.230

Figure 6-9. HOPE Pass 22 Uplink Amplitude and Phase

HOPE Pass 3 exhibits the same ringing observed on the downlink as shown in Figure 6-1. The phase for this pass shows some noise, but lacks any of the gross cloud structure expected for an early time pass, as did the downlink. Again, this pass coincides with the time striations were first evident optically. The aircraft probably flew to the northeast of the cloud transiting high on the field lines.

HOPE uplink Passes 4 and 5 missed the cloud shadow and are not included here.

HOPE Pass 6 was the next pass where fading was seen. The amplitude and phase data in Figure 6-2 appear substantially different than the downlink data (Figure 5-3). The amplitude shows a large defocus lasting for about 50 seconds with large focuses at each end lasting about 5 seconds. The phase is smooth and has a fairly Gaussian shape and exhibits far less diffraction effects.

HOPE uplink Passes 7 and 8 looks much the same as the downlink data and is not presented.

HOPE Pass 9 shown in Figure 6-3 is similar to the downlink data (Figure 5-6). This pass started at R+43 minutes and lasted about 80 seconds. For this pass the aircraft transited the striations low along the field lines, but cut most of the unstructured bulk ionization.

HOPE Passes 10 through 13 showed little or no fading and are not presented.

Pass 14, shown in Figure 6-4 was the next pass to show any significant fading during HOPE. The data shows deep fading superimposed on a slight defocus. The phase shows a large gross-cloud component with small phase bumps.

HOPE uplink Pass 15 showed strong fading but was extremely noisy and difficult to process. HOPE Pass 16 was partially lost during the change of analog tapes on the aircraft. No plots for these two passes are included.

HOPE Pass 17 was the next uplink pass to show strong fading. It is plotted in Figure 6-5. The amplitude shows strong fading with very little defocusing present. The phase is remarkably similar to the downlink shown in Figure 5-10. This uplink phase bumps should better reflect the ion cloud structure. HOPE uplink Pass 18 showed no fading and is not included here.

The phase for HOPE Pass 19 is similar in its gross shape to Pass 17 as can be seen by comparing Figures 6-5 and 6-6.

HOPE Passes 20, 21, and 22, shown in Figures 6-7, 6-8, and 6-9 were the last uplink passes to show fading. The amplitude data shows moderate fading with no large defocusing. The large isolated phase feature seen in Pass 22 (Figure 6-9) also appears in the downlink phase data (Figure 5-14). The large isolated phase feature seen in Figure 6-8 for Pass 21 may or may not be real as the downlink phase data does not show a similar feature (Figure 5-13). The phase unwrapping plotting routine could miss it or conversely have cycle skipped. It would be necessary to reprocess the data with a higher sampling rate to resolve this issue. No significant fading was observed during Passes 23 through 33 for the uplink data.

6-3 HOPE UPLINK SUMMARY.

Summarizing, the uplink propagation data for event HOPE is of high quality. The uplink data is consistent with the downlink data presented in Section 5. The uplink phase data presumably provides a better indication of the actual ion cloud structure due to its higher frequency. The uplink phase data has shown the presence of some isolated ion cloud features at late time that may relate to the rather abrupt cessation of scintillation effects. Time has not permitted a complete processing of all of the uplink data. In particular, back-propagation processing of the uplink data has not been attempted.

SECTION 7

BACK-PROPAGATION PROCESSING FOR HOPE

7-1 INTRODUCTION.

Backward propagation of the received signal diffraction pattern swept out by the aircraft can be computationally performed on a computer using thin phase screen angular spectrum techniques. The amplitude diffraction effects can, thus, effectively be removed leaving only the phase perturbations due to the integrated electron content plasma fluctuations along the propagation line-of-sight. The extent to which the amplitude fluctuations diminish is a function of the extent of the striated plasma along the line-of-sight and the amplitude and phase noise received during the measurement.

Back-propagation processing was conducted for all of the HOPE downlink passes for which doppler corrected phase data was available. The downlink data back-propagated very well with several passes showing large decreases in the S_4 scintillation index. A few uplink data passes were examined, but did not back-propagate nearly as well as measured by the decrease in the S_4 scintillation index. As the uplink data would require considerably more effort to process, it was not examined further and, with the exception of some data for JAL, it has not been included in this report.

The back-propagation processing was performed using the same routines as developed for the STRESS Experiment, although the processing interval employed here was expanded to encompass the entire cloud. This appears to allow one to visually distinguish between the gross cloud features and the random cloud properties when examining the phase power spectral density (PSD). On the other hand, it does not permit an evaluation of the differing phase PSD slopes over different portions of the occultation interval as was examined previously. For completeness the back-propagation processing routines are described in Appendix E.

A summary of the downlink back-propagation data are presented in Table 7-1. This table includes the scintillation index before and after back-propagation, the phase power spectral density break frequencies and slopes, and the back-propagation distance. The scintillation index, S_4 , is a measure of the amplitude fluctuations of the signal. The amount it decreases with back-propagation and its value after back-propagation give a good indication as to how well the pass back-propagated in a thin phase screen sense. The back-propagation distance was chosen by looking at plots of the amplitude and phase and finding the back-propagation distance where they looked the smoothest and also by computing the S_4 index and finding the distance where it was a minimum. In most cases, these two methods indicated the same distance.

The break frequencies, slopes and D.C. spectral height for the phase power spectral densities, were estimated by determining the best fit to the assumed functional form for the phase power spectral density of the random component of the phase given by

$$S_{\phi}(f) = \frac{K}{[1 + (f/f_0)^2]^{N/2}} ; \quad (7-1)$$

or in terms of the usual phase screen parameters,

$$S_{\phi}(v) = \sigma_{\phi}^2 \frac{2}{\sqrt{\pi}} \frac{\Gamma(\frac{N}{2})}{\Gamma(\frac{N-1}{2})} \frac{\ell_0}{[1 + (\ell_0 v^2)]^{N/2}} \quad (7-2)$$

where

ν = spatial frequency in cycles per kilometer

λ_0 = outer scale size (kilometers)

σ_ϕ^2 = Rayleigh phase variance (rad^2)

$10 \cdot N$ = asymptotic slope in dB per decade.

The asymptotic slope of the phase PSD is given in dB/decade or ten times the index N . It is important to note that due to the gradual roll-off (as opposed to a sharply defined break frequency), the best fit to the data is often achieved with an index N that is approximately one higher than one might estimate with a straight line asymptote.

Consistent with the assumed functional form, the break frequency is defined as the point where $\lambda_0 \nu = 1$. The real break frequency, f_0 , obtained from the data can be converted to a spatial frequency (cycles per kilometer) by dividing by the transverse field (or pattern) velocity, V_1 . Thus the outer scale size is related to f_0 through the expression

$$\lambda_0 = V_1 / f_0 \quad (7-3)$$

The phase variance is obtained from the D.C. spectral height K and the break frequency f_0 as

$$\sigma_\phi^2 = \frac{\sqrt{\pi}}{2} \frac{\Gamma(\frac{N-1}{2})}{\Gamma(\frac{N}{2})} (K f_0) \quad (7-4)$$

The transverse field velocity is the transit velocity perpendicular to the striations in the viewing plane. The transverse field velocity can, thus, be estimated by computing the velocity transverse to the magnetic field line projection from the satellite on to the aircraft constant altitude measurement plane. For most passes the aircraft was oriented to fly nearly perpendicular to the field line projection. The transverse pattern velocity was calculated from the aircraft track

and cloud track data as illustrated in Figure 7-1. The southerly transit velocities were typically ~210 m/s while the northerly transit velocities were typically ~180 m/s. Table 7-2 summarizes the transverse pattern velocity calculation, the cloud velocity, the aircraft velocity and the field line projection azimuth angle.

The back-propagation distances given in the table were originally calculated using an assumed 200 m/s transverse pattern velocity for each aircraft transit. To obtain the adjusted back-propagation distance, the back-propagation distances were then scaled according to the ratio of the square of the actual and assumed velocities and tabulated as the corrected distance. The resulting adjusted distances should be close to the slant range to the center of cloud effects. This value as indicated is found to be between 163 and 278 kilometers. Using the aircraft altitude of 11.66 kilometers and the LES-8 elevation angles defined previously in Figure 1-1, the approximate cloud transit altitude for each pass has been estimated to be between 128 and 211 kilometers as indicated in Table 7-1. These appear to be consistent with the radar and optical observation data for the actual ion-cloud altitudes.

The estimation of the outer scale size, the Rayleigh phase variance, and the spectral index is sensitive to an interpretation of the gross (or deterministic) cloud spectral shape. Any systematic approach taken tends to bias the result and becomes a somewhat subjective interpretation. As a result, several possible values of these parameters are indicated in Table 7-1 for each pass along with a value that is regarded a best estimate. The procedure used is described in Section 7-4 along with the spectral fit for the readers interpretation.

Table 7-1. HOPE Downlink Back-Propagation Summary

Pass	S_4 at Ground	S_4 Min.	Distance to Minimum (km)	Corrected Distance (km)	Phase PSD		Outer Scale f_o (km)	Spectral Height $S_4(0)$ (dB-MHz ² /Hz)	σ_{θ}^2 (rad)	Transverse Pattern Vel. V_{\perp} (m/s)	Best Fit	Intercept Altitude (km)	Comments
					Slope M (dB/Decade)	Break Freq. f_b (Hz)							
3	0.48	-	-	-	-	-	-	-	-	-	-	-	No S_4 min. found
6	1.35	-	-	-	-	-	-	-	-	-	-	-	Excellent back-propagation but gross cloud only
7	0.98	0.42	170	-	N/A	N/A	N/A	-	N/A	-	-	-	Aircraft turning - did not back-propagate well
8	1.01	-	-	-	-	-	-	-	-	-	-	-	Excellent back-propagation weak fading, one deep fade
9	1.17	0.26	159	225	30	0.079	3.00	13	1.26	238	A	153	Representative of noise only back-propagation
10	0.11	0.15	A11	-	N/A	N/A	1.19	2	0.56	-	B	-	Good back-propagation
14	0.97	0.62	179	187	30	0.087	2.34	20	2.95	204	A2	128	-
15	0.76	0.55	250	224	30	0.092	2.22	21	3.40	-	A	-	-
17	0.96	0.55	210	171	30	0.128	1.58	20.5	3.59	-	B	-	-
19	0.84	0.52	240	176	36	0.172	1.19	17	2.71	190	A	161	-
20	0.53	0.45	265	-	60	0.242	0.79	12.5	1.59	-	B	-	-
21	0.96	0.61	270	210	40	0.121	1.57	15.5	1.84	180	A2	125	-
22	0.77	0.63	170	163	40	0.089	2.13	22.5	3.53	172	A	128	-
23	0.53	0.36	310	278	40	0.102	1.86	18.5	2.38	-	B	-	-
29	0.59	0.26	480	257	50	0.224	0.80	20	3.86	-	A2	-	-
					40	0.134	1.34	22	4.08	-	B	-	-
					38	0.095	1.89	28.5	7.42	-	A	-	-
					30	0.063	2.73	27	5.62	-	A2	-	-
					44	0.110	1.56	24	4.49	-	B	-	-
					38	0.072	2.39	29.5	7.24	-	A	-	-
					30	-	-	-	-	-	-	-	S_4 min. not well defined. No break freq.
					30	0.099	1.77	20	3.15	176	A2	162	Good back-propagation
					40	0.118	1.49	20.5	3.22	-	B	-	-
					30	0.060	2.93	26	4.89	-	A	-	-
					44	0.215	0.91	17.4	2.94	196	B	128	S_4 min. not well defined
					34	0.158	1.24	20	3.76	-	A2	-	-
					50	0.261	0.75	17	2.95	-	A	-	-
					30	0.100	1.96	24	5.01	189	A	211	Good back-propagation
					40	0.046	4.07	23.5	2.86	-	A	-	-
					44	0.063	3.00	22.5	2.86	-	B	-	-
					44	0.085	2.23	18.5	2.09	146	A	208	-
					40	0.158	0.92	7.5	0.84	-	A	-	-
					60	0.074	1.98	15.5	1.24	-	B	-	-

* - Assumes constant pattern velocity of 200 m/s
 B - Best estimate
 A - Acceptable alternate
 A2 - 2nd alternate choice

Table 7-2. Transverse Pattern Velocity, V_{\perp}

Pass	$V_c \angle (\pi + \xi)$	V'_c	$V_{a/c} \angle \gamma$	Field Line Projection Angle η	$V'_{a/c}$	V_{\perp}
9	20 \angle 185°	14.9 m/s	257.9 \angle 131.6°	53°	252.8 m/s	237.9 m/s
14	"	16.4	232.8 \angle 131.5	60	220.8	204.4
15	"	16.6	177.0 \angle -41.3	61	172.9	189.5
17	"	17.1	176.0 \angle -48.0	64	163.2	180.3
19	"	17.8	180.7 \angle -53.7	68	153.7	171.5
21	"	18.5	173.1 \angle -41.2	73	157.9	176.4
22	"	18.7	240.1 \angle 137.4	74	214.7	196.0
23	"	18.9	197.7 \angle -44.4	76	170.5	189.4
29	"	19.8	180.5 \angle -49.5	86	126.5	146.3

$V'_c = |V_c| \sin(\gamma - \eta - \xi)$, ion cloud vel. perpendicular to field line projection
 $V'_{a/c} = V_{a/c} \sin(\gamma - \eta)$, aircraft velocity perpendicular to field line projection
 $V_{\perp} = V'_{a/c} - V'_c$, transverse pattern velocity.

The HOPE back-propagation phase data spans intervals that consist of unstructured gross cloud, strongly structured clouds, late time structure with little gross background cloud ionization, and noise only data. These data are contained in Figures 7-2 through 7-35. Plots are included for each pass given in Table 7-1. Plots of the back-propagated amplitude and phase are followed by plots of back-propagated phase power spectral density and the signal angular spectrum. The angular spectrum is invariant under the back-propagation processing which does not affect the angular distribution of the propagating plane waves.

The phase PSD may be converted from units of $\text{radian}^2/\text{Hz}$ to spatial units of $\text{radian}^2/\text{kilometer}$ by multiplying the ordinate by the transverse field velocity V_{\perp} and at the same time dividing the abscissa by the transverse velocity to convert from Hz to cycles/kilometer. The abrupt roll off in the phase PSD and the angular spectrum plots past 15 Hz is due to the one pole Butterworth 15 Hz filter used in the processing of the downlink data for noise reduction. The thermal noise floor appears around $-30 \text{ dB-Rad}^2/\text{Hz}$ on these plots.

The real frequency axis, f , of the angular spectrum plots can be converted to angle, θ , through the transform

$$\theta = \sin^{-1} (f\lambda/V_{\perp}) \quad (7-5)$$

where V_{\perp} is the transverse field velocity and λ is the RF wavelength ($\lambda=1.198$ meters for the downlink).

Care should be taken when comparing one pass with another because the transit time and the frequency scale can differ from pass to pass. Further, the transverse pattern velocity is different for each pass. The appropriate value for the transit velocity is given in Table 7-1. It should be noted that the angular spectrum only provides a measure of the relative power received versus angle-of-

arrival and has not been calibrated to the actual received power. The thermal noise floor appears around -30 dB-watts/Hz on these plots. The one-pole noise filter causes the abrupt roll-off in the angular spectrum beyond 15 Hz.

Passes 3 and 6, while included in Table 7-1, when back-propagated did not result in an S_4 minimum. For this reason no back-propagation data have been provided. Pass 3 exhibited some minor ringing from effects either high up the field line or from refraction in the plane of the field line projection. This pass was near the striation on-set time and, thus, presumably would not be representative of random striation effects. Passes 4 and 5 missed the cloud shadow. Pass 6 exhibited a large defocus with random fading superimposed. The lack of success in back-propagating this pass may be due in part to the large defocus which may result in significant energy being refracted along the field line projection plane.

Pass 7 appears to have occulted an unstructured portion of the ion-cloud tail to the south of the structured region as described in Section 5.2. The back-propagation was highly successful as can be seen by comparing Figures 5-4 and 7-2. The back-propagation has narrowed the Gaussian bell shape of the phase, removing the slight defocusing and spreading associated with the forward propagation of the received signal. The phase PSD shown in Figure 7-3 provides a good reference for the nominal phase PSD due to the gross cloud and can be compared with the data from other passes in order to guide one's intuition in estimating the random phase PSD. The angular spectrum shown in Figure 7-4 indicates an abrupt limit to the angular spectrum near 1.7 Hz. This is due to the finite limit to the cloud shadow. Using Equation (7-5) with a pattern velocity of approximately 200 m/s, the angular width of the cloud subtended at the aircraft is approximately 1.1 degrees. For a corrected back-propagation distance of approximately 187 kilometers, the cloud width can be estimated to be approximately 3.6 kilometers. This is reasonable given a view to LES-8 along the stretching plane of the cloud and through the thinly stretched ion cloud tail.

The aircraft turned during the fading interval of Pass 8. As a result the phase data includes a differential phase contribution from the relative change in path length of the reference K-band antenna and the subject UHF antenna which cannot be removed. Thus, the back-propagation was unsuccessful.

HOPE Pass 9 again appears to have transited the ion cloud tail, but it did cut a few striations. This pass back-propagated extremely well as can be seen by comparing Figure 7-5 with 5-6. The phase PSD reflects the striation phase structure near the center of the pass as can be seen in comparing Figure 7-3 with Figure 7-6. The random phase structure manifests itself as a shallowing of the phase spectrum slope between approximately 0.1 and 1 Hz. The angular spectrum provided in Figure 7-7 exhibits an abrupt limit near 2.6 Hz. This corresponds to a cloud width of approximately 5.9 kilometers, consistent with a pass nearer the main body of the striations.

HOPE Pass 10 has been included to provide a comparison of the back-propagated signal with no fading present. The back-propagated amplitude and phase are almost identical to the received signal (compare Figures 5-7 and 7-8). The amplitude is flat with an S_4 index of 0.15, increased slightly from 0.11 before back-propagation. The phase PSD and the angular spectrum shown in Figures 7-9 and 7-10, respectively, reflect the noise in the doppler removal process and the thermal noise floor. The small spikes evident in the phase PSD and the angular spectrum at 2 and 4 Hz is believed to be due to the receiving system hardware and is not an artifact of the subsequent processing performed. These spikes were not evident in the STRESS Experiment data. In almost all cases these spikes are below the received signal spectrum.

Passes 11, 12, and 13 show little fading or phase activity and were not back-propagated. Pass 14 was the first strong Rayleigh fading pass that back-propagated well. Only the right and left edges of the cloud appear not to have back-propagated well which may be an indication that the striations are stretched over sufficient distance along the propagation path so as not to be well represented

by a single thin phase screen. Compare Figure 7-11 with Figure 5-8. The striation phase structure appear superimposed on top of the dominant gross ion-cloud. The phase PSD shown in Figure 7-12 departs significantly from that of a smooth Gaussian bell shaped phase structure around 0.05 Hz. The first three or four points are clearly associated with the power in the gross cloud phase. The break frequency associated with the random phase PSD is approximately 0.13 Hz with approximately a 40 dB/decade slope between 0.18 and 2 Hz. However, as discussed, the best fit to the functional form described by Equation (7-1) is often achieved with an index N that is approximately one higher than one might estimate with a straight line asymptote. In this case the best fit N is 3.4 or 34 dB/decade.

The angular spectrum for Pass 14 as shown in Figure 7-13 exhibits some minor bumps at 0.27, 0.70, and 0.98 Hz. These frequencies correspond to the frequencies associated with the nearly linear slopes on either side of the gross cloud, and can be calculated as follows:

$$f_1 = \left(\frac{1}{2\pi} \right) \left(\frac{\Delta\phi}{\Delta t} \right) = \left(\frac{1 \text{ cycle}}{2 \pi \text{ rad}} \right) \left(\frac{7 \pi \text{ rad} - 0 \text{ rad}}{20 \text{ sec} - 6 \text{ sec}} \right) = +0.25 \text{ Hz}$$

$$f_2 = \left(\frac{1 \text{ cycle}}{2 \pi \text{ rad}} \right) \left(\frac{28 \pi \text{ rad} - 12 \pi \text{ rad}}{28 \text{ sec} - 20 \text{ sec}} \right) = +1.0 \text{ Hz}$$

$$f_3 = \left(\frac{1 \text{ cycle}}{2 \pi \text{ rad}} \right) \left(\frac{12 \pi \text{ rad} - 21.8 \pi \text{ rad}}{66 \text{ sec} - 54 \text{ sec}} \right) = -0.70 \text{ Hz}$$

$$f_4 = \left(\frac{1 \text{ cycle}}{2 \pi \text{ rad}} \right) \left(\frac{0.5 \pi \text{ rad} - 8 \pi \text{ rad}}{82 \text{ sec} - 68 \text{ sec}} \right) = -0.27 \text{ Hz}$$

This simply follows from the same angular association of the rate of change of signal wavefront phase with distance as expressed by Equation (7-5). It may have been illuminating to have displayed the angular spectrum as a two-sided spectrum, preserving the sense of the angle-of-arrival, however, this was not done.

HOPE Passes 15, 17, and 19 all back-propagated very well with their S_4 's going from .76, .96, and .84 to .55, .55, and .52, respectively. All three passes look similar in their shape and their statistics. They are plotted along with their angular and phase PSDs in Figures 7-14 through 7-23. The amplitude plots show some residual defocussing from the main cloud, but look very good otherwise. The back-propagated phase for these passes are smooth and show structure on top of a strong gross ion cloud.

The phase PSD's all contain resolvable gross and random components. The break frequencies and the phase PSD indices were similar for each of these passes, being approximately 0.12 Hz and 44 dB/decade, respectively. It was frequently noted in processing the PLACES data that a portion of a pass would back-propagate at a different distance than other parts indicating that the striation structure was spread over a considerable distance and that the structure cut early in the pass was, say, closer to the observer than that cut late in the pass. It would seem as if the striations were stretched along the thin ion cloud oriented at, say, 45 degrees to the path from the satellite to the aircraft, which is not unreasonable for HOPE or JAN. Pass 19 indicates two striation regions, one at 300 kilometers and one at 240 kilometers distance. The deep fade at 60 seconds on Figure 7-20 back-propagates at 300 kilometers versus 240 kilometers for the rest of the cloud. Prior to back-propagation the phase PSD slope is always near 20 dB/decade, as shown in Figure 7-15 for Pass 15. For those cases where the signal did not back-propagate well the back-propagation phase PSD may have more energy at the higher frequencies resulting in a shallower slope than it should.

The angular PSDs show some lumpiness at frequencies below .5 Hz and a dropoff to the noise floor above .5 Hz. This lumpiness is due to the small angle bending evident in the sections where the phase slope is fairly linear, as explained earlier. The angular spectrum roll-off for Pass 15 displays approximately an f^{-6} dependence.

No fading was observed on Pass 18. The back-propagation minimum S_4 for Pass 20 was not well defined. While a minimum was reached at 265 kilometers as indicated in Table 7-1, the deep fades near the center of the pass reached a minimum around 220 kilometers, where a shallow defocus was evident along with considerable residual phase interference fading. For this reason it was decided not to include back-propagation plots of this pass. At 265 kilometers the amplitude and phase were very similar to that received as shown in Figure 5-12. Since the S_4 index is more sensitive to signal focuses than fades, the effects of the background ion cloud may have biased the choice of back-propagation distance.

HOPE Pass 21 back-propagated fairly well as can be seen by comparing Figures 7-24 with the received signal in Figure 5-13. Again, a portion of the fading does not back-propagate at the same distance as the bulk of the fading. During this time frame the phase structure indicates several striation like features that may be a result of looking more nearly up the striation sheet like structure along the stretching direction of the ion cloud. (See Figure 1-1.) The back-propagated phase PSD is shown in Figure 7-25. The angular spectrum shown in Figure 7-26 displays a smooth roll-off with a slight bump at 2 Hz that may be due to the resonance in the hardware receiving system as mentioned earlier.

The phase structure of Pass 22 shown in Figure 7-27 resembles the phase structure of Pass 21. The phase must be reversed for this comparison as the aircraft flew in opposite directions on these passes. The back-propagated phase PSD and the angular spectrum are provided in Figures 7-28 and 7-29, respectively.

The next pass from HOPE which successfully back-propagated, Pass 23, is shown in Figures 7-30 through 7-32 along with its angular PSD and phase PSD. The S_4 showed a significant decrease from .53 to .36 as reflected by the fairly smooth amplitude plot. The phase plot is smooth and exhibits some structure along with a weak background ion cloud. The angular spectrum again contains a few peaks caused by the refractive bending by the edges of the gross cloud. The spike at 2 Hz is

caused by the receiving system. The angular spectrum has a break frequency of approximately 0.37 Hz or 0.13 degrees which is less than the earlier passes. The phase PSD shows the effects of the gross cloud for the first two points followed by the effects of the random phase and the noise floor. The plateau caused by the random phase structure breaks around 0.09 Hz and is followed by a 44 dB/decade slope down the noise floor.

Pass 29 exhibits some amplitude and phase bumps that are reminiscent of isolated weak structure as shown previously in Figure 5-16. This structure back-propagated extremely well as shown in Figure 7-33 at approximately the same corrected distance as Pass 23. The phase PSD shown in Figure 7-34 exhibits an extremely abrupt roll-off of nearly 60 dB/decade. The angular spectrum shown in Figure 7-35 has a break frequency of approximately 0.15 Hz which corresponds to 0.07 degrees. This pass was the last pass with noticeable scintillation activity.

7-4 PHASE PSD PARAMETER ESTIMATION.

The back-propagated phase data is dominated by a large Gaussian-like bell-shaped curve that reflects the integrated electron content through the gross (unstructured) background plasma. The contribution of the non-random gross cloud to the phase PSD must be determined in order to estimate the contributions of the random component of the phase. Any form of filtering to accomplish this separation will necessarily bias the resulting parameters. The assumed functional form for the random plasma striation phase PSD was given by Equation (7-1) as discussed in Section 7-2.

In order to obtain an obvious visual distinction between the gross cloud and the random striation effects in the phase PSD, the phase data was transformed using the phase data windowed over the entire pass. This provides resolution at the low frequencies dominated by the gross cloud. The real break frequency f_0 , the asymptotic slope $10 \cdot H$, and the D.C. spectral height $S_p(0)$ were then estimated using the templates provided in Figures 7-36 and 7-37 which follow the functional form of Equation (7-1).

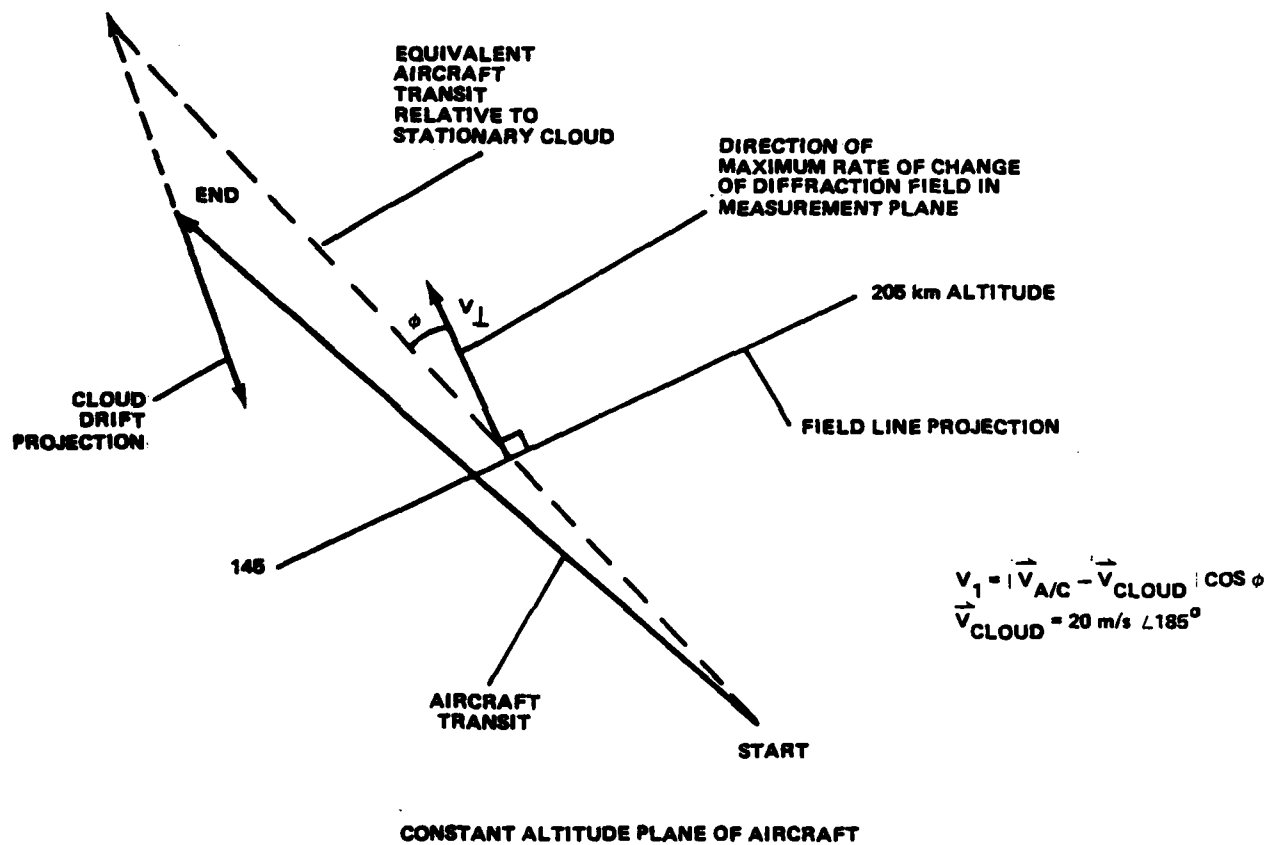


Figure 7-1. Transverse Velocity Calculation

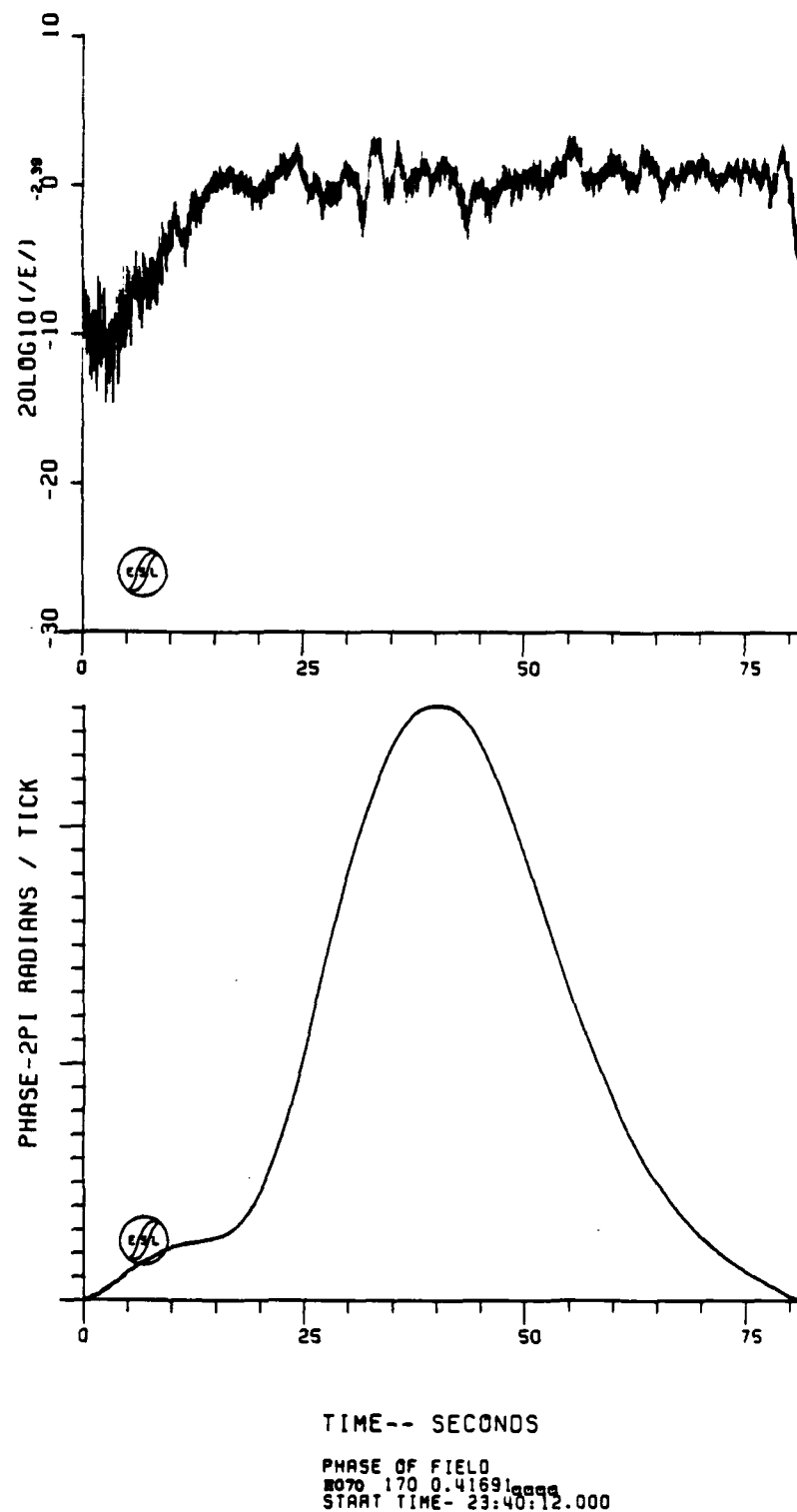


Figure 7-2. HOPE Pass 7 Downlink Back-Propagated Amplitude and Phase

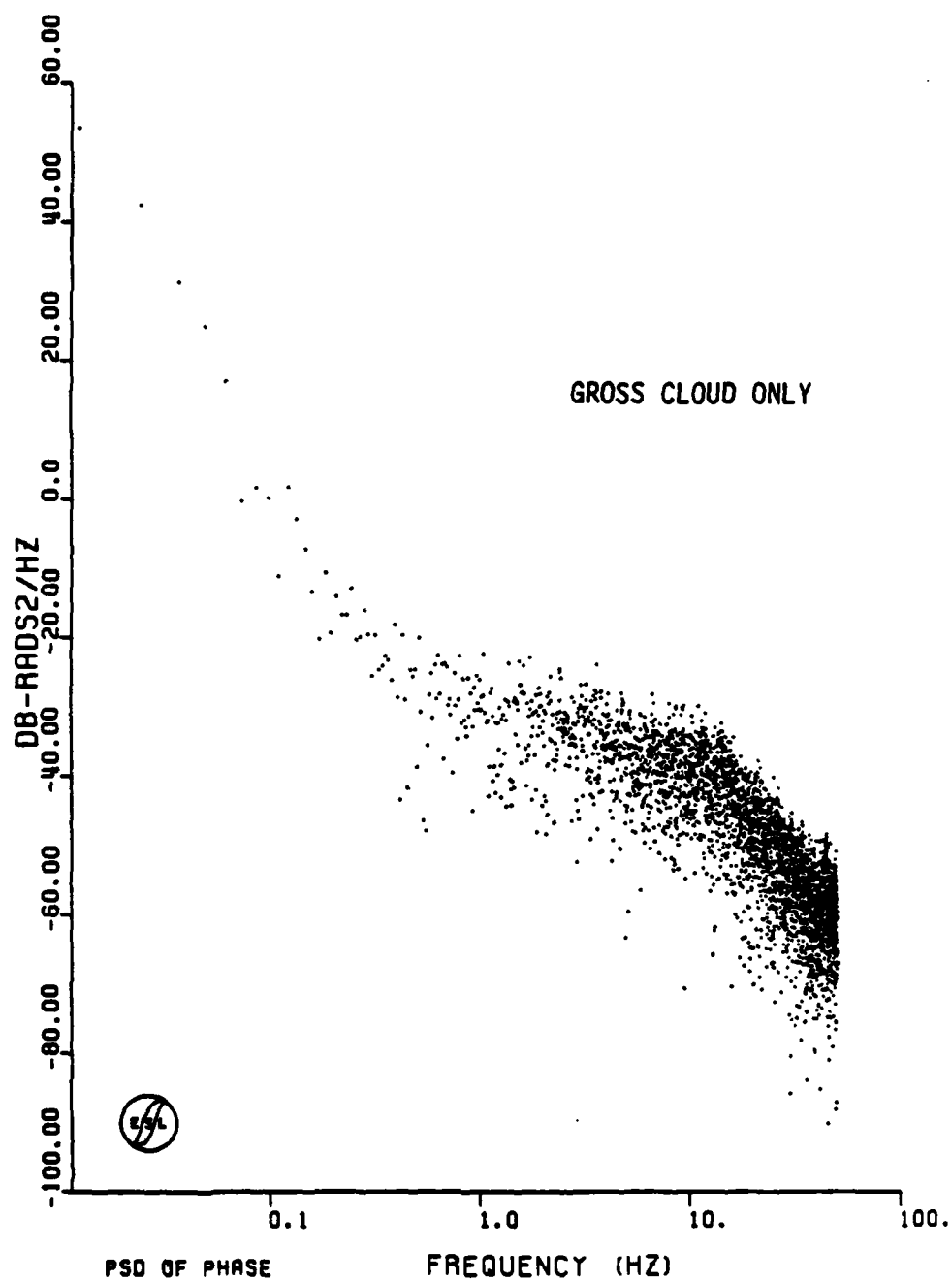


Figure 7-3. HOPE Pass 7 Downlink Back-Propagated Phase PSD

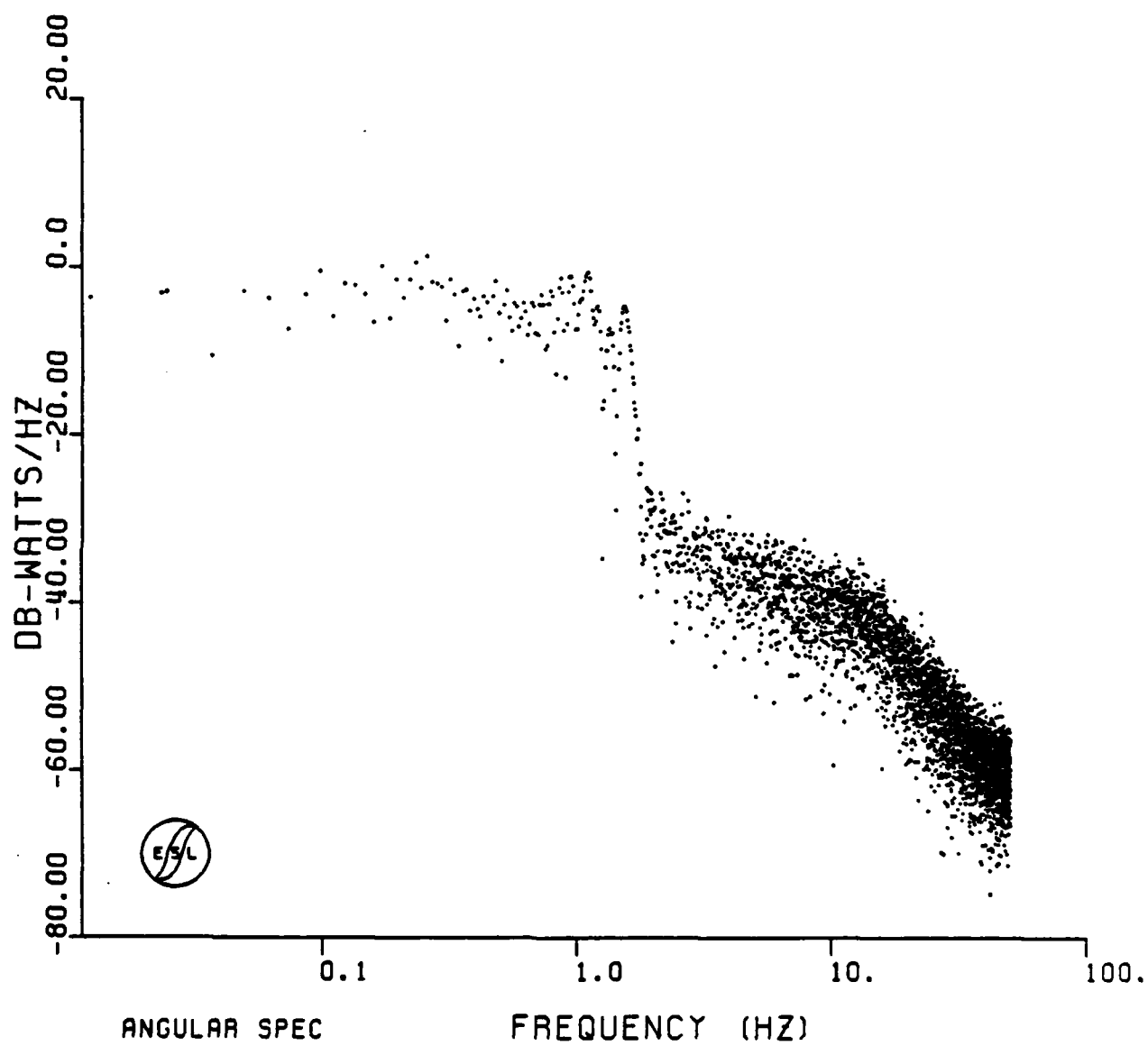


Figure 7-4. HOPE Pass 7 Downlink Angular Spectrum

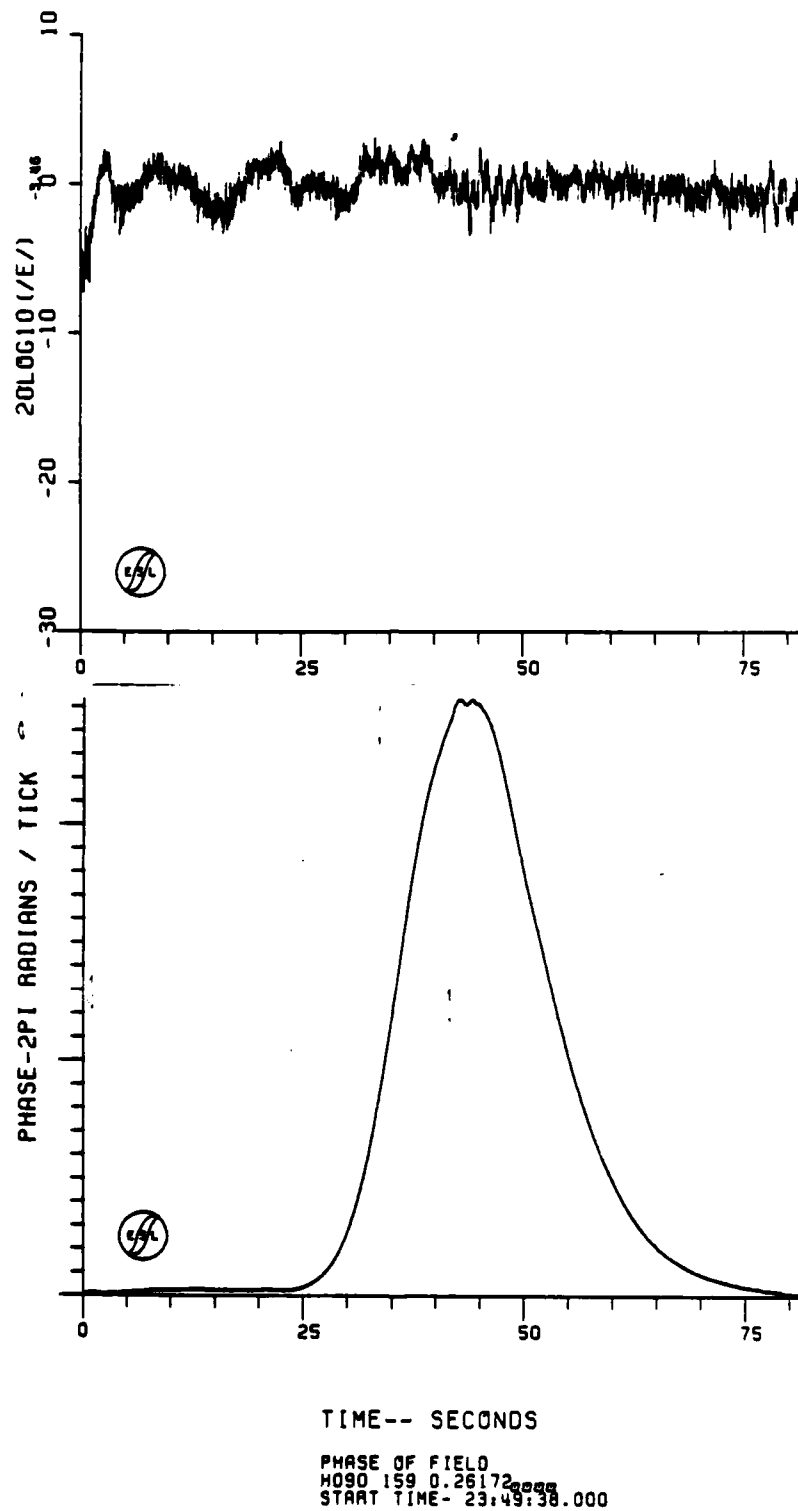


Figure 7-5. HOPE Pass 9 Downlink Back-Propagated Amplitude and Phase

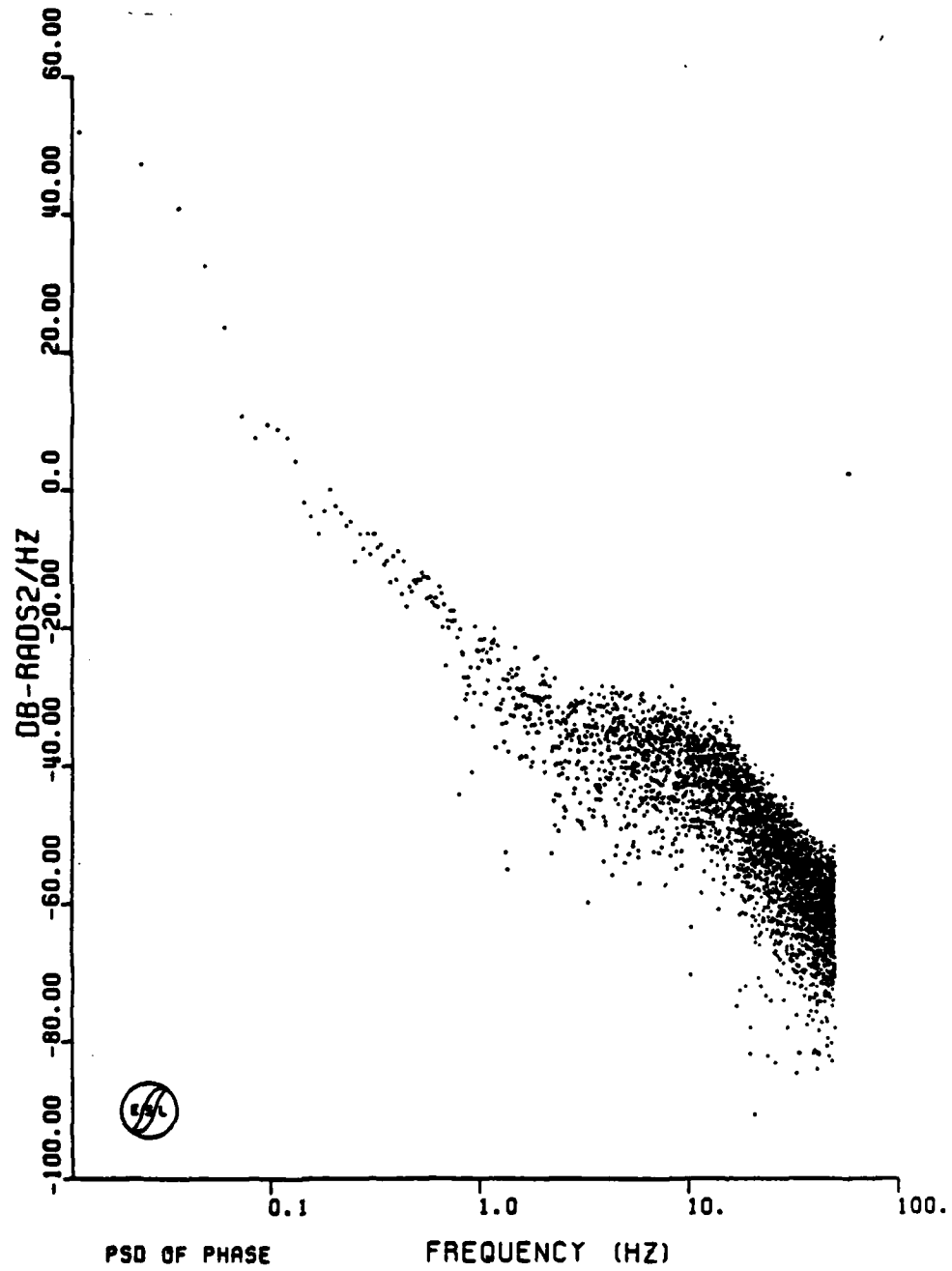


Figure 7-6. HOPE Pass 9 Back-Propagated Phase PSD

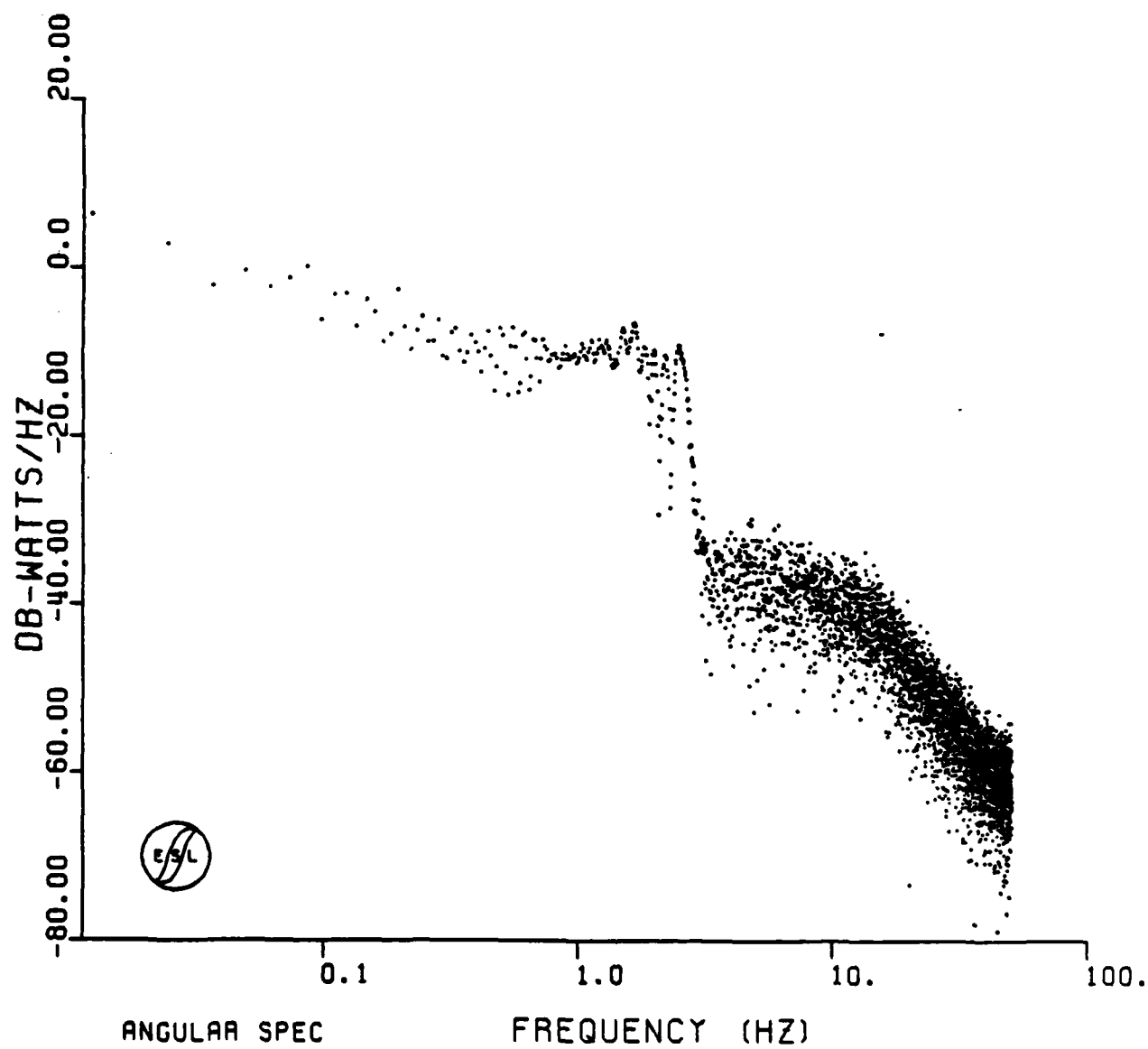


Figure 7-7. HOPE Pass 9 Downlink Angular Spectrum

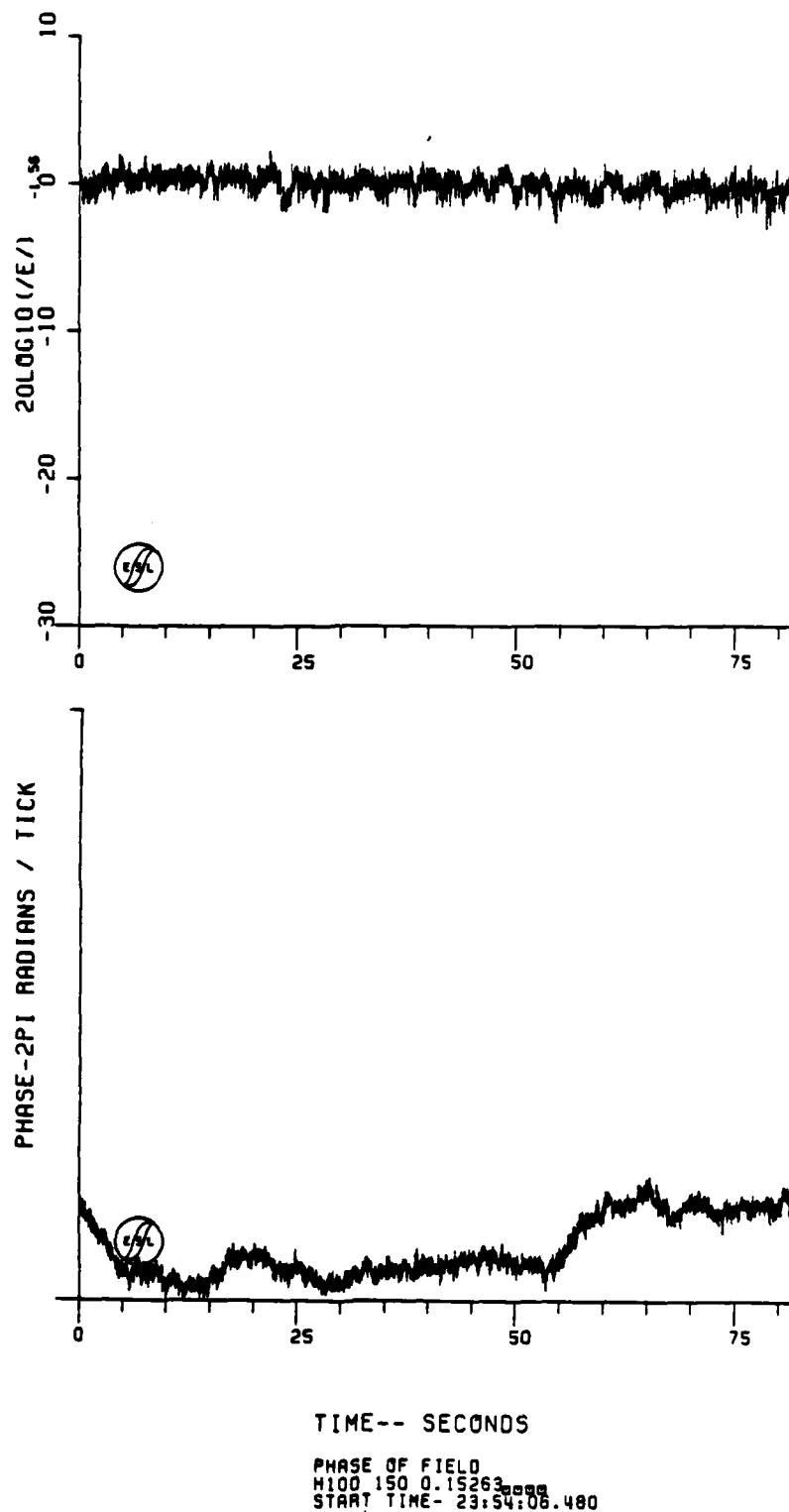


Figure 7-8. HOPE Pass 10 Downlink Back-Propagated Amplitude and Phase

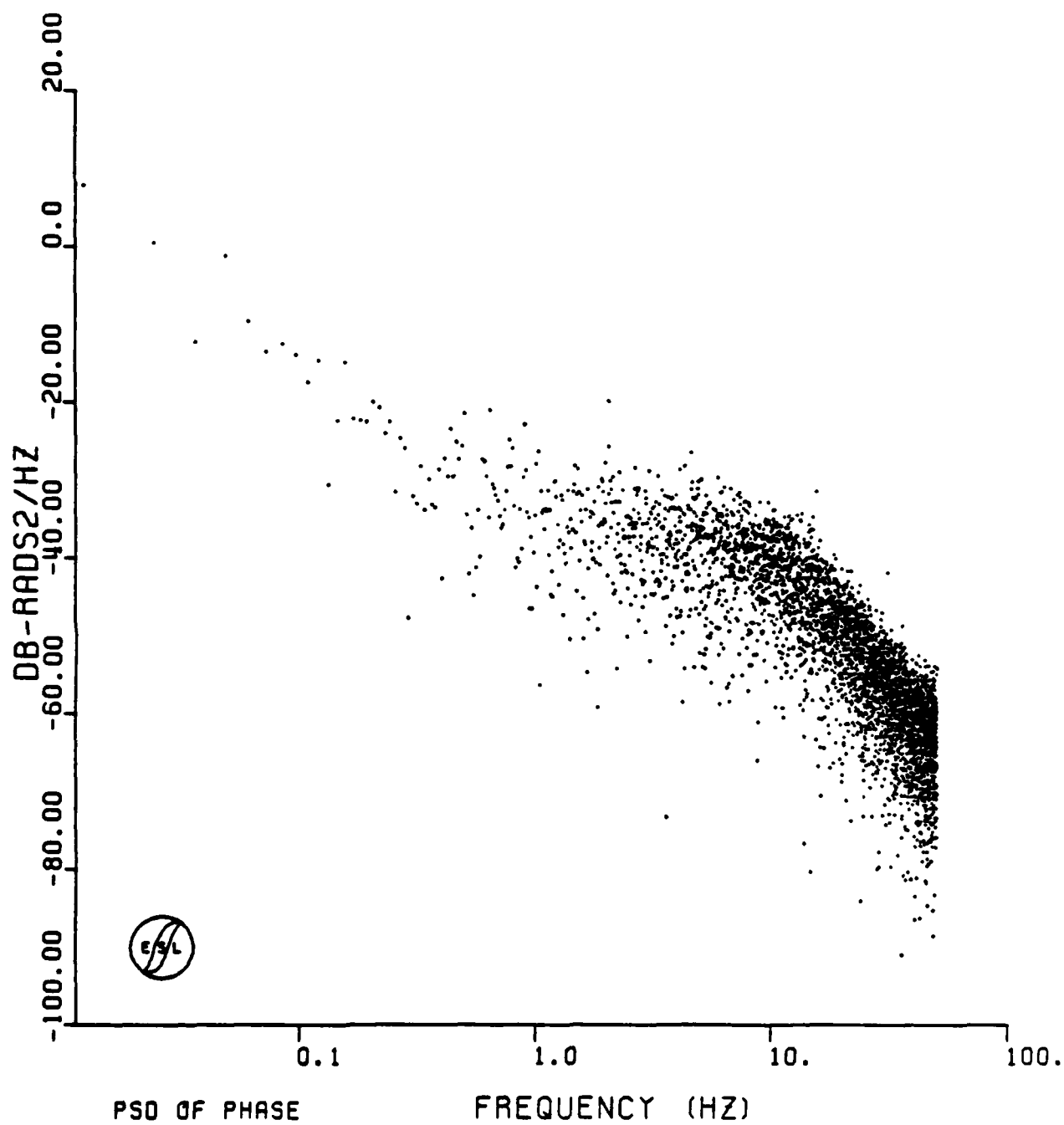


Figure 7-9. HOPE Pass 10 Downlink Back-Propagated Phase PSD

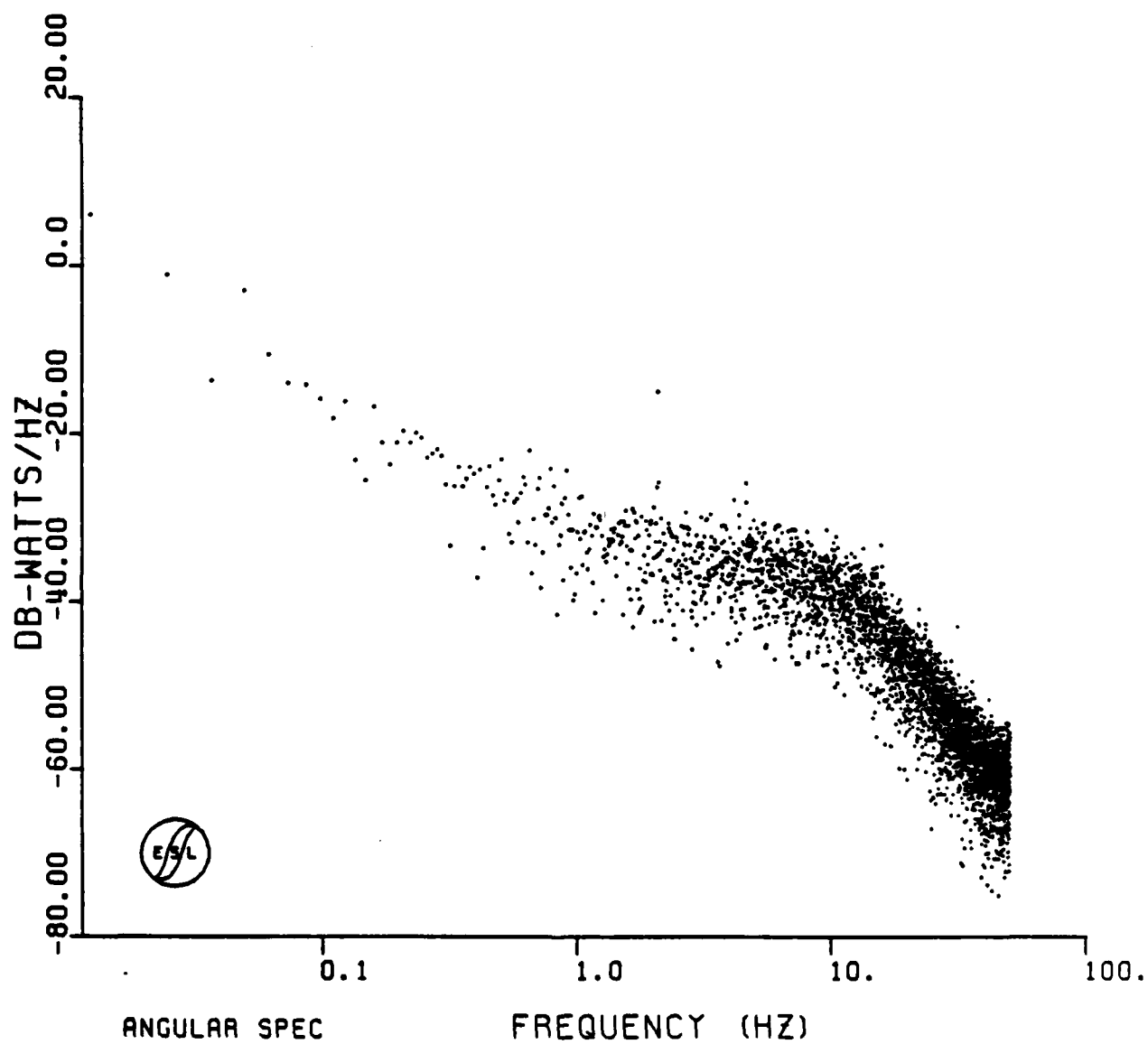


Figure 7-10. HOPE Pass 10 Downlink Angular Spectrum

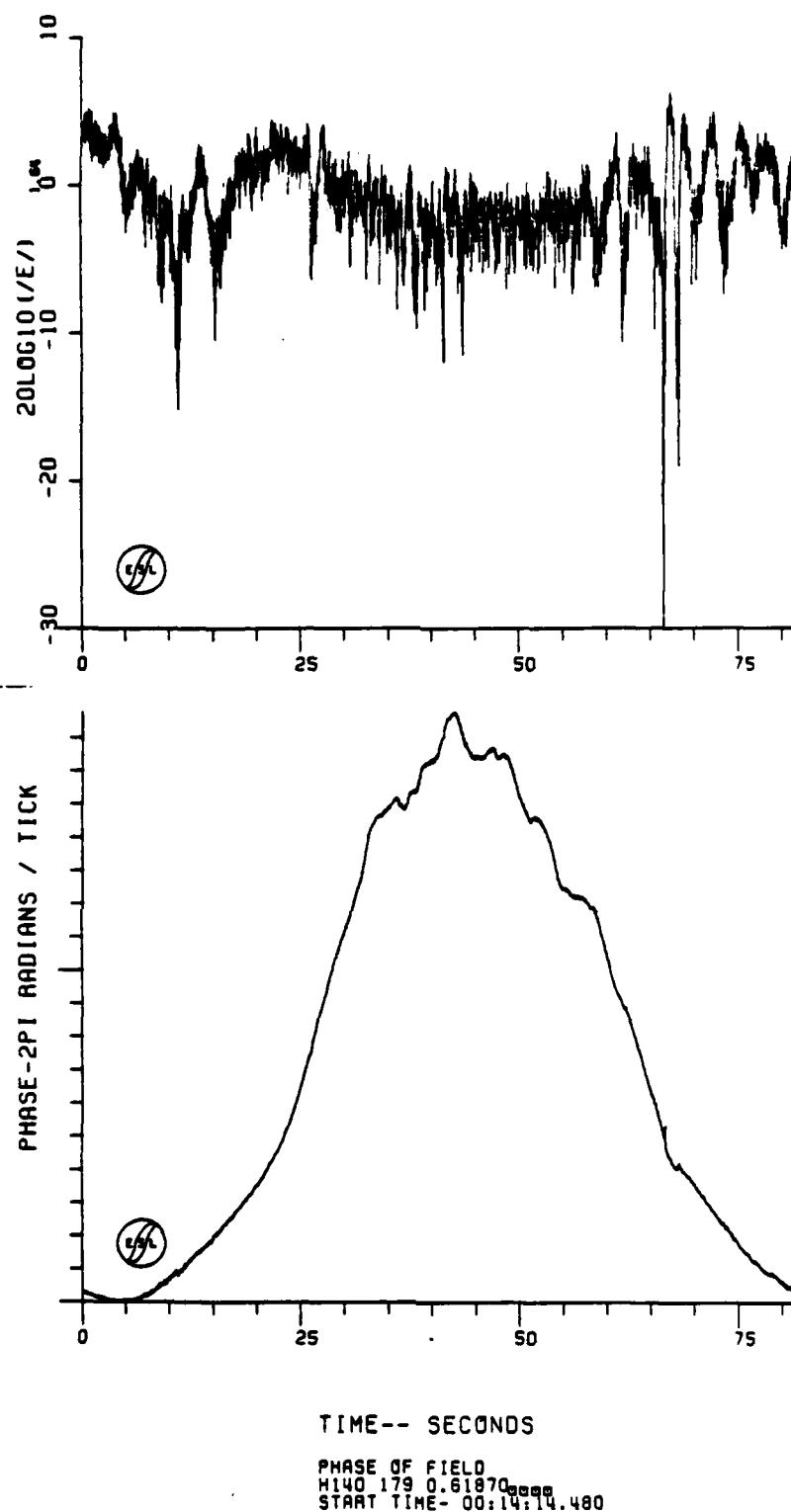


Figure 7-11. HOPE Pass 14 Downlink Back-Propagated Amplitude and Phase

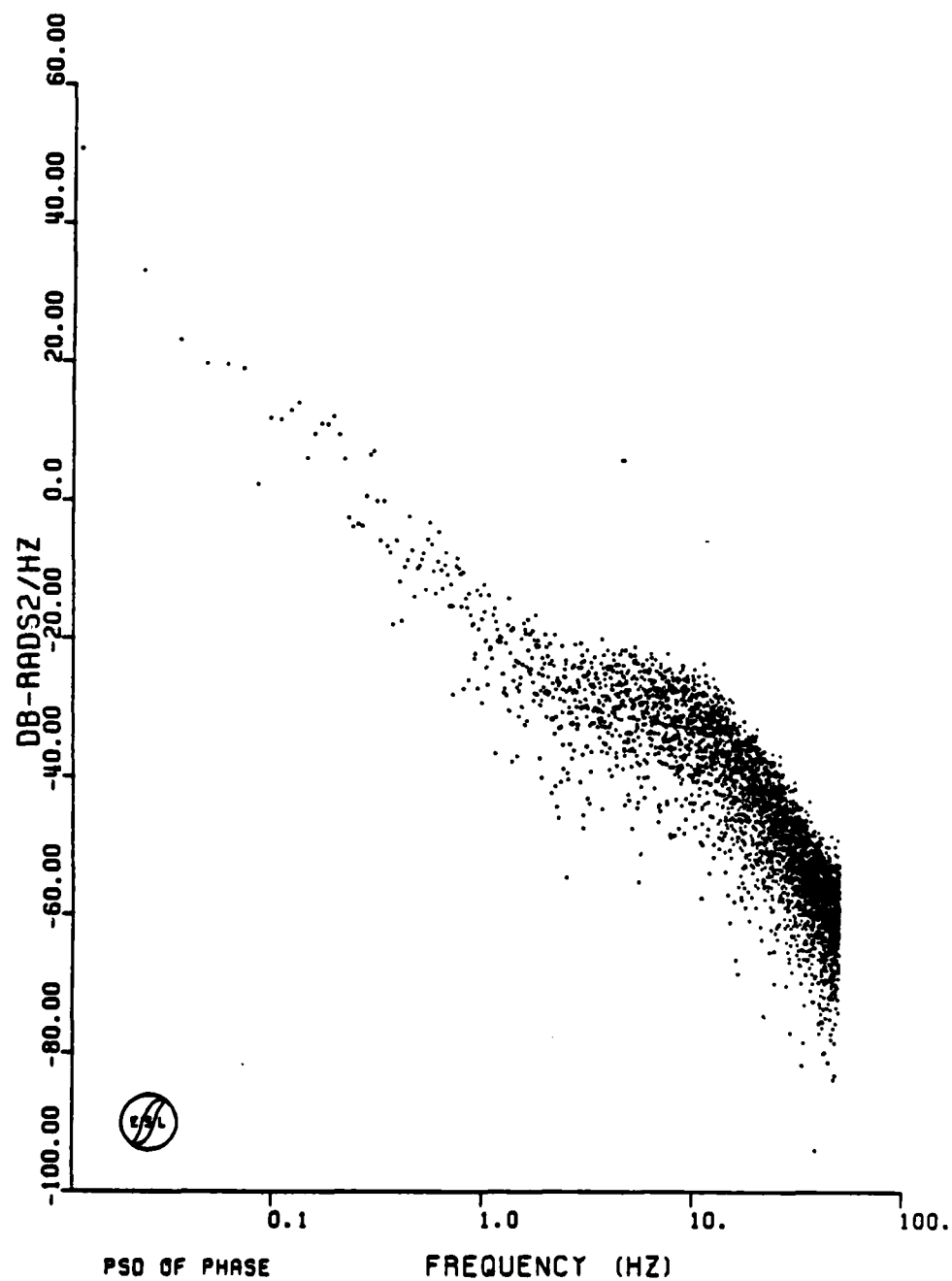


Figure 7-12. HOPE Pass 14 Back-Propagated Phase PSD

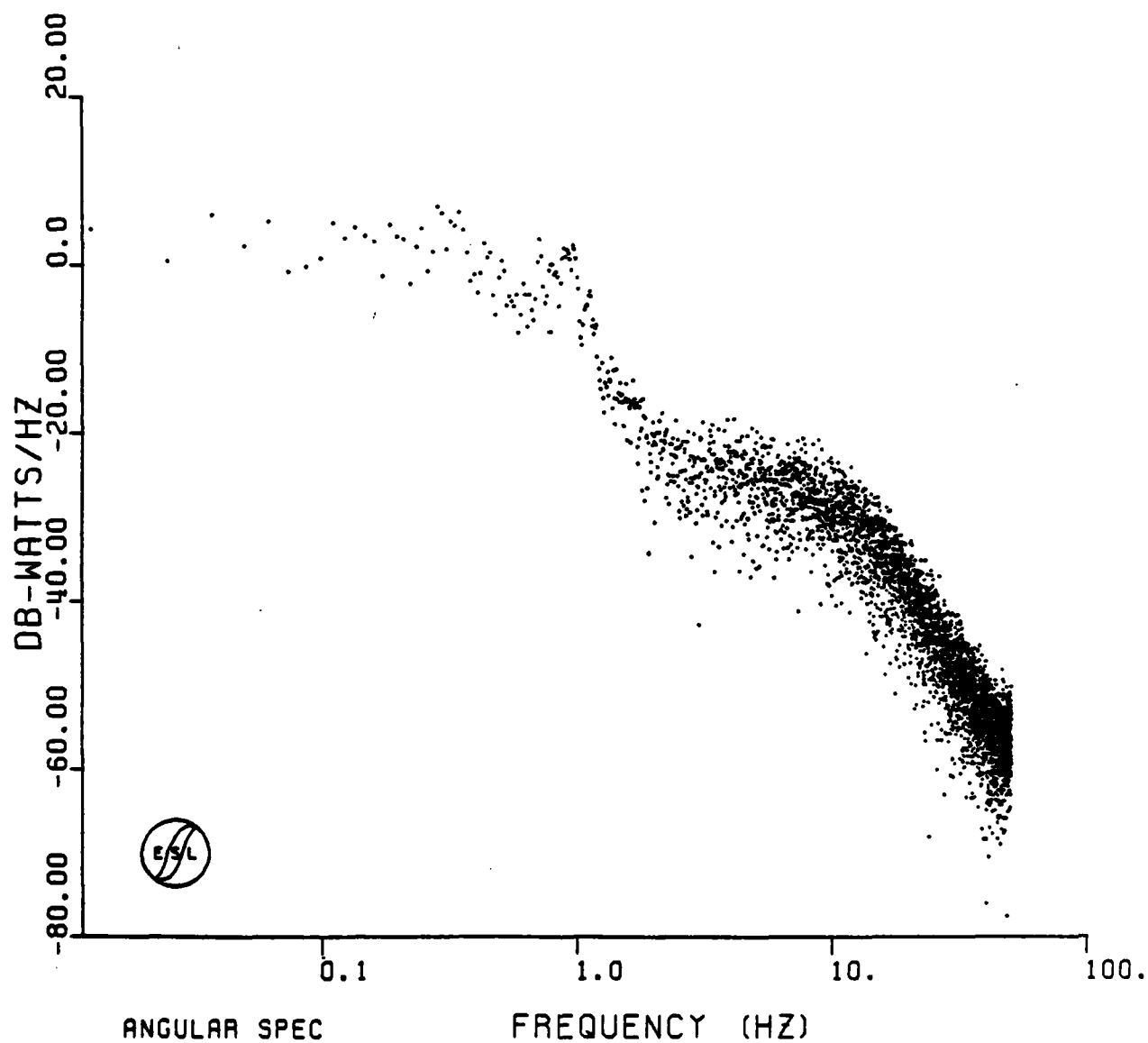


Figure 7-13. HOPE Pass 14 Downlink Angular Spectrum

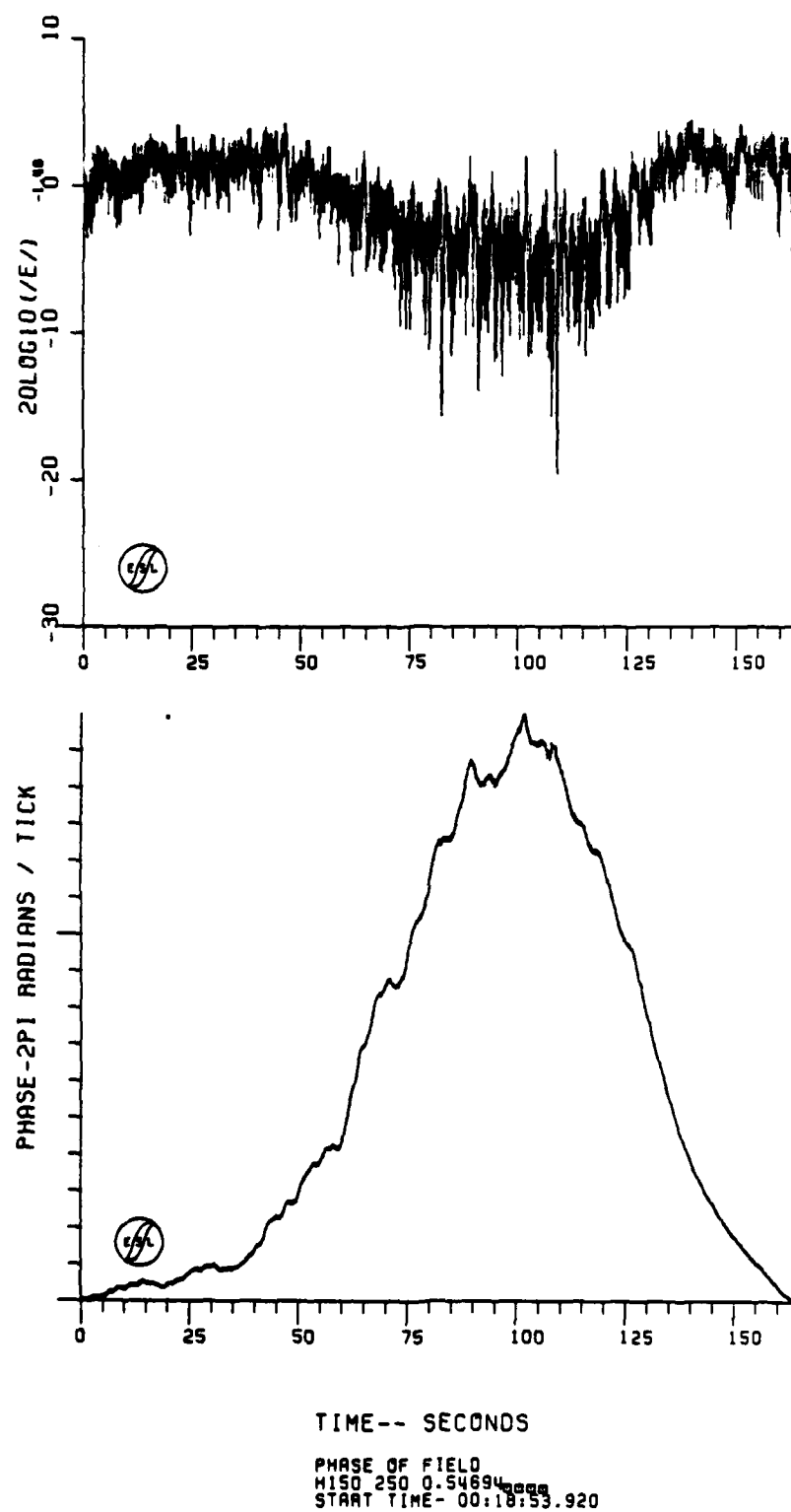


Figure 7-14. HOPE Pass 15 Downlink Back-Propagated Amplitude and Phase

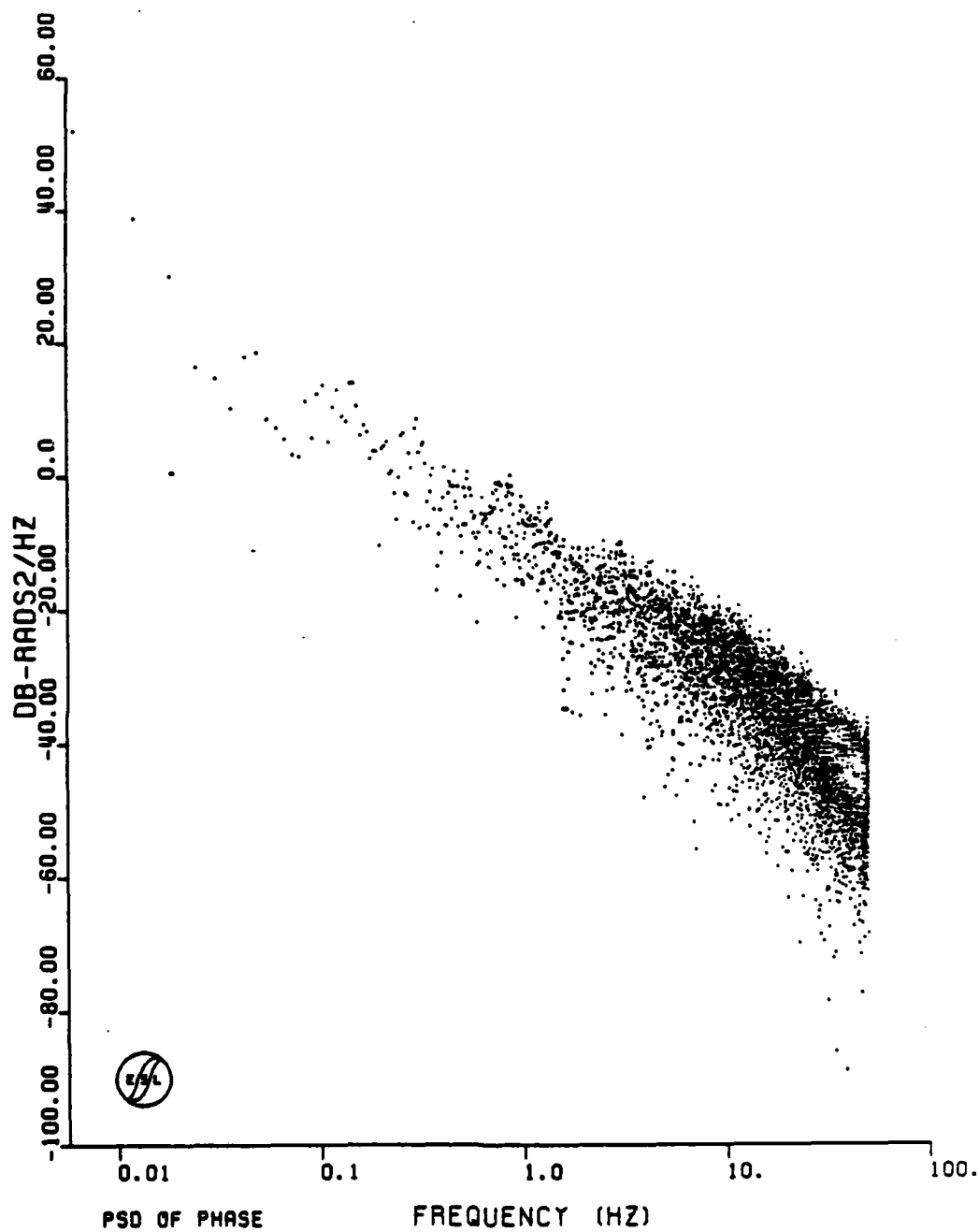


Figure 7-15. HOPE Pass 15 Received Phase PSD at Aircraft

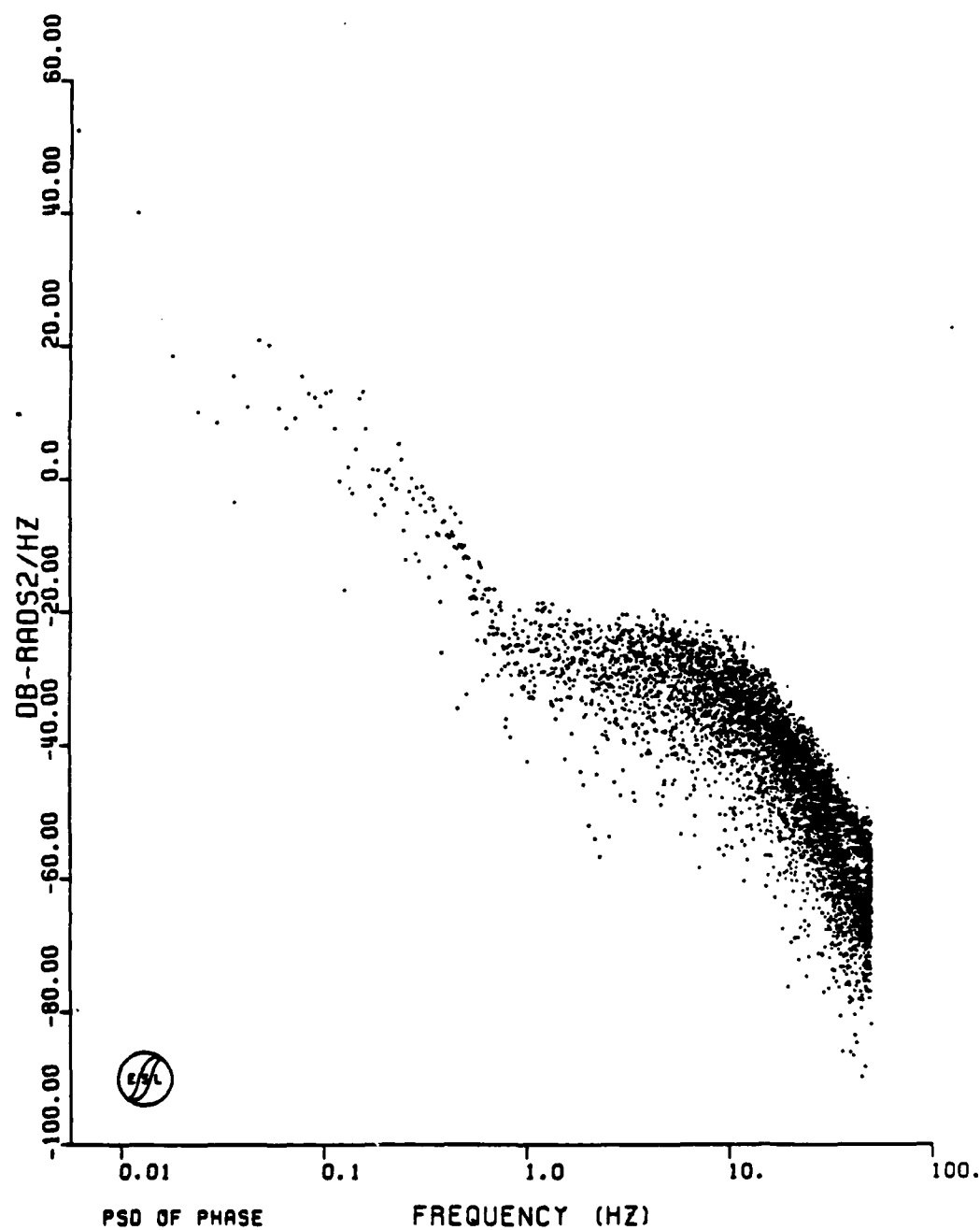


Figure 7-16 HOPE Pass 15 Back-Propagated Phase PSD

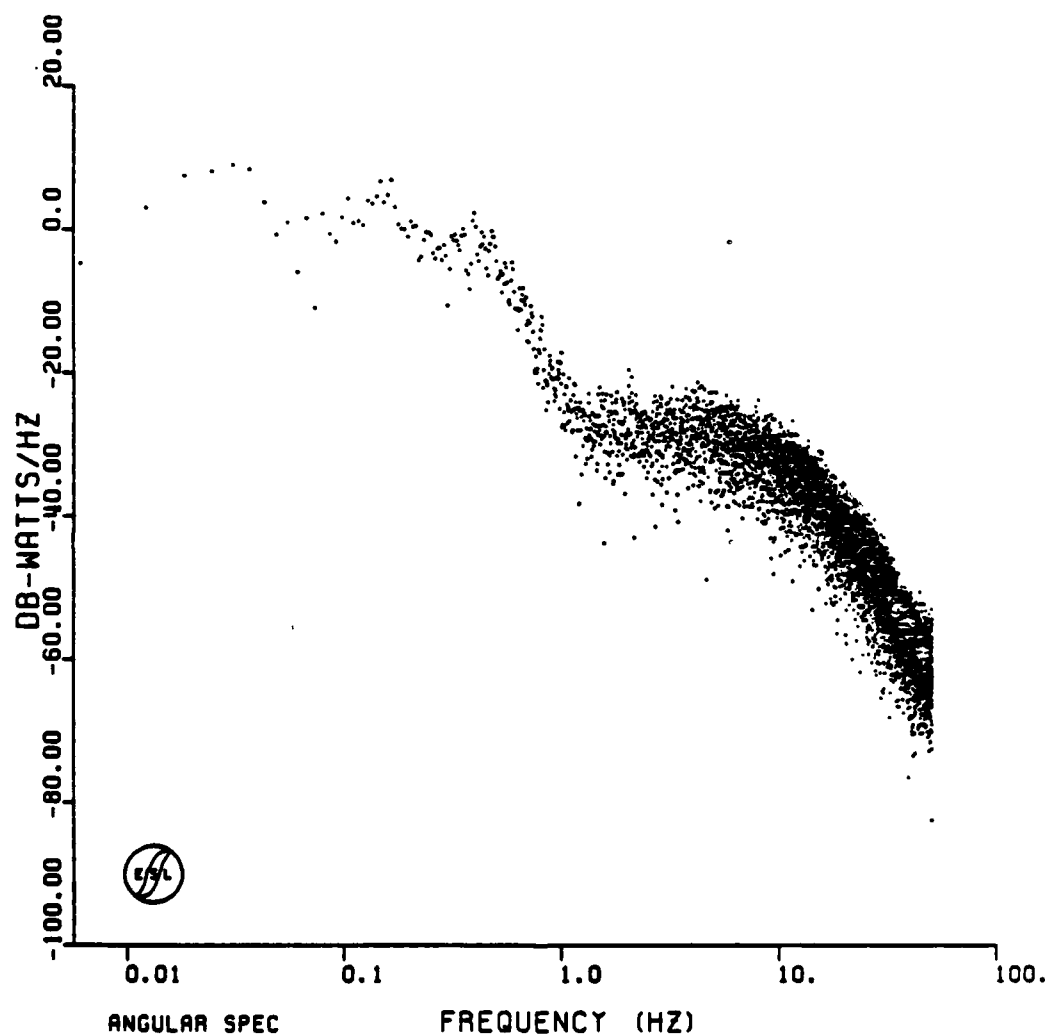


Figure 7-17. HOPE Pass 15 Downlink Angular Spectrum

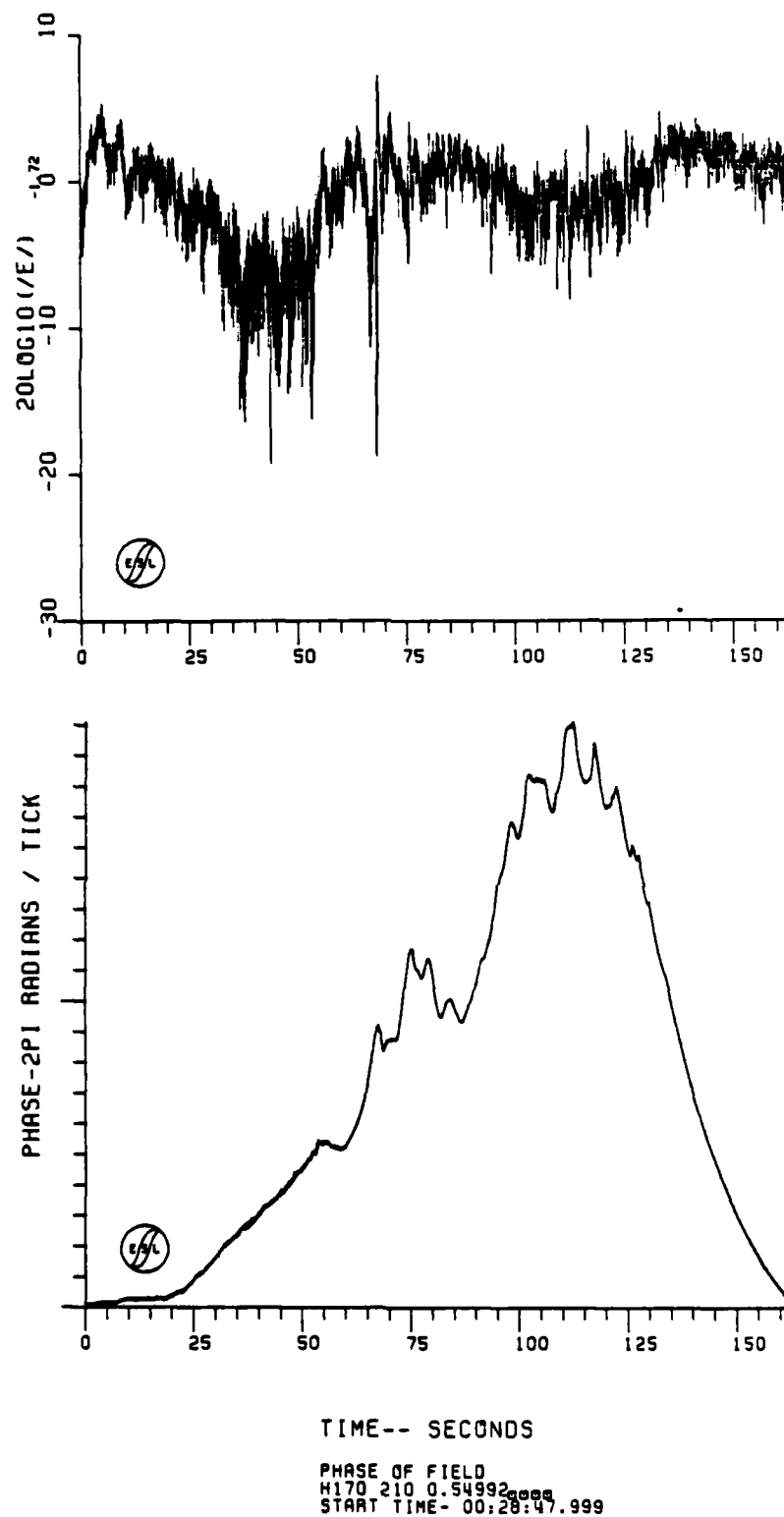


Figure 7-18. HOPE Pass 17 Downlink Back-Propagated Amplitude and Phase

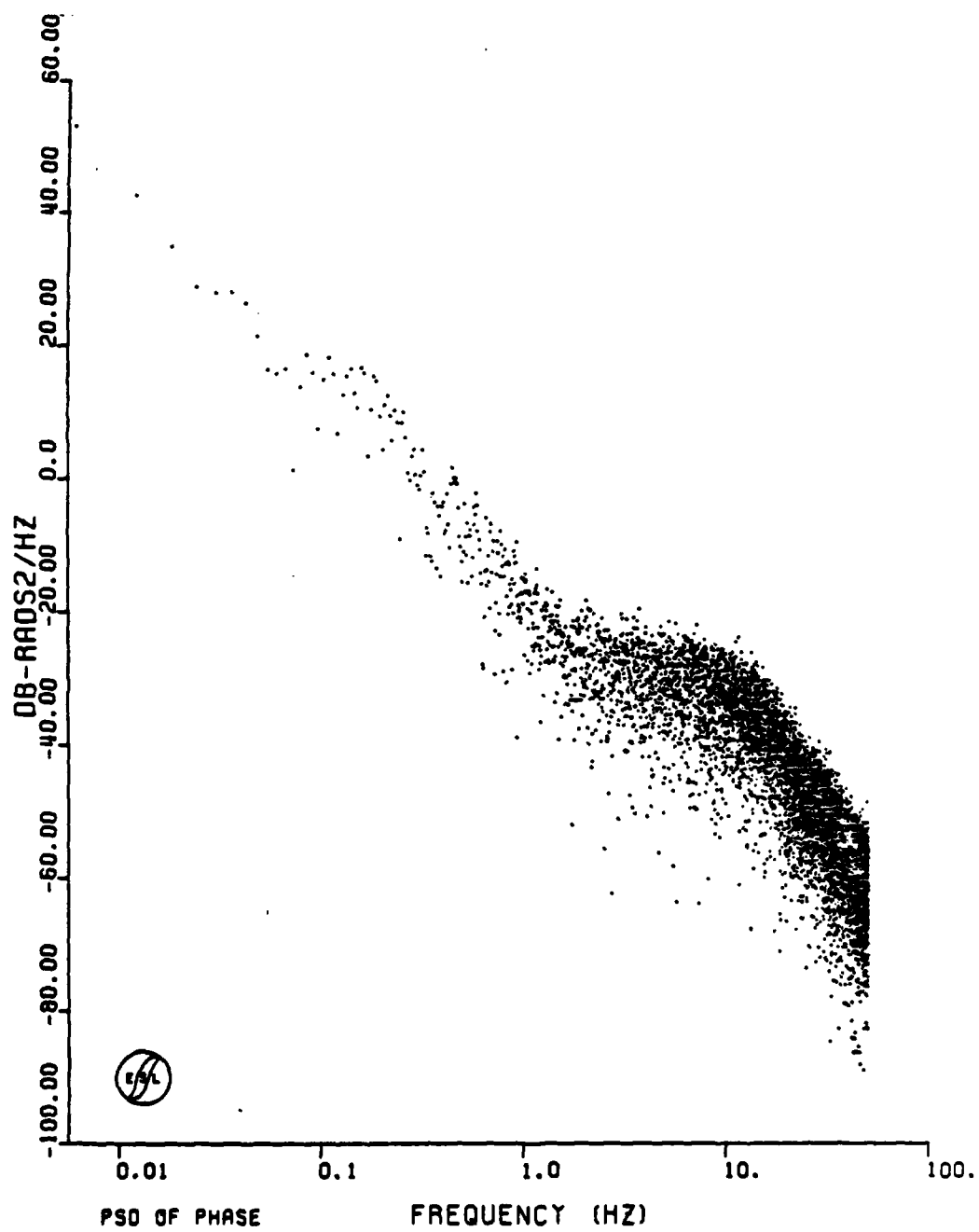


Figure 7-19. HOPE Pass 17 Back-Propagated Phase PSD

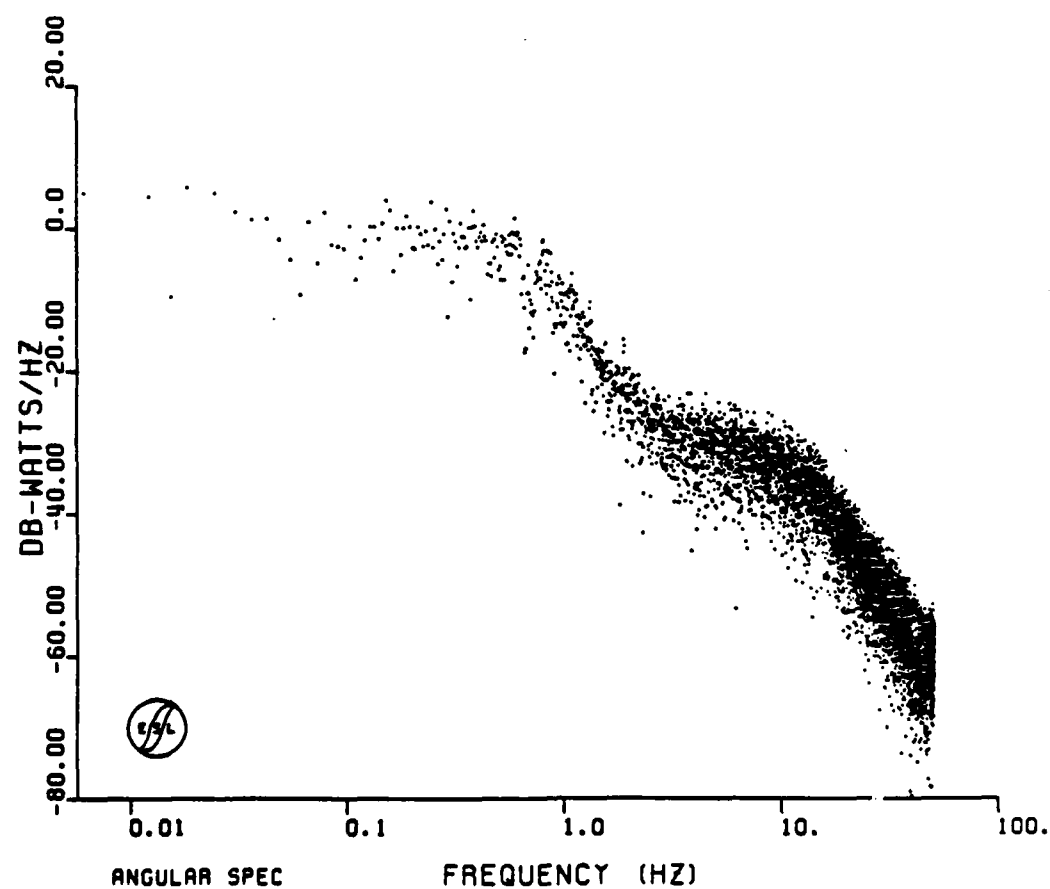
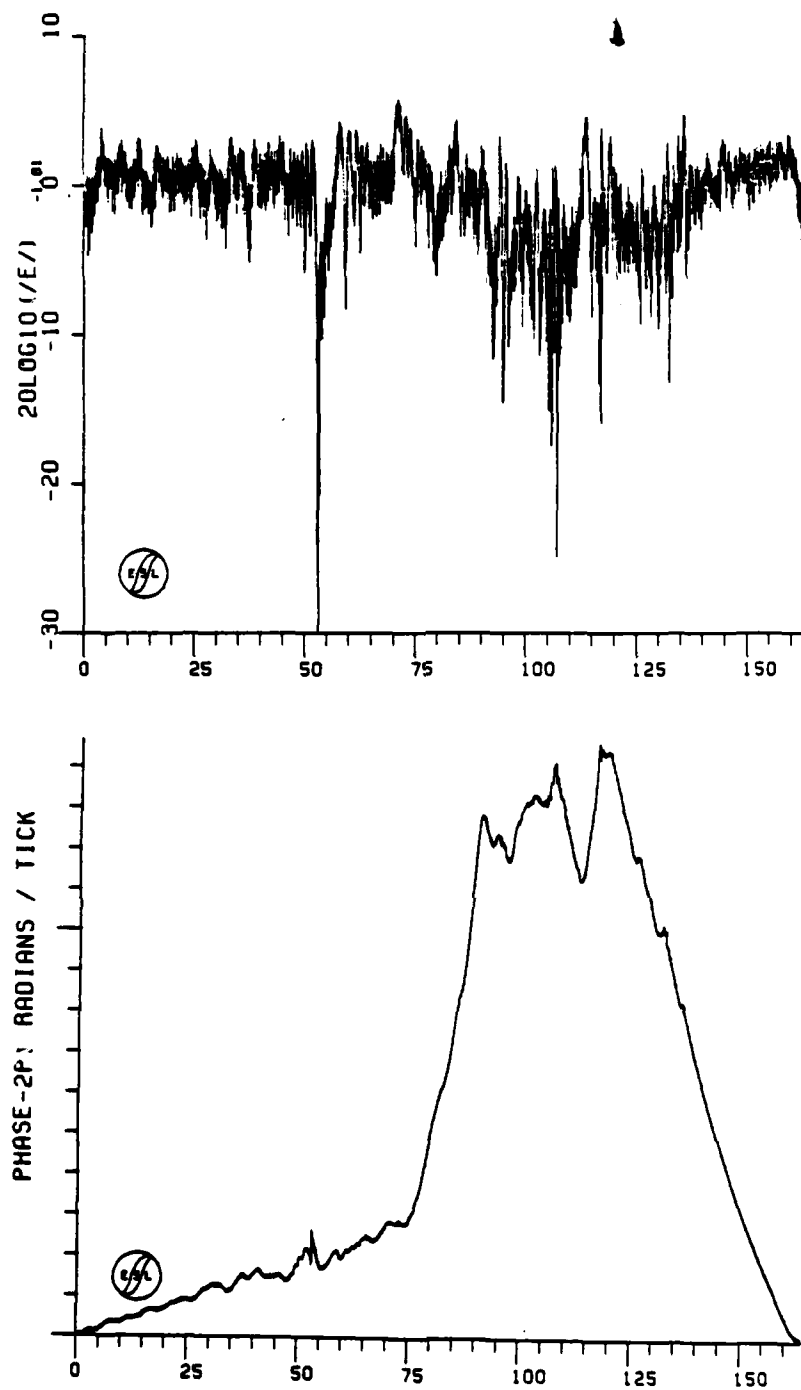


Figure 7-20. HOPE Pass 17 Downlink Angular Spectrum



TIME-- SECONDS

PHASE OF FIELD
 H190 240 0.50882
 START TIME- 00:42:38.479

Figure 7-21. HOPE Pass 19 Downlink Back-Propagated Amplitude and Phase

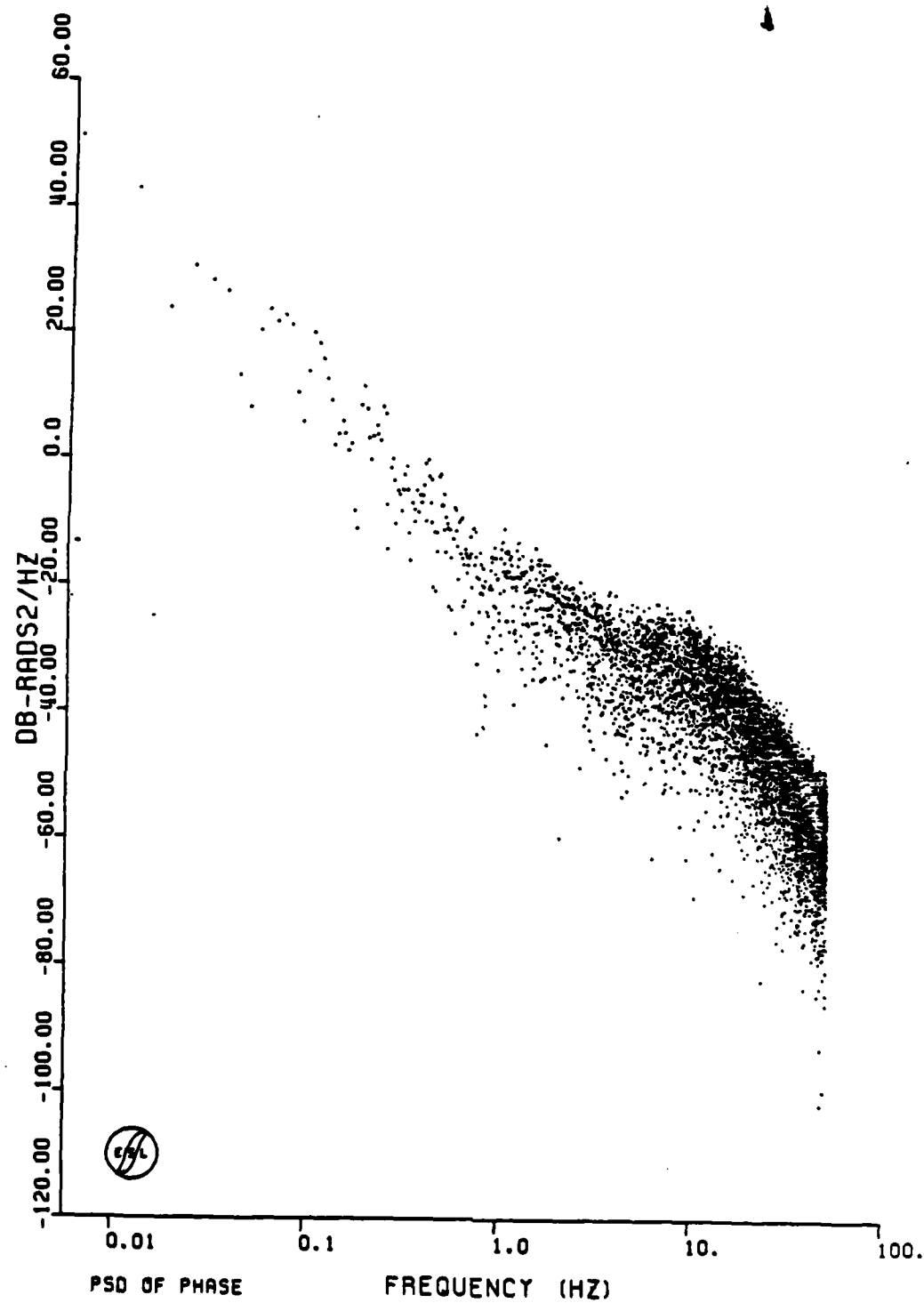


Figure 7-22. HOPE Pass 19 Back-Propagated Phase PSD

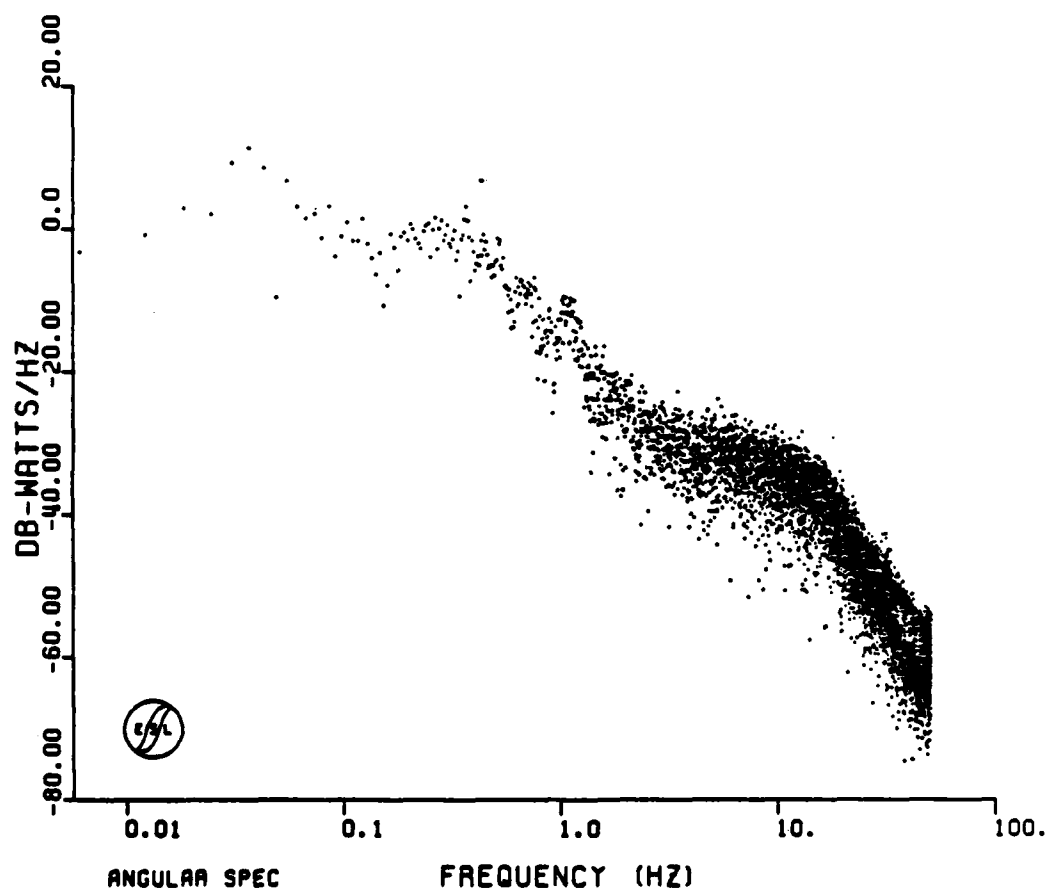


Figure 7-23. HOPE Pass 19 Downlink Angular Spectrum

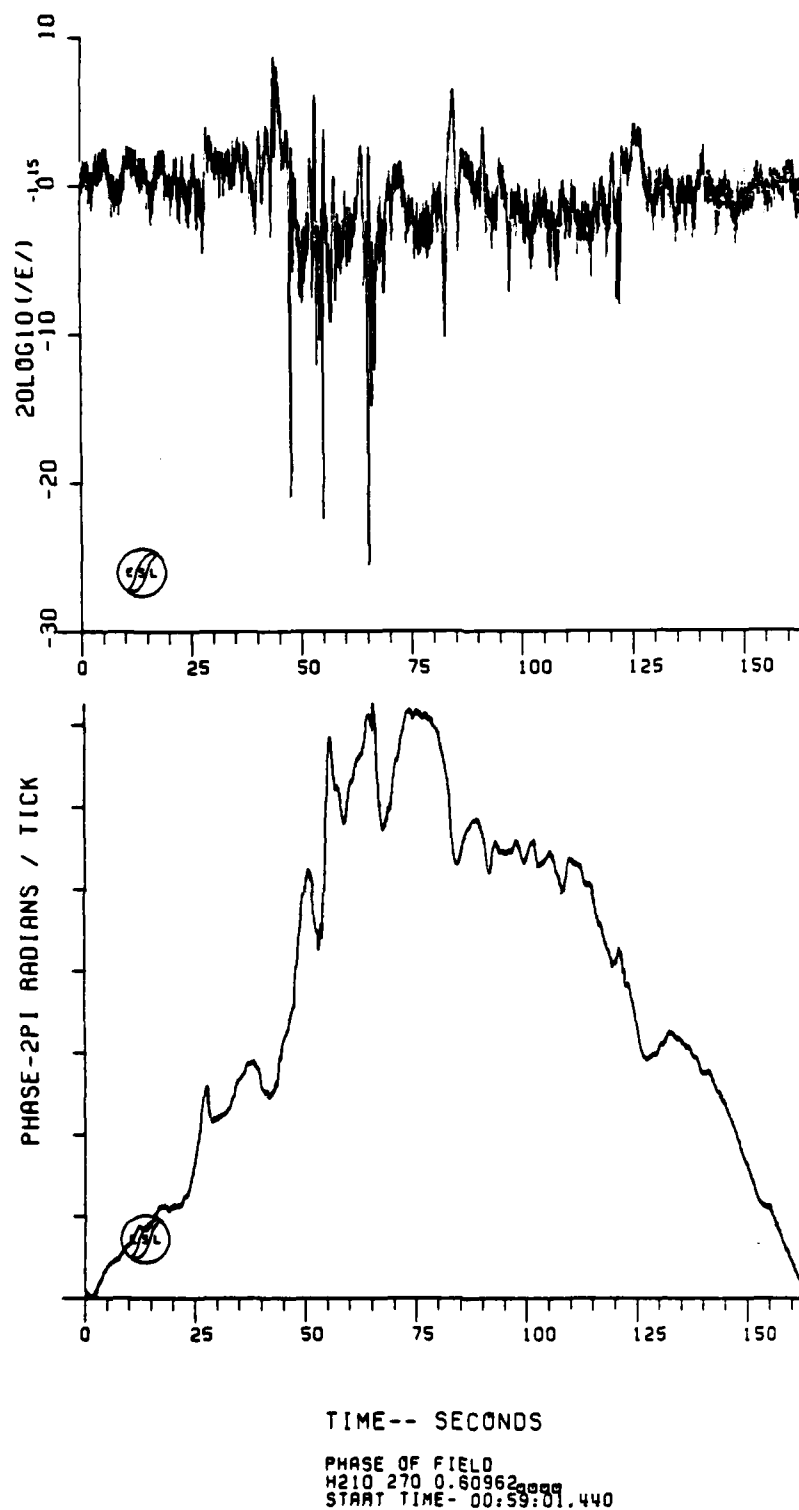


Figure 7-24. HOPE Pass 21 Downlink Back-Propagated Amplitude and Phase

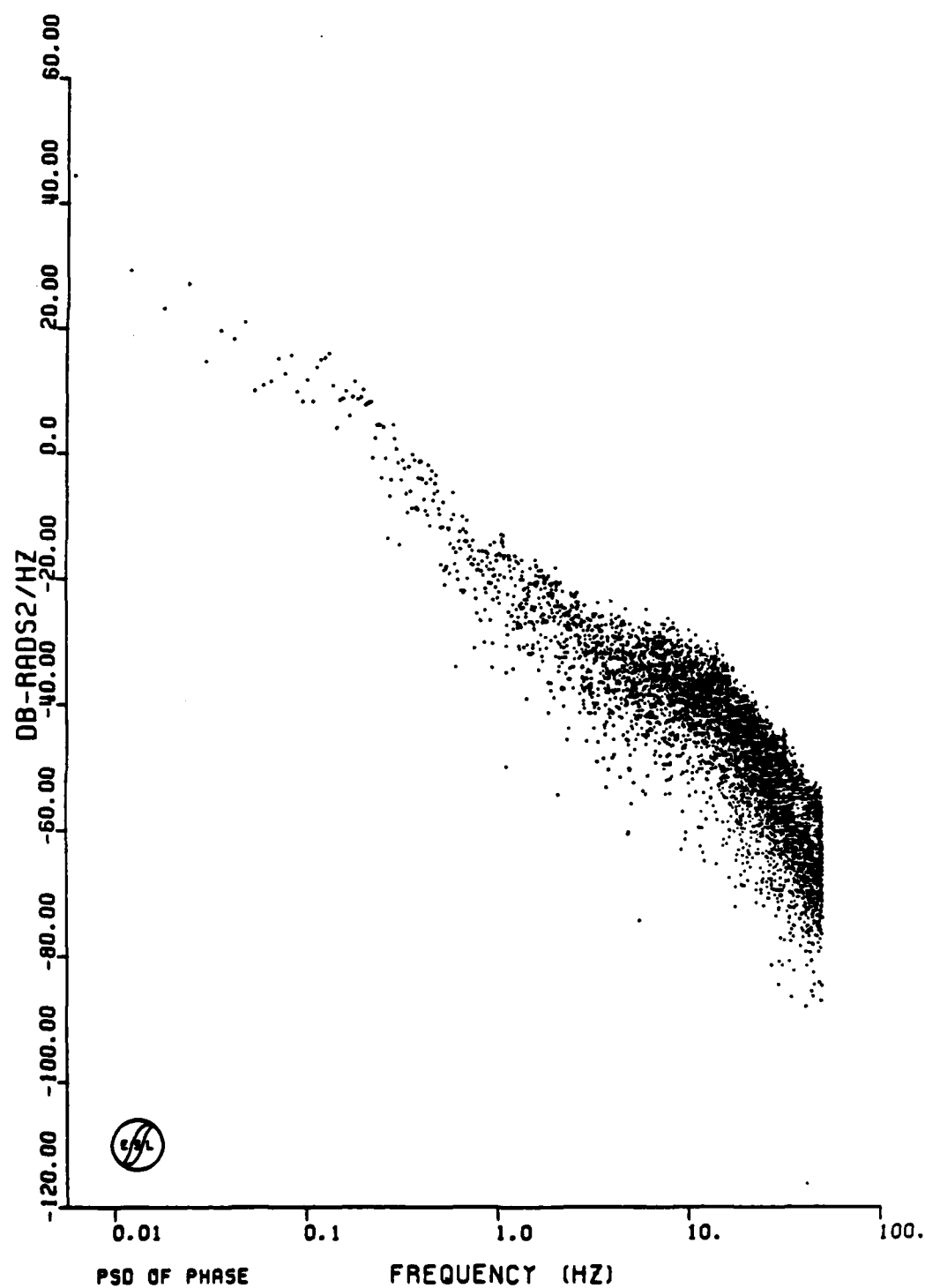


Figure 7-25. HOPE Pass 21 Back-Propagated Phase PSD

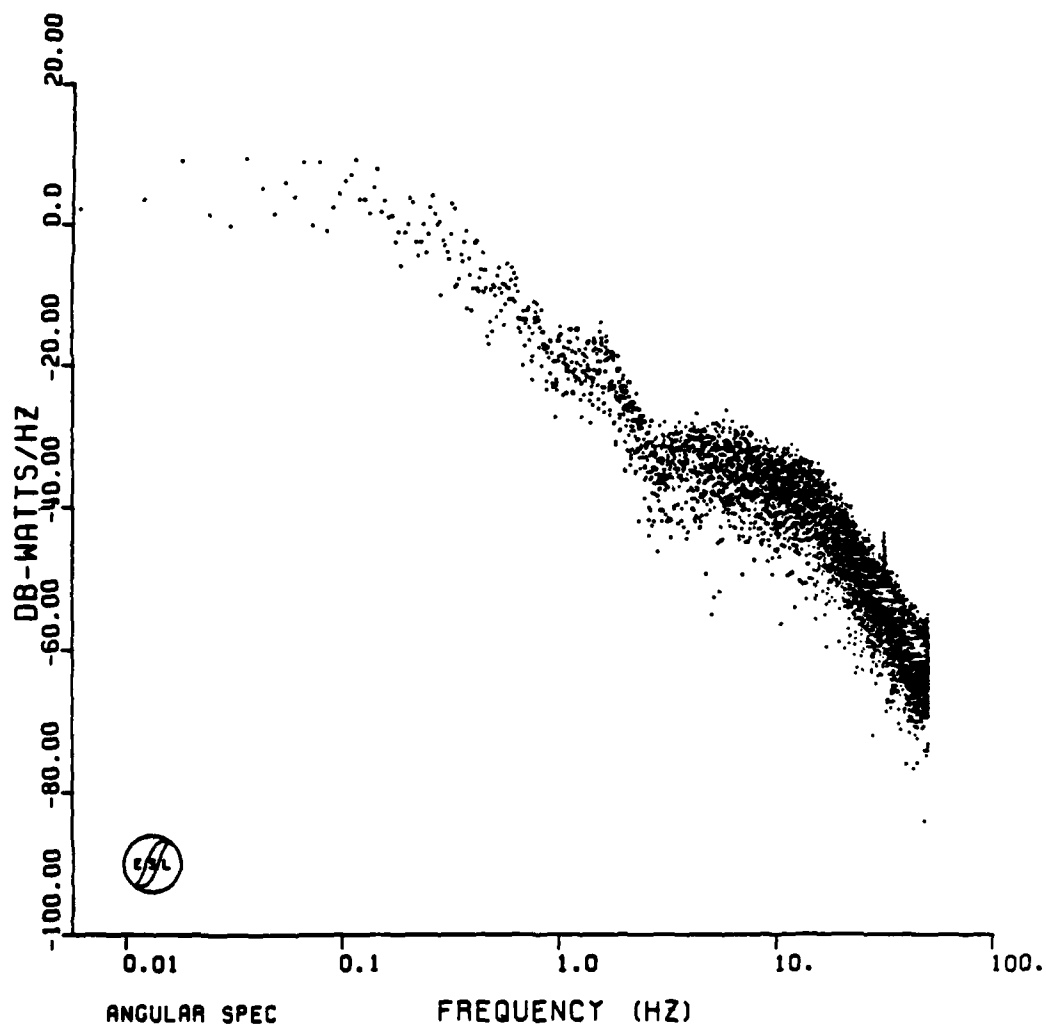
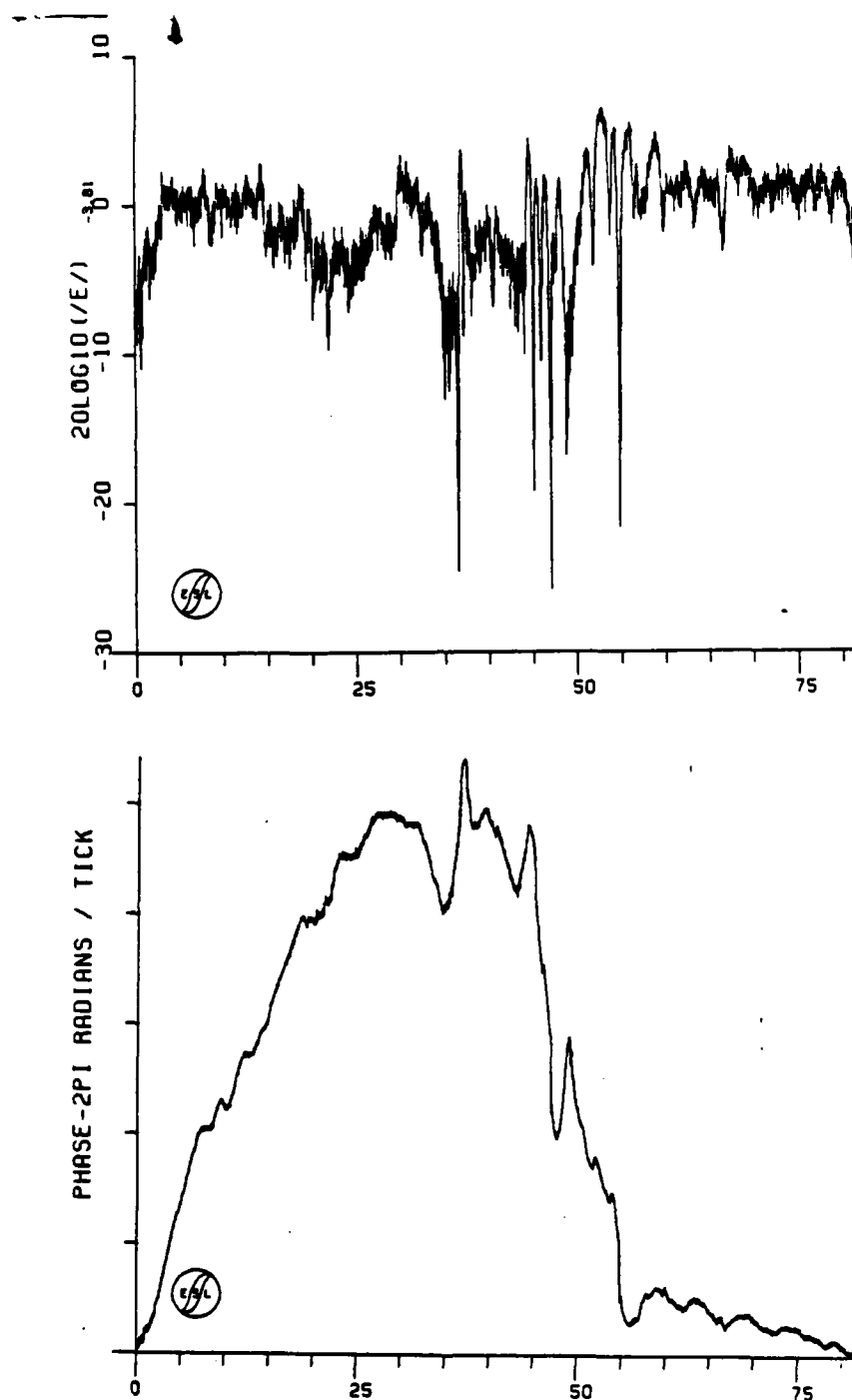


Figure 7-26. HOPE Pass 21 Downlink Angular Spectrum



TIME-- SECONDS

PHASE OF FIELD
 H220 170 0.625210000
 START TIME- 01:04:40.480

Figure 7-27. HOPE Pass 22 Downlink Back-Propagated Amplitude and Phase

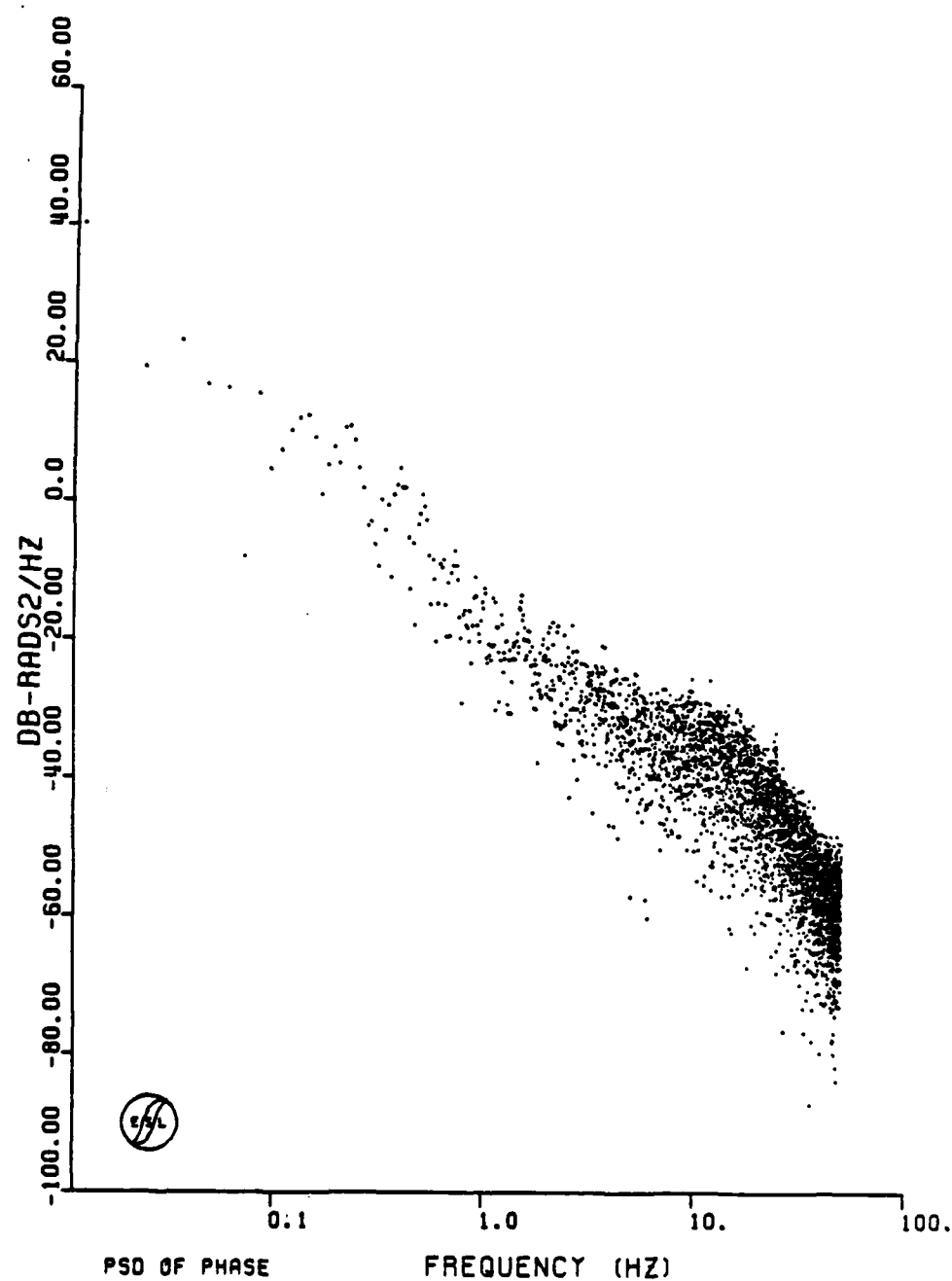


Figure 7-28. HOPE Pass 22 Back-Propagated Phase PSD

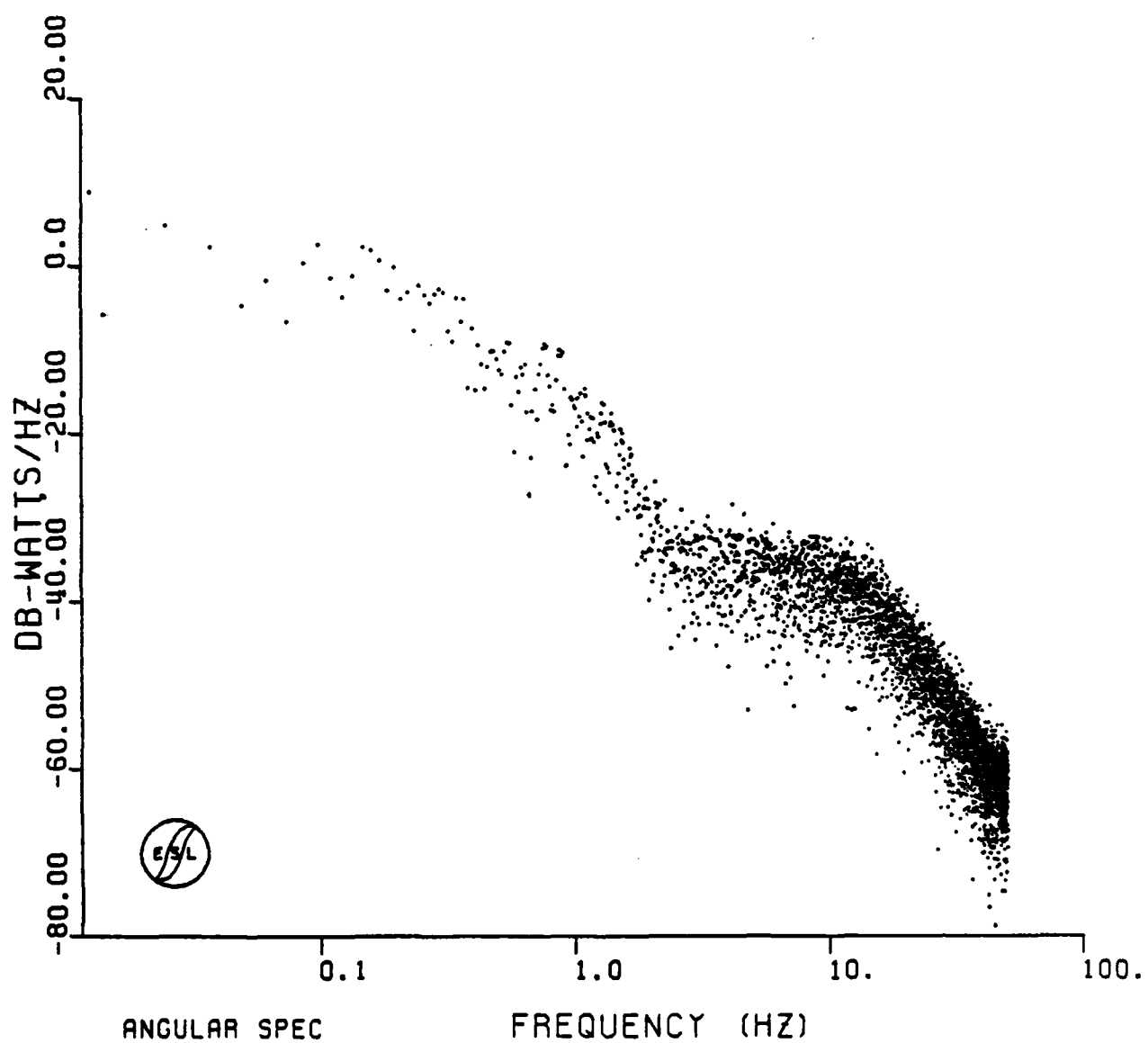


Figure 7-29. HOPE Pass 22 Downlink Angular Spectrum

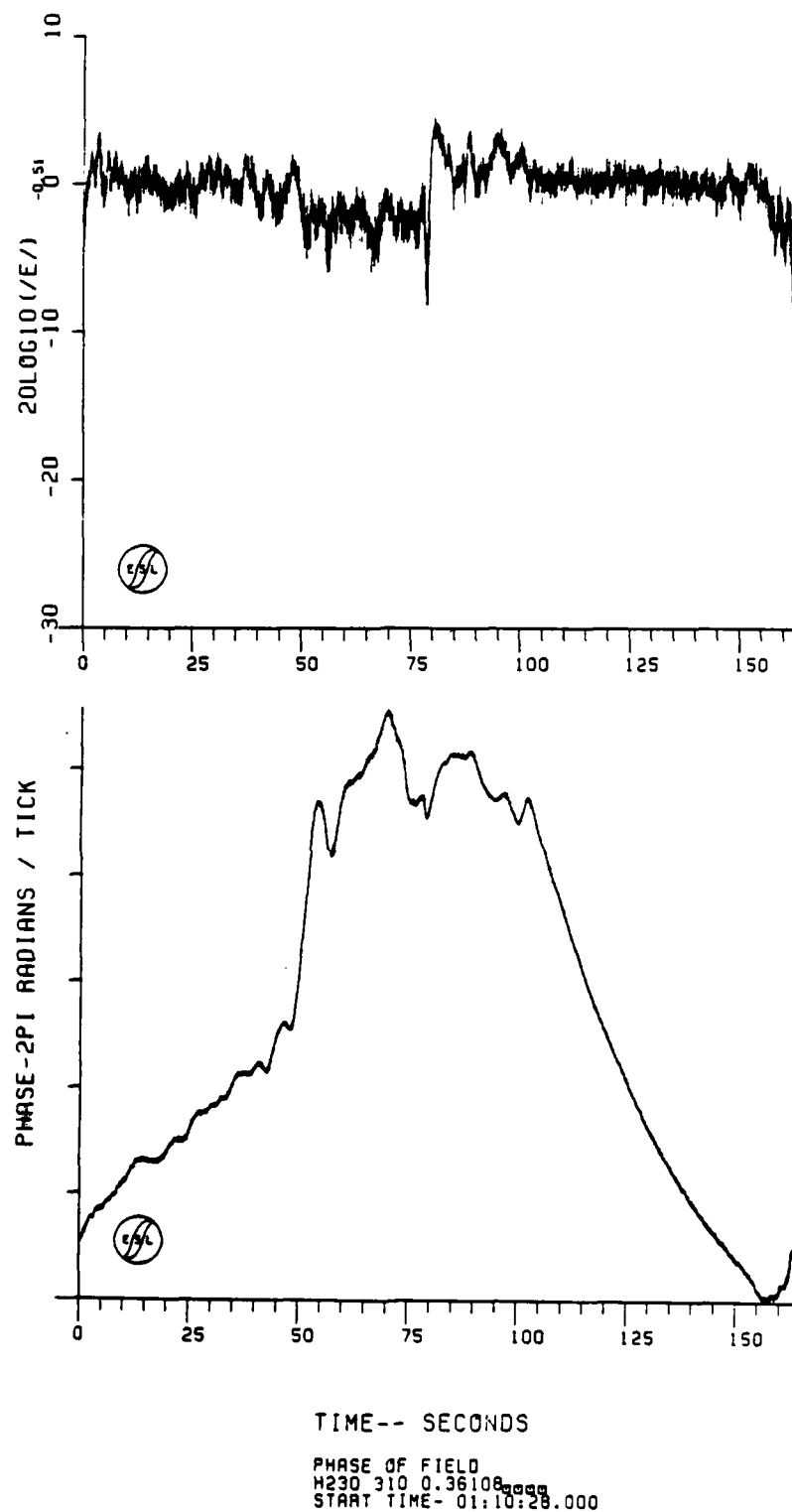


Figure 7-30. HOPE Pass 23 Downlink Back-Propagated Amplitude and Phase

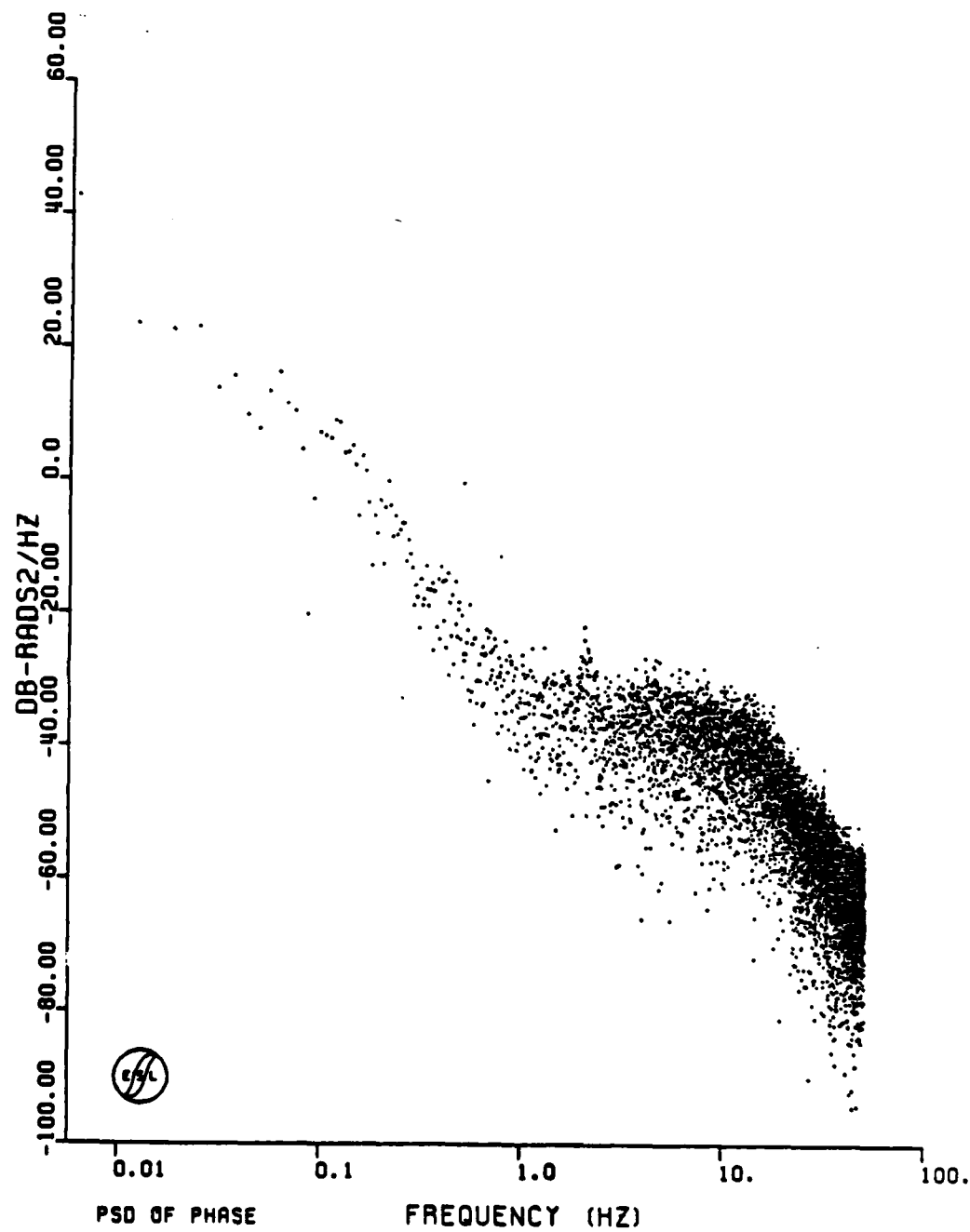


Figure 7-31. HOPE Pass 23 Back-Propagated Phase PSD

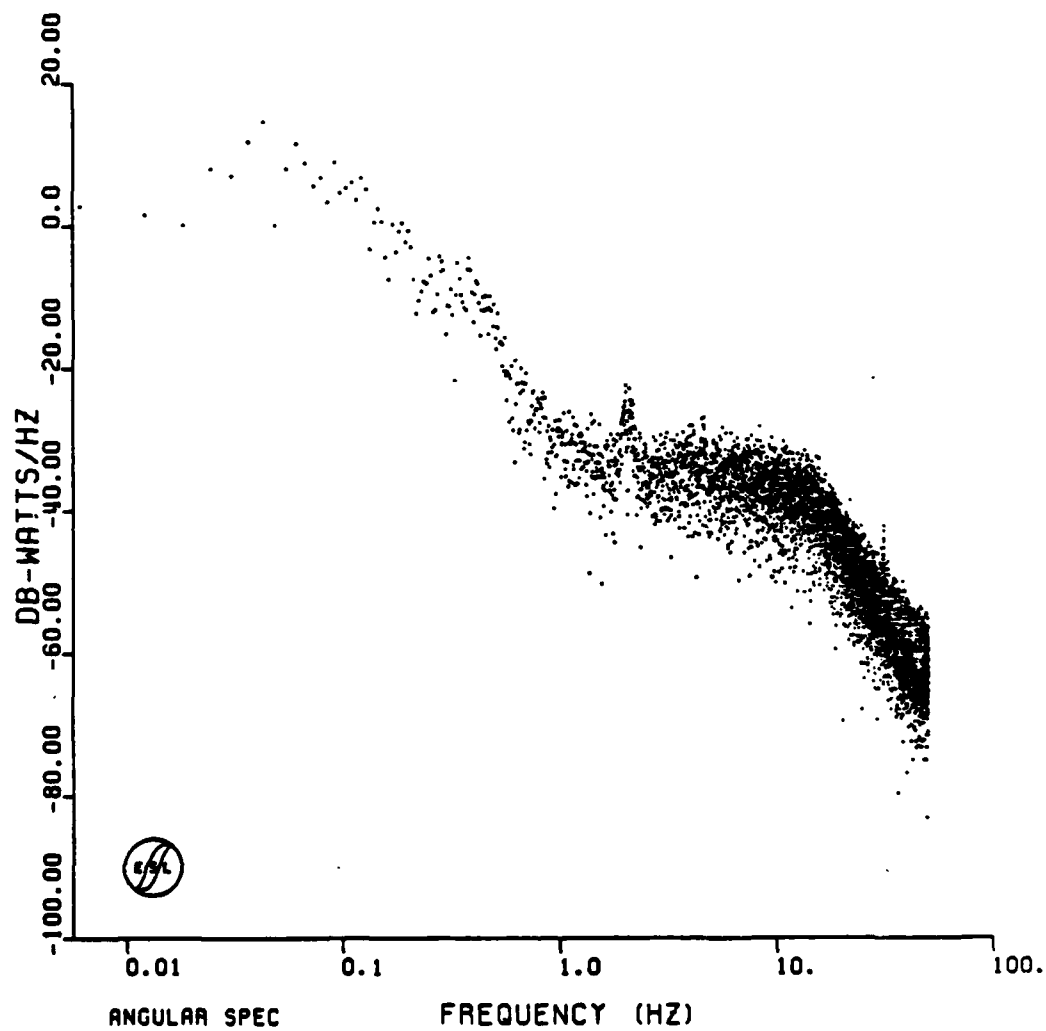


Figure 7-32. HOPE Pass 23 Downlink Angular Spectrum

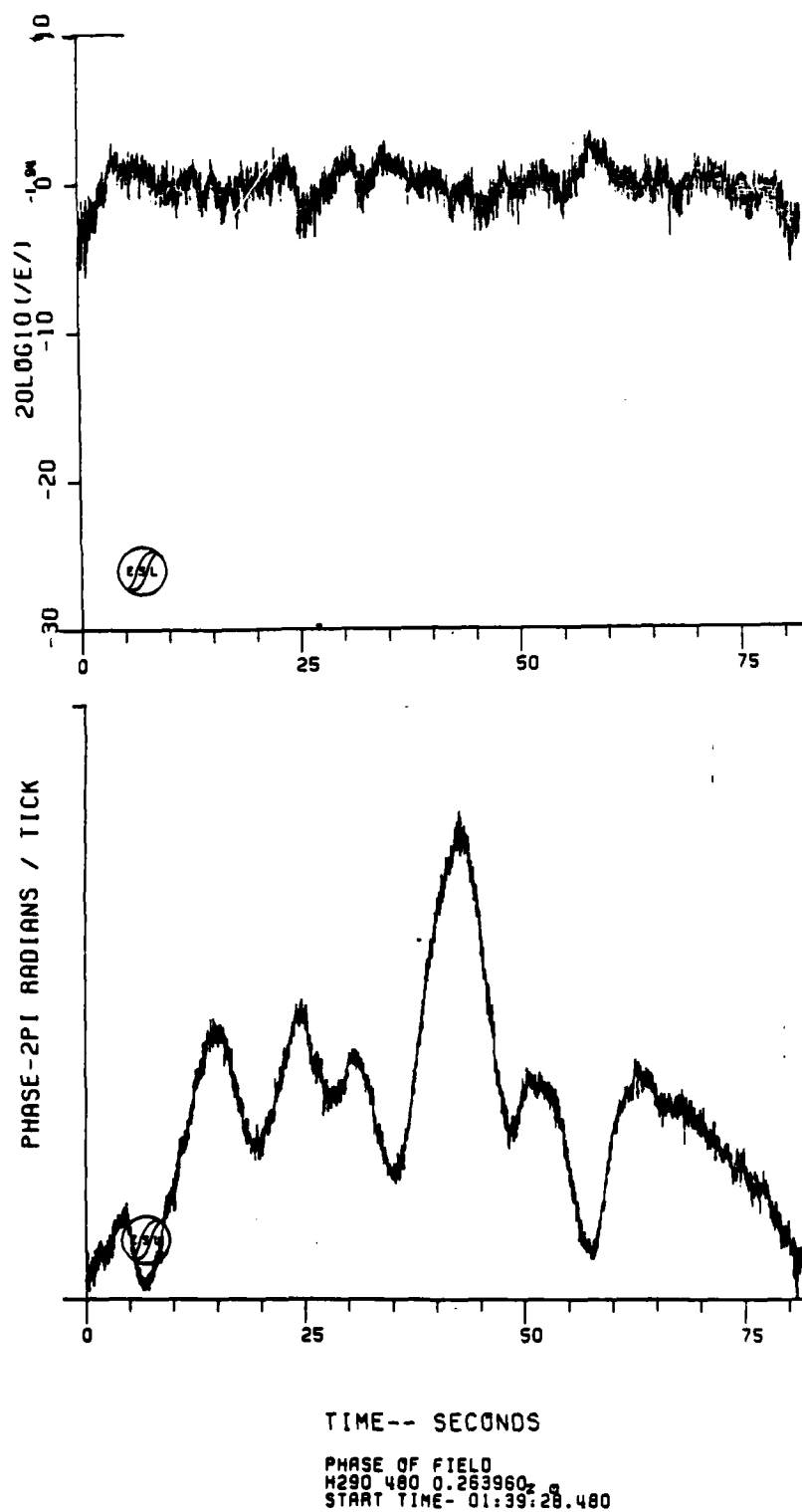


Figure 7-33. HOPE Pass 29 Back-Propagated Amplitude and Phase

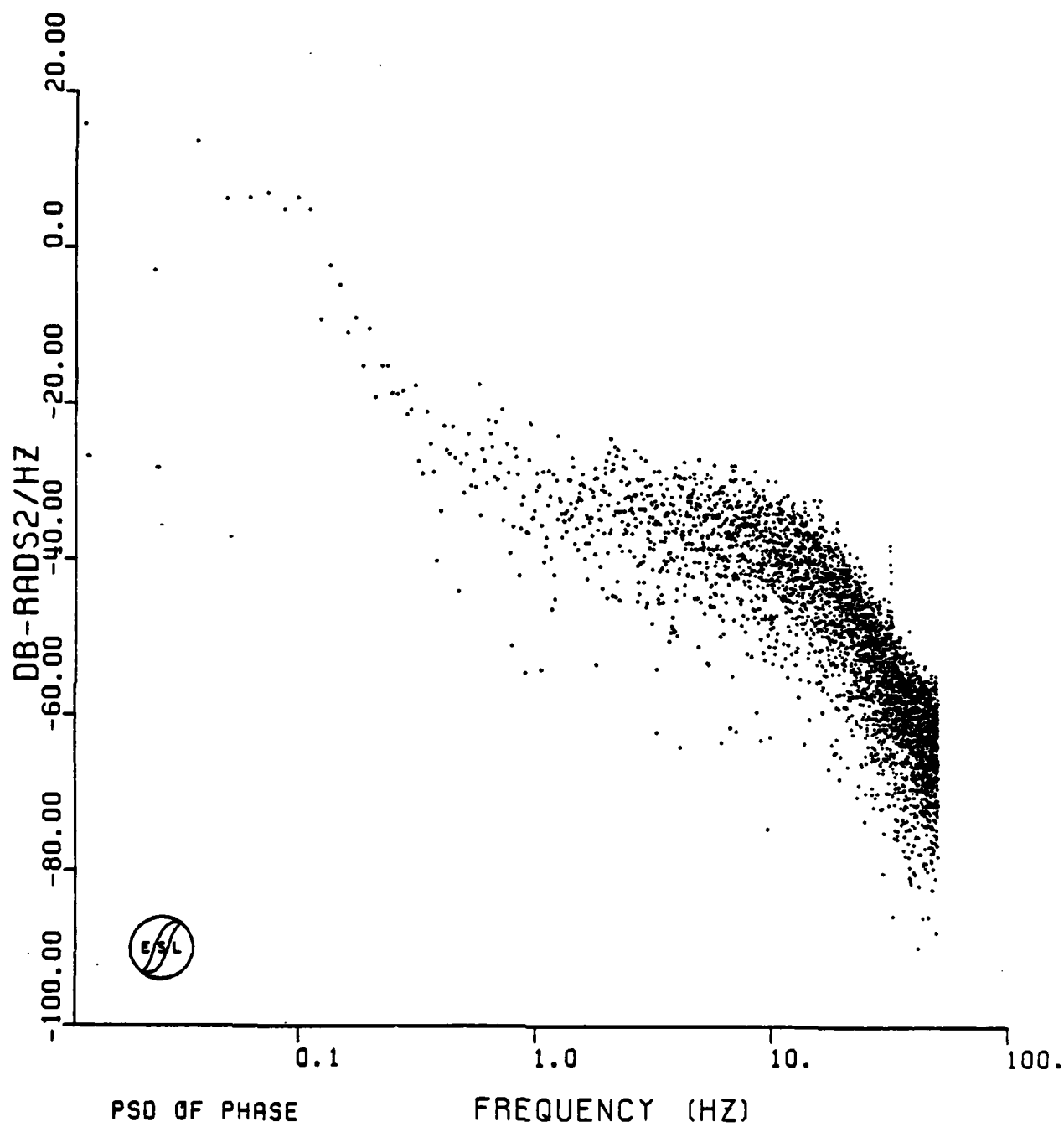


Figure 7-34. HOPE Pass 29 Back-Propagated Phase PSD

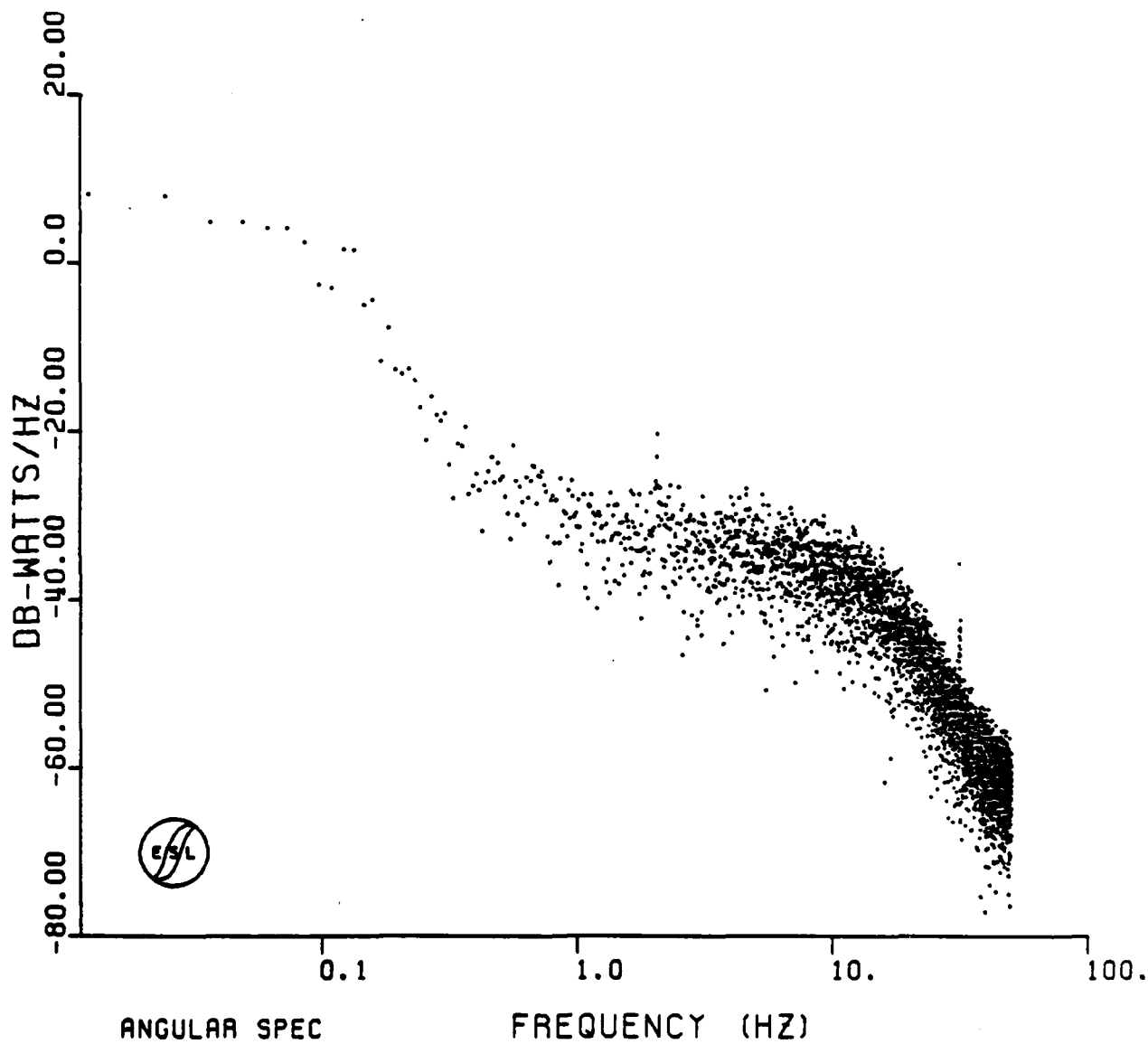


Figure 7-35. HOPE Pass 29 Angular Spectrum

One alternative is to visual distinction of the gross and random portions of the PSD is to average transforms of detrended phase data from shorter segments of the pass. Depending upon the segment chosen, there may not be sufficient resolution to permit a break frequency to be distinguished. Also, the piecewise linear removal of the gross cloud phase will leave some residual non-linear phase component that will distort the phase data in some unknown and segment dependent way. Nonetheless, this approach was successfully used in processing the STRESS Experiment data.

A systematic computerized technique to estimate the random phase contribution would seem desirable, but is not without its difficulties. For instance, a least squares fit to spectral index between 0.2 and 1.0 Hz may result in a more systematic result for the spectral index. If used, equal spacing of points on the frequency axis would be employed to avoid driving the results by the large number of points at the higher frequency end of the spectrum. Unfortunately, the break frequency depends on the choice of σ_ϕ^2 or visa versa. If one filters the data to estimate and remove the gross cloud, the phase variance and the break frequency will depend to some extent on the filtering employed. The phase variance and thus the break frequency depends on the residual gross cloud phase. For instance, a running average of the phase data over, say, a 15 second interval (equivalent to ~3 kilometers in distance) is equivalent to multiplying the phase PSD by a SINC^2 or $(\sin x/x)^2$ function with the first null at 0.067 Hz. The "random" phase PSD can then be estimated by subtracting this modified PSD from the original; e.g.,

$$S_{\phi_R}(f) = S_{\phi}(f) (1 - \text{sinc}^2(\pi 15 f)) \quad (7-6)$$

For some passes the gross cloud is swept out in approximately 30 seconds, thus, the averaging time must not be made too long or the gross cloud shape will not be replicated accurately. Too short of an averaging time, say, 10 seconds and the first null occurs near the likely break frequency of 0.1 Hz.

In the absence of a clearly superior method for estimating the outer scale size, and recognizing that others may wish to employ their own approach, a quick subjective visual method was chosen using the templates shown in Figures 7-36 and 7-37. The phase for Pass 9 (see Figure 7-5) also follows a Gaussian shape and the first spectral sidelobe in Figure 7-38 is approximately 5 dB higher than for Pass 7. Thus, we associate this feature with the gross cloud. Accordingly the best fit to the random phase component is believed to be as shown in Figure 7-38.

Table 7-1 summarizes the parameter fits obtained for those passes that successfully back-propagated. In most cases several different fits to the data are possible depending upon which features of the PSD are interpreted as resulting from the gross cloud phase, and whether a fit is made to the highest power points on the PSD or on the average. For each pass an attempt has been made to obtain at least one alternate fit to the data in order to gain insight as to the possible variance of the estimate. The interpretation of the values in Table 7-1 are facilitated by Figures 7-38 through 7-55 which show the corresponding curve fits to the back-propagated phase PSD data.

Figure 7-38 and 7-39 shows what is regarded as the best fit to the HOPE Pass 9 data while Figure 7-39 provides an alternate fit. The phase PSD for Pass 7 which consisted entirely of a Gaussian shaped gross cloud indicates a bump or lobe around 0.1 Hz approximately $2 \text{ dB radian}^2/\text{Hz}$ in magnitude (see Figure 7-3). Alternatively, the fit shown in Figure 7-39 may be appropriate if the first spectral sidelobe is not influenced by the gross cloud feature. As this pass did not transit significant structure and the fading was relatively weak, the analytic formulation of Equation (7-1) is not necessarily expected to provide a good fit to the data.

The first three points of the phase PSD for Pass 14 shown in Figure 7-40 are clearly associated with the gross cloud. The phase shown in Figure 7-11 appears to have an underlying Gaussian shape, thus, we would expect any corresponding spectral sidelobe in the phase PSD to be of low magnitude. Indeed, the first sidelobe

is ~13 dB higher than for Pass 9. Thus, we associate this feature with the gross cloud effects. Accordingly the best fit to the random component of the spectral data is given in Figure 7-40. Figure 7-41 provides two alternate fits that associate the roll-off at $20 \text{ dB-rad}^2/\text{Hz}$ as due to random components.

Four possible fits to the PSD of Pass 15 are given in Figures 7-42 and 7-43. Again, the phase structure has an underlying Gaussian shape. The phase PSD first sidelobe is ~30 dB down from the first point like the previous pass, and again we associate the first sidelobe as due to the gross cloud phase. The middle curve was taken as the best fit with the highest curve being the logical alternate choice if the first spectral peak is associated with the random phase. Some of the spectral bumps are undoubtedly due to the periodic low frequency phase structure evident in Figure 7-14. Figure 7-43 serves to illustrate that if the bumps are ignored that a much steeper slope is required to fit the data. Generally, our estimates are biased towards the higher power points, but below any spectral peaks.

The back-propagated phase for Pass 17 also exhibits a low frequency periodic striation structure as was shown in Figure 7-18. This appears to result in large bumps in the phase PSD as shown in Figure 7-44. The phase due to the gross ion cloud appears somewhat rectangular over its highest portion. The corresponding phase PSD should, therefore, resemble a sinc function for which the first sidelobe peak is approximately 15 dB down from the mainlobe peak. The first sidelobe peak of Figure 7-44 is 18 dB down in good agreement with this interpretation. Thus, in this case we take as the best fit the curve shown in Figure 7-44 that ignores the first peak. An alternative curve through the first spectral sidelobe is shown in Figure 7-45. The spectral bumps would imply that there are a few preferential sizes of large spatial size (~5 kilometers) at this time. Being late in the lifetime of the cloud ($R+1^{h22m}$) this may indicate that a statistically complete cascade of sizes has not resulted, and/or may be related to striation freezing.

From numerical simulations of barium striation development under conditions of gradient-drift convective instabilities it has been demonstrated that an initially unstable gradient first steepens and then finger-like striations and depletions develop. The size of the primary striations is controlled by the initial gradient^[6] (~5 kilometers for these barium releases). When the unstable plasma is completely isolated from the background ionosphere, the primary striations bifurcate, generating smaller structures which in turn bifurcate resulting in a cascade of striation sizes down to some small size where classical diffusion can rapidly dissipate the structure. It is believed that E-region coupling can effectively result in an anomalous diffusion that in turn exhibits the bifurcation process so that the primary structures persist much longer than expected (freezing phenomenon)^[7].

The back-propagated phase shown in Figure 7-21 for Pass 19 strongly resembles a rectangular pulse. Thus, we anticipate a sinc function shape due to the gross cloud should appear in the phase PSD with a first sidelobe peak approximately 15 dB down. The first spectral sidelobe peak in Figure 7-46 is indeed 15 dB down. For this reason we believe the best fit to the random phase data is given by the curve with the 44 dB/decade slope given in Figure 7-45. The large finger like features to the phase may cause the obvious spectral lobing. However, because of the strong rectangular phase shape to the phase, there is some question as to whether the second sidelobe is also an artifact of the gross cloud. There appears to be an additional component to the phase spectrum that appears as a bump around 1 Hz. An attempt to fit this feature requires a 30 dB/decade slope as shown in Figure 7-46. This bump also appears in the data for Passes 21 and 22. It is no longer evident in Pass 23, although there are three points near 1.3 Hz that are suggestive of this feature. Figure 7-46 provides an alternate fit for this pass.

The gross cloud component of the back-propagated phase shown in Figure 7-24 resembles a rounded pulse; thus, we associate the first spectral sidelobe in the PSD which is 13 dB down with the gross cloud. The best fit to the random data is provided in Figure 7-48. Figure 7-49 provides two alternative fits to Equation (7-1).

The gross cloud component for Pass 22 is still significant although diminishing (see Figure 7-27). Again, due to the phase shape we associate the first spectral sidelobe peak which is approximately 12 dB down with the gross cloud. Hence, we believe the random data component is best described by the curve with the 44 dB/decade slope shown in Figure 7-50. Figure 7-51 provides two other alternative fits to the spectral data.

The best and alternate fits to the phase PSD for Pass 23 are shown in Figures 7-52, 7-53, and 7-54. Again a range of curve fits are possible depending upon how the lower frequency points are fit. The gross cloud component of the phase PSD for this pass should resemble a sinc function with the first sidelobe ~15 dB down, as measured on Figure 7-52. For this reason we believe the curve shown in Figure 7-52 represents the best fit to the random component of the data. Figures 7-53 and 7-54 provide alternate fits assuming the first sidelobe is due to random phase fluctuations.

The propagation effects appear to dissipate following Pass 29. Only weak fading occurred during this pass. The phase structure (Figure 7-33) does not indicate significant background ionization, thus, the phase PSD shown in Figure 7-55 is entirely associated with random striation structure. The best fit to the data would appear to be near the 60 dB/decade roll-off.

The outer scale size, the back-propagated phase PSD slope and the rms phase for these passes have been plotted in Figures 7-56, 7-57, and 7-58 versus time after release, respectively. Those values corresponding to the best estimate are connected by the solid line from pass to pass. The dotted line connects those points that result from a fit that includes the first spectral sidelobe peak. Passes 9 and 29 are not representative of Rayleigh fading and, thus, a phase process that should necessarily fit the analytic formulation of Equation (7-1). Thus, these points are shown, but not connected to the curves drawn. The peak integrated electron content shown has been estimated from the peak phase as given previously in Figure 5-17. This provides a comparison of the R¹S phase with the

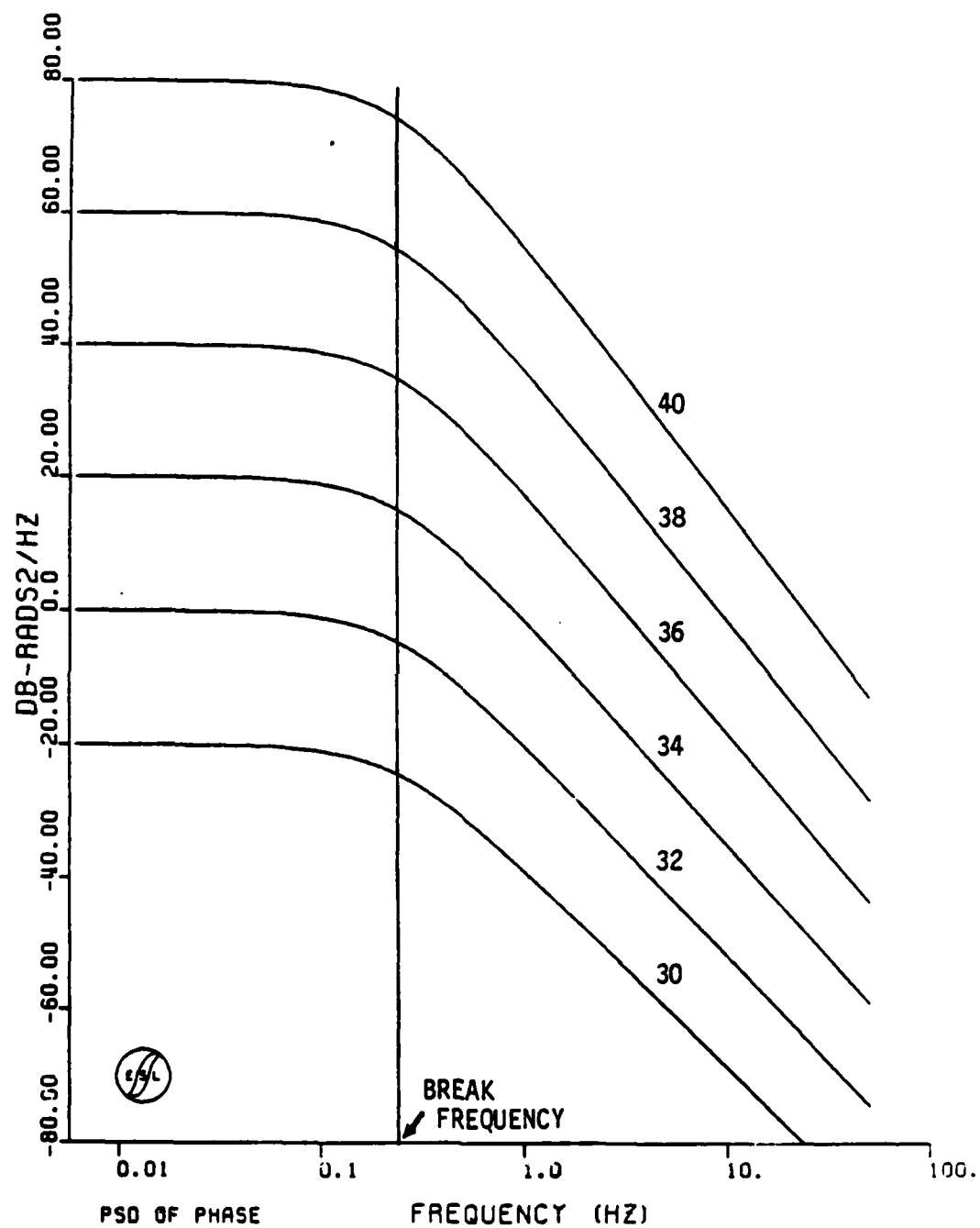


Figure 7-36. Phase PSD Template for Slopes from 30 to 40 dB/Decade

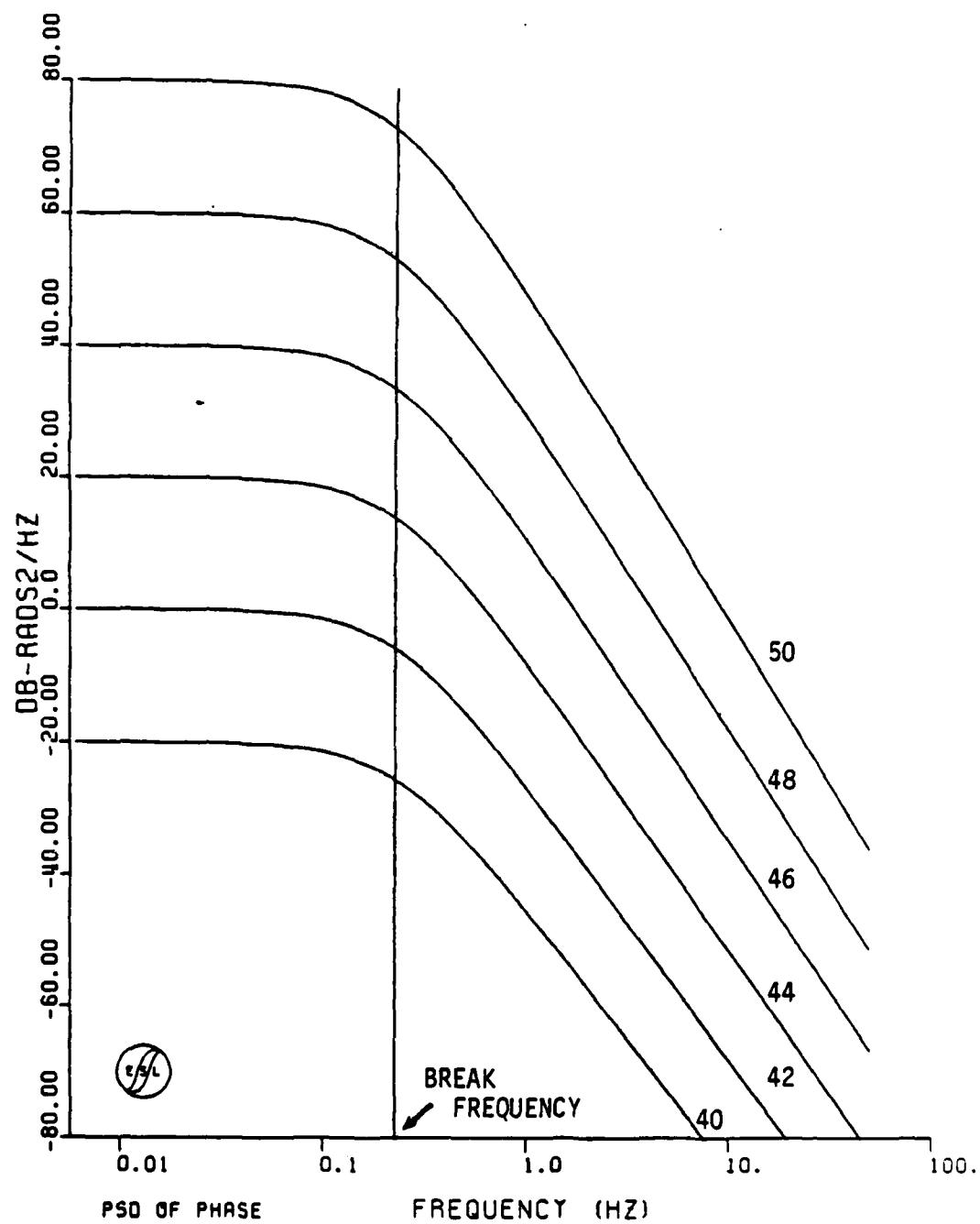


Figure 7-37. Phase PSD Template for Slopes from 40 to 50 dB/Decade

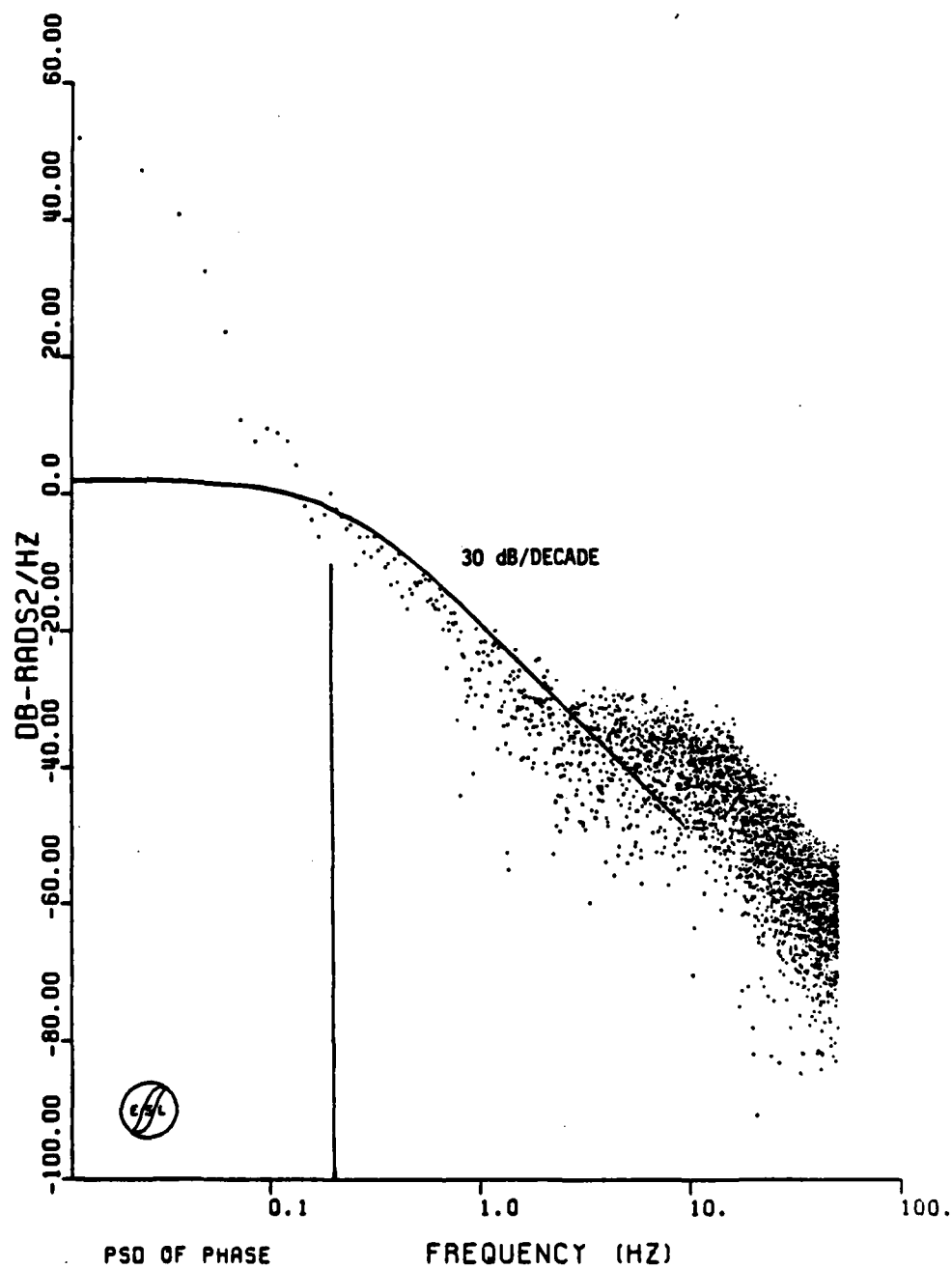


Figure 7-38. Best Fit to HOPE Pass 9 Back-Propagated Phase PSD

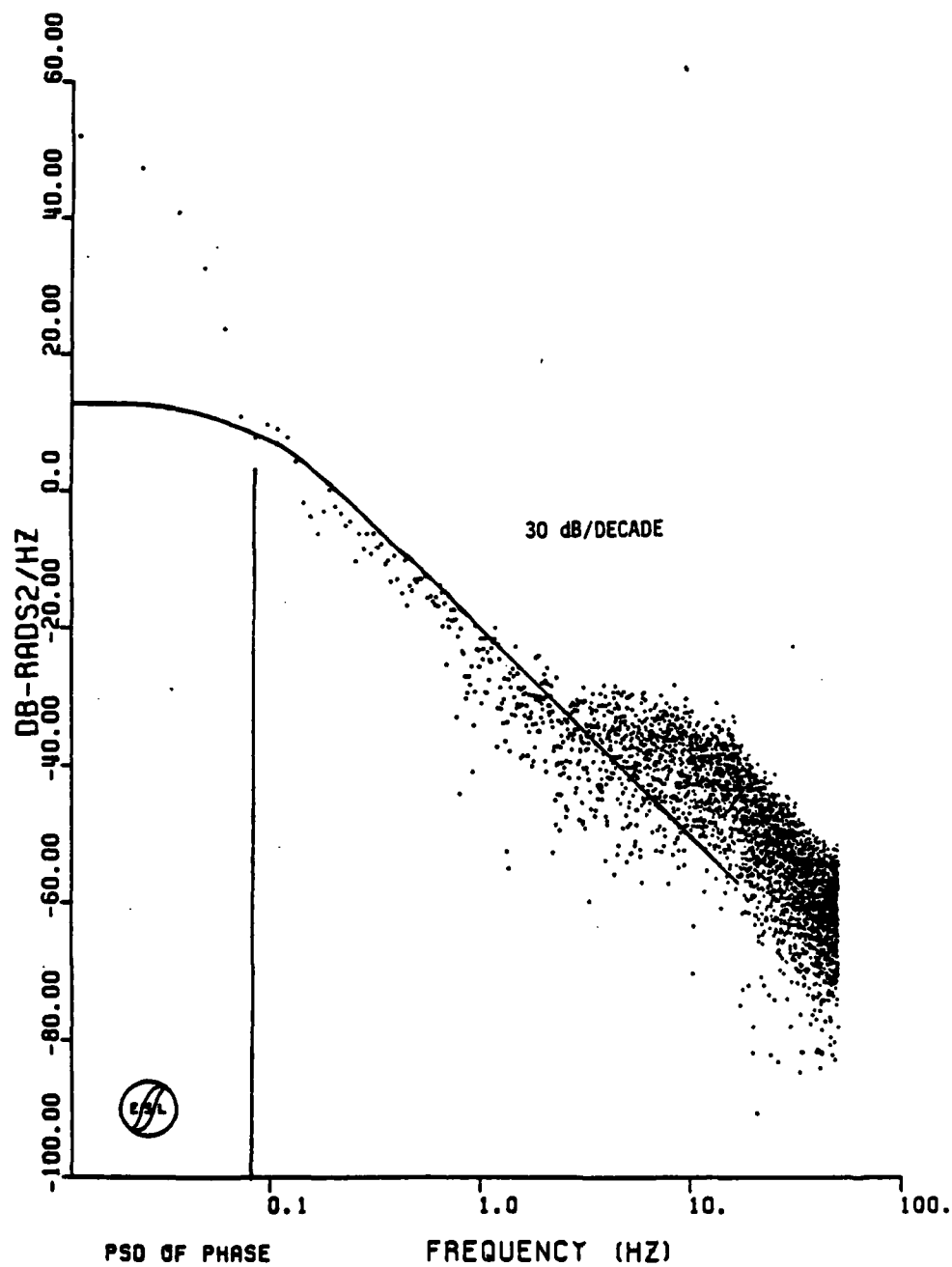


Figure 7-39. Alternate Fit to HOPE Pass 9 Back-Propagated Phase PSD

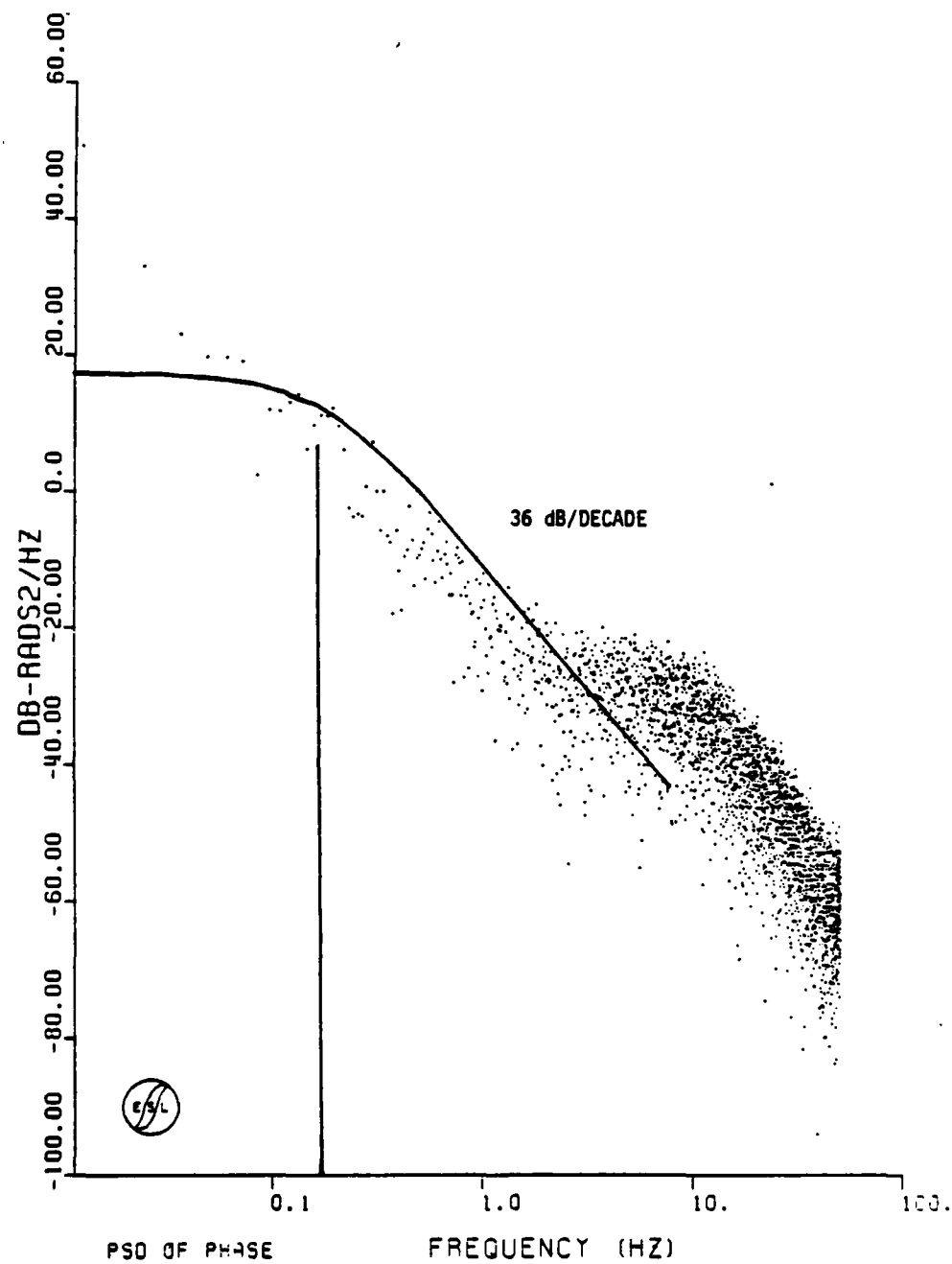


Figure 7-40. Best Fit to HOPE Pass 14 Back-Propagated Phase PSD

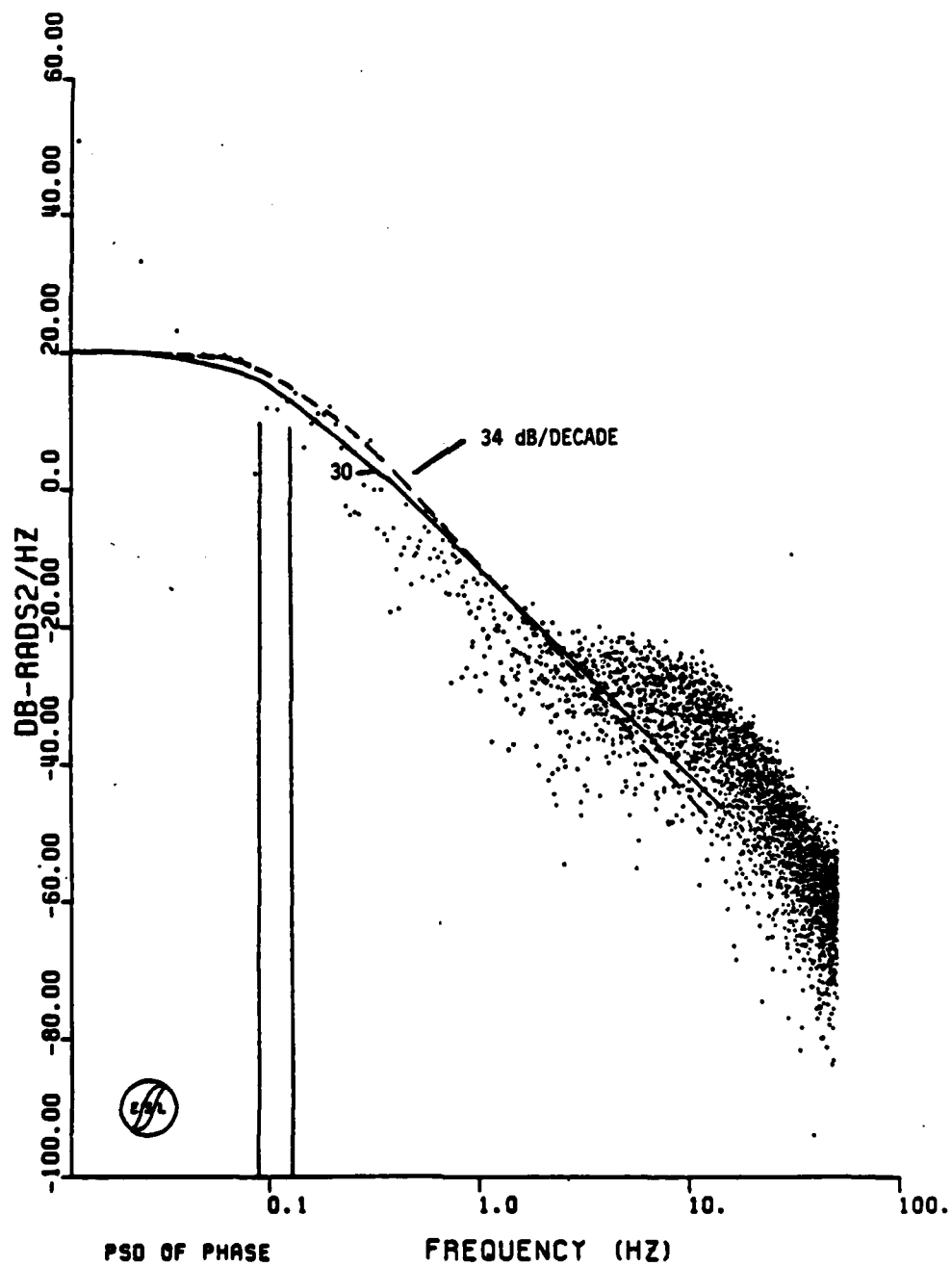


Figure 7-41. Alternate Fit to HOPE Pass 14 Back-Propagated Phase PSD

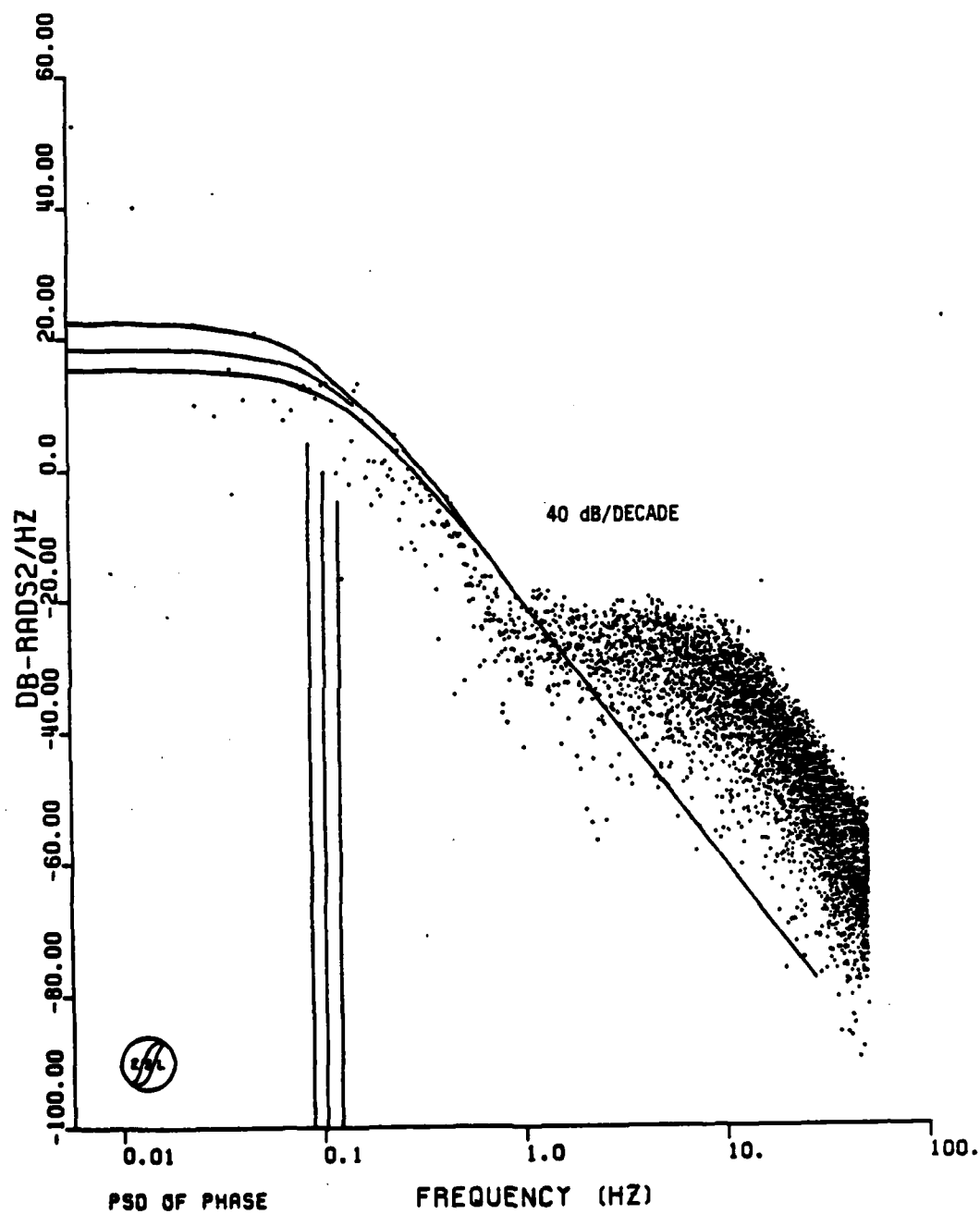


Figure 7-42. Best and Alternate Fits to HOPE Pass 15 Back-Propagated Phase PSD

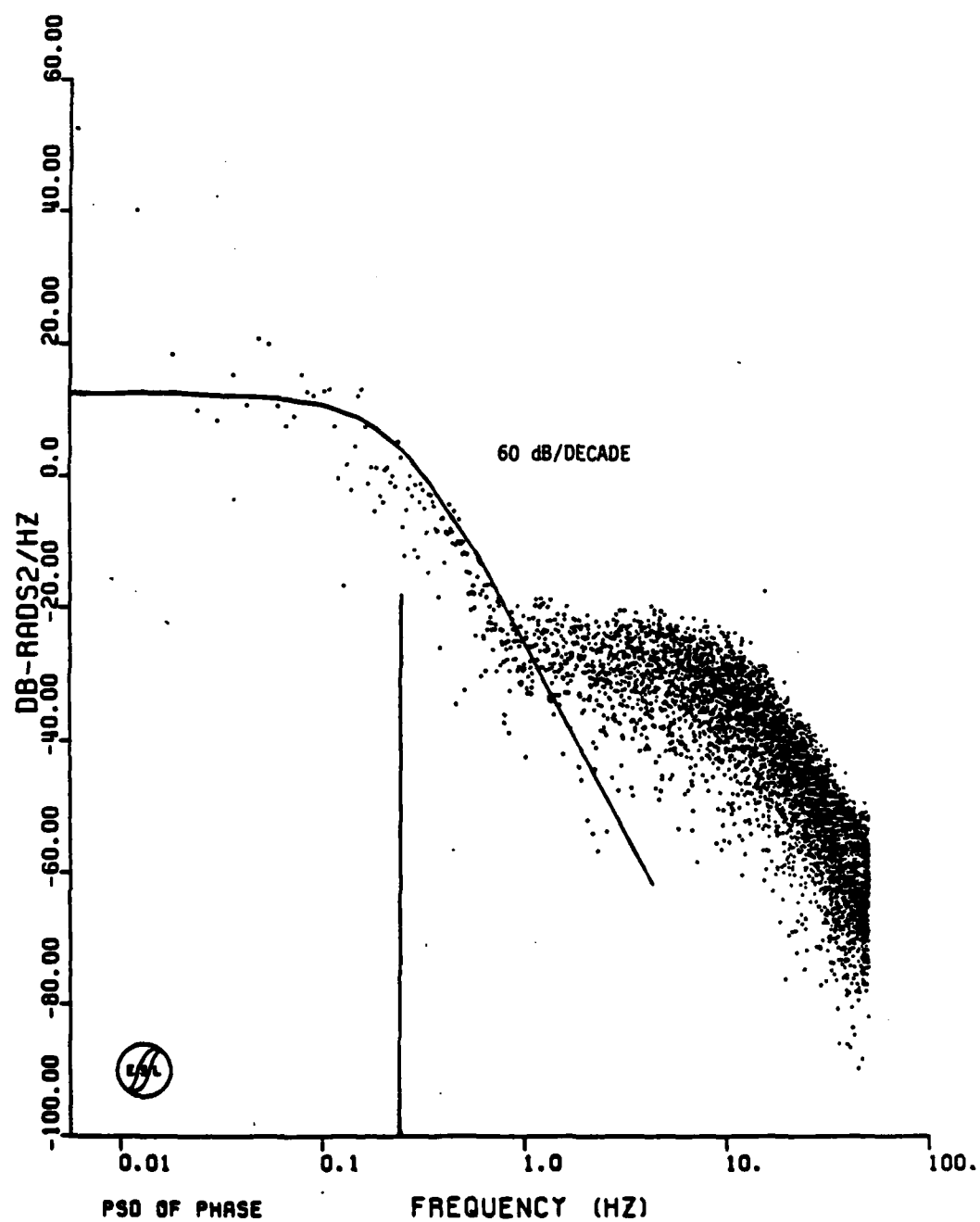


Figure 7-43. Extreme Fit to HOPE Pass 15 Back-Propagated Phase PSD

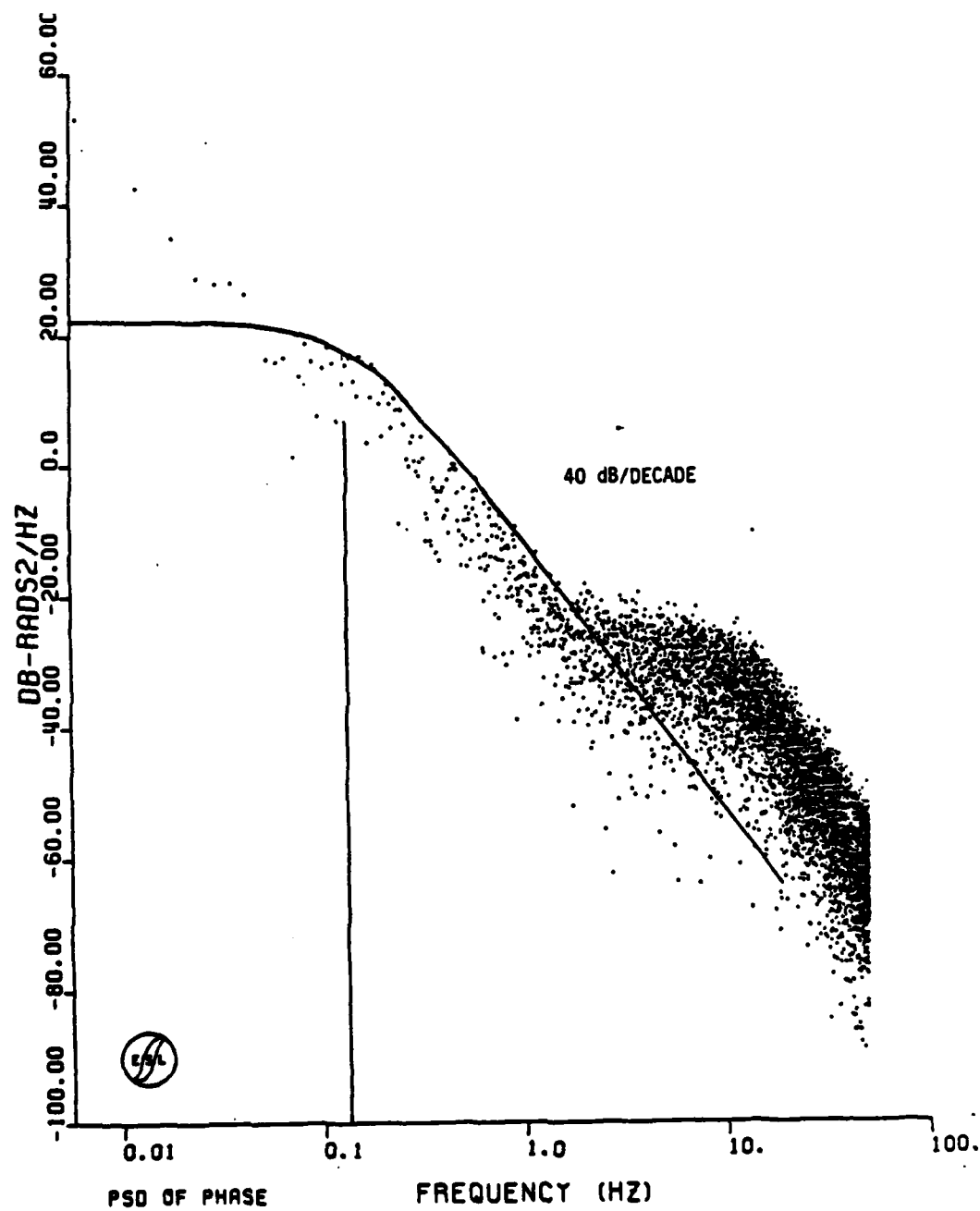


Figure 7-44. Best Fit to HOPE Pass 17 Back-Propagated Phase PSD

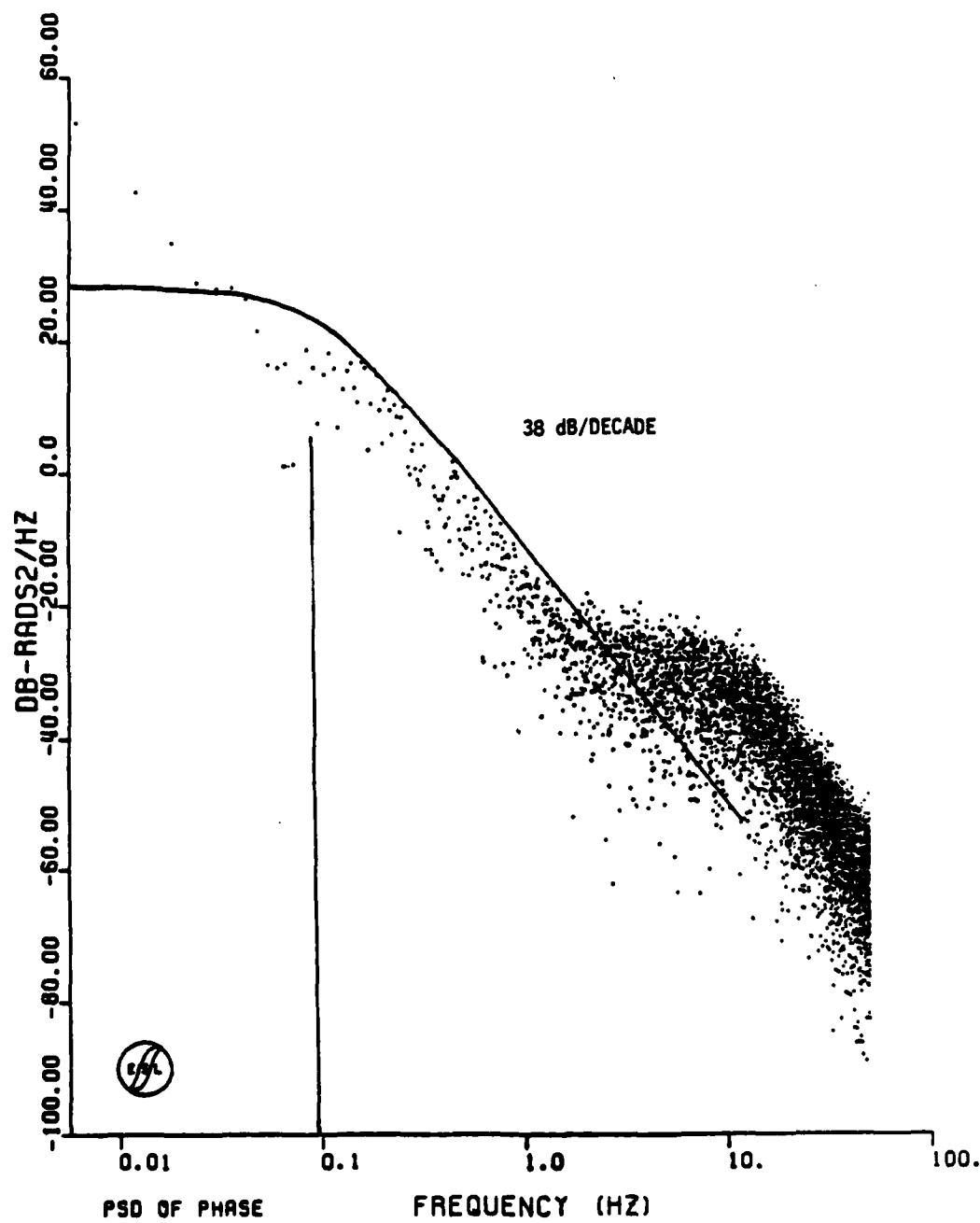


Figure 7-45. Alternate Fit to HOPE Pass 17 Back-Propagated Phase PSD

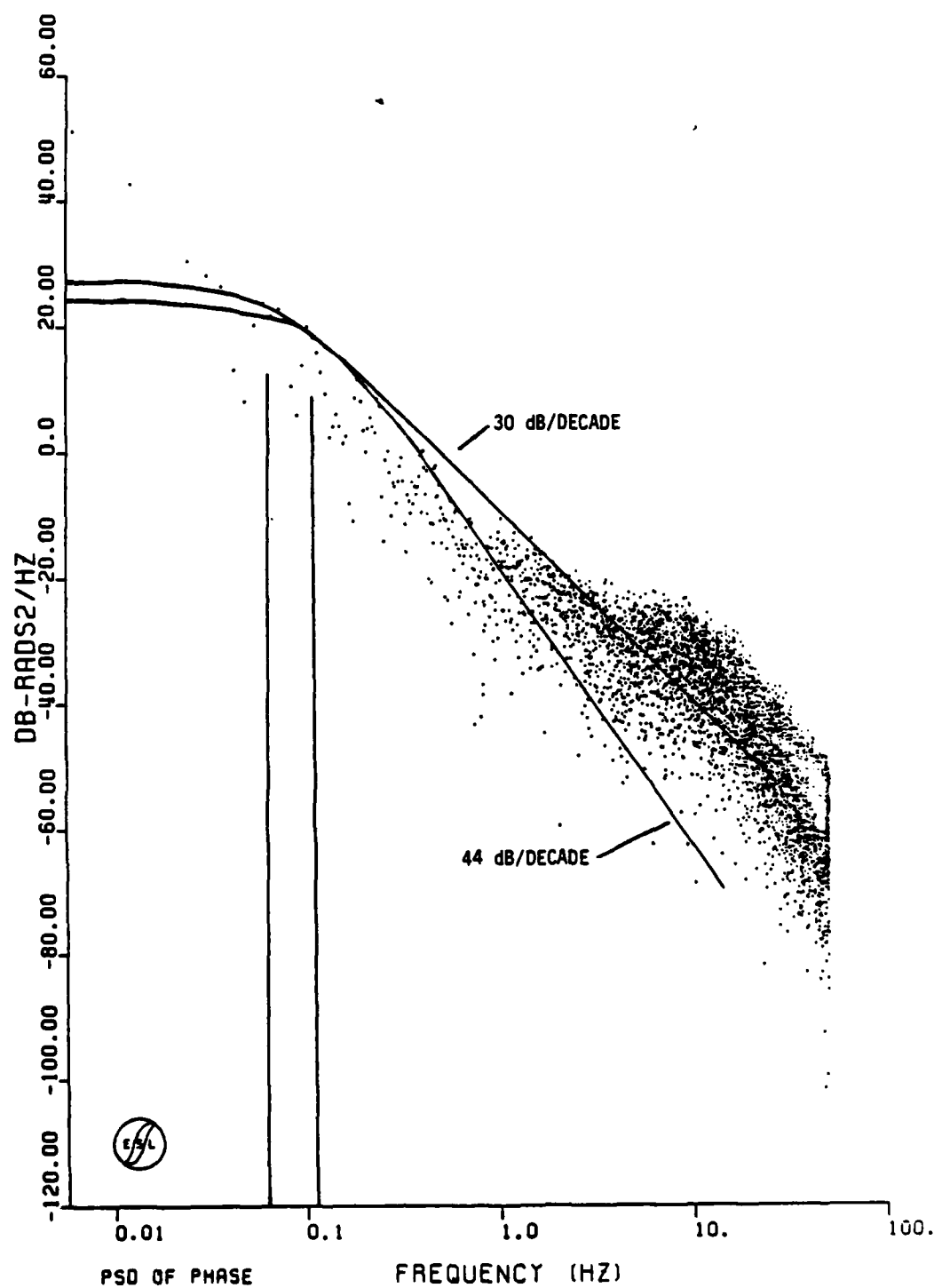


Figure 7-46. Best and Alternate Fit to HOPE Pass 19 Back-Propagated Phase PSD

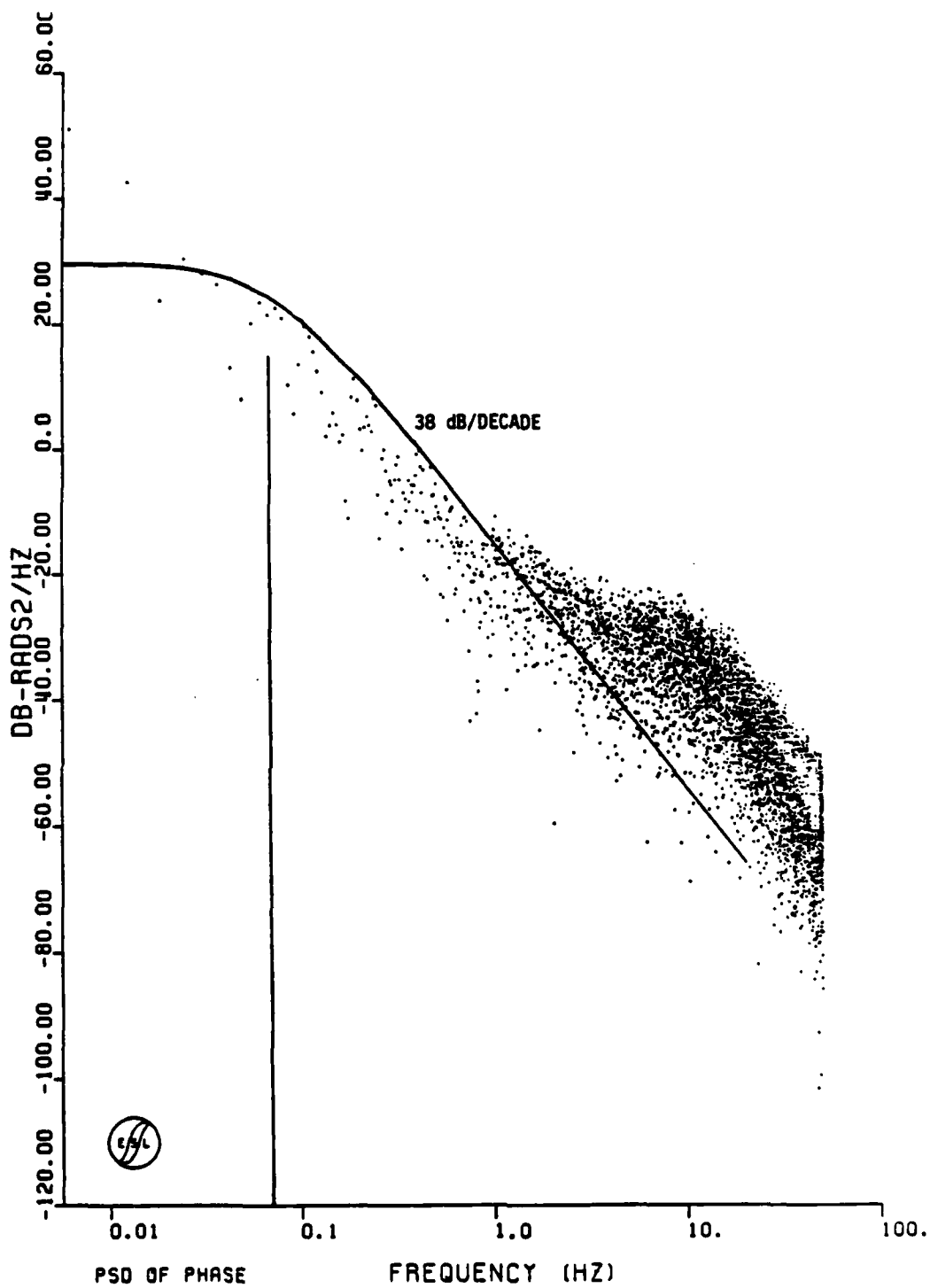


Figure 7-47. Alternate Fit to HOPE Pass 19 Back-Propagated Phase PSD

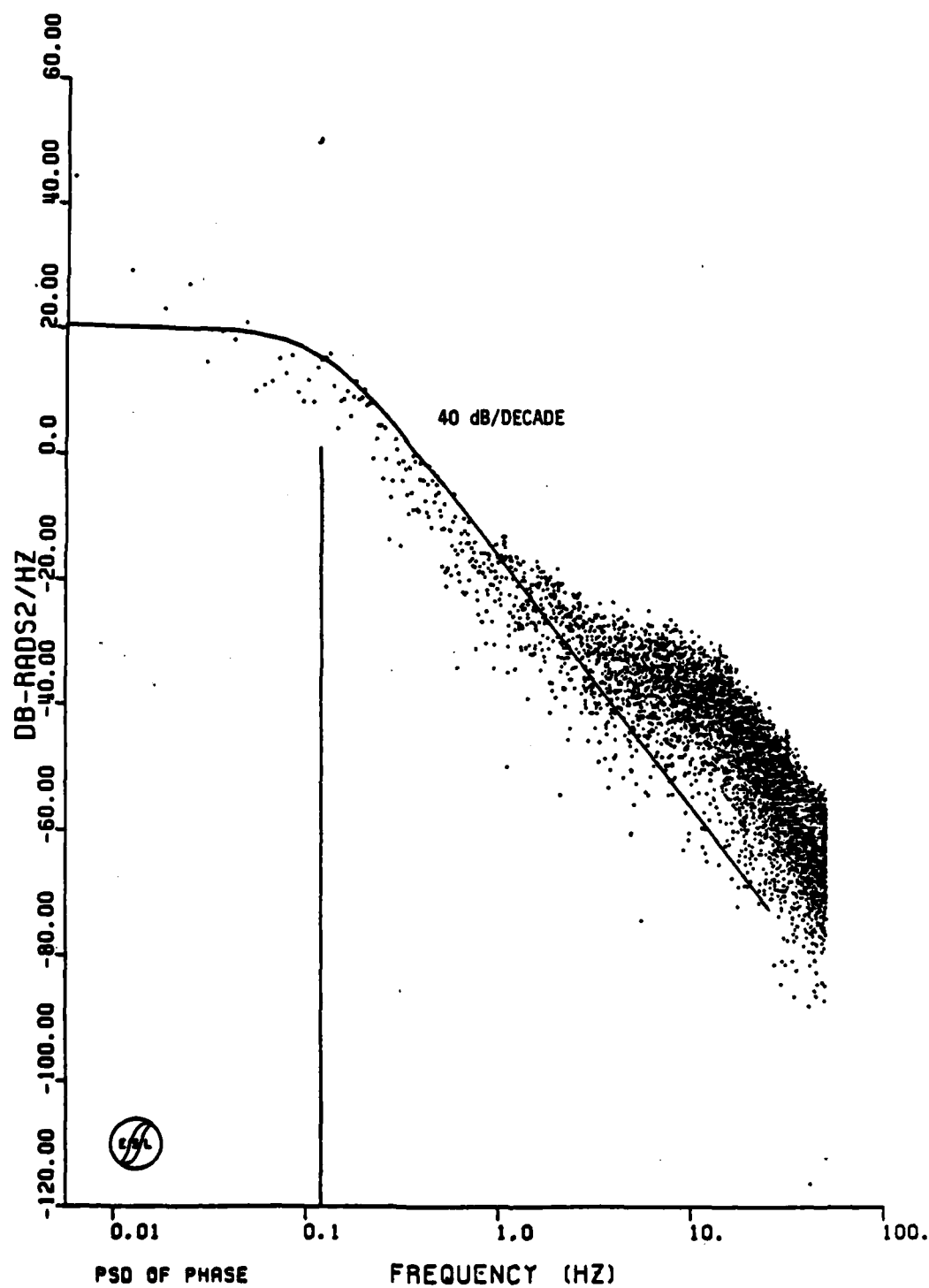


Figure 7-48. Best Fit to HOPE Pass 21 Back-Propagated Phase PSD

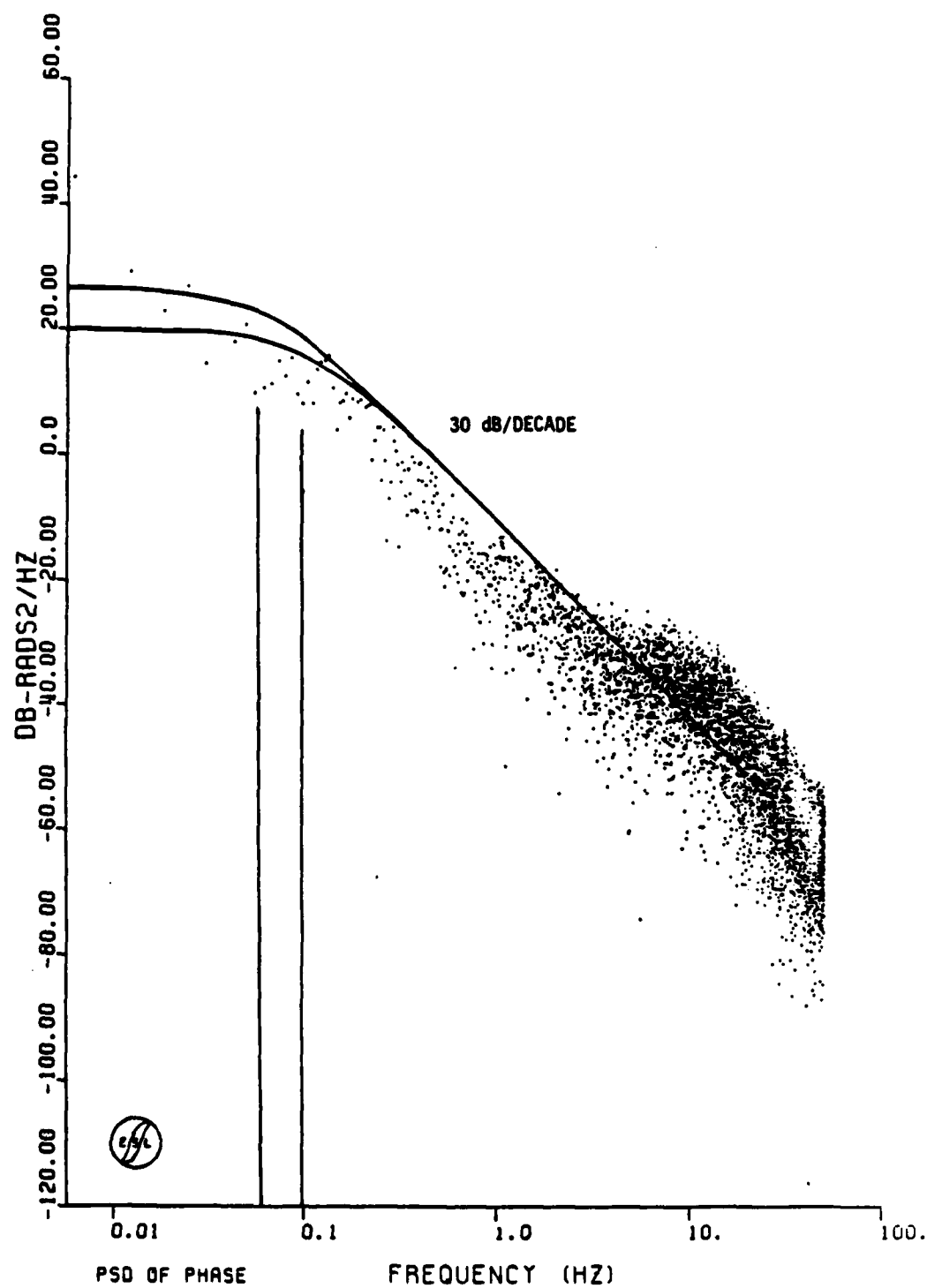


Figure 7-49. Alternate Fit to HOPE Pass 21 Back-Propagated Phase PSD

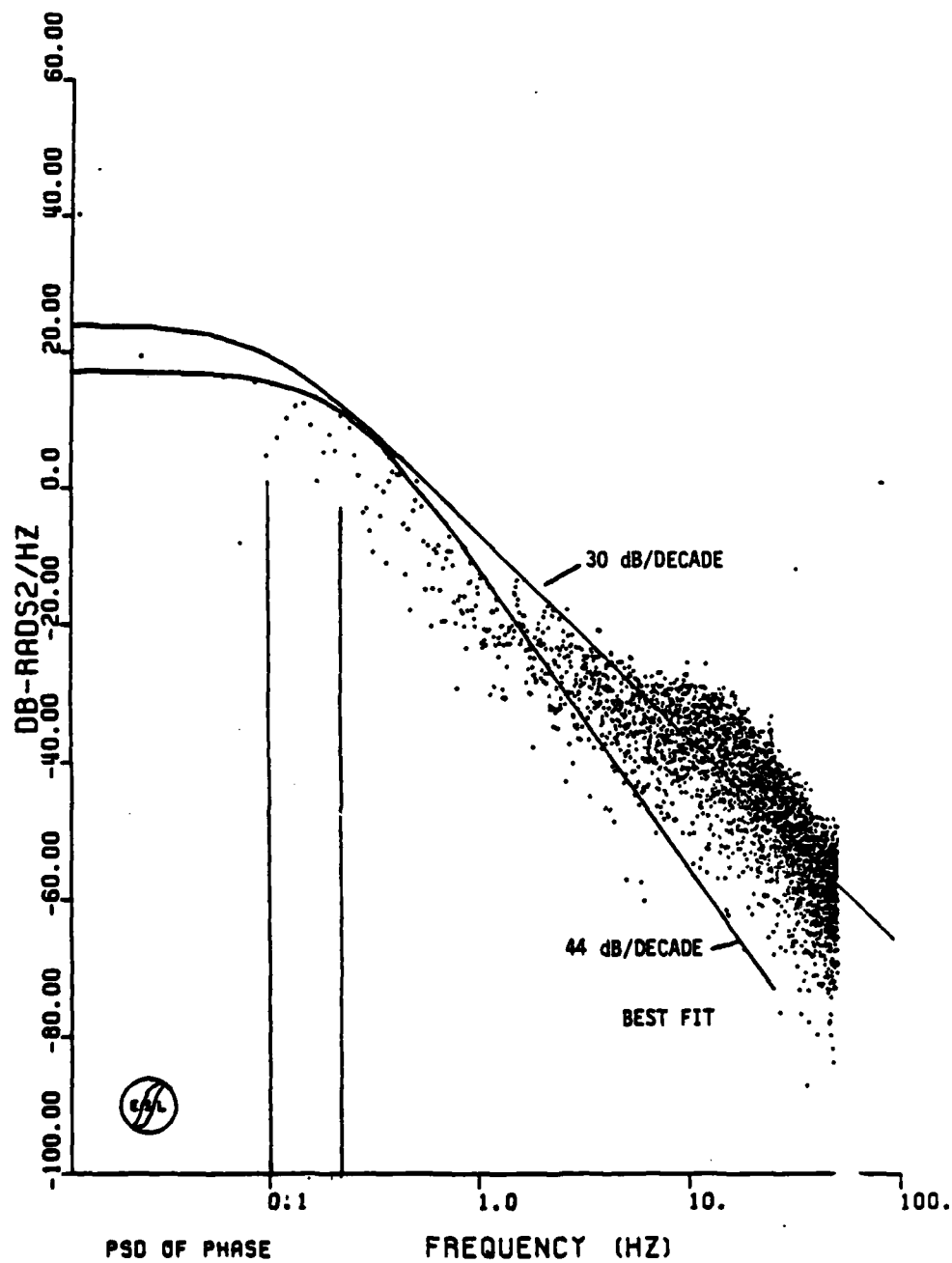


Figure 7-50. Best Fit to HOPE Pass 22 Back-Propagated Phase PSD

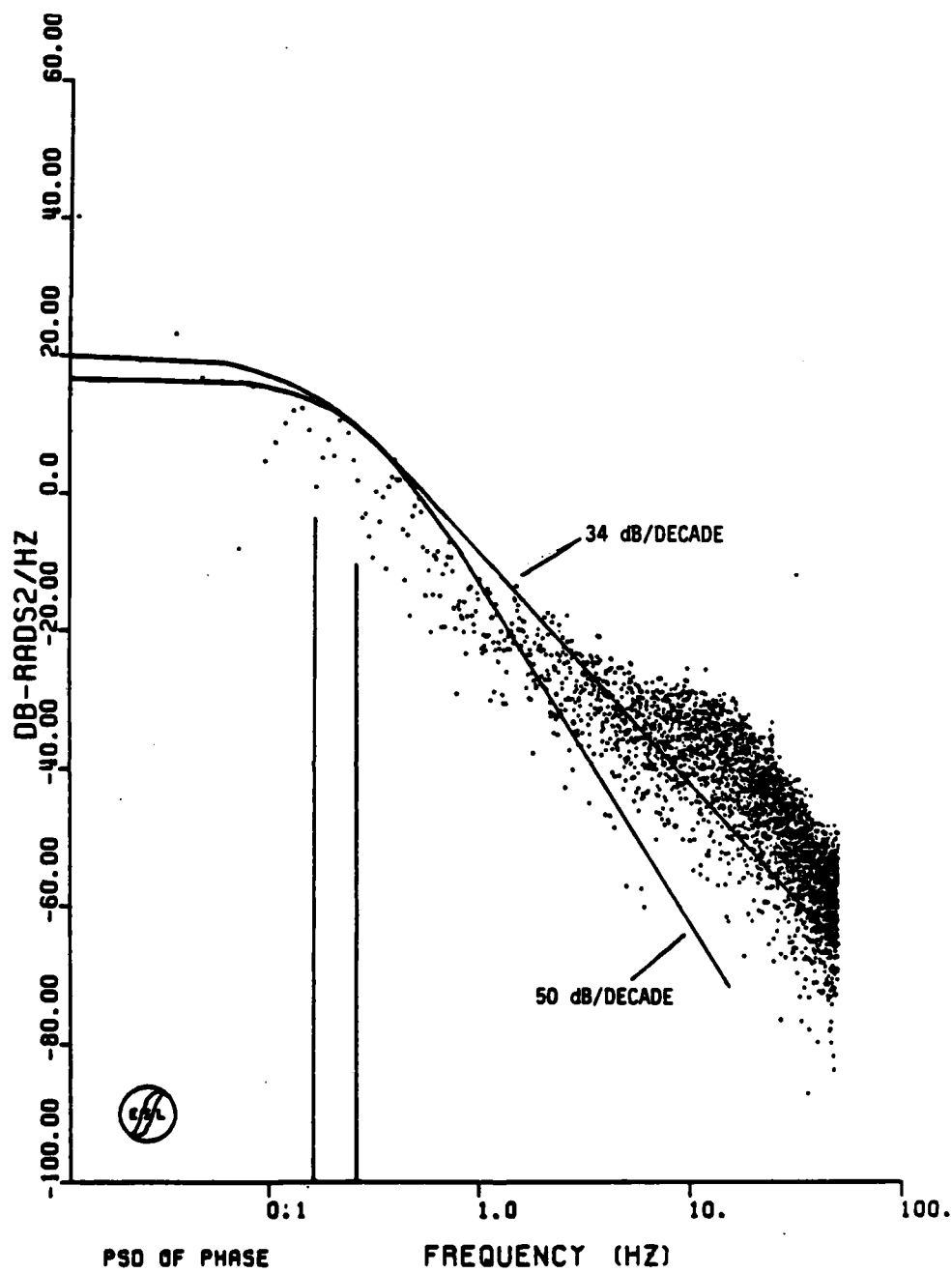


Figure 7-51. Alternate Fit to HOPE Pass 22 Back-Propagated Phase PSD

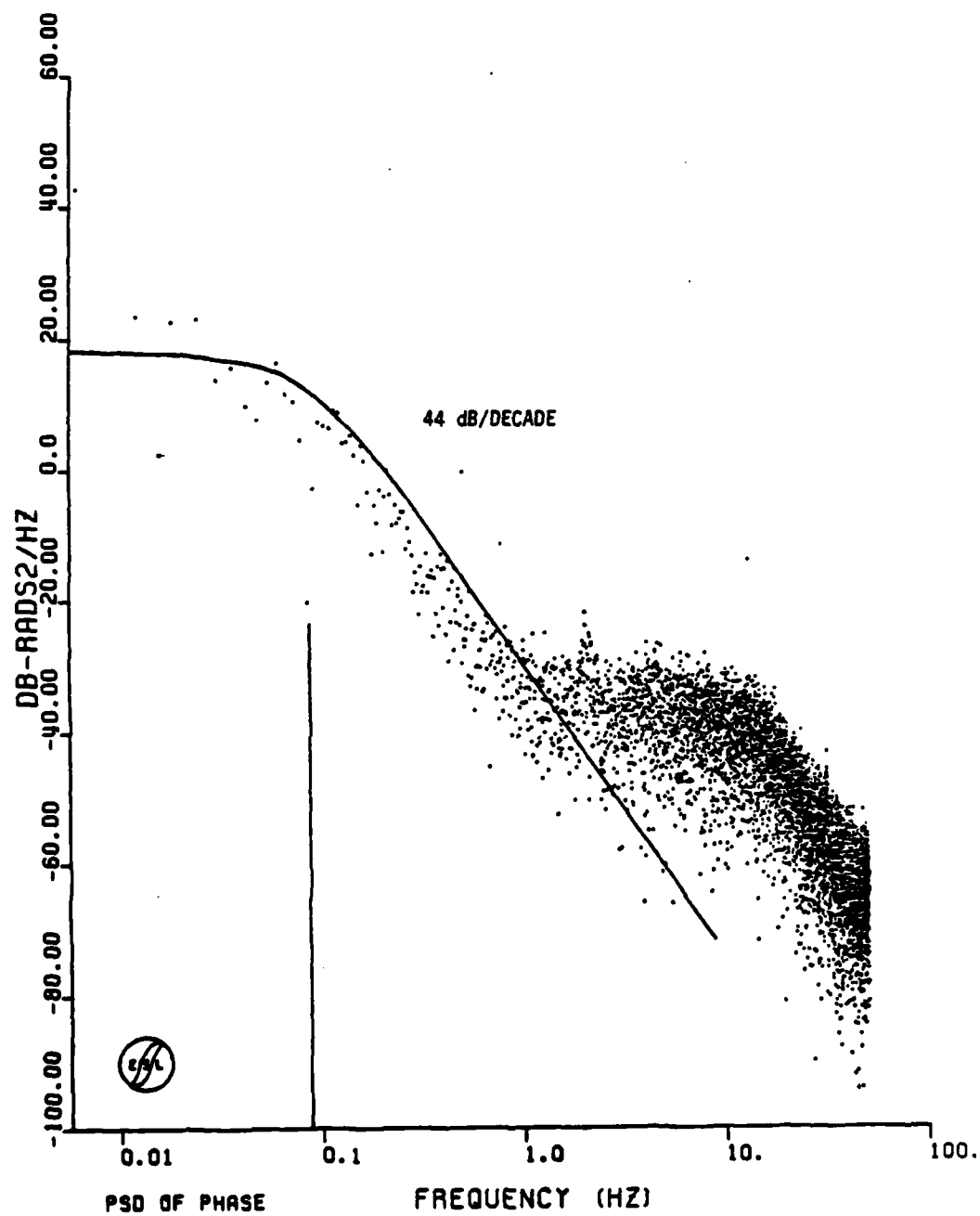


Figure 7-52. Best Fit to HOPE Pass 23 Back-Propagated Phase PSD

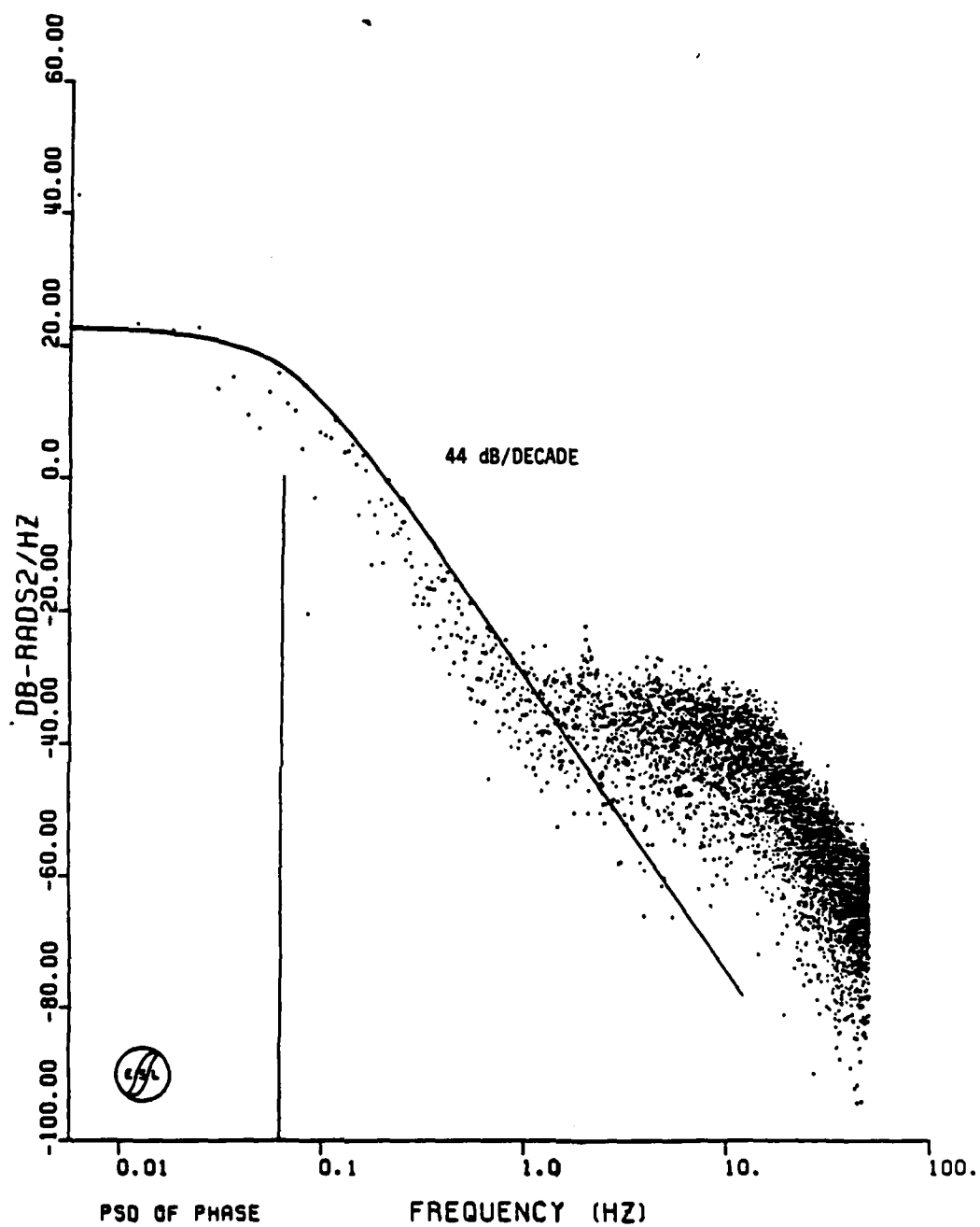


Figure 7-53. Alternate Fit to HOPE Pass 23 Back-Propagated Phase PSD

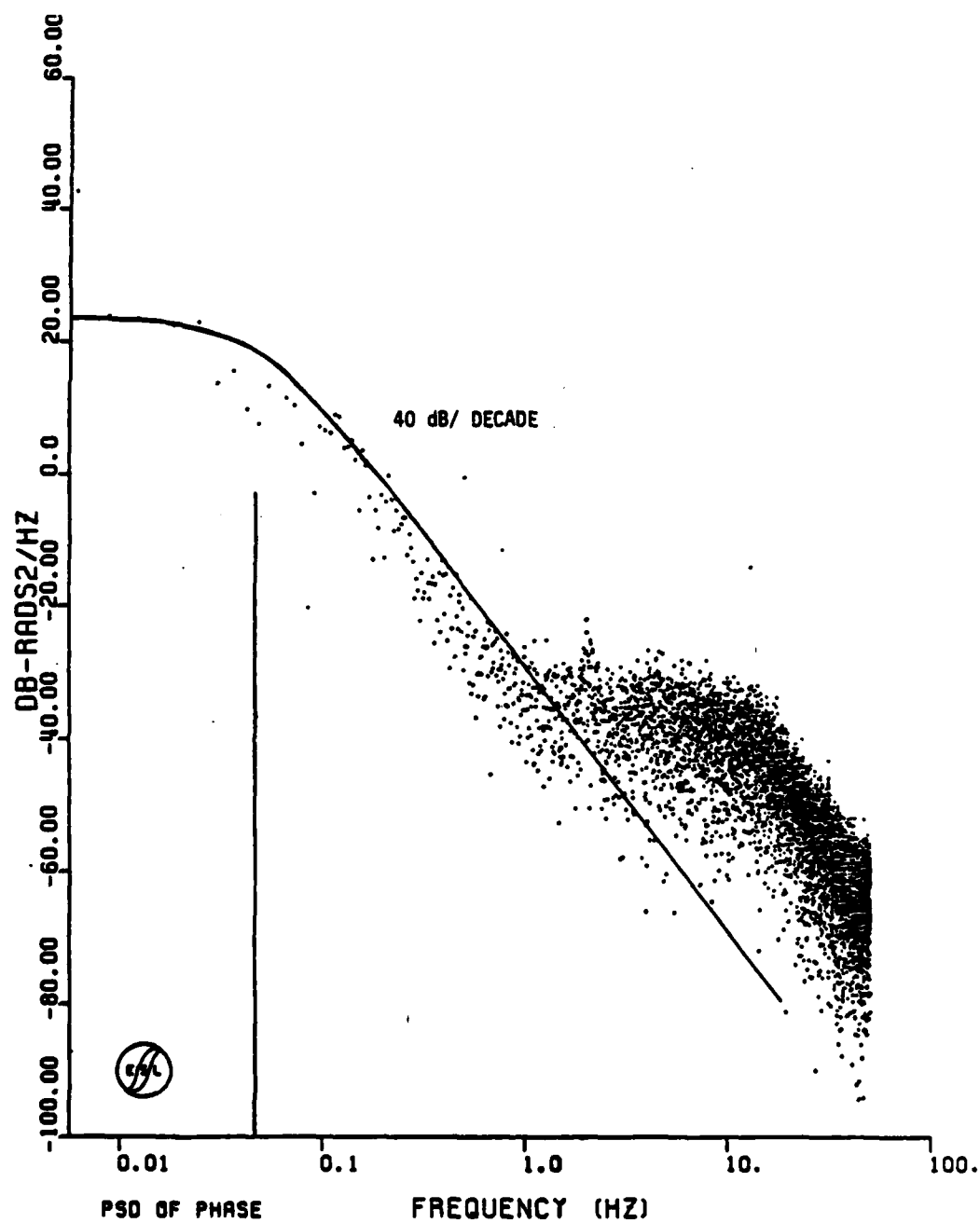


Figure 7-54. Second Alternate Fit to HOPE Pass 23 Back-Propagated Phase PSD

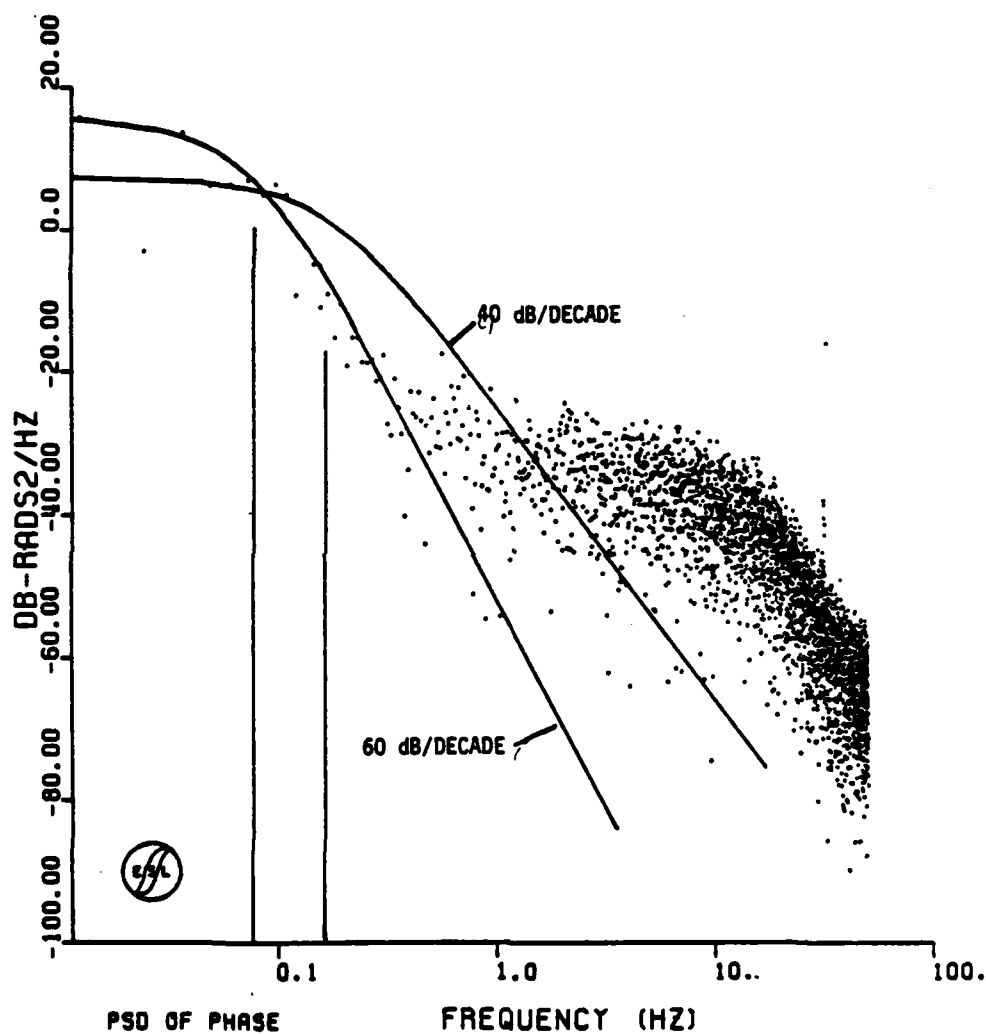


Figure 7-55. Best and Alternate Fit to HOPE Pass 29 Back-Propagated Phase PSD

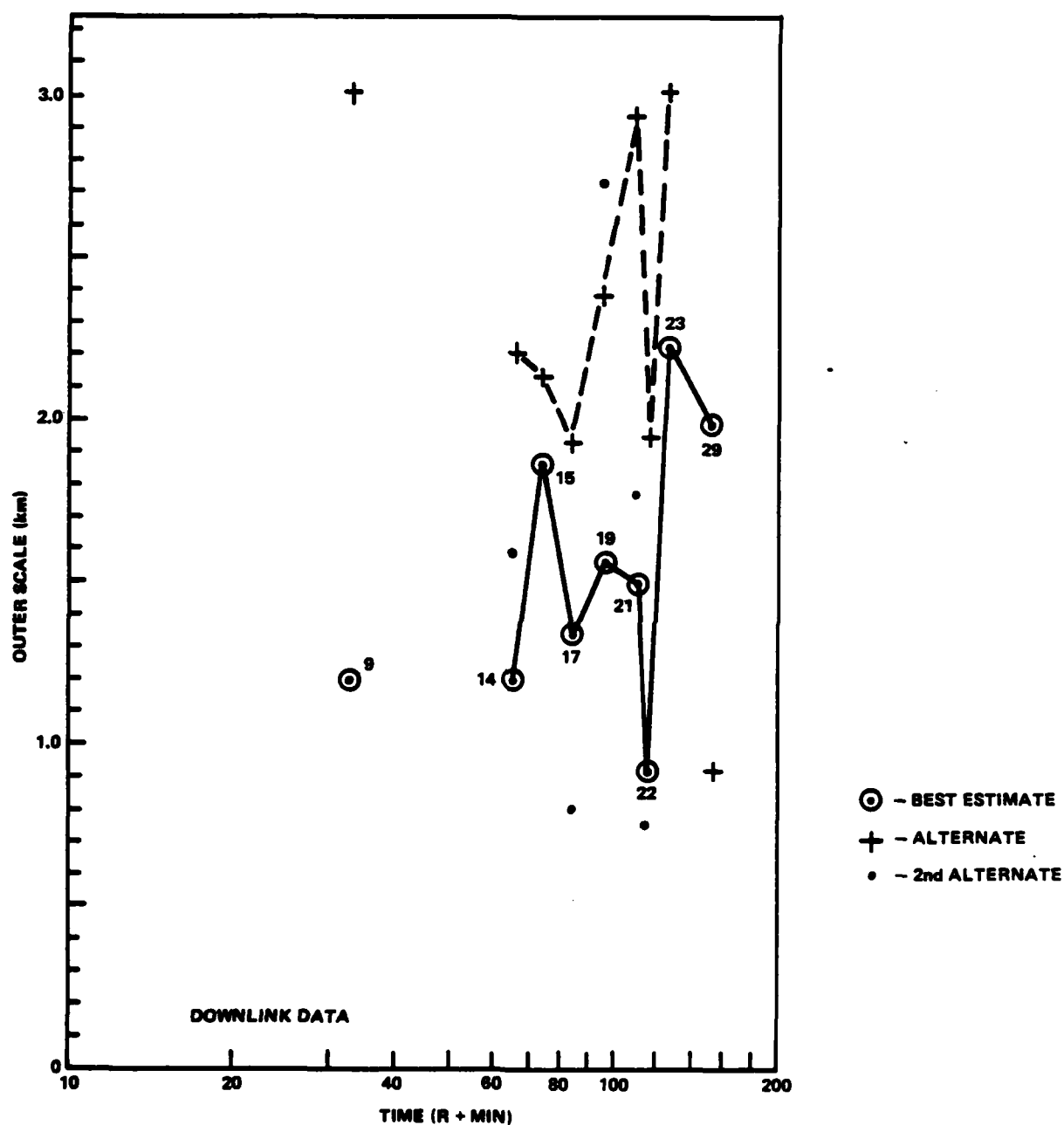


Figure 7-56. Outer Scale Versus Time for HOPE

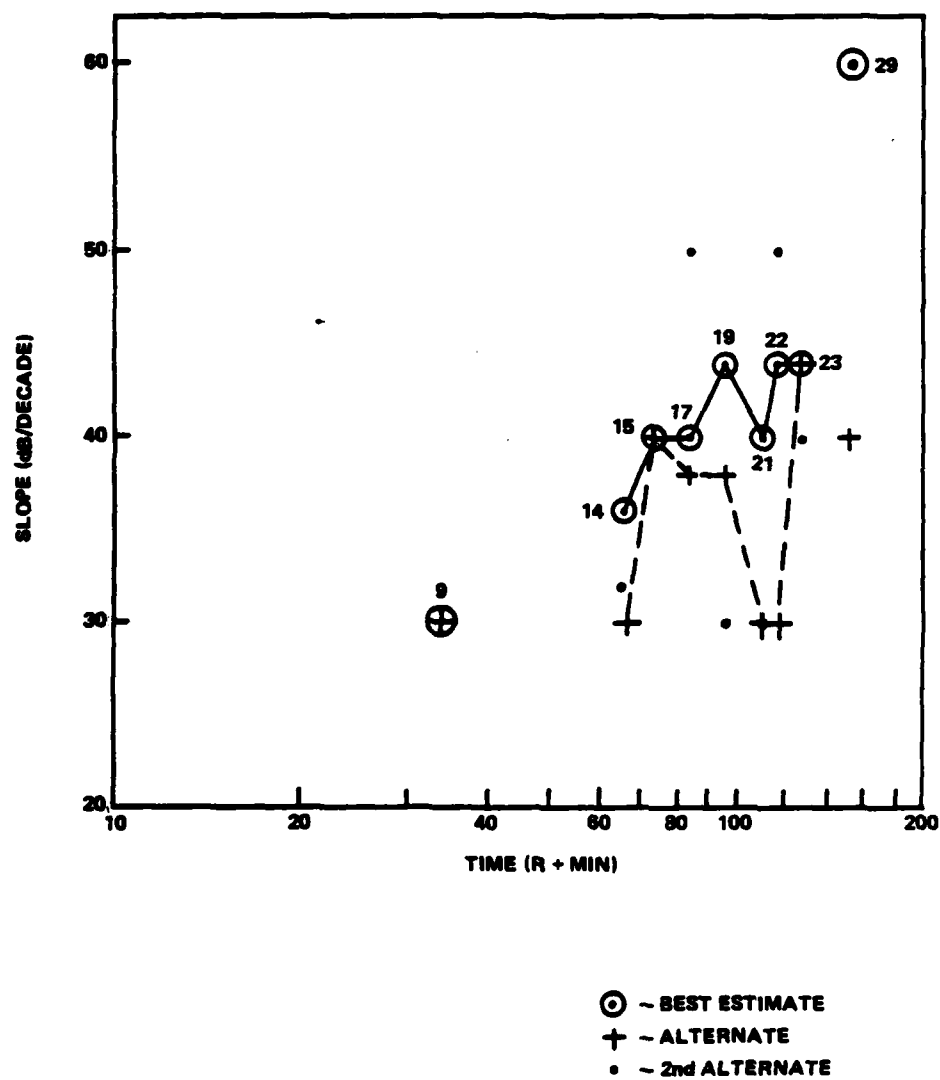


Figure 7-57. Back-Propagated Phase PSD Slope Versus Time for HOPE

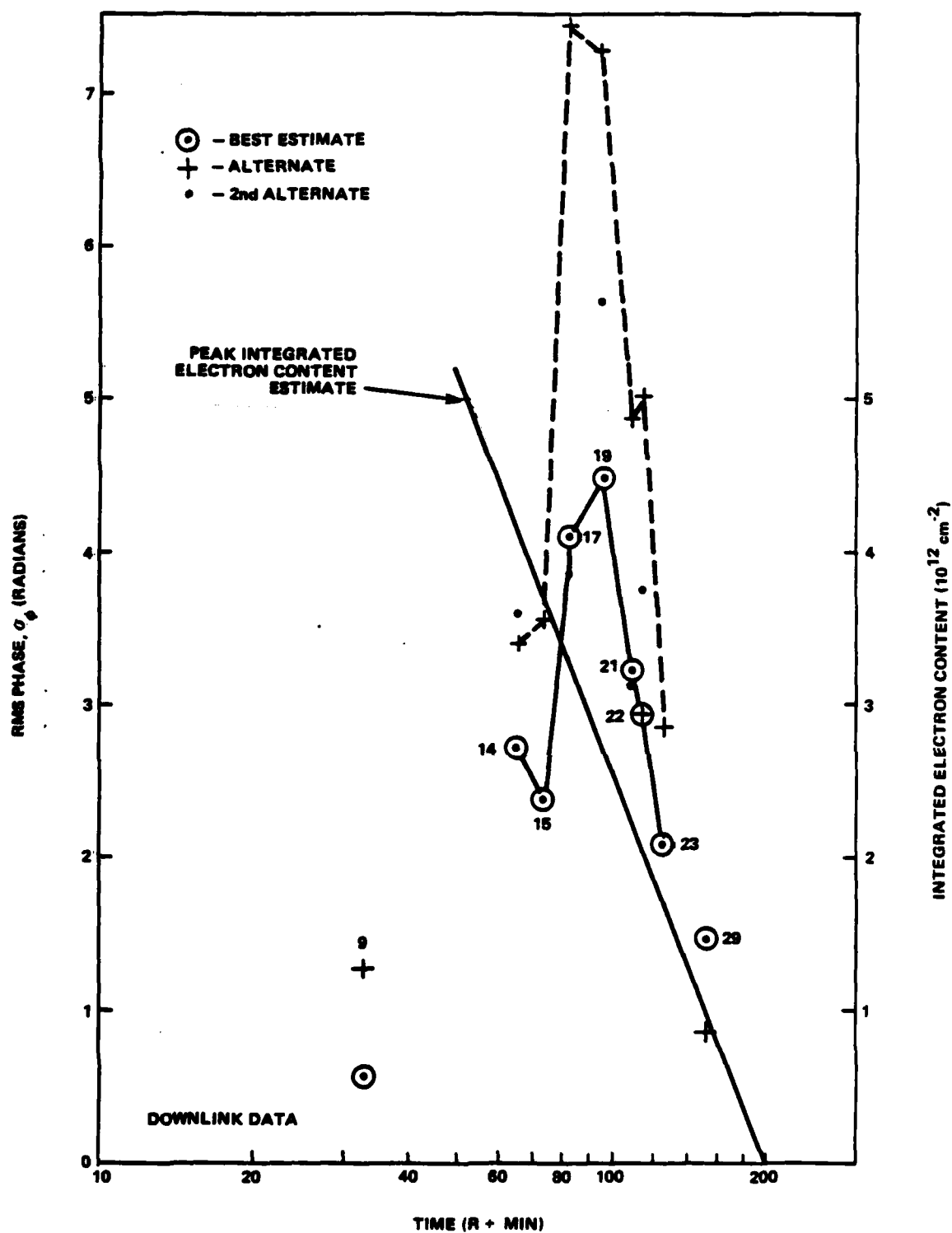


Figure 7-58. RMS Phase Versus Time for HOPE

decay in the integrated electron content through the ion cloud. Fading effects appear to dissipate as the background ion cloud ionization approaches the background ionosphere.

SECTION 8

IRIS OVERVIEW

8-1 GENERAL.

It was during IRIS, the third barium release, that the beacon rocket experiment was successfully executed. Unfortunately, just prior to release on IRIS, an oscillator failed in the airborne K-band receiver. This resulted in no usable uplink data on IRIS and no doppler correction for the downlink tone data. Manual doppler compensation was used throughout the night. This permitted good amplitude data to be obtained on the downlink signal as presented in Section 9; however, uncompensated doppler excursions in the phase data made back-propagation attempts unsuccessful.

Two beacon rockets were fired during this release, both resulting in good data. The Beacon Experiment results are presented in Reference 3.

8-2 RELEASE GEOMETRY.

The third barium release, IRIS, was on 8 December 1980 and occurred at 23:13:08. It was released at an altitude of 182.2 kilometers and a latitude and longitude of 28.7633°N and 87.1853°W. The projection of this release point is 30.7635°N and 86.0093°W. The cloud projection moved in a south-southeast direction during the entire experiment. Fading was last observed about 3 degrees south and 0.75 degrees east of the release point projection at R+2 hours 30 minutes. Plots of the cloud track projection and aircraft ground track are in Figures 8-1 and 8-2. Figures 8-3, 8-4, and 8-5 show the aircraft ground track for each hour with intervals of strong fading indicated.

No cloud tracking data was available between release and R+12 minutes. Optics track data was used from R+12 minutes to R+15 minutes and radar track data was used thereafter. The release being low and west of the planned release point

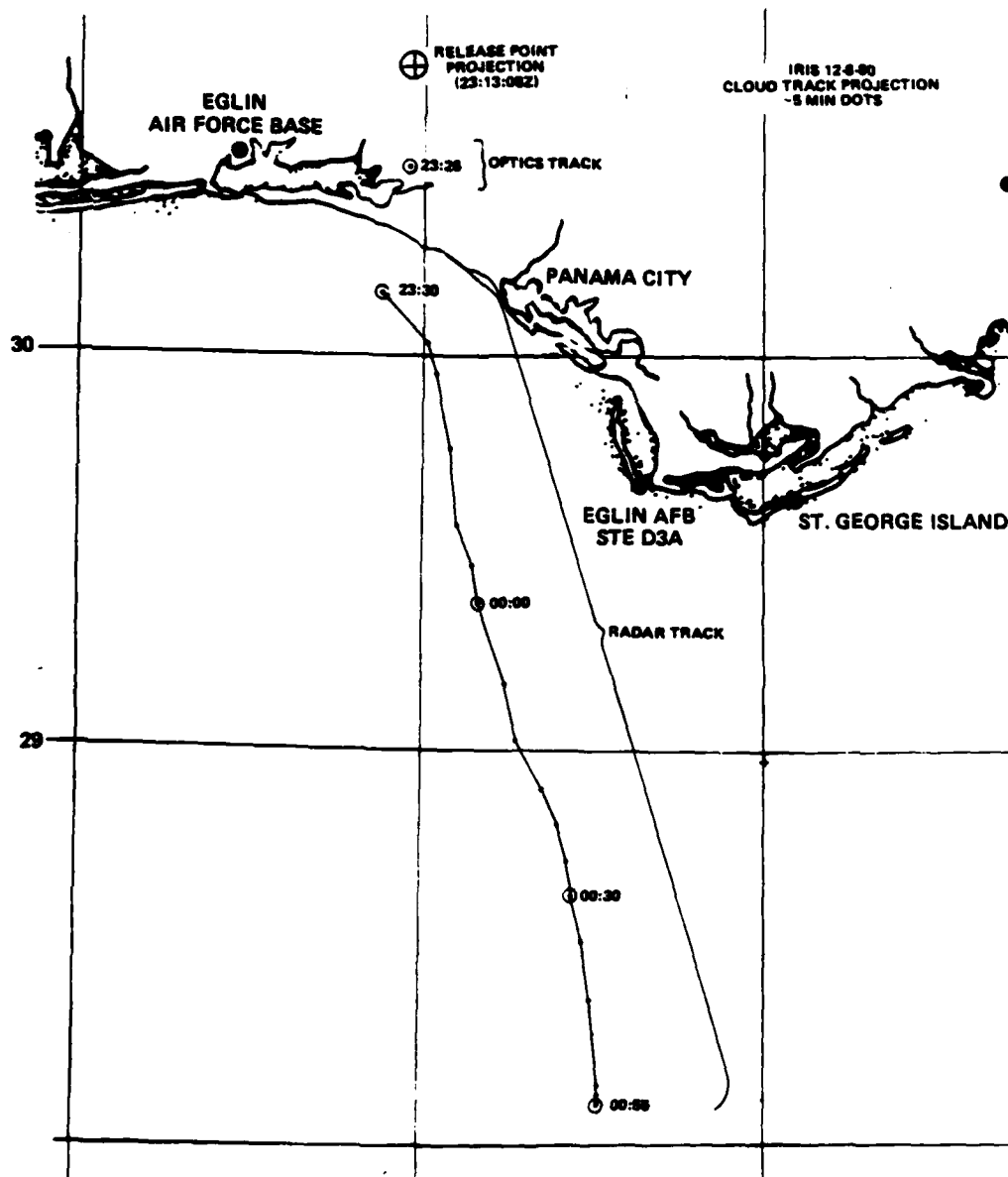


Figure 8-1. Ion Cloud Track Projection for IRIS

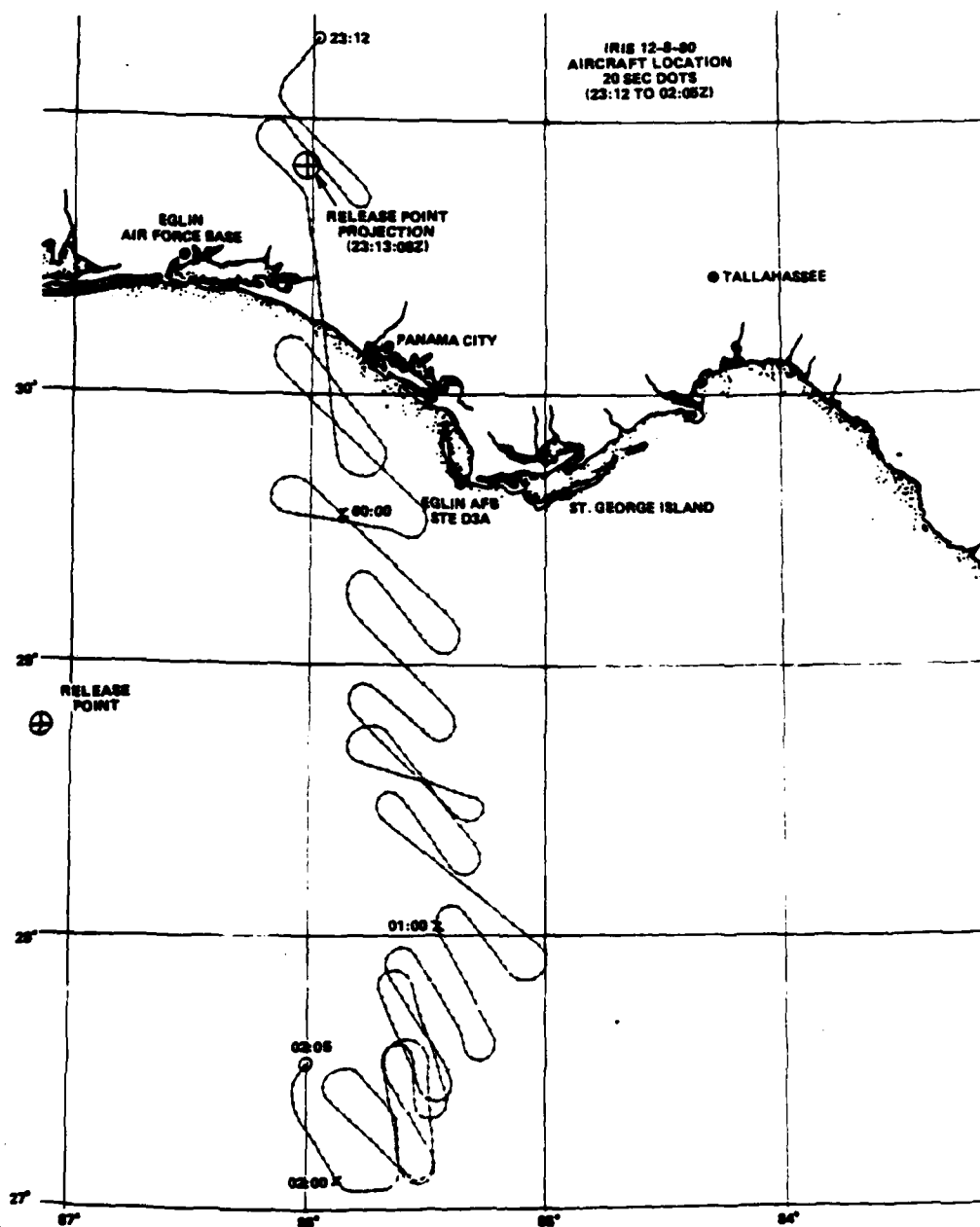


Figure 8-2. Aircraft Ground Track for IRIS

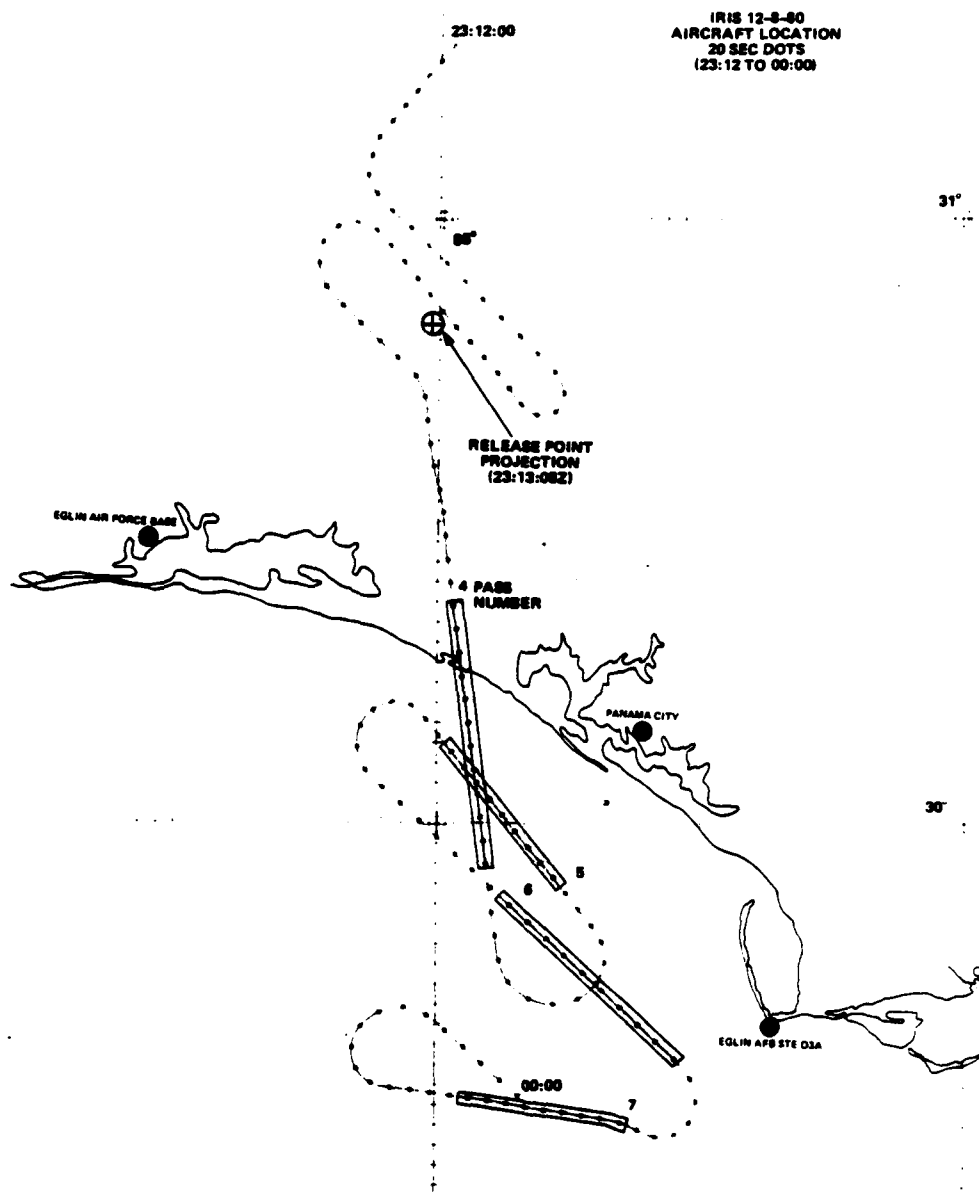


Figure 8-3. Aircraft Ground Track for IRIS from 23:12 to 00:00Z.
Periods of Deep Fading are Shaded.

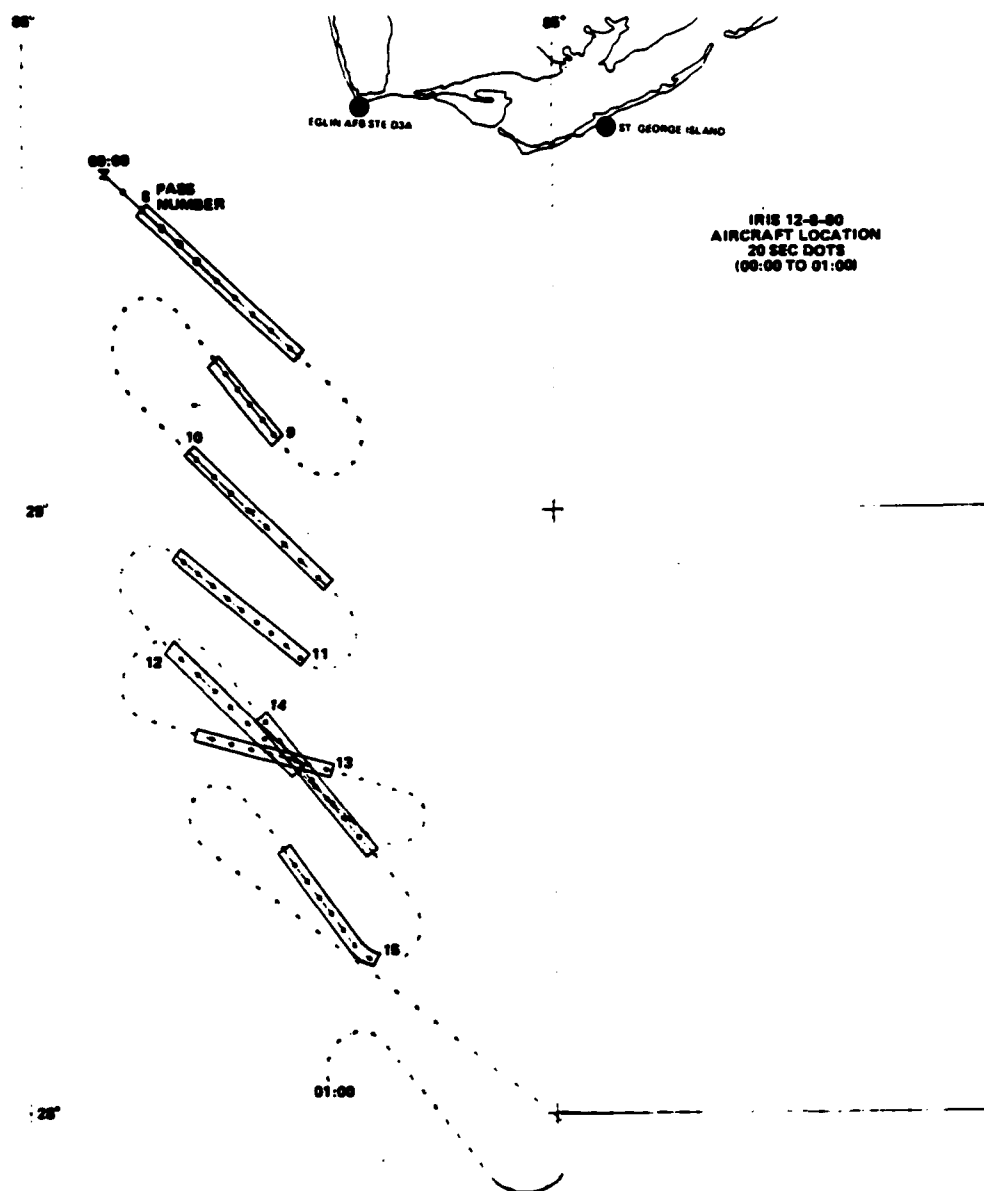


Figure 8-4. Aircraft Ground Track for IRIS from 00:00 to 01:00Z. Periods of Deep Fading are Shaded.

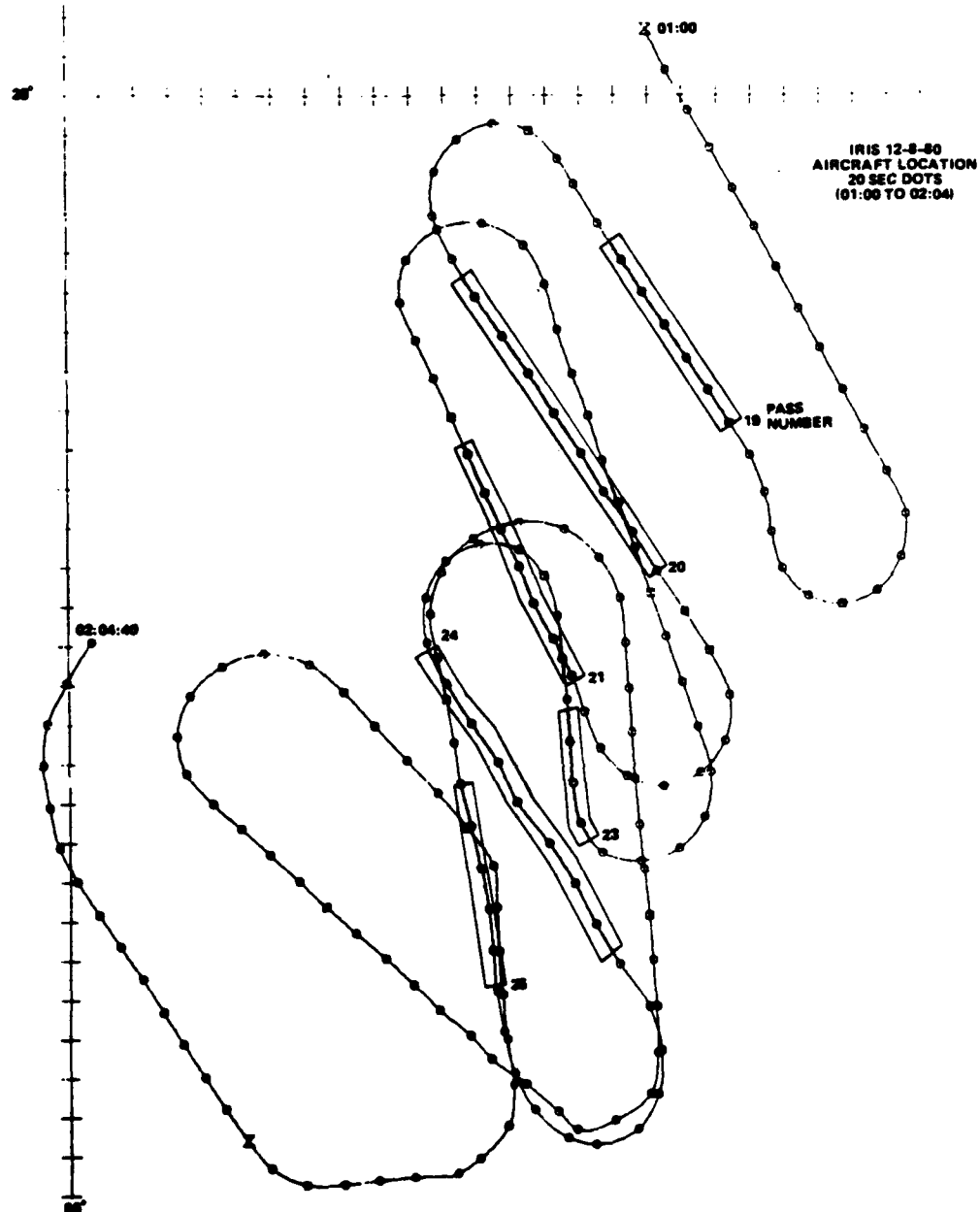


Figure 8-5. Aircraft Ground Track for IRIS from 01:00 to 02:04Z. Periods of Deep Fading are Shaded.

resulted in the radar not acquiring the release as planned. The radar track provided a consistent indication of the striation location throughout the night.

8-3 FADING DATA SUMMARY.

A total of 31 passes were made ending at R+2 hours 48 minutes. A summary of these passes is given in Table 8-1. The first strong fading was seen at R+16 minutes, the fourth pass. Moderate to strong fading was present during 17 of the next 22 passes with the last strong fading ending at R+2 hours 26 minutes. The last fading observed ended at R+2 hours 44 minutes during Pass 29. Downlink amplitude data is available for all 31 passes. K-band lock was never achieved during this experiment due to an oscillator failure, consequently no usable uplink data was recorded. Manual doppler correction was used throughout the night as indicated in Table 8-1. The downlink data is presented in the next section.

Table 8-1. Aircraft Data Summary for IRIS

Pass No.	Time	K-Lock	Comments
1	23:15:30-23:18:10	No, manual doppler correction	No fading
2	23:19:40-23:23:10	No, manual doppler correction	Weak diffraction ringing
3	23:25:10-23:28:20	No, manual doppler correction	No fading
4	23:29:20-23:34:20	No, manual doppler correction	Strong fading, large defocus
5	23:38:30-23:41:30	No, manual doppler correction	Strong fading, large defocus, second fading object
6	23:46:30-23:49:40	No, manual doppler correction	Strong fading
7	23:51:50-23:54:50	No, manual doppler correction	Strong fading
8	00:00:40-00:03:30	No, manual doppler correction	Strong fading
9	00:06:50-00:08:30	No, manual doppler correction	Strong fading
10	00:13:20-00:15:50	No, manual doppler correction	Strong fading
11	00:18:10-00:20:40	No, manual doppler correction	Strong fading

Table 8-1. -- Continued

Pass No.	Time	K-Lock	Comments
12	00:23:20-00:26:00	No, manual doppler correction	Strong fading
13	00:30:30-00:32:50	No, manual doppler correction	Strong fading
14	00:37:00-00:39:40	Yes, no uplink tone	Weak fading
15	00:41:50-00:44:20	Yes, no uplink tone	Strong fading
16	00:48:00-00:52:00	Yes	No fading
17	00:56:00-00:58:00	Yes	No fading
18	01:00:40-01:03:40	No, manual doppler correction	No fading
19	01:07:00-01:08:50	No, manual doppler correction	Moderate fading
20	01:11:50-01:14:20	No, manual doppler correction	Strong fading
21	01:17:50-01:20:00	No, manual doppler correction	Strong fading
22	01:23:30-01:26:00	No, manual doppler correction	No fading
23	01:27:50-01:29:20	No, manual doppler correction	Moderate fading
24	01:31:30-01:34:10	No, manual doppler correction	Moderate fading
25	01:38:00-01:39:40	No, manual doppler correction	Moderate fading

Table 8-1. -- Continued

Pass No.	Time	K-Lock	Comments
26	01:44:00-01:46:00	No, manual doppler correction	No fading
27	01:47:30-01:49:40	No, manual doppler correction	Weak fading
28	01:54:00-01:55:00	No, manual doppler correction	No fading
29	01:56:00-01:57:00	No, manual doppler correction	Weak fading
30	01:58:00-01:59:00	No, manual doppler correction	No fading
31	02:00:00-02:01:30	No, manual doppler correction	No fading

SECTION 9

IRIS DOWNLINK TONE DATA

9-1 INTRODUCTION.

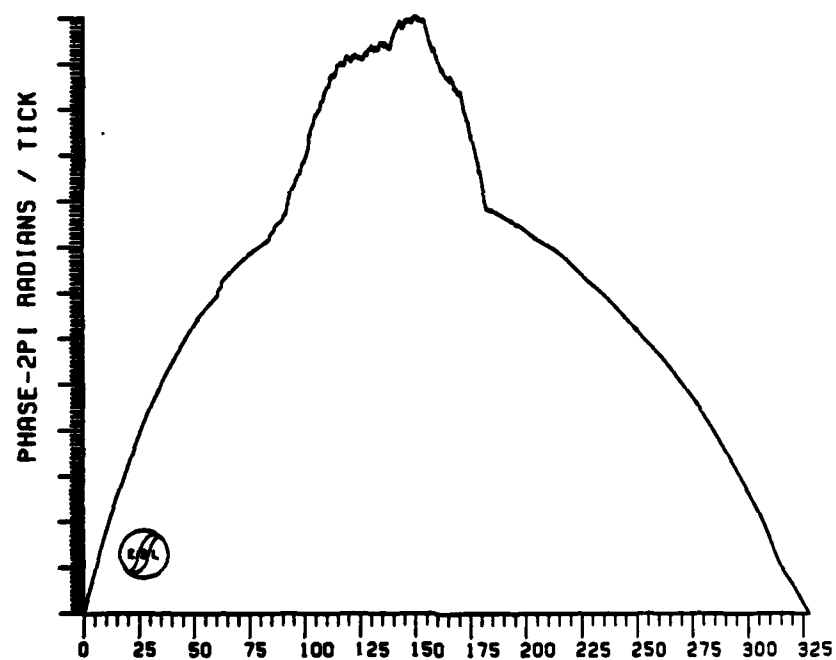
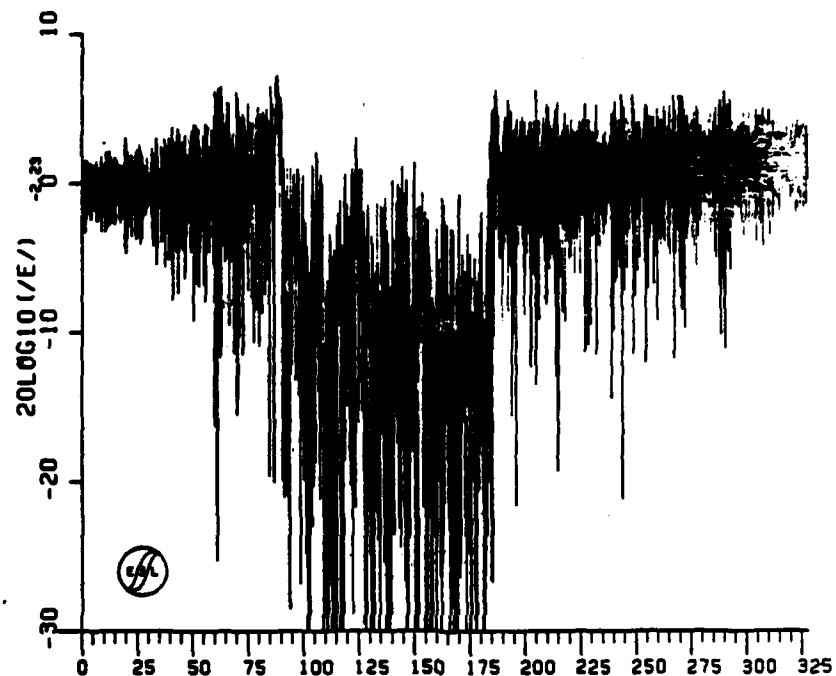
Measurements of the downlink tone amplitude were successfully conducted following the IRIS release. Due to the manual doppler compensation employed throughout the experiment, the phase data were corrupted by the uncompensated aircraft motion. Thus, the detrended phase data does not accurately reflect the barium cloud phase structure. Examples of the measured phase are included here for reference. Attempts at back-propagation of these data records were unsuccessful as the uncompensated doppler results in an artificial defocusing due to the long term phase trend as well as minor random effects.

9-2 DOWNLINK PROPAGATION MEASUREMENTS DURING IRIS.

A total of 31 passes were made following release with substantial fading seen on 17 of these. A summary of these passes were given in Table 8-1. Plot of the received tone data are given in Figures 9-1 through 9-11.

The release was low and slightly west of the planned release point. This resulted in the radar not acquiring the ion cloud upon the initial release. Additionally, this resulted in the aircraft being north of the ion cloud shadow for the first three passes and thus no fading was observed. The striation on set times as observed optically from C-6 and Tyndall were $R+10^m$ (2323:08Z) and $R+9^{m44s}$ (2322:52Z), respectively. The first strong fading was seen on the fourth pass at $R+16$ minutes.

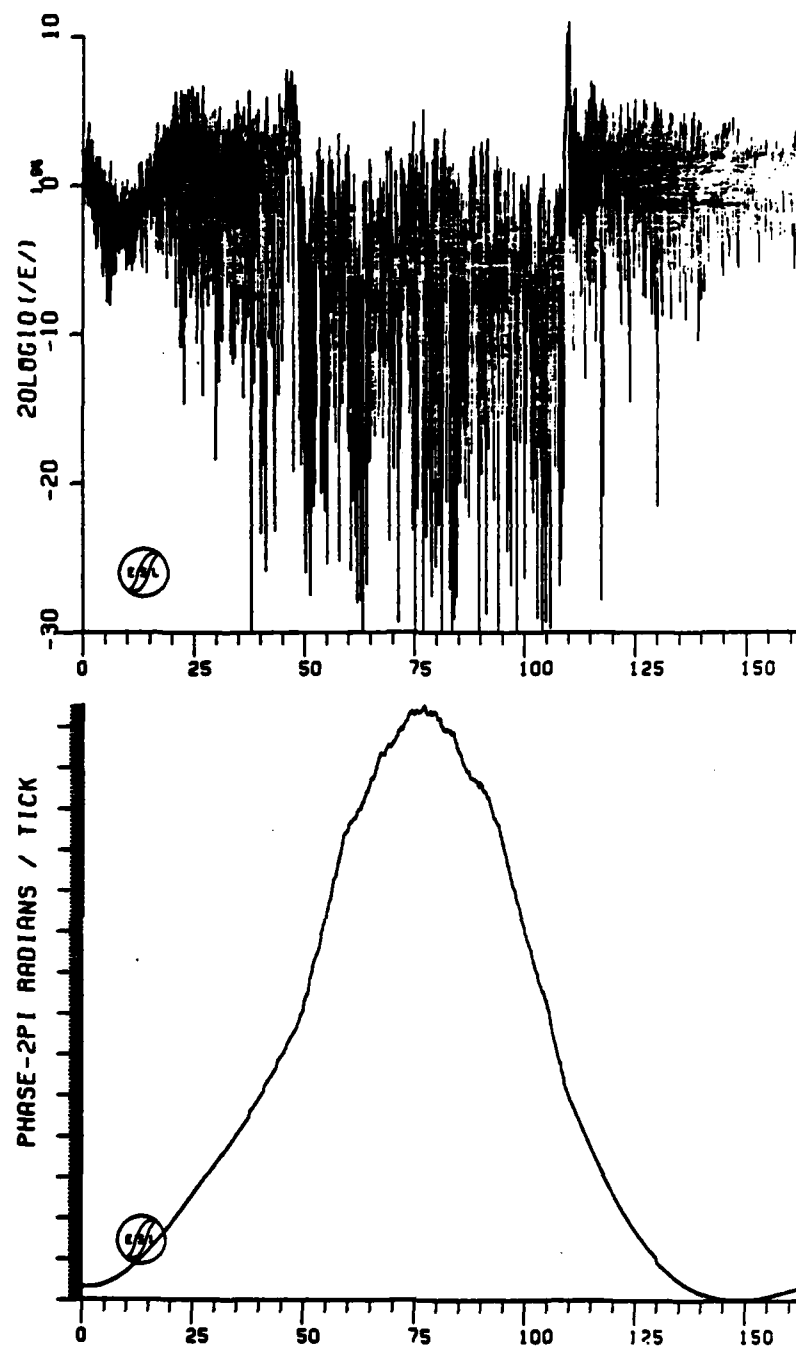
Both Passes 4 and 5 occurring at $R+16$ minutes and $R+26$ minutes show strong irregular fading indicating that striations were present at this time. These passes are shown in Figures 9-1 and 9-2. Their fading also exhibited a -15 dB defocus indicating that the aircraft flew almost directly under the main



TIME-- SECONDS

PHASE OF FIELD
104040381100HZ
START TIME- 23:29:11.998

Figure 9-1. IRIS Pass 4 Downlink Amplitude and Phase



TIME-- SECONDS

PHASE OF FIELD
105 010582 100HZ
START TIME- 23:38:25.998

Figure 9-2. IRIS Pass 5 Downlink Amplitude and Phase

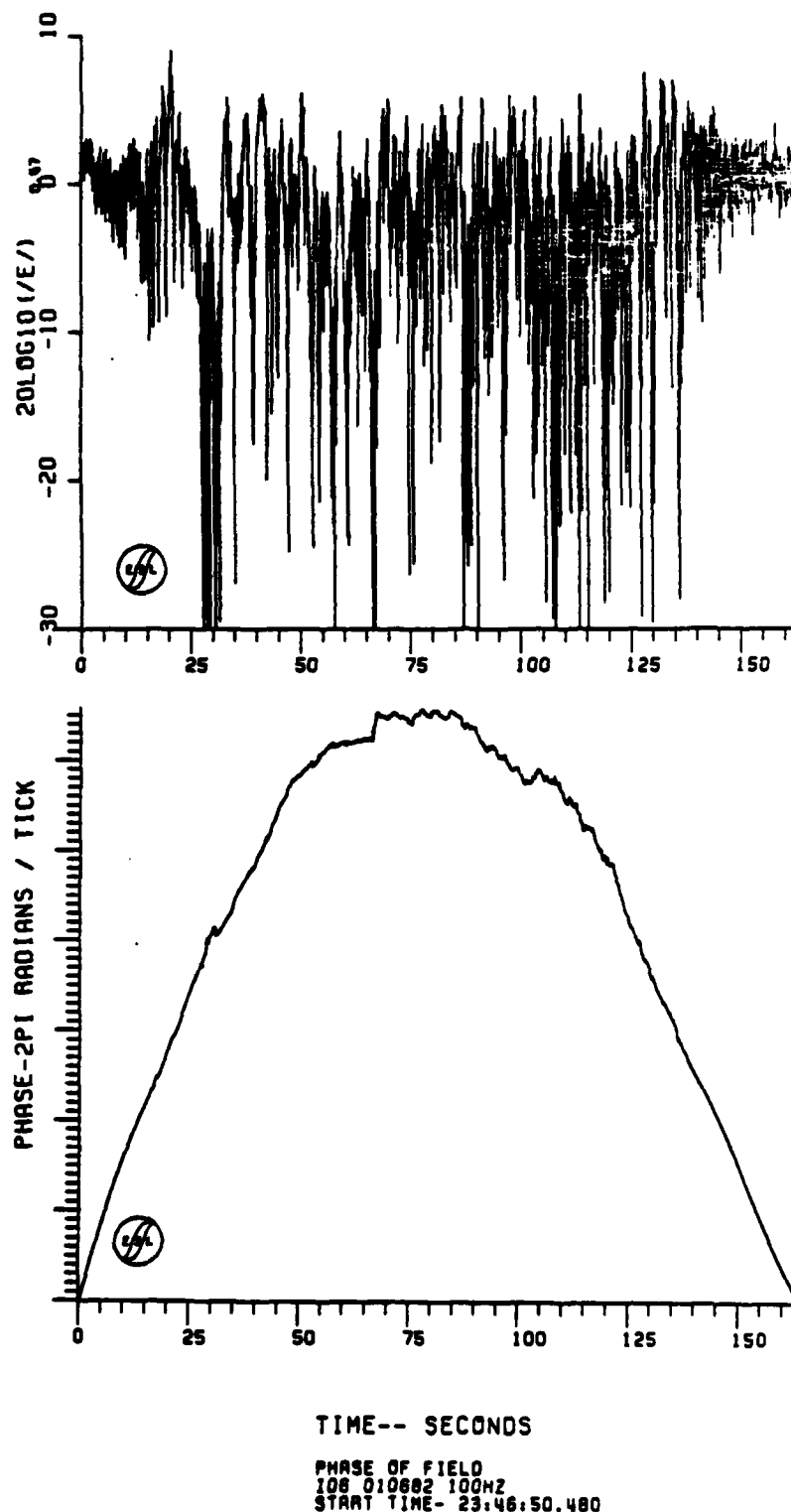


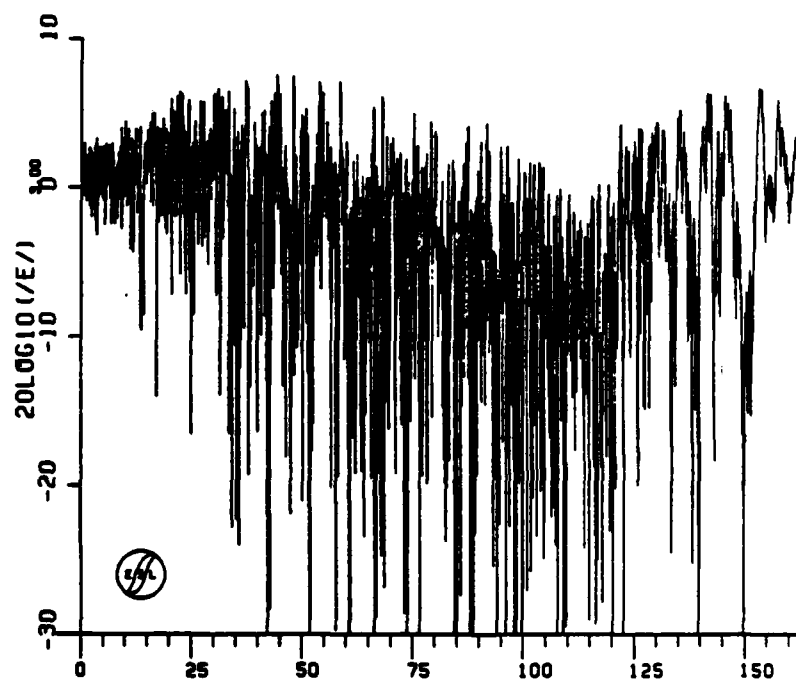
Figure 9-3. IRIS Pass 6 Downlink Amplitude and Phase

DSN-ESL4157, IRIS, TEST, ON031081
REC. NO. 52 53 54 55 56 57 58 59

PS0318
DTAN

11/24/81

17:02:20

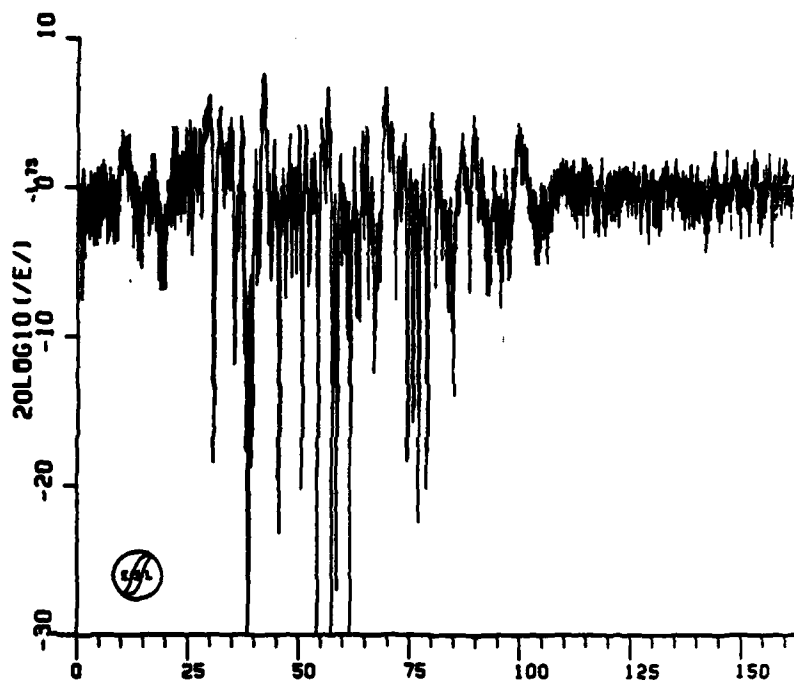


TIME-- SECONDS

MAGNITUDE OF FIELD
107031181100HZ
START TIME- 23:51:45.440

Figure 9-4. IRIS Pass 7 Downlink Amplitude

DSN-ESL4157. IRIS. TEST. 0N031081 PSD318 11/23/81 17:40:58
 REC. NO. 63 64 65 66 67 68 69 70 07AM



TIME-- SECONDS

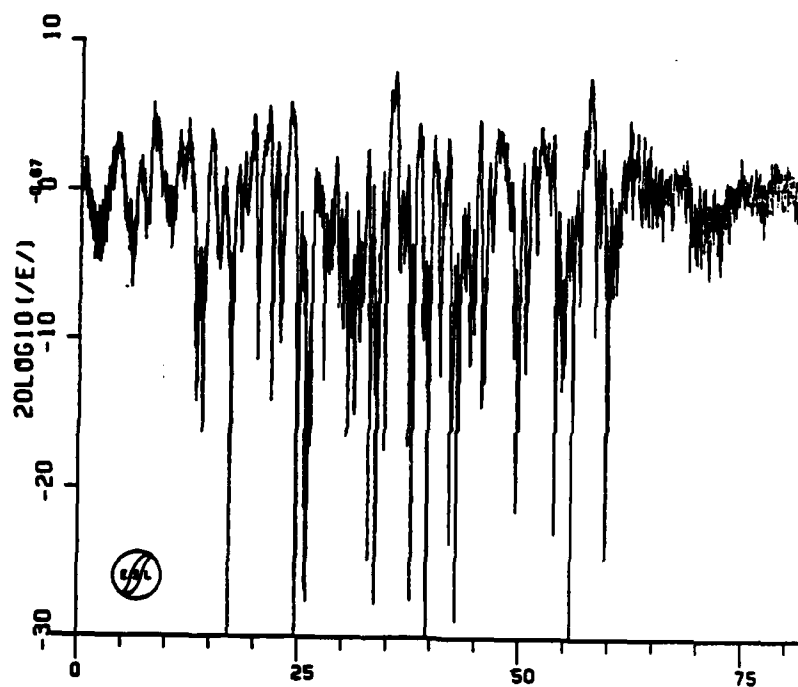
MAGNITUDE OF FIELD
 108031181100HZ
 START TIME- 00:01:20.959

Figure 9-5. IRIS Pass 8 Downlink Amplitude

DSN-ESL4157, IRIS, TEST, ON031081
REC. NO. 77 78 79 80

PS0318
DTM

11/24/81 17:08:42



TIME-- SECONDS

MAGNITUDE OF FIELD
109031181100HZ
START TIME- 00:07:07.920

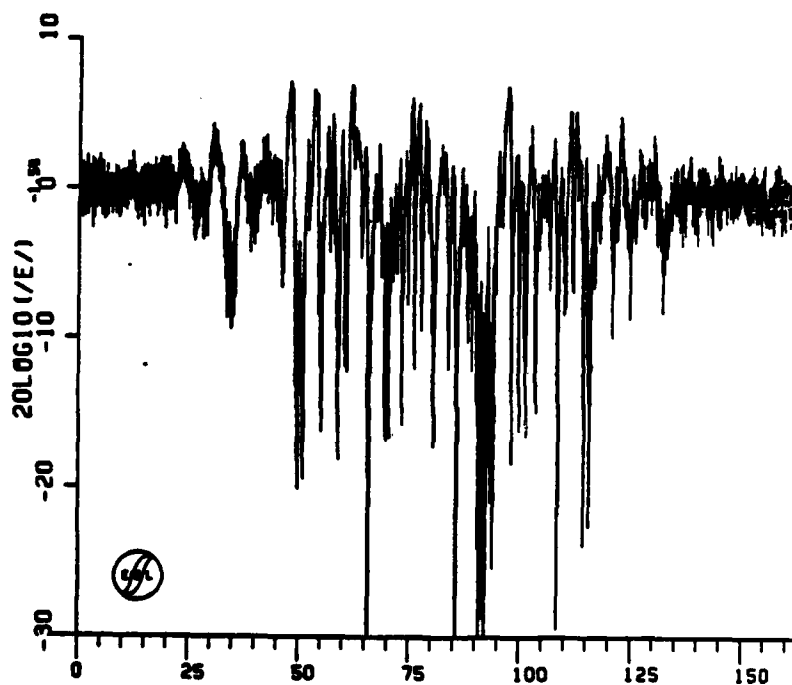
Figure 9-6. IRIS Pass 9 Downlink Amplitude

DSN-ESL4157. IRIS. TEST. 0N031081
REC. NO. 01 02 03 04 05 06 07 08

PS0318
DTRM

11/23/81

17:36:52



TIME-- SECONDS

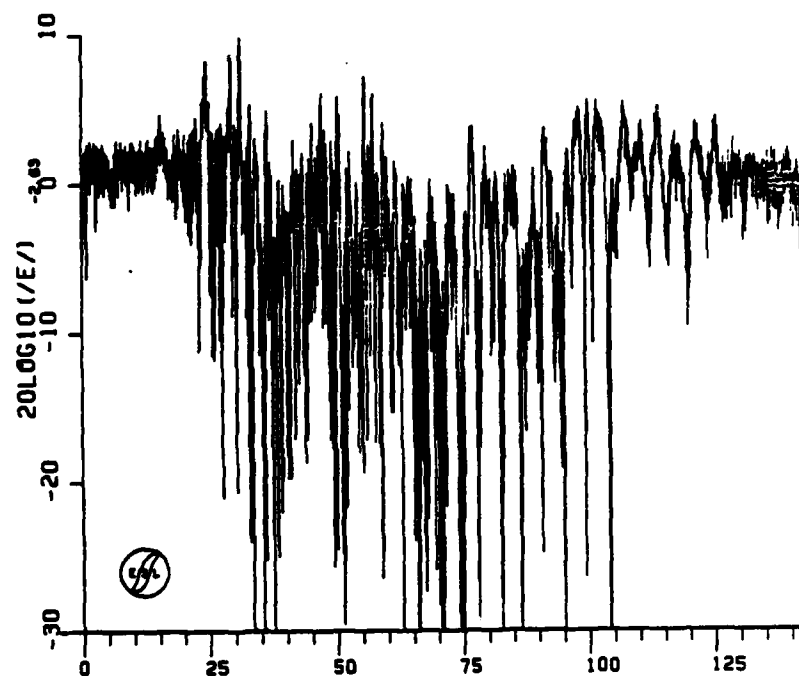
MAGNITUDE OF FIELD
110031181100HZ
START TIME- 00:19:08.000

Figure 9-7. IRIS Pass 10 Downlink Amplitude

DSN-ESL4157.IRIS.TEST.0N031081
REC. NO. 89 90 91 92 93 94 95

PS0318
DTAN

11/30/81 17:02:02



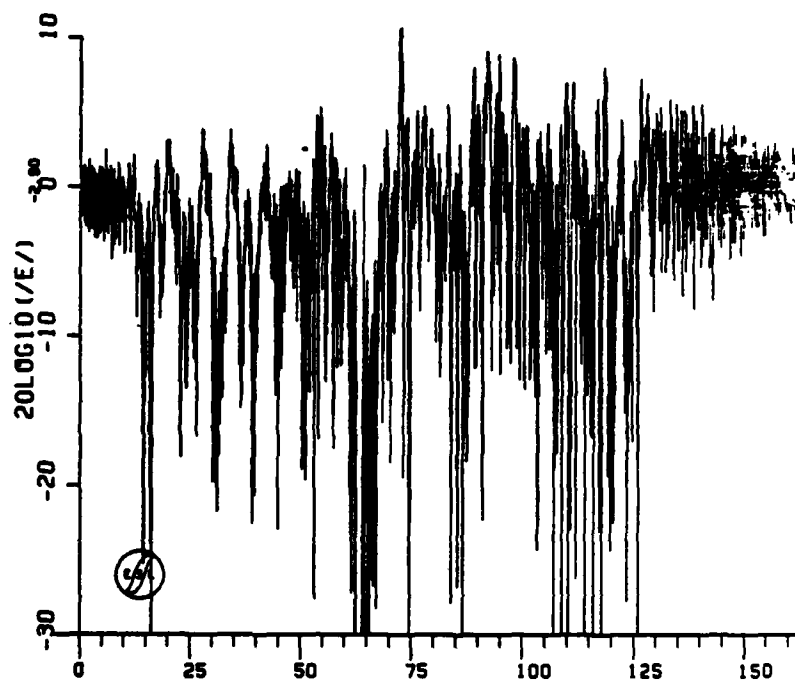
TIME-- SECONDS

MAGNITUDE OF FIELD
111031181100HZ
START TIME- 00:17:56.000

Figure 9-8. IRIS Pass 11 Downlink Amplitude

DSN-ESL4157.IRIS.TEST.0N031081 PS0318
REC. NO. 97 98 99 100 101 102 103 104 NO DTRM

11/24/81 11:57:23

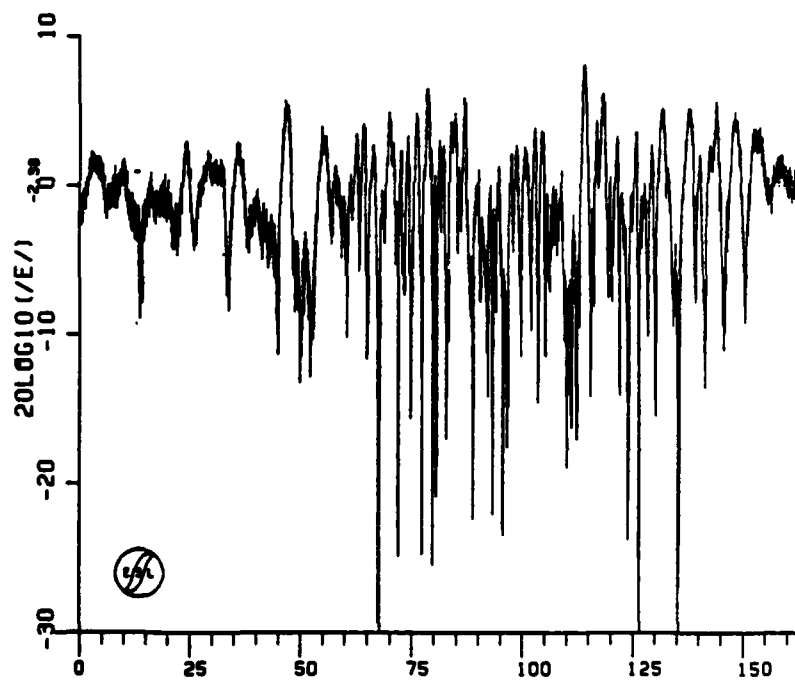


TIME-- SECONDS

MAGNITUDE OF FIELD
112031181100HZ
START TIME- 00:23:16.000

Figure 9-9. IRIS Pass 12 Downlink Amplitude

OSN=ESL4157. IRIS. TEST. 0N031081 PSD318 11/24/81 11:57:56
 REC. NO. 149 150 151 152 153 154 155 156 NO DTRM



TIME-- SECONDS

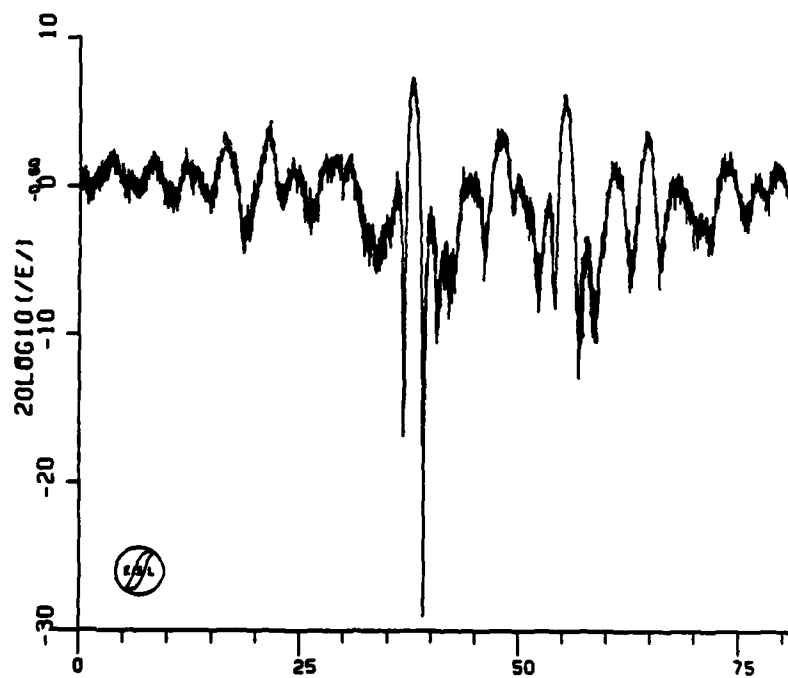
MAGNITUDE OF FIELD
 120031181100M2
 START TIME- 01:11:36.000

Figure 9-10. IRIS Pass 20 Downlink Amplitude

DSN-ESL4157. IRIS. TEST. CN031081
REC. NO. 192 193 194 195

P50318
NO DTRN

11/24/81 12:03:06



TIME-- SECONDS

MAGNITUDE OF FIELD
125031181100M7
START TIME- 01.37.57.440

Figure 9-11. IRIS Pass 25 Downlink Amplitude

cloud and that the gross cloud still had a large electron content. Pass 4 lasted about twice as long as Pass 5 because the aircraft's path was about 40 degrees from perpendicular to the magnetic field line projections and traveling in the same direction as the cloud as can be seen in Figure 9-3. The aircraft's path was close to perpendicular to the magnetic field line projections in most of the other passes. The fading seen during these two passes is very similar to fading seen during the STRESS experiment. The received phase with doppler is included for these two passes to show the effect of doppler. A linear trend of about 1000 cycles per pass has been removed from the raw data. In Pass 4 it is fairly obvious where the cloud separates from the doppler phase trend. Nonetheless, the doppler is still noisy enough that attempts at removing it and back-propagating were unsuccessful. The distinction between the cloud phase and the doppler is less obvious in Pass 5 and all subsequent passes. Unsuccessful attempts at back-propagation were also made on other passes, especially Passes 5 and 6 that bracket the time frame of interest for the Beacon experiment.

The aircraft transited the ion cloud shadow on Pass 5 approximately 5 minutes 33 seconds prior to the beacon rocket occultation experiment and again on Pass 6 - 2 minutes 37 seconds after the beacon occultation. The FPS-85 radar data provides ion cloud contours near these passes. The aircraft position is available from the FPS-16 radar track and the satellite ephemeris data is known. From this data the intersection geometry of the path connecting the aircraft and the satellite with the ion cloud geometry can be determined. This is shown in Figure 9-12 for the Pass 5 prior to occultation and in Figure 9-13 for the Pass 6 following occultation. The shape of the ion cloud contour at 160 kilometers altitude was obtained from the FPS-85 radar data near the time of each pass.⁽⁸⁾ The ion cloud center at 160 kilometers altitude has been translated to correspond with the cloud center at the time of each aircraft transit. The maximum ion cloud density is close to 160 kilometers altitude at the time of these passes.

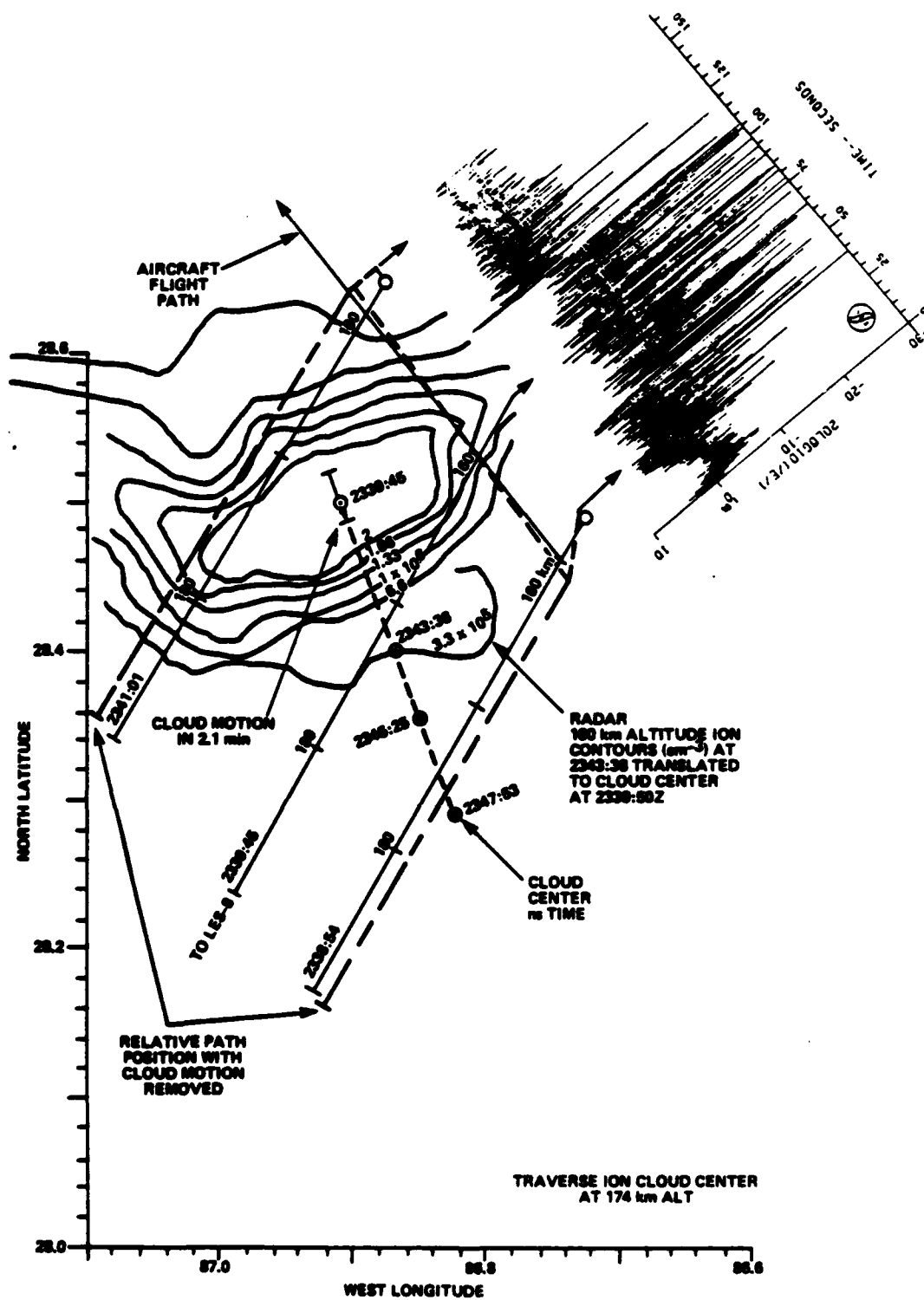
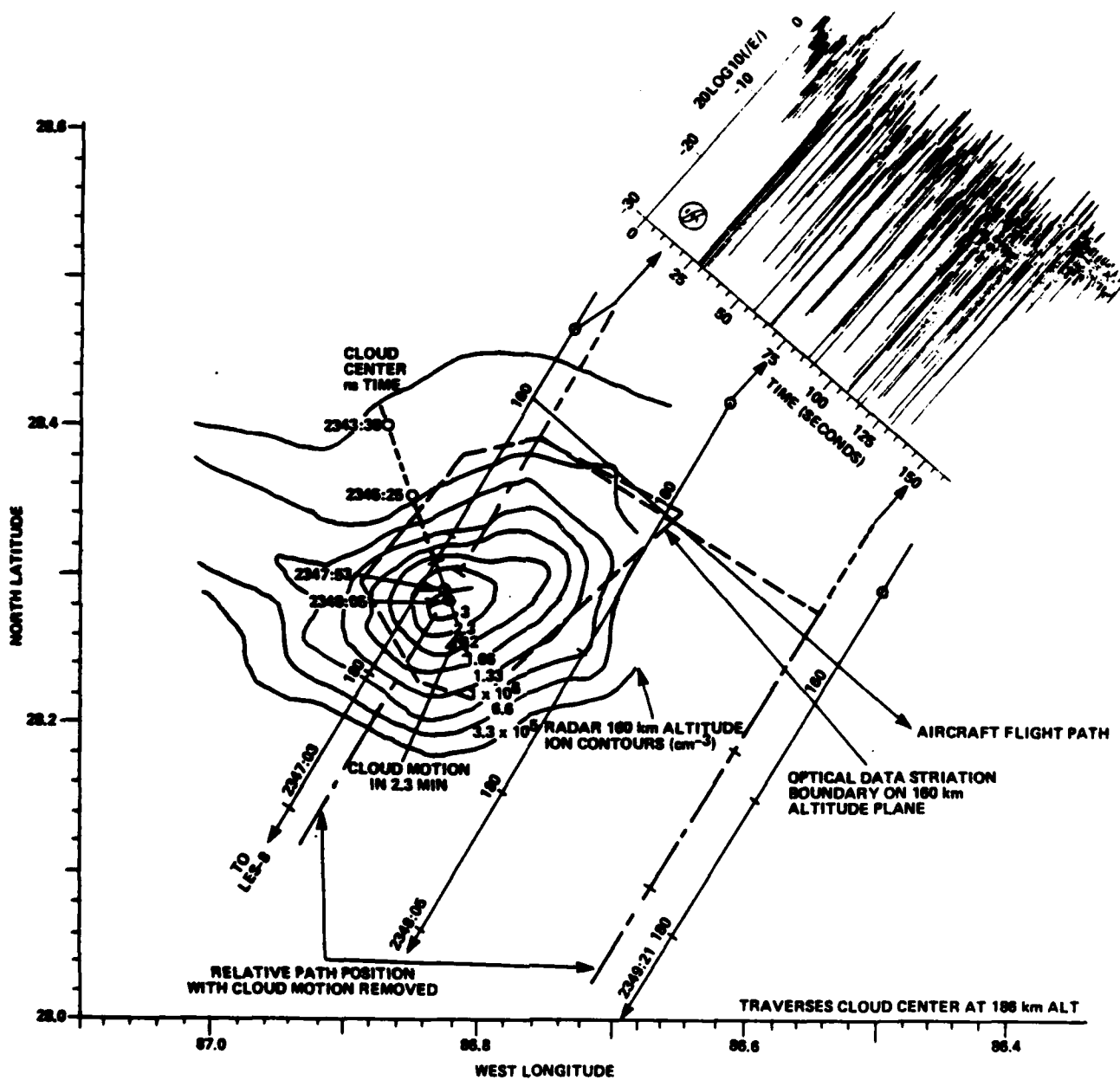


Figure 9-12. IRIS Pass 5 Aircraft Occultation Geometry



On Pass 5 the propagation path cut the field line through the cloud center approximately 174 kilometers in altitude. The aircraft slice through the cloud appears to extend from approximately 157 to 185 kilometers in altitude. The aircraft propagation path slice through the 160 kilometer altitude plane is nearly orthogonal to the beacon rocket slice because of the near vertical transit of the rocket as opposed to the constant altitude transit of the aircraft. Nonetheless, some of the same field lines are cut.

As the aircraft takes approximately 2 minutes to traverse the fading region, the position of the cloud center moves appreciably with respect to the ion cloud contours as shown. The position of the ray path at the beginning and end of the pass corrected for the relative cloud motion are also shown. In effect for Pass 5, relative to the contour drawn, the fading begins somewhat further south (the cloud was further north) and the fading ends further north (the cloud has moved south). The aircraft was in level flight throughout the fading intervals shown.

There appears to be good correlation between the ion contours drawn (appropriate to 3 minutes 48 seconds) and the observed fading. The shallow defocus shown in Figure 9-12 coincides reasonably well with the transit of the most dense part of the cloud, however, it does occur slightly southeast of the apparent cloud center. Further, it would appear that there is substantial fading to the southeast of the 6.6×10^5 ion contour. The ion cloud contour map results from an average of approximately 1 minute of data; thus, it is possible that cloud center position provided is lagging slightly behind the true center due to cloud motion. However, the cloud motion over a 1 minute interval is too small to account for the apparent scintillation activity to the southeast.

The trend for striations to the southeast (or east) appears even greater during Pass 6, 8 minutes later, as shown in Figure 9-13. The propagation path cut the field line through the cloud center approximately 186 kilometers in altitude, nearly 12 kilometers higher than on Pass 5. The propagation path slice

through the cloud appears to extend from approximately 160 to 196 kilometers altitude. The fading data indicates that substantial scintillation activity exists to the southeast (or east) well beyond the 3.3×10^5 ion contour. The aircraft, satellite and ion cloud track data are well defined and have little reason to be suspect.

Also shown on Figure 9-13 is the approximate boundary⁽⁹⁾ of the visible striations as defined from photographs taken from C-6, Tyndall, D-3, St. George Island, D-4, and the aircraft around 2345Z and translated to the ion cloud center during Pass 6. This would imply that these leading striations are not highly visible.

Pass 7 also provided strong fading data with a slight shallow defocus. This pass was approximately 5 minutes prior to the second beacon experiment occultation. Passes 8, 9, and 10 are shorter in duration and show less fading intensity than the earlier passes and the following two passes, Pass 11 and 12, indicating that the aircraft was not in optimum location during these passes. Pass 8 was approximately $2\frac{1}{2}$ minutes after the second beacon experiment occultation.

Plots of Passes 20 and 25 are given in Figures 2-38 and 2-39 and indicate typical late time scintillation activity. The other passes after Pass 12 either do not show fading or were out of the bandwidth of the filters in the recording equipment at the aircraft. The lack of doppler correction caused the bandwidth of the signal being recorded to be larger than usual and consequently was lost or distorted during the recording process. The real time strip chart data was not affected by this problem and is available during these passes.

9-3 IRIS SUMMARY.

Summarizing, the amplitude fading data was of good quality for most of the passes while usable phase data was non-existent due to the lack of K-band lock. The data near the beacon rocket occultation times provides an interesting correlation of the aircraft data with the FPS-85 radar ion cloud contours and the optical

striation data. These data provide a strong indication that striations diffuse outward leading the main ion cloud. This may partially explain the difficulty in occulting the late time striations based on the radar ion cloud track center point.

SECTION 10

JAN OVERVIEW

10-1 GENERAL.

While JAN, the fourth release, provided excellent propagation data for over 3 hours, cloud tracking data was available only during the first 48 minutes. Thereafter the aircraft was positioned solely based on the real time fading data received via the FLTSATCOM link with the aircraft. Downlink propagation data are presented in Section 11 and the uplink propagation data are shown in Section 12. Back-propagation of the downlink data are presented in Section 13. A few uplink data passes were examined but did not back-propagate well and are not presented. A comparison of Pass 10 uplink and downlink back-propagated data are included in Section 13. It is believed good uplink back-propagation results can be achieved, but the uplink was given a low priority in this effort due to additional processing effort required.

10-2 RELEASE GEOMETRY.

JAN, the fourth barium release, occurred on 12 December 1980 at 23:13:42. It was released at an altitude of 183.7 kilometers and a latitude and longitude of 29.1961°N and 86.9778°W. The ion cloud from this release initially drifted on an approximate 40 degree azimuth and then stopped for a few minutes. It then drifted very slowly west for the remainder of the experiment, with the last observation ending up about 1 degree west of the initial release point projection.

Optics tracking was used until approximately R+48 minutes. It gave reasonably consistent information on the cloud location during this time but the track showed some abrupt changes. Radar tracking was available for the remainder of the experiment, but was inconsistent with the fading observed. The striated portion of the ion cloud was followed using the real time fading displays and

the radar tracking of the aircraft. A plot of the available cloud tracking data is shown on Figure 10-1. A plot of the aircraft ground track is given in Figure 10-2. Figures 10-3, 10-4, and 10-5 show the aircraft ground track during each hour along with periods of strong fading.

10-3 FADING DATA SUMMARY.

A total of 35 passes were made ending at R+3 hours 33 minutes. Table 10-1 contains a summary of these passes. Diffraction ringing with large ~15 dB defocus was seen during the first three passes. Strong fading was present for all 18 passes between R+24 minutes and R+1 hour 2 minutes. Very good data was received during this time. Moderate to strong fading was present in four of the next eight passes ending at R+2 hours 12 minutes. Fading was seen as late as R+2 hours 54 minutes.

Uplink and downlink data was received for all passes. K-band lock was not lost during this release. Overall, the highest quality uplink data was obtained during JAN and the highest quality downlink data was obtained during JAN and HOPE.

Table 10-1. Aircraft Data Summary for JAN

Pass No.	Time	K-Lock	Comments
1	23:14:00-23:15:40	Yes ↓	Moderate diffraction ringing
2	23:18:10-23:20:50		Diffraction ringing with large -15 dB defocus
3	23:24:30-23:27:30		Diffraction ringing with large -15 dB defocus
4	23:32:50-23:34:40		Strong fading, but short
5	23:37:00-23:38:40		Strong fading
6	23:42:20-23:44:00		Strong fading
7	23:47:10-23:48:40		Strong fading
8	23:53:20-23:57:00		Strong fading
9	00:00:20-00:02:20		Strong fading
10	00:05:50-00:08:10		Strong fading
11	00:13:50-00:15:20		Strong fading
12	00:19:30-00:21:30		Strong fading
13	00:24:10-00:26:00		Strong fading
14	00:30:40-00:32:20		Strong fading
15	00:34:40-00:36:30		Strong fading
16	00:41:40-00:44:10		Strong fading
17	00:47:50-00:49:50		Strong fading
18	00:53:40-00:56:30		Strong fading
19	01:00:00-01:02:40		Strong fading
20	01:07:20-01:10:00		Strong fading
21	01:12:50-01:15:00		Strong fading
22	01:19:10-01:20:40		Weak fading
23	01:23:00-01:25:00		Strong fading
24	01:28:00-01:30:40		Moderate fading
25	01:33:40-01:35:10		Moderate fading
26	01:38:30-01:41:20		Weak fading, large focus
27	01:45:30-01:47:30		No fading

Table 10-1. --Continued

Pass No.	Time	K-Lock	Comments
28	01:51:50-01:53:30	Yes ↓	Weak fading
29	01:55:30-01:57:00		Weak fading
30	01:59:40-02:01:20		No fading
31	02:03:20-02:07:20		Weak fading
32	02:09:30-02:14:00		No fading
33	02:20:00-02:25:00		No fading
34	02:30:30-02:37:00		No fading
35	02:39:00-02:46:50		No fading

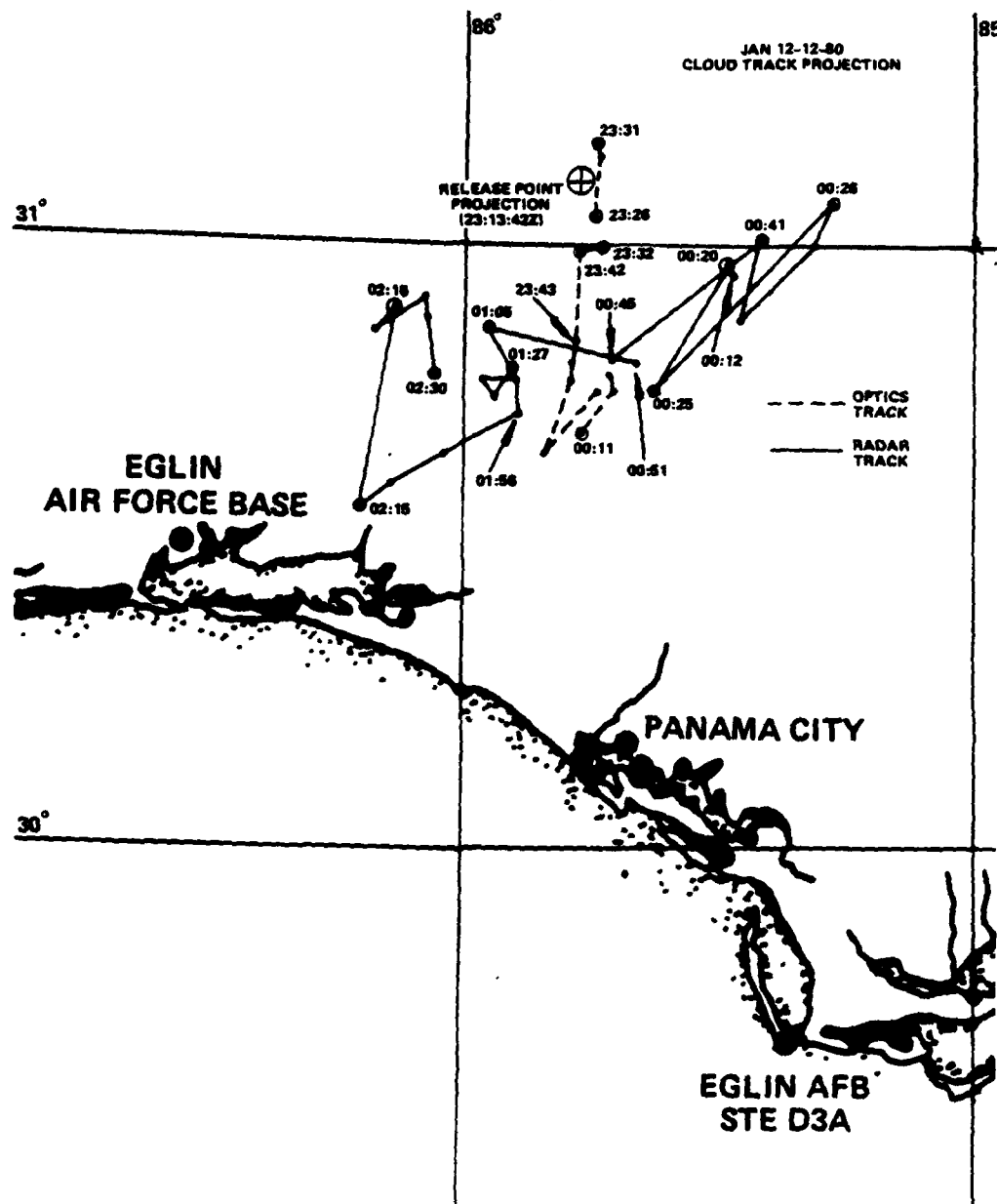


Figure 10-1. Ion Cloud Track Projection for JAN

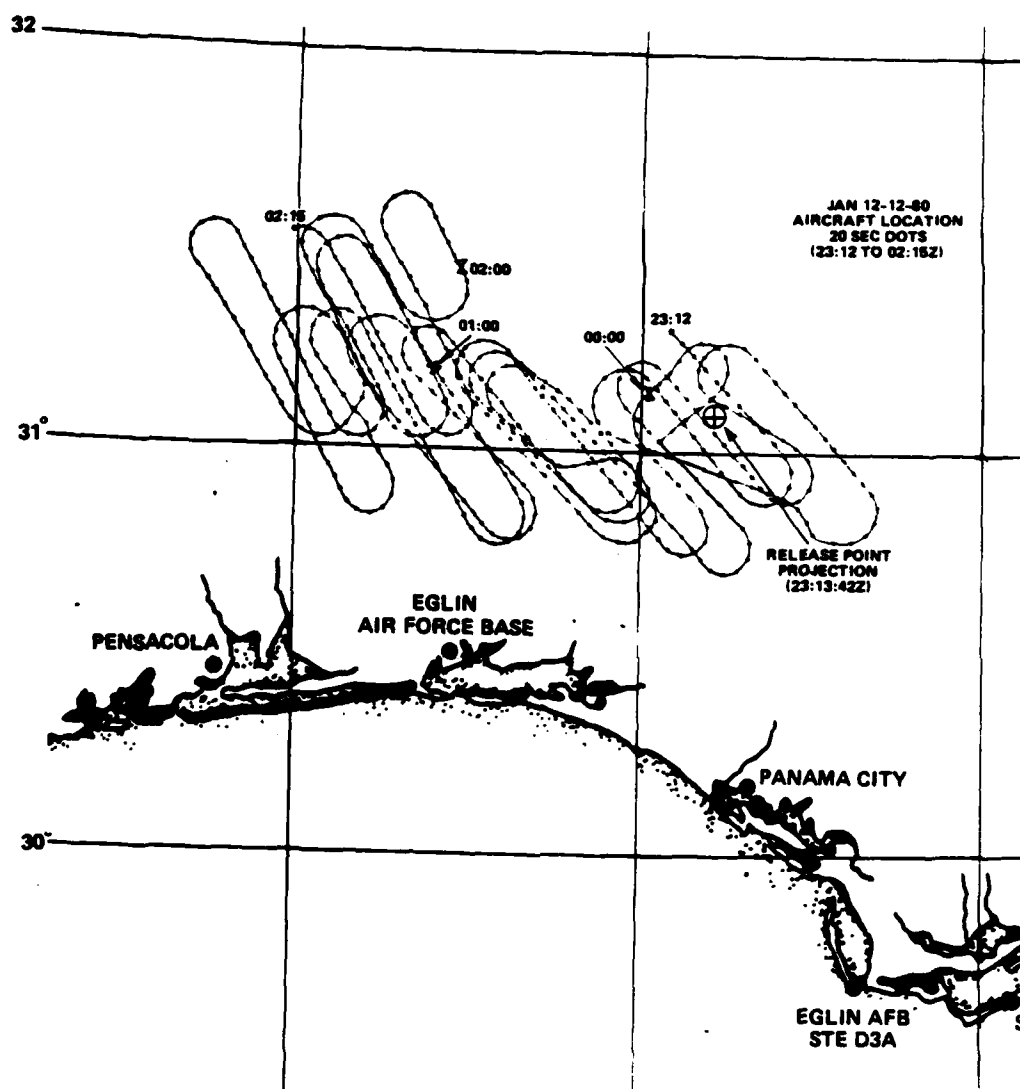


Figure 10-2. Aircraft Ground Track for JAN

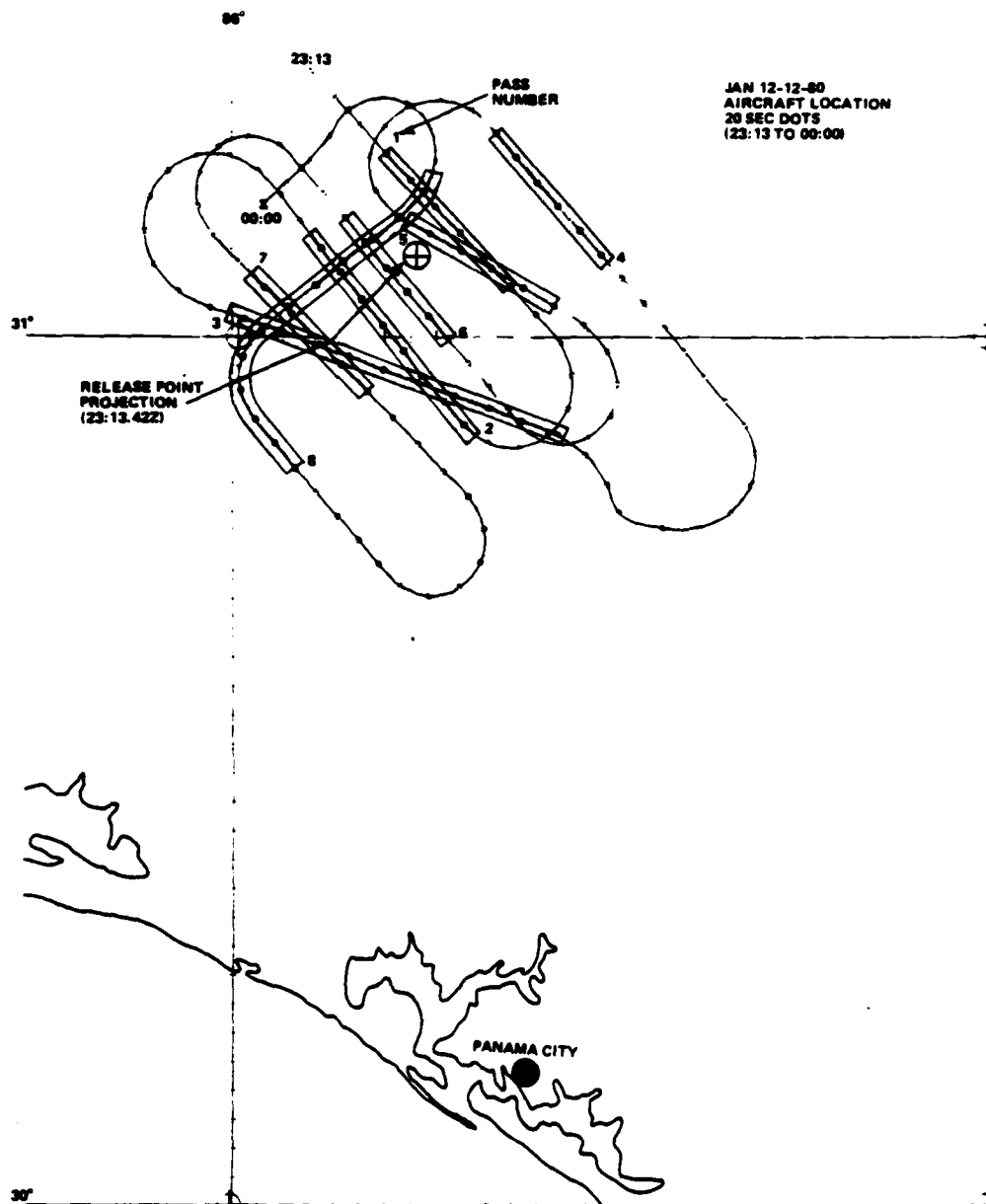


Figure 10-3. Aircraft Ground Track for JAN from 23:13 to 00:00Z. Periods of Deep Fading are Shaded.

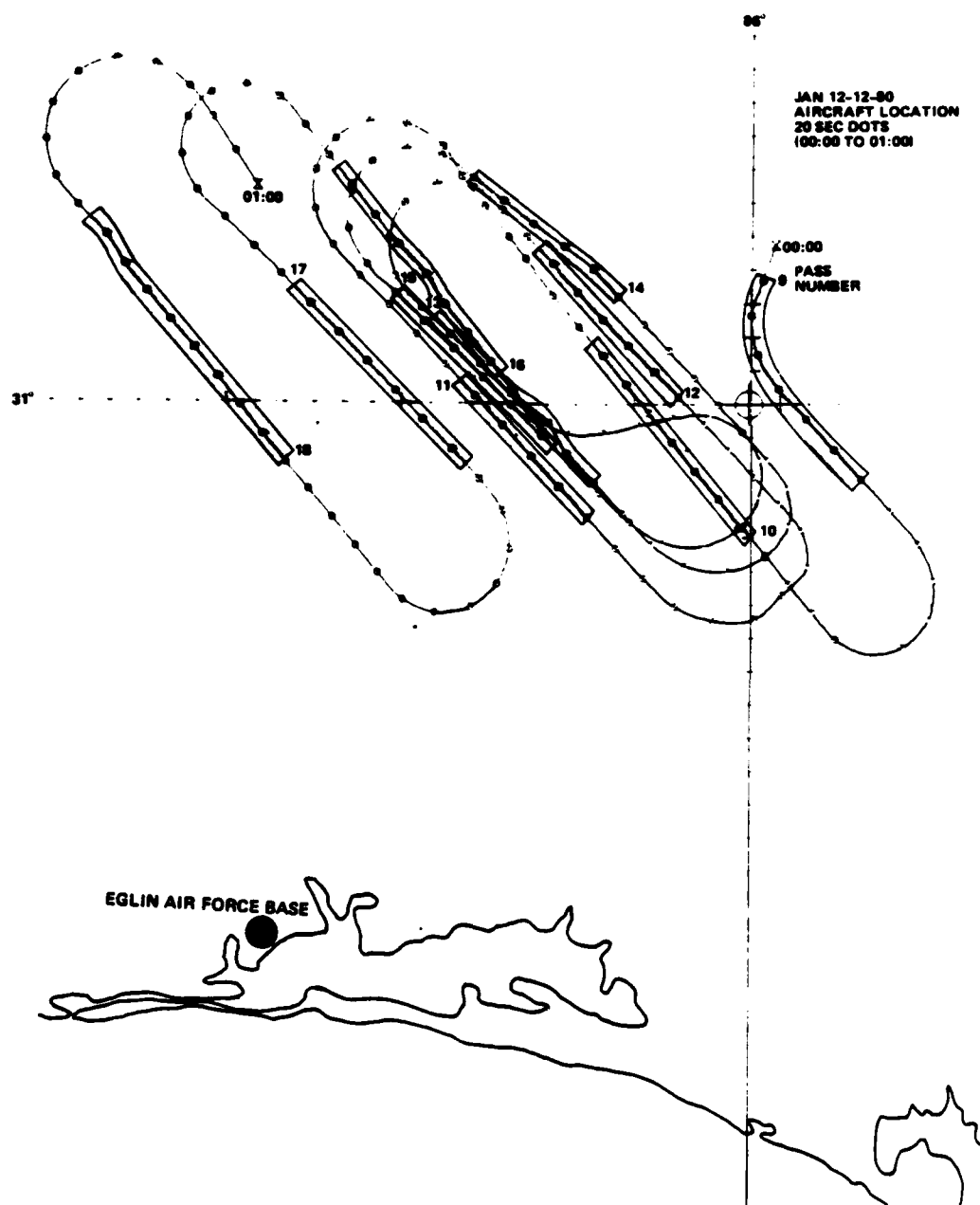


Figure 10-4. Aircraft Ground Track for JAN from 00:00 to 01:00Z. Periods of Deep Fading are Shaded.

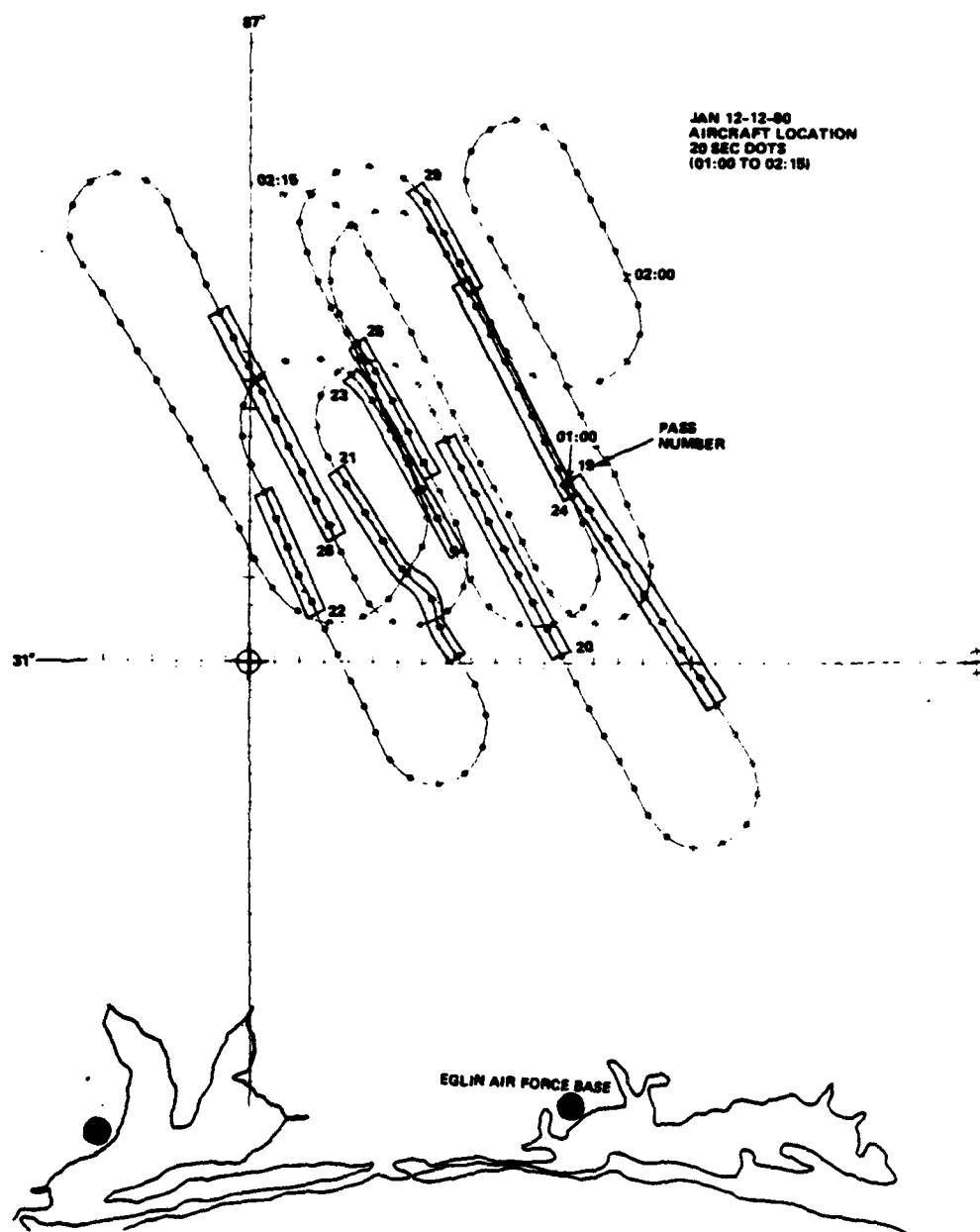


Figure 10-5. Aircraft Ground Track for JAN from 01:00 to 02:15Z. Periods of Deep Fading are Shaded.

SECTION 11
JAN DOWNLINK TONE DATA

11-1 INTRODUCTION.

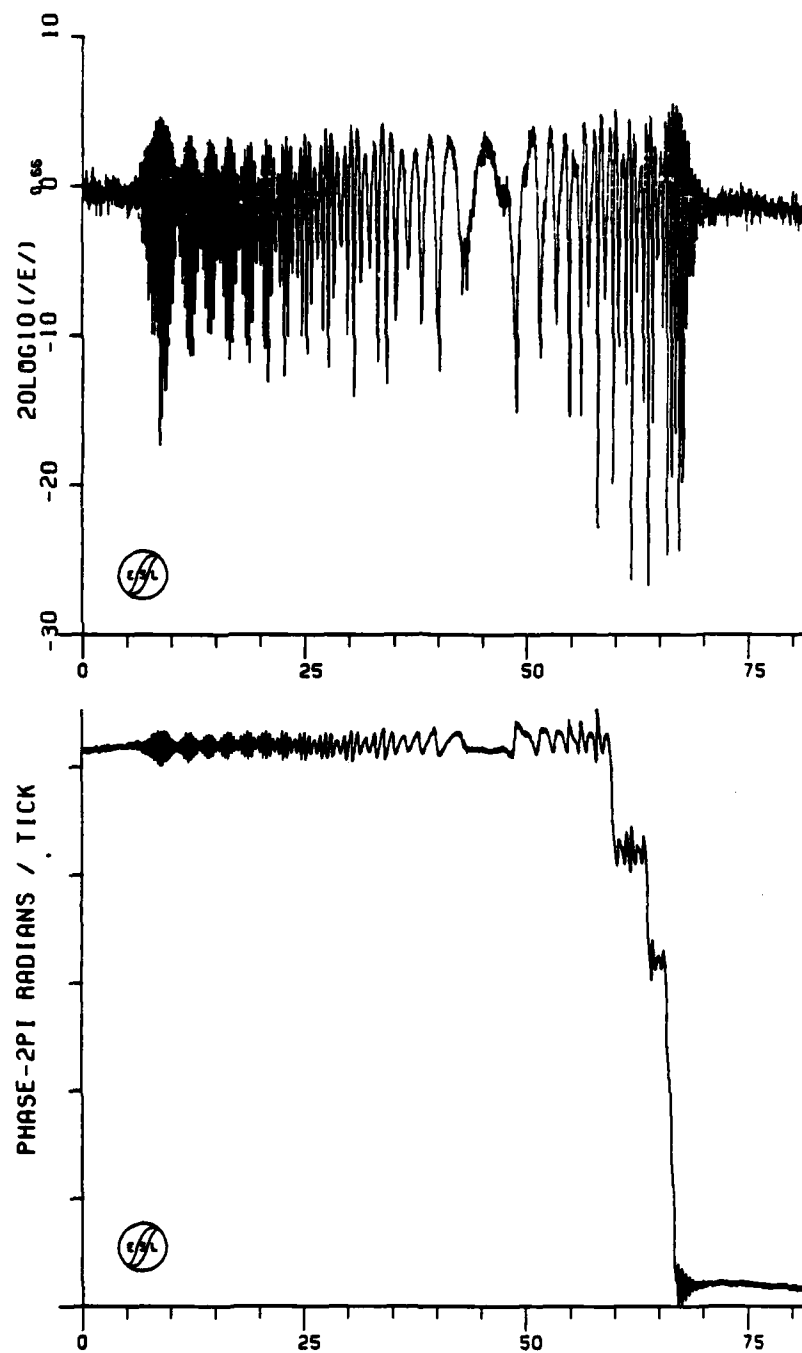
Downlink tone amplitude and phase measurements were made following the JAN release. These measurements were made using a 250 MHz signal transmitted from LES-8 through the barium ion cloud to the KC135/662 aircraft. The signal processing employed is described in Appendix B.

11-2 DOWNLINK PROPAGATION MEASUREMENTS DURING JAN.

A total of 35 passes were made following this release with fading seen as late as R+2 hours 55 minutes. A summary of these passes were given in Table 10-1. Plots of the received downlink amplitude and phase are given in Figures 11-1 through 11-22. The fading data shows the usual progression of effects from diffraction ringing at early times to strong scintillation as the striations develop, eventually weakening as the ionization diminishes. The first three passes were reminiscent of the early HOPE passes.

The aircraft was slightly north of the release point projection at the time of release. This release point projection is northeast of the planned release point projection. The aircraft flew into the cloud shadow approximately 34 seconds after release. As indicated in Figure 11-1, strong diffraction ringing was observed similar to that seen in GAIL Passes -3 and -2, the first two passes seen during GAIL. The phase plot exhibits a cycle skipping of the phase unwrapping routine as the plane exits the cloud shadow.

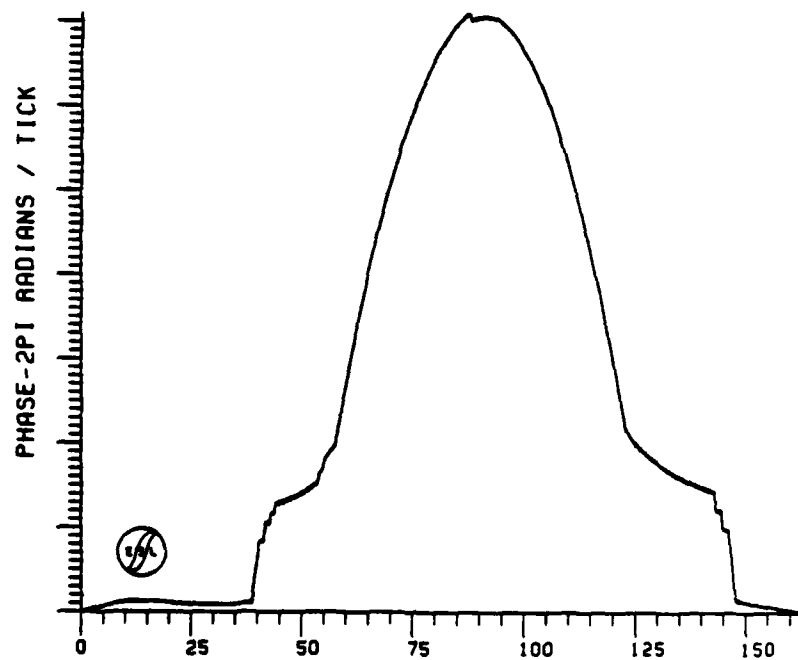
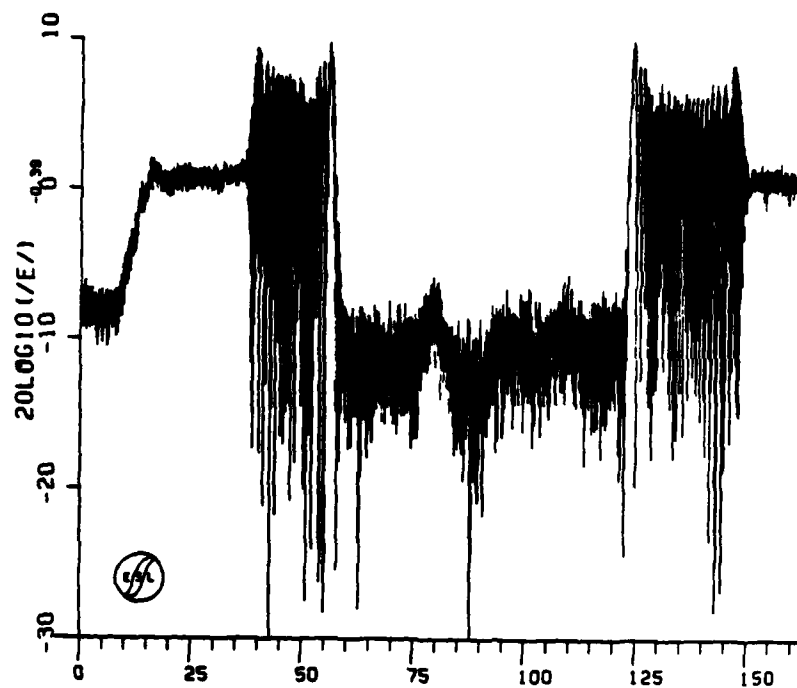
Passes 2 and 3 exhibited strong defocuses caused by the build-up of ionization in the main cloud. These passes shown in Figures 11-2 and 11-3 are similar to HOPE Pass 1. The striation on-set times as observed from the A-105, C-6, and Tyndall sites were R+11^m 11^s, R+12^m 36^s, and R+13^m 07^s, respectively. Pass 3, centered at R+12^m, exhibits the same 15 dB defocus as Pass 2.



TIME-- SECONDS

PHASE OF FIELD
J01051881100HZ
START TIME- 23:14:08.480

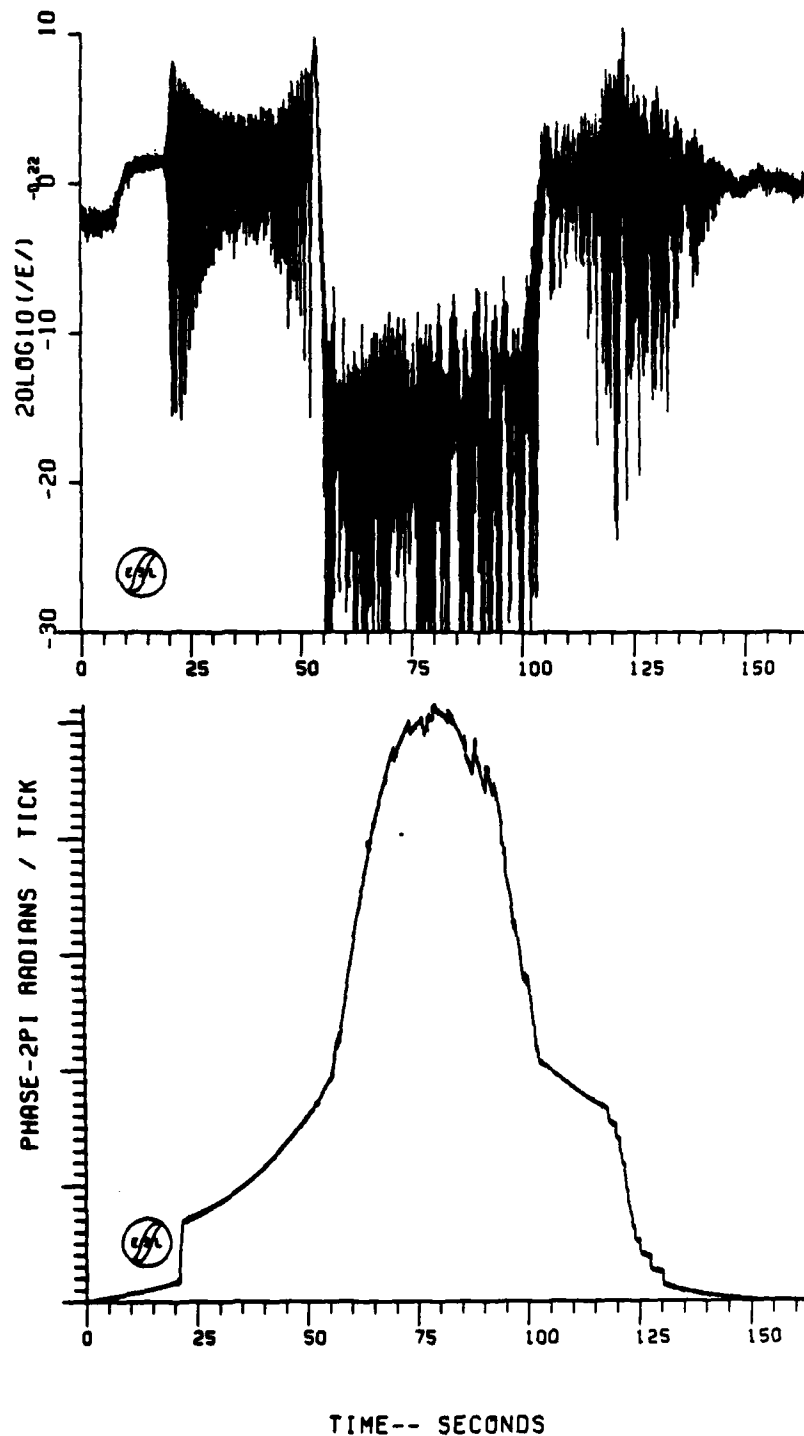
Figure 11-1. JAN Pass 1 Downlink Amplitude and Phase



TIME-- SECONDS

PHASE OF FIELD
J02052281100HZ
START TIME- 23:18:07.999

Figure 11-2. JAN Pass 2 Downlink Amplitude and Phase



PHASE OF FIELD
 J03052281100HZ
 START TIME- 23:24:28.000

Figure 11-3. JAN Pass 3 Downlink Amplitude and Phase

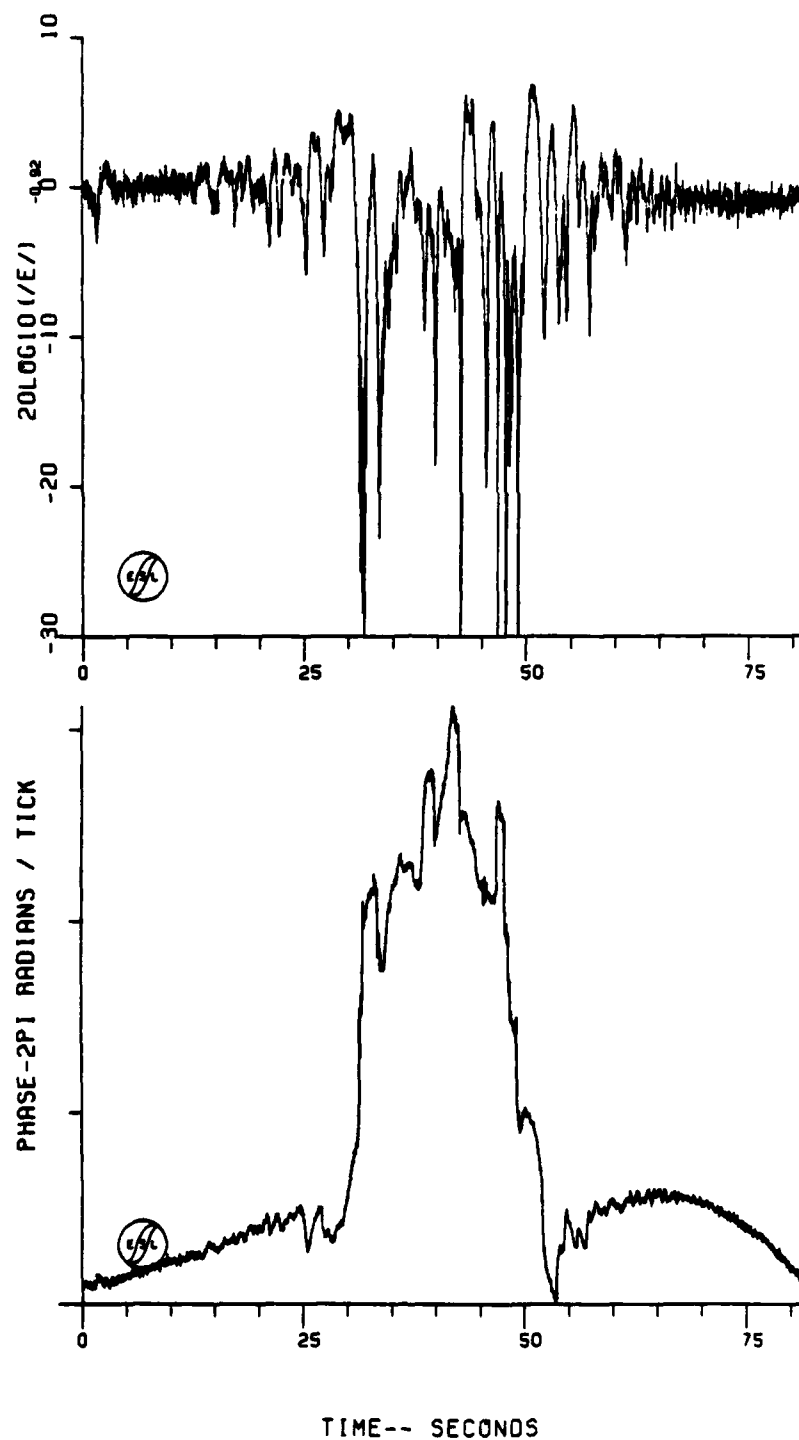


Figure 11-4. JAN Pass 4 Downlink Amplitude and Phase

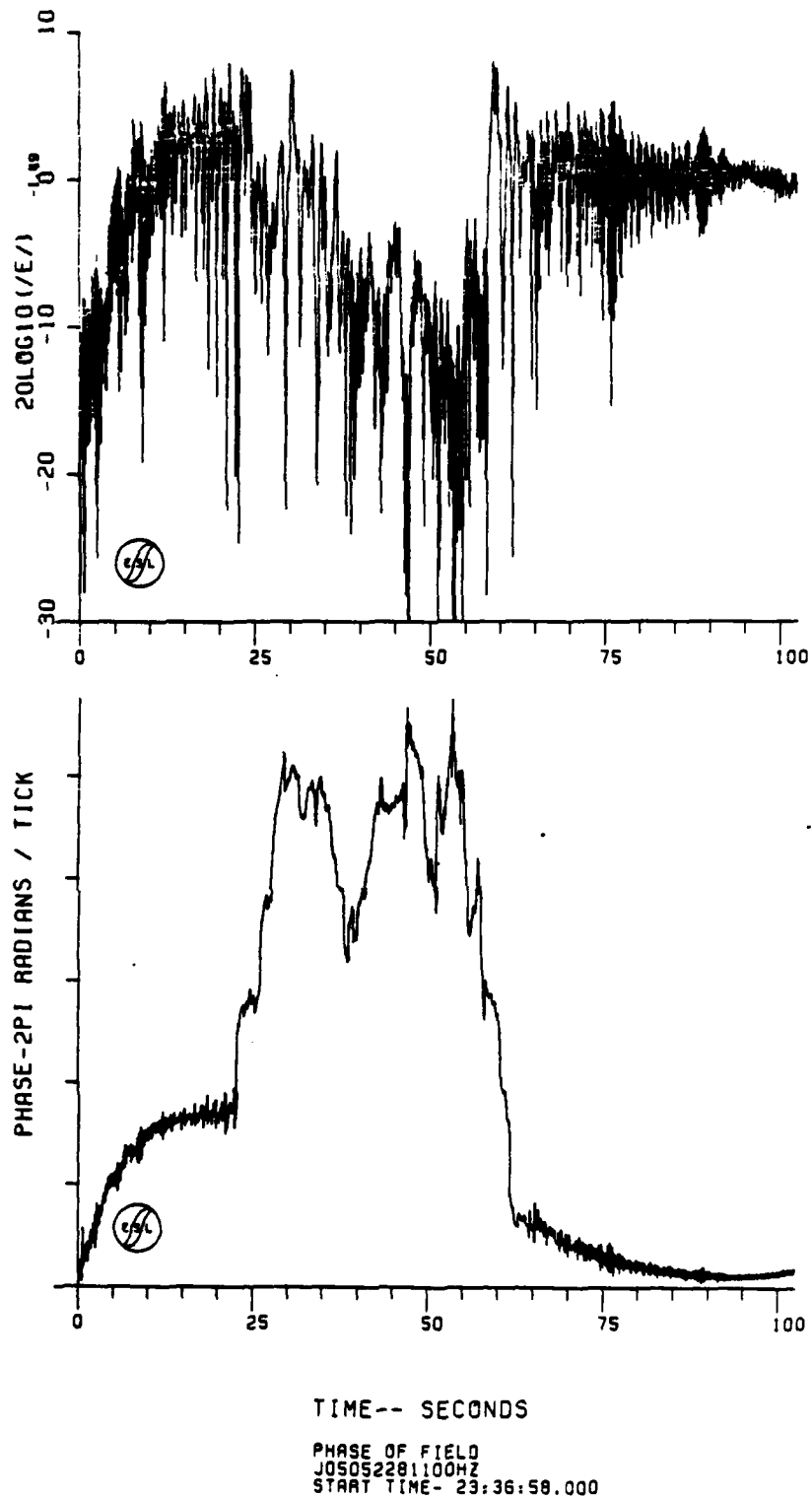
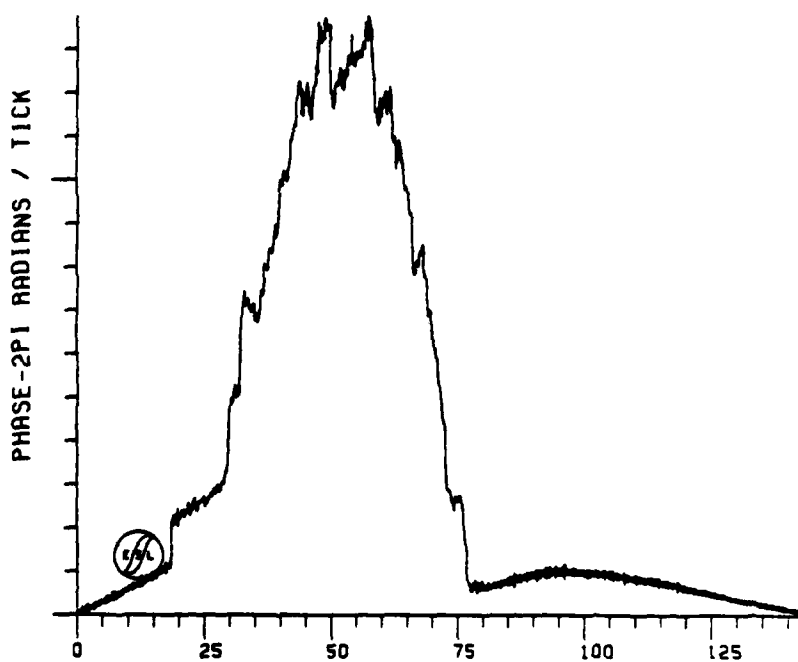
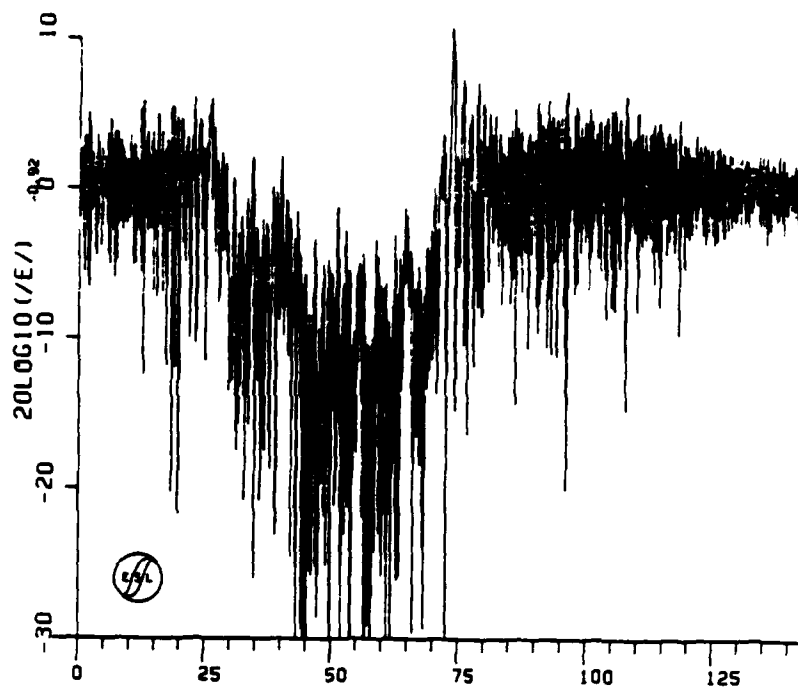


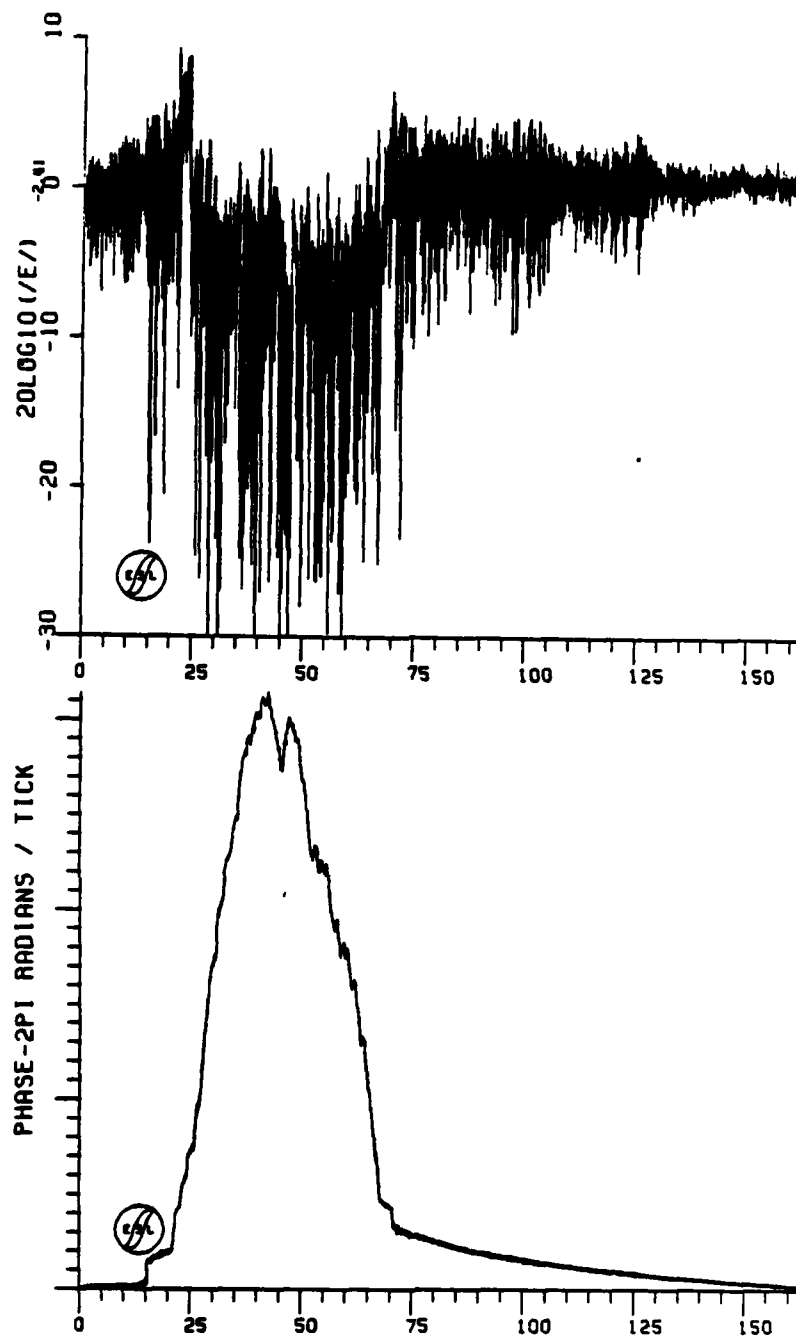
Figure 11-5. JAN Pass 5 Amplitude and Phase



TIME-- SECONDS

PHASE OF FIELD
J06052281100HZ
START TIME- 23:42:18.000

Figure 11-6. JAN Pass 6 Amplitude and Phase



TIME-- SECONDS

PHASE OF FIELD
J07052281100HZ
START TIME- 23:47:08.000

Figure 11-7. JAN Pass 7 Downlink Amplitude and Phase

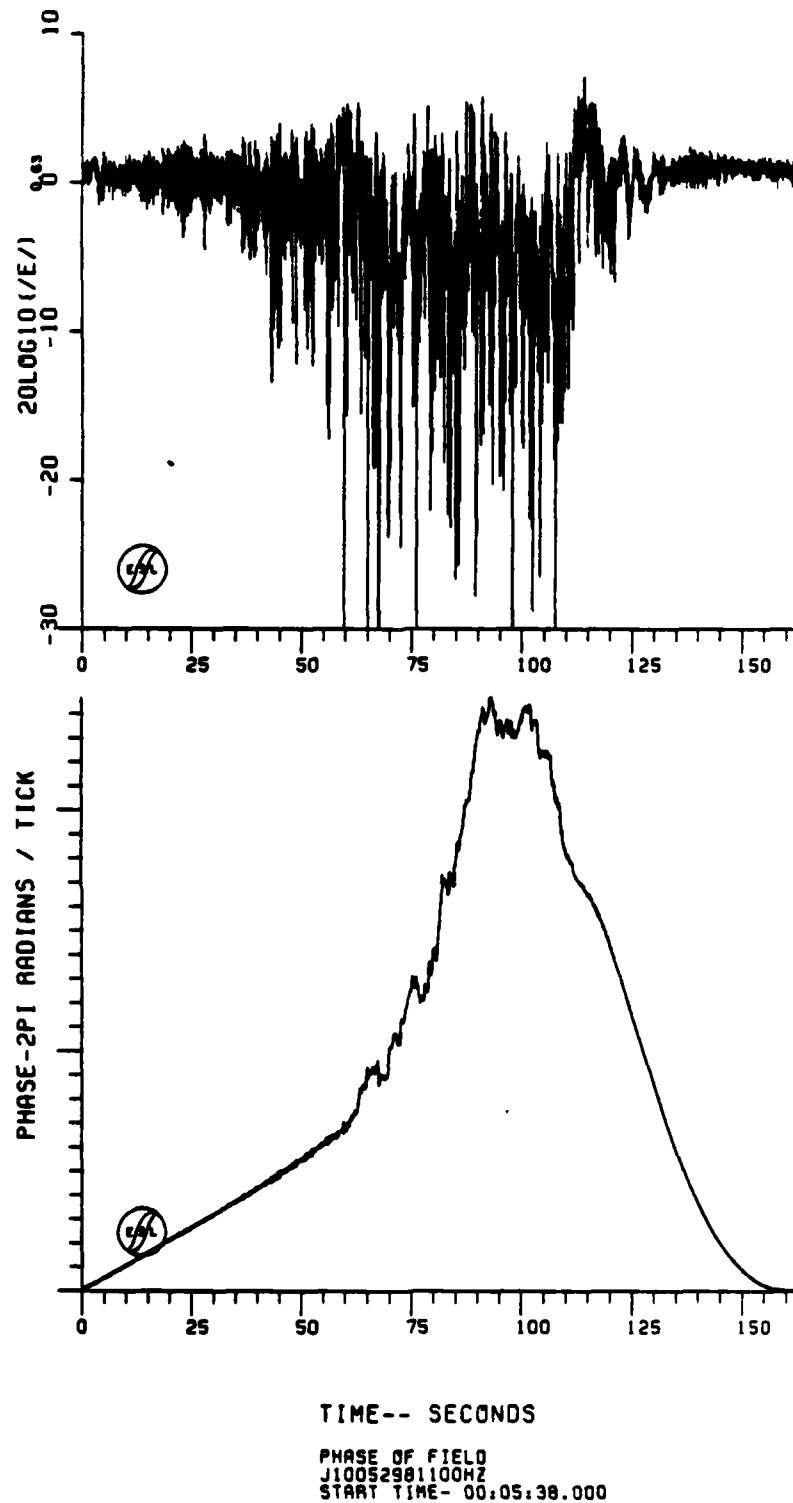


Figure 11-8. JAN Pass 10 Downlink Amplitude and Phase

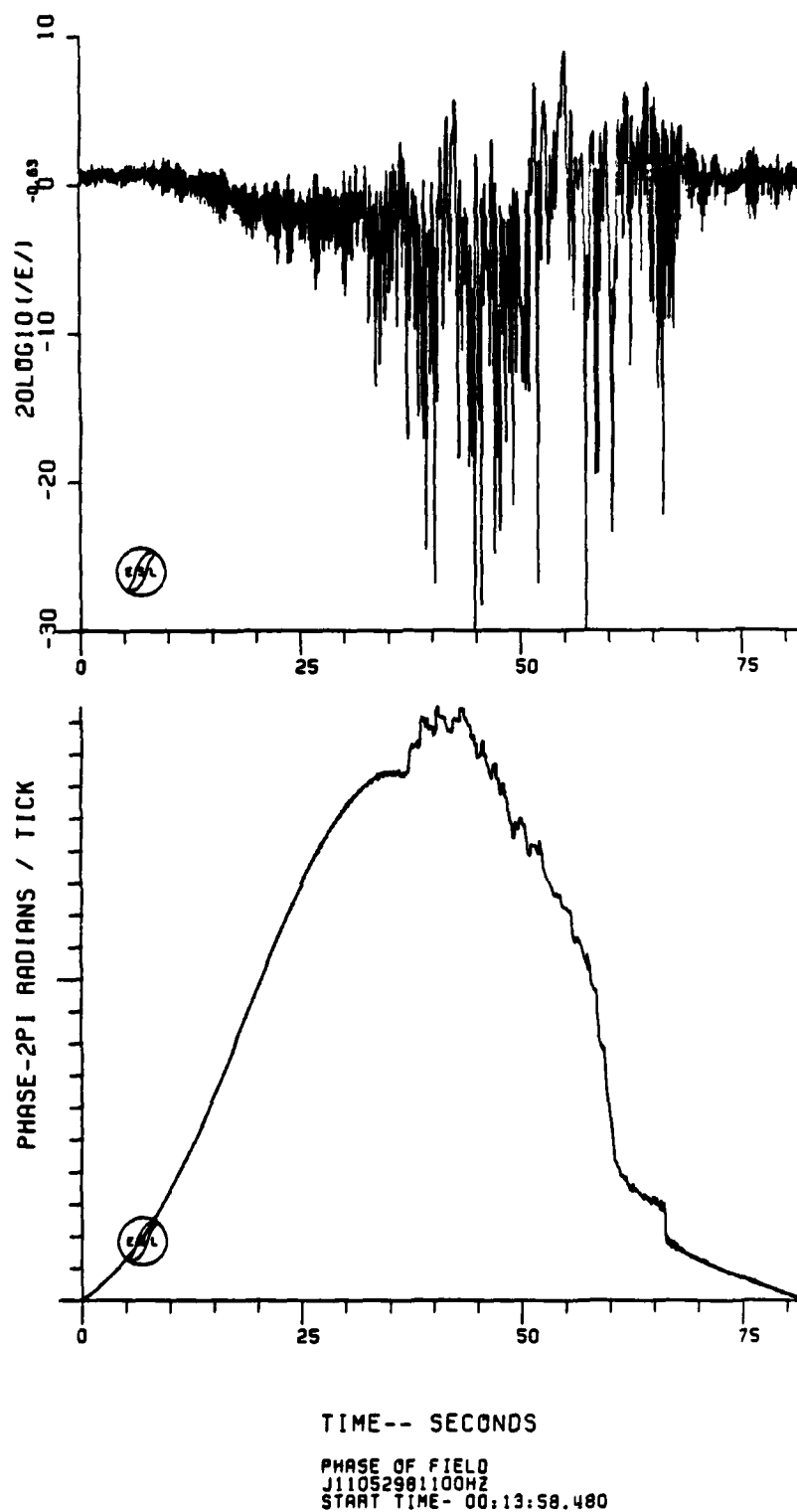
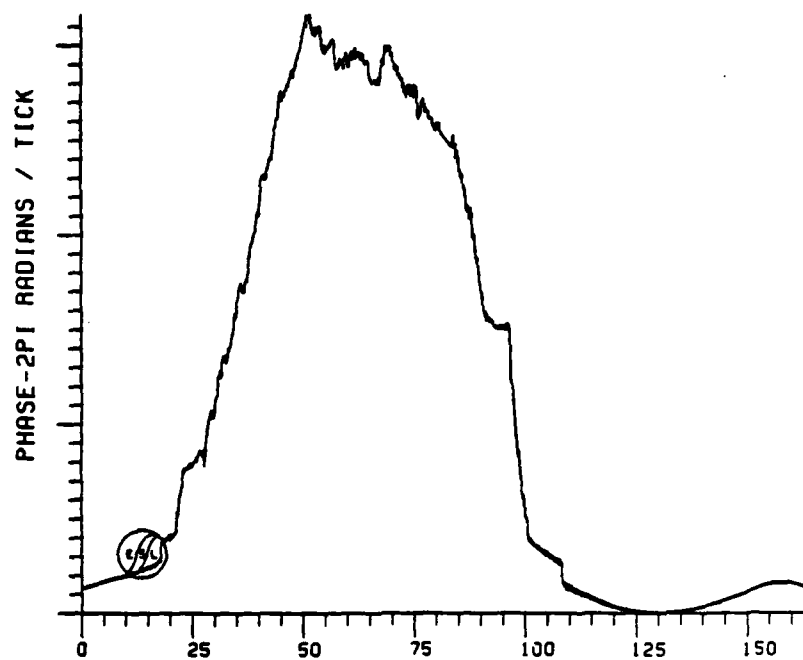
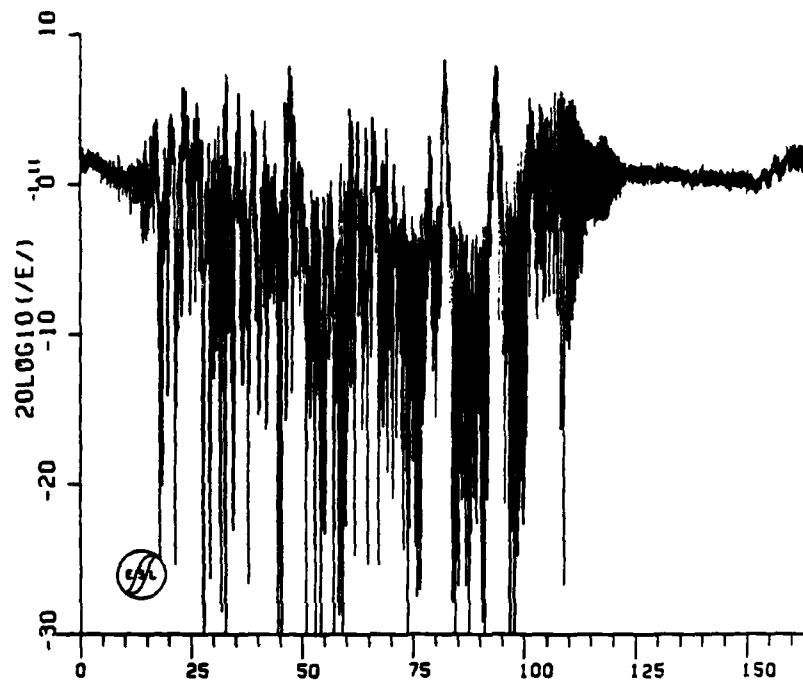


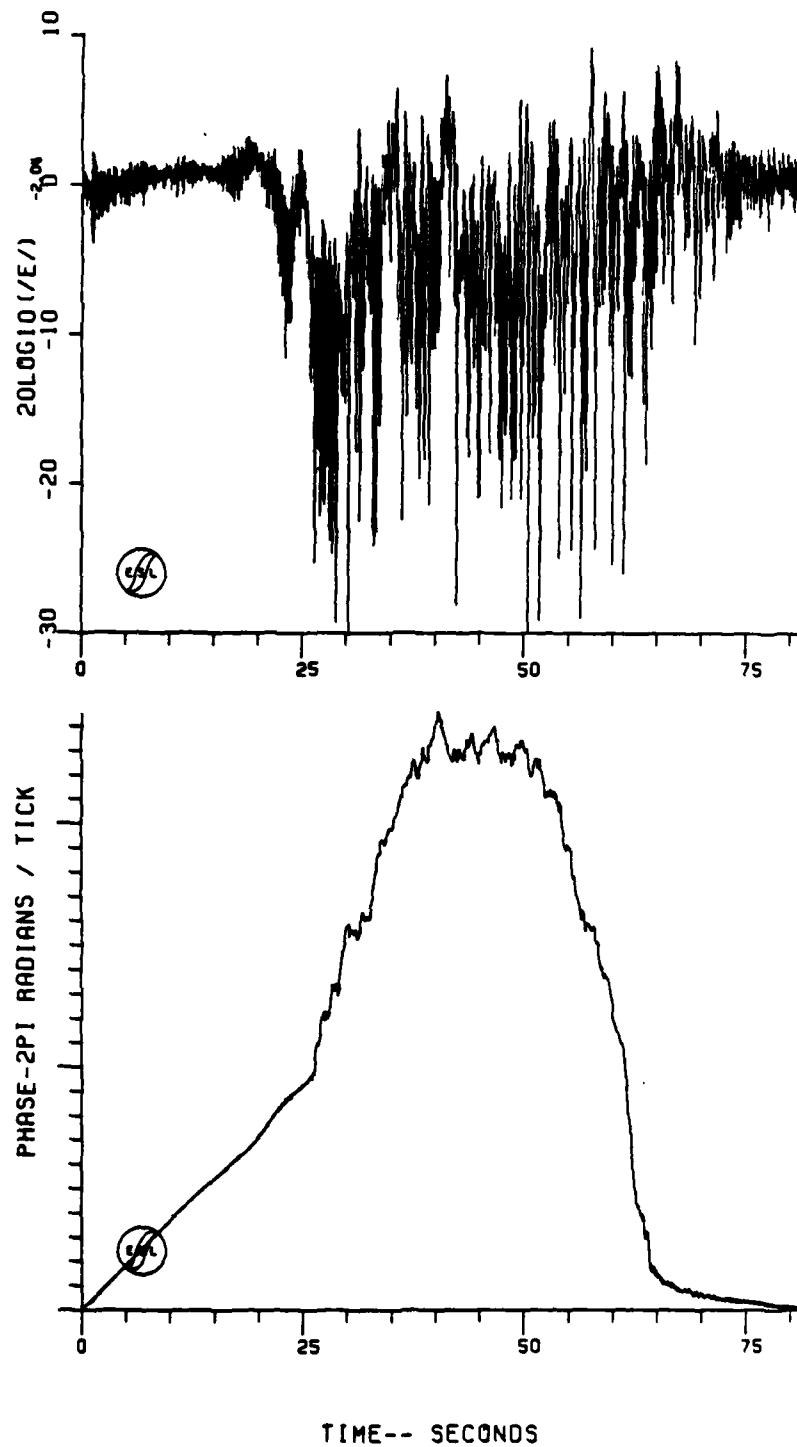
Figure 11-9. JAN Pass 11 Downlink Amplitude and Phase



TIME-- SECONDS

PHASE OF FIELD
J12052981100HZ
START TIME- 00:19:28.000

Figure 11-10. JAN Pass 12 Downlink Amplitude



TIME-- SECONDS

PHASE OF FIELD
J13052981100HZ
START TIME- 00:24:28.480

Figure 11-11. JAN Pass 13 Downlink Amplitude and Phase

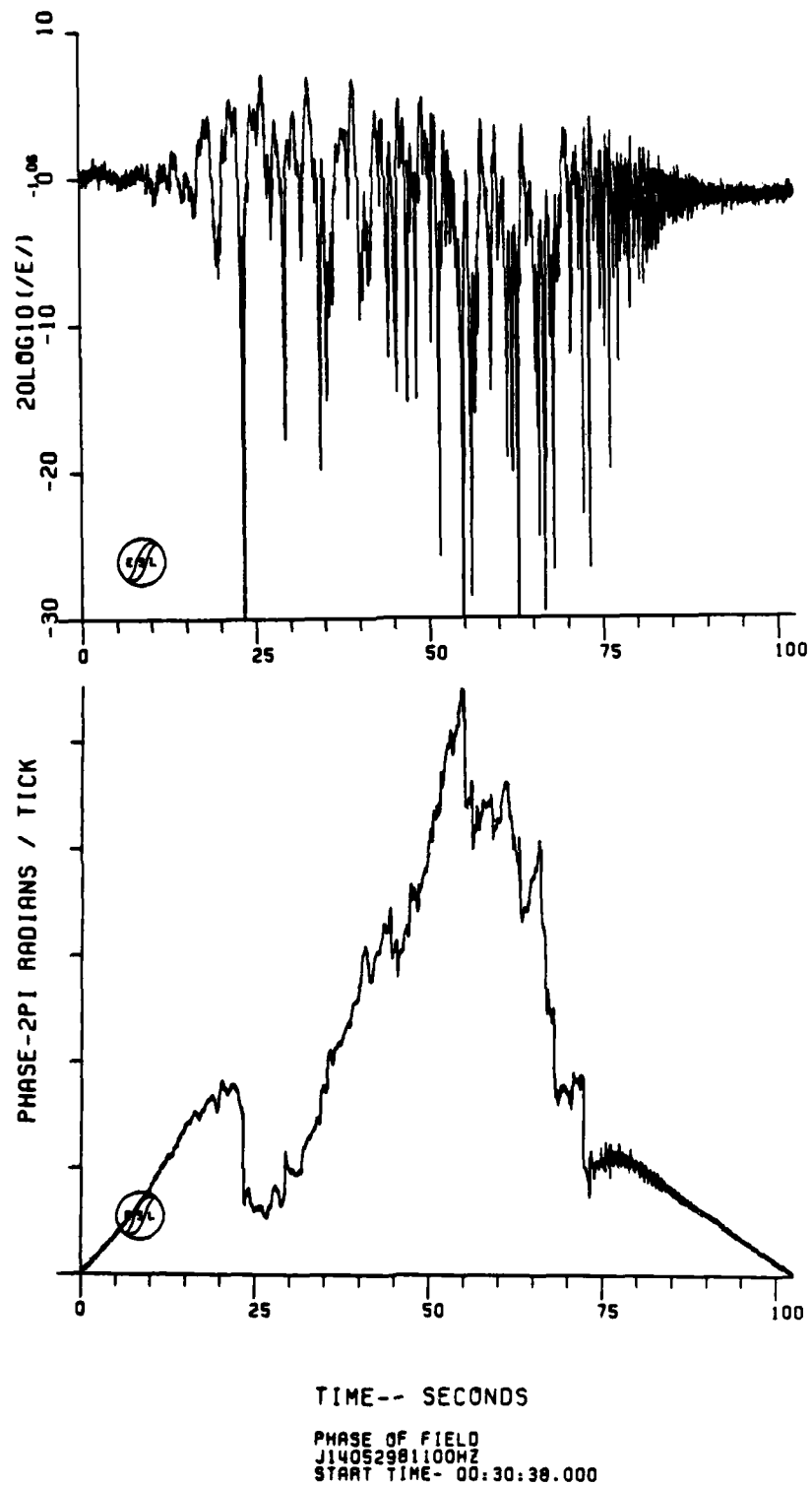


Figure 11-12. JAN Pass 14 Downlink Amplitude and Phase

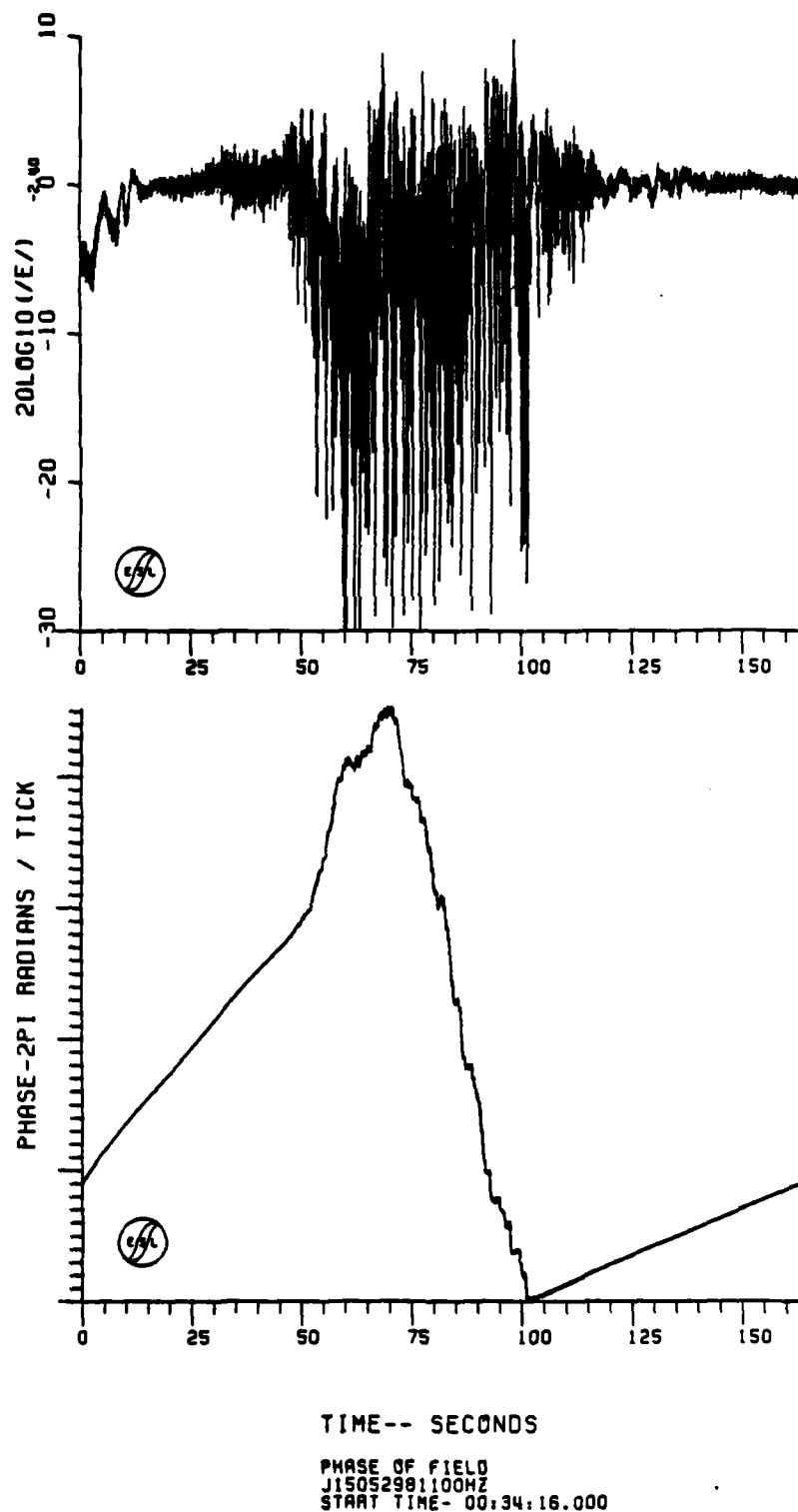


Figure 11-13. JAN Pass 15 Downlink Amplitude and Phase

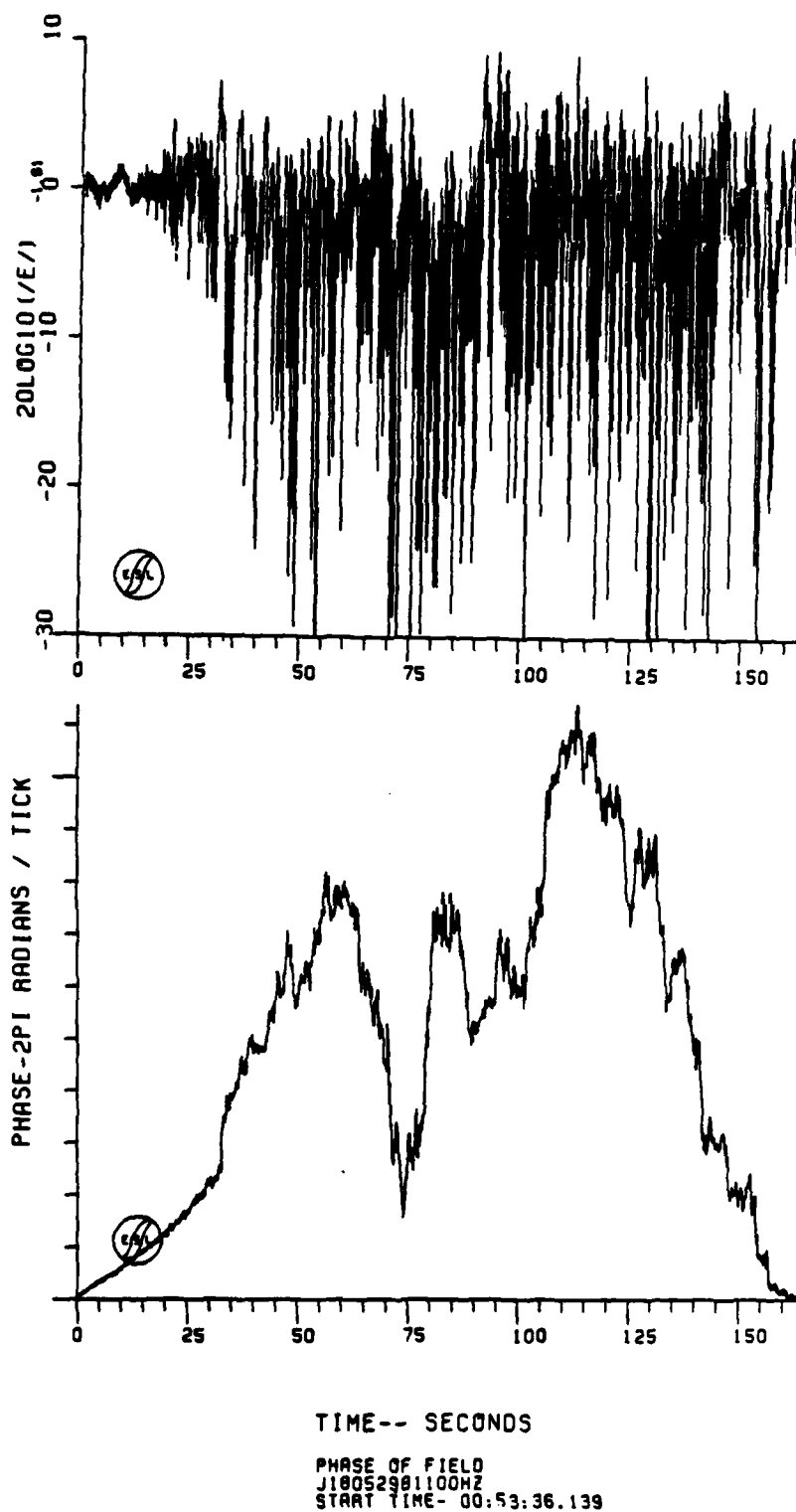
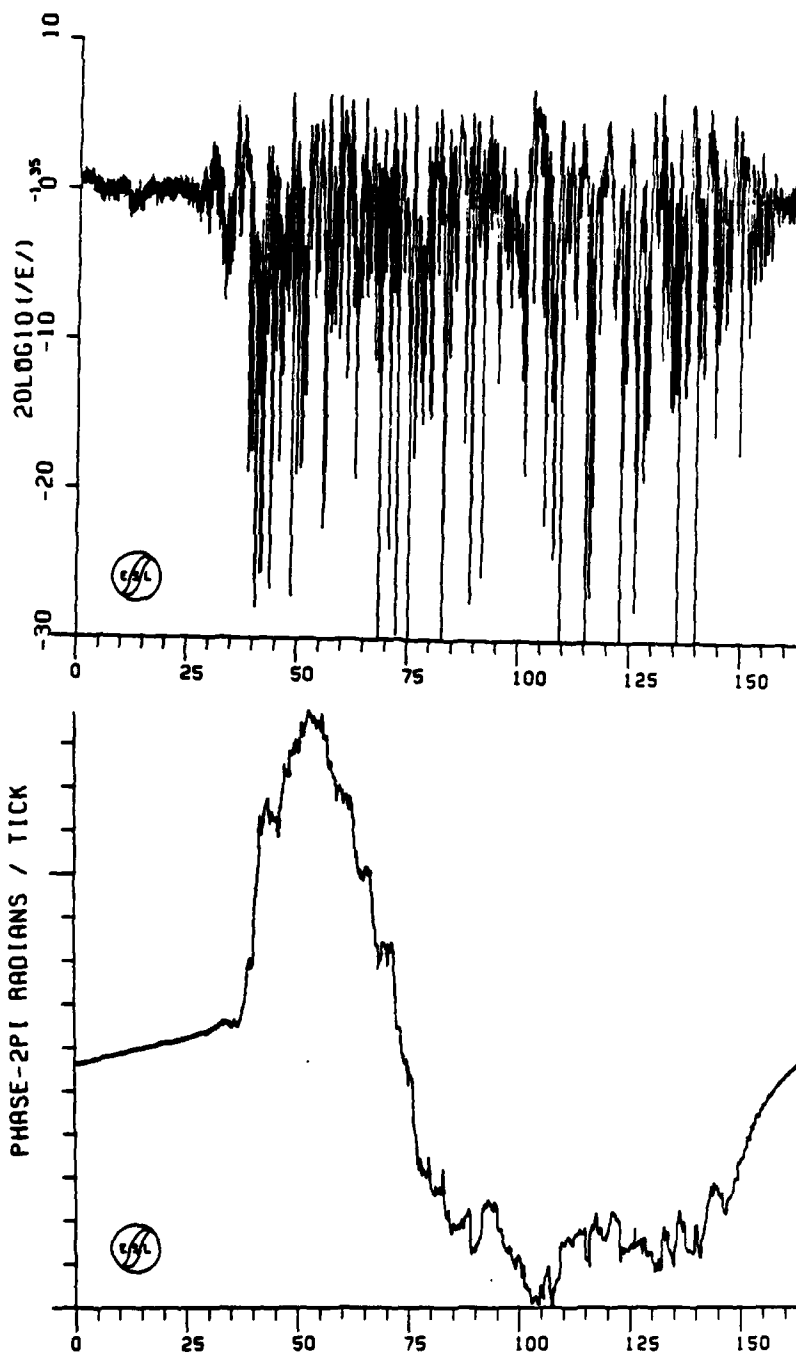


Figure 11-14. JAN Pass 18 Downlink Amplitude and Phase



TIME-- SECONDS

PHASE OF FIELD
J20052981100HZ
START TIME- 01:07:10.140

Figure 11-15. JAN Pass 20 Downlink Amplitude and Phase

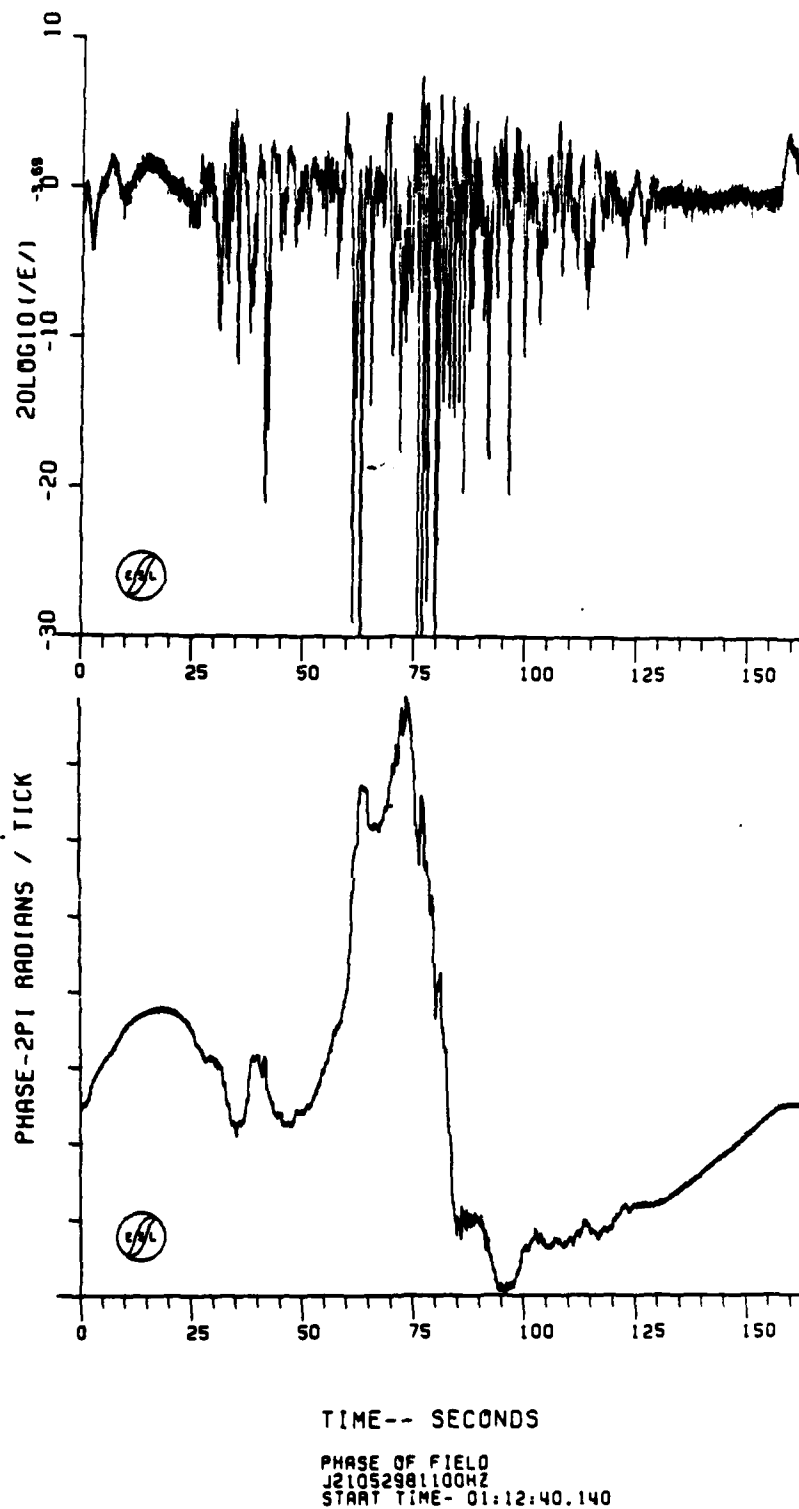
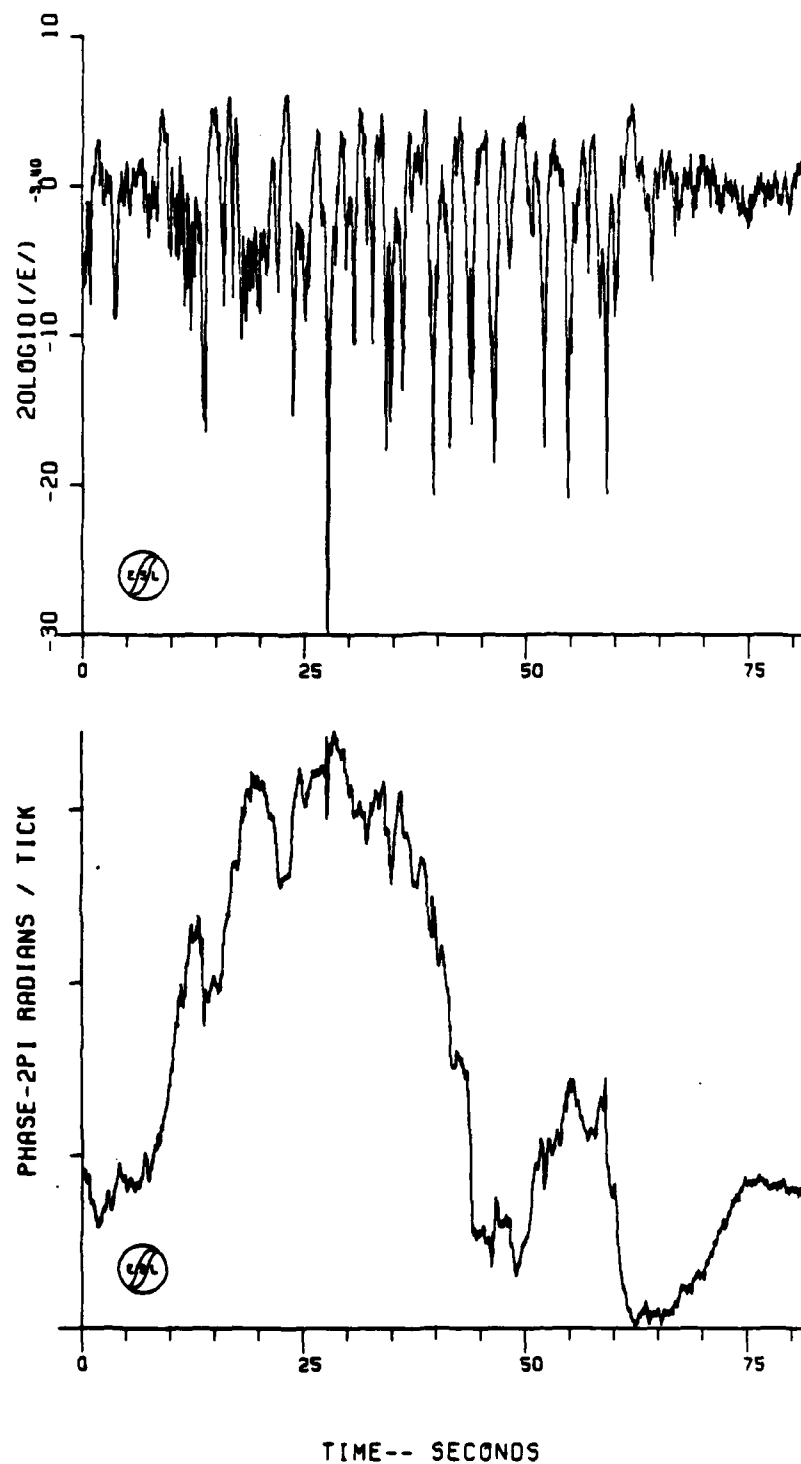
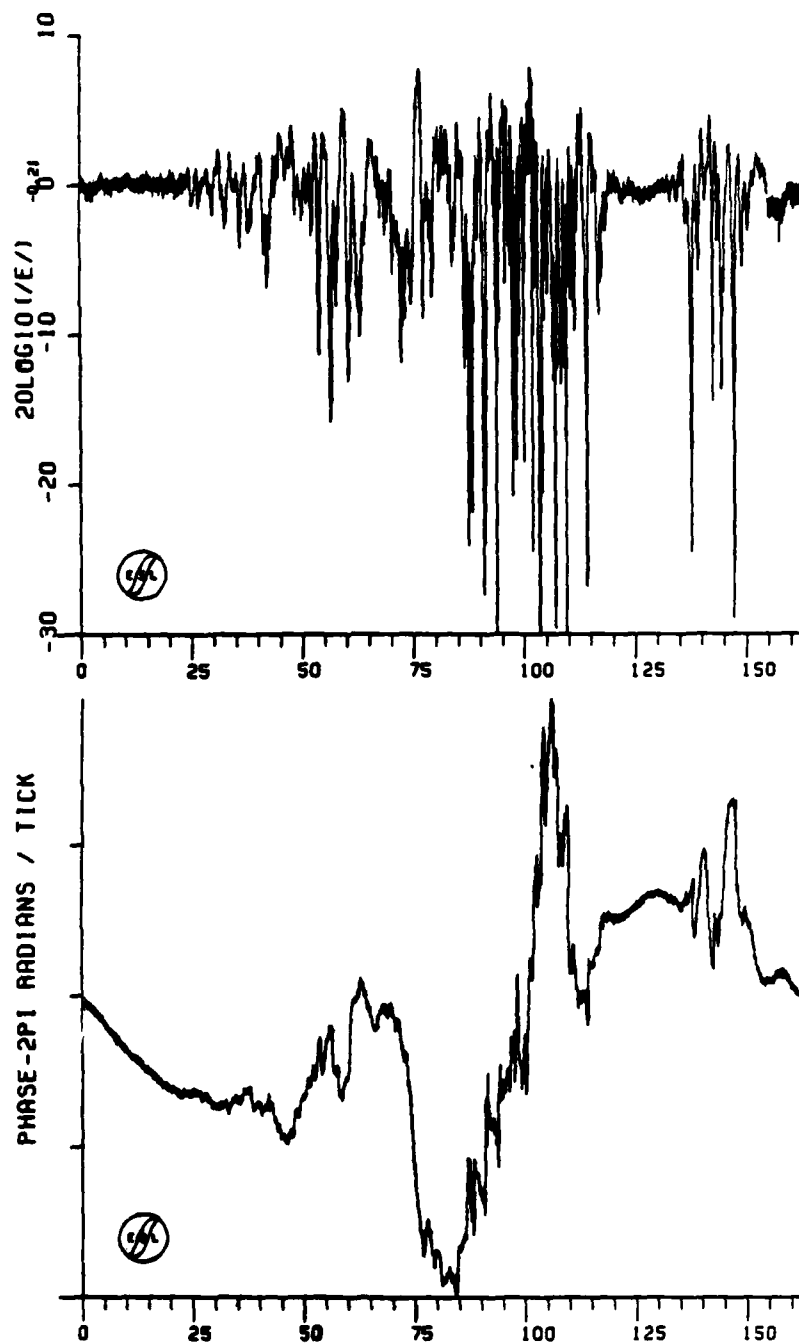


Figure 11-16. JAN Pass 21 Downlink Amplitude and Phase



PHASE OF FIELD
J23052981100HZ
START TIME- 01:23:31.100

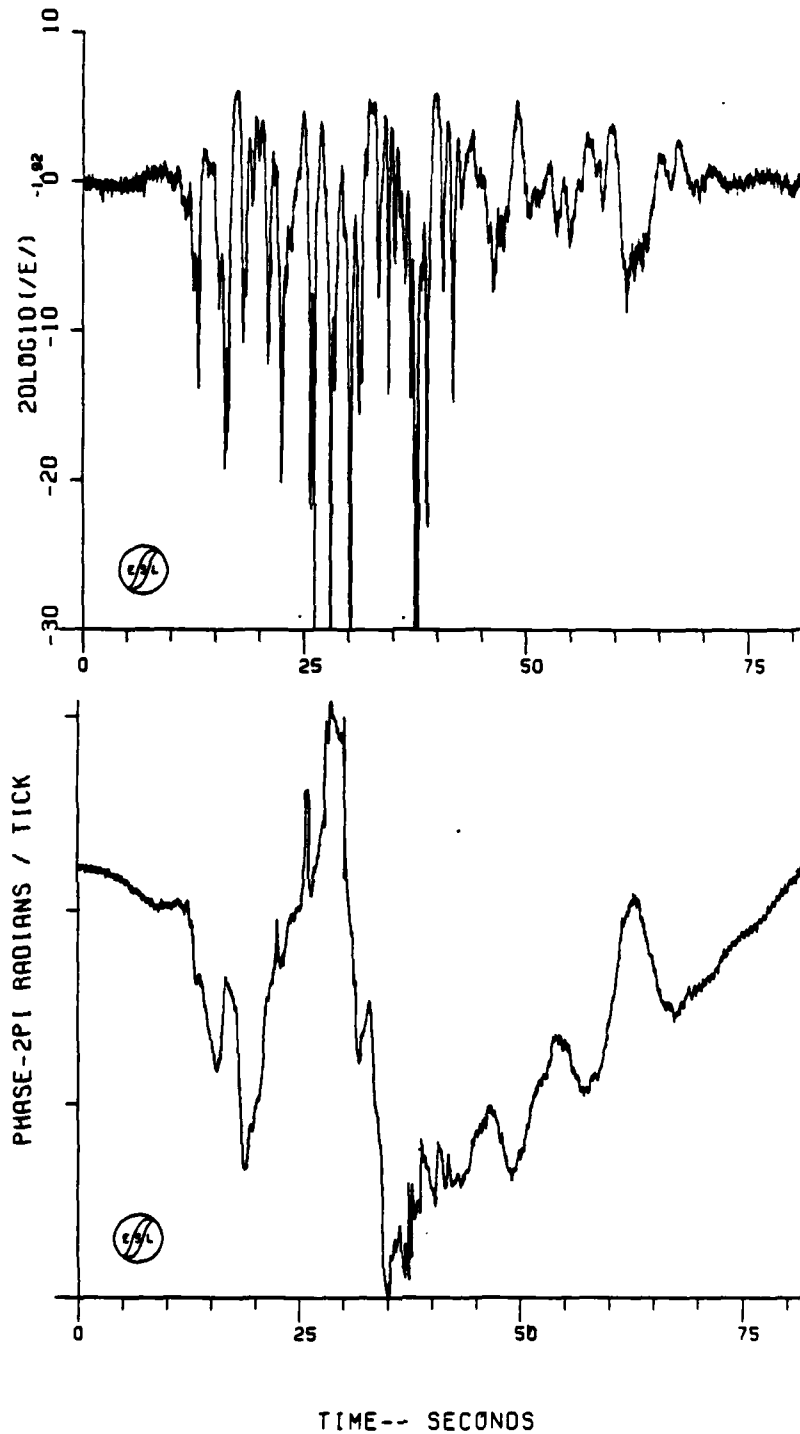
Figure 11-17. JAN Pass 23 Downlink Amplitude and Phase



TIME-- SECONDS

PHASE OF FIELD
J24052981100HZ
START TIME- 01:27:50.140

Figure 11-18. JAN Pass 24 Downlink Amplitude and Phase



TIME-- SECONDS

PHASE OF FIELD
J25052981100HZ
START TIME- 01:33:50.620

Figure 11-19. JAN Pass 25 Downlink Amplitude and Phase

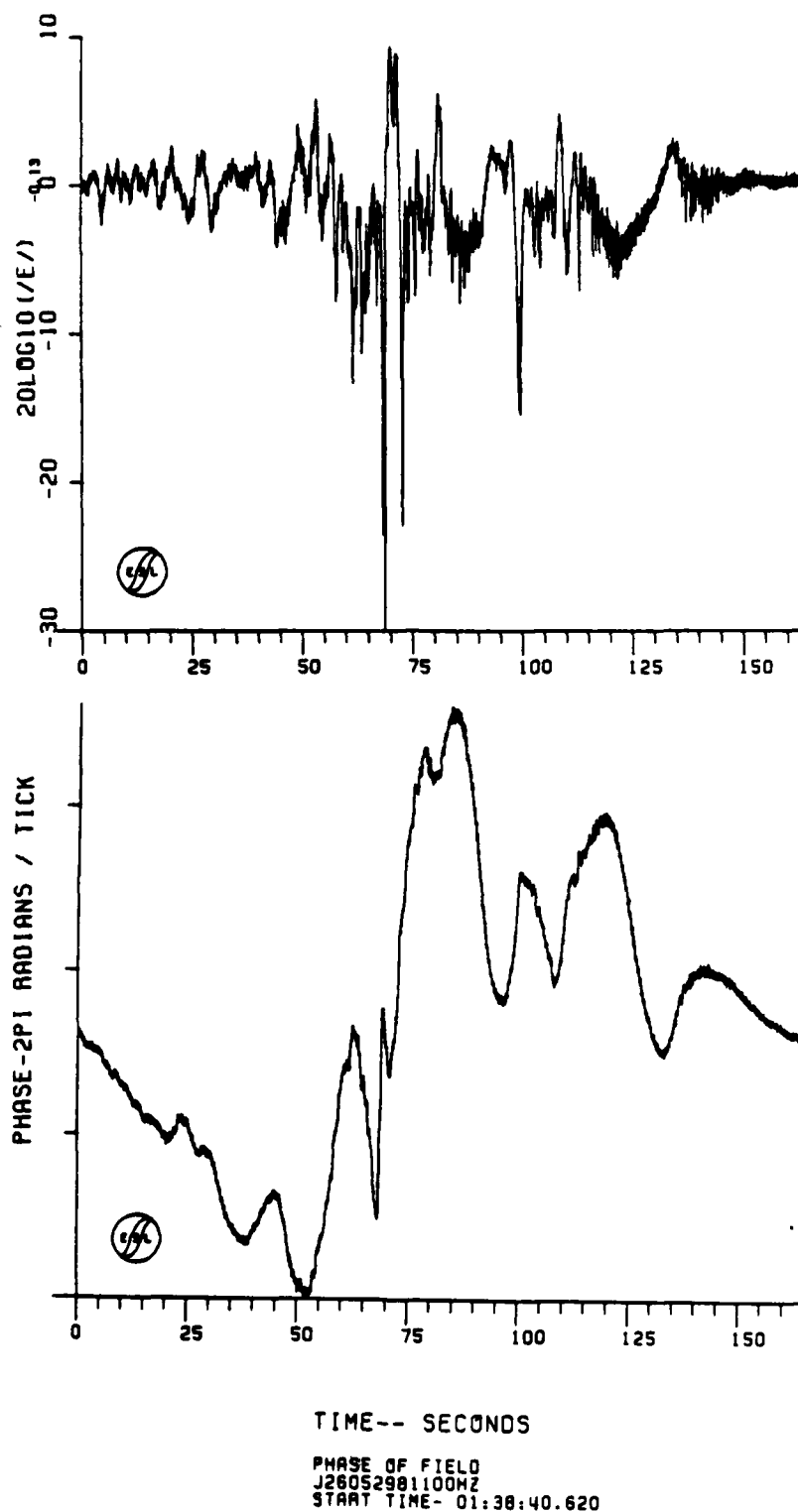
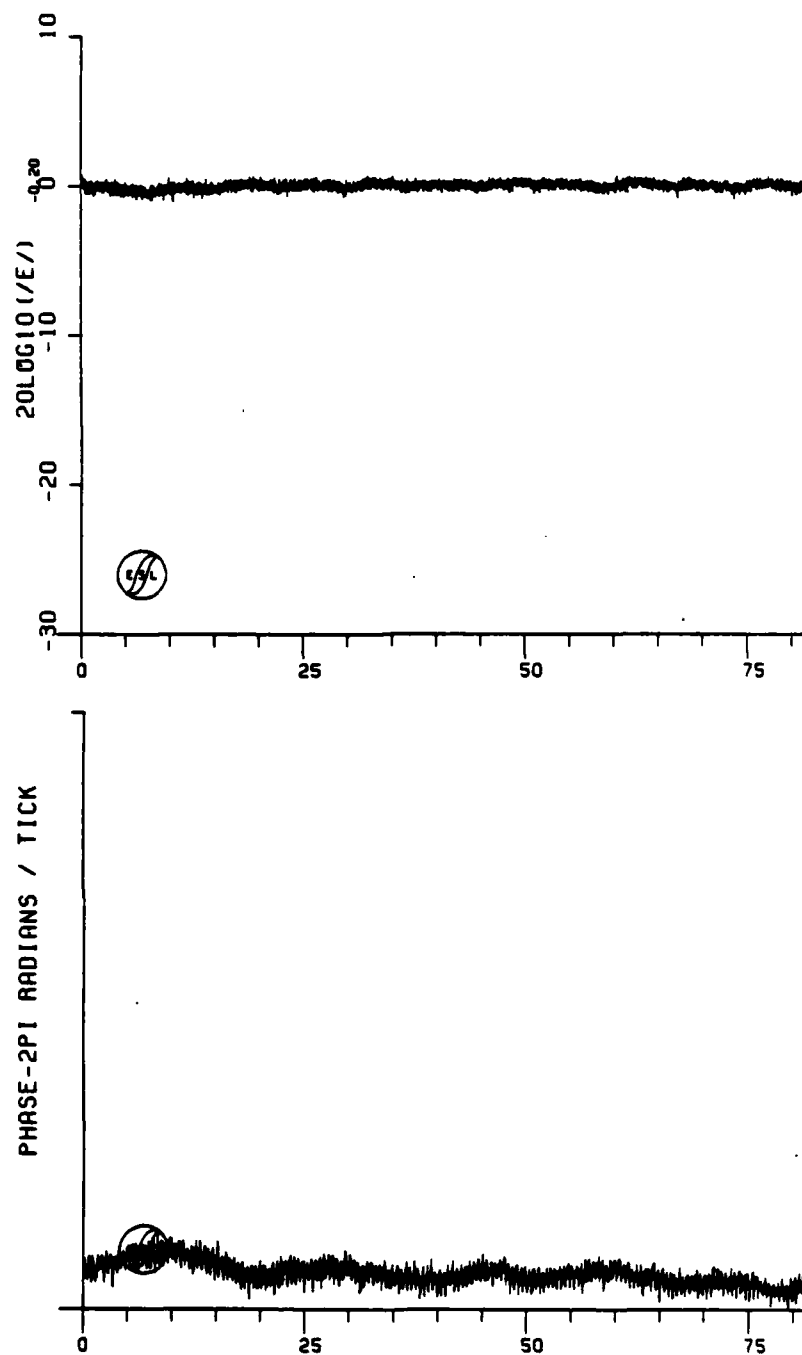


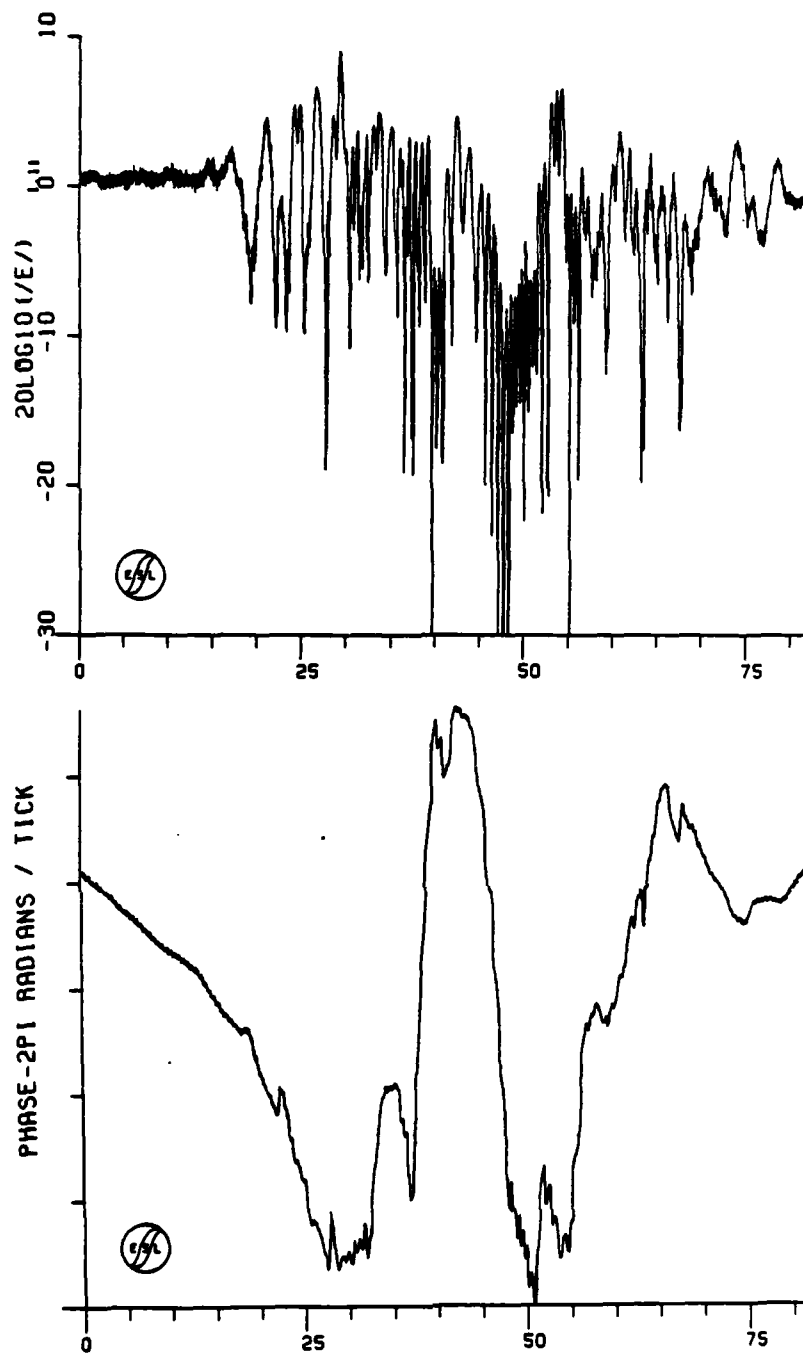
Figure 11-20. JAN Pass 26 Downlink Amplitude and Phase



TIME-- SECONDS

PHASE OF FIELD
J27052981100HZ
START TIME- 01:45:20.140

Figure 11-21. JAN Pass 27 Amplitude and Phase



TIME-- SECONDS

PHASE OF FIELD
J29052981100HZ
START TIME- 01:55:24.140

Figure 11-22. JAN Pass 29 Downlink Amplitude and Phase

However, there appears to be random scintillation fading superimposed. The leading edge exhibits smooth diffraction ringing corresponding to the northwest side of the ion cloud. The southeast side produces more random fading at this time.

JAN Pass 4 was to the north of the release point projection as shown in Figure 10-3. Only a short fading interval was noted with little phase windup as shown in Figure 11-4. This propagation path was presumably high up the field lines catching only the tips of a few striations as reflected in the phase data.

Passes 5, 6, and 7 all exhibit a shallow defocus as shown in Figures 11-5, 11-6, and 11-7. Passes 4, 5, 6, and 7 progressively scan the fading shadow region in a northeast to a southwest progression. Pass 8 traced out the fading pattern in a southwest to northeast pass. Unfortunately the motion of the cloud during this time is not well known. However, based on Pass 8 it is clear that the cloud did not drift significantly during this time. Pass 8 and Pass 9 were not included among the plots and presented as the aircraft executed a turn during these passes which distorts the phase data. The location of these passes and the fading intervals are shown on Figures 10-3 and 10-4 of the prior section. Pass 9 was near parallel to the magnetic field projection and to the north of the cloud. As the plane turned southeast, it served to define the north-south extent of the fading region.

Pass 10 enters the cloud from the southeast side. The phase structure reflects the striation development on this side of the ion cloud as shown in Figure 11-8. The amplitude data indicates that the striations are stretched out leading the main ion cloud to the southeast or south. Likewise Pass 11 which enters the cloud from the northwest reflects a fairly smooth initial phase windup followed by a random fluctuation imposed by the striation phase interference fading on the southeast side of the cloud. Pass 11 amplitude and phase are shown in Figure 11-9.

Pass 12 exhibits a shallow defocus of a few dB as shown in Figure 11-10. For this pass which should be further up the field lines but near that of Pass 10, the fading is nearly symmetric with the gross ion cloud bell shaped phase curve. This pass is just slightly north of Pass 10. The gross phase windup is greater than that of Pass 10 indicating the main ion cloud at this time was north of Passes 10, 11, and 13. Pass 13, shown in Figure 11-11, is in the same vicinity as Pass 11 and exhibits slightly greater phase windup, reflecting the subsequent southwesterly movement of the cloud.

Pass 14, slightly to the north of Pass 12, likewise indicates the cloud has moved to the southwest. This pass appears to have intersected the striations high up the magnetic field lines.

Pass 15 shown in Figure 11-13 appears to have been nearly through the center of the ion cloud. The total phase windup may be less than the maximum shown. The uplink data for this pass shows considerably less phase windup, indicating a value more of the order of 15 cycles. The phase again reflects the smooth ion cloud structure to the northwest side. This pass is nearly an hour and a half after release and still indicates a cohesive striation unit with little moderation of effects.

The analog tape in the aircraft was changed between the 15th and 16th passes. Its plot is not included due to filter start-up transients in the digitized data. It should be possible to process this pass with some special processing should it prove to be of interest. Pass 17 has not been included because the phase of the signal was very noisy. The cause of this phase noise is not understood, but may have been due to a momentary loss of K-band phase lock.

Passes 18 and 20 demonstrate the strong fading at 2 hours. These data are shown in Figures 11-14 and 11-15. These passes most likely were not through the peak density portion of the ion cloud. Pass 19 has not been included as it exhibited the same phase noise problem as during Pass 17.

Pass 21 was apparently high up the field lines to the west of Pass 20. The data indicates a short interval of deep fading as shown in Figure 11-16. Pass 22 was further west of Pass 21 and did not exhibit strong fading and, thus, was not plotted here. Pass 23 (Figure 11-17), just to the north of Pass 21, shows little gross cloud windup and only moderate fading depth.

None of the subsequent passes show evidence of a strong gross cloud phase windup. Pass 24 could imply that the striations are beginning to drift apart. Pass 24 occurs at $R+2^h 15^m$ and is shown in Figure 11-18. This pass is in the same vicinity as Pass 19. Pass 25, near Pass 23, is shown in Figure 11-19. This pass too shows a moderation of the fading intensity. The shallow fading at the end of the pass occurs on the southeast side of the transit. The shallow fading at the beginning of Pass 24 was also on the southeast side of the transit.

Pass 26 shown in Figure 11-20 only shows as few cycles of phase activity with one large focus. Pass 27 which was to the west of Pass 26 and near Pass 22 shows no activity whatsoever. This is plotted in Figure 11-21 as an example of the signal amplitude and phase during level flight without fading activity present.

Pass 28, back through the vicinity of Pass 23 and 25, did not exhibit any significant fading and is not shown. Pass 29 is shown in Figure 11-22 and was the last strong fading observed. This pass was at $R+2^h 42^m$. Pass 29 was on the northern extreme of Pass 24. Subsequent passes in that vicinity failed to detect any significant fading. We believe that the striations dissipated by this time, however, it is possible that the drift direction could have changed to due north causing the aircraft to transit to the south of the main striation region. An examination of the total phase windup or total integrated electron content versus time would imply the ionization dissipated to that of the background ionosphere. This is evident in the total phase windup of each subsequent aircraft pass. The phase windup varied from 109π radians in Pass 2 to 5π radians in Pass 29 as shown in the preceding figures. The total integrated electron content is shown plotted for JAN versus time on a log scale in Figure 11-23.

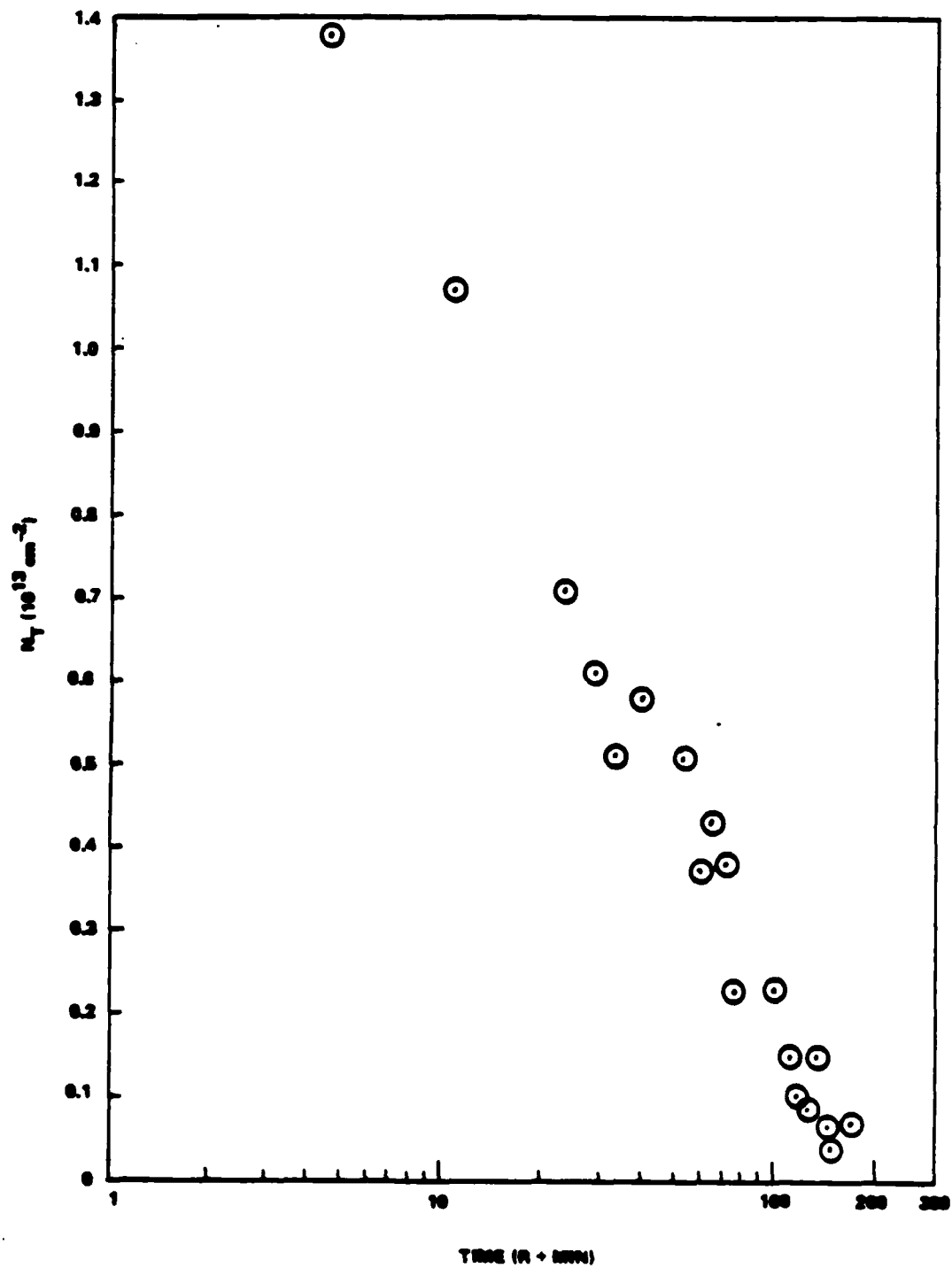


Figure 11-23. Integrated Electron Content Versus Time for JAN

11-3

JAN SUMMARY.

Summarizing, the downlink propagation data for event JAN is of high quality and appears to give good information about the cloud development. The data appears similar to that of HOPE, including the initial 15 dB defocus through the eventual dissipation of fading effects.

SECTION 12

JAN UPLINK TONE DATA

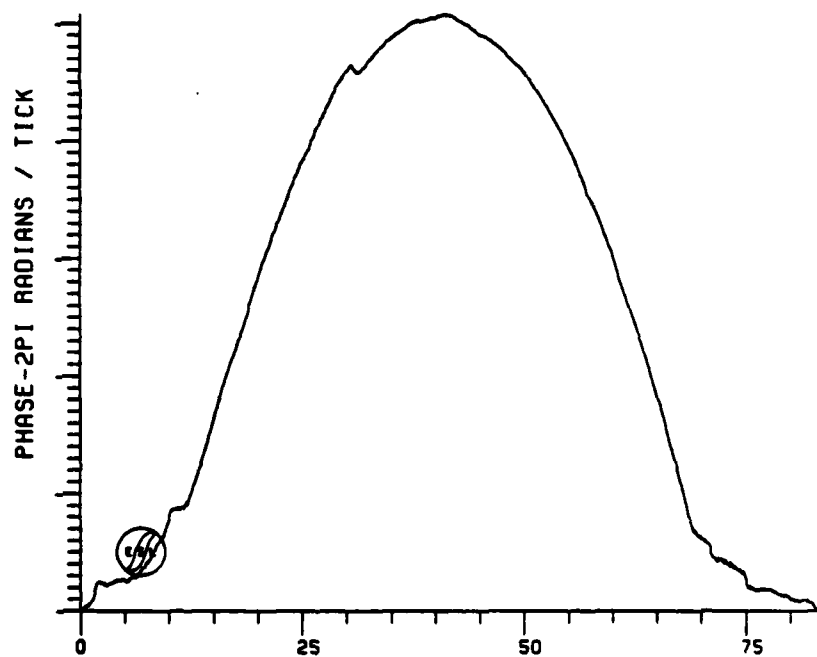
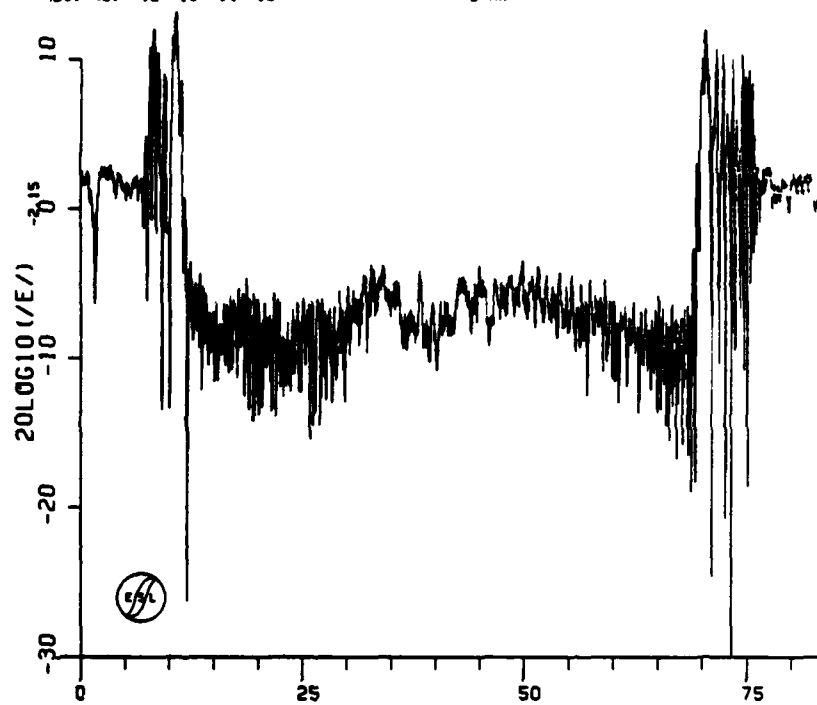
12-1 INTRODUCTION.

Measurements of the uplink tone amplitude and phase were successfully made following the JAN release. The uplink tone signal is transmitted from the aircraft (doppler pre-corrected) at 341 MHz to the LES-8 satellite. The doppler pre-correction is provided by the K-band (39.6 GHz) reference signal generated at the satellite coherently with the downlink tone. At the satellite, the inphase and quadrature components of the signal are sampled and sent back down on the K-band data link (reference signal) to the aircraft. The uplink data requires a significant amount of computer processing in order to extract the signal amplitude and phase as described in Appendix B and D. Except for the satellite processing non-idealities described in Appendix B, the uplink data should provide a better estimate for the cloud integrated electron content on back-propagation processing, since the link frequency is at 341 MHz as opposed to 250 MHz where diffraction effects are worse. Loss of K-band lock results in the loss of doppler correction for both the uplink and downlink tones as well as the loss of the K-band data link. While the loss of the K-band phase lock was a problem during the earlier releases, it was not a problem during JAN.

12-2 UPLINK PROPAGATION MEASUREMENTS DURING JAN.

Uplink data was received during all 35 passes made following this release. A summary of these passes were given in Table 10-1. Plots of the processed uplink tone data are given in Figures 12-1 through 12-22. Plots of the JAN downlink tone data for the same passes were given in Section 11.

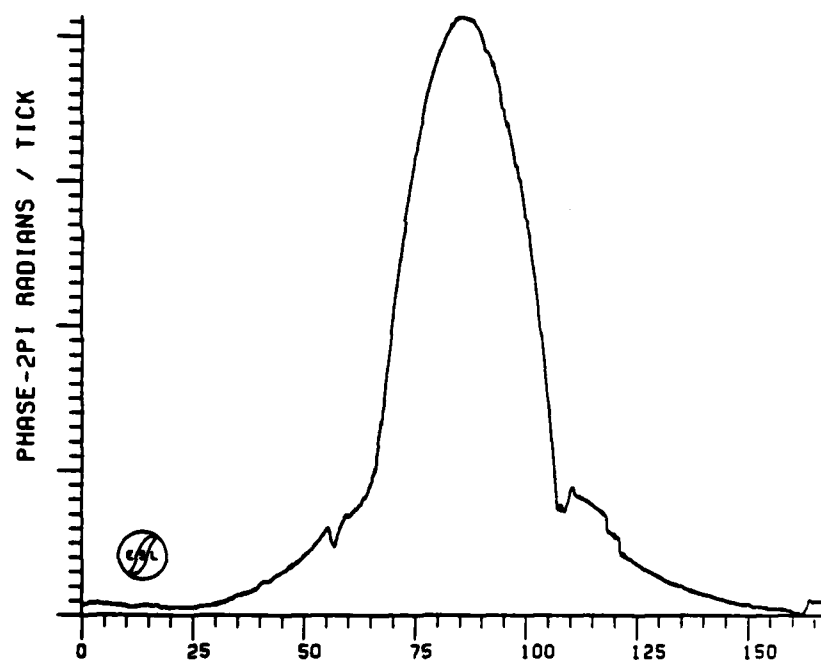
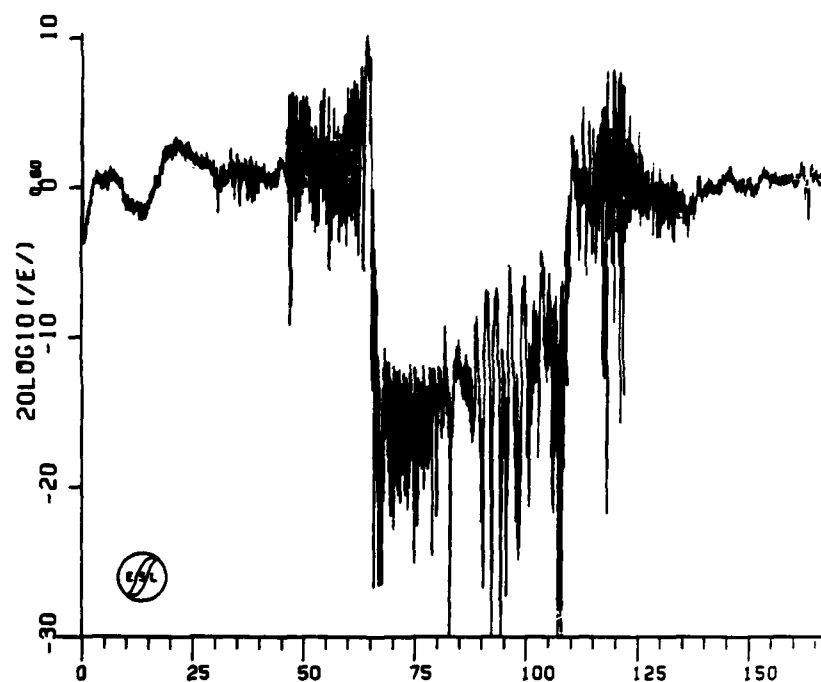
It is interesting to note that the uplink did not exhibit diffraction ringing on the first pass as did the downlink. This difference is presumably due to the 36 percent higher uplink frequency. As no fading was observed, a plot for Pass 1 has not been included.



TIME-- SECONDS

PHASE OF FIELD
UJ02 050501 15HZ
START TIME- 23:18:57.652

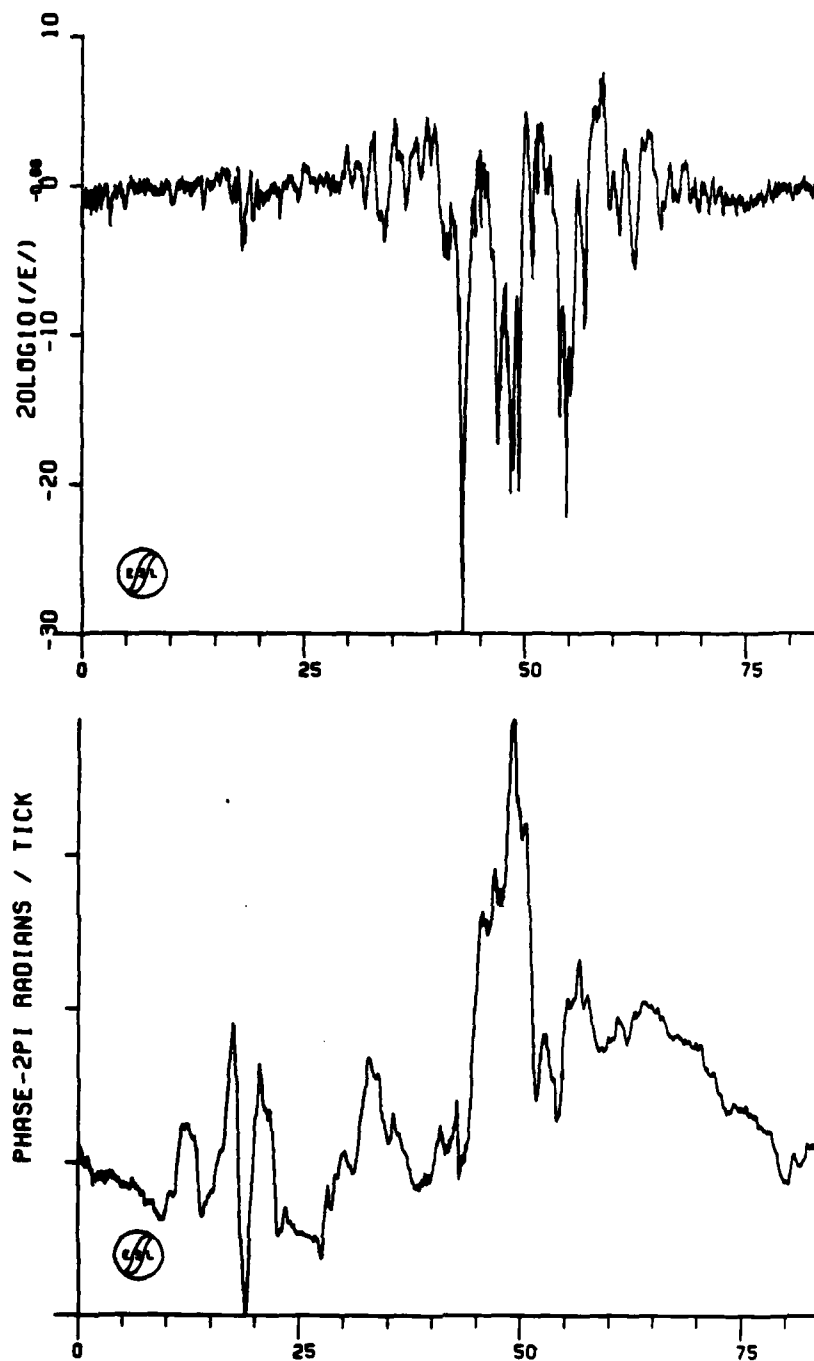
Figure 12-1. JAN Pass 2 Uplink Amplitude and Phase



TIME-- SECONDS

PHASE OF FIELD
UJ03 050581 15HZ
START TIME- 23:24:21.775

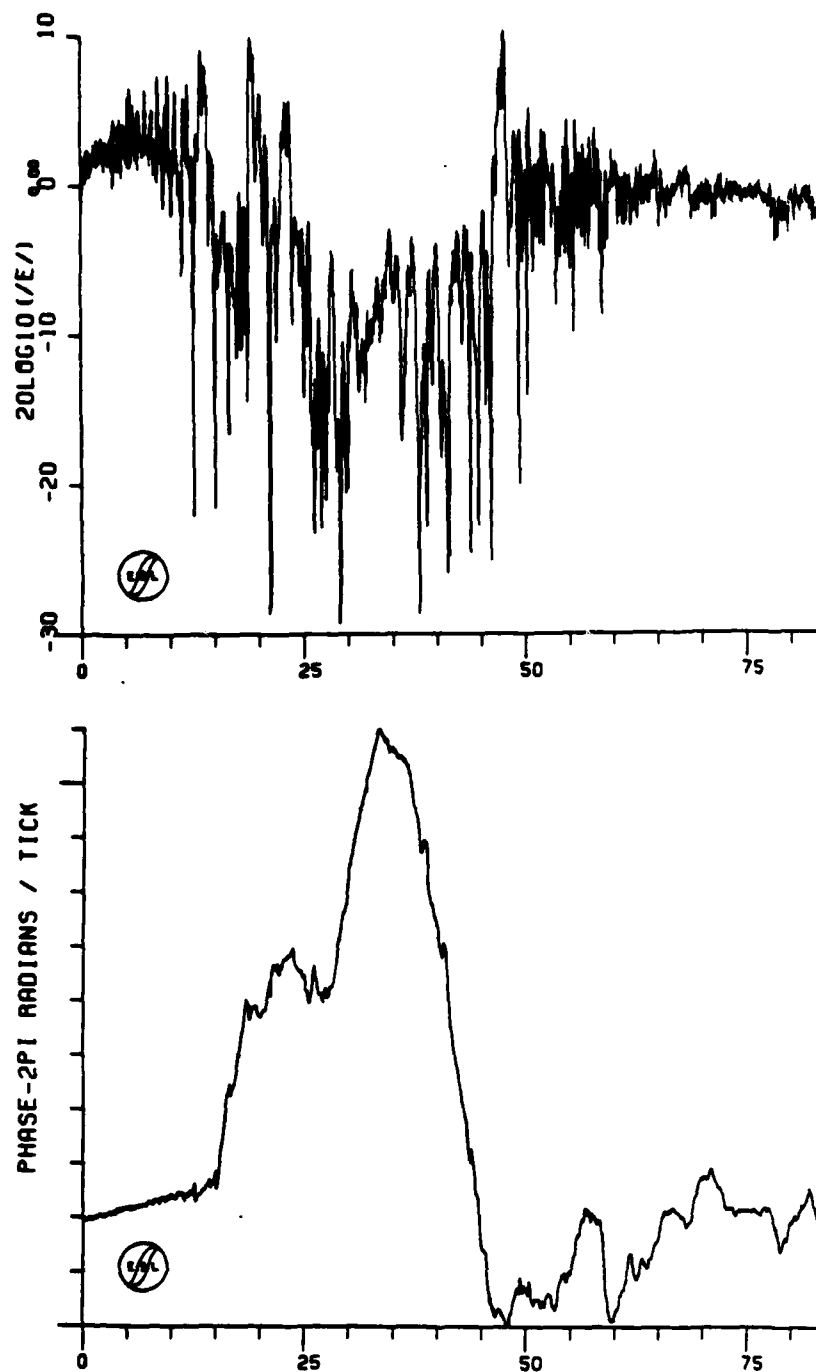
Figure 12-2. JAN Pass 3 Uplink Amplitude and Phase



TIME-- SECONDS

PHASE OF FIELD
UJ04 050581 15HZ
START TIME- 23:33:00.421

Figure 12-3. JAN Pass 4 Uplink Amplitude and Phase



TIME-- SECONDS

PHASE OF FIELD
UJOS 050581 15HZ
START TIME- 23:37:09.253

Figure 12-4. JAN Pass 5 Uplink Amplitude and Phase

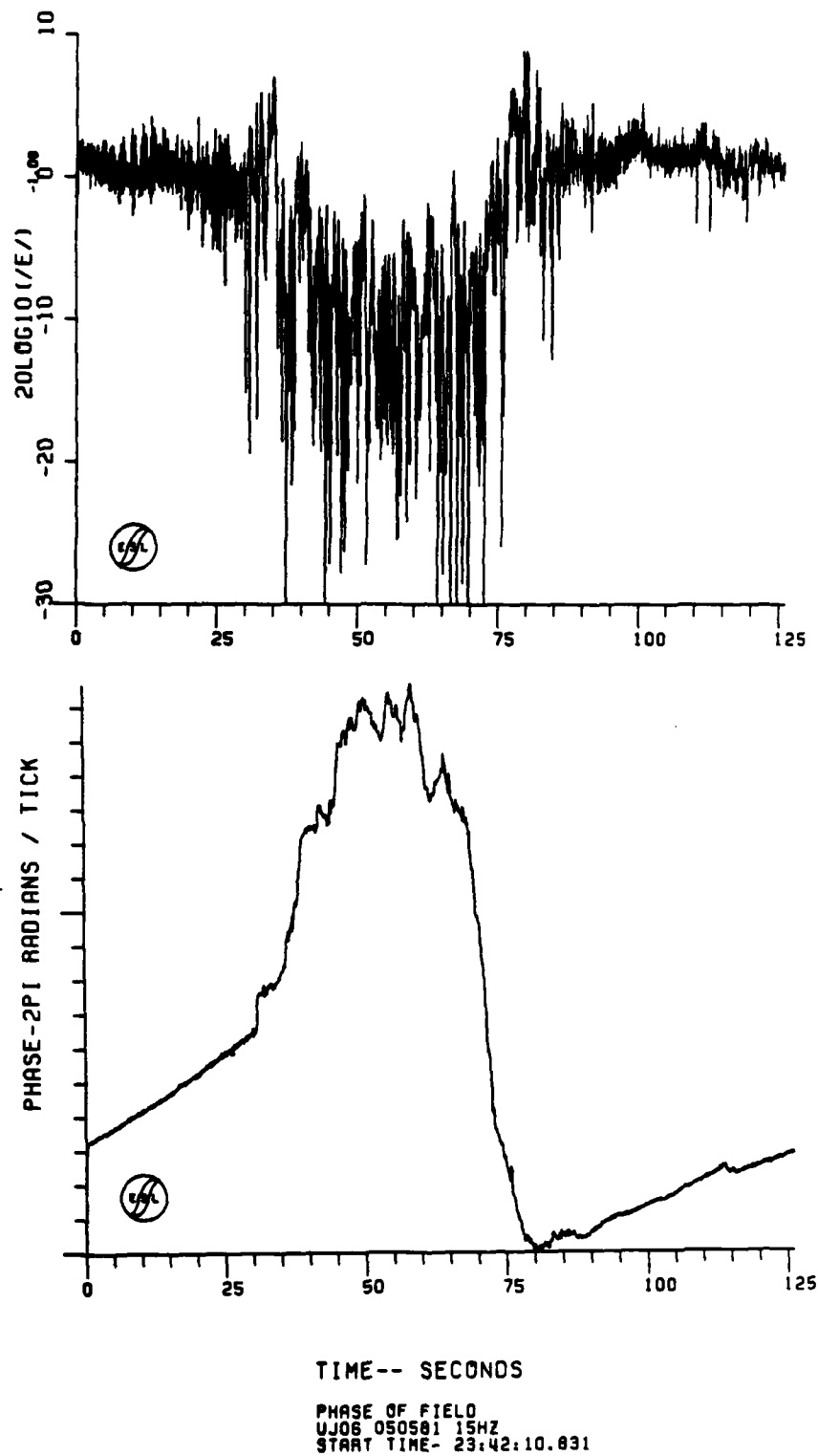
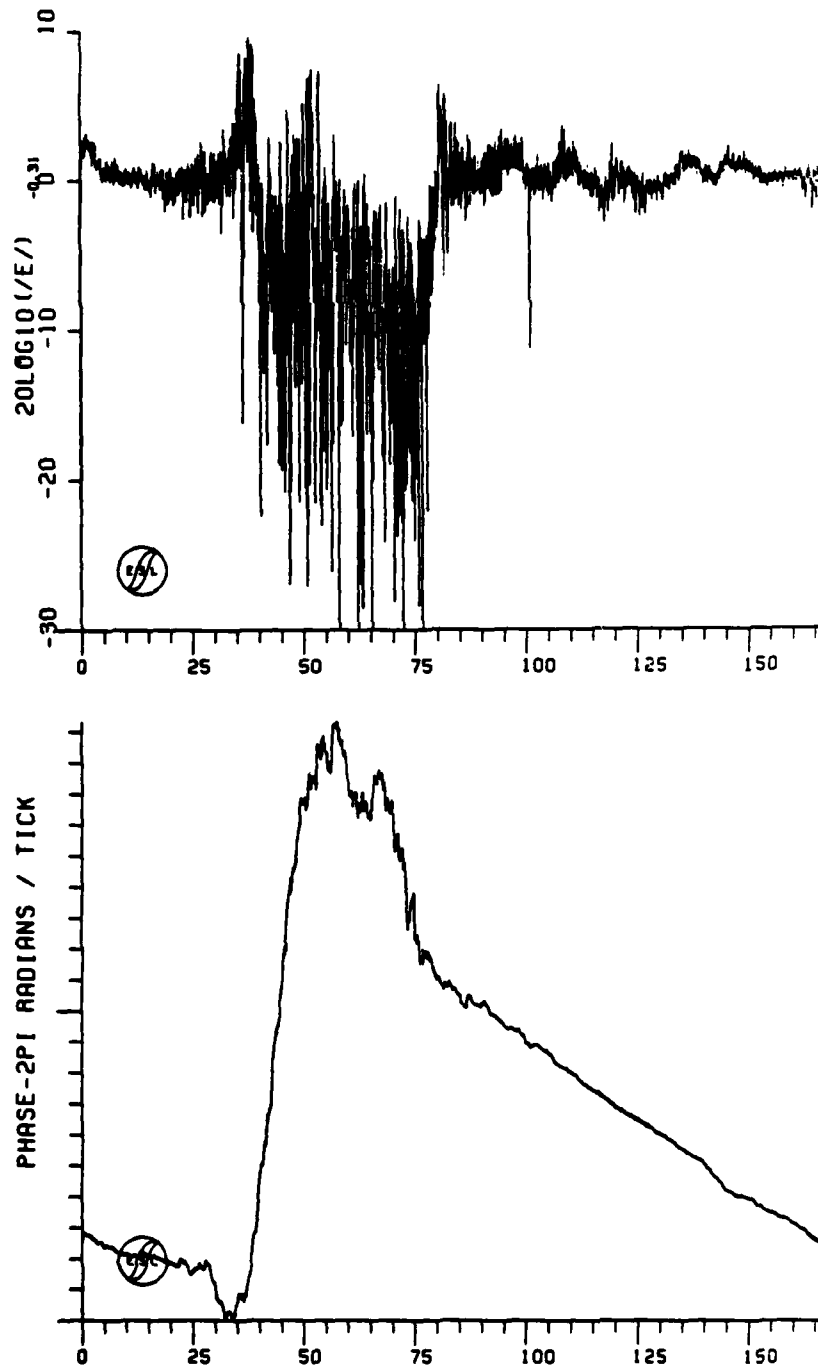
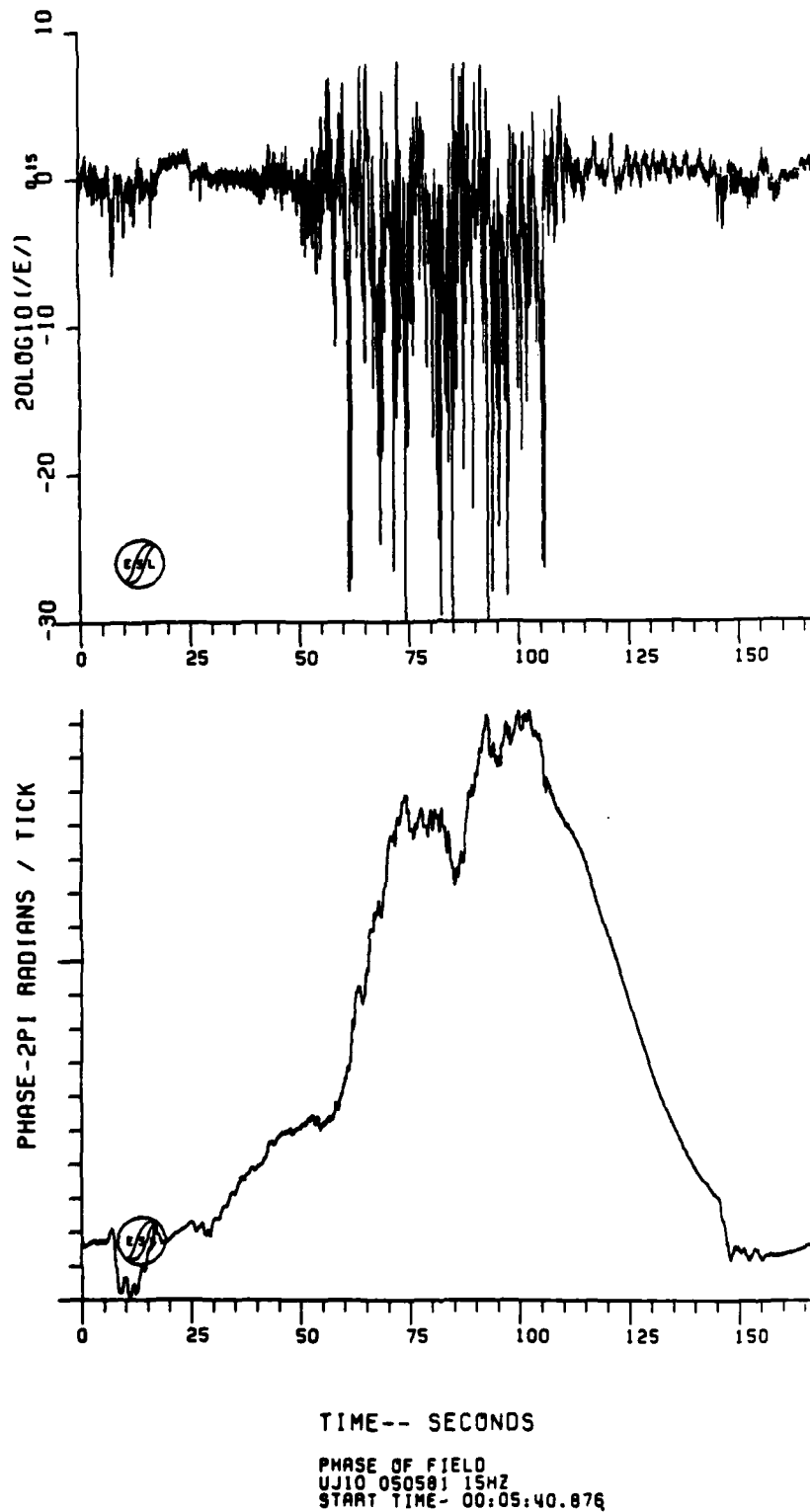


Figure 12-5. JAN Pass 6 Uplink Amplitude and Phase



TIME-- SECONDS
 PHASE OF FIELD
 UJ07 050581 15HZ
 START TIME- 23:46:56.527

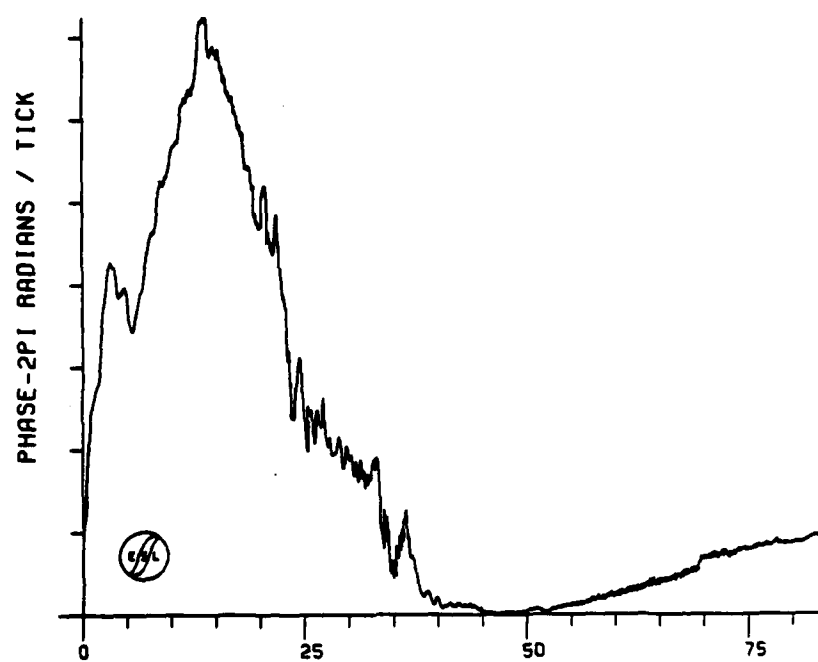
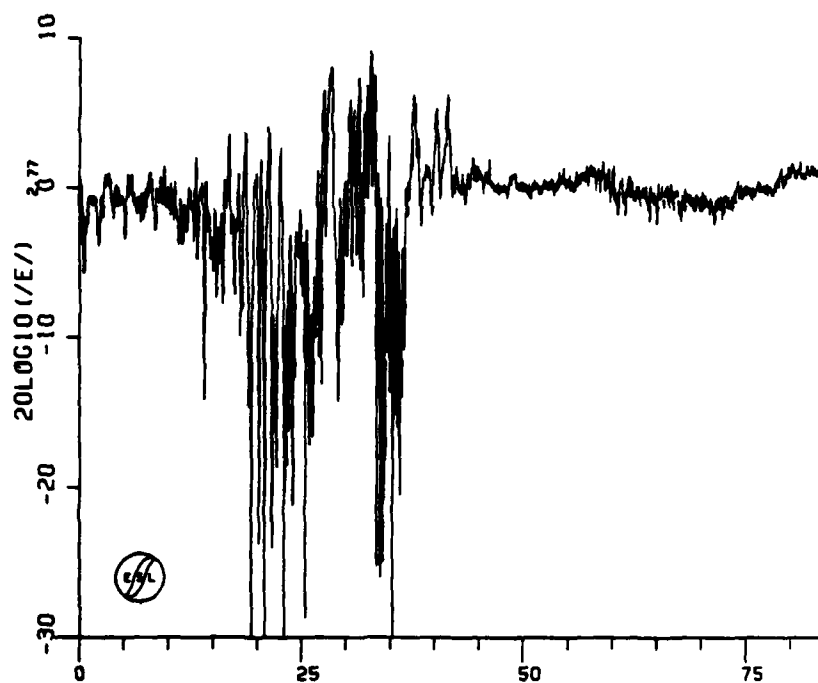
Figure 12-6. JAN Pass 7 Uplink Amplitude and Phase



TIME-- SECONDS

PHASE OF FIELD
UJ10 050581 15HZ
START TIME- 00:05:40.876

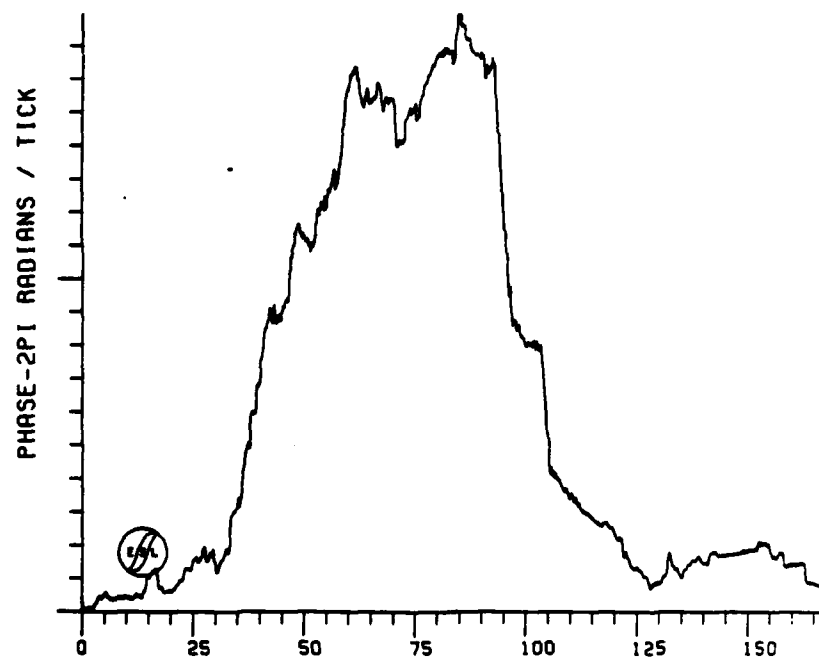
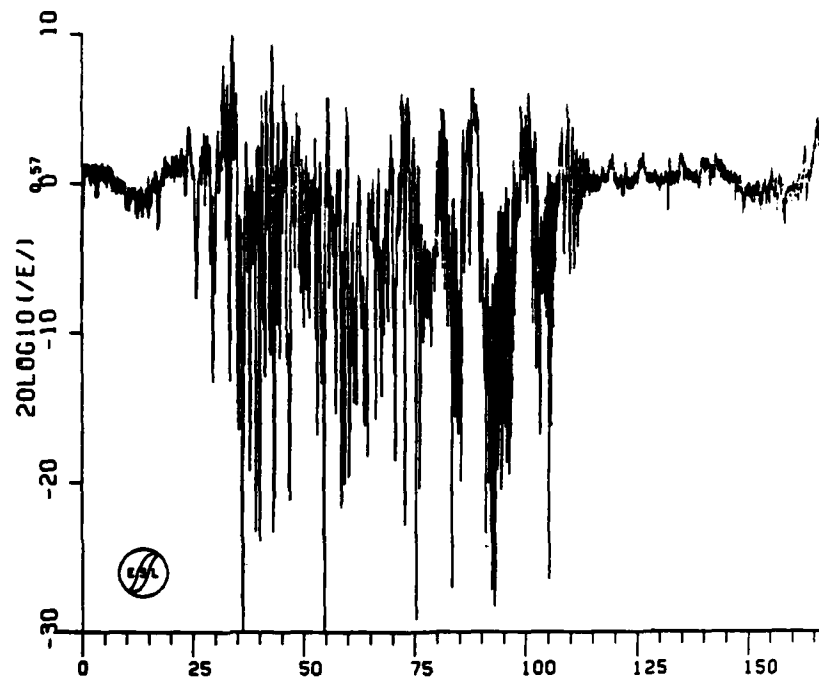
Figure 12-7. JAN Pass 10 Uplink Amplitude and Phase



TIME-- SECONDS

PHASE OF FIELD
UJ11 050581 15HZ
START TIME- 00:14:22.073

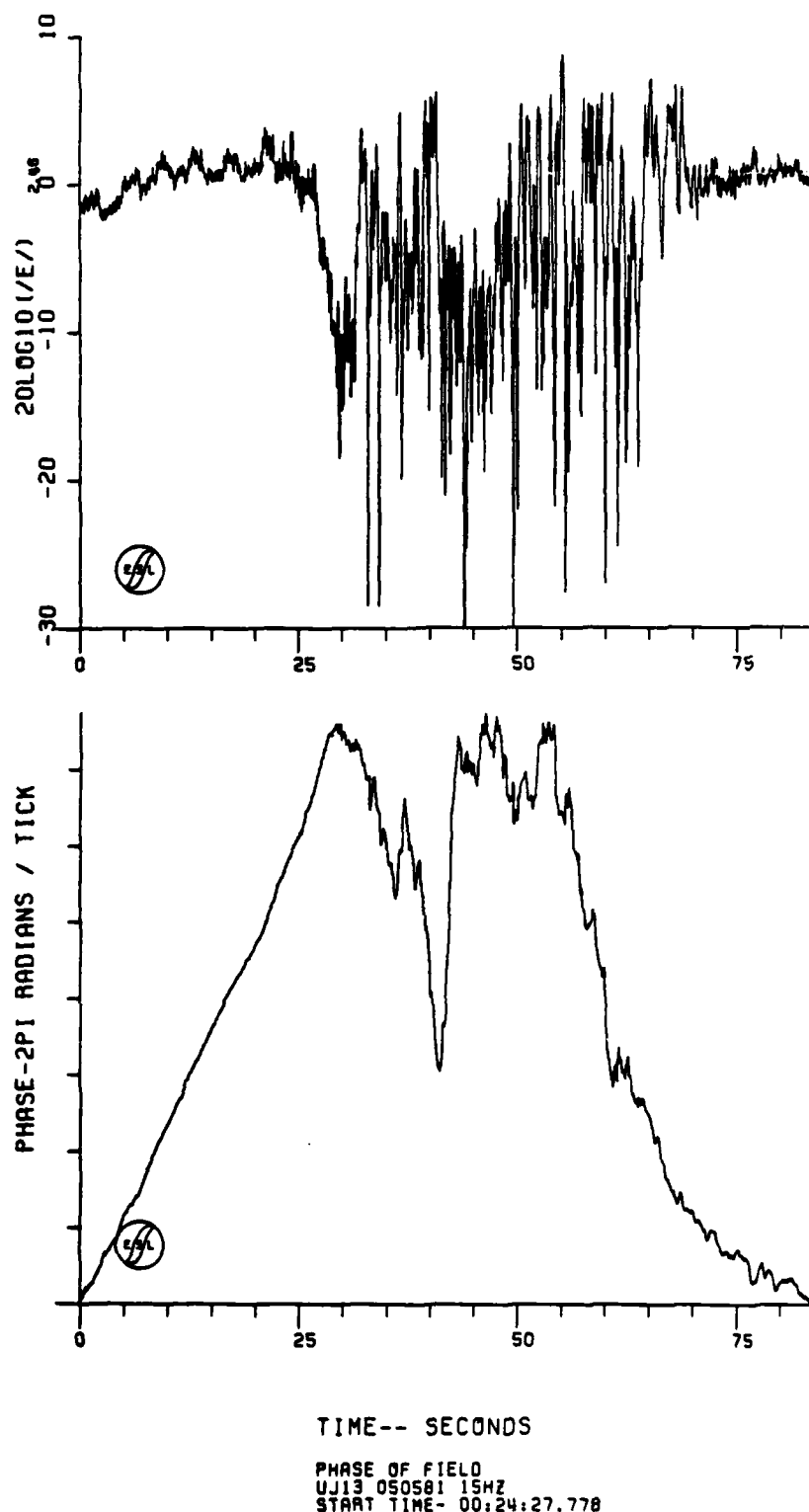
Figure 12-8. JAN Pass 11 Uplink Amplitude and Phase



TIME-- SECONDS

PHASE OF FIELD
UJ12 050501 15HZ
START TIME- 00:19:21.100

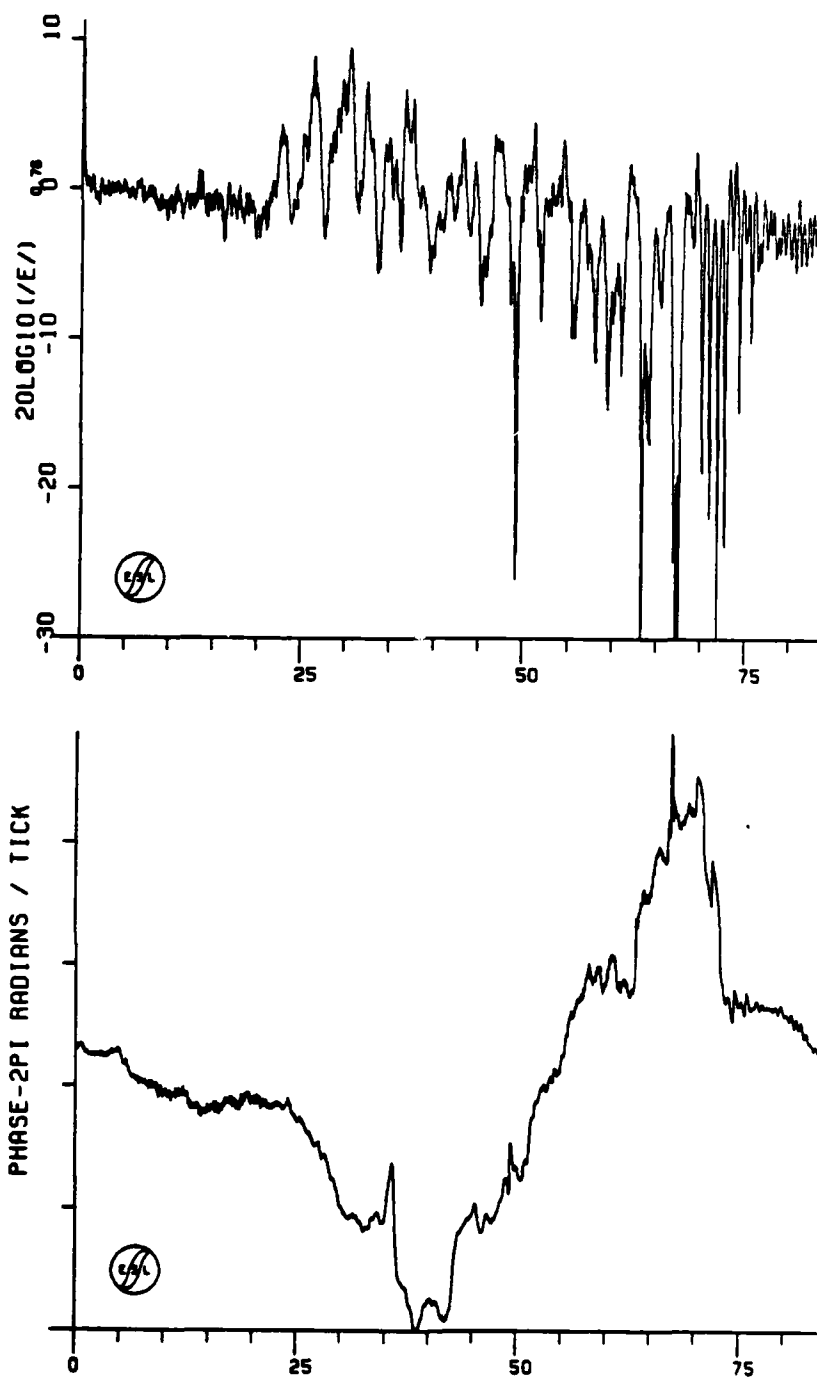
Figure 12-9. JAN Pass 12 Uplink Amplitude and Phase



TIME-- SECONDS

PHASE OF FIELD
UJ13 050581 15HZ
START TIME- 00:24:27.778

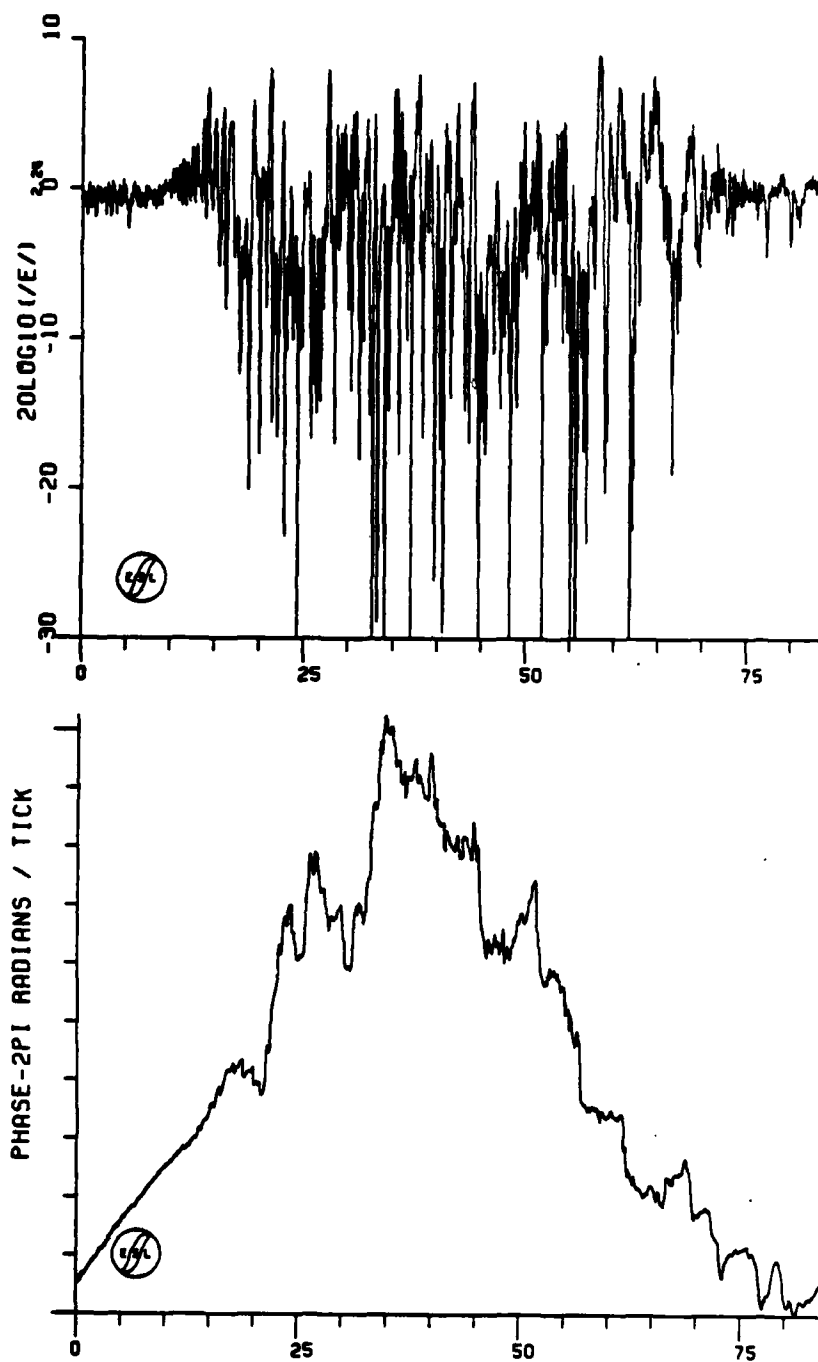
Figure 12-10. JAN Pass 13 Uplink Amplitude and Phase



TIME-- SECONDS

PHASE OF FIELD
UJ14 050501 15HZ
START TIME- 00:30:33.868

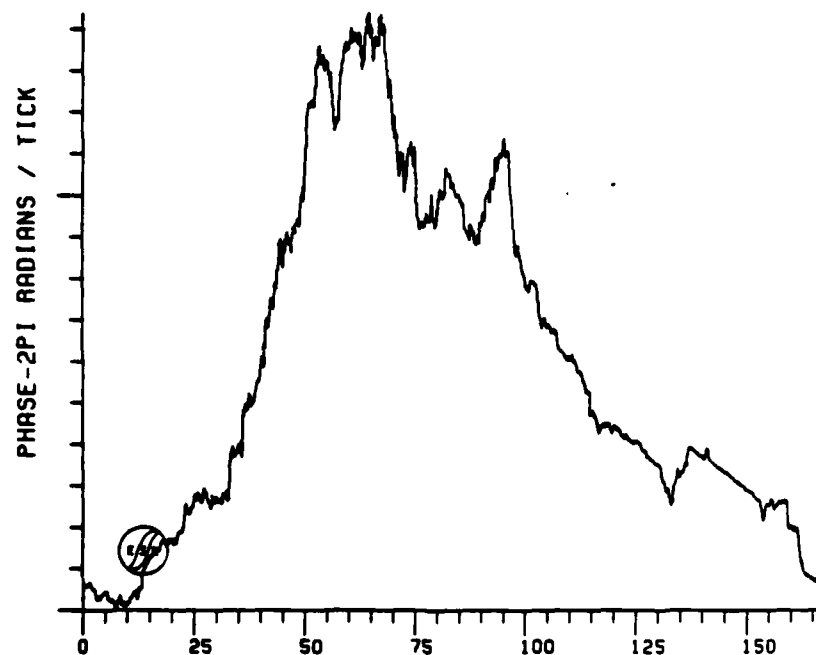
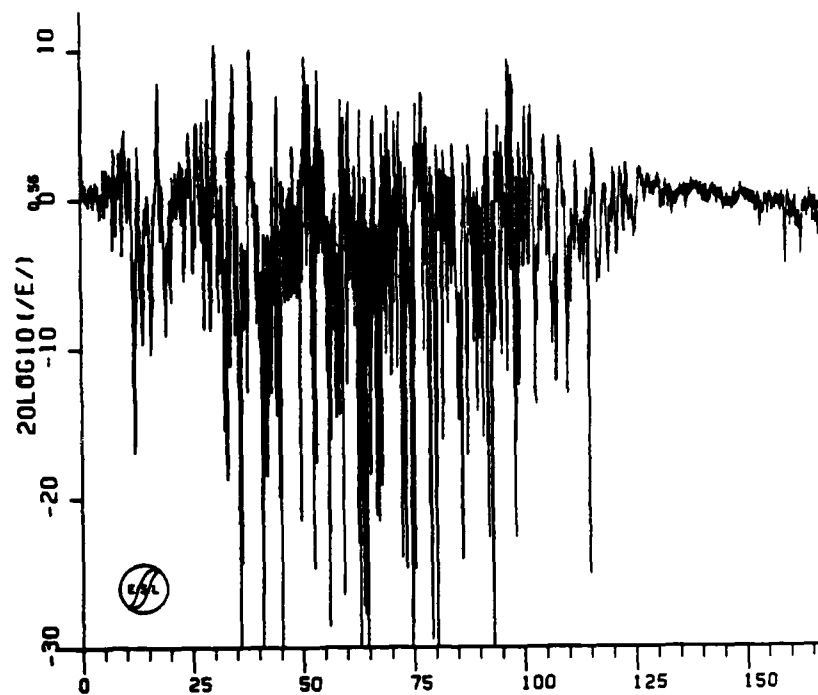
Figure 12-11. JAN Pass 14 Uplink Amplitude and Phase



TIME-- SECONDS

PHASE OF FIELD
UJ15 050581 15HZ
START TIME- 00:34:50.350

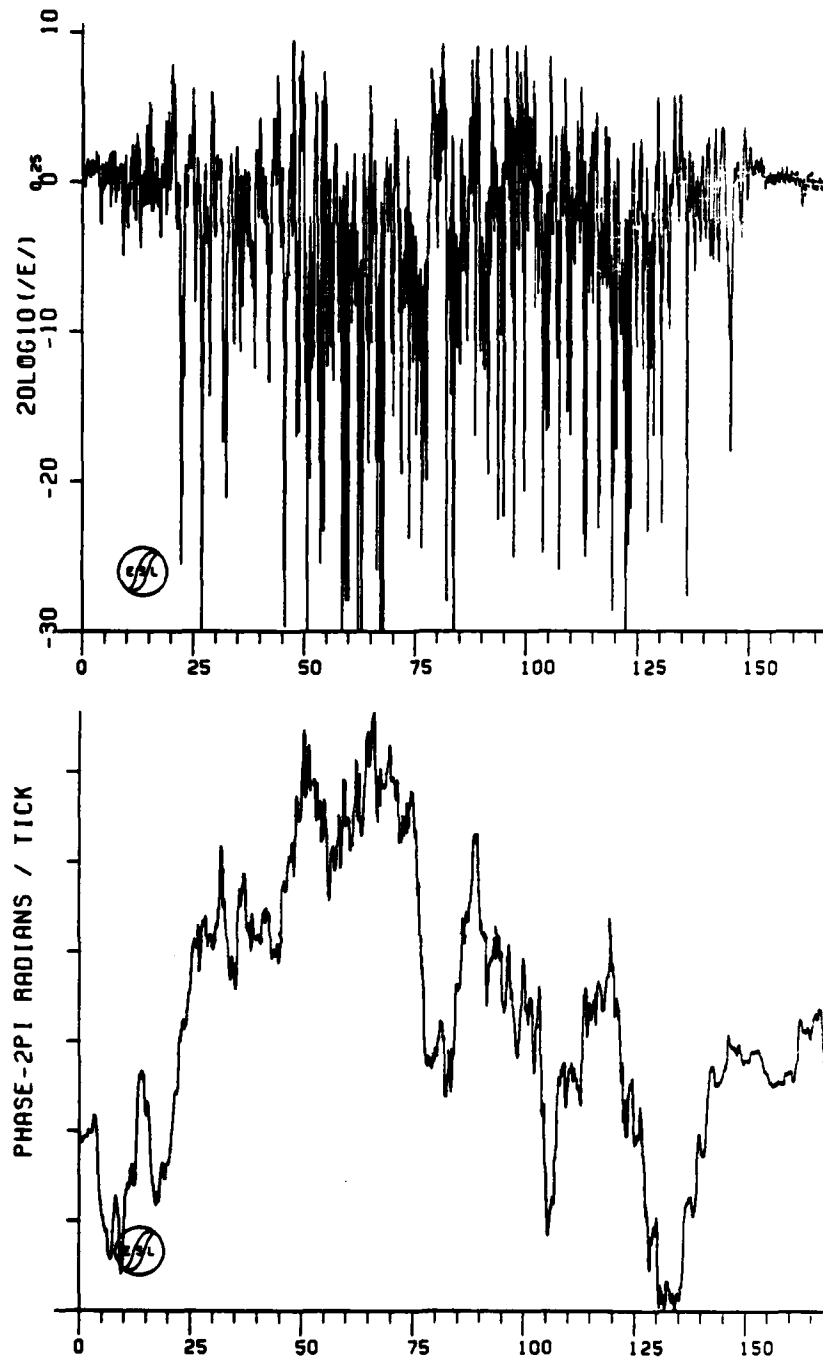
Figure 12-12. JAN Pass 15 Uplink Amplitude and Phase



TIME-- SECONDS

PHASE OF FIELD
UJ16 050501 15HZ
START TIME- 00:35:23.747

Figure 12-13. JAN Pass 16 Uplink Amplitude and Phase



TIME-- SECONDS

PHASE OF FIELD
UJ18 050581 15HZ
START TIME- 00:53:48.048

Figure 12-14. JAN Pass 18 Uplink Amplitude and Phase

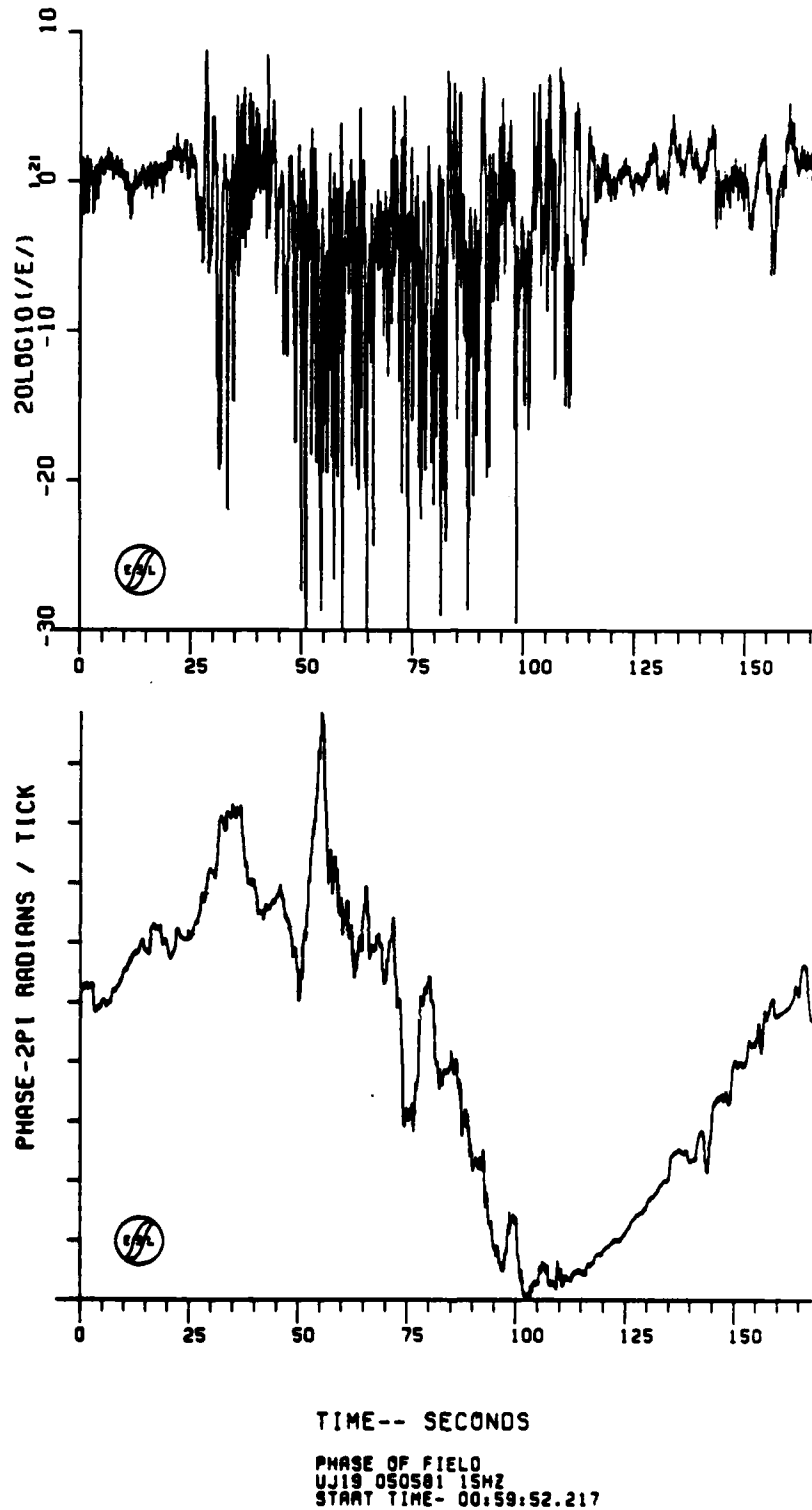
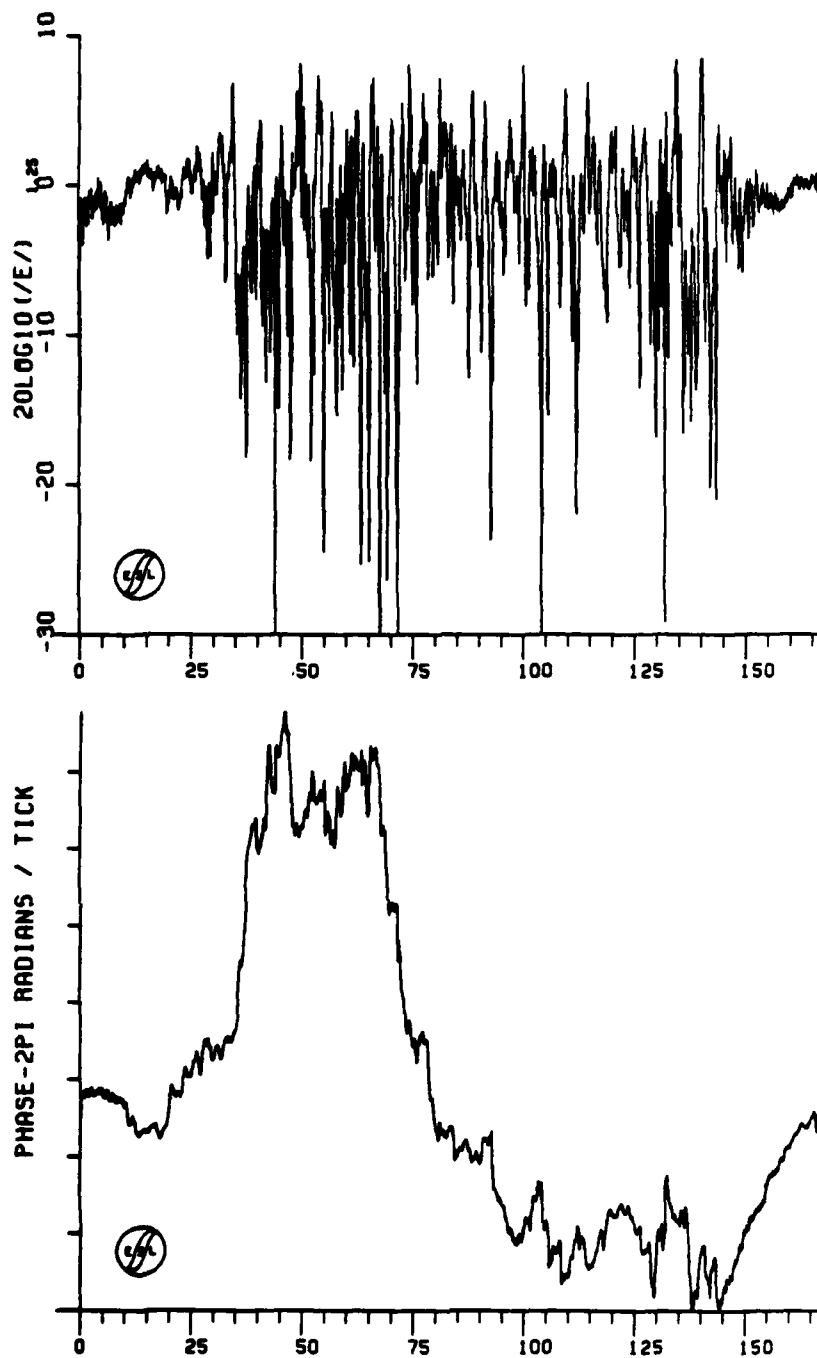


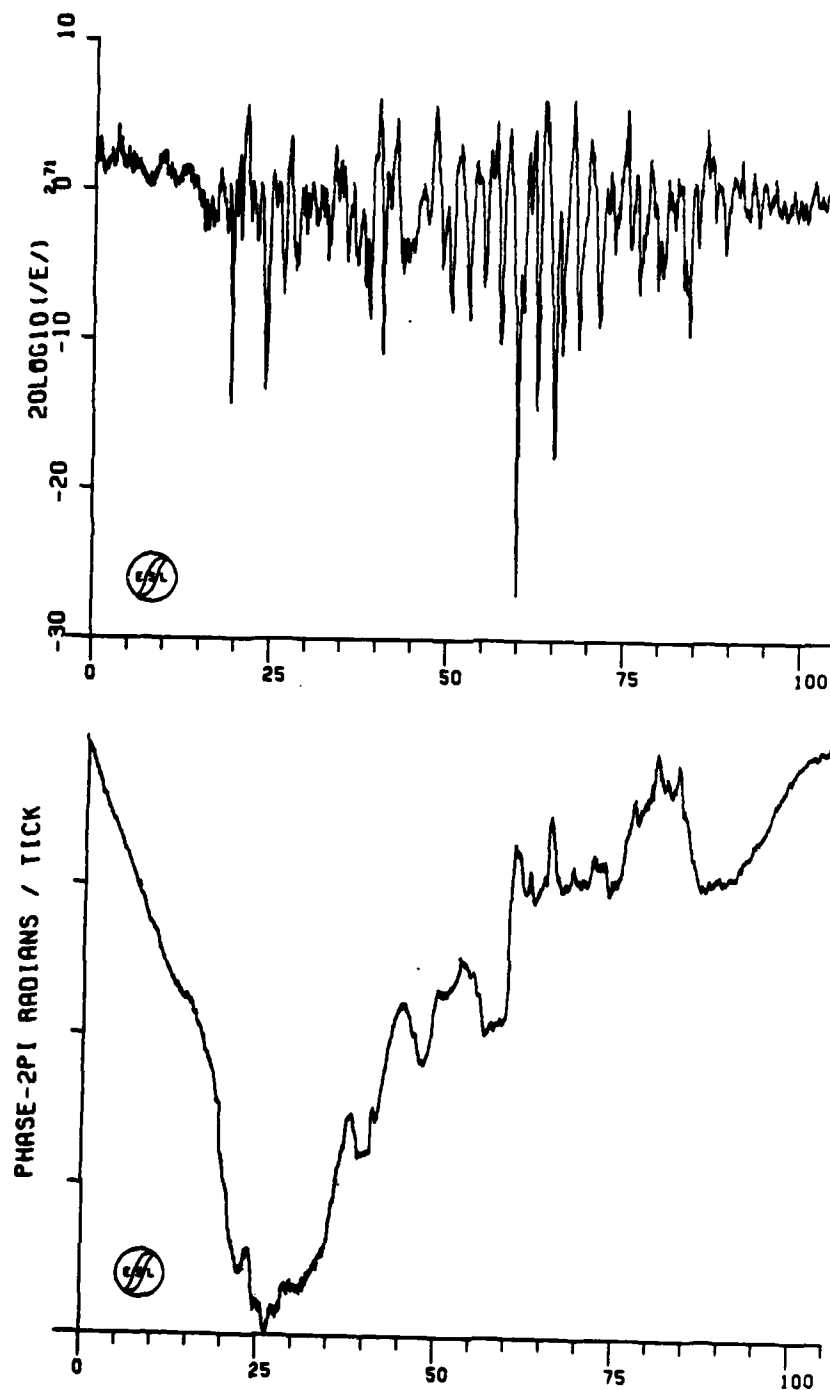
Figure 12-15. JAN Pass 19 Uplink Amplitude and Phase



TIME-- SECONDS

PHASE OF FIELD
UJ20 050501 15HZ
START TIME- 01:07:14.585

Figure 12-16. JAN Pass 20 Uplink Amplitude and Phase



TIME-- SECONDS

PHASE OF FIELD
UJ23 050501 15HZ
START TIME- 01:23:06.383

Figure 12-17. JAN Pass 23 Uplink Amplitude and Phase

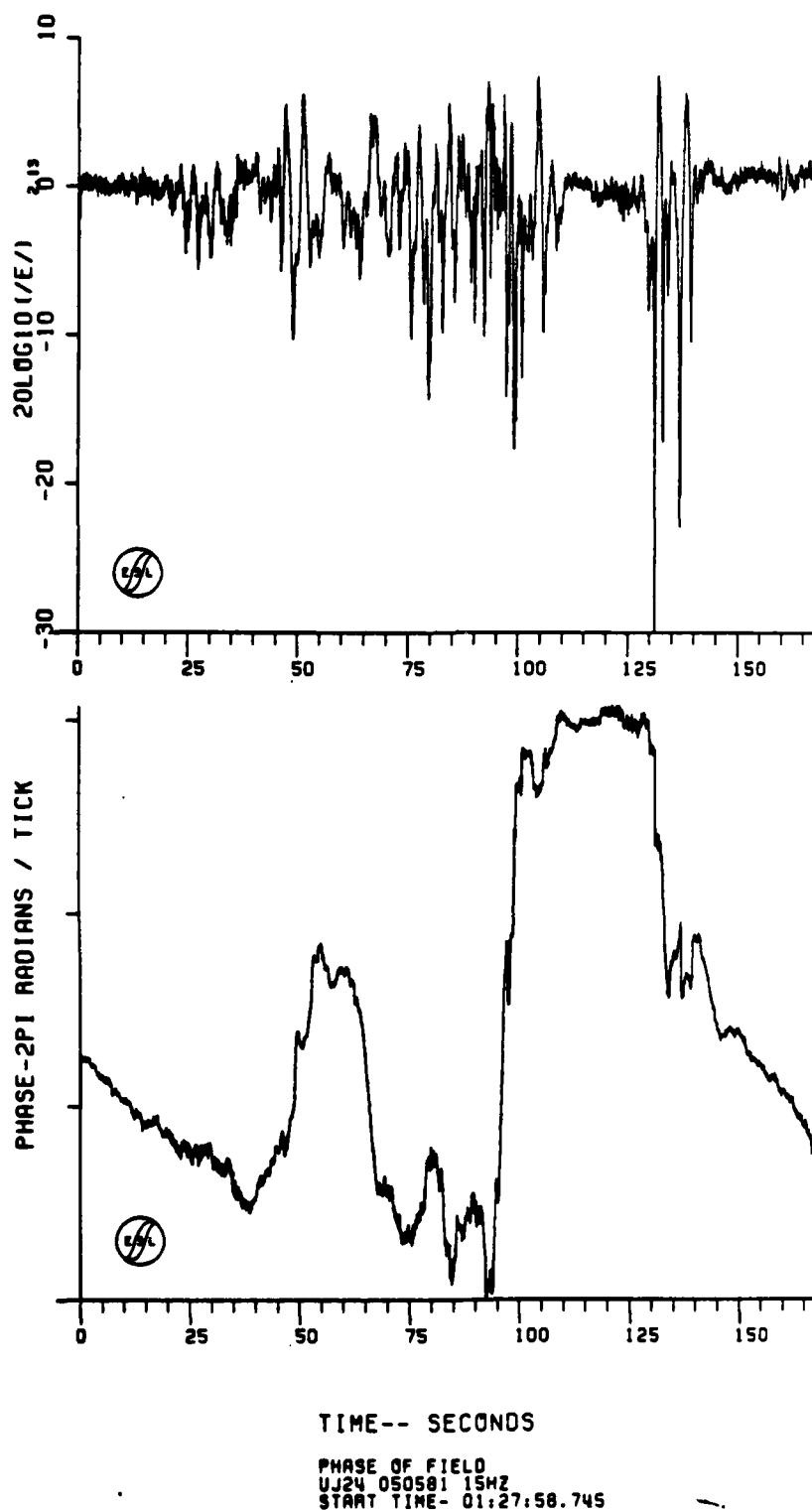


Figure 12-18. JAN Pass 24 Uplink Amplitude and Phase

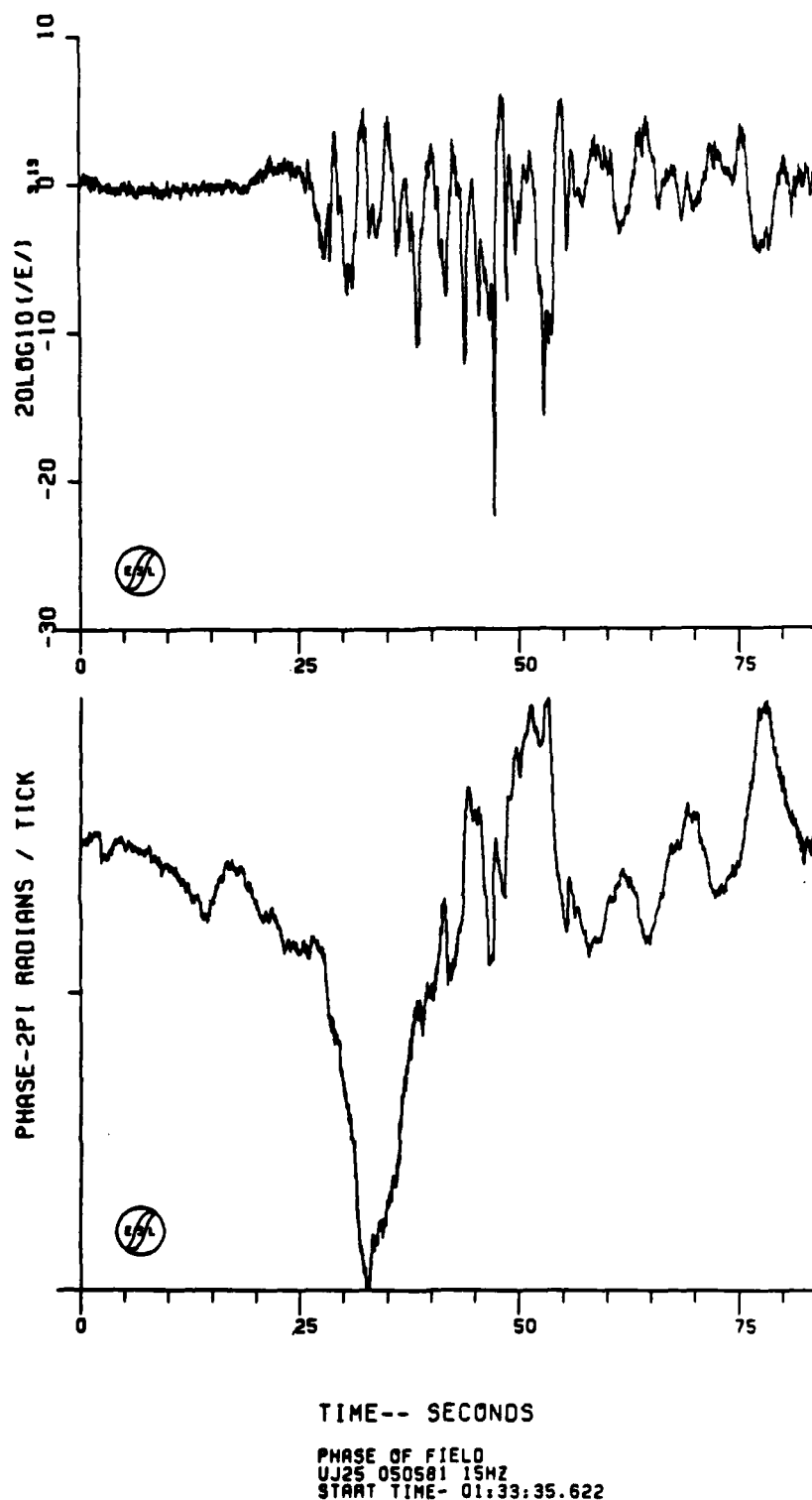
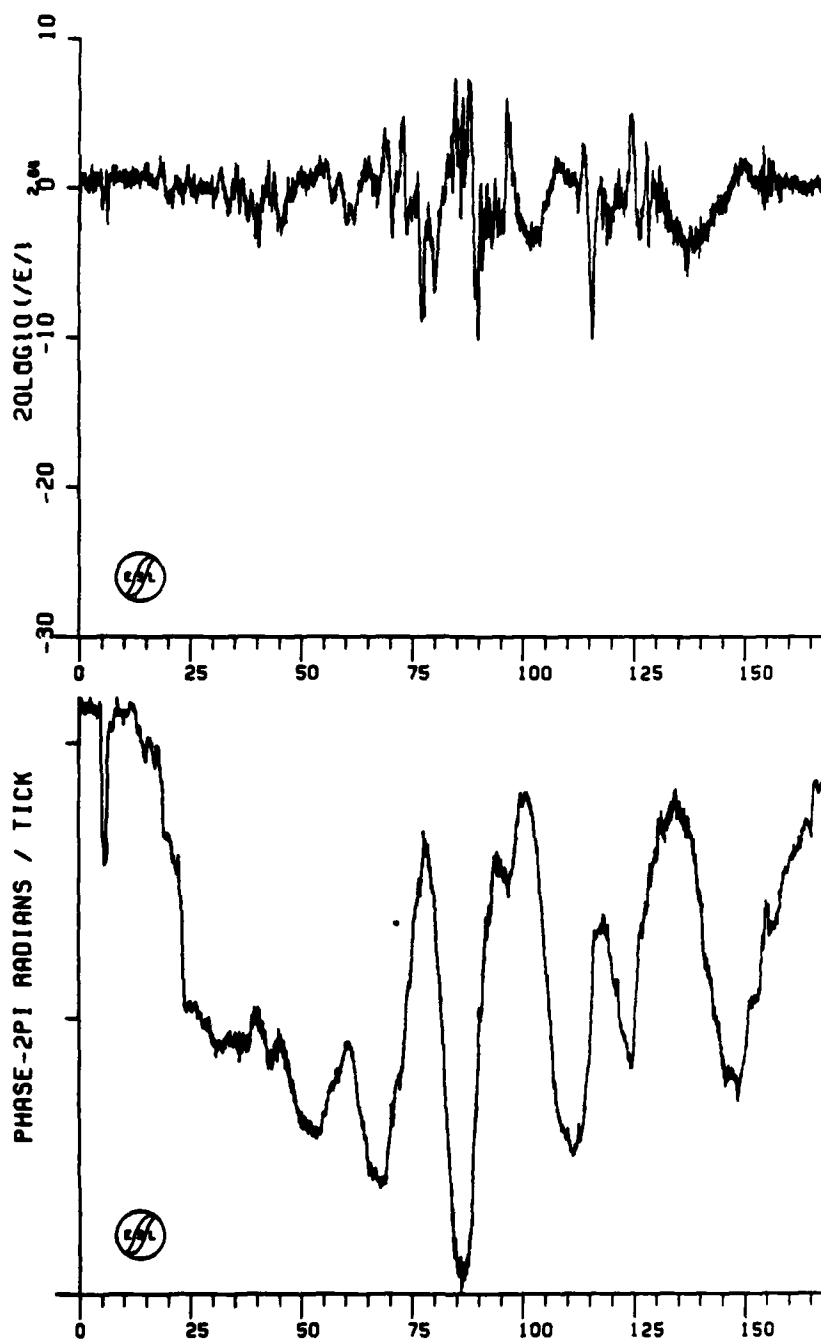


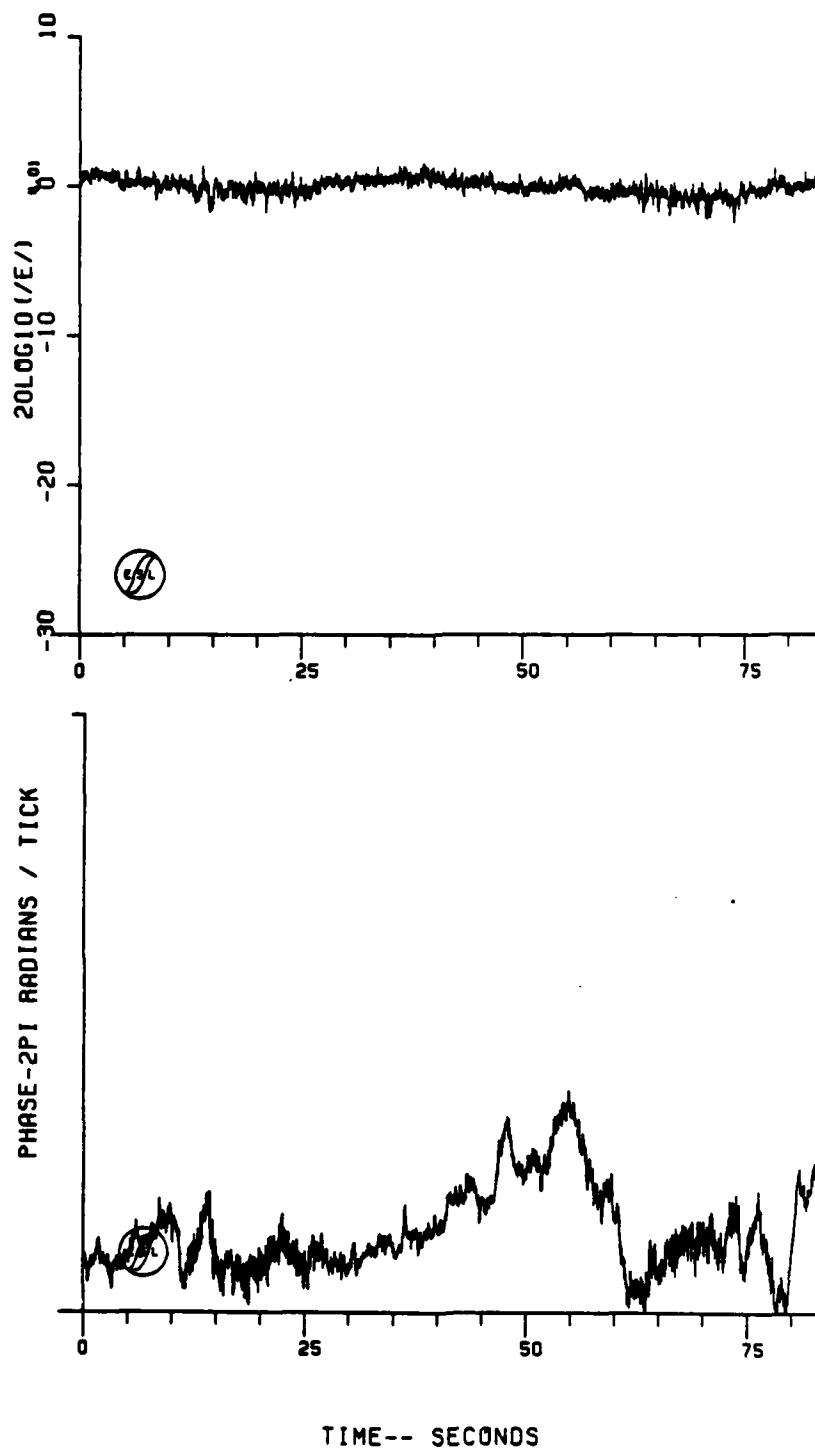
Figure 12-19. JAN Pass 25 Uplink Amplitude and Phase



TIME-- SECONDS

PHASE OF FIELD
UJ26 050581 15HZ
START TIME- 01:38:25.432

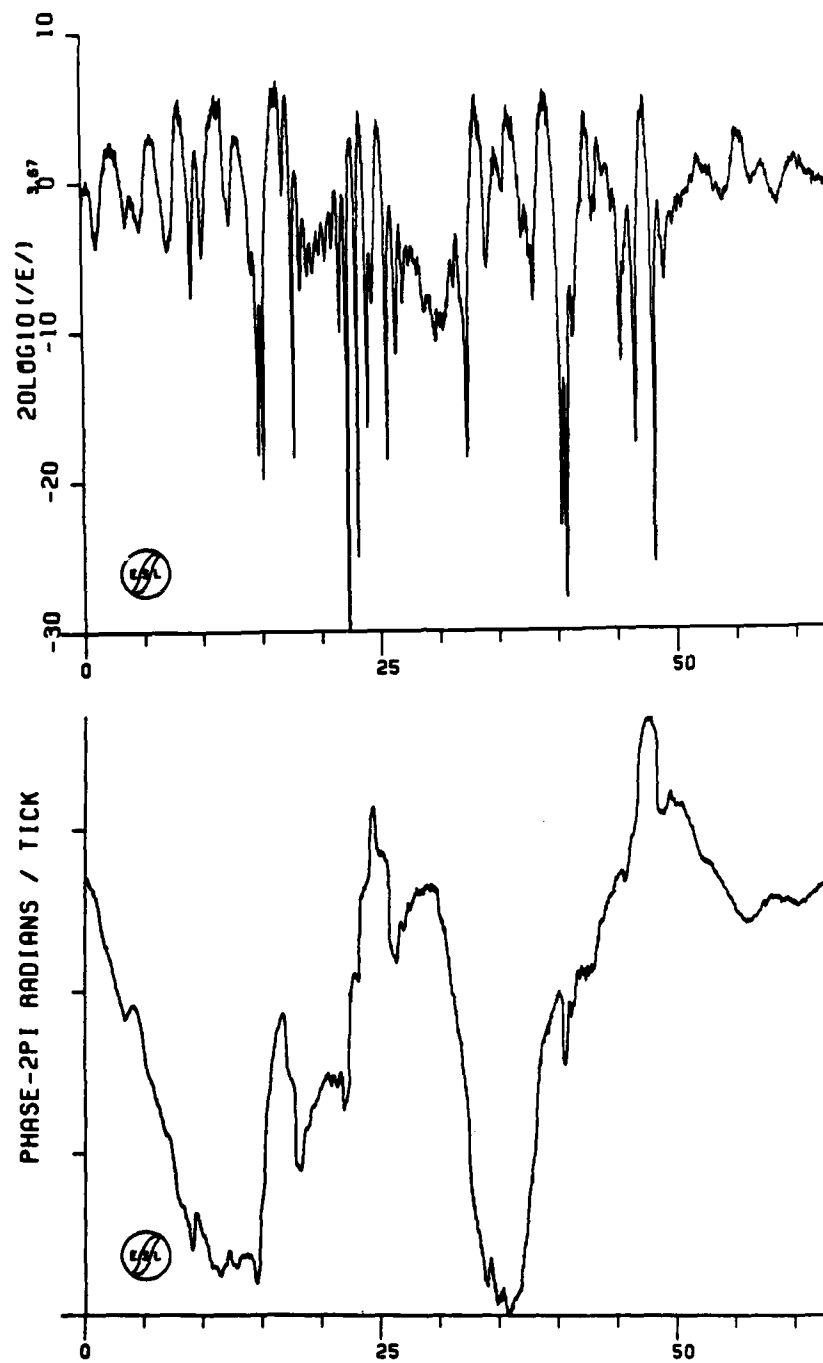
Figure 12-20. JAN Pass 26 Uplink Amplitude and Phase



TIME-- SECONDS

PHASE OF FIELD
UJ27 050581 15HZ
START TIME- 01:46:08.782

Figure 12-21. JAN Pass 27 Uplink Amplitude and Phase



TIME-- SECONDS

PHASE OF FIELD
UJ29 050581 15HZ
START TIME- 01:55:42.725

Figure 12-22. JAN Pass 29 Uplink Amplitude and Phase

JAN Pass 2 strongly resembles the downlink tone data, including the abrupt ion cloud edge on the southeastern side of the cloud (beginning of the pass) as can be seen from Figure 12-1. The amplitude shows a large defocus of -10 dB lasting approximately 55 seconds with diffraction ringing on the ends. The phase follows the large Gaussian bell shape of the gross ion cloud. A cycle skip in the phase unwrapping routine can be seen at 30 seconds on this plot.

JAN Pass 3 also shows a large defocus on the northwest side of the cloud (see Figure 12-2). Pass 3 coincides with the time of the first observable striation structure. Like the downlink, the data exhibits smooth diffraction ringing on the northern side of the cloud and more random fading on the southern side.

JAN Pass 4 again mirrors the downlink data and is plotted in Figure 12-3. This pass was presumably high up the field lines and caught only the tips of a few leading striations.

Passes 5, 6, and 7 all exhibit the shallow defocus feature seen on the downlink as displayed in Figures 12-4, 12-5, and 12-6. Both the uplink and the downlink data (Figure 11-7) on Pass 7 exhibit a small diffraction in the main ion cloud phase windup.

A similar trend can be seen in the Pass 10 data, Figure 12-7, although not as pronounced. While strong fading was observed during Passes 8 and 9 they are not included here because the aircraft was in a turn during part of these passes.

The amplitude data for Pass 11, shown in Figure 12-8, is similar to that of Figure 11-9 for the downlink, however, the phase data look substantially different. Based on the downlink data a phase windup of approximately 13 cycles is anticipated as opposed to the 7 cycles observed. This may be due to undetected cycle slipping in the processing routines or a reflection of the diffraction effects distorting the phase data, thus, the need for back-propagating processing.

The amplitude and phase on the uplink of Pass 12 tracks extremely well with that of the downlink. Compare Figure 12-9 with Figure 11-10.

Pass 13 shows two, large defocuses that are somewhat hidden by the rapid amplitude fluctuations on the downlink. Compare Figures 12-10 with Figure 11-11. Pass 14 data shown in Figure 12-11 appears unusual in that a large number of focuses are apparent in the data. This behavior may be an artifact of the uplink processing and should be treated cautiously.

Pass 15 exhibits the same strong fading seen on the downlink. Pass 15 is shown in Figure 12-12. This is one of the most intense fading passes observed at late time during JAN. The uplink phase data does not indicate a large background ion cloud for this pass.

JAN Pass 16, while not shown for the downlink, is shown here for the uplink data in Figure 12-13. Pass 15 and 16 were in close proximity and both display intense fading. The phase of Pass 16 exhibits the usual steep edge on the southeastern side of the cloud.

Pass 17 has not been included due to the unusually large phase noise observed. The cause of this phase noise is not understood, although it was also observed on the downlink for this pass and may have been due to a momentary loss of K-band phase lock.

Passes 18, 19, and 20 shown in Figures 12-14, 12-15, and 12-16 illustrate the intense fading that persisted at 2 hours after release. Pass 19 was not provided on the downlink due to the phase noise problem that occurred only on Passes 17 and 19, however, it did not appear to impact the uplink data on Pass 19. Both the uplink and the downlink phase during Pass 20 indicate that a high density background ion cloud was traversed on the southeastern side of the transit.

The uplink and downlink fading on Pass 23 as shown in Figure 12-17 are very similar. The phase on the uplink appears to have inadvertently been plotted upside down. Passes 21 and 22 have not been shown here. They show only a few 5 dB fades.

Pass 24 shown in Figure 12-18, indicates as does the downlink data, that the striations may be beginning to drift apart. It would appear that the down-sampling of the uplink tone data has resulted in a few cycles skips around 100 seconds on this plot.

Pass 25 also indicates a lessening of fading intensity. This data is shown in Figure 12-19. Pass 26 shows only a cycle or so of phase activity with one large signal focus as shown in Figure 12-20. The downlink also exhibited this fading pattern (see Figure 11-20).

Pass 27 did not exhibit any fading or phase activity as shown in Figure 12-21. It is included here as an indication of the quality of the uplink data in the absence of fading. Likewise, Pass 28 did not display any fading and has not been plotted.

Pass 29 shown in Figure 12-22 was the last strong fading observed during JAN. The phase data shows many of the same features as seen on the downlink data in Figure 11-22. None of the subsequent passes resulted in any significant fading.

12-3 JAN UPLINK SUMMARY.

Summarizing, the uplink propagation data for event JAN is of high quality and reflects the same progression of effects as does the downlink data presented in Section 11. The uplink phase data potentially provide a better indication of the actual ion cloud structure due to its higher radio frequency. Time has not permitted a complete processing of all of the uplink data. In particular, only a limited attempt at back-propagation processing has been attempted.

SECTION 13

BACK-PROPAGATION PROCESSING FOR JAN DOWNLINK

13-1 INTRODUCTION.

Back-propagation processing was performed for each JAN pass. Only a few of these passes back-propagated very well as measured by the decrease in the S_4 scintillation index. This section presents the results of this back-propagation processing. The approach used is the same as that described in Section 7 for HOPE.

13-2 JAN BACK-PROPAGATION SUMMARY.

Back-propagation processing was performed for all of the JAN downlink data and a few of the uplink data passes. Only a few of these passes back-propagated very well as measured by the decrease in the S_4 scintillation index. Those passes between R+25 minutes and R+2 hours did not back-propagate well in the sense that significant residual amplitude fluctuations would remain; in some cases the amplitude fluctuations from one portion of the cloud would not reach a minimum at the same distance as other portions of the cloud. Thus, during this period the occultation geometry was presumably such that the propagation path was oriented along the stretching direction of the ion cloud, providing depth that is not well represented by a single phase screen.

Generally, the uplink back-propagation processing was given a low priority due to the additional processing effort required and data from only a few passes are presented here.

A summary of the downlink back-propagation data are presented in Table 13-1. This table includes the scintillation index before and after back-propagation, the phase power spectral density break frequencies and slopes, and the back-propagation distance.

Table 13-1. JAN Downlink Back-Propagation Summary

Pass	S_4 at Ground	S_4 Min.	Distance to Minimum ^a (km)	Corrected Distance (km)	Phase PSD		Outer Scale f_o (km)	Spectral Height $S_4(f)$ (dB-Hz ² /Hz)	σ_θ (rad)	Transverse Pattern Vel. V_L (m/s)	Intercept Altitude (km)	Comments
					Slope M (dB/Decade)	Break Freq. f_o (Hz)						
1	0.619				-	-						No S_4 min.
2	1.38	0.312	306		N/A	N/A						Good back-propagation, gross cloud only
3	1.09	0.427	289		N/A	N/A						Poor back-propagation, striation on-set
4	0.670	0.271	342		40	0.22		10				Good back-propagation
5	1.09	0.615	300		-	-						Poor back-propagation
6	0.88	0.589	292		-	-						
7	0.695	0.430	159		-	-						
10	0.567	0.538	240		30	0.20		18.5				
11	0.762	0.617	150		40	0.18		17.0				
12	0.942	0.781	225		24	0.18		19.0				
13	0.813	0.628	200		-	-						
14	0.774	0.684	198		-	-						
17	0.741	0.633	111		-	-						
18	0.934	0.841	220		-	-						
20	0.784	0.691	200		-	-						
21	0.557	0.477	110		22	0.11		13.0				
23	0.726	0.374	133		30	0.22		11.0				Good back-propagation
24	0.679	0.386	184		-	-						
25	0.684	0.254	127		40	0.14		18.0				
26	0.720	0.332	180		40	0.068		18.0				
27	0.065	0.110	None		-	-						Noise only - no fading
28	0.358	0.221	184		-	-						Weak fading
29	0.838	0.598	124		38	0.17		20				Fair back-propagation

^a Assumes 200 m/s pattern velocity

The JAN back-propagation data spans intervals of the early time unstructured cloud through the late time striation structure as it dissipates into the background ionosphere. These data are shown in Figures 13-1 through 13-36. Plots are included of the back-propagated amplitude and phase, the back-propagated phase power spectral density (PSD), and the signal angular spectrum. Section 7-3 described the procedure to convert the real frequency axes to their spatial or angular units. When comparing one pass with another the differences in the aircraft velocity orthogonal to the magnetic field line projection must be taken into account as this changes from pass to pass.

JAN Pass 2 back-propagated extremely well as measured by the S_4 scintillation index, going from 1.38 to 0.31. The back-propagated amplitude and phase are shown in Figure 13-1 and may be compared to the received signal shown in Figure 11-2. Note that the Gaussian shaped phase which now reflects the gross ion cloud ionization has narrowed significantly from that of the received signal which reflects the angular spreading of the received energy. Figure 13-2 is a plot of the phase PSD. The first spectral sidelobe is approximately 65 dB down from the peak as expected for the nearly Gaussian shape of the phase. The angular spectrum is shown in Figure 13-3. The abrupt drop in the angular spectrum is due to the finite size of the ion cloud.

The striation on-set time observed optically coincides with Pass 3. The received signal phase shown in Figure 11-3 reflects significant angular diffraction effects superimposed on the same basic Gaussian phase structure of the previous pass. This pass back-propagated poorly as shown in Figure 13-4. Significant residual amplitude effects remain although the diffraction ringing at the edges due to the gross cloud have back-propagated properly. This is typical of many of the passes processed for JAN. We assume that there must be significant structure developed with significant spatial extent along the propagation direction that may not be entirely obvious from optical observations for this pass. The

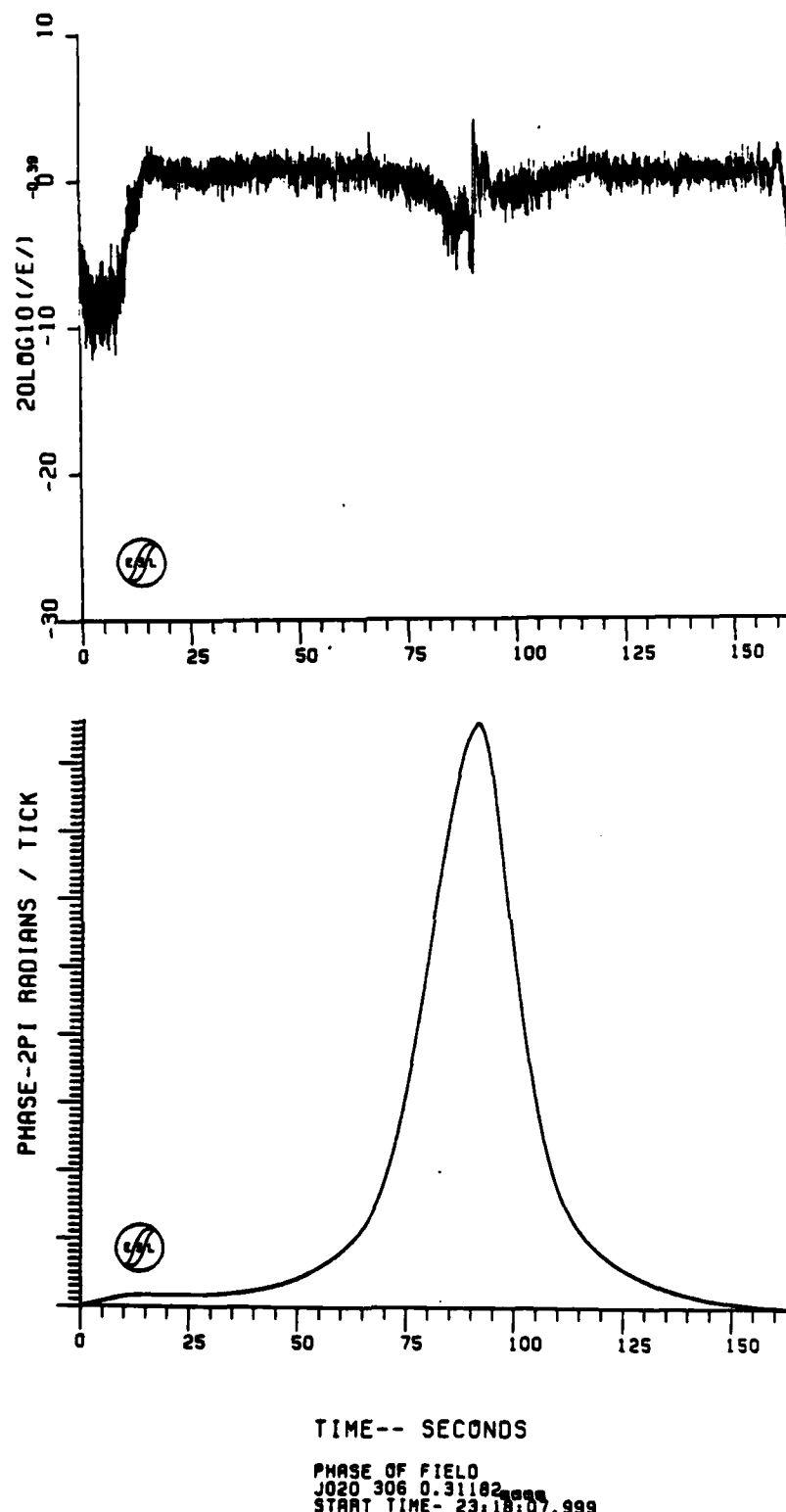


Figure 13-1. JAN Pass 2 Downlink Back-Propagated Amplitude and Phase

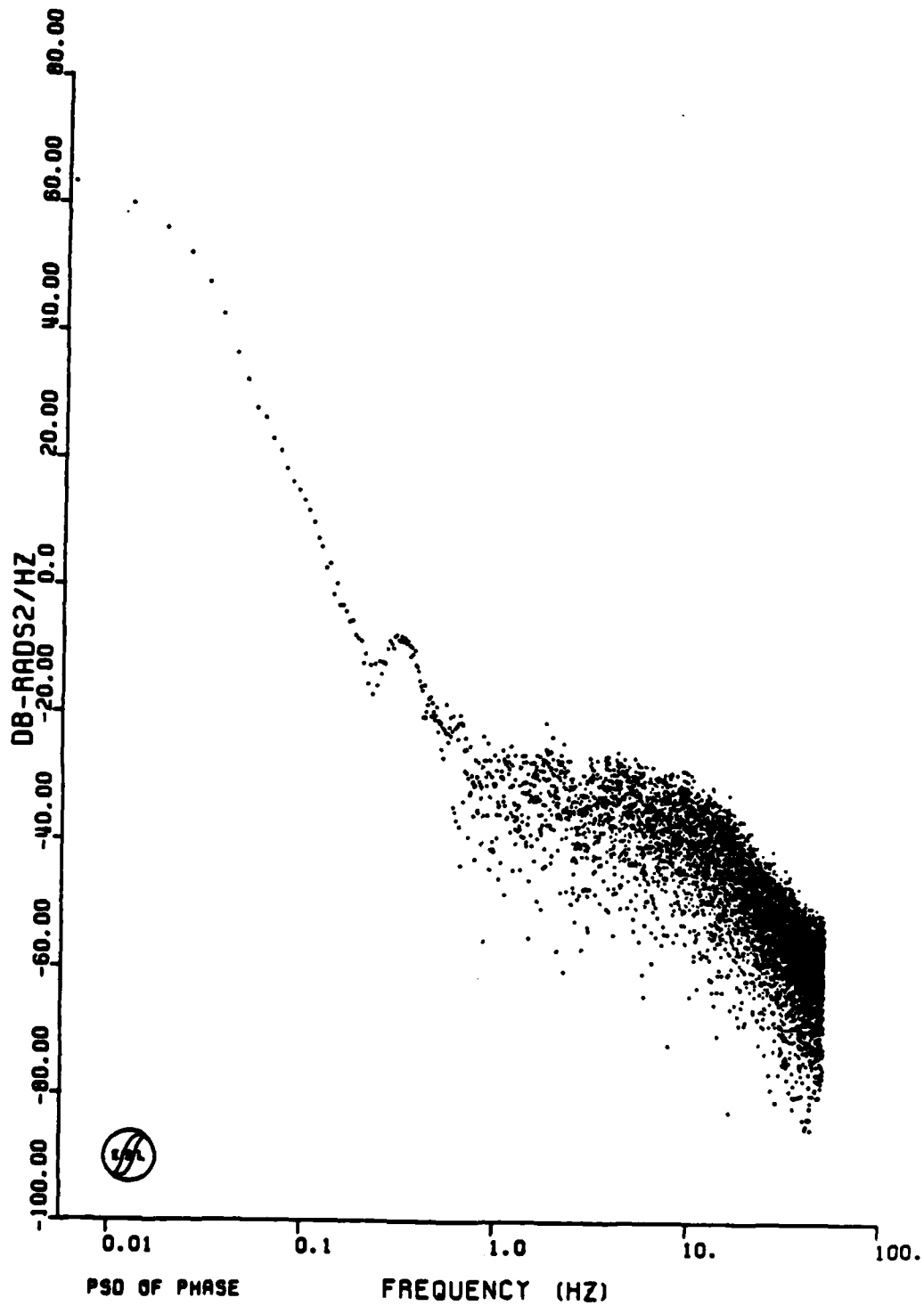


Figure 13-2. JAN Pass 2 Downlink Back-Propagated Phase PSD

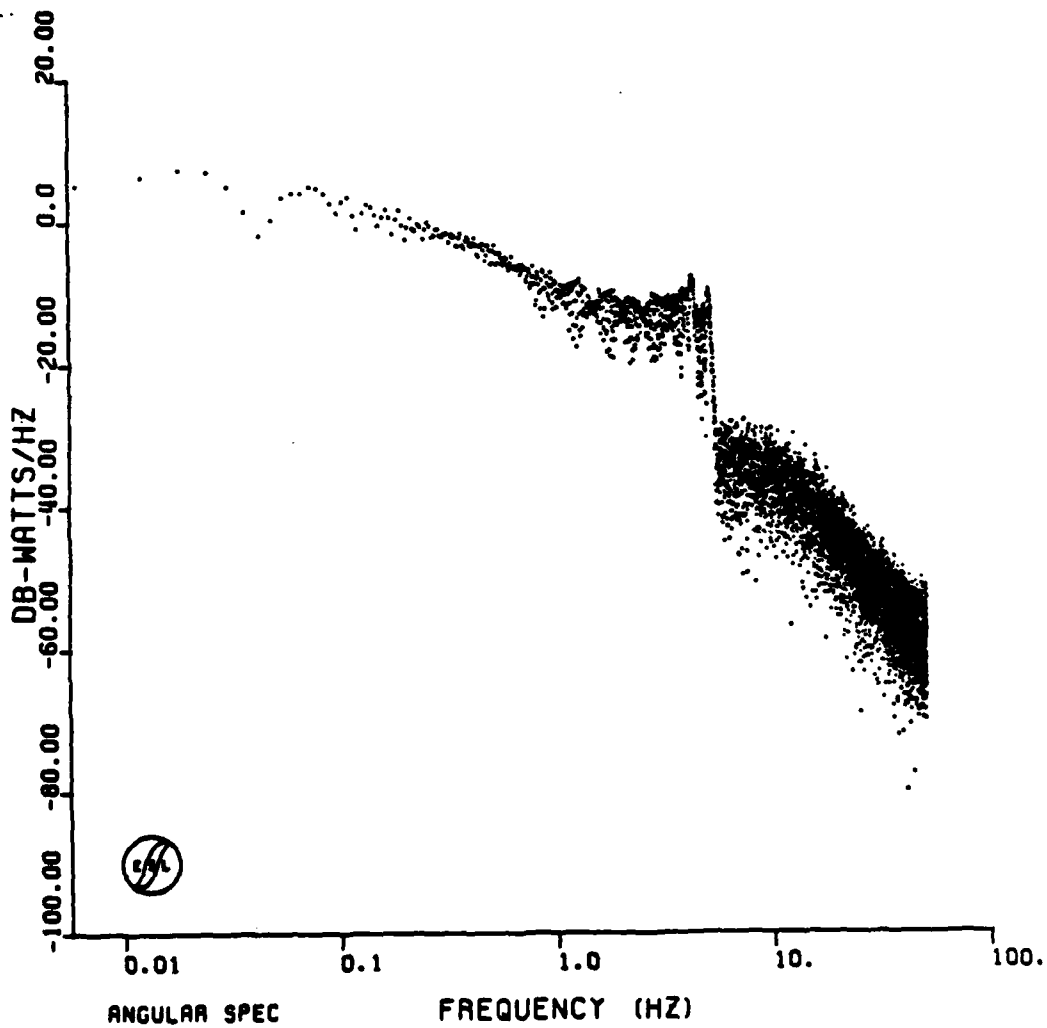
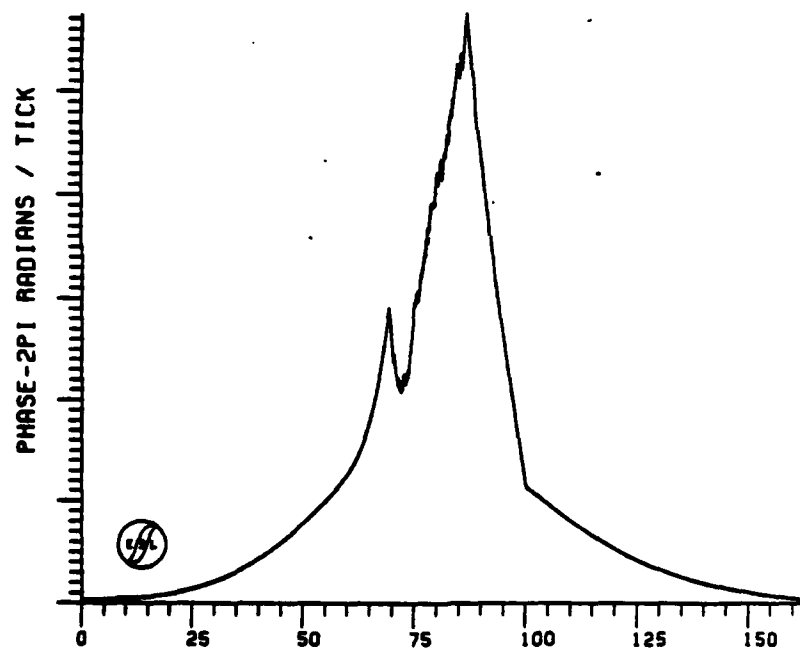
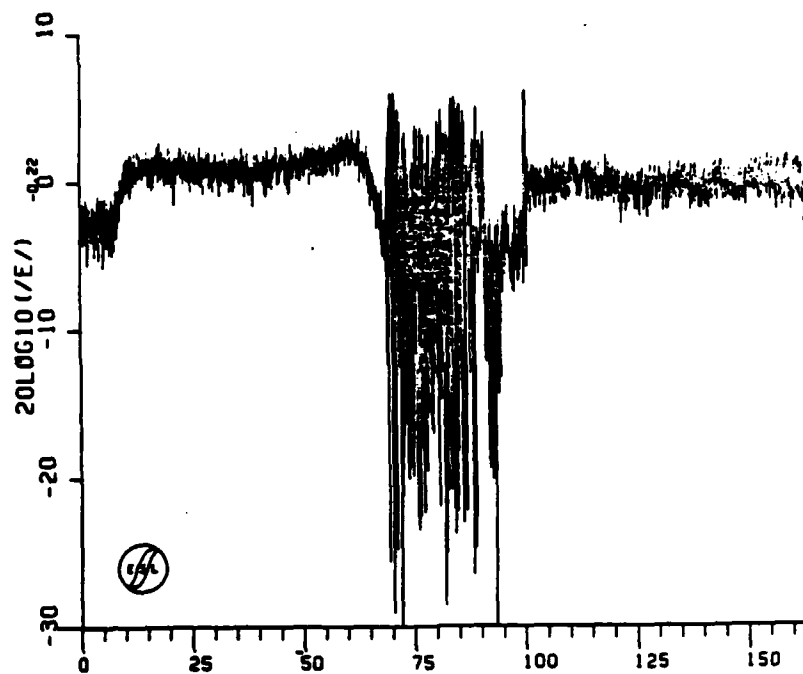


Figure 13-3. JAN Pass 2 Downlink Angular Spectrum



TIME-- SECONDS

PHASE OF FIELD
 J030 289 0.42758
 START TIME- 23:24:28.000

Figure 13-4. JAN Pass 3 Downlink Back-Propagated Amplitude and Phase

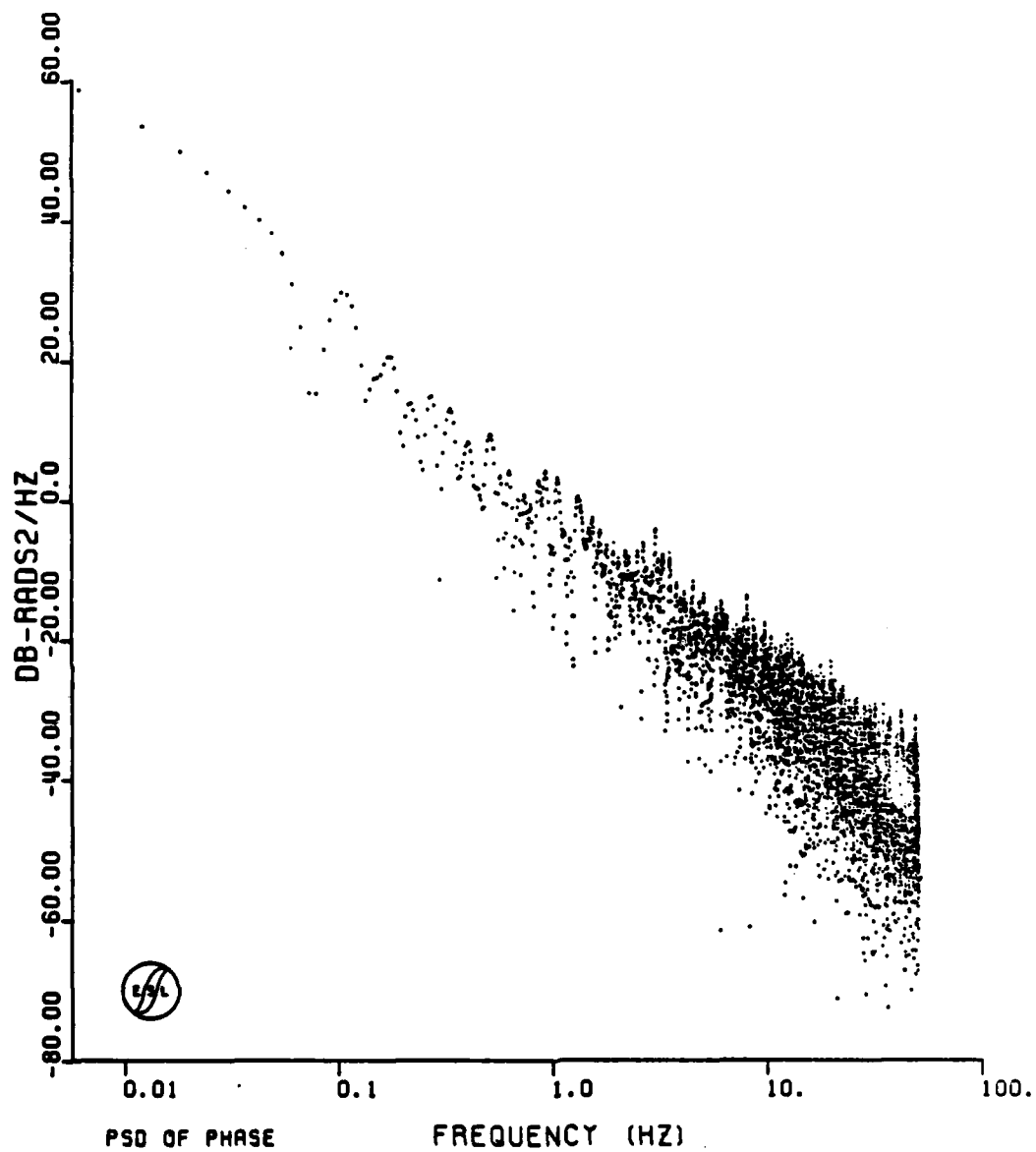


Figure 13-5. JAN Pass 3 Downlink Back-Propagated Phase PSD

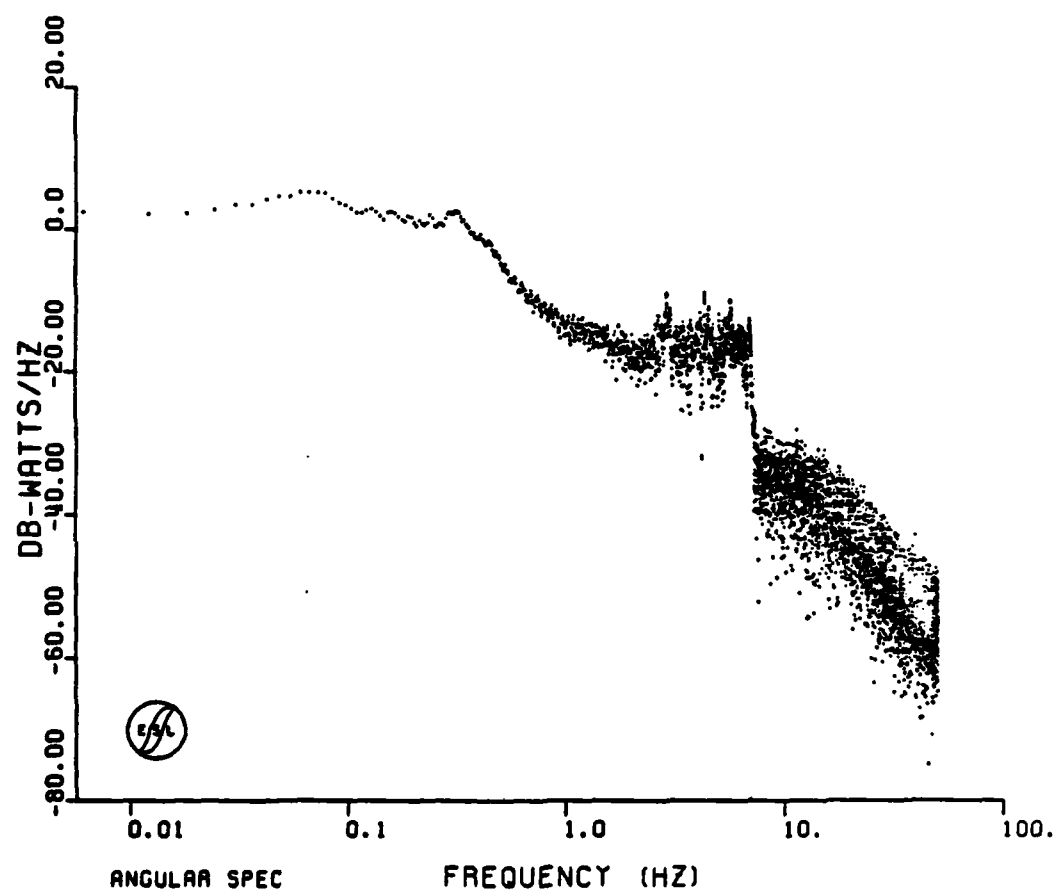
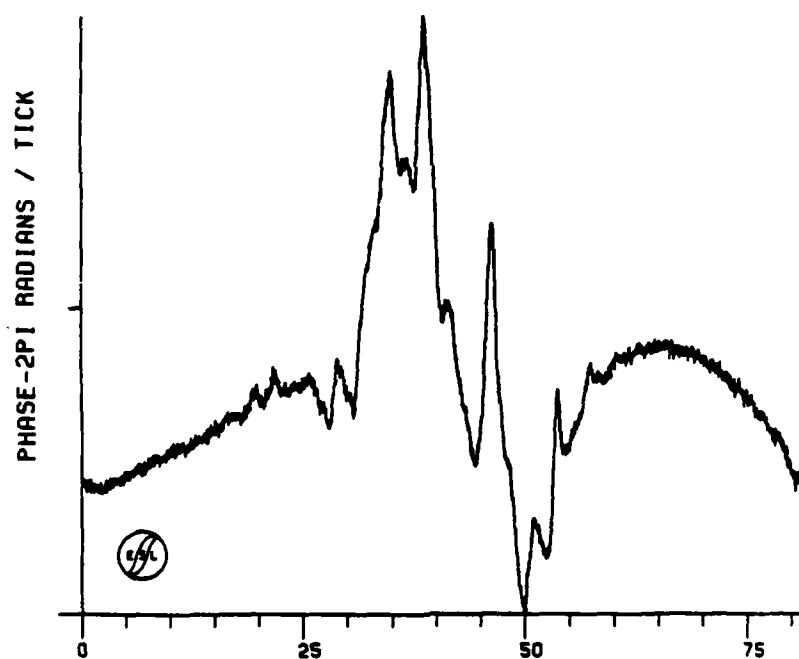
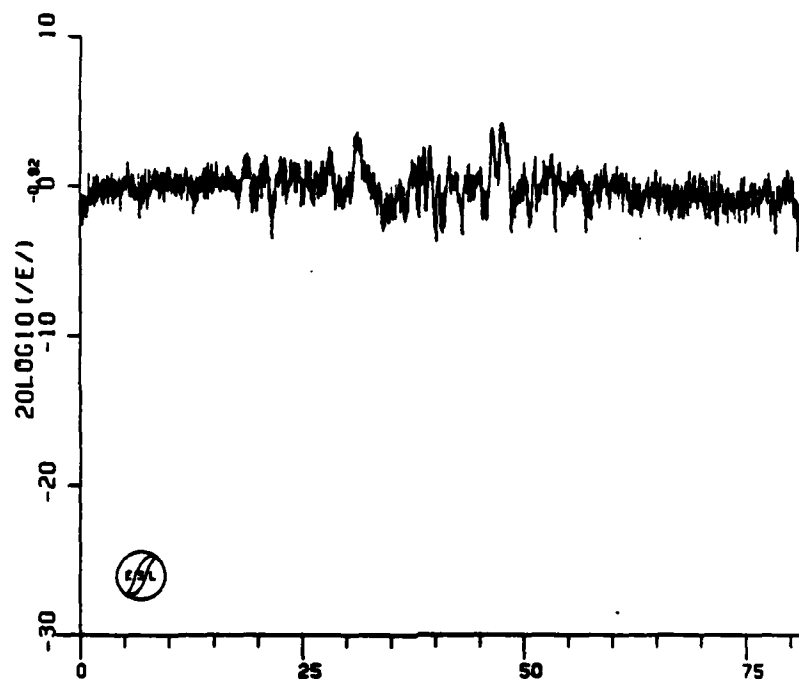


Figure 13-6. JAN Pass 3 Downlink Angular Spectrum



TIME-- SECONDS

PHASE OF FIELD
 J040 342 0.27143
 START TIME- 23:32:58.480

Figure 13-7. JAN Pass 4 Downlink Back-Propagated Amplitude and Phase

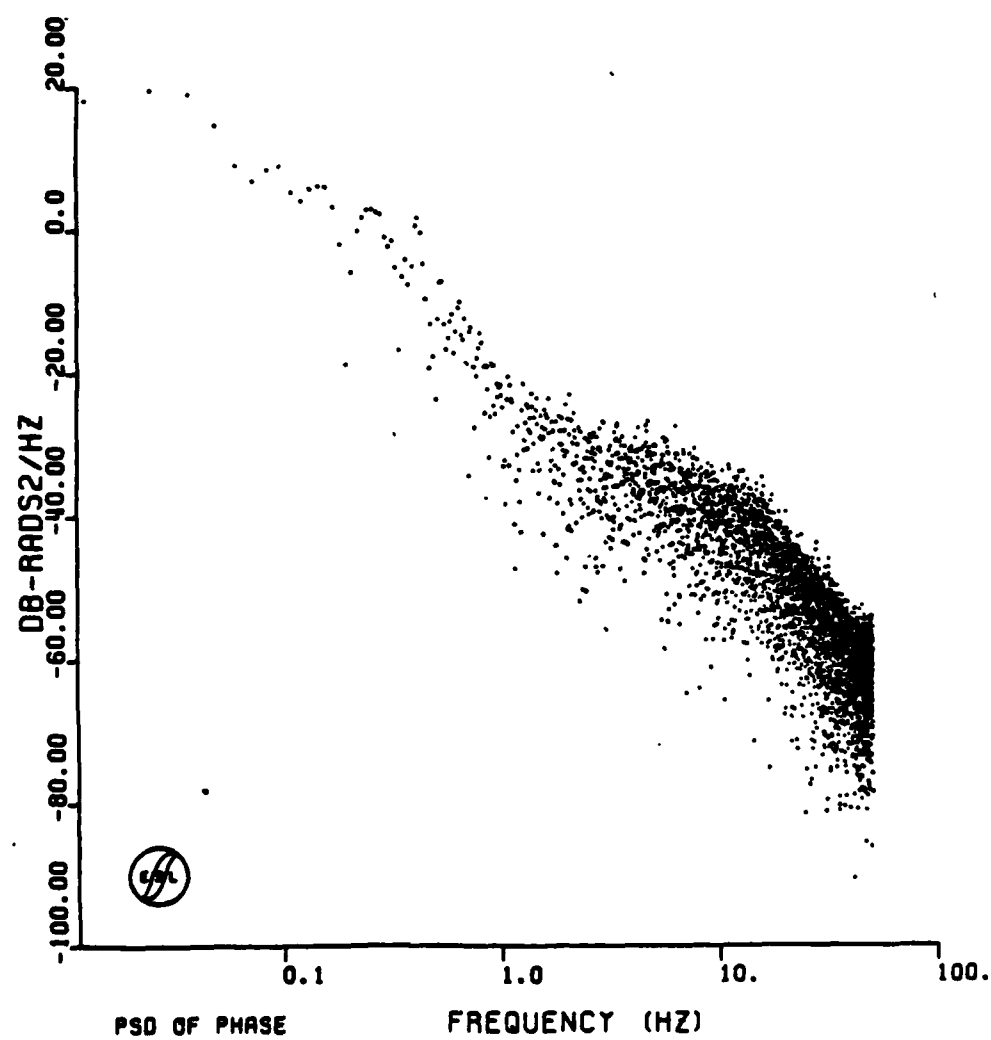


Figure 13-8. JAN Pass 4 Downlink Back-Propagated Phase PSD

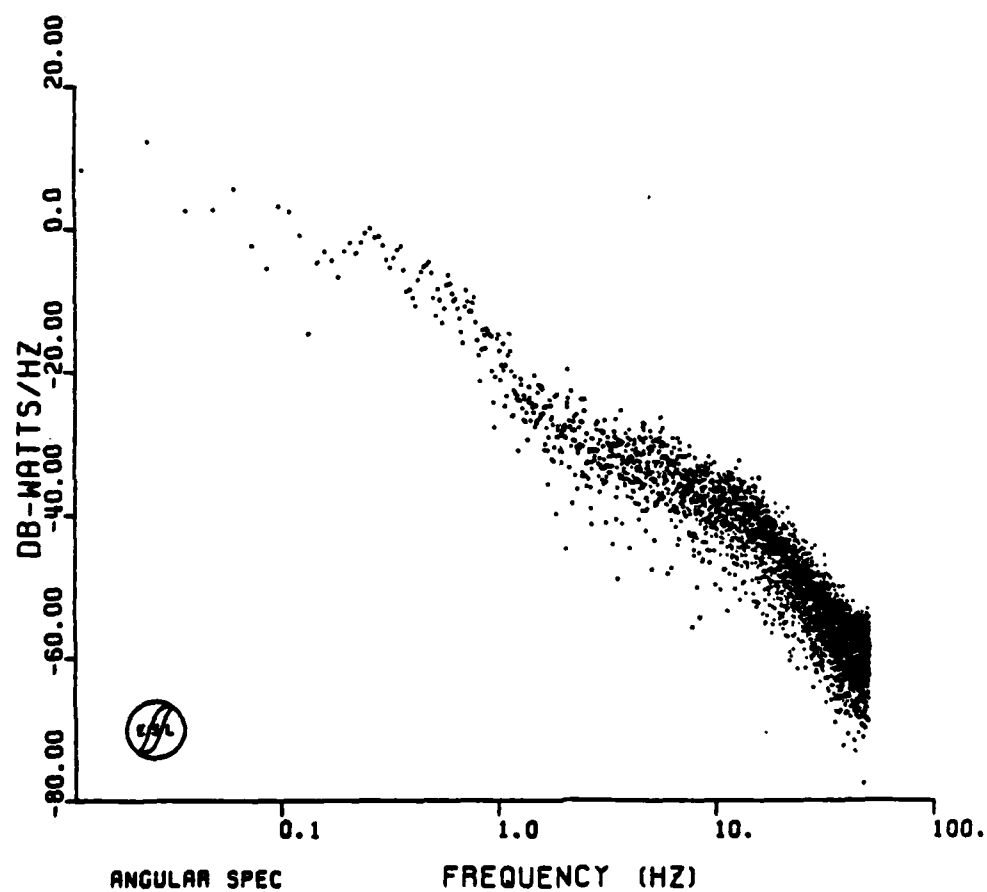
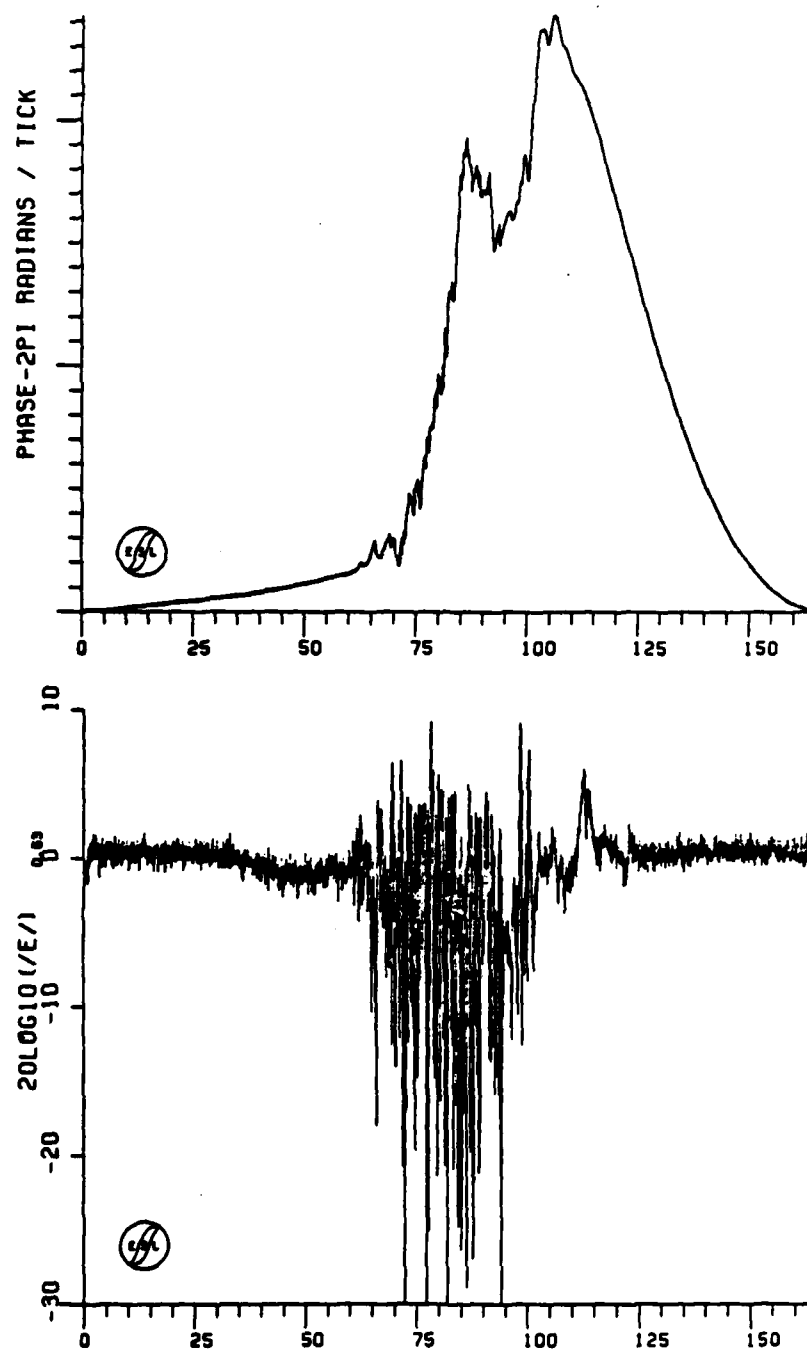


Figure 13-9. JAN Pass 4 Downlink Angular Spectrum



TIME-- SECONDS

MAGNITUDE OF FIELD
J100 240 0.537714.00
START TIME- 00:05:38.000

Figure 13-10. JAN Pass 10 Downlink Back-Propagated Amplitude and Phase

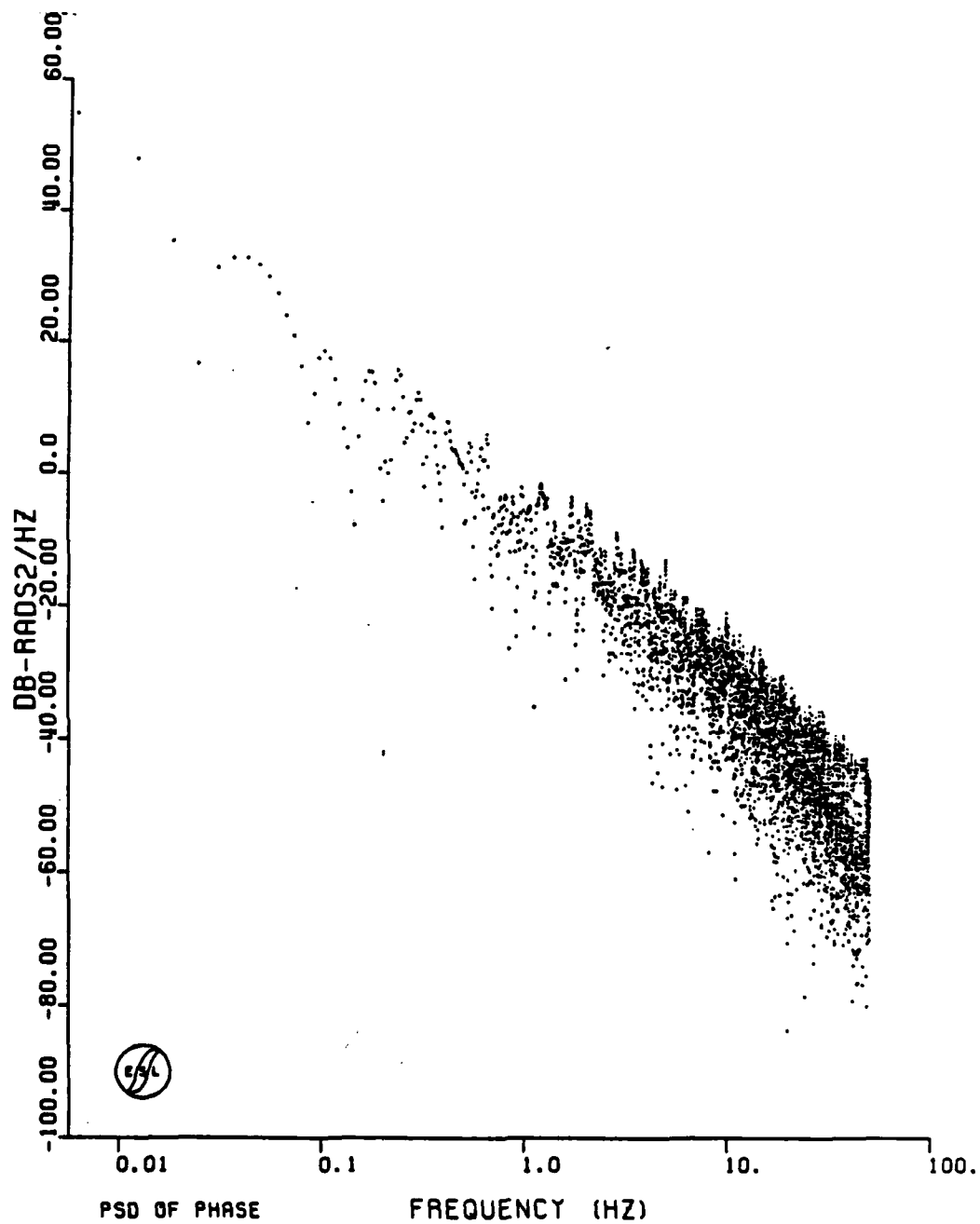


Figure 13-11. JAN Pass 10 Downlink Back-Propagated Phase PSD

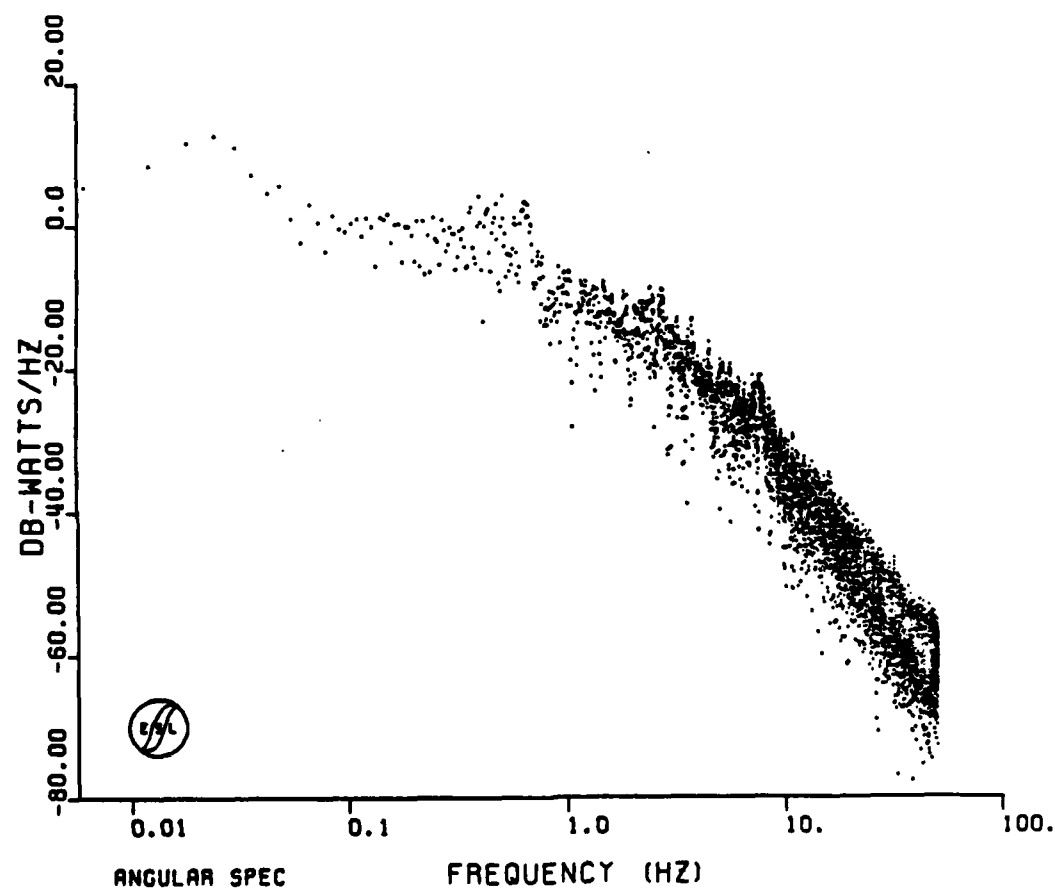


Figure 13-12. JAN Pass 10 Downlink Angular Spectrum

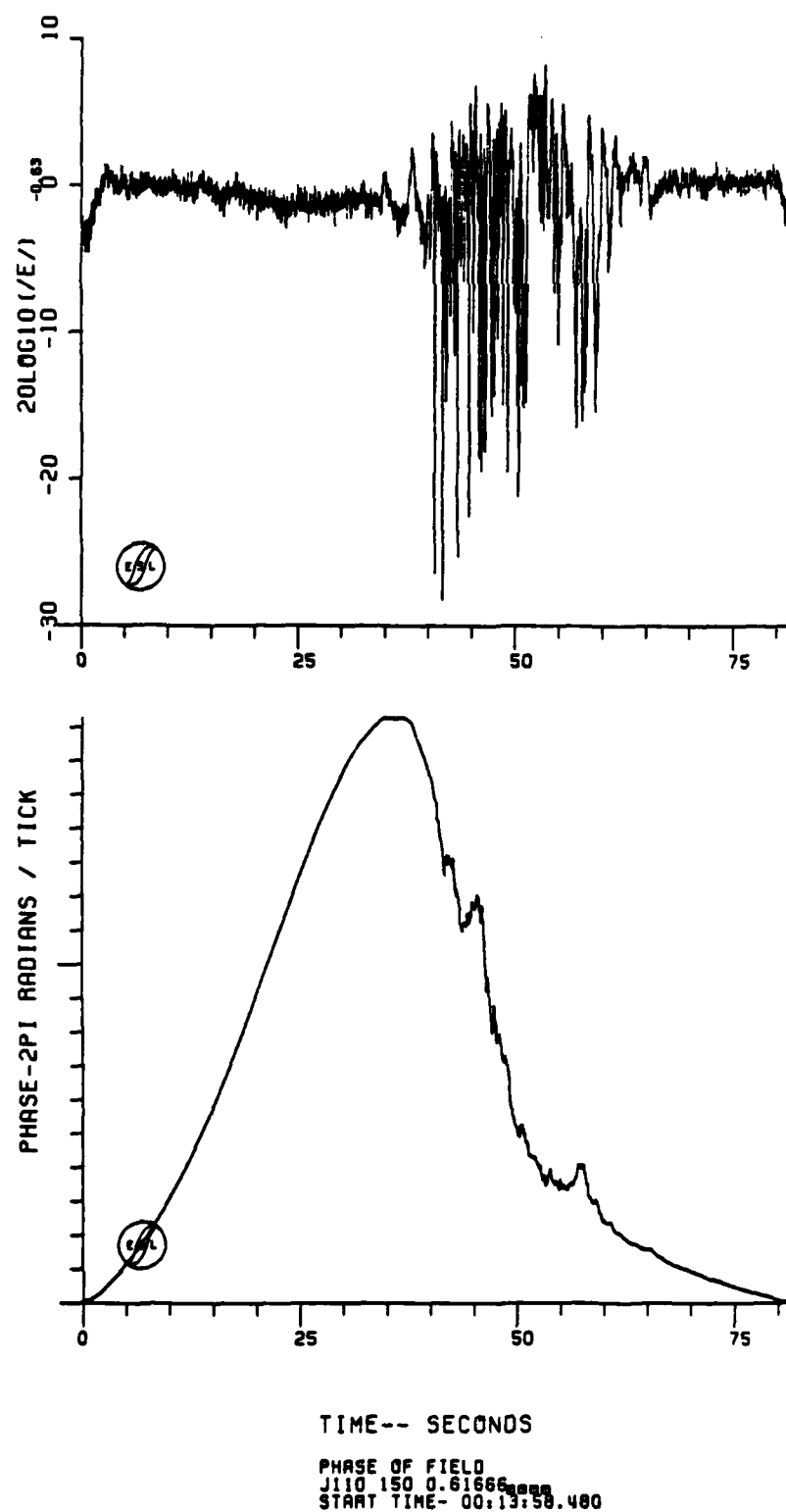


Figure 13-13. JAN Pass 11 Downlink Back-Propagated Amplitude and Phase

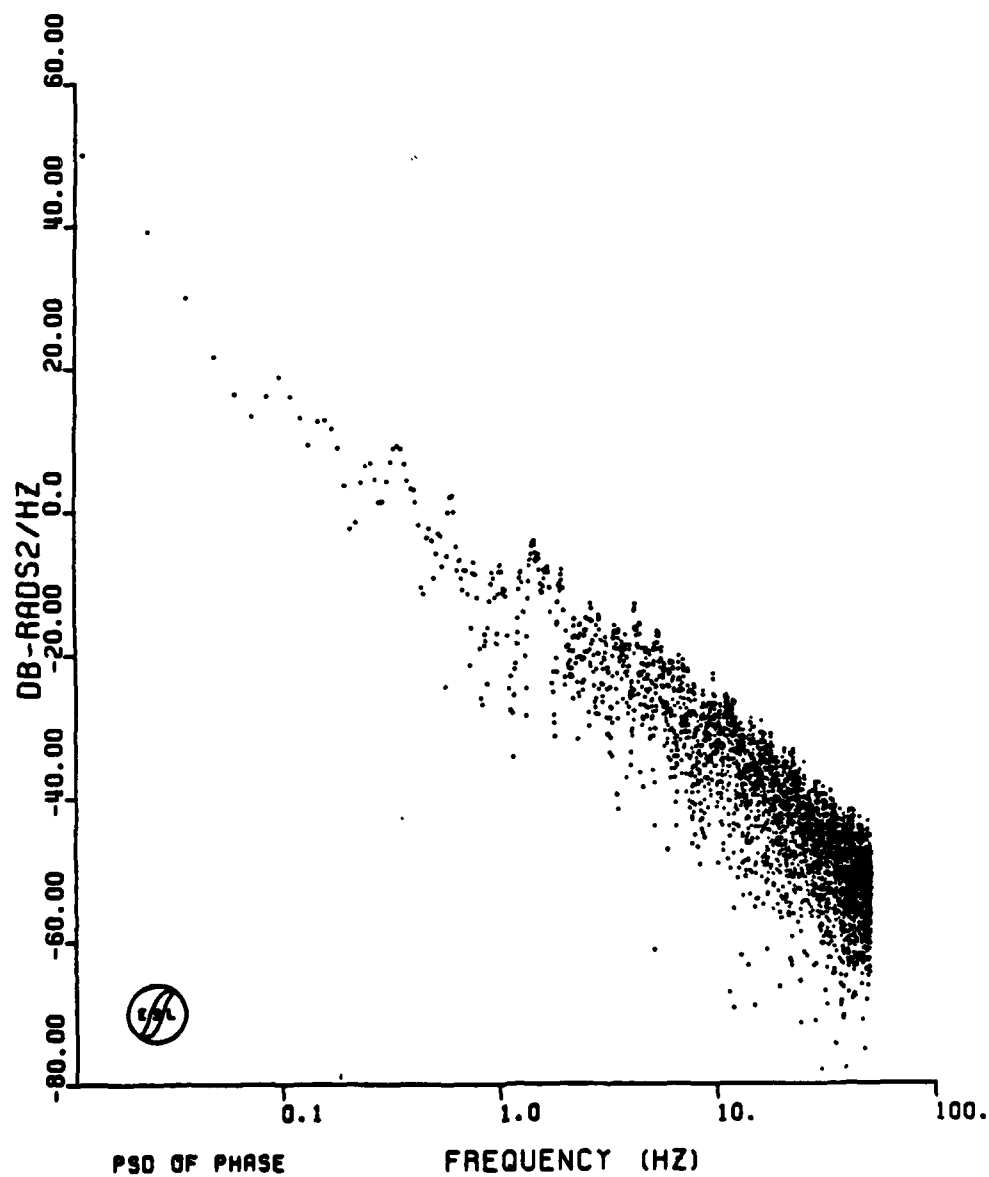


Figure 13-14. JAN Pass 11 Downlink Back-Propagated Phase PSD

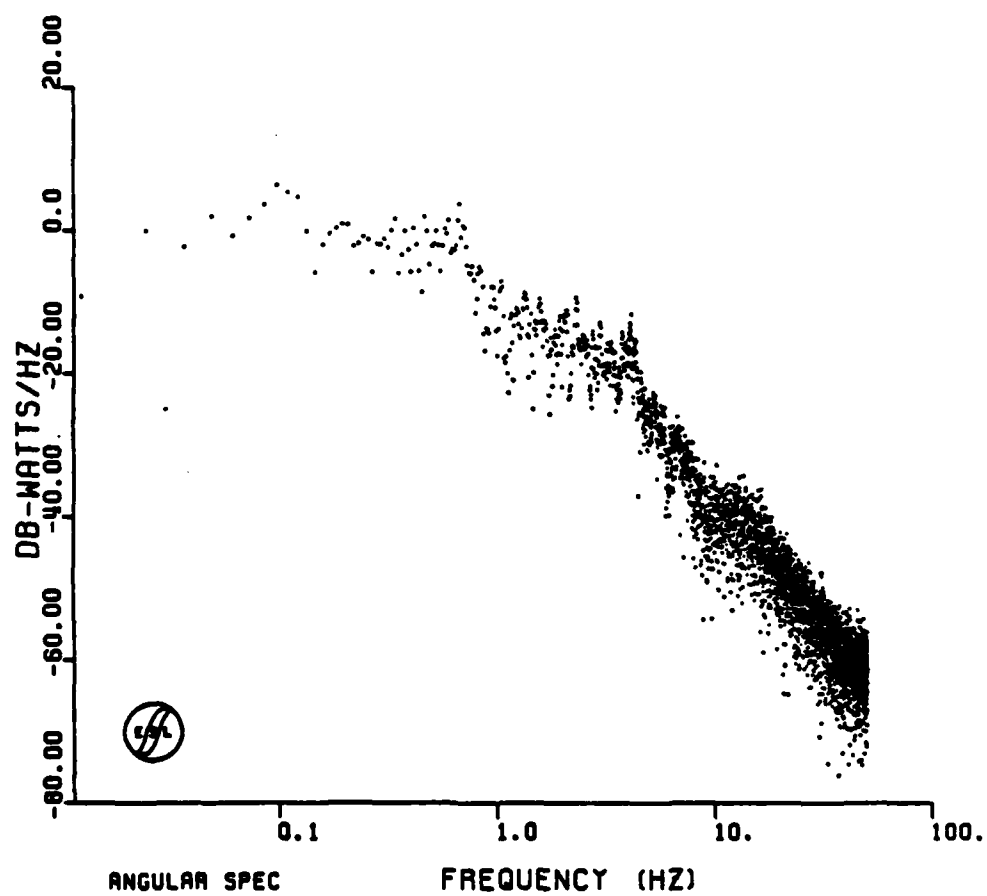
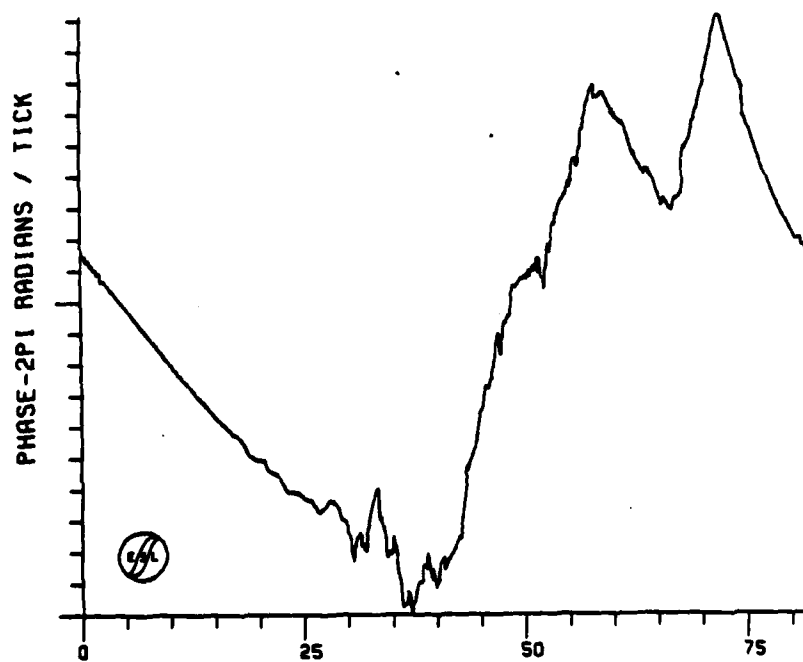
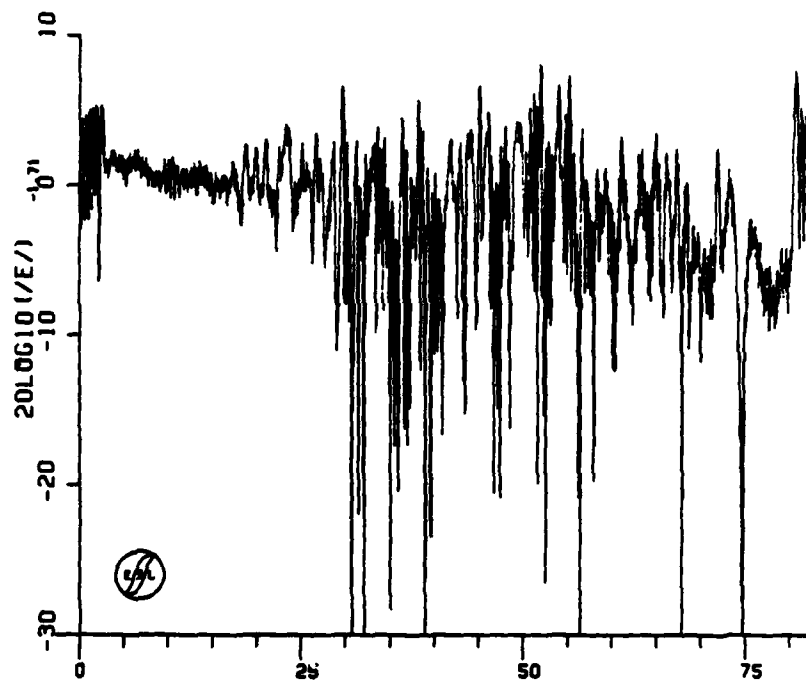


Figure 13-15. JAN Pass 11 Downlink Angular Spectrum



TIME-- SECONDS

PHASE OF FIELD
J120 225 0.78146
START TIME- 00:19:28.000

Figure 13-16. JAN Pass 12 Downlink Back-Propagated Amplitude and Phase

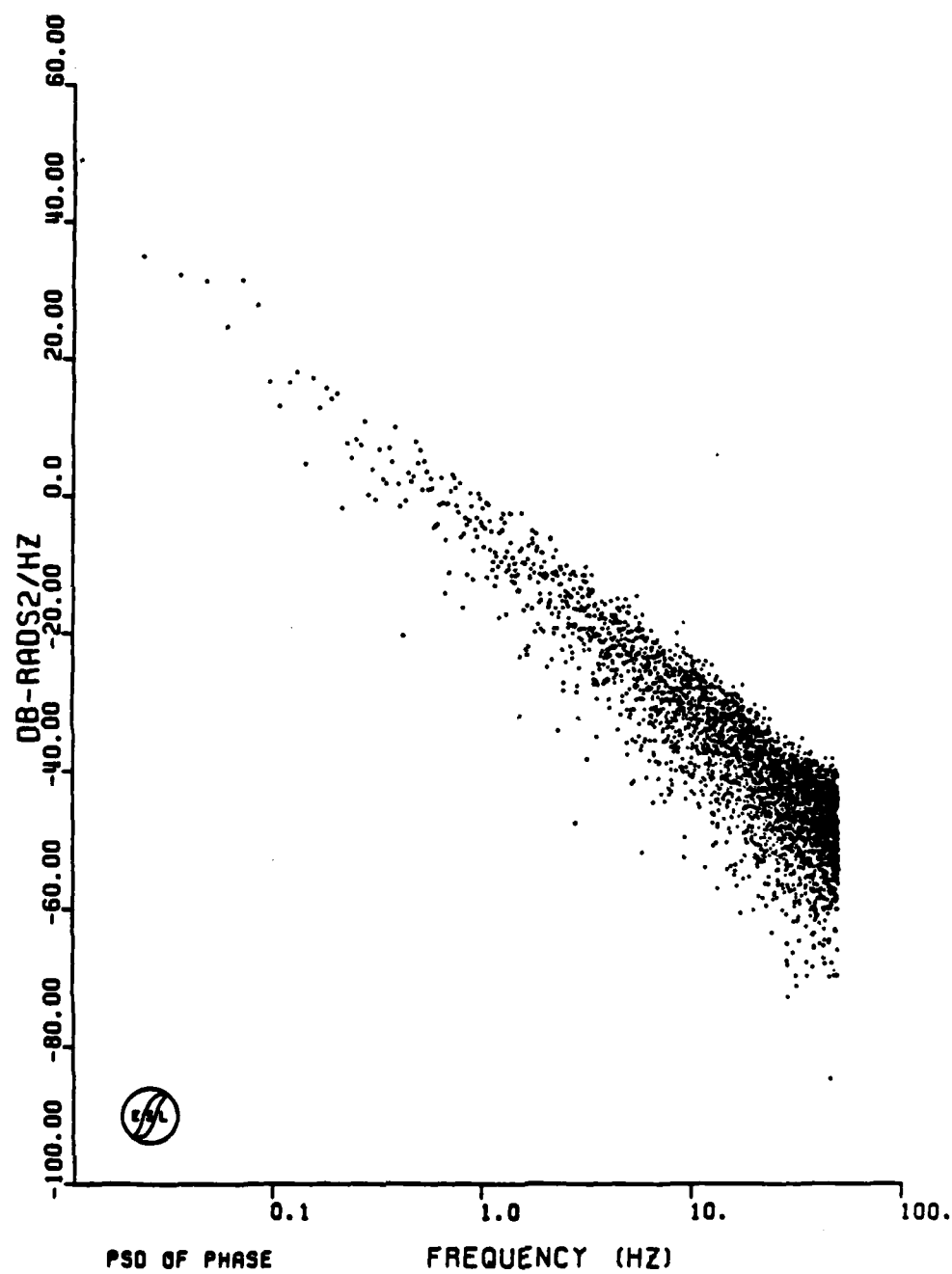


Figure 13-17. JAN Pass 12 Downlink Back-Propagated Phase PSD

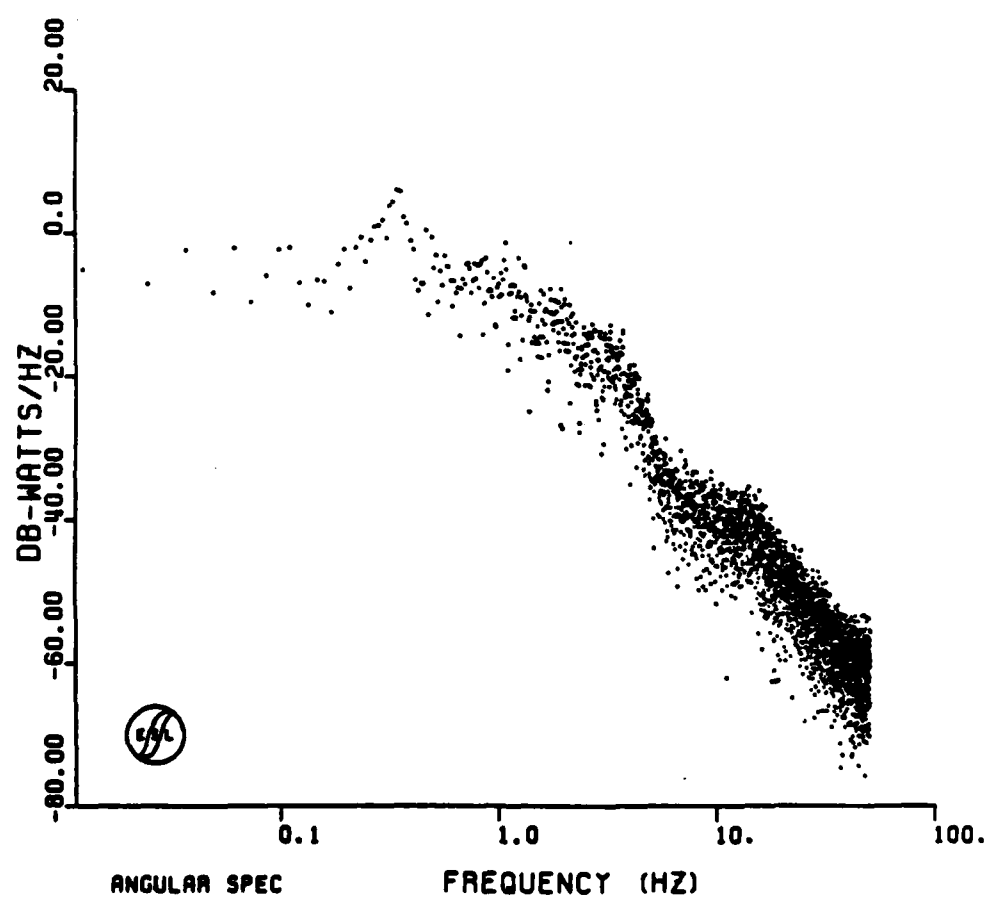


Figure 13-18. JAN Pass 12 Downlink Angular Spectrum

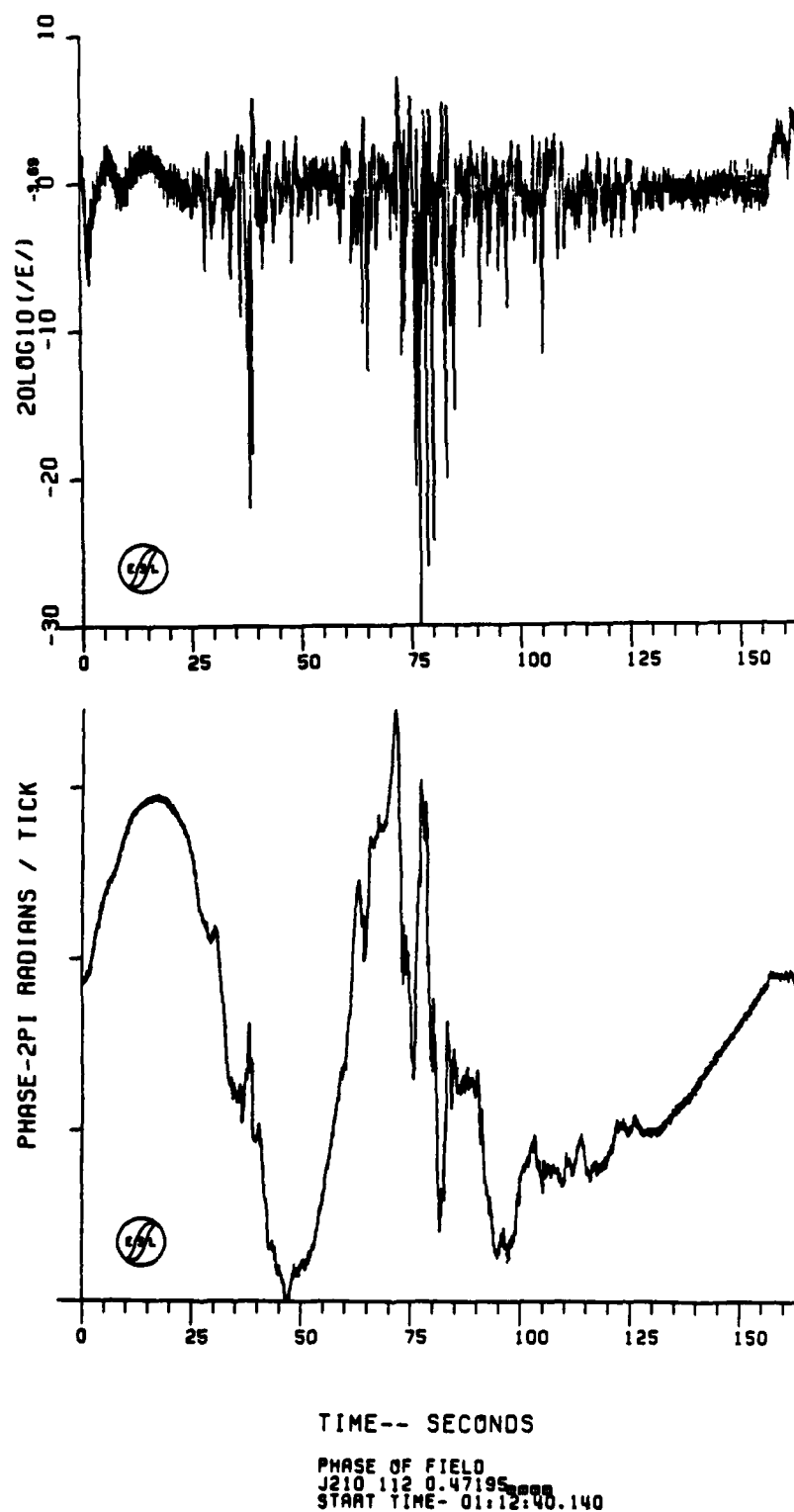


Figure 13-19. JAN Pass 21 Downlink Back-Propagated Amplitude and Phase

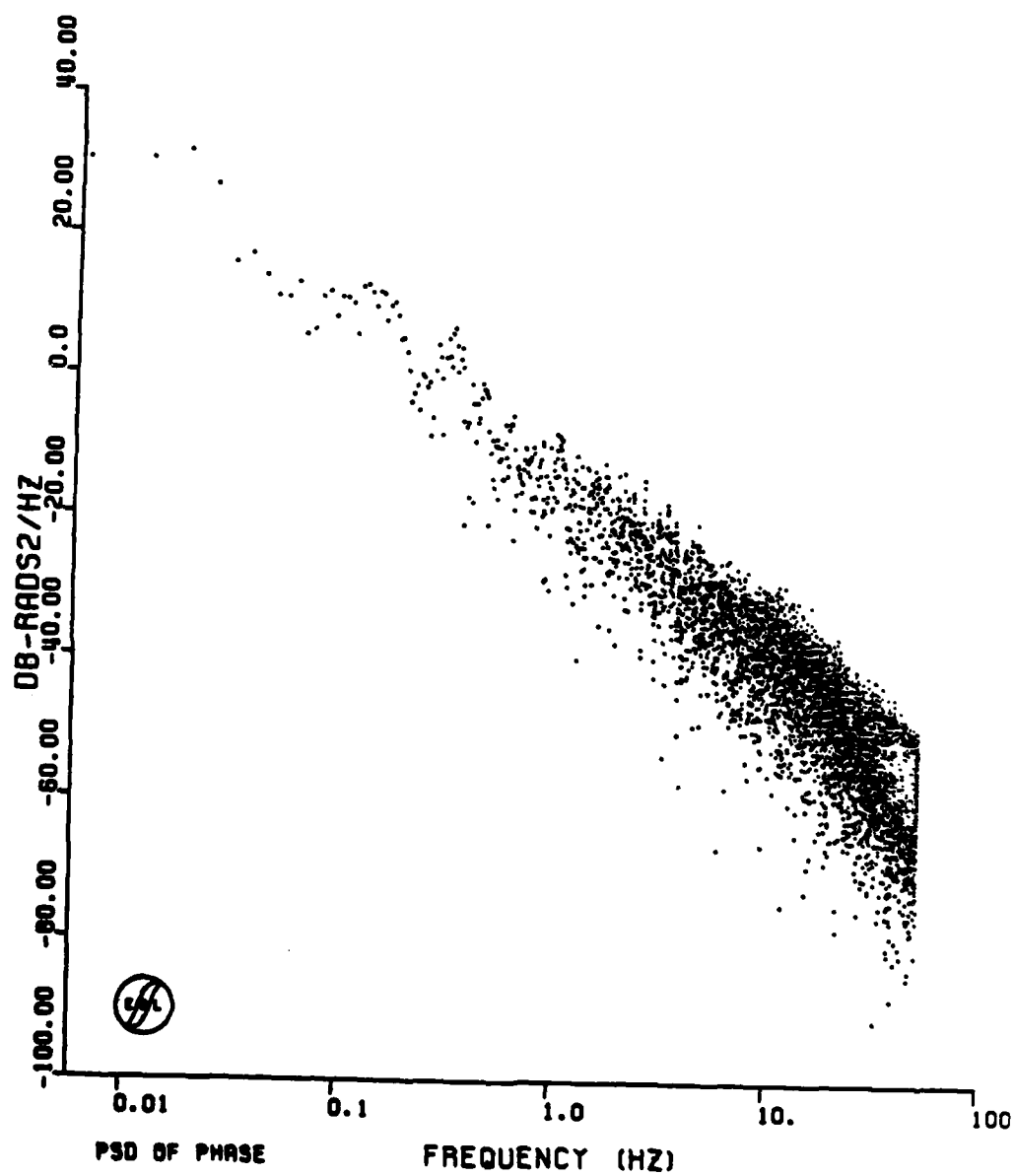


Figure 13-20. JAN Pass 21 Downlink Back-Propagated Phase PSD

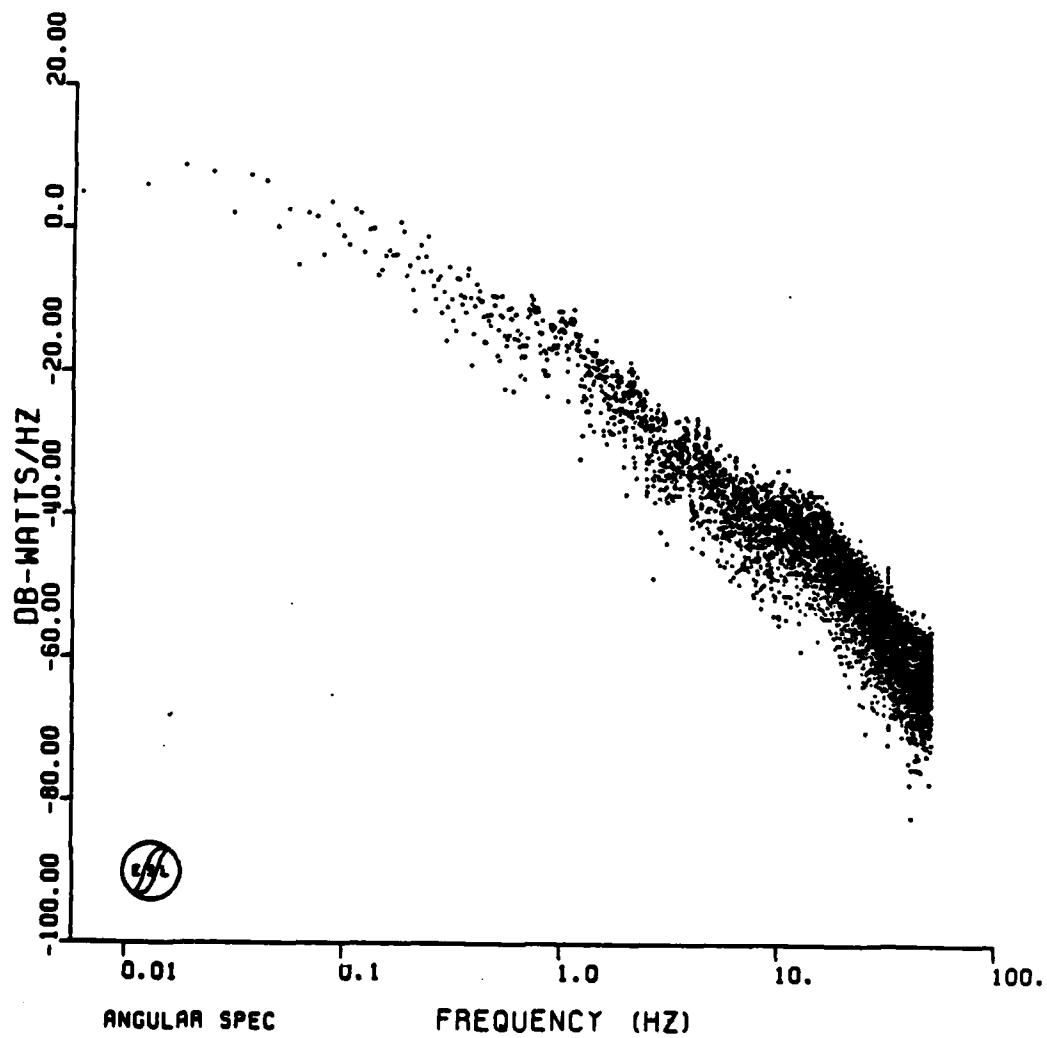


Figure 13-21. JAN Pass 21 Downlink Angular Spectrum

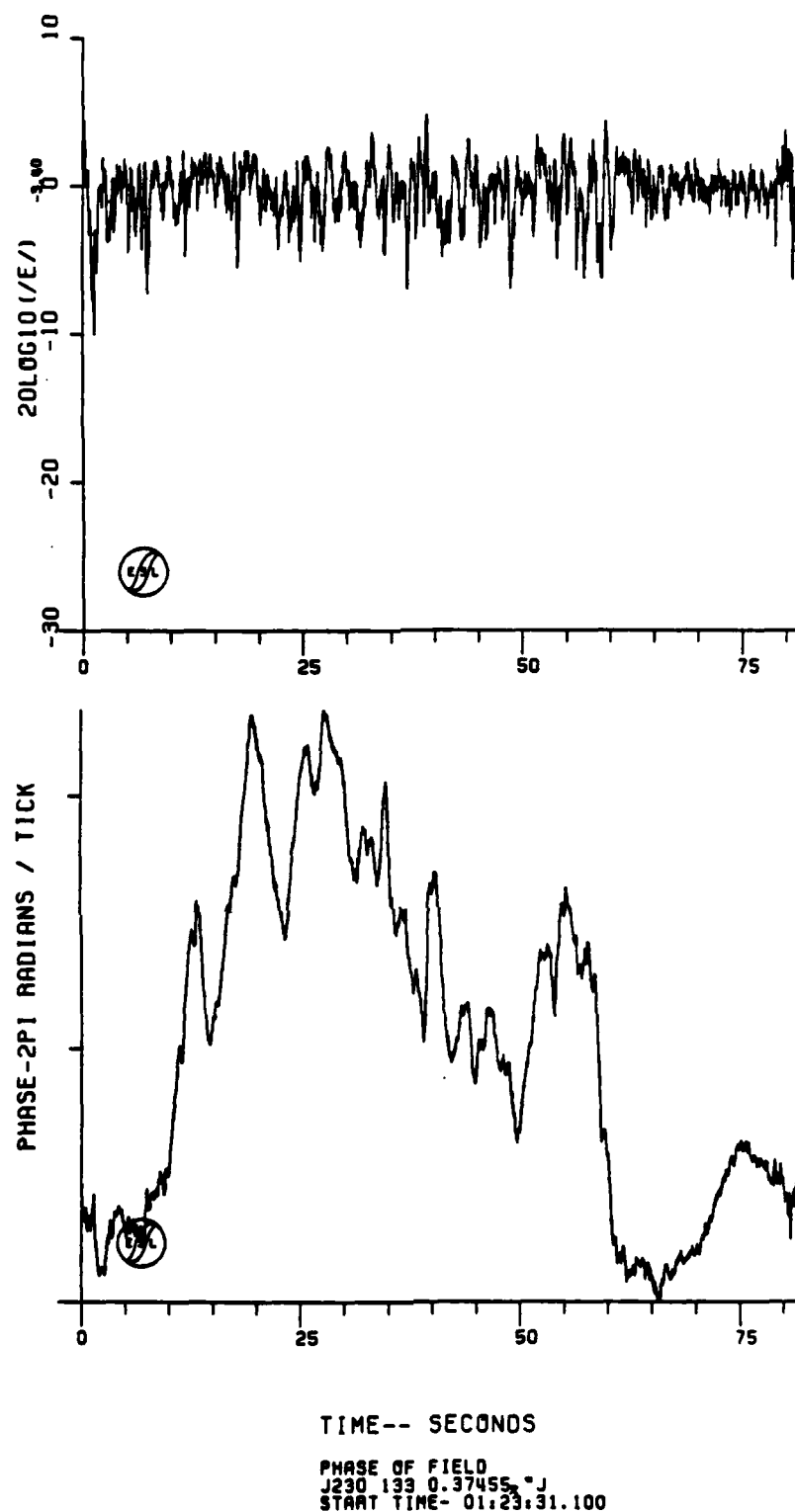


Figure 13-22. JAN Pass 23 Downlink Back-Propagated Amplitude and Phase

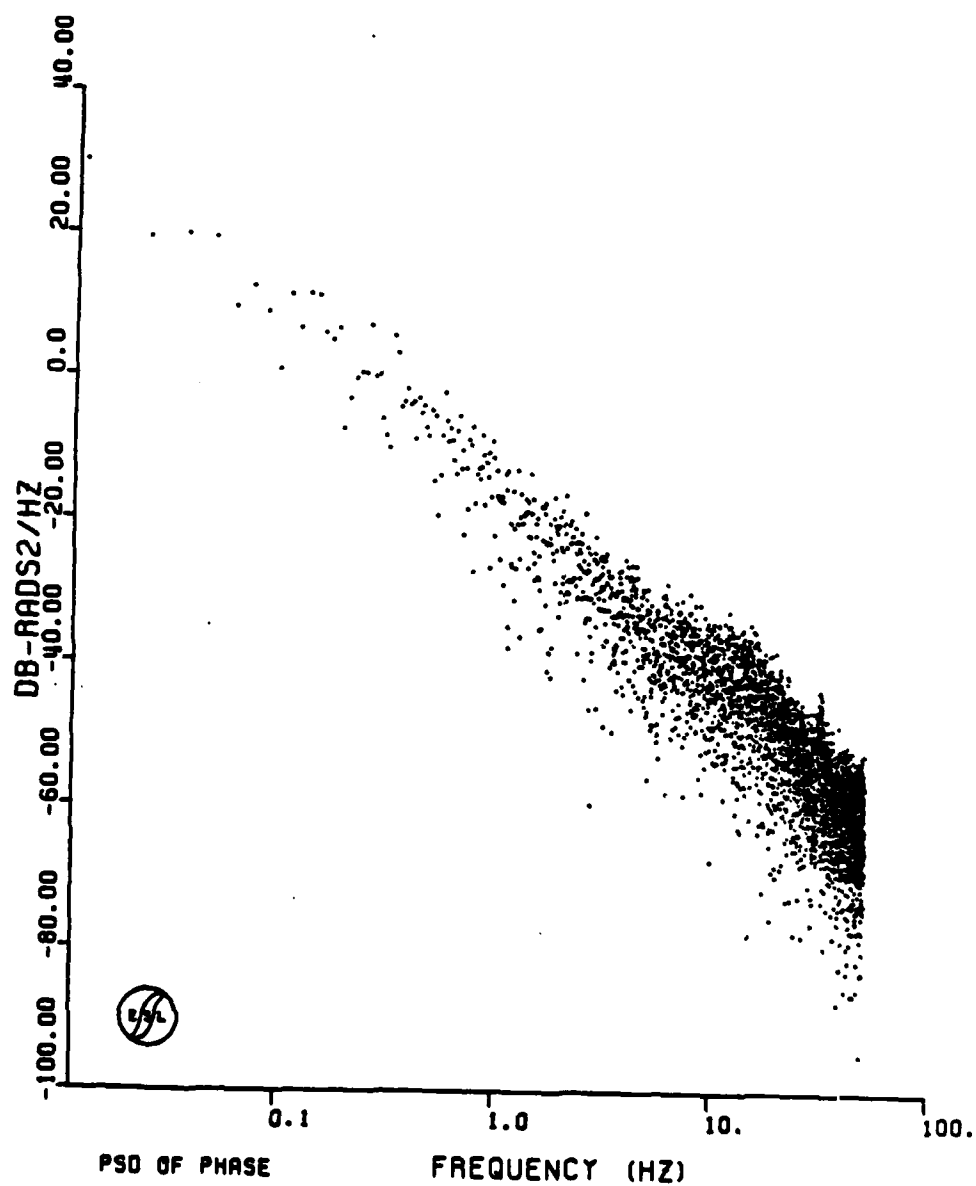


Figure 13-23. JAN Pass 23 Downlink Back-Propagated Phase PSD

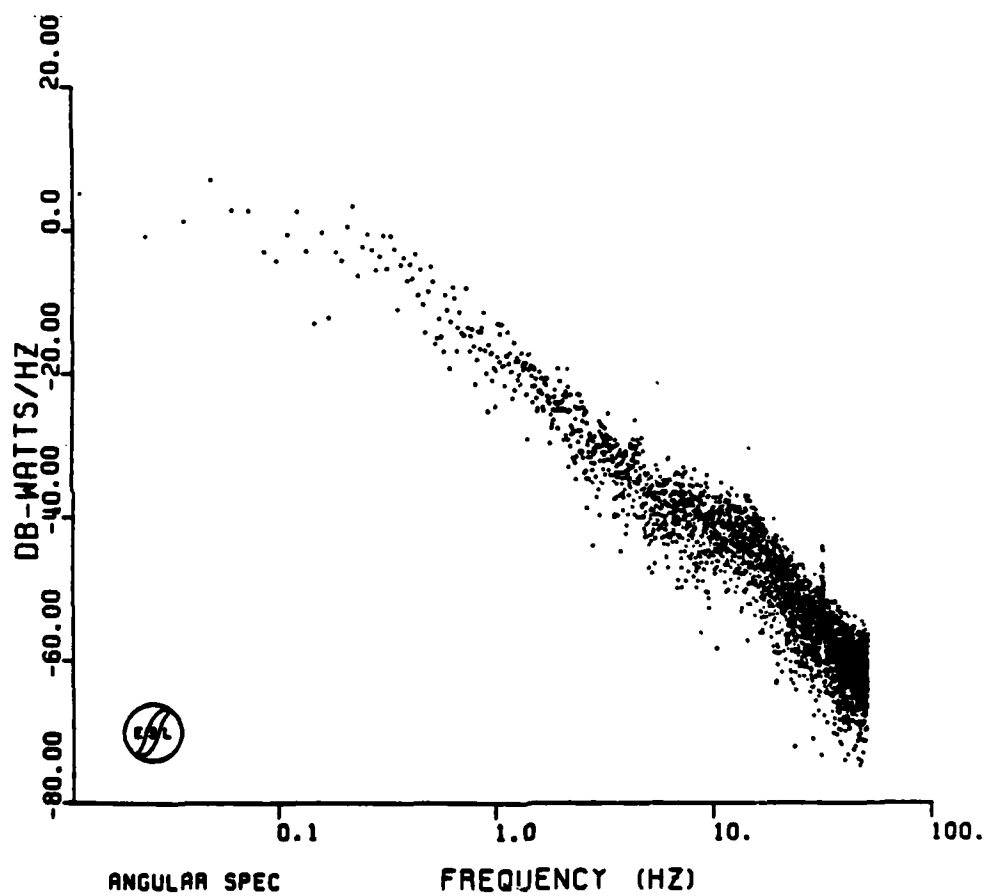
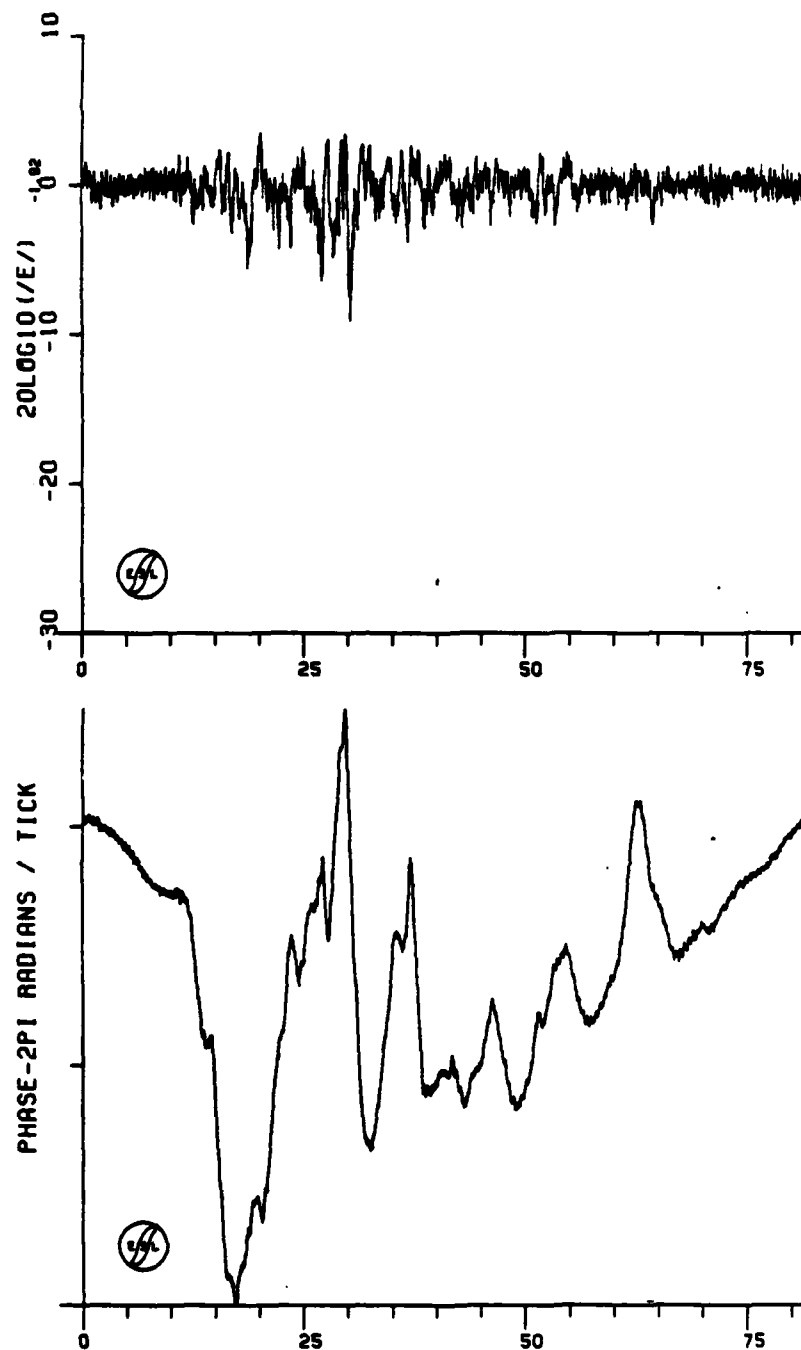


Figure 13-24. JAN Pass 23 Downlink Angular Spectrum



TIME-- SECONDS

PHASE OF FIELD
J250 127 0.25442 "J"
START TIME- 01:33:50.820

Figure 13-25. JAN Pass 25 Downlink Back-Propagated Amplitude and Phase

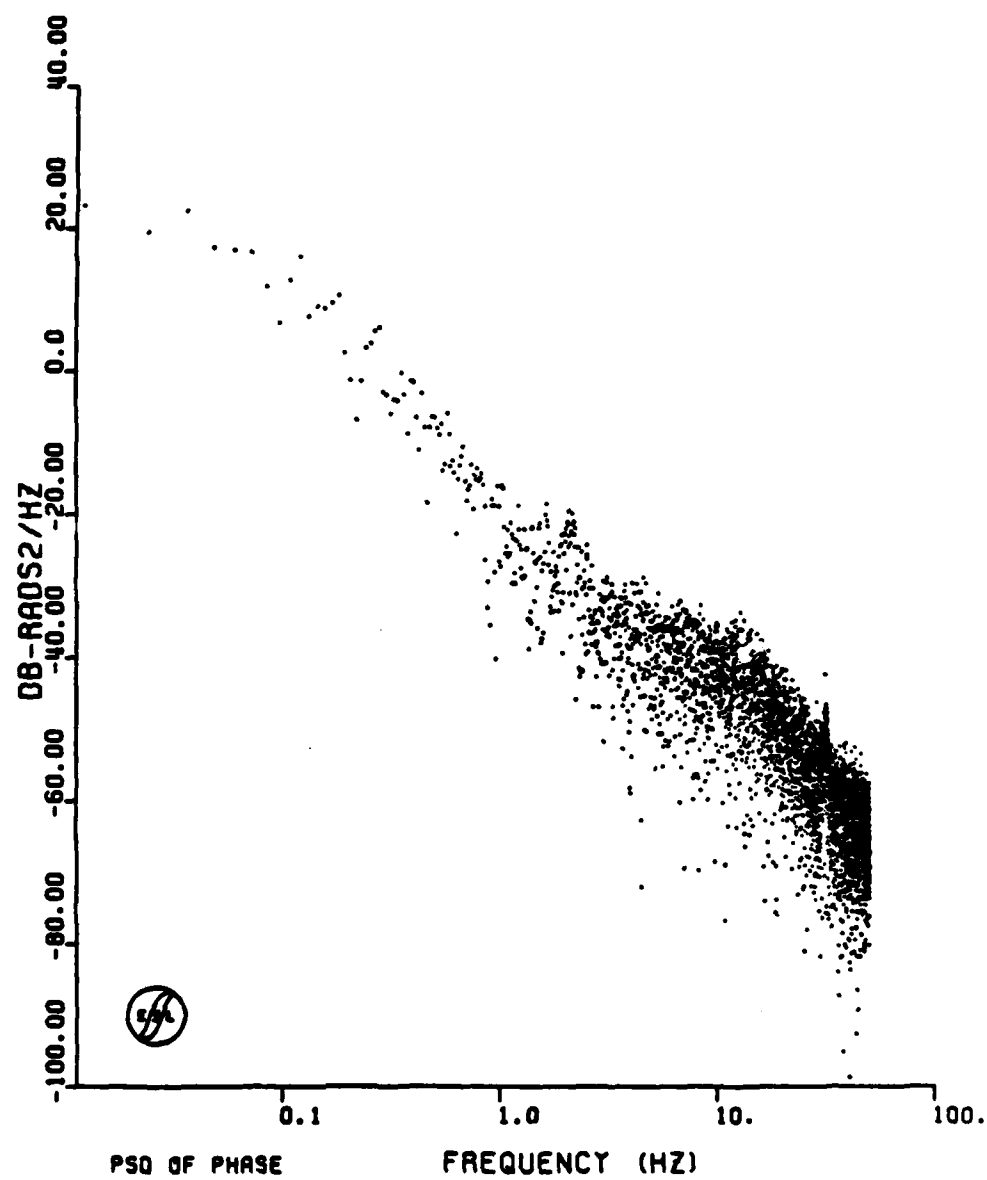


Figure 13-26. JAN Pass 25 Downlink Back-Propagated Phase PSD

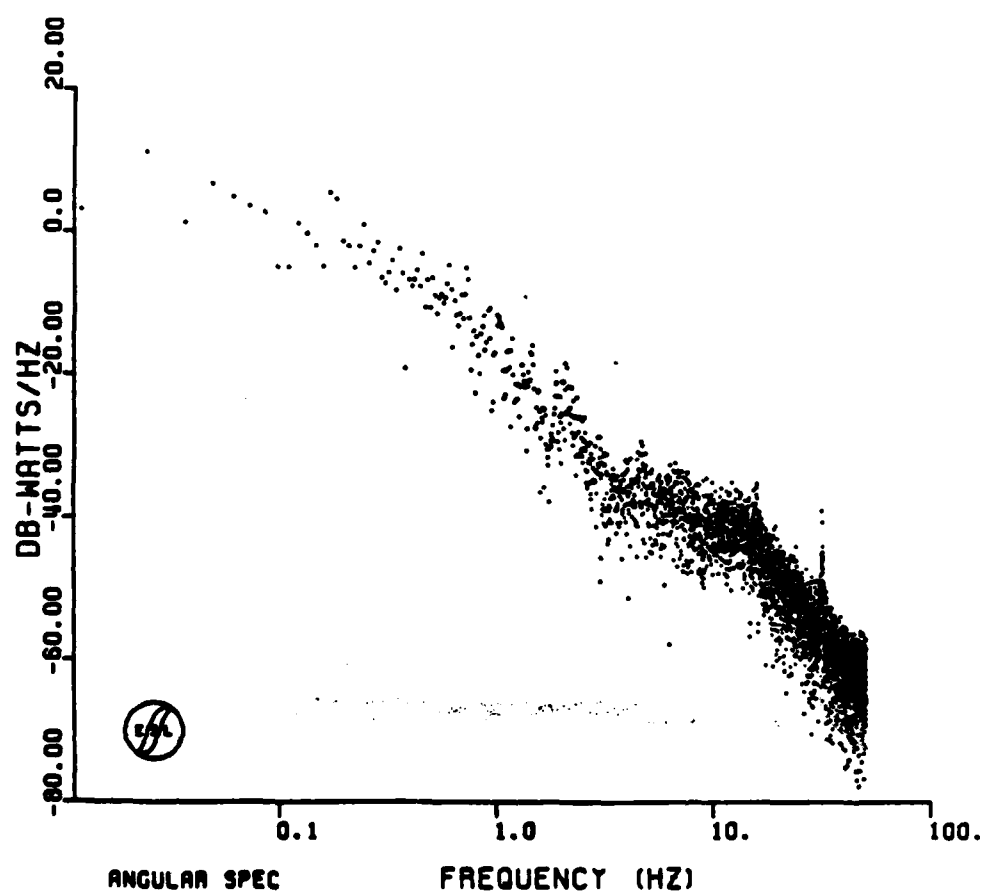
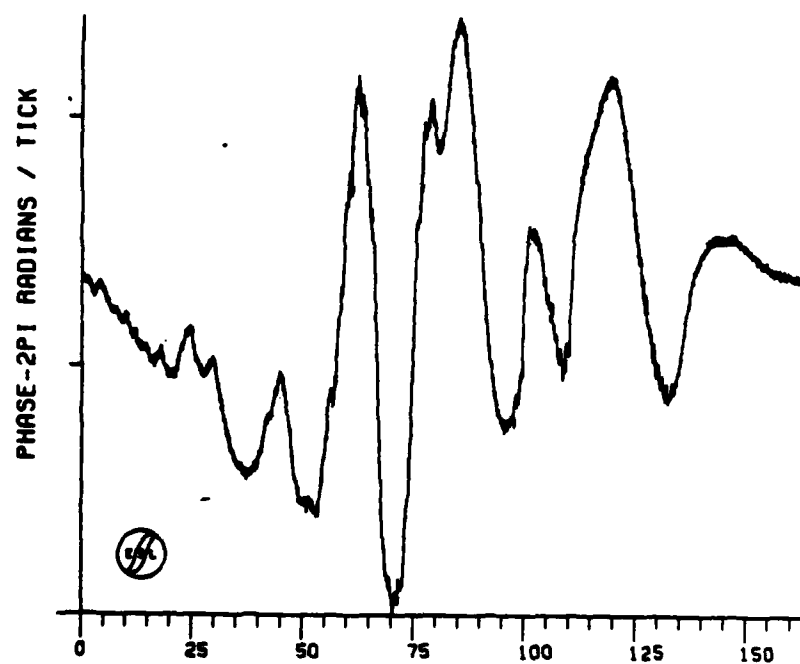
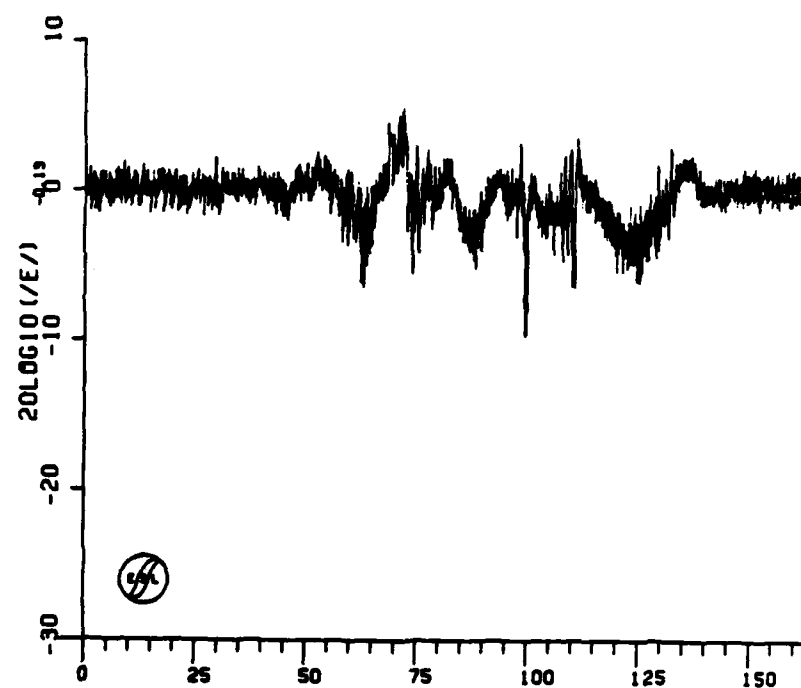


Figure 13-27. JAN Pass 25 Downlink Angular Spectrum



TIME-- SECONDS

PHASE OF FIELD
J260 180 0.33260
START TIME- 01:38:40.620

Figure 13-28. JAN Pass 26 Downlink Back-Propagated Amplitude and Phase

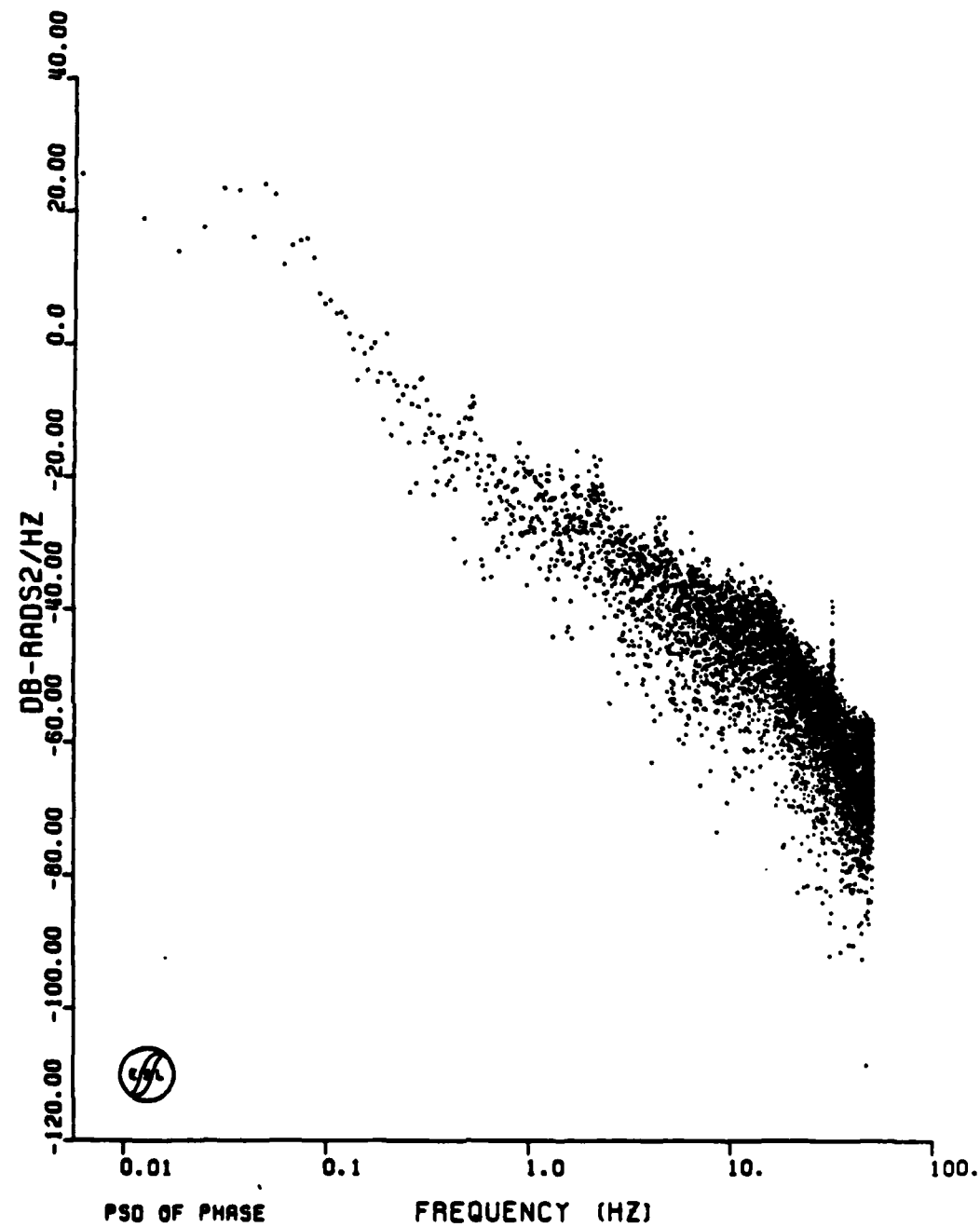


Figure 13-29. JAN Pass 26 Downlink Back-Propagated Phase PSD

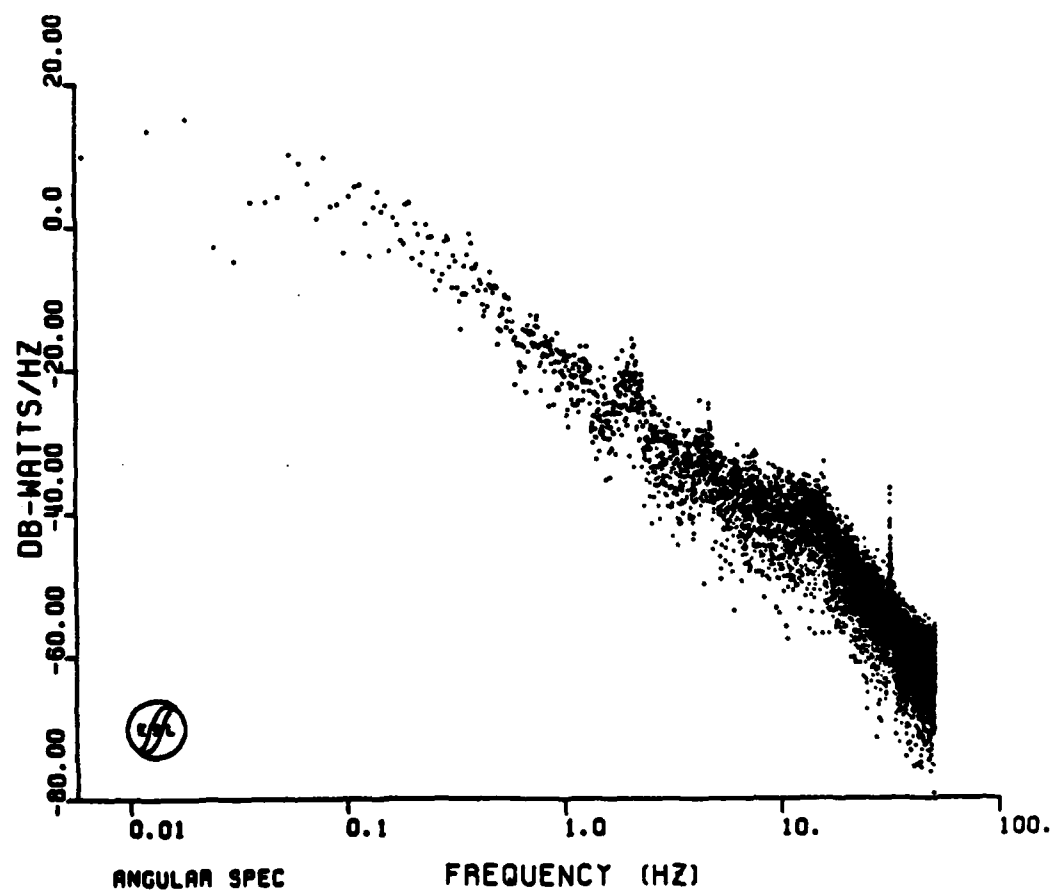
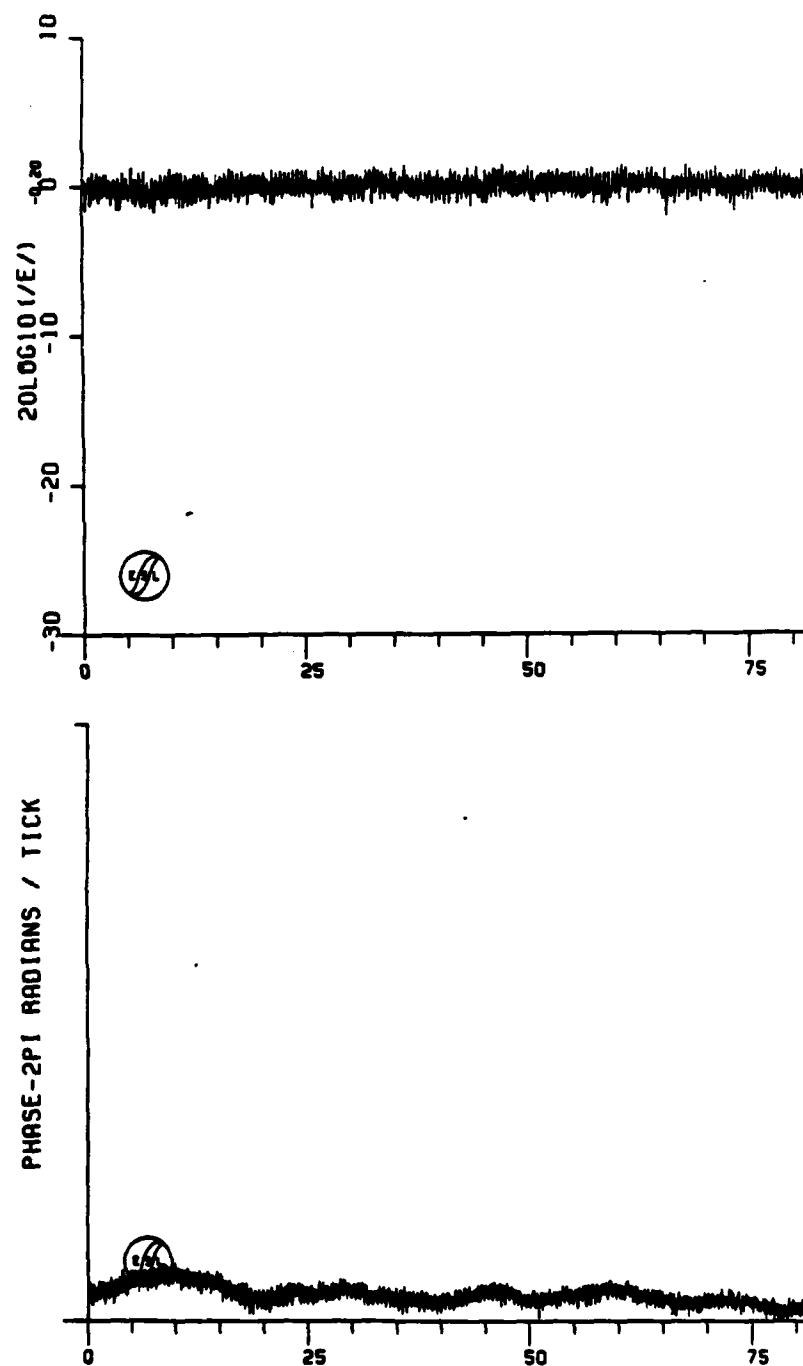


Figure 13-30. JAN Pass 26 Downlink Angular Spectrum



TIME-- SECONDS

PHASE OF FIELD
J270 150 0.11782
START TIME- 01:45:20.140

Figure 13-31. JAN Pass 27 Downlink Back-Propagated Amplitude and Phase

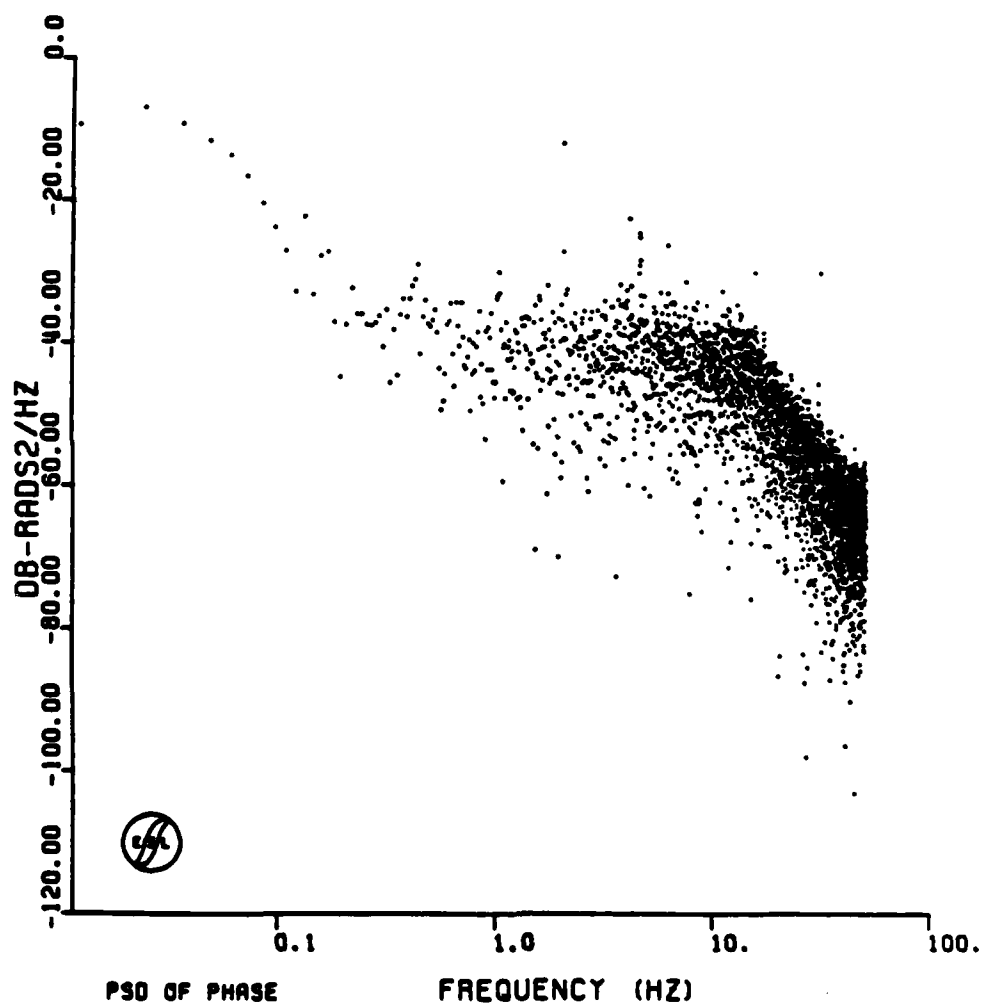


Figure 13-32. JAN Pass 27 Downlink Back-Propagated Phase PSD

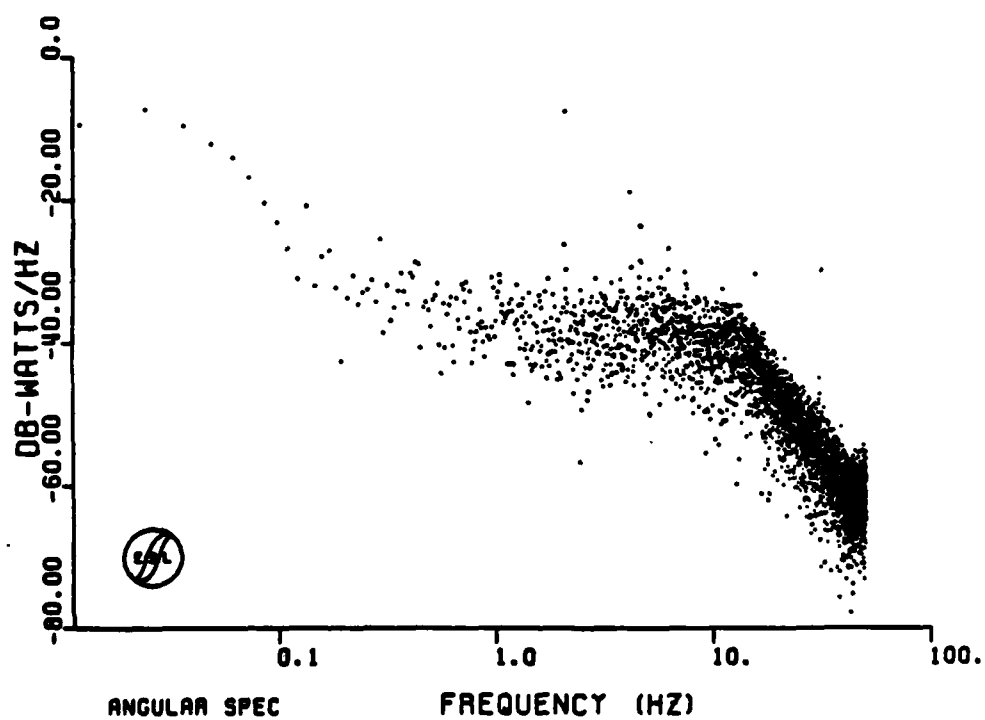
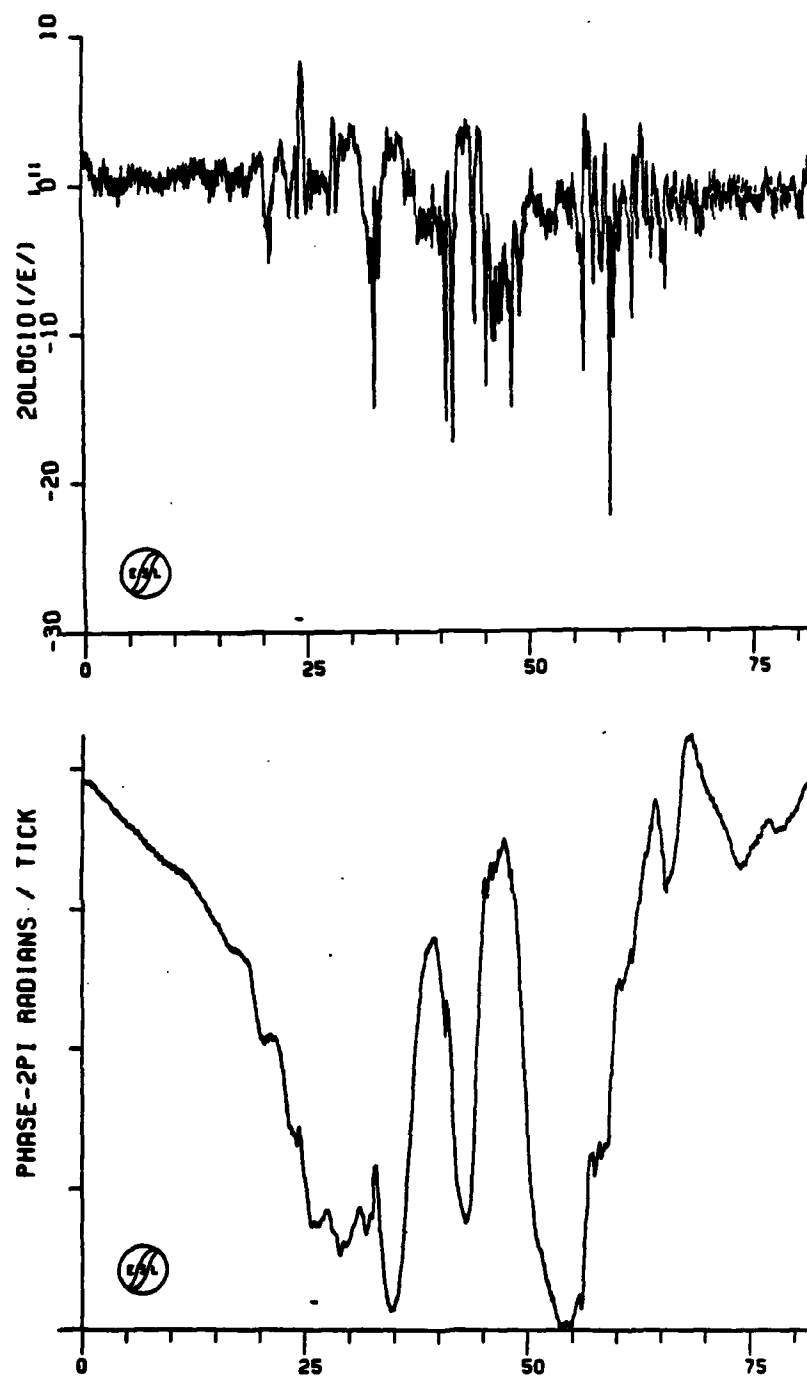


Figure 13-33. JAN Pass 27 Downlink Angular Spectrum



TIME-- SECONDS

PHASE OF FIELD
J290 124 0.59854
START TIME- 01:55:24.140

Figure 13-34. JAN Pass 29 Downlink Back-Propagated Amplitude and Phase

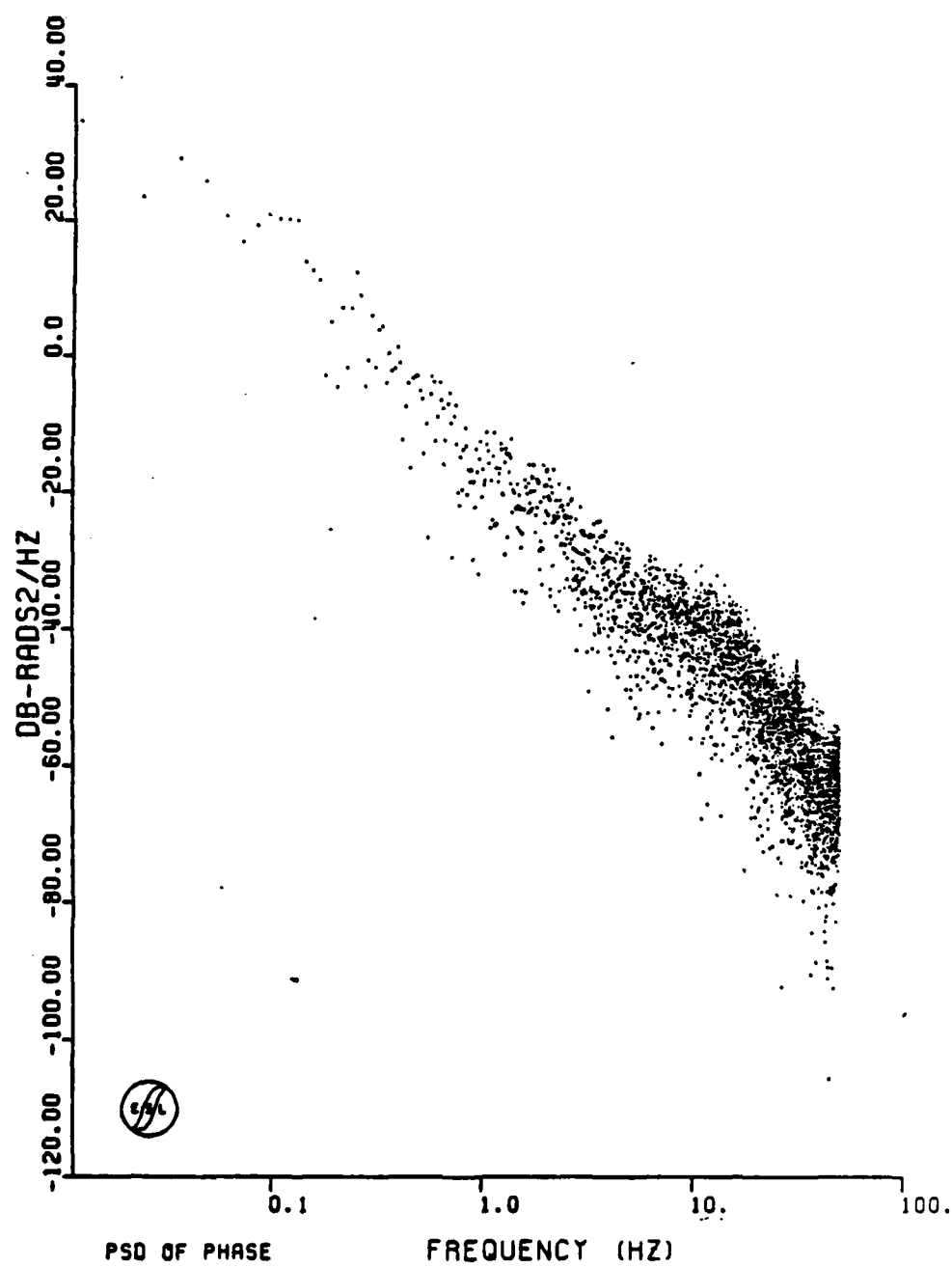


Figure 13-35. JAN Pass 29 Downlink Back-Propagated Phase PSD

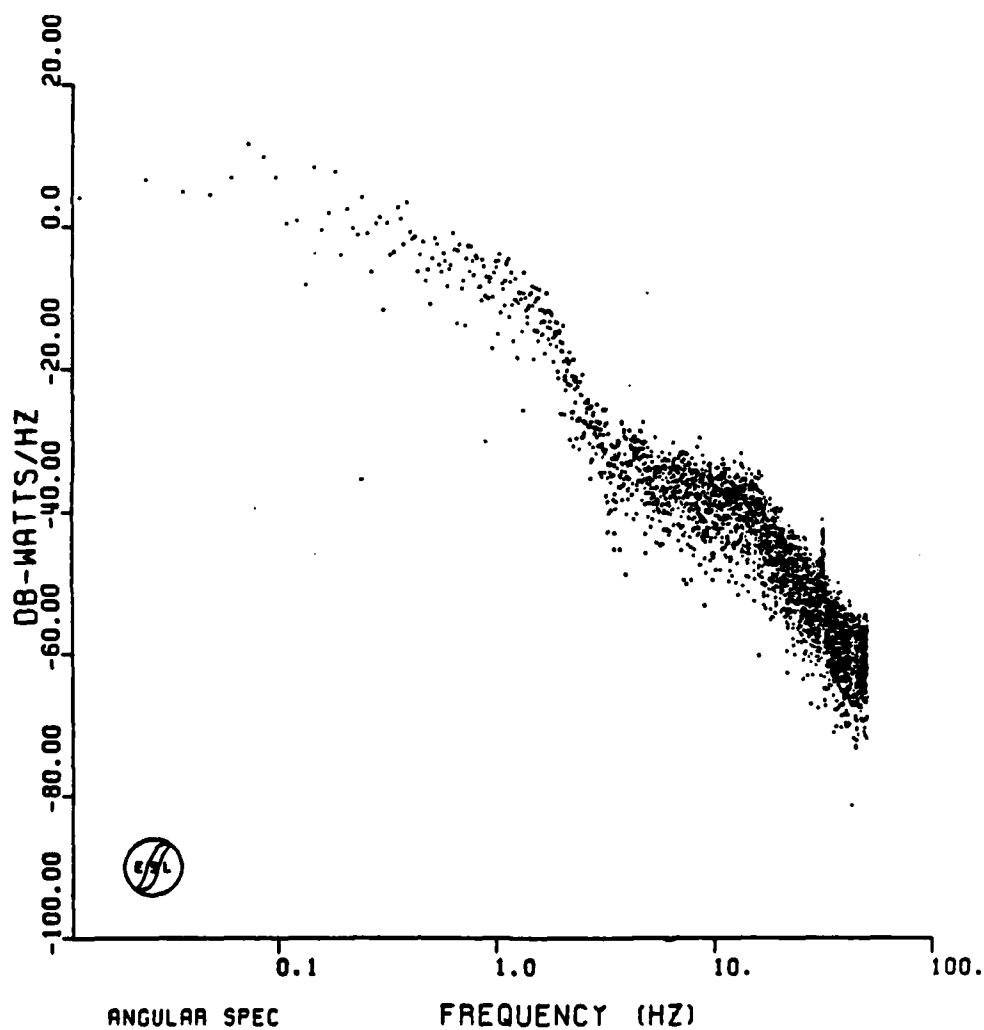


Figure 13-36. JAN Pass 29 Downlink Angular Spectrum

phase PSD is shown in Figure 13-5 and the angular spectrum is given in Figure 13-6. Since the phase resembles a triangular spike, the phase spectrum is expected to follow a sinc^2 function with the first spectral lobe approximately 26 dB down as shown. Significant number of lobes are evident in the data, thus, the phase data presumably contains significant diffraction effects and does not provide a good measure of the plasma integrated electron content. The angular spectrum which is invariant under the back-propagation processing is shown in Figure 13-6.

Pass 4 back-propagated very well as can be seen by comparing Figure 13-7 with Figure 11-4. The S_4 index decreased from 0.67 to 0.27, a significant decrease. Note however, that there is little gross ion cloud phase windup for this pass and only small random phase fluctuations. The propagation path for this pass was presumably high up the field lines catching only the tips of a few striations as reflected in the phase data. Figure 13-8 and 13-9 show the corresponding phase PSD and angular spectrum, respectively.

Passes 5 through 9 did not back-propagate well and are not shown. Pass 10 too did not back-propagate well as shown by Figure 13-10. This is typical of the earlier passes that are not shown. The diffraction ringing at the edges of the pass have back-propagated, but, the striation effects on the left portion of the gross phase structure remain. In Section 13-4 this data is compared with the uplink back-propagated data. Figures 13-11 and 13-12 display the corresponding downlink phase PSD and angular spectrum.

The back-propagated signal for JAN Pass 23 is shown in Figure 13-22. Again this pass back-propagated very well with the S_4 index dropping from 0.73 to 0.37. The phase exhibits finger-like perturbations. The phase PSD and the angular spectrum is shown in Figure 13-23.

Pass 25 also back-propagated well as can be seen by comparing Figure 11-17 with Figure 13-25. The phase PSD and the angular spectrum both contain a bump around 2 Hz that is believed to be due to the receiving equipment. These are shown in Figures 26 and 27.

JAN Pass 26 provides another example of a pass that partially back-propagated. Figure 13-28 shows the amplitude and phase. Most of the rapid interference fading back-propagated but the shallow defocusing/focusing remains. The phase structure again resembles finger-like perturbations. Figures 13-29 and 13-30 show the back-propagated phase PSD and the angular spectrum evident at late times.

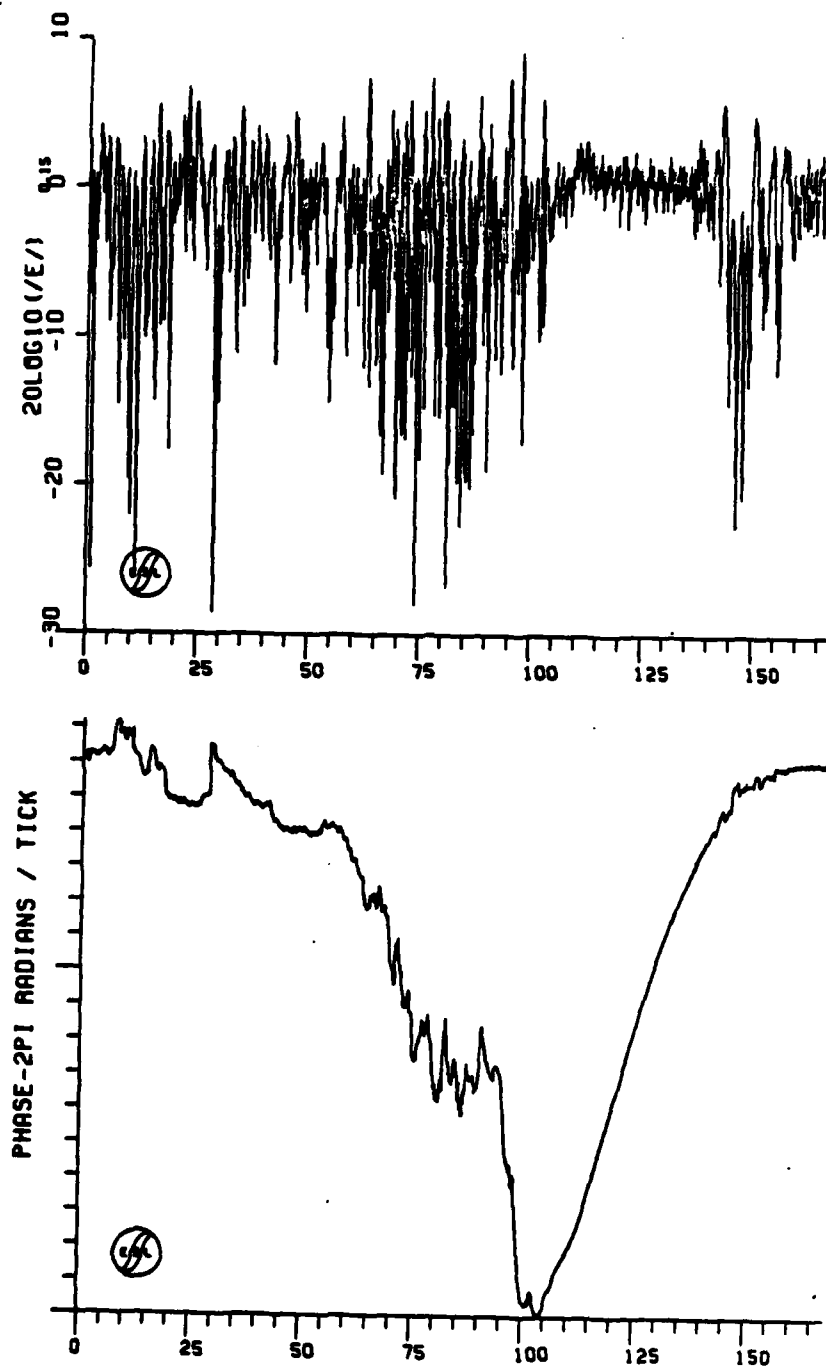
JAN Pass 27 provides an example of a noise only pass. Figures 13-31, 13-32, and 13-33 show the noise after back-propagation 150 kilometers. The resonance spikes evident in the phase PSD and the angular spectrum are believed due to the receiving equipment. For most passes these spikes are below the signal spectrum. The 20 dB/decade roll-off in these spectrums at 15 Hz is due to the low pass filter used to reduce the noise.

Pass 29 was the last pass to contain significant fading. Figure 13-34 shows the back-propagated signal. Again, the back-propagation was only partially successful in eliminating the rapid phase interference fading at a single distance. The phase PSD and the angular spectrum are shown in Figures 13-35 and 13-36, respectively.

13-4 BACK-PROPAGATED JAN UPLINK DATA.

Generally the uplink back-propagation processing was given a low priority. Generally the uplink data suffers from the same problem as the downlink data in that few appear to back-propagate well. JAN Pass 10 and Pass 23 are shown here in Figures 13-37 through 13-41 as two representative samples.

The uplink back-propagated amplitude and phase for Pass 10 is shown in Figure 13-37. The back-propagation distance is the same as that for the downlink shown in Figure 13-10. The uplink received amplitude and phase is shown in Figure 12-7 prior to back-propagation. In back-propagation 240 kilometers, the scintillation index increases from 0.60 to 0.75. Interestingly, however, the gross



TIME-- SECONDS

PHASE OF FIELD
 UJ10-240 0.746834.00
 START TIME- 00:05:40.876

Figure 13-37. JAN Pass 10 Uplink Back-Propagated Amplitude and Phase

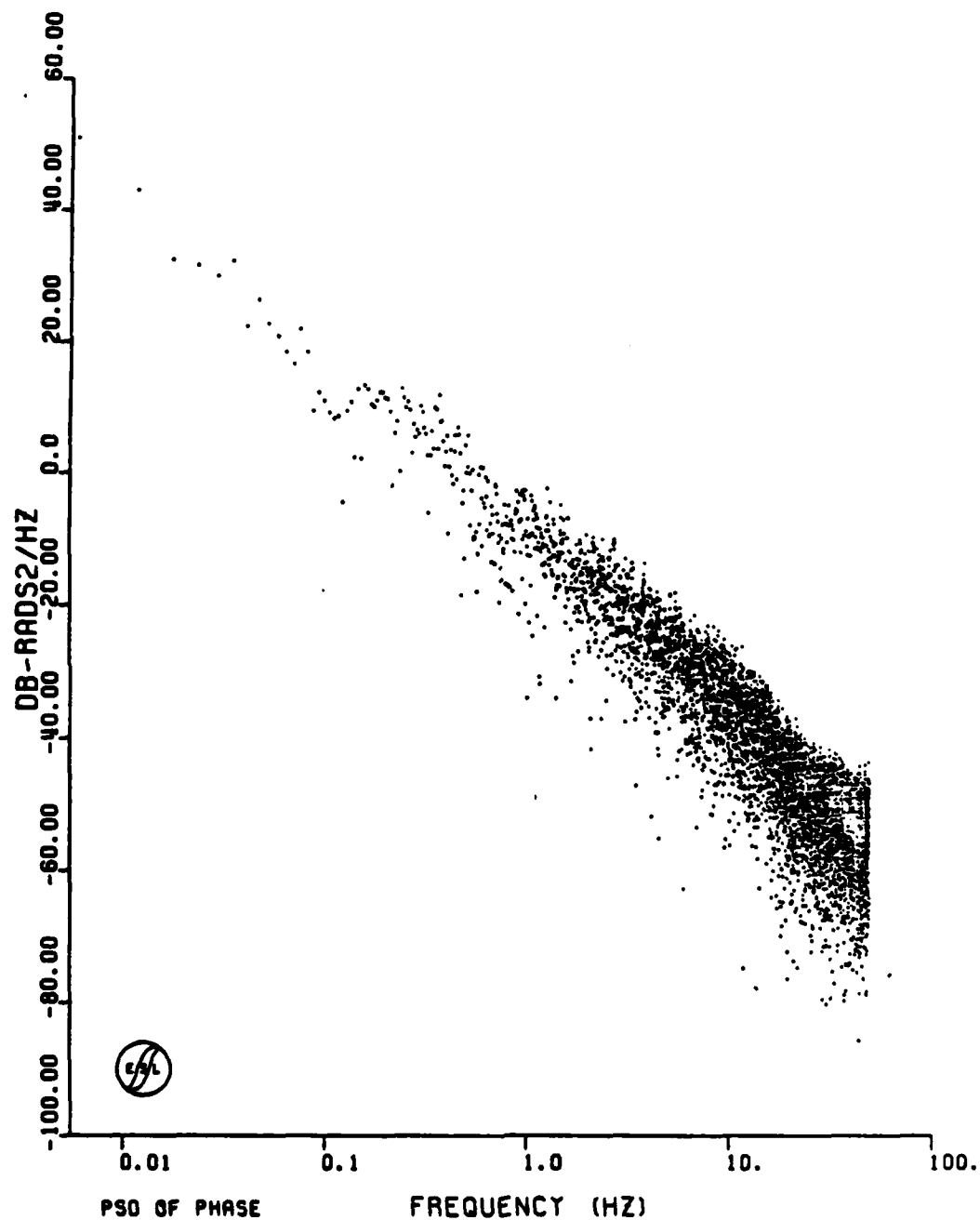


Figure 13-38. JAN Pass 10 Uplink Back-Propagated Phase PSD

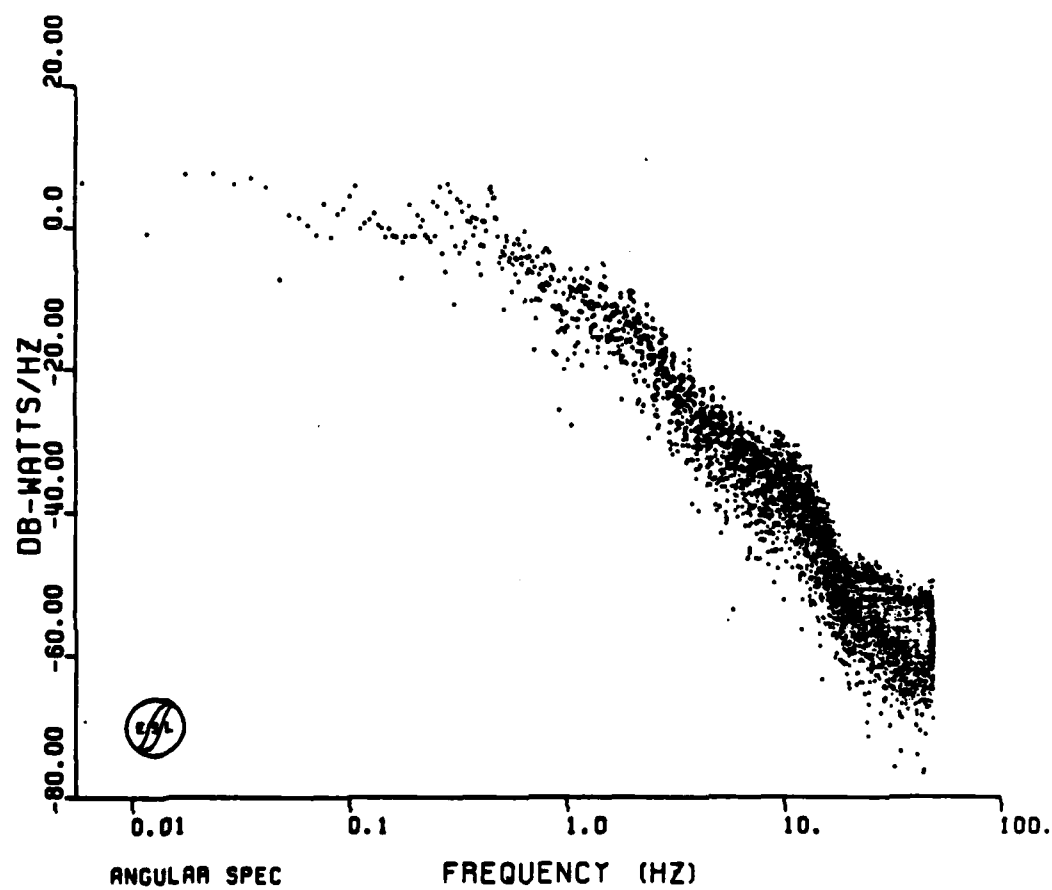


Figure 13-39. JAN Pass 10 Uplink Angular Spectrum

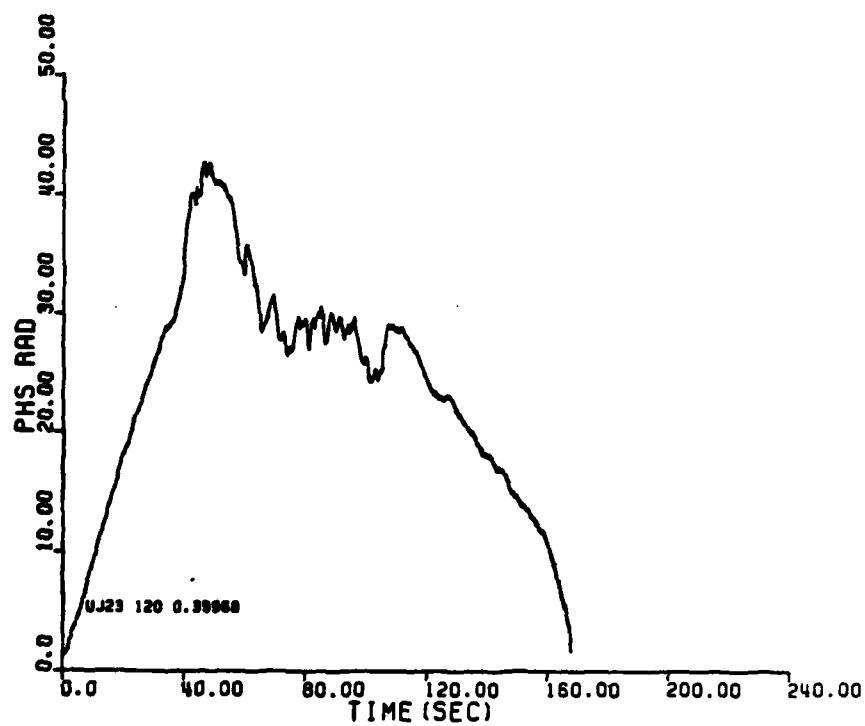
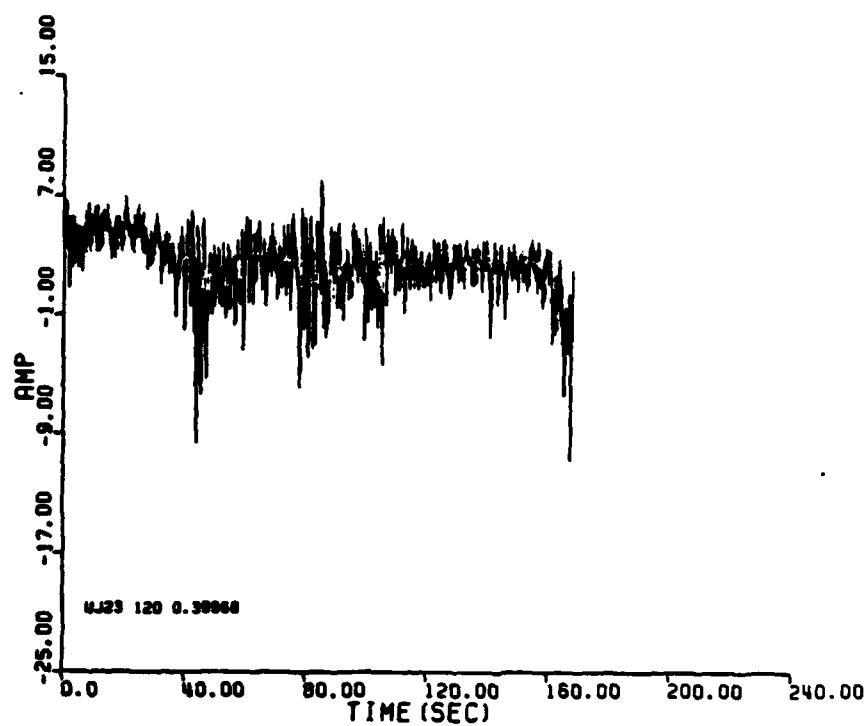


Figure 13-40. JAN Pass 23 Uplink Back-Propagated Amplitude and Phase at 120 Kilometers

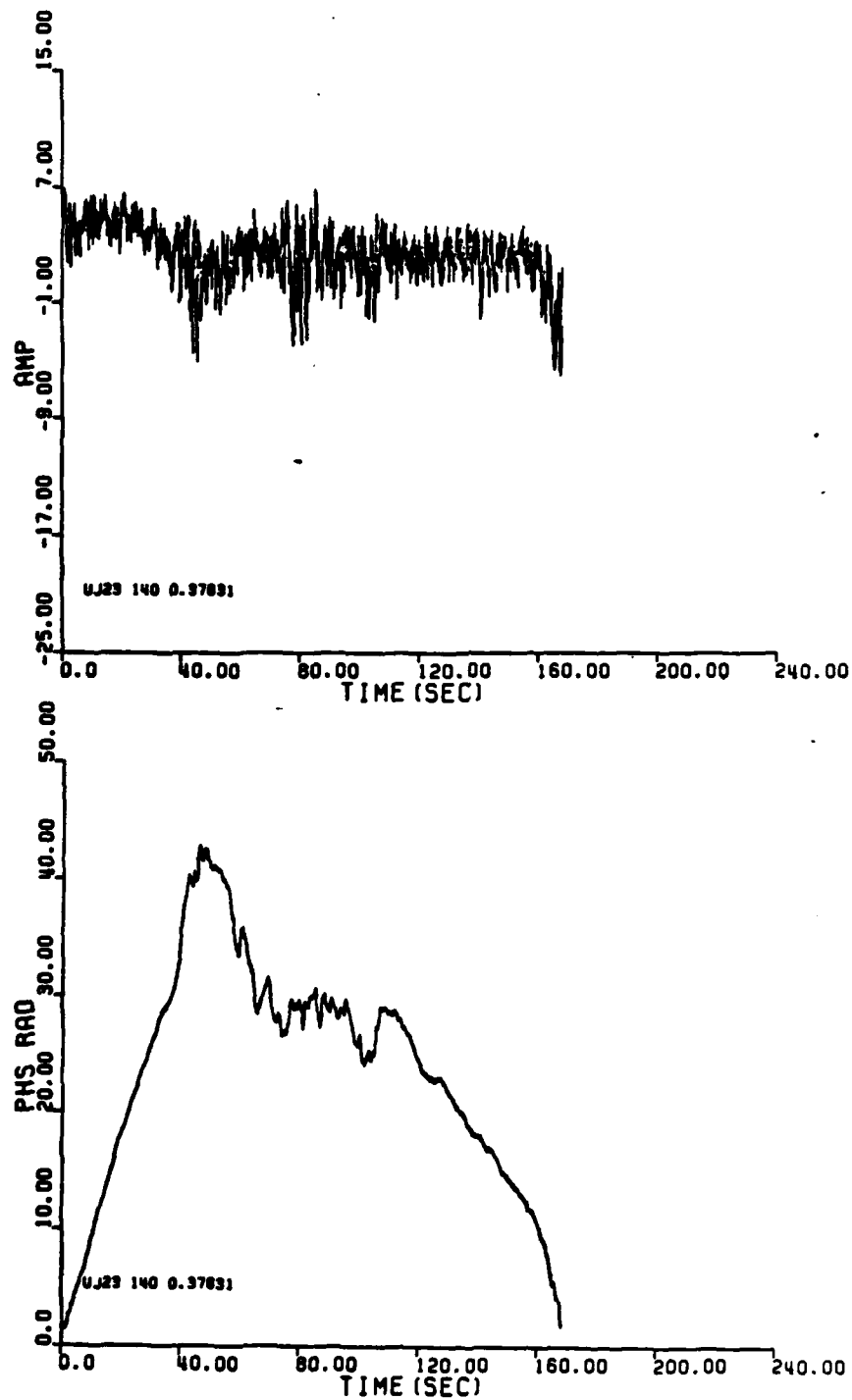


Figure 13-41. JAN Pass 23 Uplink Back-Propagated Amplitude and Phase at 140 Kilometers

phase structure on the right hand side appears to match rather well with the downlink back-propagated phase, including the prominent bifraction at the peak, as can be seen by comparing Figure 13-37 with Figure 13-10. The phase is plotted in Figure 13-37 for the uplink must be inverted. Significant diffraction effects remain on the left hand side of the peak phase where the agreement is not as good. The ratio of the downlink peak phase divided by the uplink peak phase ($34\pi/48\pi=0.71$) is nearly equal to the ratio of their propagation frequencies ($250/341 \text{ MHz}=0.73$) as it should.

The phase PSD's for the uplink and downlink are significantly alike. When overlayed the slopes are the same and both exhibit a slight bump around 0.2 Hz. The angular spectrum shown in Figure 31-39 and 13-12 differ, of course, due to the different propagation frequencies.

JAN Pass 23 back-propagated reasonably well as shown in Figure 13-40 and may be compared with Figure 12-17. If detrended and plotted to the same scale as the downlink this would more closely resemble the downlink data. Figure 13-41 shows the back-propagated phase and amplitude at a distance of 140 kilometers as opposed to the 120 kilometer distance of Figure 13-40. Generally this serves to illustrate that the phase structure is reasonably insensitive to the precise back-propagation distance provided that the residual phase interference fading effects are not too severe.

SECTION 14

REFERENCES

1. Dr. James Marshall, et.al.; PLACES Quick-Look Report for Beacon and Aircraft Experiments, DNA 5737F, 31 March 1981.
2. Roger Swanson, Dr. James Marshall, Allen Johnson, "PLACES Airborne Experiment," AFWAL-TR-81-1250, May 1982.
3. Dr. James Marshall, Jeff Lehman, Gary Elston, "PLACES Beacon Experiment Test Results," to be published.
4. Dr. C. Prettie, A. Johnson, Dr. J. Marshall, T. Grizinski, R. Swanson, Project STRESS Satellite Communication Test Results, AFWAL-TR-17-158, July 1977.
5. W. Boquist, "PLACES Ground Optics Project Preliminary Test Results," Technology International Corp., May 1981 (unpublished).
6. M. Keskinen, B. McDonald, and S. Ossakow, "Preliminary Numerical Study of the Outer Scale Size of Ionospheric Plasma Cloud Striations," NRL Memorandum Report 4124; 3 December 1979.
7. B. McDonald, S. Ossakow, S. Falesak, N. Zabusky, "Scale Sizes and Lifetimes of F-Region Plasma Cloud Striations as Determined by the Condition of Marginal Stability," NRL Memorandum Report 4383; 1980.
8. V. Gonzales, "Radar Tracking of Barium Ion Clouds: Results of the PLACES Experiment," DNA 5851F, August 1981.
9. Dr. C. Prettie, Private Communication, 12 March 1982.

APPENDIX A

AIRCRAFT EQUIPMENT CONFIGURATION

The aircraft equipment configuration used during the PLACES experiment is shown in Figure A-1. Also shown in Figure A-1 are the track assignments used in recording the data both on the Ampex AR-200 analog tape recorder and on the 8-channel strip chart recorders.

The format shown for the analog tape recorder was essentially the same as that used during the 1977 STRESS experiment. The 8-channel strip chart recorder format was new and intended to accommodate and display the uplink fading data together with the downlink data. The display of the K-band video spectrum was intended to provide a reference as to the strength of K-band lock and it divides the uplink and downlink data on the chart display. In addition, a lock indicator of the K-band receiver was remoted to a marker pen. The log envelope output on the uplink tone processor had degraded to the point where it was believed to be of marginal quality, and thus was not recorded. The aircraft heading data from the INS was recorded on a digital tape recorder. The K-band antenna azimuth and elevation was displayed on the strip chart and recorded on the analog tape recorder.

The Dorne Margolin antenna was used for the UHF LES-8 uplink. The uplink power was set to a point approximately 6 dB below saturation at the satellite. The Collins Crossed Dipole was used for receipt of the UHF LES-8 downlink tone.

The downlink tone and a 1 kHz reference tone ($\text{PRE-D} + 1 \text{ kHz}$) were sent over a 500 kHz channel on the Atlantic FLTSATCOM (23°W) satellite to the CCF Mission Control at Eglin AFB. This was the same signal as recorded on Track 10 of the analog recorder. It was FM modulated using a 10 kHz zero to peak frequency deviation under non-fading conditions. Using a 50 kHz IF receive bandwidth at the Eglin ground station, a peak signal enhancement (focus) of approximately 9.5 dB

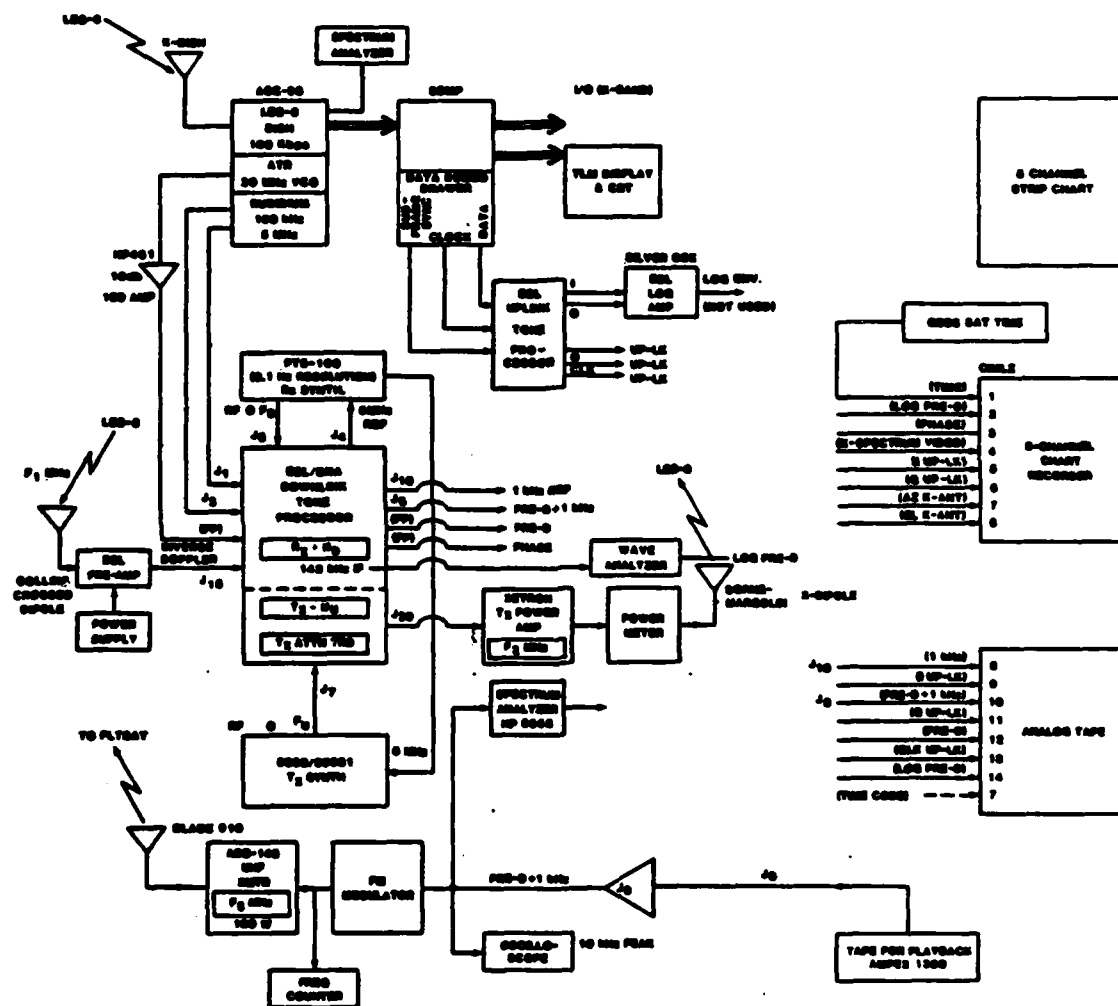


Figure A-1. Aircraft Equipment Configuration

could be accommodated without distortion. An AGC was not used at the modulator, otherwise long signal enhancements (focus and defocus) would not be accurately reproduced. A blade antenna on the top side of the aircraft was used for this link together with the ARC-146 transmitter. Approximately 100 watts of the 1 kW available transmitter power was required on the FLTSATCOM link.

The K-band receiver provides the K-band doppler to the downlink tone processor on a 20 MHz VCO output. The K-band receiver also demodulated the I-Q uplink samples sent down on this K-band link. These samples were output to the uplink tone processor along with subframe sync and clock data.

APPENDIX B

DATA PROCESSING AND DISPLAY OVERVIEW

B-1 DOWNLINK TONE PROCESSING.

The downlink tone data was processed in essentially the same manner during PLACES as during STRESS. The analog tape had a reference signal modulated at 1 kHz and the fading signal modulated at 500 Hz. The reference signal was stripped off and used as the clock for digitizing the 500 Hz fading signal at 4 kHz, thus, removing tape playback frequency errors from the fading signal. The digitized data was then put through a 500 Hz digital phase lock loop (DPLL) the output of which was used to down-convert the original data to baseband from 500 Hz. The baseband data was then put through a 15 Hz 2-pole Butterworth filter, removing the 1 kHz residual from the DPLL cosine demodulation and some of the high frequency noise on the signal. The fading data spectral bandwidth is generally much less than 15 Hz, thus, the phase shifting characteristics of a Butterworth filter does not affect the desired signal. This data was then down-sampled by a factor of 40 to 100 Hz and stored on disk as the final data to be plotted and propagated. See Appendix C for a more detailed explanation of the processing.

B-2 UPLINK TONE PROCESSING.

The uplink data was processed identically during PLACES as during STRESS. A detailed description can be found in Appendix D. Some additional processing was done on the HOPE uplink data which was not done on any other PLACES data. The HOPE uplink data had much more noise than desired between 10 and 30 Hz. This was removed by convolving the time signal with a rect function which was 8 samples long. This is equivalent to multiplying the angular spectrum by a sinc^2 with its first zero at 12.5 Hz. This additional processing brought the noise down considerably and left the lower frequency signal relatively untouched. Plots of HOPE

Pass 20 uplink before and after this processing, including their power spectrums, are shown in Figures B-1 through B-6.

B-3 BACK-PROPAGATION PROCESSING.

The back-propagation processing was done identically during PLACES as during STRESS. This processing is explained in detail in Appendix E.

B-4 AMPLITUDE PLOTS.

The amplitude plots were made by converting the amplitude squared data into dB and scaling such that the average power was 0 dB. All 2048 point data records were plotted by connecting each point by straight lines. Generally each plot consists of about four to eight records. The amount in dB by which the amplitude was scaled to achieve an average power of 0 dB is given on the left axis of each amplitude plot. This provides a measure of the relative received signal power from pass to pass at the 0 dB level on the amplitude plot.

B-5 PHASE PLOTS.

The phase plots were made by first converting the phase from Modulo 2π to continuous phase and linear detrending. In most cases, the linear trend was small being less than 10π radians. This data was then plotted by connecting all of the points with straight lines.

B-6 ANGULAR SPECTRUM PLOTS.

The angular spectrum plots were made by 1) converting the signal to amplitude and phase components, 2) changing the phase from Modulo 2π to continuous, 3) linear detrending the continuous phase, 4) recombining the amplitude and phase, and 5) fast Fourier transforming this data. The resultant was then 6) magnitude squared, 7) summed and divided by 2 such that the negative and positive frequency points were folded on top of each other yielding only positive frequency components, and 8) plotted on log-log plot. 2^N (8192 or 16,384) original signal points were used in all cases, with N normally equaling 13 or 14.

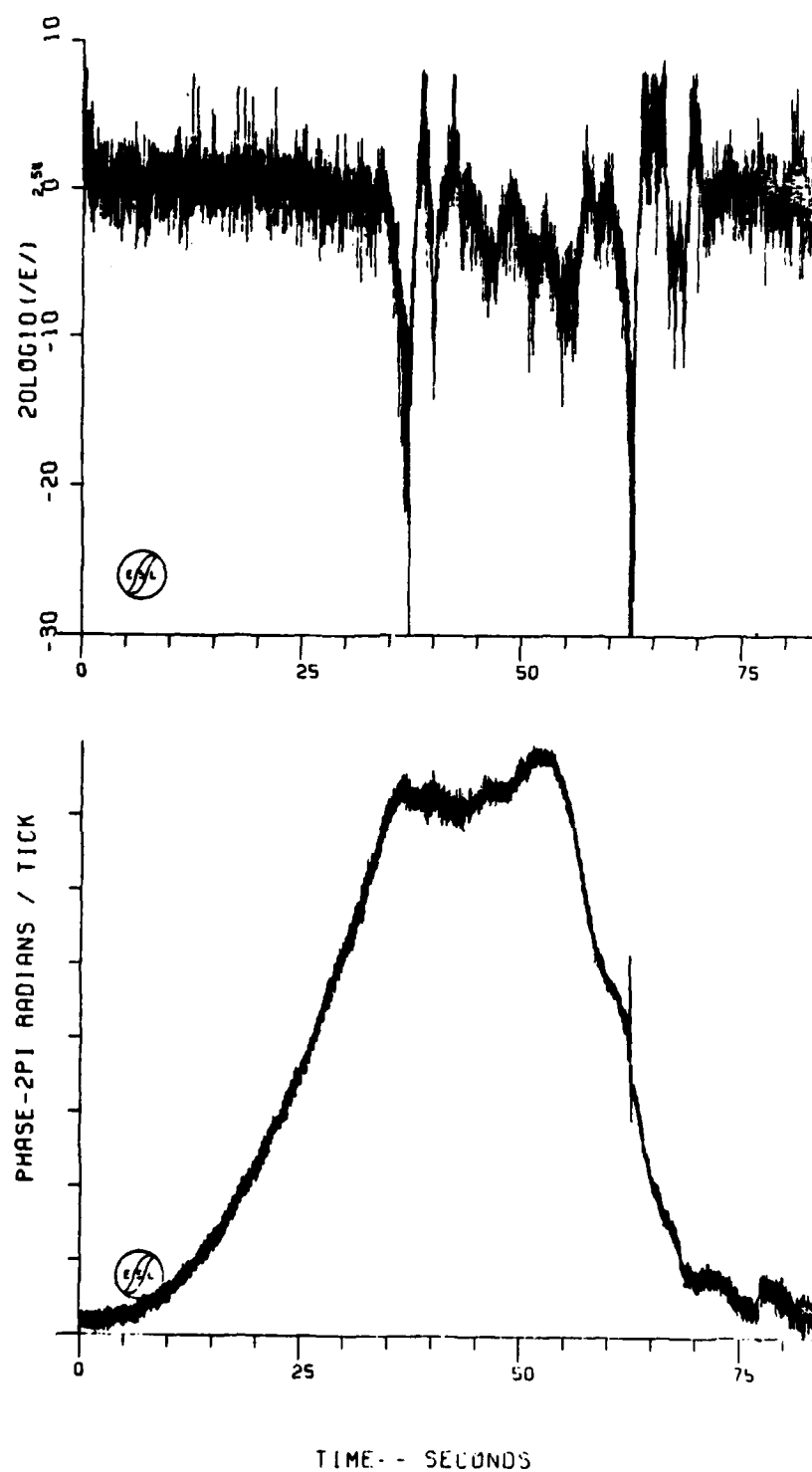


Figure B-1. HOPE Pass 20 Uplink Amplitude and Phase Before Filtering

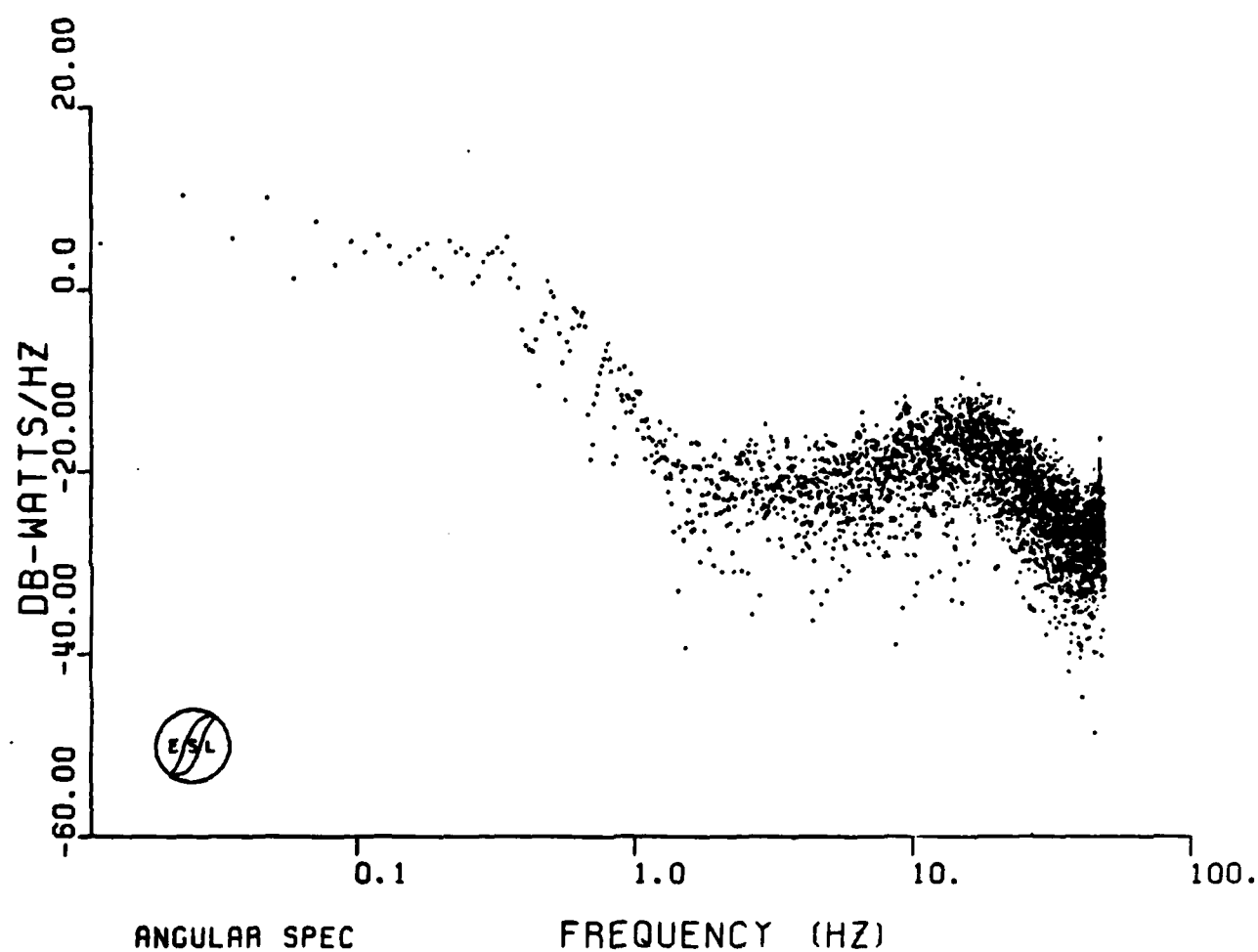
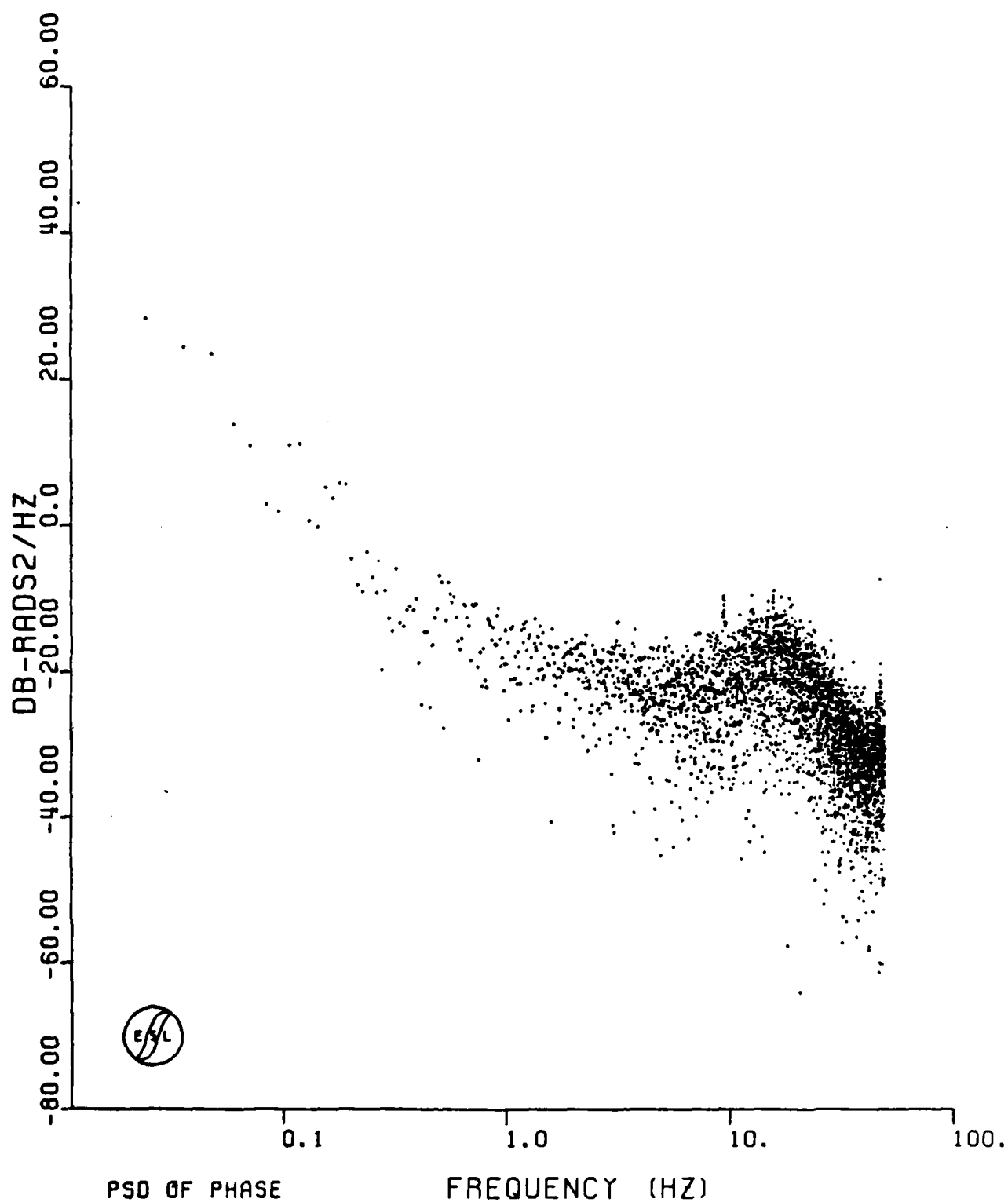


Figure B-2. HOPE Pass 20 Uplink Angular Spectrum Before Filtering



PSD OF PHASE

FREQUENCY (HZ)

Figure B-3. HOPE Pass 20 Uplink Phase Spectrum Before Filtering

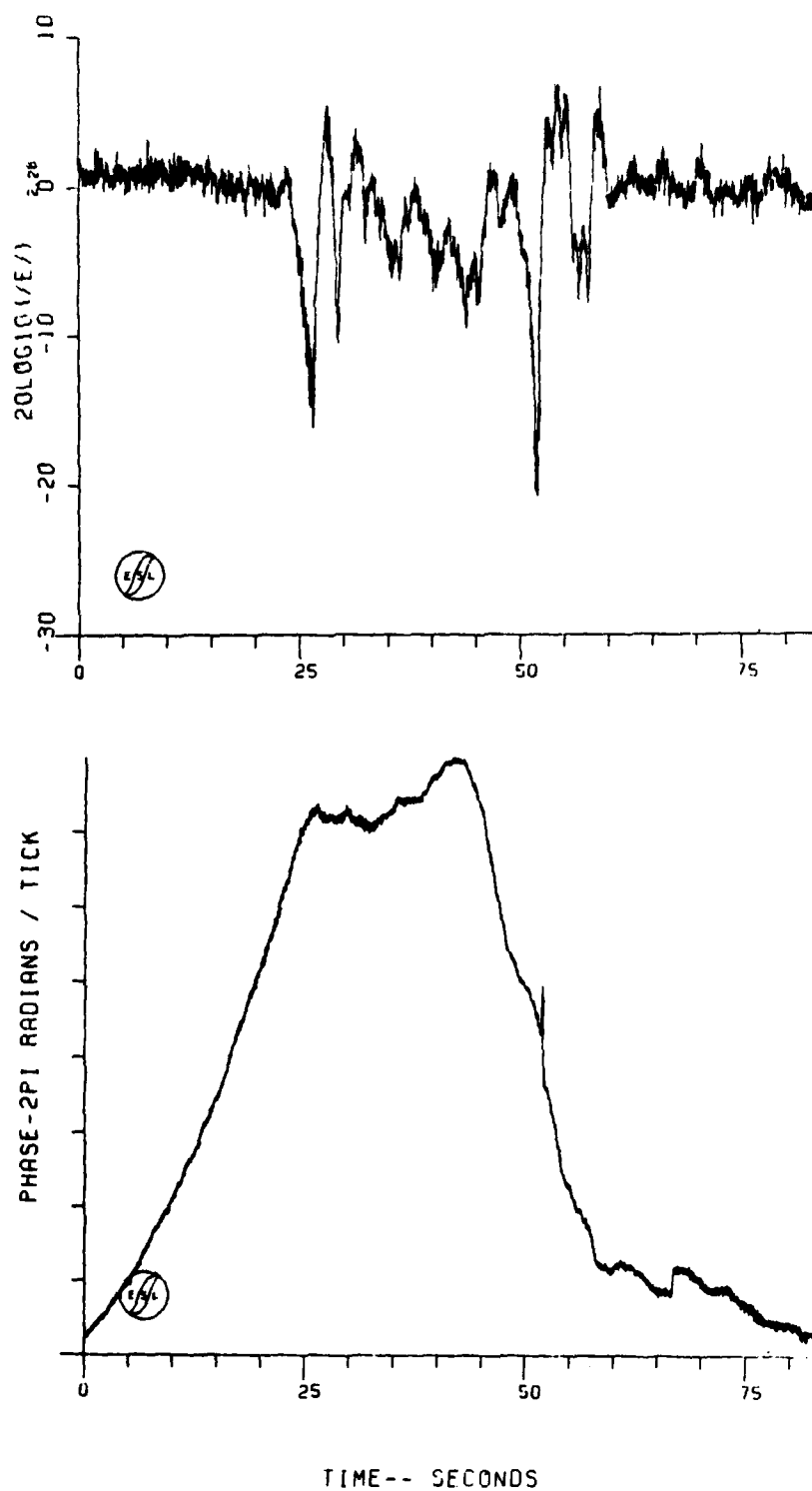


Figure B-4. HOPE Pass 20 Uplink Amplitude and Phase After Filtering

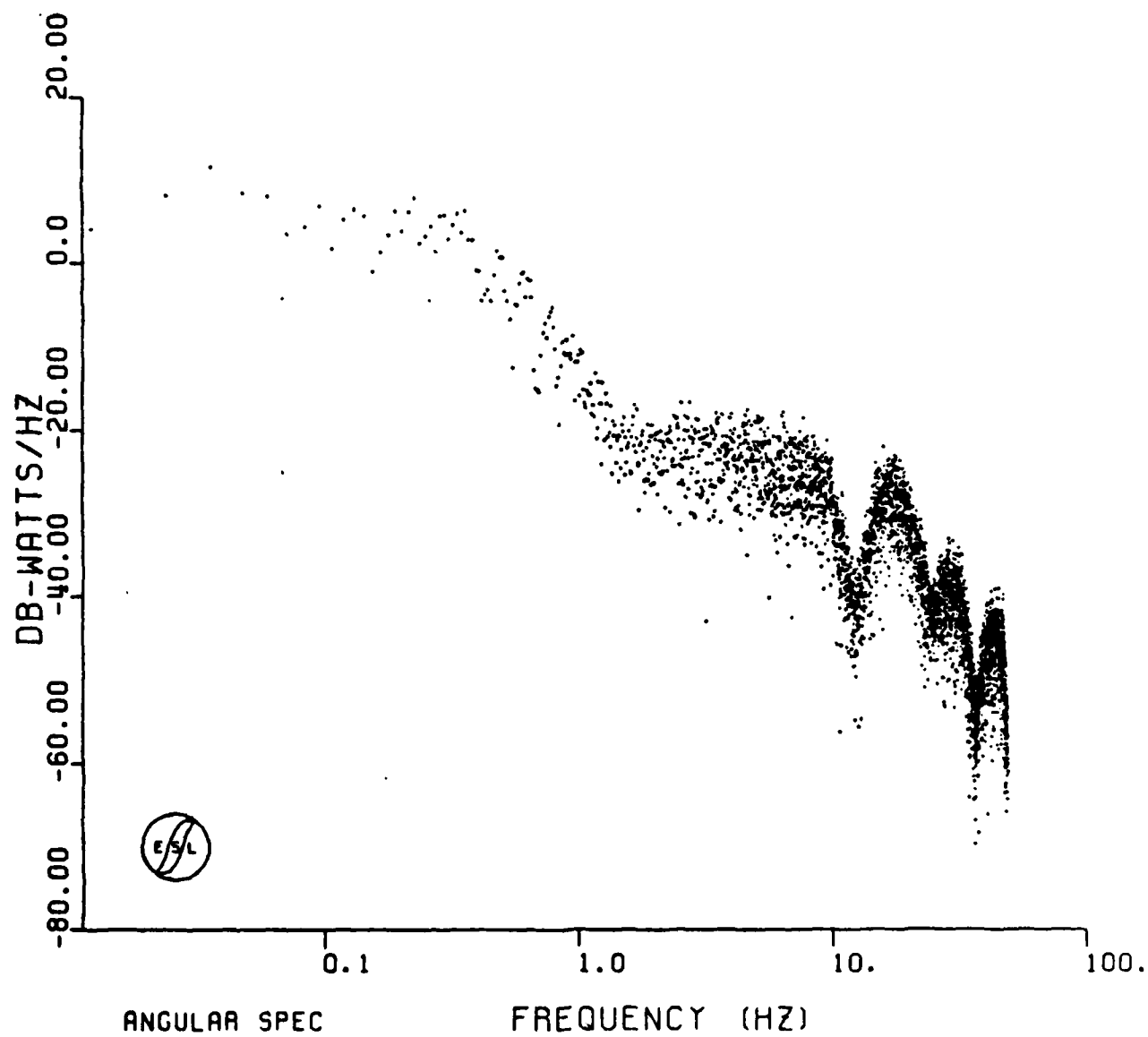
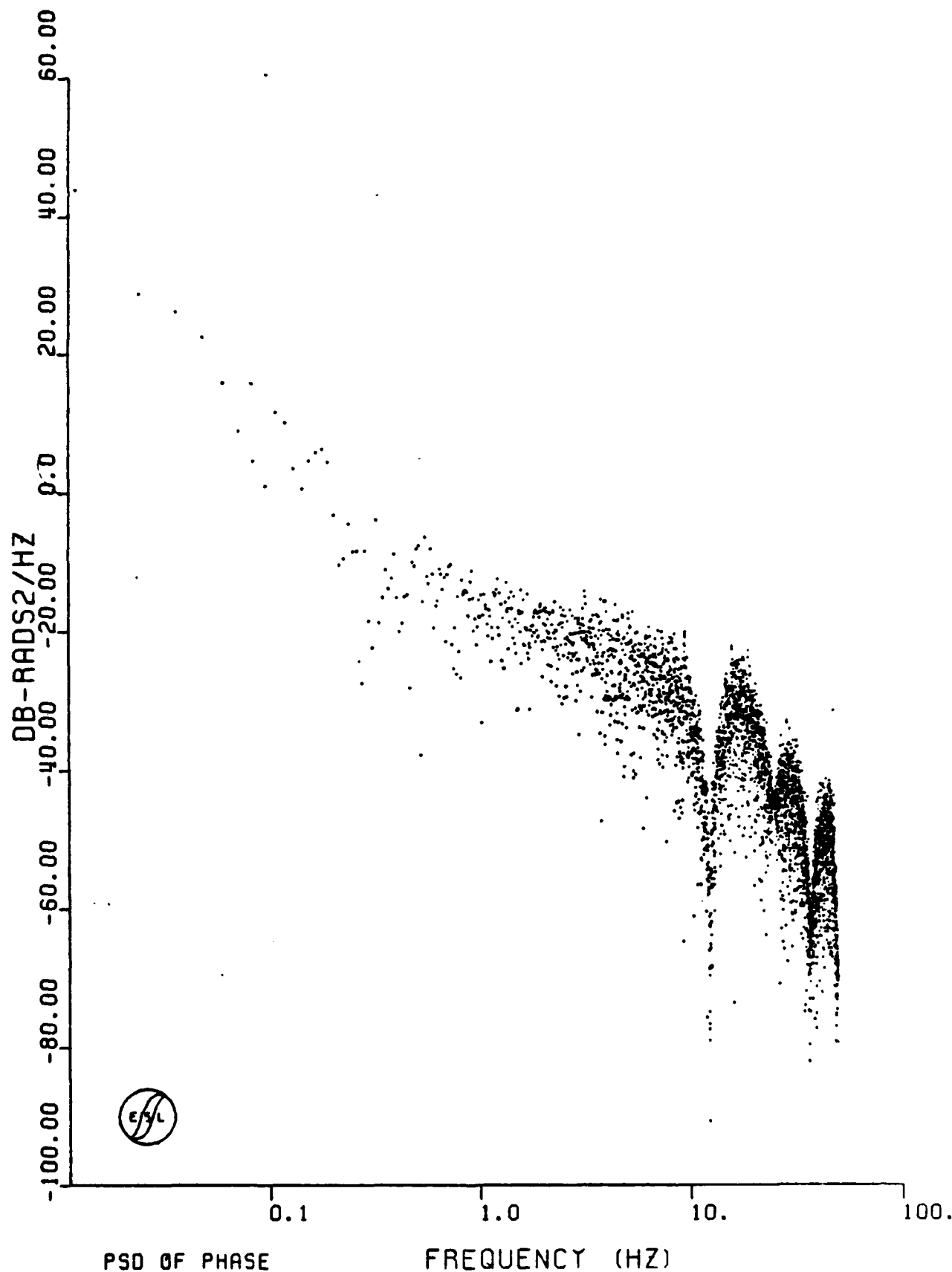


Figure B-5. HOPE Pass 20 Uplink Angular Spectrum After Filtering



PSD OF PHASE

FREQUENCY (HZ)

Figure B-6. HOPE Pass 20 Uplink Phase Spectrum After Filtering

APPENDIX C

DOWNLINK TONE DATA PROCESSING SUMMARY

C-1 INTRODUCTION.

This appendix is included to provide a basic understanding of the data processing performed on the downlink tone. Link calculations are provided in Appendix F.

C-2 DOWNLINK TONE PROCESSING.

The measurement of phase data on the downlink tone is made possible by phase referencing the UHF tone to signals divided down from the LES-8 or LES-9 100 Kbps K-band doppler signals shown conceptually in Figure C-1. The downlink tone fading is measured, recorded and processed as shown in Figures C-2 and C-3.

Recordings of the down-converted doppler corrected signal is the real time output of each flight test. The UHF signal is down-converted to a frequency that is nominally 500 Hz. Recorded on the same FM tape track is a 1 kHz reference tone. The same 1 kHz reference tone is also recorded alone on a separate tape track. Analog tape data is processed after the test in the ESL Tape Center. The analog 500 Hz plus 1 kHz track is 8-bit digitized at a 4 K sample per second rate and stored on digital tape for subsequent computer processing. The nominal level of the 500 Hz signal on the tape is equal to the 1 kHz reference signal level during nonfading signal conditions.

The IBM 370 software demodulator program shown in Figure C-3 is used to convert the digitized analog data into a format suitable for plot generation and back-propagation. The output of the demodulator software is the amplitude and phase of the envelope of the 500 Hz data sampled at a 100 sample pairs per second rate and formatted into 2048 point files. Plots of the amplitude and phase are generated by a subsequent software routine as shown in the figure, and are back-propagated. The purpose of the processing indicated in the demodulator software

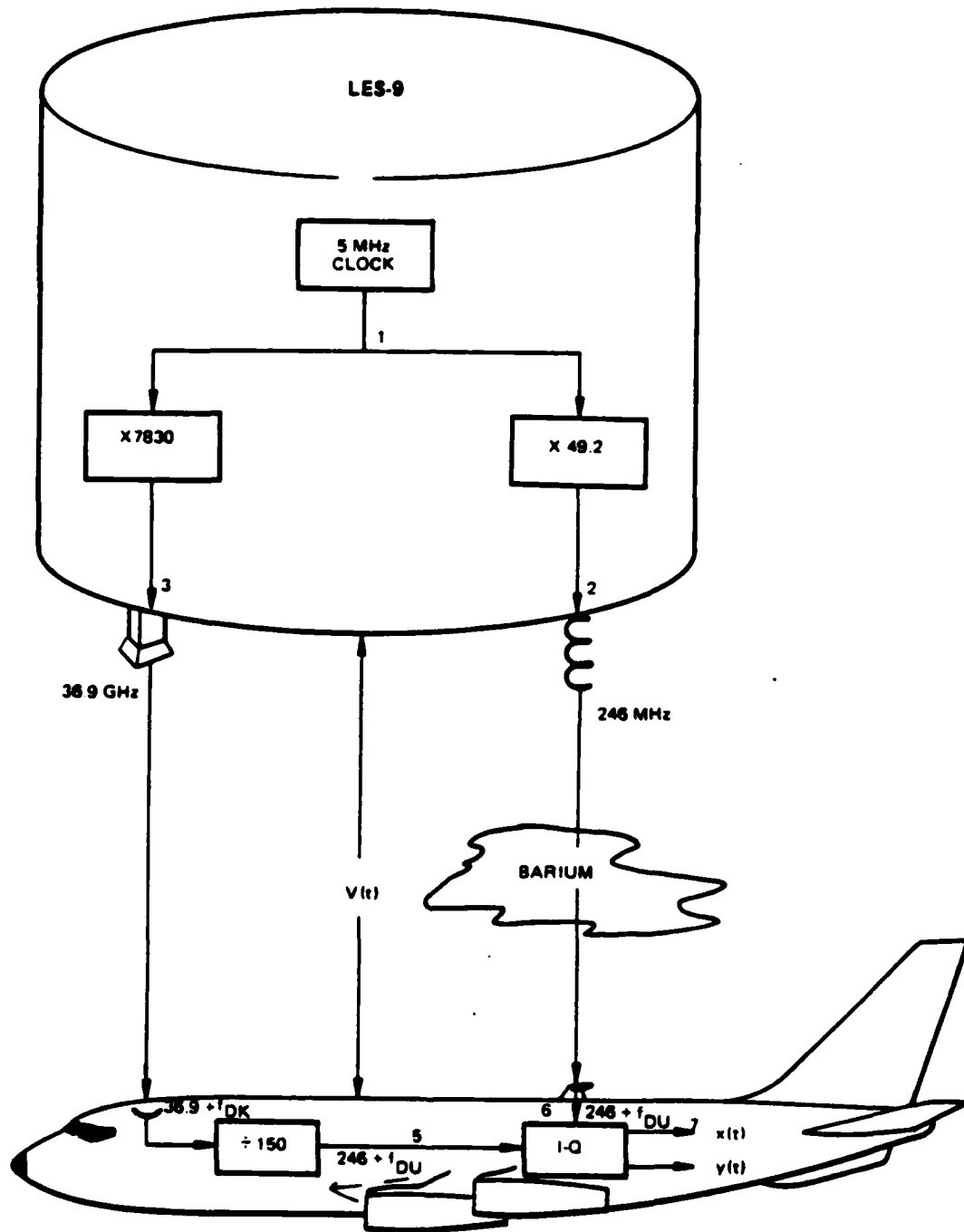


Figure C-1. Conceptual Downlink Data Doppler Correction

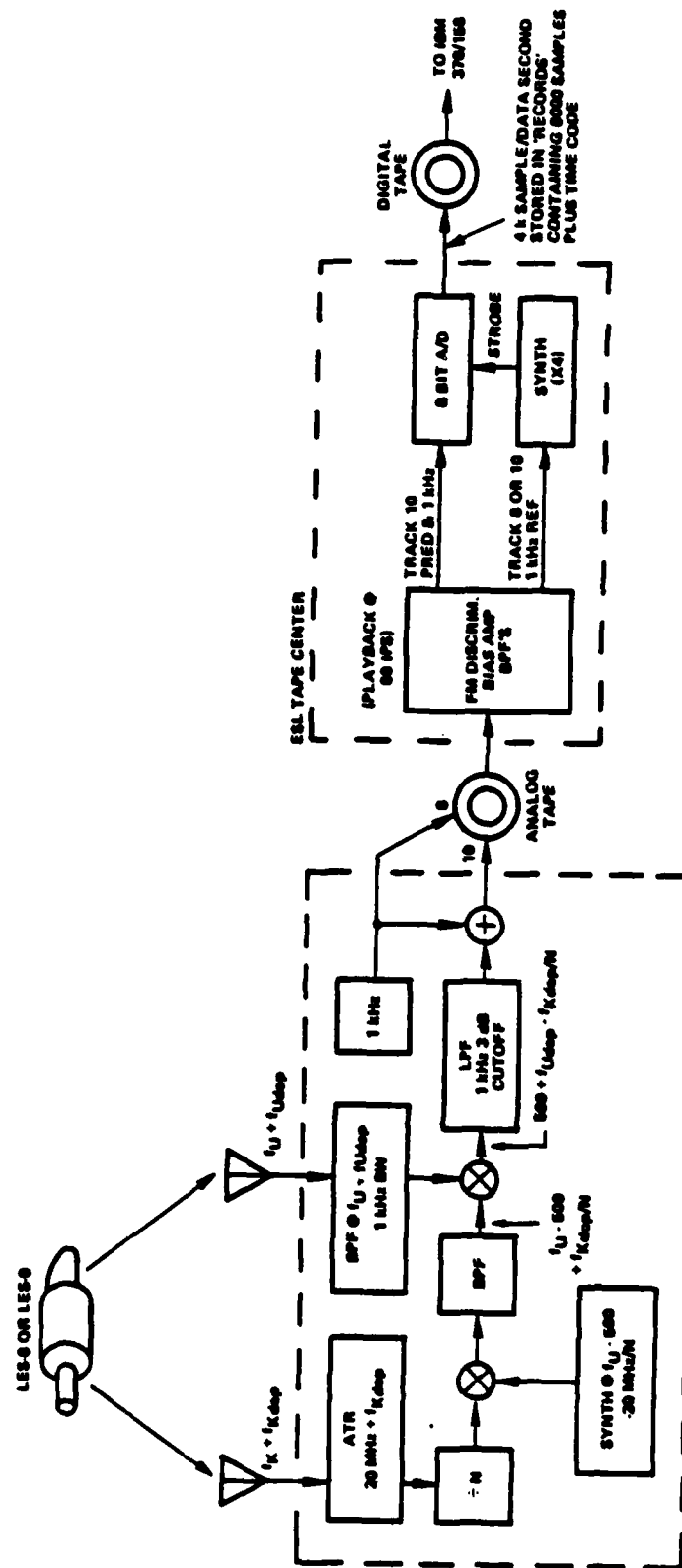


Figure C-2. Conceptual Measurement of Downlink Tone Fading from LES-9. Note that in Use with LES-8 the Output of the ATR is Conceptually $f_u - 500 + f_{k_dop}/N$ and the Intermediate Doppler Inversion Process is Bypassed

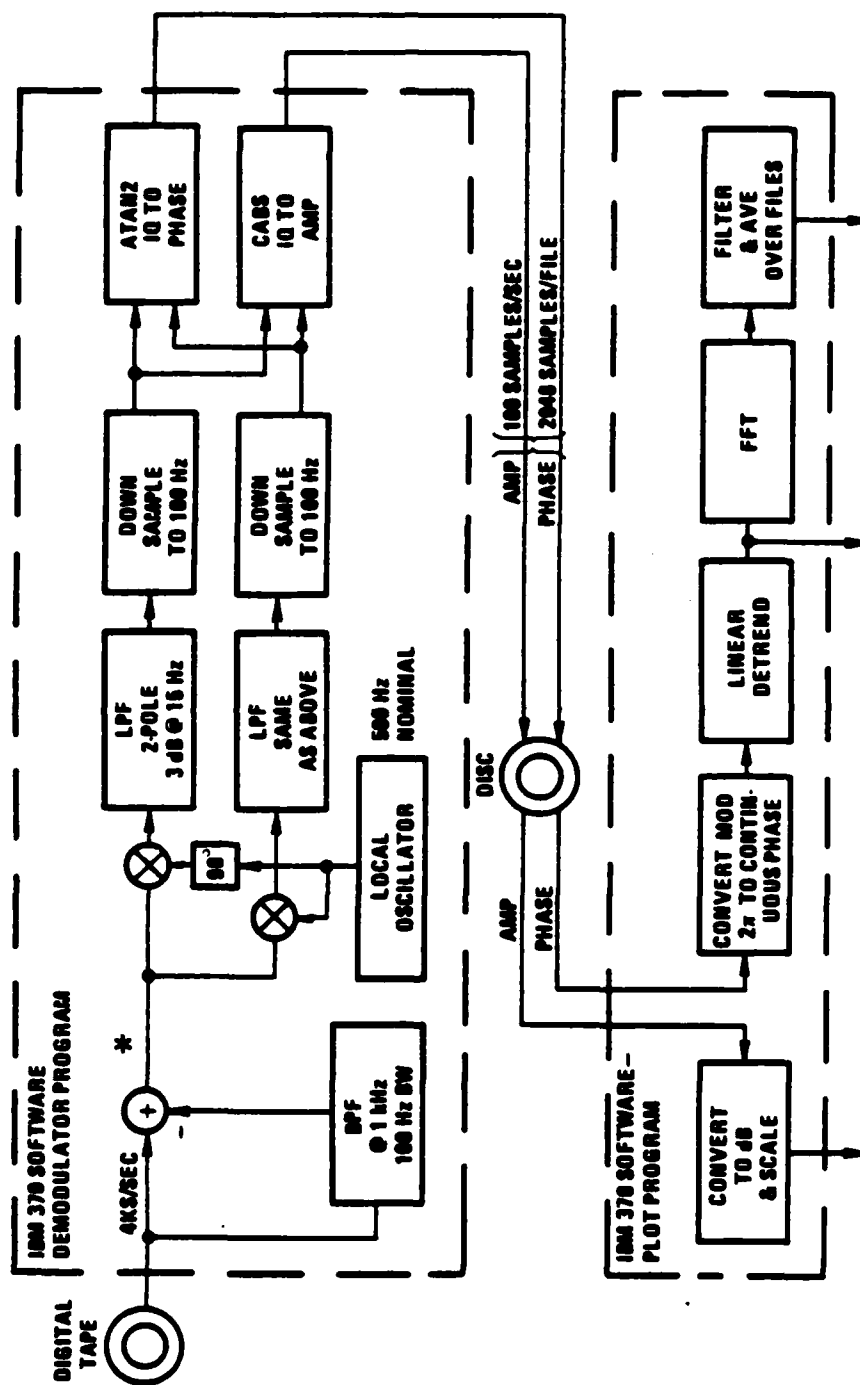


Figure C-3. Software Processing of the Downlink Tone Fading Data

block diagram is straightforwardly understood, with an exception perhaps of the 1 kHz bandpass notch filter. The purpose of this filter was to strip out the 1 kHz signal from the data stream to allow automatic local oscillator frequency determination by zero-crossing software (not shown) from signals at the asterisk. This software is necessary if the residual frequency error on the downlink is large. The data recorded during PLACES was sufficiently close in frequency to the nominal 500 Hz value that automatic local oscillator frequency determination was not needed. The local oscillator frequency settings provided at the aircraft minimize the need for this correction.

2000
2001

APPENDIX D

UPLINK TONE DATA PROCESSING SUMMARY

D-1 INTRODUCTION.

This appendix is included to provide a basic understanding of the data processing performed on the uplink tone. Link calculations are provided in Appendix F.

D-2 UPLINK TONE PROCESSING.

Obtaining data from the aircraft uplink to the LES satellites involves a significant amount of data processing. The aircraft transmits signals that are doppler precorrected in a manner figuratively illustrated in Figure D-1.

The systems on the satellite which process the UHF uplink tone transmitted from the aircraft are shown in Figure D-2. The signal received at the satellite is amplified by the UHF FRONT END. The DOWN-CONVERTER down converts the signal from UHF to HF. The "SAMPLES" BASEBAND CONVERTER hard limits the signal, down-converts it to baseband, and converts the coherent and quadrature outputs of the baseband down-conversions to digital data streams using 1-bit sampling (hard quantizing). The SIGNAL PROCESSOR formats the sample data stream together with synchronization and telemetry data. The formatted data is DPSK modulated and sent via K-band back down to the aircraft. The K-dish system must be used to transmit the high data rate required.

Figure D-3 shows in more detail the DOWN-CONVERTER and the "SAMPLES" portion of the BASEBAND CONVERTER. The DOWN-CONVERTER acts as simple mixer and merely translates the uplink UHF signal down in frequency. The actual DOWN-CONVERTER on the satellite is more complex than that illustrated but the effective translation is the same. The first BPF of the BASEBAND CONVERTER filters the translated signal to a bandwidth of 75 kHz. The hard-limiter system (HL/FIL)

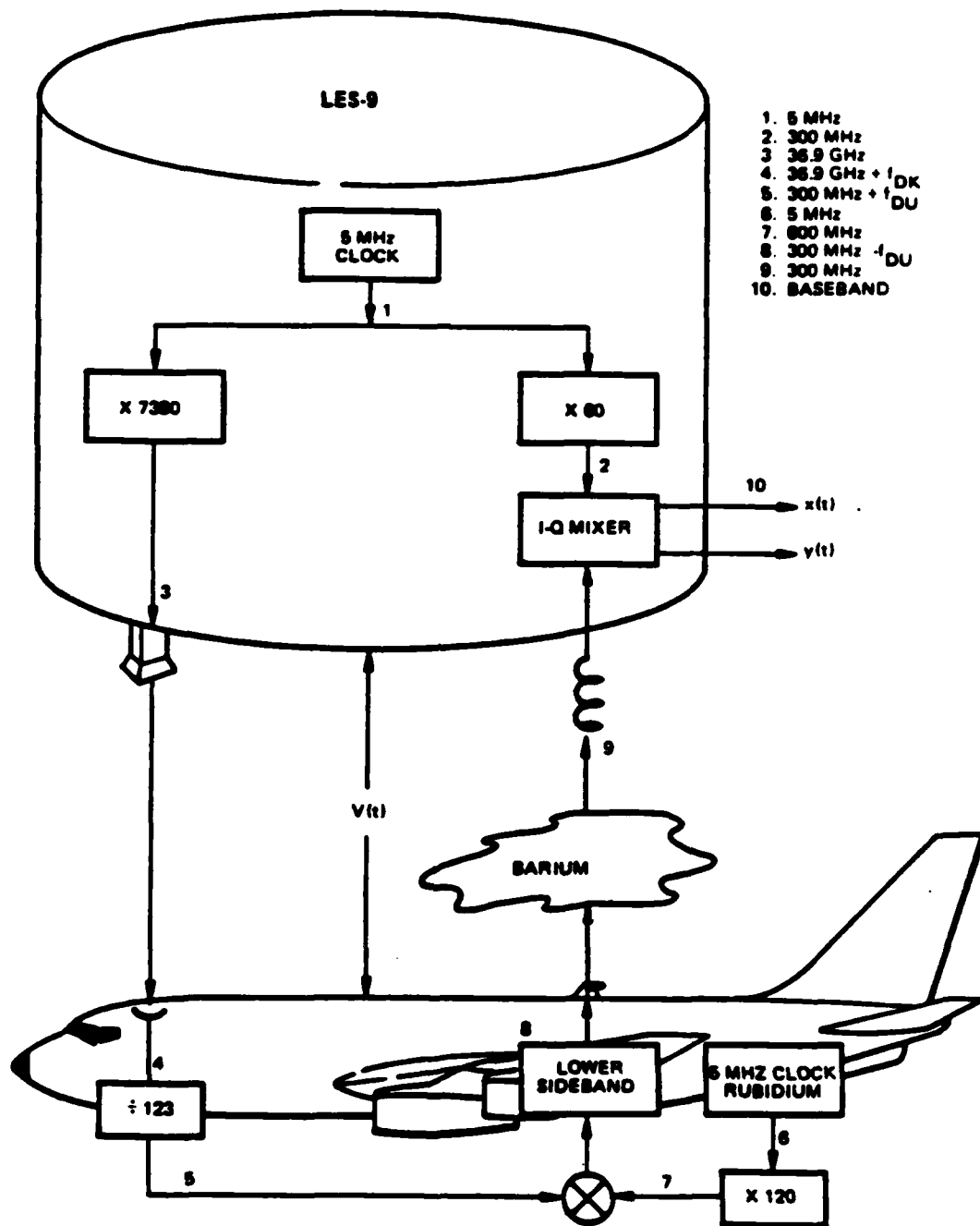


Figure D-1. Simplified Uplink Doppler Correction

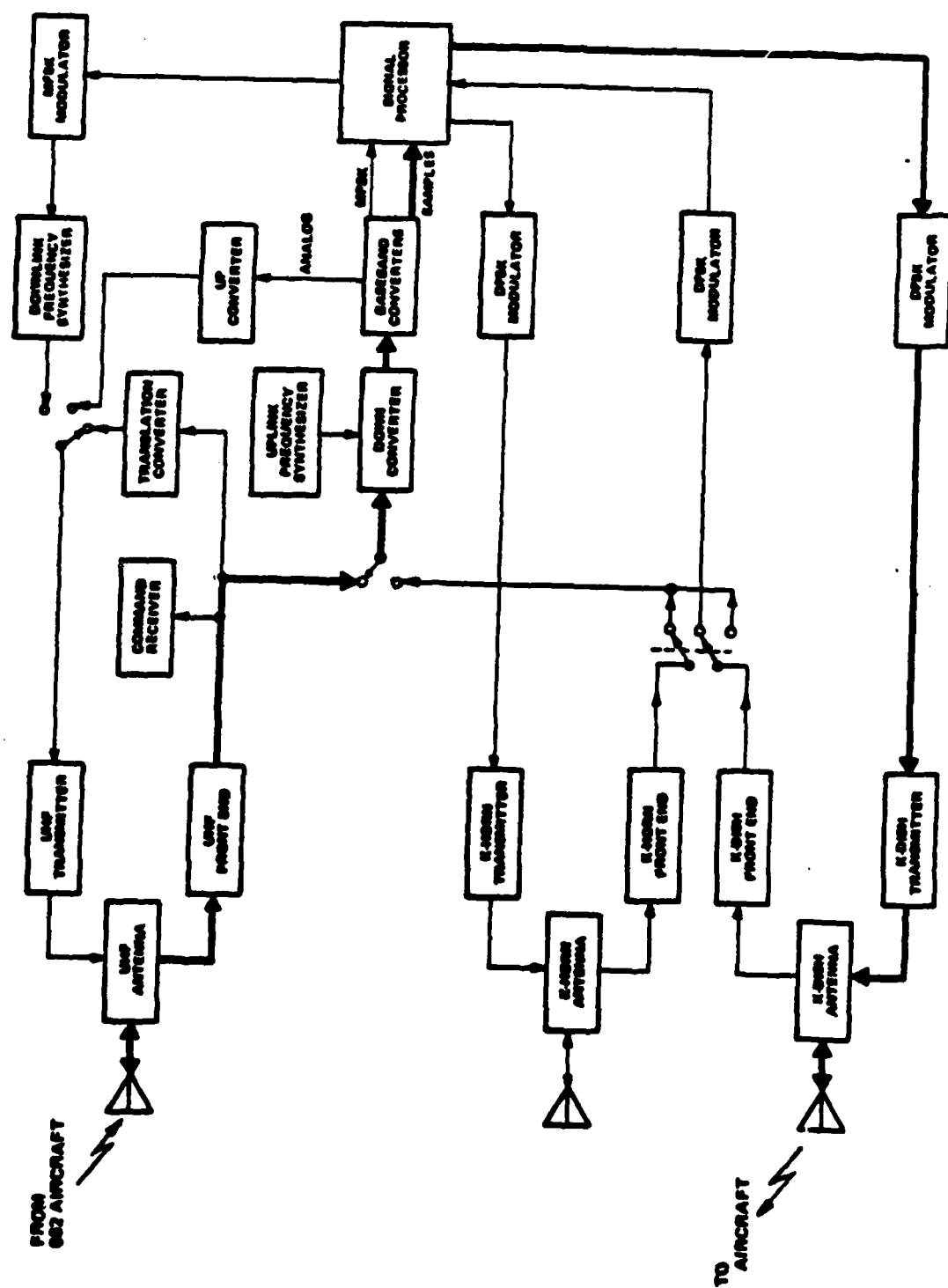


Figure D-2. Uplink Data Tone LES Satellite Signal Path

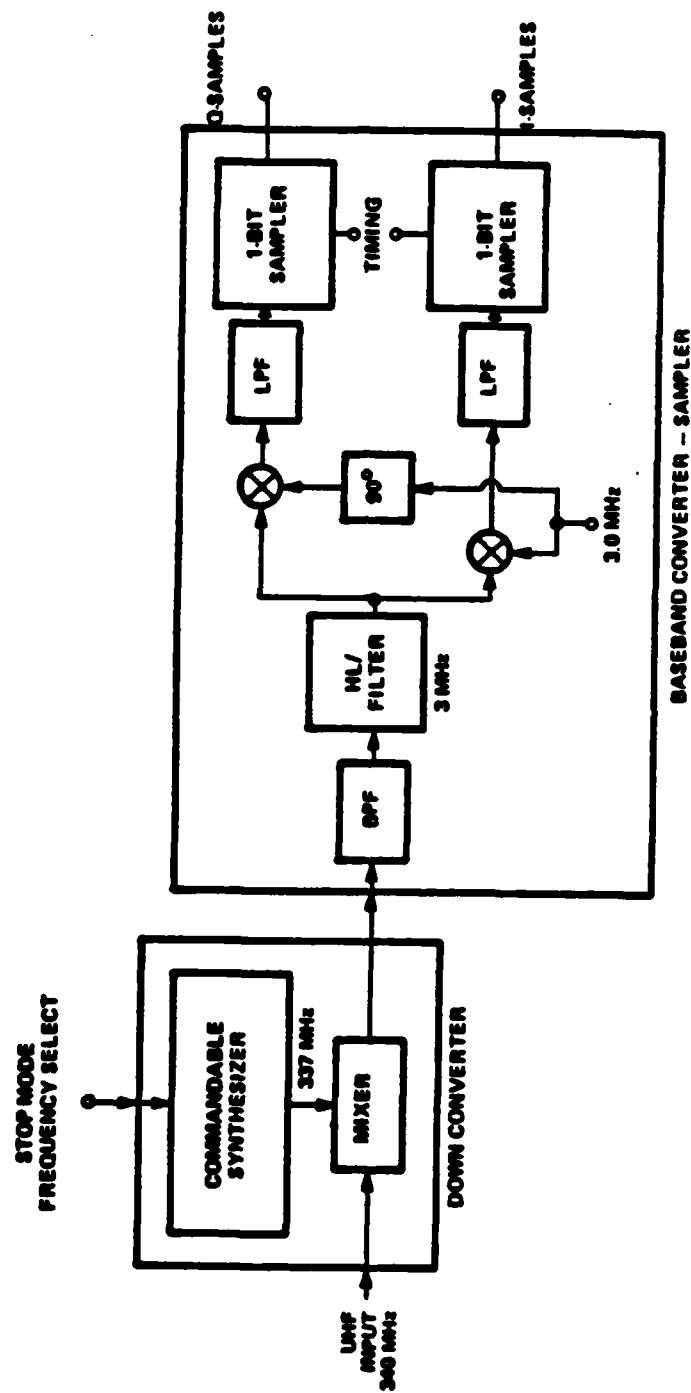


Figure D-3. Satellite Down Converter and Sampler

hard limits the received signal and filters out the higher frequency components from the hard-limiter output. The signal is then mixed down to baseband with an I-Q mixer. The I arm and Q arm signals are low-pass filtered to a cutoff frequency of 35 kHz before they are 1-bit sampled each at a 50 kilobit per second rate.

The SIGNAL PROCESSOR uses a 50-bit frame format into which the I and Q samples are put. The first bit position is for the SYNC bit which is always a "1" and is conventionally used by the report-back and crosslink demodulators to achieve frame synchronization. The next bit position is dedicated to bits of the forward message. The third and fourth bit positions are dedicated to telemetry information and the fifth through fiftieth bit positions carry the I and Q samples alternating between I and Q. In the formatting process, some of the I and Q samples from the BASEBAND CONVERTER are dropped in order to accommodate the bits in the 1 through 4 bit positions. Two out of 25 bits are lost from both the I and Q channels in this manner. The effective I and Q data rates are, as a consequence, each decreased to 46 kilobits per second.

This transmitted data stream is to be demodulated and processed at the aircraft for eventual recovery of the inphase and quadrature signals. The technique used in recovering the signals from the hard quantized data relies on the fact that the diffracted field received at the satellite is of a low power, comparable to the received noise power. As each bit in the sample stream is a measure of whether or not the signal plus noise voltage at some instant of time is greater than 0, the summation of a number of these bits over an interval represents a probability estimate of this voltage being greater than 0 within that interval. It is this computed probability that will be used to recover the original I and Q signals. The block diagram for the aircraft processing is contained in Figure D-4. In the aircraft the demodulated data stream is sorted and serially fed into a pair of 256 bit shift registers and UP/DOWN counters. By comparing the delayed bit from the shift register with a current bit from the I/Q sort, the counters generate a running sum of the number of 1's in a 256 bit window. The counter output is then

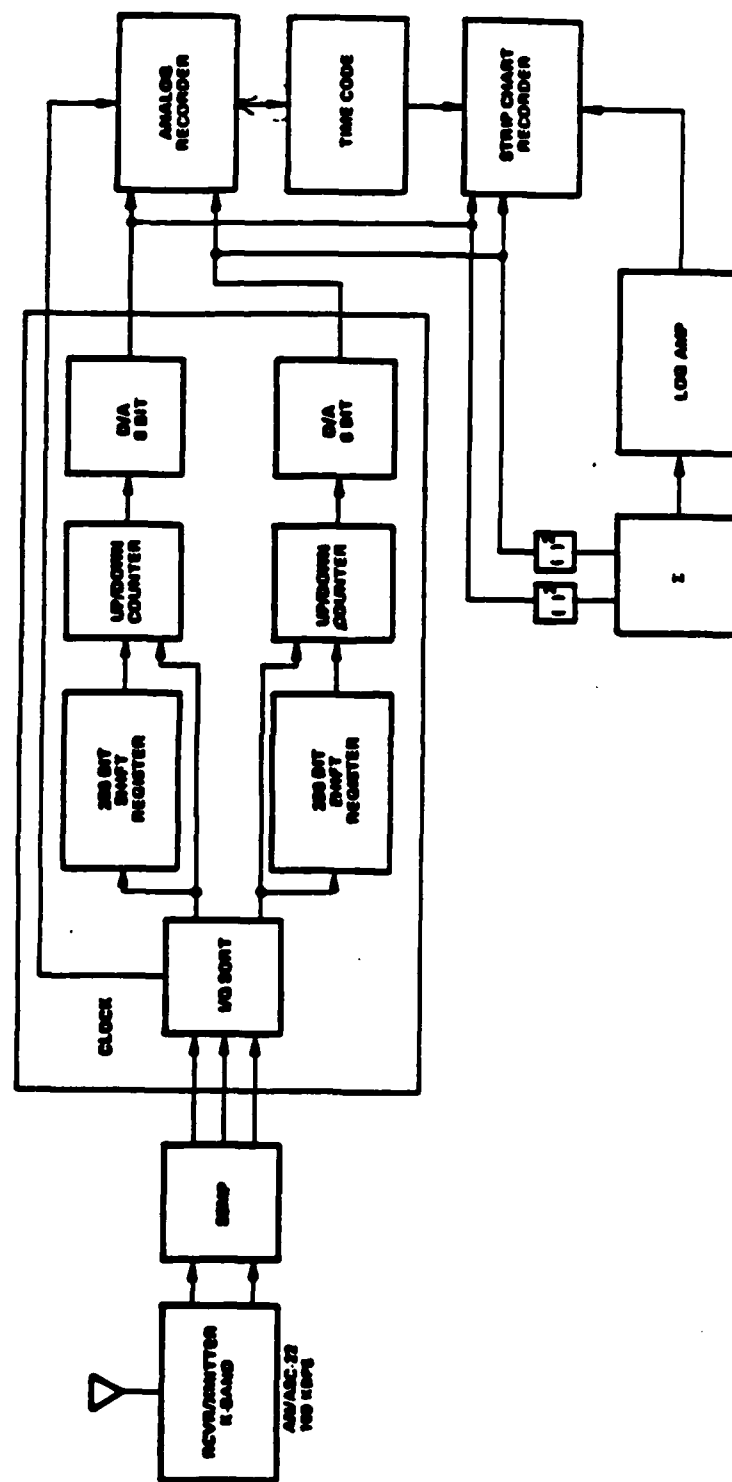


Figure D-4. Aircraft Equipment for Uplink Tone Data Processing

converted once every 2.78 milliseconds to an analog voltage, displayed on strip chart, and FM recorded on analog tape along with time frame data. Computer implemented processing to follow this step treats the recorded data as probability estimates made over the window time frame. At the incoming data rate of 46K bits per second this 256 bit window derives its probability estimate from a 5.56 milliseconds window.

At ESL, the recordings of the samples are processed to estimate the propagation parameters of interest by estimating the voltages in the I and Q channels at the satellite. The SYNC bit will be identified and the bits in the first 4 bit positions of the frame will be ignored. The I samples will then be separated from the Q samples, the two streams being used to estimate the coherent and quadrature components of the diffracted signal envelope.

The I and Q samples carry information about the signal amplitude and phase statistically. The tone transmitted by the aircraft is intentionally given a relatively low output power level so that the signal strength at the satellite is about equal to the noise power in the hard limiter - hard quantizer processing bandwidth. Decisions of the hard quantizer are thereby influenced not only by the signal but also by the noise. The noise is almost independent from sample to sample and influences each decision independently. The signal strength in either the I or Q channel is slowly varying and for this reason the signal influences many consecutive decisions. By noting the trend of the samples over periods when the signal is approximately constant, not only can the presence of the signal be detected, but its strength relative to the noise power can also be evaluated. This fact is the basis of the data reduction scheme to be used to measure amplitude and phase.

Recovery of the signal can be demonstrated by considering a function of the form;

$$s(t) = A+n(t) . \quad (1)$$

Here A represents the I or Q channel signal and $n(t)$ is the white Gaussian noise of variance σ^2 present in the channel. For the case of concern, I and Q may be taken as constant since the dependency of the barium induced fluctuations on time is much slower than the variation of the noise. Over the 5.56 milliseconds window over which probability is estimated, A is essentially constant. The data obtained for the uplink configuration confirms these assumptions.

As $n(t)$ is a zero mean Gaussian noise process over the processing bandwidth, the probability that $s(t)$ is much greater than 0:

$$P[s(t) > 0] = \frac{1}{\sqrt{2\pi\sigma^2}} \int_{-A}^{\infty} e^{-x^2/2\sigma^2} dx . \quad (2)$$

If a quantity \hat{p} is now defined as the function of samples in a string of samples (the 256 sample window) that are greater than 0, it will approximate the above probability. The output realized by the up-down counters, scaled by 256, is this estimate. It remains to implement the inverse of the above equation so that A can be obtained from \hat{p} . Rearranging Equation (2) yields:

$$P[s(t) > 0] = \frac{1}{\sqrt{2\pi}} \int_{-\infty}^{A/\sigma} e^{-x^2/2} dx$$

equivalently:

$$\hat{p} = \frac{1}{\sqrt{2\pi}} \int_{-\infty}^{A/\sigma} e^{-x^2/2} dx . \quad (3)$$

Software processing uses Equation (3) to generate a table of values of \hat{p} and A/σ from which the ratio of I or Q to noise variance can be obtained from \hat{p} . Noting that this method actually obtains A/σ and that σ is constant, the final amplitudes estimated are seen to be linearly scaled from the actual values.

Processing begins with the development of histograms representing the probability windows realized on the digital tape. As mentioned earlier, this initialization step is necessary due to channel imbalances encountered in the steps leading up to the generation of the digital tape. Although these windows would be expected to have values from 0 to 256 distributed about the midpoint of this interval, this distribution is not realized. Computation of the histogram allows a determination of the actual window limits. As an example, it may be found that the histogram reveals values only in the range of 30 to 150. It is evident that a net channel gain of less than unity and a negative offset have appeared in the data. The initialization step, where the histograms are determined, compensates for this by indicating to the generation step the correct limits for the look-up table that it forms. A flow chart of the software for the initialization step appears in Figure D-5. Finally it is noted that a data reduction by a factor of 4 is also performed on this data. This step is the summing of 4 probability estimates to yield a single estimate and resulting window width of 1024. Summation is provided to suppress high frequency noise in the reconstructed data. The look-up tables are actually created from this wider window.

Figure D-6 presents the flow chart of the program that generates the recovered in-phase and quadrature signals and writes them to disk. Look-up tables are first generated from the window widths provided by the initialization procedure. Construction of these tables is accomplished through the selection of a set of integers in the range provided from the initialization, and scaling these to provide a probability range from 0 to 1. Equation (3) is then employed to compute values of A/σ and store these at array locations corresponding to the integers from which their computation was scaled. Final recovery of the I or Q channel

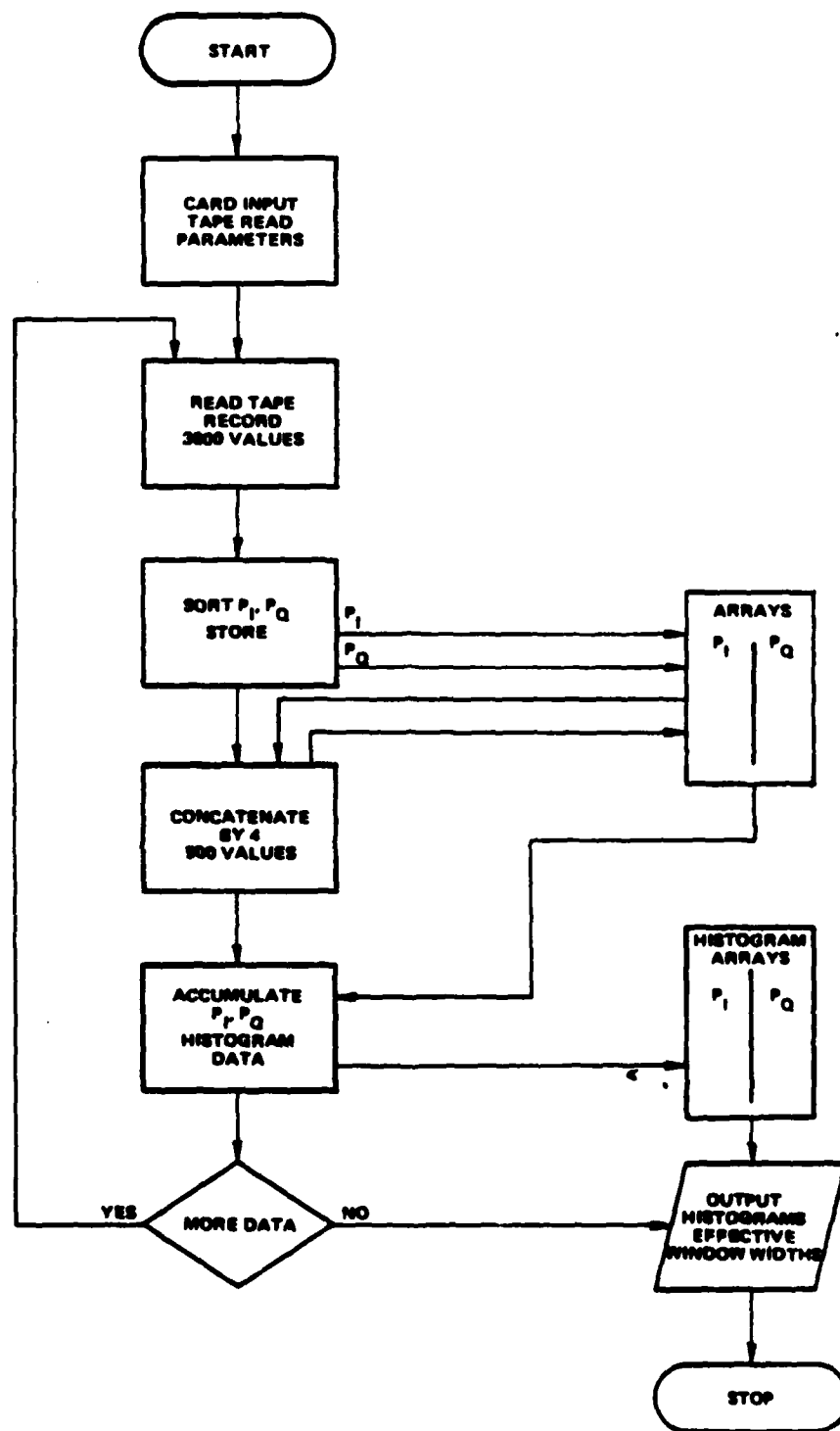


Figure D-5. Flowchart for Determination of Histograms to Set Uplink Data Processing Parameters

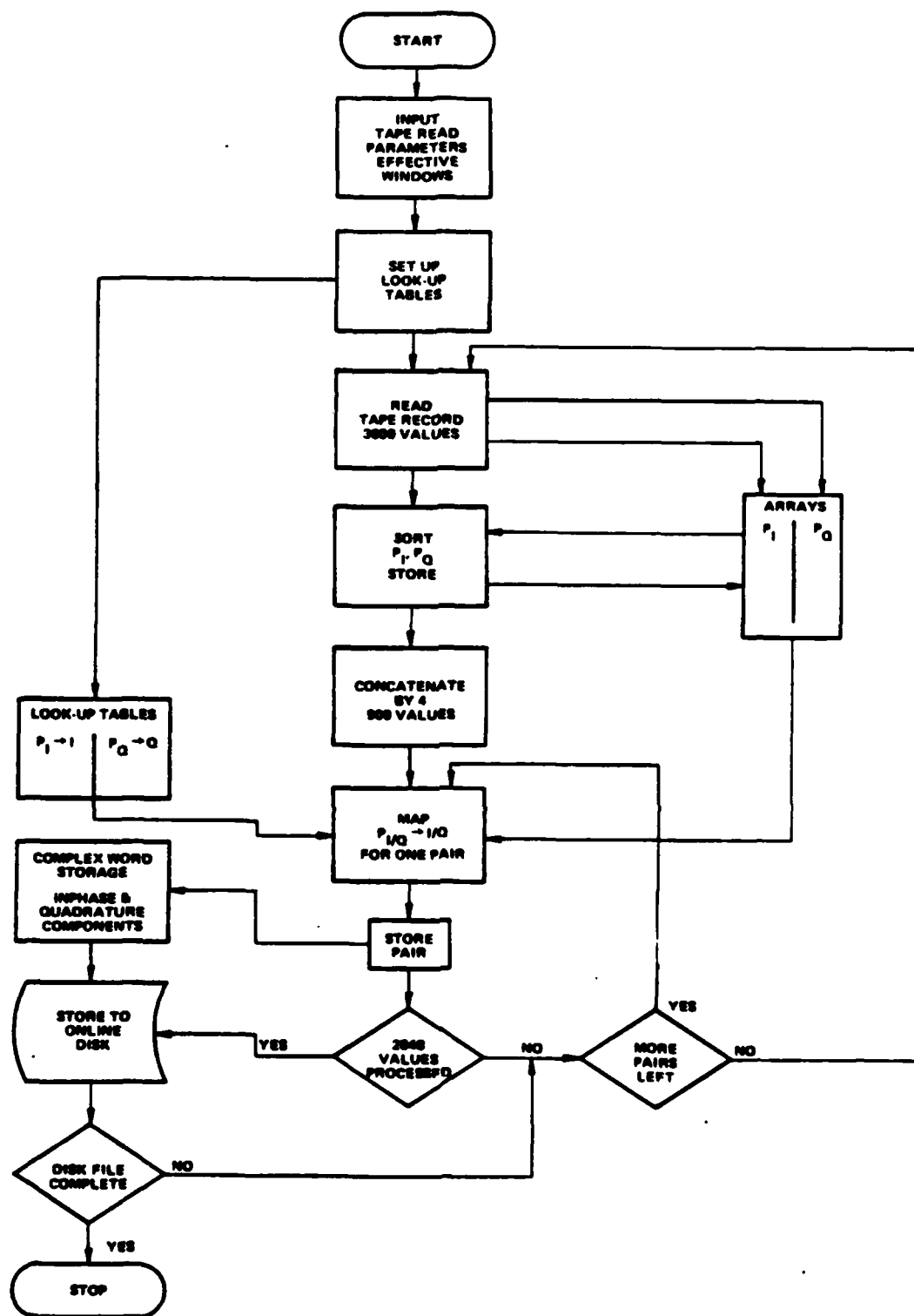


Figure D-6. Flowchart for Uplink Data Signal Recovery Software

amplitude-to-noise variance ratio is effected by selecting that value in the look-up array with subscript identical to the integral (0-1024) probability estimate. Figure D-7 shows an example of one such look-up table. These steps are followed for both I and Q signals until a 2048 point record is generated. Upon completion of the record it is stored to on-line disk. The creation of the 2048 point disk file is repeated until an entire pass has been reconstructed. Program execution is then halted.

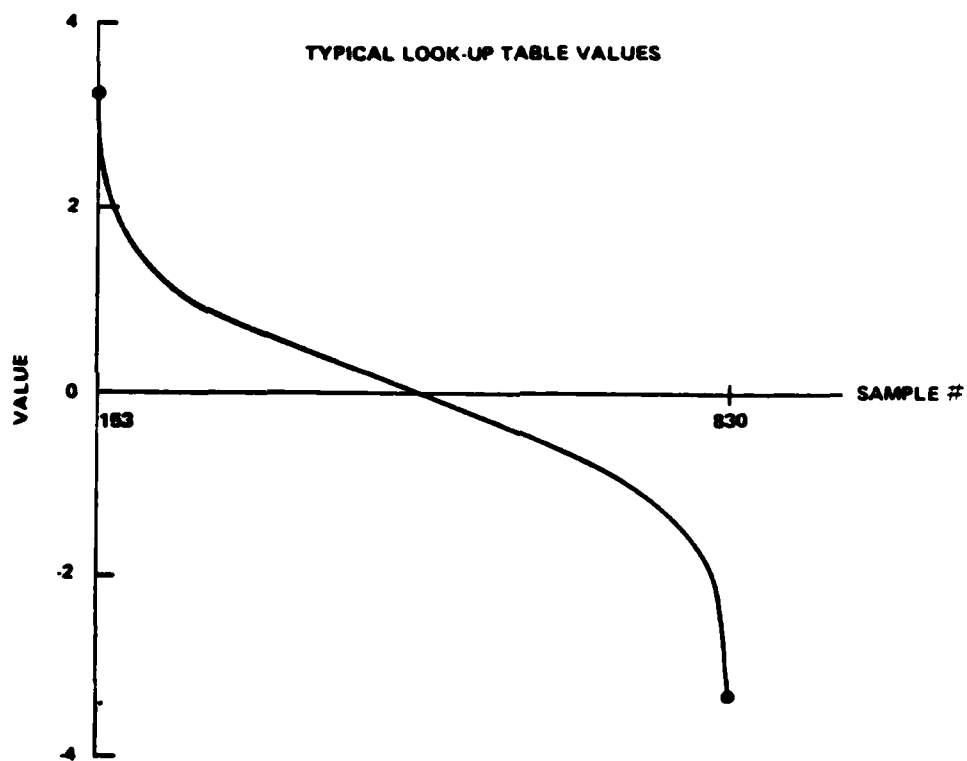


Figure D-7. Plot of a Typical Look-up Table Value Versus Sample Value

APPENDIX E

BACK-PROPAGATION PROCESSING

The local effect of a plasma on an RF wave propagating through it is to increase the signal phase velocity. The cumulative effect is a wavefront phase shift proportional to the ray path integrated electron content. Free space propagation of signal wavefronts away from the plasma irregularities introduces diffraction effects that are manifested as amplitude scintillations and an increase in the high frequency spectral content of the wavefront phase fluctuations. The purpose of back-propagation is to process out these diffraction effects in order to obtain a measurement of integrated electron content fluctuations.

The processed tone data is used as input to a two-dimensional free space propagation code allowing calculation of the field at various distances away from the ground. Of the numerous resulting fields, the field whose normalized rms power fluctuations (S_4 scintillation index) are least, is chosen as the field at the striated ion cloud. In this manner, the back-propagation processing determines an approximation to the distance to the cloud and an approximation to the integrated electron content fluctuation of the ion cloud.

Free space propagation is performed using angular spectrum techniques. The propagation processing of signal data can be viewed as a dispersive filtering. The Fourier transform of the received data (or angular spectrum) is calculated and this filtering is performed in the transform domain. (Because of the properties of solutions to the Helmholtz equation, the Fourier transform of the field is closely related to the complex angular spectrum; hence, the naming of the technique.) This transform is multiplied by a filter function with constant amplitude and nonlinear phase dependence. The phase shift in cycles ϕ , as a function of the frequency parameter, f , of the transform is given by

$$\phi(f) = z(1 - (f\lambda)^2)^{1/2}/\lambda$$

where λ is the free space signal wavelength and z is the desired propagation distance. The inverse transform produces the desired field at the distance z .

In the above equation for the phase shift of the dispersive propagation filter, the transform parameter is implicitly assumed to be given in terms of a spatial frequency. The transformation between the time dependence of the data and the spatial dependence required for the propagation filtering is made by assuming a constant speed across the cloud fading. While using a speed close to the exact speed on each pass was possible, it was found practical to assume a nominal speed at 200 m/s in all of the processing. Analysis has showed that a difference between the assumed and actual speed in making this time-to-space transformation has imperceptible effect on the phase of the field at the back-propagation distance which minimizes the scintillation index. It was found that the sole effect of the differences in assumed and actual speeds is a change in the back-propagation distance that minimizes the scintillation index. This change was found to be systematic; the ratio of actual back-propagation distance to that resulting from an assumed speed. The validity of these findings were upheld by the results of comparisons between back-propagations of STRESS data using the assumed 200 m/s velocity and those using actual velocities. For each pass the actual distance can later be computed using the appropriate scaling with the actual pass velocity. The actual distances are physically meaningful and represent an estimate of the approximate slant range to the region of cloud effects.

The back-propagation processing of the PLACES data was performed in two steps. The first step was to find the back-propagation distance that minimized the scintillation index. Positive and negative distances were searched to find an approximate minimum with a 10 kilometer resolution. A search with 1 kilometer resolution around the approximate minimum determined the actual minimum. The second step was to create a data file of the field back-propagated to the determined distance for subsequent plotting and processing. The software algorithm for this second step is illustrated in Figure E-1; the first step has a similar flowchart with an added facility to determine, in an iterative manner, the distance with minimum scintillation index (S_4).

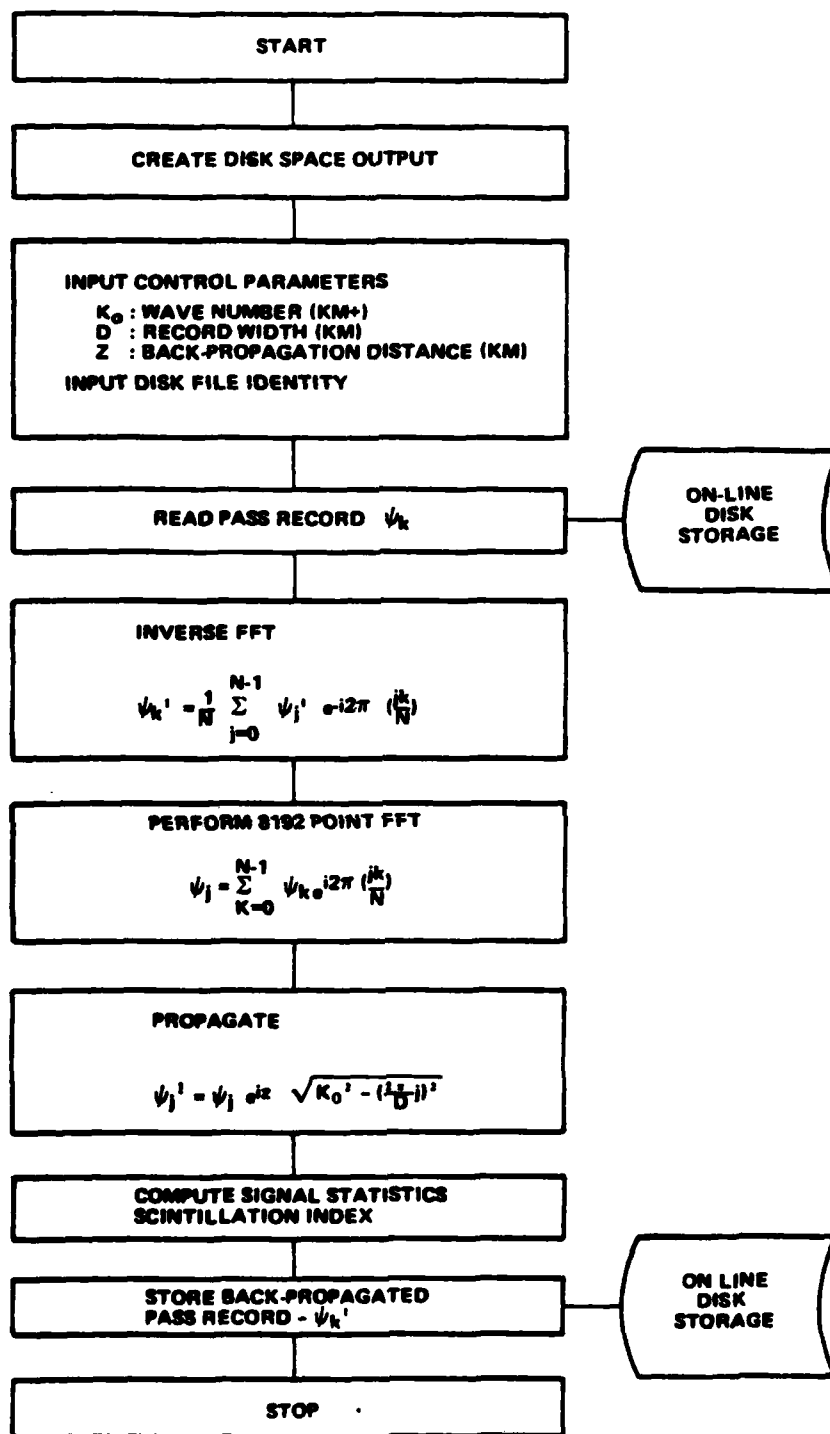


Figure E-1. Flowchart of PATS Code for Free-Space Propagation

The effects of noise and distortion manifested themselves in the back-propagation processing. The predominant sources of these signal degradations are apparently additive thermal noise, phase noise, and, for the uplink data, imperfect uplink signal estimation.

The effects of additive noise on the back-propagation is to cause amplitude fluctuations in the field over and above the diffraction induced effects. As a result, even if diffraction effects are fully removed by the processing, the scintillation index will not be zero (it will, however, be minimum). The power spectrum of the phase of the field at this back-propagation distance will have a noise floor with power spectrum identical to the spectrum of the non-propagated noise. This noise floor thus reflects the filtering performed in the data processing. Indeed, the 15 Hz cutoff of the downlink data filter and the 12.5 Hz cutoff of the uplink processing are both readily apparent in the power spectra of the back-propagated phases.

In performing back-propagation of both uplink and downlink data, it was noted in weak fading passes that the scintillation index increased significantly (.1) over a small distance (± 1 kilometer) from the initial distance. This rapid increase in the scintillation index is attributable to high frequency (1-20 Hz) components of phase noise. Previous analysis has shown that low frequency (less than 1 Hz) phase noise has negligible effect on the back-propagated phase. The high frequency phase noise discovered in the data processing subsequent to the STRESS experiment is observed to cause effects identical to the additive thermal noise effects once the field has been propagated more than 10 kilometers. This phase noise raised the expected power spectral density resolution limit approximately 8 to 12 dB radians squared per Hz in the propagated field phase power spectrum. The source of this noise is uncertain. It does appear to be stronger from LES-8 than LES-9, suggesting that the satellite UHF or K-band synthesizers may be its source.

As during STRESS in back-propagating uplink data, the scintillation index dependence with distance was occasionally observed to have high frequency oscillation superimposed upon it. The oscillations have magnitudes as large as .03 and periods typically of 4 kilometers. The regularity of the oscillations when observed imply a coherent noise or distortion. In some cases, readjustment of the uplink data estimation gain compression curves ameliorates the problem, suggesting distortion of the uplink signal as the likely possible source. The effects of this signal distortion on the back-propagated phase are surmised to be minor.

S_4 values for the uplink data at the ground differ significantly from the unity value more so than would be expected if the fading were truly Rayleigh distributed. The deviation from unity can be attributed to one important source of error and to one less important source. The source of primary importance is the signal focus compression effects of the uplink tone system. While an attempt was made to remove these effects through processing, some compression often remains. Note that while the fading distribution may be close to Rayleigh in the 5 dB through 20 dB fade levels, significant processing related compression may occur in the 0 dB and above focus region. The S_4 index (normalized rms power fluctuation) is sensitive more to the focus regime than to the fade regime. A significant deviation from unity for fading situations close to Rayleigh distributed is thus, understandable, suggesting perhaps that the S_4 index is not a parameter of prime interest.

The less important source of error is the effect of non-fading intervals in the interval used to determine the S_4 parameter causing the S_4 to assume lower values. These intervals typically occur at the beginnings and endings of the pass. This effect can be circumvented in the majority of the passes by restricting the sampling interval used to determine S_4 to a central region of the fading data from the pass.

It should be noted that the phase at the ground is not proportional to the integrated content of the cloud; diffraction effects alter its form somewhat, and, the power spectrum of the phase at the ground has a shallower slope than the power spectrum of the phase at the cloud.

APPENDIX F

AIRCRAFT EXPERIMENT LINK CALCULATIONS

F-1 INTRODUCTION.

The aircraft link calculations are provided in this section for reference. Link calculations are provided for the uplink and downlink tones and for the K-band doppler reference signal.

F-2 DOWNLINK TONE.

The link calculations for the downlink UHF tone is provided in Table F-1. The predicted received carrier power-to-noise power density ratio (C/KT) is computed to be 46.1 dB-Hz. The value measured (Reference 2) during the STRESS experiment was 46 to 47 dB and will vary somewhat from pass-to-pass depending on the aircraft antenna coupling to the satellite. There was no apparent degradation over the 3 years since STRESS in the overall signal quality. A 2 or 3 dB SNR improvement appears to have been realized, possibly through a combination of more favorable geometry and hardware/antenna changes on the aircraft. A quick look at the downlink C/KT indicate approximately 50 to 51 dB-Hz during PLACES.

The real time fading indicator on the aircraft used the log output of an HP 3890 wave analyzer. The detection bandwidth is approximately 100 Hz providing a signal-to-noise ratio of 26 dB on the real time strip-chart display.

The downlink tone ground processing software at the CCF at Eglin AFB and ESL used a 15 Hz bandwidth, resulting in approximately 34 dB SNR on the CCF real time displays in the figures presented in this report.

Table F-1. Link Calculation Downlink Tone to Aircraft

XMTR Power	37.8 dBm	6W
Antenna Gain	9 dB	
EIRP	46.8 dBm	
Space Loss	171.9 dB	@ 245 MHz, E1=35° R=38,193 km SL=171.6 dB, E1=50° R=37,091
Polarization Loss	0.4 dB	3 dB to 3 dB
Receiver Gain	3 dB	
Received Power	-122.5 dBm	
Noise Density	-168.6 dBm/Hz	T=1000°
C/kT	46.1 dB-Hz	
Noise Power	-148.6 dBm	100 Hz BW - real time a/c indicator
a/c Strip Chart SNR	26.1 dB	Real time on a/c
Noise Power	-156.8 dBm	15 Hz BW Real time @ CCF
SNR	34.2 dB	CCF displays

F-3 UPLINK TONE.

Table F-2 provides a link calculation for the uplink tone. The uplink power level is set to approximately 0 dB SNR at the satellite. The corresponding effective C/KT is approximately 42.8 dB-Hz. During the STRESS experiment the uplink power was set by noting when the satellite output signal power began to compress as the uplink power was increased. The uplink power was then backed off about 8 dB. This would have resulted in a C/KT of approximately 38 dB-Hz at the satellite. A value of around 39 dB-Hz was observed in the ESTHER data. The same procedure was used during PLACES.

The real time fading indicators use 256 bit averaging windows on the I and Q data, which corresponds to approximately a 360 Hz bandwidth or 17.2 dB SNR. Post processing the data in 1024 bit windows results in approximately 23 dB SNR. These outputs can be averaged further as necessary.

F-4 K-BAND DOPPLER REFERENCE.

Table F-3 gives an approximate link calculation for the K-band downlink to the 662 aircraft. This calculation indicates there is approximately 4 dB of margin at the 100 Kbps data rate. A dB or so of implementation loss in the modem along with possible satellite output power degradation over time and potential antenna pointing errors make this link somewhat marginal. The tracking loop SNR is, however, high and there is generally ample margin to loss of phase lock (and thus loss of the downlink tone doppler correction).

Table F-2. Link Calculation Uplink Tone Aircraft-to-Satellite

XMTR Power	44.4 dBm	(27.5W) adj. for 0 dB SNR (100W max)
Antenna Gain	2 dB _i	<u>+2</u> dB
EIRP	46.4 dBm	
Space Loss	175.9 dB	@ 388.4 MHz, 35°E1, R=38,193 km
Polarization Loss	0.5 dB	<u>+0.5</u> dB 5 dB to 3 dB
Receiver Gain	10 dB _i	<u>+1</u> dB
Incident Power	-120.0 dB	<u>+2.3</u> dB
Noise Density	-167.8 dBm/Hz	
C/kT	47.8 dB-Hz	
Noise Power	-120 dBm	<u>+1</u> dB in 60 kHz
SNR	0 dB	<u>+2.5</u> dB at input to limiter
SNR _{AL/samp}	-5 dB	Simulation results (after limiter and Sampler)
C/kT _{AL/samp}	42.8 dB	
SNR	17.2 dB	in 256 bit window (~350 Hz BW) real time
SNR	23.2 dB	in 1024 bit window (~90 Hz BW) post process

Table F-3. Approximate K-band Downlink Calculation

XMTR Power	26.2 dBm	(.4 watt)
Antenna Gain	<u>42.6 dBi</u>	(3' dish)
EIRP	68.8 dBm	
Space Loss	216.0 dB	@ 38 GHz
Receiver Ant. Gain	<u>47.0 dBi</u>	
Received Power	-100.2 dBm	
Noise Power Density	<u>-164.5 dBm/Hz</u>	9.5 dB noise figure
C/kT	64.3 dB-Hz	
Loop SNR	50.3 dB	25 Hz BW
E_b/N_0 Required	10.3 dB	10^{-5} BER DPSK
R_D	50 dB	100 Kbps
C/kT Required	60.3 dB/Hz	
Margin	4.0 dB	

DISTRIBUTION LIST

DEPARTMENT OF DEFENSE

Defense Nuclear Agency

ATTN: NAFO
ATTN: RAAE, P. Lunn
ATTN: STNA
ATTN: RAEE
ATTN: NATD
3 cy ATTN: RAAE
4 cy ATTN: TITL

Defense Technical Information Center

12 cy ATTN: DO

Field Command

Det 1, Defense Nuclear Agency
Lawrence Livermore Lab
ATTN: FC-1

Field Command

Defense Nuclear Agency
ATTN: FCPR

DEPARTMENT OF THE ARMY

BMD Advanced Technology Center

ATTN: ATC-R, W. Dickinson
ATTN: ATC-O, W. Davies
ATTN: ATC-T, M. Capps
ATTN: ATC-R, D. Russ

BMD Systems Command

ATTN: BMDSC-HLE, R. Webb
2 cy ATTN: BMDSC-HW

US Army Nuclear & Chemical Agency

ATTN: Library

US Army Satellite Comm Agency

ATTN: Document Control

DEPARTMENT OF THE NAVY

Naval Ocean Systems Center

ATTN: Code 532
ATTN: Code 5323, J. Ferguson
ATTN: Code 5322, M. Paulson

Naval Research Laboratory

ATTN: Code 4780
ATTN: Code 4780, S. Ossakow
ATTN: Code 4187
ATTN: Code 7500, B. Wald
ATTN: Code 4700
ATTN: Code 4720, J. Davis
ATTN: Code 7950, J. Goodman
ATTN: Code 6700

Theater Nuclear Warfare Proj Office

ATTN: PM-23, D. Smith

DEPARTMENT OF THE AIR FORCE

Air Force Geophysics Laboratory

ATTN: OPR, H. Gardiner
ATTN: OPR-1
ATTN: LKB, K. Champion
ATTN: CA, A. Stair
ATTN: PHY, J. Buchau
ATTN: R. Babcock
ATTN: R. O'Neil

Air Force Technical Applications Ctr

ATTN: TN

Air Force Weapons Laboratory

ATTN: SUL
ATTN: NTYC
ATTN: NTN

Air Force Wright Aeronautical Lab

ATTN: A. Johnson
ATTN: W. Hunt

Air University Library

ATTN: AUL-LSE

DEPARTMENT OF ENERGY CONTRACTORS

Los Alamos National Laboratory

ATTN: MS670, J. Hopkins
ATTN: P. Keaton
ATTN: MS664, J. Zinn
ATTN: T. Kunkle, ESS-5
ATTN: R. Jeffries
ATTN: D. Simons
ATTN: J. Wolcott

DEPARTMENT OF DEFENSE CONTRACTORS

Berkeley Research Associates, Inc

ATTN: J. Workman
ATTN: C. Prettie
ATTN: S. Brecht

Charles Stark Draper Lab, Inc

ATTN: D. Cox
ATTN: J. Gilmore
ATTN: A. Tetewski

ESL, Inc

4 cy ATTN: J. Marshall
4 cy ATTN: J. Lehman
4 cy ATTN: W. Solbrig

JAYCOR

ATTN: J. Sperling

Kaman Tempo

ATTN: DASIAC

DEPARTMENT OF DEFENSE CONTRACTORS (Continued)

Kaman Tempo
ATTN: DASIAC

M.I.T. Lincoln Lab
ATTN: D. Towle

Mission Research Corp
ATTN: R. Bogusch
ATTN: F. Fajen
ATTN: R. Hendrick
ATTN: C. Lauer
ATTN: S. Gutsche
ATTN: D. Knepp
ATTN: R. Bigono
ATTN: R. Kilb
ATTN: Tech Library
ATTN: F. Guigliano
ATTN: G. McCartor

Pacific-Sierra Research Corp
ATTN: H. Brode, Chairman SAGE

Physical Dynamics, Inc
ATTN: E. Fremouw

R&D Associates
ATTN: B. Yoon

Rand Corp
ATTN: B. Bennett

DEPARTMENT OF DEFENSE CONTRACTORS (Continued)

R&D Associates
ATTN: W. Wright
ATTN: W. Karzas
ATTN: R. Turco
ATTN: C. Greifinger
ATTN: M. Gantsweg
ATTN: F. Gilmore
ATTN: H. Ory
ATTN: P. Haas

Rand Corp
ATTN: E. Bedrozian
ATTN: C. Crain
ATTN: P. Davis

SRI International
ATTN: R. Tsunoda
ATTN: J. Vickrey
ATTN: W. Chesnut
ATTN: R. Leadabrand
ATTN: R. Livingston
ATTN: D. McDaniels
ATTN: M. Baron
ATTN: G. Price
ATTN: D. Neilson
ATTN: A. Burns
ATTN: W. Jaye
ATTN: J. Petrickes
ATTN: C. Rino
ATTN: V. Gonzales
ATTN: G. Smith